Notes on Numerical Fluid Mechanics
and Multidisciplinary Design 147

Marianna Braza
Kerry Hourigan
Michael Triantafyllou *Editors*

# Advances in Critical Flow Dynamics Involving Moving/Deformable Structures with Design Applications

## Proceedings of the IUTAM Symposium on Critical Flow Dynamics Involving Moving/Deformable Structures with Design Applications, June 18–22, 2018, Santorini, Greece

Springer

# Notes on Numerical Fluid Mechanics and Multidisciplinary Design

Volume 147

Notes on Numerical Fluid Mechanics and Multidisciplinary Design publishes state-of-art methods (including high performance methods) for numerical fluid mechanics, numerical simulation and multidisciplinary design optimization. The series includes proceedings of specialized conferences and workshops, as well as relevant project reports and monographs.

More information about this series at http://www.springer.com/series/4629

Marianna Braza · Kerry Hourigan ·
Michael Triantafyllou
Editors

# Advances in Critical Flow Dynamics Involving Moving/Deformable Structures with Design Applications

Proceedings of the IUTAM Symposium on Critical Flow Dynamics Involving Moving/Deformable Structures with Design Applications, June 18–22, 2018, Santorini, Greece

Springer

*Editors*
Marianna Braza
Institut de Mécanique des Fluides de
Toulouse, UMR 5502-CNRS-INPT-UPS
Toulouse, France

Kerry Hourigan
Department of Mechanical
and Aerospace Engineering
Monash University
Clayton, VIC, Australia

Michael Triantafyllou
Department of Mechanical Engineering
Massachusetts Institute of Technology
Cambridge, MA, USA

ISSN 1612-2909 ISSN 1860-0824 (electronic)
Notes on Numerical Fluid Mechanics and Multidisciplinary Design
ISBN 978-3-030-55593-1 ISBN 978-3-030-55594-8 (eBook)
https://doi.org/10.1007/978-3-030-55594-8



This Springer imprint is published by the registered company Springer Nature Switzerland AG
The registered company address is: Gewerbestrasse 11, 6330 Cham, Switzerland

# Preface

## Critical Flow Dynamics Involving Moving/Deformable Structures with Design Applications

Co-chaired by Marianna Braza, Kerry Hourigan and Michael Triantafyllou

Progress in understanding turbulence and flow control is enabling scientists to improve aerodynamic/hydrodynamic performance by reducing drag, increasing lift or thrust and reducing noise under critical conditions that may result in massive separation, strong vortical dynamics, amplification of harmful instabilities (flutter and buffet) and flow-induced vibrations. These topics have been among the principal objectives of the IUTAM Symposium held in Santorini Island, Greece, from June 18 to 22, 2018.

Theory together with large-scale simulations and experiments has shown new features of turbulent flow in the boundary layer over bodies and in thin shear layers immediately downstream of separation. A new insight was provided in the structure of turbulent–non-turbulent (TNT) and turbulent–turbulent (TT) interfaces regarding these critical phenomena. Spontaneous and artificially generated fluctuations were proved able to affect the turbulent flow and these interfaces, and to modify the vortex dynamics leading to reduction of noise and drag. Electromechanical actuation and energy conversion were shown to be highly effective for the analysis and optimization of the fluid–structure interaction, and a variety of physical mechanisms were investigated thanks to the use of novel smart actuators to affect morphing.

This symposium investigated a combination of new insights into turbulent flow interacting with actively deformable structures, leading to new ways of adapting and controlling the body shape and vibrations, to respond to these critical conditions.

Furthermore, the symposium topics included "smart," bio-inspired methods together with new dynamically controlled aerodynamic and hydrodynamic shapes in order to attenuate the harmful effects and to increase performance and safety, by considering also critical conditions like gusts.

Progress in these areas is receiving a great deal of impetus from international research groups, especially stimulated by major contracts related to this topic, involving key multinational industrial companies particularly in aeronautics and naval architecture, stimulated by targeted government programs. This symposium succeeded at bringing together the leading international groups of researchers working in the scientific communities.

The present IUTAM Symposium included advanced theoretical approaches, and experimental and simulation methods showing in synergy how smart designs lead to considerable benefits compared to conventional ways. The symposium has drawn together the scientific advances in the state of the art and established important outlooks of research concerning these topics, according to the following sessions:

- Theoretical aspects of fluid–structure interaction (FSI) involving separation
- Instability and transition studies related to critical phenomena in FSI
- Intelligent materials, morphing, actuation, energy conversion
- Bio-inspired methods for smart wing design
- Experimental techniques for the dynamics of separation in VIV, MIV, TIV
- Compressibility effects related to unsteady separation in FSI
- Direct numerical simulation of unsteady separated flows
- Turbulence modeling approaches involving FSI: advanced statistical (URANS) and hybrid (URANS-LES)
- Coupling strategies CFD-SM
- Dynamically controlled aerodynamic and hydrodynamic shapes and vibrations for improved design.

This symposium brought together renowned scientists in the above fields and contributed to advancing the physical comprehension, simulation and modeling methods regarding critical flow dynamics around moving/deformable structures.

A general outcome was that the scientific communities learned much from one another, and this meeting brought new research ideas and new concepts for smart designs.

The present volume has been edited by:

Toulouse, France — Marianna Braza
marianna.braza@imft.fr

Clayton, Australia — Kerry Hourigan
kerry.hourigan@monash.edu

Cambridge, USA — Michael Triantafyllou
mistetri@mit.edu


DESOL
SPA HOTEL

# Contents

# Flow Induced Vibrations

# Alteration of the Spanwise Structure of the Turbulent Flow Past a Cylinder Subjected to Vortex-Induced Vibrations


**Simon Gsell, Rémi Bourguet, and Marianna Braza**

**Abstract** The three-dimensional structure of the flow downstream of a circular cylinder, either fixed or subjected to vortex-induced vibrations, is investigated by means of numerical simulation, at Reynolds number 3900, based on the cylinder diameter and current velocity. The flow exhibits pronounced fluctuations distributed along the span in all studied cases. Qualitatively, it is characterized by spanwise undulations of the shear layers separating from the body and the development of vortices elongated in the plane normal to its axis (planar vortices). A dominant spanwise wavelength is identified; it tends to decrease as a function of the streamwise distance in the shear layers and then slowly increases further in the wake. The spanwise structure of the flow is differently altered in these two regions, once the cylinder vibrates. In the shear-layer region, an amplification of vorticity spanwise fluctuations is accompanied by a reduction of the spanwise wavelength; it is found to decrease as a function of the instantaneous Reynolds number based on the instantaneous flow velocity seen by the moving body, following the global trend of the wavelength versus Reynolds number previously reported for fixed cylinders. In the wake region, the flow spanwise structure is essentially unaltered compared to the fixed body case, in spite of the major distortions of the streamwise and cross-flow length scales.

Keyword Vortex-induced vibrations · Turbulent wake · Direct numerical simulation

S. Gsell (✉)
Aix Marseille Univ, CNRS, Centrale Marseille, M2P2 Marseille, France
e-mail: simon.gsell@univ-amu.fr

R. Bourguet · M. Braza
Institut de Mécanique des Fluides de Toulouse, IMFT, Université de Toulouse, CNRS, Toulouse, France



M. Braza et al. (eds.), *Advances in Critical Flow Dynamics Involving Moving/Deformable Structures with Design Applications*, Notes on Numerical Fluid Mechanics and Multidisciplinary Design 147,
https://doi.org/10.1007/978-3-030-55594-8_2

## 1 Introduction

The flow patterns developing downstream of slender bodies with bluff cross-section have been the object of intense research in the past decades and the circular cylinder wake has often been used as canonical configuration in this context [1]. Particular attention was paid to the vortex patterns emerging in the plane perpendicular to the cylinder axis, including in the case where the body oscillates in the current [2]. The present study focuses on the structures of the flow occurring in the spanwise direction.

In the fixed cylinder case, the three-dimensional transition of the flow occurs through a spanwise undulation of the primary wake vortices. Depending on the Reynolds number $Re$, based on the cylinder diameter and oncoming flow velocity, different regimes associated to distinct spanwise wavelengths may be observed. A wavelength of the order of one body diameter (i.e. the typical wavelength of a regime called 'mode B' [3]) persists over a wide range of $Re$, as reported by Mansy et al. [4] ($Re \in [300, 2200]$), Wu et al. [5, 6] ($Re \in [200, 1800]$), Lin et al. [7] ($Re = 10{,}000$), Chyu and Rockwell [8] ($Re = 10{,}000$) and Hayakawa and Hussain [9] ($Re = 13{,}000$). The small-scale spanwise vortices, that appear in the detached shear layers for $Re > 1000$ approximately [10–16], also undergo a three-dimensional transition, as pointed out by Wei and Smith [17] and Rai [16]. Prior works suggested that this flow region is associated with a spanwise wavelength (of the order of 0.5 body diameters) lower than that observed further in the wake [4, 8, 18].

The streamwise evolution of these spanwise patterns and their possible alteration when the body oscillates are investigated here on the basis of numerical simulation results. The Reynolds number is set to 3900, as often selected in prior works as a typical case of the early turbulent regime [19]. The flow past a fixed cylinder is considered first, as a reference configuration. The spanwise patterns developing once the cylinder oscillates are investigated in conditions naturally arising for a bluff body free to move in the current, by considering typical cases of vortex-induced vibrations (VIV) [20] issued from a prior parametrical study [21] and covering wide ranges of oscillation amplitudes and frequencies. A detailed analysis has been reported in a recent paper [22]; the main observations are presented in this proceeding. The methodology employed in this study is briefly described in Sect. 2 and the principal results are presented in Sect. 3.

## 2 Method

The physical system is analogous to that described in [21]. A rigid circular cylinder is immersed in a current. The Reynolds number, based on the cylinder diameter and oncoming flow velocity is set to 3900. In the following, all flow quantities are made non-dimensional by the cylinder diameter, flow velocity and fluid density. In oscillating body cases, the cylinder is mounted on an elastic support allowing displacements in the in-line and cross-flow directions, i.e. the directions parallel and

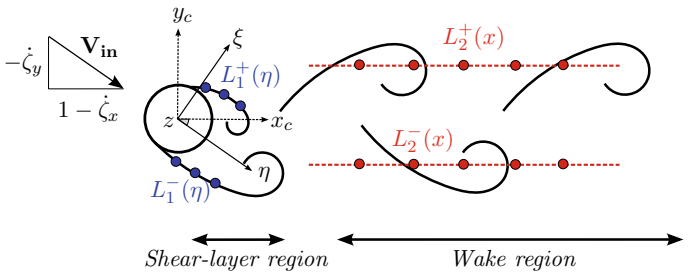


**Fig. 1** Schematic view of the spanwise lines $L_1$ and $L_2$ along which flow quantities are analyzed. Reproduced from Gsell et al. [22]

normal to the oncoming flow. The structural damping of the oscillator is set to zero. Its stiffness controls the structural natural frequency, which is varied through the reduced velocity $U^*$, defined as the inverse of the non-dimensional natural frequency. Three values of the reduced velocity are selected in the present study, $U^* \in \{3, 6, 9\}$. These values correspond to distinct VIV regimes, generally referred to as initial, upper and lower branches [21, 23], and allow to cover wide ranges of oscillation amplitudes and frequencies.

The behavior of the coupled flow-structure system is predicted by direct numerical simulation of the three-dimensional Navier-Stokes equations. The computations are performed with the finite-volume code Numeca Fine/Open (www.numeca.com). The Navier-Stokes equations are expressed in the cylinder frame which avoids any grid deformation. The frame motion is taken into account by adding inertial terms in the Navier-Stokes equations [21, 24]. The spanwise length of the body is set to 10 diameters. The numerical domain extends from −30 diameters to 90 diameters in the in-line direction, and from −30 diameters to 30 diameters in the cross-flow direction. The numerical mesh is composed of $45 \times 10^6$ cells. Details of the numerical method, as well as convergence and validation results have been reported in previous papers [21, 22].

A quantitative analysis of the spanwise wavelengths emerging in the flow is performed by monitoring the cross-flow vorticity fluctuations along spanwise lines placed in the wake, as illustrated in Fig. 1. Two frames attached to the body center are represented: the frame $(x_c, y_c, z)$, in translation with respect to the laboratory frame $(x, y, z)$, and the frame $(\eta, \xi, z)$, where the $\eta$ axis is parallel to the instantaneous oncoming flow $\boldsymbol{V_{in}}$, defined as $\boldsymbol{V_{in}} = [1 - \dot{\zeta}_x, -\dot{\zeta}_y, 0]$ in the laboratory frame, where $\dot{\zeta}_x$ and $\dot{\zeta}_y$ are the non-dimensional body velocities in the $x$ (in-line) and $y$ (cross-flow) directions. Two flow regions are considered, the shear-layer region (lines $L_1$) and the wake region (lines $L_2$). Lines $L_1$ are placed in the detached shear layers, which are automatically tracked during post-processing. These lines may therefore move in the laboratory frame, in particular when the body oscillates. On the other hand, lines $L_2$ in the wake region are fixed in the laboratory frame; their cross-flow positions correspond to regions of maximum and minimum time-averaged spanwise vorticity,

i.e. regions crossed by the positive and negative wake vortices. Details regarding the definitions of the monitoring lines and data processing techniques are reported in [22].

## 3 Results

A global visualization of the three-dimensional flow is presented in Fig. 2. In the four studied cases, an instantaneous iso-surface of the $Q$-criterion [25] is colored by iso-contours of the cross-flow vorticity ($\omega_y$). The $Q$-criterion highlights a number of small, elongated vortices, mainly aligned in the $(x, y)$ plane. These vortices have often been described as streamwise vortices in prior studies. However, due to their alignment in the $(x, y)$ plane and their oblique orientation in this plane, the term planar vortices is preferred in the following to designate these flow structures. The planar vortices are observed both in the fixed and oscillating body cases. While body motion is generally expected to decrease the three-dimensionality of the flow, the

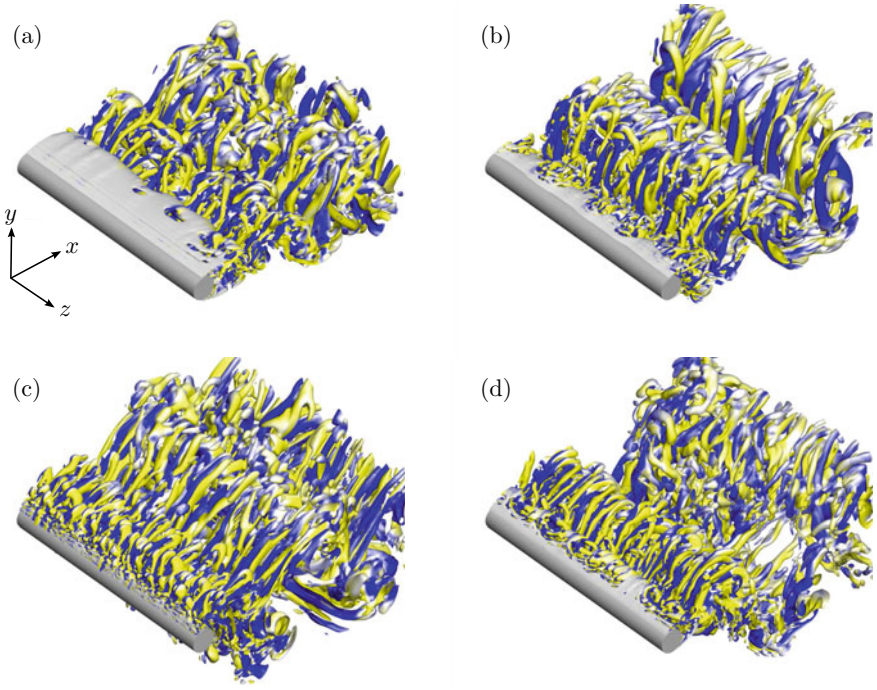


**Fig. 2** Global visualization of the three-dimensional flow: instantaneous iso-surface of the $Q$-criterion ($Q = 0.1$) colored by iso-contours of the cross-flow vorticity ($\omega_y \in [-1, 1]$) in the (**a**) fixed and (**b**–**d**) oscillating body cases, for (**b**) $U^* = 3$, (**c**) $U^* = 6$ and (**d**) $U^* = 9$. Reproduced from Gsell et al. [22]

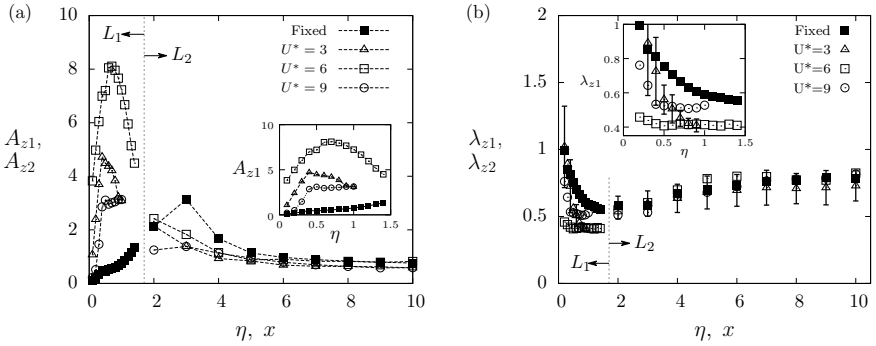


**Fig. 3** Quantitative analysis of the spanwise fluctuations of the cross-flow vorticity: streamwise evolution of the typical fluctuation **a** amplitudes and **b** wavelengths, in the fixed and oscillating body cases. In **b**, error bars indicate the typical time-variability of the wavelength for $U^* = 3$ (case of maximum variability). Reproduced from Gsell et al. [22]

'density' of planar vortices in the wake region and their magnitude do not significantly vary from one case to the other. In this region, the planar vortices tend to be more regularly aligned in the $(x, y)$ plane when the body oscillates. This suggests that body motion may be associated with an homogenization of the three-dimensional patterns. The planar vortices are generally observed over the entire body length. They define a typical spanwise length scale of the flow structure. Localized regions without planar vortices may however be encountered ($U^* = 9$, Fig. 2d), suggesting some possible amplitude modulations of the three-dimensional patterns.

A closer view of the three-dimensional flow near the body suggests that the formation of planar vortices tend to be enhanced when the cylinder oscillates. Moreover, shear-layer visualizations issued from the tracking procedure mentioned in Sect. 2 indicate a spanwise undulation of the shear layers; the undulation amplitudes are more pronounced in oscillating body cases [22].

A quantitative analysis of the spanwise structure of the flow is presented in Fig. 3, which shows the streamwise evolution of the typical amplitudes ($A_{z1}$ and $A_{z2}$) and wavelengths ($\lambda_{z1}$) and $\lambda_{z2}$) of spanwise fluctuations of the cross-flow vorticity, along lines $L_1$ and $L_2$ (see Fig. 1). In the fixed body case, a continuous increase of the spanwise fluctuation amplitude, as a function of the streamwise distance, is observed in the shear-layer region. The amplitude keeps increasing at the beginning of the wake region and a maximum value is reached close to $x = 3$, i.e. near the region of formation of the spanwise wake vortices. When the cylinder oscillates, the amplitude of the spanwise fluctuations is dramatically altered in the shear-layer region; it is generally larger in this case. For example, the peak amplitude in this region for $U^* = 6$ is roughly 6 times larger than in the fixed body case. The streamwise trend of $A_{z1}$ is comparable in the three oscillating body cases: a steep increase in the very near region (close to the area of spanwise vortex formation), followed by a much lower increase or a decrease. Some slight differences can be noted in the wake region for $x \in [2, 4]$. Further downstream ($x > 4$), the relatively constant amplitudes are

close in all studied cases, including in the fixed body case. The global upstream shift of the peak amplitude in the oscillating body cases, compared to the fixed body case, may be connected to an upstream shift of the spanwise vortex formation region. The evolution of $A_{z1}$ and $A_{z2}$ suggests that the alteration of the spanwise fluctuations, associated with body motion, is essentially localized close to the cylinder, in the shear-layer region.

The streamwise evolution of the spanwise wavelengths is depicted in Fig. 3b. In the fixed body case, the wavelength exhibits a continuous streamwise evolution. Distinct trends can be observed in the shear-layer and wake regions: the wavelength decreases as a function of the streamwise distance in the shear-layer region while it tends to increase with $x$ further downstream. A minimum wavelength close to 0.5 diameters is noted around $x = 2$. The overall trend of the wavelength is similar for oscillating body cases. The alteration of the wavelength associated with body motion is concentrated in the shear-layer region. In this region, lower minimum values of $\lambda_{z1}$, still close to 0.5 diameters, can be reached once the cylinder oscillates. It appears that the spanwise wavelength tends to decrease as a function of the instantaneous Reynolds number, i.e. based on the instantaneous flow velocity seen by the moving body: the global decreasing trend of the wavelength versus Reynolds number, previously reported for fixed cylinders [4, 6], persists in the oscillating body case when considering the instantaneous Reynolds number. The present results indicate that the spanwise wavelength scales with the momentum thickness of the boundary layer at separation. The momentum thickness is altered when the cylinder moves and it is found to decrease when the instantaneous Reynolds number increases, which may explain the above trend. This discussion is detailed in [22]. In contrast, there is no major modification of $\lambda_{z2}$ in the wake region. The variation of the wavelength between the different cases is generally smaller than its time variability for a given case (indicated by error bars for $U^* = 3$, which is the case of maximum variability). In addition, the variation of $\lambda_{z2}$ in this region is negligible compared to the variation of the $(x, y)$ typical length scales of the wake.

**Acknowledgements** This study is part of a Ph.D. work [26] funded by the French Ministry of Research. It was performed using HPC resources from GENCI (Grants No. x20152a7184 and No. c20162a7184).

## References

1. Williamson, C.H.K.: Vortex dynamics in the cylinder wake. Annu. Rev. Fluid Mech. **28**(1), 477–539 (1996)
2. Williamson, C.H.K., Roshko, A.: Vortex formation in the wake of an oscillating cylinder. J. Fluids Struct. **2**(4), 355–381 (1988)
3. Williamson, C.H.K.: The existence of two stages in the transition to three-dimensionality of a cylinder wake. Phys. Fluids **31**(11), 3165–3168 (1988)
4. Mansy, H., Yang, P.-M., Williams, D.R.: Quantitative measurements of three-dimensional structures in the wake of a circular cylinder. J. Fluid Mech. **270**, 277–296 (1994)

5. Wu, J., Sheridan, J., Soria, J., Welsh, M.C.: An experimental investigation of streamwise vortices in the wake of a bluff body. J. Fluids Struct. **8**(7), 621–635 (1994)
6. Wu, J., Sheridan, J., Hourigan, K., Soria, J.: Shear layer vortices and longitudinal vortices in the near wake of a circular cylinder. Exp. Thermal Fluid Sci. **12**(2), 169–174 (1996)
7. Lin, J.-C., Vorobieff, P., Rockwell, D.: Three-dimensional patterns of streamwise vorticity in the turbulent near-wake of a cylinder. J. Fluids Struct. **9**(2), 231–234 (1995)
8. Chyu, C., Rockwell, D.: Evolution of patterns of streamwise vorticity in the turbulent near wake of a circular cylinder. J. Fluid Mech. **320**, 117–137 (1996)
9. Hayakawa, M., Hussain, F.: Three-dimensionality of organized structures in a plane turbulent wake. J. Fluid Mech. **206**, 375–404 (1989)
10. Bloor, M.S.: The transition to turbulence in the wake of a circular cylinder. J. Fluid Mech. **19**(02), 290–304 (1964)
11. Braza, M., Chassaing, P., Minh, H.H.: Numerical study and physical analysis of the pressure and velocity fields in the near wake of a circular cylinder. J. Fluid Mech. **165**, 79–130 (1986)
12. Prasad, A., Williamson, C.H.K.: The instability of the shear layer separating from a bluff body. J. Fluid Mech. **333**, 375–402 (1997)
13. Kim, J., Choi, H.: Instability of the Shear Layer Separating from a Circular cylinderC Technical report, DTIC Document (2001)
14. Rajagopalan, S., Antonia, R.A.: Flow around a circular cylinder—structure of the near wake shear layer. Exp. Fluids **38**(4), 393–402 (2005)
15. Thompson, M.C., Hourigan, K.: The shear-layer instability of a circular cylinder wake. Phys. Fluids (1994-present), **17**(2), 021702 (2005)
16. Rai, M.M.: A computational investigation of the instability of the detached shear layers in the wake of a circular cylinder. J. Fluid Mech. **659**, 375–404 (2010)
17. Wei, T., Smith, C.R.: Secondary vortices in the wake of circular cylinders. J. Fluid Mech. **169**, 513–533 (1986)
18. Williamson, C.H.K., Wu, J., Sheridan, J.: Scaling of streamwise vortices in wakes. Phys. Fluids **7**(10), 2307–2309 (1995)
19. Beaudan, P., Moin, P.: Numerical experiments on the flow past a circular cylinder at sub-critical Reynolds number. Technical report, Department of Mechanical Engineering, Stanford University (1994)
20. Williamson, C.H.K., Govardhan, R.N.: Vortex-induced vibrations. Annu. Rev. Fluid Mech. **36**, 413–455 (2004)
21. Gsell, S., Bourguet, R., Braza, M.: Two-degree-of-freedom vortex-induced vibrations of a circular cylinder at Re = 3900. J. Fluids Struct. **67**, 156–172 (2016)
22. Gsell, S., Bourguet, R., Braza, M.: Three-dimensional flow past a fixed or freely vibrating cylinder in the early turbulent regime. Phys. Rev. Fluids **3**(1), 013902 (2018)
23. Jauvtis, N., Williamson, C.H.K.: The effect of two degrees of freedom on vortex-induced vibration at low mass and damping. J. Fluid Mech. **509**, 23–62 (2004)
24. Newman, D.J., Karniadakis, G.E.: A direct numerical simulation study of flow past a freely vibrating cable. J. Fluid Mech. **344**, 95–136 (1997)
25. Hunt, J.C.R., Wray, A.A., Moin, P.: Eddies, streams, and convergence zones in turbulent flows. Technical Report S88, Center for Turbulence Research (1988)
26. Gsell, S.: Vortex-induced vibrations of a rigid circular cylinder. Ph.D. thesis, University of Toulouse (2016)

# Vortex-Induced Vibration of Symmetric Airfoils Used in Vertical-Axis Wind Turbines


**Bridget Benner, Daniel Carlson, Banafsheh Seyed-Aghazadeh, and Yahya Modarres-Sadeghi**

**Abstract** The present work considers a flexibly-mounted NACA 0021 airfoil, allowed to oscillate in the crossflow direction to investigate its Vortex-Induced Vibration (VIV) response at different angles of attack. This airfoil is considered, since it is one of the airfoils used in Vertical-Axis Wind Turbine (VAWT) designs. Based on the experimental results of the current work, for smaller angles of attack, $\alpha$, no oscillation was observed. Oscillations started at $\alpha = 60°$, with a rather small amplitude and small lock-in range, and grew in peak amplitude and width of the lock-in range through $\alpha = 90°$, where VIV persisted for a wide range of reduced velocities: $1.7 < U^* < 12$ (where $U^* = U/f_nD$, is the reduced velocity, $U$ is the flow velocity, $f_n$ is the structure's natural frequency in otherwise still water, and $D$ is the chord length) and reached an amplitude of $A^* = 1.93$ (defined as $A^* = A/D$, where $A$ is the amplitude of oscillations and $D$ is the chord length of the airfoil). Flow visualizations were conducted using Bubble Image Velocimetry (BIV) technique, with image pairs captured by a high-speed camera. These flow visualizations indicated 2S vortex shedding patterns in the wake of the oscillating airfoils at a frequency equal to the oscillation frequency, confirming that the observed oscillations are VIV.

**Keywords** Vortex-induced vibration · Vertical-axis wind turbine

## 1 Introduction

Vortex-induced vibration (VIV) occurs in bluff bodies when the frequency of vortex shedding off the body locks-in with the structure's natural frequency. Once the oscillations start, the shedding frequency deviates from that predicted for a fixed bluff body using Strouhal law and matches the frequency of oscillations for a range of reduced

B. Benner · D. Carlson · Y. Modarres-Sadeghi (✉)
University of Massachusetts Amherst, Amherst, MA, USA
e-mail: modarres@engin.umass.edu

B. Seyed-Aghazadeh
Miami University, Oxford, OH, USA



M. Braza et al. (eds.), *Advances in Critical Flow Dynamics Involving Moving/Deformable Structures with Design Applications*, Notes on Numerical Fluid Mechanics and Multidisciplinary Design 147,
https://doi.org/10.1007/978-3-030-55594-8_3

velocities (a dimensionless number relating the flow velocity to the structural natural frequency). This range of large-amplitude oscillations is called the lock-in range. VIV has been extensively studied for the model case of a flexibly-mounted cylinder placed in flow [1, 2]. Other cases where VIV has been observed in a bluff-body with non-circular cross-section have been considered as well [3–5]. For bluff bodies with non-circular cross-sections, a non-zero mean lift force acts on the body, which could result in another type of response with lower oscillation frequency compared with the shedding frequency and larger amplitude of oscillations compared with what is observed in VIV, called galloping. A combined VIV and galloping response is sometimes observed in these cases.

In order for VIV to be observed in a streamlined structure (i.e. an airfoil), the airfoil needs to be placed at relatively large angles of attack such that vortices are shed in the wake of the body. One practical example of an airfoil that is placed at large angles of attack is observed in VAWTs. VAWTs have been considered recently as a viable alternative for floating offshore wind turbines [6, 7] and therefore deeper understanding of how they behave is of great significance. This need for a deeper understanding of the behavior of airfoils at large angles of attack has led to recent numerical and experimental studies on VIV of airfoils.

Skrzypiński et al. [8] studied VIV of a DU96-W-180 airfoil placed at an angle of attack of 90° using a numerical technique with forced motion in the chordwise direction, and reported "the possibility of the lock-in phenomenon" [8]. Ehrmann et al. [9] performed experimental work in a wind tunnel to study the influence of a sharp edge on the reduction of VIV magnitude using three elastically-mounted airfoil shapes (NACA-0018) at a fixed angle of attack of 90°. They concluded that one sharp edge is enough to reduce VIV magnitude. Zou et al. [10] developed a model to predict VIV of an airfoil using a free wake aerodynamic code and compared their results with measured data for a DU96-W-180 airfoil as well as results obtained for the same airfoil via numerical studies by Skrzypiński et al. [8].

The existing studies on VIV of an airfoil placed at large angles of attack have all been focused on a single angle of attack. In order to obtain an overall view of the airfoil's behavior at various angles of attack, pinpoint the angle of attack at which VIV starts and observe how the magnitude of the response and the width of the lock-in range changes with varying angles of attack, the current work focuses on a series of experiments on a symmetric airfoil that is extensively used in the current designs of VAWTs.

## 2 Experimental Setup and Results

### *2.1 Experimental Setup*

The experiments were conducted in a re-circulating water tunnel, with a test section of 1.27 m × 0.5 m × 0.38 m and a turbulence intensity of less than 1% for up to

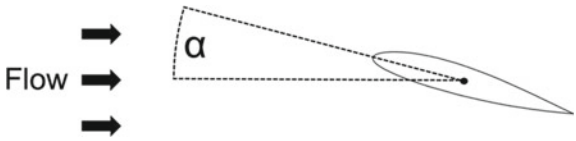


**Fig. 1** The flow direction and the angle of attack

a flow velocity of $U = 0.3$ m/s. A NACA-0021 airfoil was printed of ABS plastic with a chord of 4.13 cm and a length of 23.9 cm. The airfoil was affixed to a surface-piercing cylindrical extension with a diameter of 12.7 mm, such that the entire airfoil length was submerged and the cylindrical attachment was submerged 50% into the water, 2.5 cm in the water, out of a total extension length of 5.0 cm. The cylindrical extension served to minimize the surface wake effects at the free surface. The airfoil-cylinder assembly was mounted on low-damping air bearings free to move in the crossflow direction (i.e., perpendicular to the direction of the incoming flow) and springs extended from the metal plate to a fixed housing. This air bearing setup was used before for other VIV studies (e.g. Seyed-Aghazadeh et al. [3]) by the authors. The structural damping ratio was found to be $\zeta = 0.0067$ and the natural frequency in air $f_{na}$ ~ 0.61 Hz. The total moving mass of the system was $m = 0.225$ kg, resulting in a mass ratio of $m^* = 3.64$, where the mass ratio is defined as $m^* = m/\rho V_d$, where $m$ is the total moving mass of the system (including the airfoil, extensions, air bearings, mounting bracket, force sensor and various cabling) and $V_d$ is the volume of the airfoil and the submerged portion of the cylindrical extension. The natural frequency of the airfoil in water, $f_{nw}$, was obtained for each angle of attack (Fig. 1) by measuring the peak frequency of the vibrating structure decaying from an initial displacement for at least 50 cycles.

## *2.2 An Overall View of the Response*

The displacement time histories were measured for all angles of attack over a range of varying reduced velocities. These time histories were used to obtain the magnitude and frequency of oscillation at each point and the summary of these results are plotted in Fig. 2 as the dimensionless amplitudes of the airfoil crossflow oscillations, $A^*$, versus the reduced velocity, $U^*$, at varying angles of attack, $\alpha$. For angles of attack smaller than $\alpha = 55°$, no oscillations are observed in the entire reduced velocity range tested. Very small-amplitude oscillations are observed for $\alpha = 60°$, in a range of $5.8 < U^* < 6.7$ and a peak amplitude of $A^* = 0.063$ is observed at $U^* = 6.5$. At larger angles of attack, $\alpha = 65°$–$90°$, non-zero amplitudes are observed within a range of reduced velocities, resembling the lock-in range of a typical VIV response. For $\alpha = 65°$ the non-zero magnitudes are observed for $5.5 < U^* < 8.0$, with a maximum magnitude of $A^* = 0.497$ observed at $U^* = 6.838$. As the angle of attack is increased, the lock-in range becomes wider, and the maximum amplitude of oscillation becomes larger, such that the widest lock-in range, $1.7 < U^* < 12$, is observed for $\alpha = 90°$

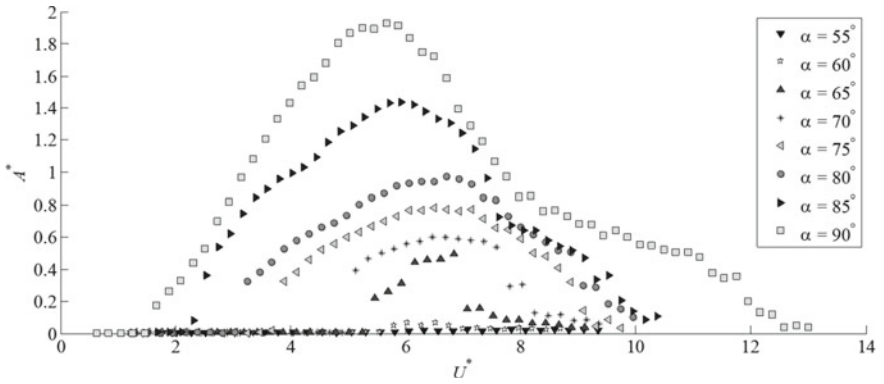


**Fig. 2** Dimensionless amplitude of the crossflow oscillations, $A* = A/D$, versus the reduced velocity, $U* = U/f_{nw}D$, and the angle of attack, $\alpha$

when the chord length of the airfoil is completely perpendicular to the incoming flow direction. The largest peak amplitude of oscillations, $A* = 1.93$, is also observed at $U* = 5.7$ for $\alpha = 90°$. For all the cases where oscillations are observed the oscillation frequency remains close to the structure's natural frequency.

## 2.3 Sample Cases and the Higher Harmonic Contributions

In Fig. 3, time histories of the airfoil's dimensionless amplitude and the dimensionless force coefficient, which acts on the airfoil in the cross-flow direction, are plotted together with their corresponding frequency contents for a sample case of $\alpha = 85°$, at a reduced velocity of $U* \sim 5.9$. In these plots $t*$ is time normalized by the natural frequency of the system in still water. The amplitude of the response is $A* = 1.4$. The dimensionless crossflow force coefficient is found as $C_y = 2F_y/\rho DU^2L$, where $F_y$ is the flow force measured using the force sensor in the crossflow direction and $L$ is the length of the airfoil.

In frequency plots the frequency is normalized by the natural frequency of the system in still water and therefore the peak oscillating frequency stays very close to unity. This is expected in a typical VIV response, since the flow forces are due to the shedding of vortices and the oscillations start when the frequency of vortex shedding equals the natural frequency of oscillation. The resulting oscillation, therefore, is expected to have a frequency equal to that of the natural frequency of the system. What is more interesting in the frequency response is the contribution of higher harmonic components of the main frequency in the frequency contents of both displacement and forces. This is clear in the frequency plots for displacement and force, where higher harmonics at twice and three times the crossflow oscillation frequencies are observed. The second higher harmonics are observed due to the system's asymmetry. The third higher harmonic is due to the contribution of the fluctuating drag force in the

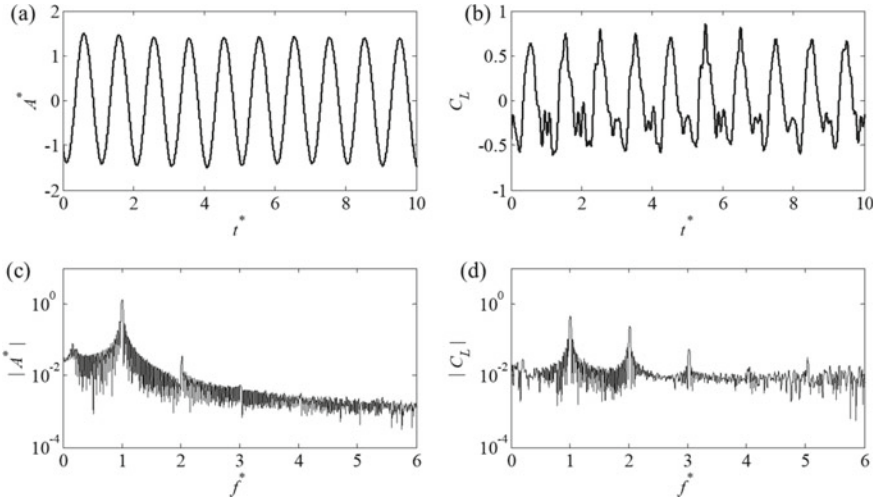


**Fig. 3** Sample time history and fast Fourier transform (FFT) plots of the airfoil's **a** dimensionless amplitude and **b** lift coefficient in the cross-flow direction together with **c**, **d** their corresponding frequency contents, measured using the force sensor and displacement sensor for $U^* \sim 5.9$ at $\alpha = 85°$. In the above plots, $C_L = 2F_L/\rho DU^2L$ and $t^* = tf_{nw}$

force measured in the cross-flow direction. It is known that the fluctuating drag force has a frequency twice the shedding frequency (since the force in the drag direction sees two vortices of similar strength during every period of crossflow oscillations). Since the structure oscillates in flow, the crossflow force has a component of the lift force (perpendicular to the relative velocity of the structure with respect to the incoming flow) and drag force (in line with that relative velocity). By considering the components of lift and drag in the crossflow direction, one can show that third harmonic contributions can be observed in the crossflow direction.

## *2.4 The Wake Pattern*

BIV flow visualizations were performed to study the shedding pattern of the airfoil at varying angles of attack in the range of $\alpha = 0°$–$90°$. Figure 4 shows the vortices formed in the wake of the airfoil at $\alpha = 0°, 20°, 60°, 65°$, and $80°$ at a reduced velocity of $U^* \sim 5.7$. The images were produced using a Phantom Miro M110 high-speed camera positioned underneath the water tunnel recording at 100 fps. Distinct vortex shedding patterns at this reduced velocity are observed for angles of attack $\alpha = 65°$ and $\alpha = 80°$, when the airfoil is experiencing VIV. At both angles of attack $\alpha = 65°$ and $\alpha = 80°$, for a reduced velocity of $U^* \sim 5.7$, two single vortices are shed per cycle of oscillation (2S pattern).

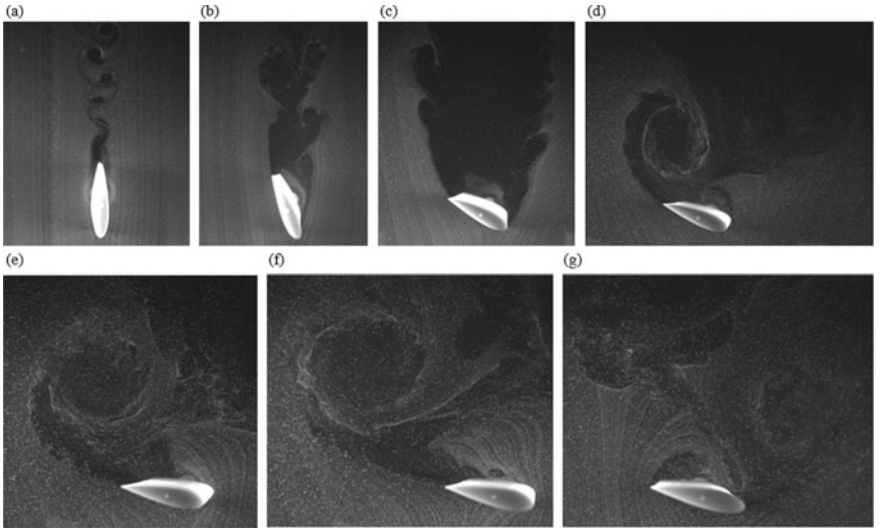


**Fig. 4** Flow visualization for wake of the airfoil at $U^* \sim 5.7$ at angles of attack of **a** $\alpha = 0°$, **b** $\alpha = 20°$, **c** $\alpha = 60°$, **d** $\alpha = 65°$, **e–g** $\alpha = 80°$

## 3 Conclusions

Flow-induced oscillations of a NACA-0021 airfoil at various angles of attack in the range of $0° < \alpha < 90°$ were studied experimentally over a range of reduced velocities of $0.6 < U^* < 13.0$ and a range of Reynolds numbers of $600 < Re < 13{,}300$. The airfoil was free to oscillate in the crossflow direction only, perpendicular to the incoming flow. Non-zero amplitudes were observed for angles of attack in the range of $\alpha = 60°$–$90°$ over a range of reduced velocities specific to each angle of attack. The $\alpha = 90°$ case exhibited the widest lock-in range ($1.7 < U^* < 12$) and the largest peak amplitude ($A^* = 1.93$ at $U^* = 5.7$). For all cases where oscillations were observed ($\alpha = 65°$–$90°$), the dimensionless oscillation frequency had a value of $f^* \sim 1$ at the beginning of the lock-in range and gradually increased to $1.2 < f^* < 1.4$. Flow visualizations indicated 2S vortex shedding patterns in the wake of the oscillating airfoils at particular angles of attack when the shedding frequency was equal to the oscillation frequency, confirming that the observed oscillations are due to VIV.

During operation, vertical-axis wind turbines are known to encounter every possible angle of attack. Thus, for certain flow velocities and structural natural frequencies, vertical axis turbines are shown to experience VIV, which could have a deleterious effect on the fatigue life of the turbine as a whole.

**Acknowledgements** This research is supported in part by the National Science Foundation under NSF award numbers EEC-1460461 and CBET-1437988.

## References


1. Williamson, C.H.K., Govardhan, R.: Vortex-induced vibrations. Annu. Rev. Fluid Mech. **36**, 413–455 (2004)
2. Sarpkaya, T.: A critical review of the intrinsic nature of vortex-induced vibrations. J. Fluids Struct. **19**, 389–447 (2004)
3. Seyed-Aghazadeh, B., Carlson, D., Modarres-Sadeghi, Y.: Vortex-induced vibration and galloping of prisms with triangular cross-sections. J. Fluid Mech. **817**, 590–618 (2017)
4. Nemes, A., Zhao, J., Lo Jacono, D., Sheridan, J.: The interaction between flow-induced vibration mechanisms of a square cylinder with varying angles of attack. J. Fluid Mech. **710**, 102–130 (2012)
5. Zhao, J., Leontini, J., Lo Jacono, D., Sheridan, J.: Fluid-structure interaction of a square cylinder at different angles of attack. J. Fluid Mech. **747**, 688–721 (2014)
6. Sun, X., Huang, D., Wu, G.: The current state of offshore wind energy technology development. Energy **41**, 298–312 (2012)
7. Paquette, J., Barone, M.: Innovative offshore vertical-axis wind turbine rotor project. In: EWEA 2012 Annual Event, Copenhagen, Denmark (2012)
8. Skrzypiński, W., Gaunaa, M., Sørensen, N., Zahle, F., Heinz, J.: Vortex-induced vibrations of a DU96-W-180 airfoil at 90° angle of attack. Wind Energy **17**, 1495–1514 (2014)
9. Ehrmann, R.S., Loftin, K.M., Johnson, S., White, E.B.: Lock-in of elastically mounted airfoils at a 90° angle of attack. J. Fluids Struct. **44**, 205–215 (2014)
10. Zou, F., Riziotis, V.A., Voutsinas, S.G., Wang, J.: Analysis of vortex-induced and stall-induced vibrations at standstill conditions using a free wake aerodynamic code. Wind Energy **18**, 2145–2169 (2015)

# Flow Past an Oscillating Cylinder: Effects of Oscillation Mode on Wake Structure


**S. Peppa, L. Kaiktsis, C. E. Frouzakis, and G. S. Triantafyllou**

**Abstract** We present a computational study of three-dimensional flow past a cylinder forced to oscillate both transversely and in-line with respect to a uniform stream. The cylinder oscillates with a frequency in the in-line direction equal to twice the transverse oscillation frequency, thus following a figure-eight trajectory; for a flow from left to right, the figure-eight is traversed in either a counter-clockwise or a clockwise direction in the upper half plane. Flow simulations were performed for $\mathrm{Re} = 400$ (for which the unforced flow is fully three-dimensional) for different cases, defined in terms of the oscillation mode (counter-clockwise or clockwise motion) and the ratio of transverse oscillation frequency to the natural frequency of vortex shedding ($F =$ 0.8, 0.9, 1.0 and 1.1). The results demonstrate that the effect of cylinder oscillation on the flow structure and forces differs substantially between the counter-clockwise and the clockwise oscillation mode. For the counter-clockwise mode, forcing at low amplitude decreases the flow three-dimensionality, with the wake becoming increasingly three-dimensional for transverse oscillation amplitudes higher than 0.25–0.30 cylinder diameters. For the case of clockwise mode, a strong stabilizing effect is found: the wake becomes two-dimensional for a transverse oscillation amplitude of 0.20 cylinder diameters, and remains so at higher amplitudes.

**Keywords** Fluid-structure interactions · Wake instability · DNS · Bluff-bodies

S. Peppa (✉)
Department of Naval Architecture, University of West Attica, Athens, Greece
e-mail: speppa@uniwa.gr

L. Kaiktsis · G. S. Triantafyllou
Department of Naval Architecture and Marine Engineering, NTUA, Athens, Greece
e-mail: kaiktsis@naval.ntua.gr

G. S. Triantafyllou
e-mail: gtrian@deslab.ntua.gr

C. E. Frouzakis
Department of Mechanical and Process Engineering, ETH Zurich, Zurich, Switzerland
e-mail: frouzakis@lav.mavt.ethz.ch



M. Braza et al. (eds.), *Advances in Critical Flow Dynamics Involving Moving/Deformable Structures with Design Applications*, Notes on Numerical Fluid Mechanics and Multidisciplinary Design 147,
https://doi.org/10.1007/978-3-030-55594-8_4

## 1 Introduction

Flows past bluff bodies exhibit very rich physics. To shed light on the wake dynamics, several numerical studies of three-dimensional flow past a stationary cylinder have been performed. Studies relevant to Vortex Induced Vibration (VIV) have considered the flow past a cylinder oscillating either in the transverse or the in the in-line direction with respect to the incoming stream. The present study concerns the flow past an oscillating cylinder following a figure-eight trajectory, commonly encountered in VIV. Direct Numerical Simulation (DNS) of three-dimensional flow past a circular cylinder is performed, at a Reynolds number of 400. The Navier-Stokes equations for incompressible flow are solved using the spectral element code nek5000 [1].

A postulate of previous literature studies of flow past an oscillating cylinder is that cylinder motion organizes the flow, bringing it closer to two-dimensional flow. Indeed, it has been shown that, in the case of transverse cylinder oscillation, in the Reynolds number range up to 300–400, the flow is characterized mostly by two-dimensionality at oscillation amplitudes above 10% of the cylinder diameter [2, 3]. The stabilizing effect of forcing in the case of transverse cylinder oscillation has been further confirmed and quantified by the Floquet stability analysis calculations of [4].

In this paper, following our previous study [5], we perform three-dimensional simulations past an oscillating cylinder for a wider range of oscillation frequencies, to investigate the wake dynamics, and relate it to the direction in which the figure-eight is traversed. Several numerical experiments with different oscillation frequencies are employed for the two oscillation modes considered (counter-clockwise and clockwise motion). A ratio of in-line and transverse oscillation amplitude $\varepsilon = 0.2$ is used, based on experimental observations reported in [6], whereas the transverse oscillation amplitude varies from 0 to 0.60 cylinder diameters.

## 2 Formulation and Numerical Method

We consider flow of an incoming uniform stream past a cylinder of diameter $D$. The velocity of the fluid far upstream the cylinder is $U_\infty$, the density and kinematic viscosity of the fluid are, $\rho$ and $\nu$, respectively. The Reynolds number of the flow, defined as $Re = U_\infty \cdot D/\nu$, is equal to 400, a value identical to the one used in the two-dimensional simulations reported in [7], and close to that in the experiments of [8]. We use a Cartesian coordinate system formed by *x-axis*, parallel to the incoming flow, *y-axis*, normal to the flow, and *z-axis*, along the cylinder span. The cylinder oscillates around a mean position, with transverse amplitude $A_y$ and in-line amplitude $A_x$. The in-line oscillation frequency is twice the transverse frequency, $f_x = 2f_y$. The instantaneous displacement of the cylinder in the $y$-direction is:

$$\eta_y = A_y \sin(2\pi f_y t) \tag{1}$$

while the corresponding displacement in the $x$-direction can be:

$$\eta_x = \pm A_x \sin(2\pi f_x t) = \pm A_x \sin(4\pi f_y t) \tag{2}$$

For a flow stream from left to right, the plus (+) sign in Eq. (2) corresponds to a motion which is counter-clockwise in the upper $x$-$y$ plane and the minus (−) sign to a clockwise motion in the upper $x$-$y$ plane. It is noted that, in general, the in-line oscillation can be characterized by a phase shift with respect to the transverse oscillation, i.e. $\eta_x = A_x \sin(4\pi f_y t + \theta)$, resulting in different trajectories and direction of the cylinder motion. The figure-eight counter-clockwise and clockwise motion correspond to values of phase shift $\theta = 0$ and $\theta = \pi$, respectively.

The fluid forces acting on the cylinder in the transverse and in-line direction are the lift and drag force, respectively. The total lift and drag force, per cylinder unit length, are scaled with the dynamic pressure, yielding the lift and drag coefficient, respectively:

$$F_y = \frac{1}{2}\rho U_\infty^2 D C_L \tag{3}$$

$$F_x = \frac{1}{2}\rho U_\infty^2 D C_D \tag{4}$$

The instantaneous lift coefficient, $C_L$, can be decomposed into the time-averaged value, $<C_L>$ and an instantaneous fluctuation, $C_L'$, i.e. $C_L =< C_L > + C_L'$, where $< C_L >= 1/T \int_0^T C_L dt$, with $T$ representing a large integration time. Correspondingly, the decomposition of the drag coefficient, $C_D$, is: $C_D =< C_D > + C_D'$ where $< C_D >= 1/T \int_0^T C_D dt$.

We will denote the root mean square (r.m.s.) of $C_L'$ and $C_D'$ by $C_{L,RMS}$ and $C_{D,RMS}$, respectively.

From dimensional analysis it follows that all non-dimensional force coefficients are functions of: the Reynolds number, the reduced y-amplitude, $A_y/D$, the relative x-amplitude, $\varepsilon = A_x/A_y$, and the frequency ratio $F = f_y/f_s$ (where $f_s$ is the natural frequency of the Kármán vortex street). Each of the two directions in which the figure eight trajectory can be traversed defines a different physical problem [9]; thus the dynamics also depends on the oscillation mode (counter-clockwise or clockwise).

The governing equations are the Navier–Stokes and incompressibility equations. For convenience, we non-dimensionalize all lengths with respect to $D$, all velocities with respect to $U_\infty$, time with respect to $D/U_\infty$, and pressure with respect to $\rho U_\infty^2$. Then the incompressibility and Navier–Stokes equations read:

$$\nabla \cdot \vec{u} = 0 \tag{5}$$

$$\frac{\partial \vec{u}}{\partial t} + \vec{u} \cdot \nabla \vec{u} = -\nabla p + \frac{1}{Re}\nabla^2 \vec{u} \tag{6}$$

where $\vec{u}$ is the absolute velocity vector, and $Re$ is the Reynolds number of the flow.

On the cylinder surface, the instantaneous fluid velocity is equal to that of the cylinder, i.e. $\vec{u} = \vec{u}_x + \vec{u}_y = d\eta_x/dt\vec{i} + d\eta_y/dt\vec{j}$, where $(\eta_x, \eta_y)$ is now the non-dimensional cylinder displacement, and $\vec{i}$, $\vec{j}$ are the unit vectors in the $x$- and $y$-direction. To avoid the reconstruction of the computational grid at each time step, we use a frame of reference that is fixed on the cylinder. Taking that $\vec{u}$ represents the relative, with respect to the moving cylinder, velocity, the incompressibility equation remains the same, while the momentum equation (Eq. 6) changes to:

$$\frac{\partial \vec{u}}{\partial t} + \vec{u} \cdot \nabla \vec{u} = -\nabla p + \frac{1}{Re}\nabla^2 \vec{u} - \frac{d^2\eta_x}{dt^2}\vec{i} - \frac{d^2\eta_y}{dt^2}\vec{j} \tag{7}$$

i.e. a d'Alambert acceleration is present at the right-hand side of Eq. (7). This means that, in order to find the actual force components acting on the cylinder, one has to subtract from the computed forces the "dynamic Archimedes" forces, which are equal to $-(\pi/4)\rho D^2 d^2\eta_y/dt^2\vec{j}$ and $-(\pi/4)\rho D^2 d^2\eta_x/dt^2\vec{i}$, for the lift and drag force, respectively. Moreover, the flow boundary conditions corresponding to $x$-$y$ cross-sections are modified as follows: (i) at the inflow and at the side boundaries, $\vec{u}_y = -d\eta_y/dt\vec{j}$, $\vec{u}_x = 1\vec{i} - d\eta_x/dt\vec{i}$, (ii) on the cylinder surface, the instantaneous fluid velocity is reduced to $\vec{u} = 0$, (iii) at the outflow, the Neumann-type boundary condition is maintained, $\partial\vec{u}/\partial\eta = 0$. Finally, periodic boundary conditions are prescribed for the end planes in the spanwise direction.

The parallel code Nek5000 [1], based on the Spectral Element Method [10, 11] is used to solve Eqs. (5) and (7) subject to the new boundary conditions. The code has been validated and resolution tests have confirmed the accuracy of the present simulations [5].

With reference to the cylinder centre, the computational domain extends 20 diameters upstream and 60 diameters downstream. In the vertical direction the domain is symmetrical, extending up to 17 diameters from the cylinder center. The domain length in the spanwise direction ($z$-direction) is chosen to be $L_z = 2\pi$, which is deemed sufficient based on experimental observations regarding the spanwise wavelength, as well as on published three-dimensional computational studies of flow past a cylinder (see [12] and references therein, [13]).

In $x$-$y$ planes, the discretization consists of 2056 spectral elements. In the $z$-direction, a total of 10 element layers are used. Thus, 20,560 three-dimensional spectral elements are used in total, each with $8 \times 8 \times 8$ elemental resolution. The spectral element grid is illustrated in Fig. 1. A third-order semi-implicit temporal scheme is employed for time discretization [14]; the time step is $\Delta t = 0.001$.

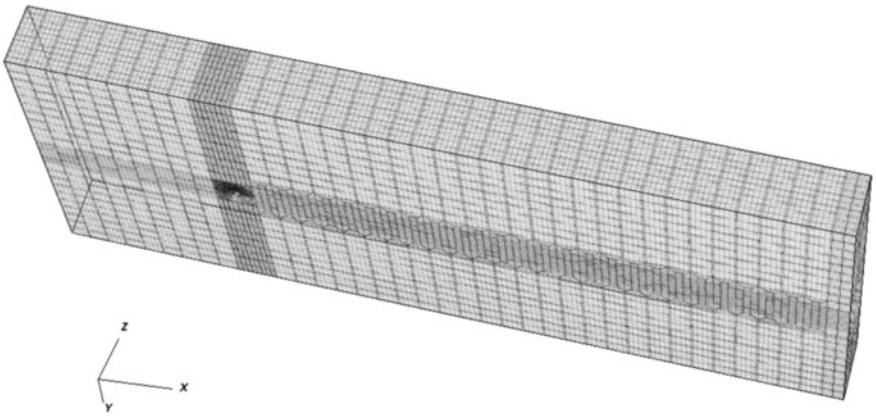


**Fig. 1** Spectral element grid for three-dimensional flow past a circular cylinder used in the simulations

## 3 Results

We have performed DNS of flow past an oscillating cylinder with transverse oscillation frequency close to the frequency of vortex formation behind a stationary cylinder. The cylinder follows a figure-eight trajectory which is traversed into two distinct ways: (i) counter-clockwise and (ii) clockwise in the upper *x*-*y* plane. In the present simulations, four values of frequency ratio were studied, $F = 0.8, 0.9, 1.0$ and $1.1$, for a constant value of amplitude ratio ε equal to 0.2, while the corresponding transverse oscillation amplitude varies from 0 to 0.60 of the cylinder diameter. We assume that the flow is past an infinitely long circular cylinder, approximated here with a finite domain length in the spanwise direction, with periodic boundary conditions for the end planes.

For each numerical experiment, corresponding to a certain combination of frequency and oscillation amplitude, the flow is computed until a statistical steady state is reached, within which the flow mean quantities are time-independent. Simulations are initialized from flow fields corresponding to lower oscillation amplitudes with a smooth increase in amplitude. After reaching the constant amplitude regime, the governing equations are further integrated in time until a statistical steady state is reached.

The magnitude of non-dimensional lift forces, expressed in terms of $C_{L,RMS}$ versus the transverse oscillation amplitude, is shown in Fig. 2a, b. It is assessed that, for clockwise motion, the lift fluctuations increase substantially with oscillation amplitude, while, for counter-clockwise motion, there is a milder dependence on $A_y/D$. For counter-clockwise cylinder motion with $F = 1.0$, the curves of lift forces remain almost flat for oscillation amplitude 0.10–0.50, whereas, for oscillation with $F = 1.1$, the magnitude of the lift force decreases in the range of high values of $A_y/D$.

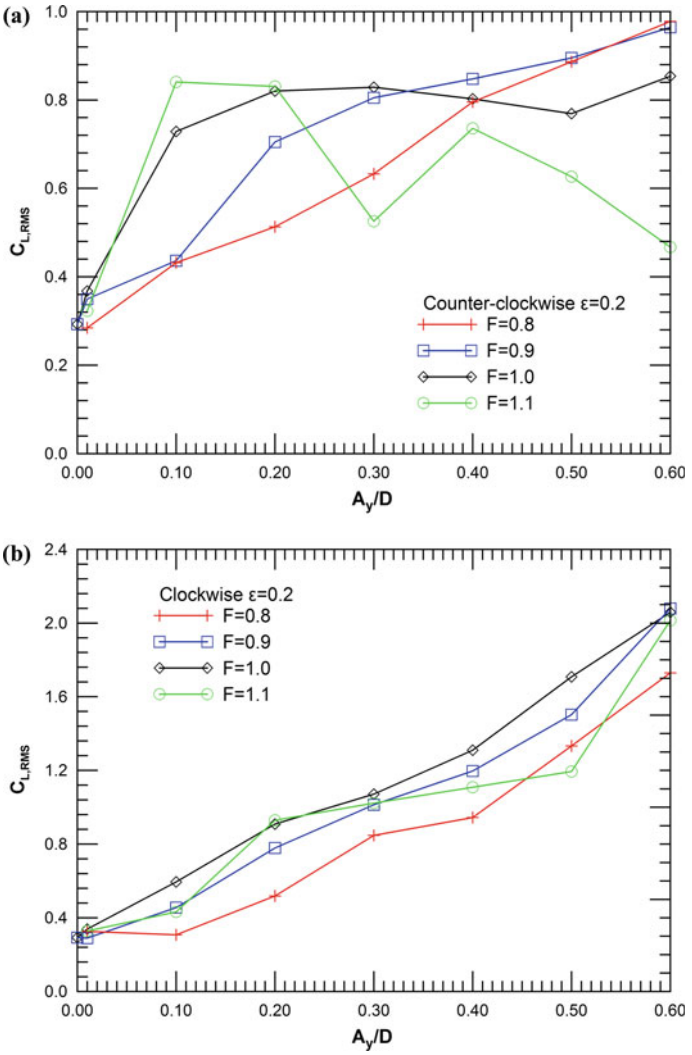


**Fig. 2** Variation of the rms of the lift coefficient $C_{L,RMS}$ for counter-clockwise (**a**) and clockwise (**b**) oscillation with $\varepsilon = 0.2$ as a function of the non-dimensional amplitude $A_y/D$, for frequency ratios F = 0.8, 0.9, 1.0 and 1.1

The variation of the mean drag coefficient $<C_D>$, for the two oscillation modes is shown in Fig. 3a, b. For counter-clockwise oscillation, the drag force exhibits a monotonic increase with oscillation amplitude, as demonstrated in Fig. 3a, which suggests the absence of a major transition in the shedding mode; the case of F = 1.1 appears as a possible exception. Higher values of time-averaged drag coefficient are found for resonant forcing with counter-clockwise oscillation, suggesting a wider wake. For the clockwise mode, drag forces exhibit in general a monotonic increase

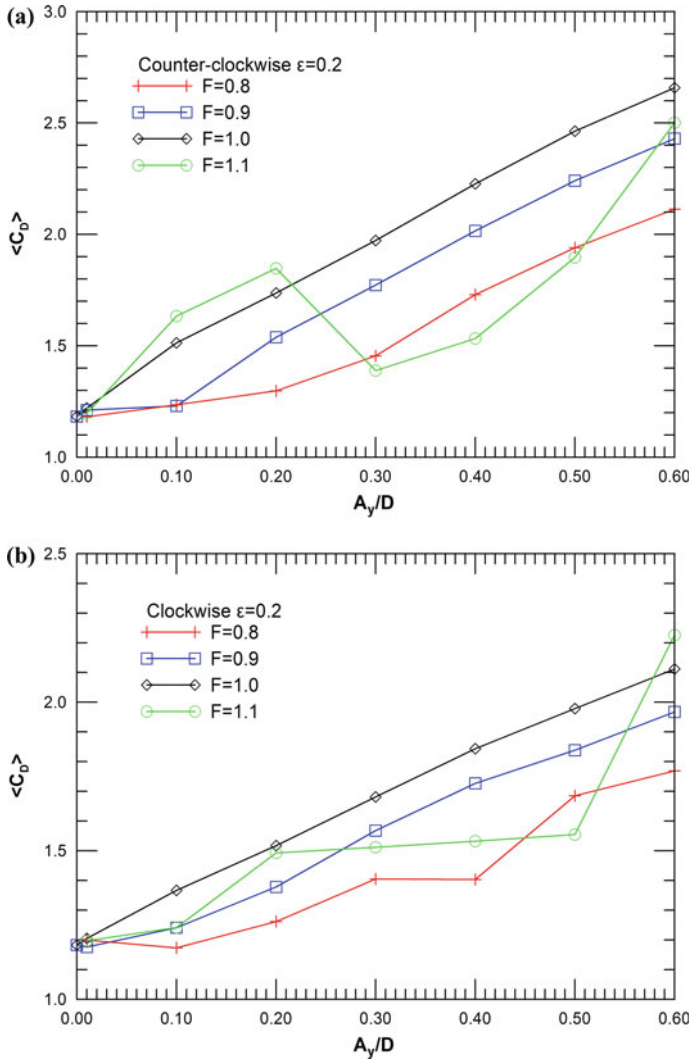


**Fig. 3** Variation of the mean drag coefficient $<C_D>$ for counter-clockwise (**a**) and clockwise (**b**) oscillation with $\varepsilon = 0.2$ as a function of the non-dimensional amplitude $A_y/D$, for frequency ratios $F = 0.8$, 0.9, 1.0 and 1.1

with transverse oscillation amplitude, as demonstrated in Fig. 3b, suggesting the absence of a major transition in the shedding mode, with flat regions present for $F = 0.8$ and $F = 1.1$.

Visualizations of the wake in terms of vorticity isocontours illustrate the three-dimensionality effects and the overall structure of the vortex street. The visualizations presented here correspond to the cylinder mean position, i.e., $\eta_y/D = \eta_x/D = 0$, at different oscillation amplitudes. The variation in flow structure can be related to the

variation of forces on the cylinder, although the relation is by no means straightforward. First results for the case of flow past an oscillating cylinder have been presented in [5], showing the effect of counter-clockwise cylinder motion with F = 1.0 on flow structures, for representative values of transverse oscillation amplitude.

The present results demonstrate a strong stabilizing effect (return to two-dimensional flow) for clockwise cylinder motion. In particular, Fig. 4 presents instantaneous vorticity isocontours, plotted at the moment that the cylinder occupies its mean position, at different oscillation amplitudes, for clockwise cylinder motion with F = 0.9 and F = 1.0. For F = 0.9, for an oscillation amplitude $A_y/D = 0.40$ (see Fig. 4b), strong vortex tubes are present, while the streamwise rolls have disappeared in the near wake, and the entire wake is two-dimensional at large times. The same effect is observed for F = 1.0, already for the lower oscillation amplitude $A_y/D = 0.20$ (see Fig. 4c, d). This return to two-dimensional flow is associated with the clear monotonic increase of forces with oscillation amplitude, as shown in Figs. 2b and 3b.

The trend of reducing wake three-dimensionality with oscillation amplitude is also noted for the counter-clockwise oscillation mode at moderate oscillation amplitude, as shown in Fig. 5. In particular, for F = 0.9 and transverse oscillation amplitude equal to 0.30, the wake is characterized by reduced levels of vortex tube deformation in the near wake mostly (Fig. 5b). The wake complexity increases again at higher oscillation amplitudes (see Fig. 5c), corresponding to transverse oscillation amplitude of 0.60. The decrease and subsequent increase of wake three-dimensionality with oscillation amplitude is also found for F = 1 (see Fig. 5e, f, corresponding to transverse oscillation amplitude of 0.3 and 0.6, respectively).

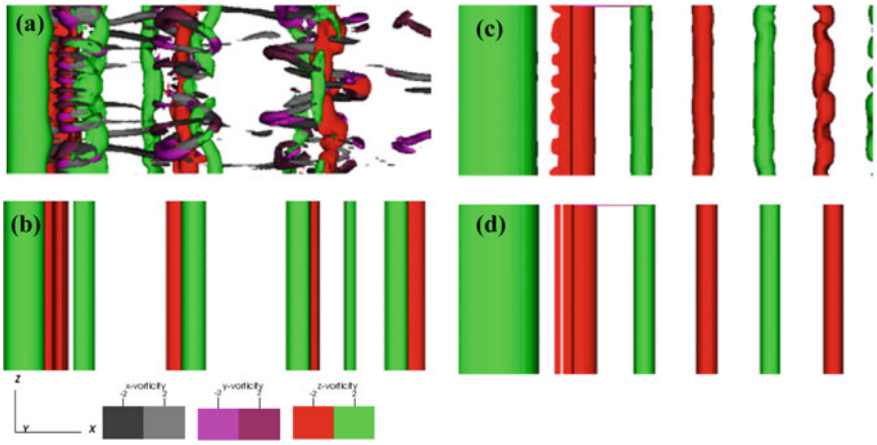


**Fig. 4** Clockwise mode: instantaneous vorticity isosurfaces (top view) of three-dimensional flow for a cylinder oscillating at: (i) F = 0.9 and $A_y/D = 0.30$ (**a**), 0.40 (**b**) and (ii) F = 1.0 and $A_y/D = 0.20$ at t = 10T (**c**), 0.20 at t = 30T (**d**), T being the oscillation period

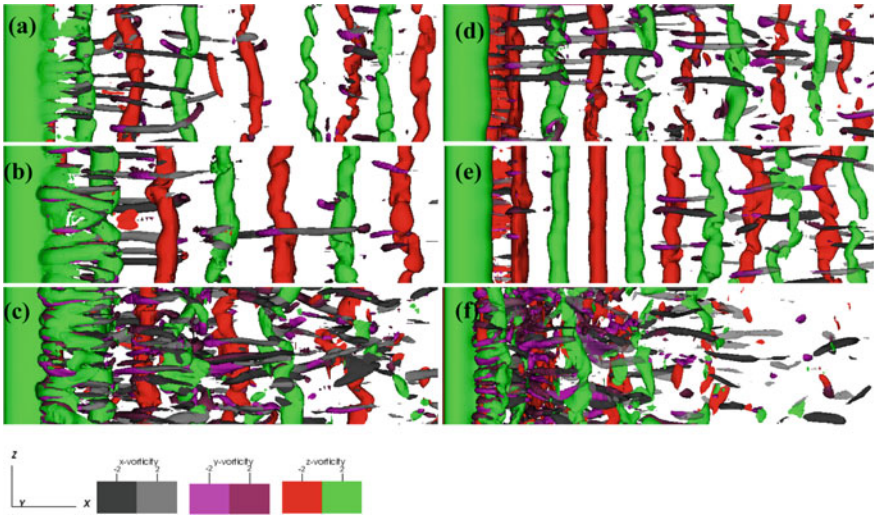


**Fig. 5** Counter clockwise mode: instantaneous vorticity isosurfaces (top view) of three-dimensional flow for a cylinder oscillating at: (i) F = 0.9 and $A_y/D = 0.10$ (**a**), 0.30 (**b**), 0.60 (**c**) and (ii) F = 1.0 and $A_y/D = 0.10$ (**d**), 0.30 (**e**), 0.60 (**f**)

## 4 Conclusions

In this paper, computational results for three-dimensional flow past an oscillating cylinder, undergoing a figure-eight trajectory, have been presented. Flow simulations were performed for Re = 400 (for which the unforced flow is fully three-dimensional) for different cases, characterized by the type of cylinder motion (counter-clockwise or clockwise) and the ratio of transverse oscillation frequency to the natural frequency of vortex shedding.

The present results demonstrate that the cylinder oscillation mode critically affects the wake three-dimensionality and overall structure. Counter-clockwise motion has a stabilizing effect when the cylinder oscillates at moderate amplitudes, in terms of reducing the three-dimensionality in the near wake, an effect which is most pronounced at F = 1.0; the wake three-dimensionality increases at higher oscillation amplitudes. Moreover, the present results show that, in the case of the clockwise mode, the cylinder oscillation has a strong stabilizing effect, with the flow becoming two-dimensional at different transverse oscillation amplitude, depending on the frequency of oscillation; flow two-dimensionality is maintained for high oscillation amplitudes.

**Acknowledgements** This work was supported by computational time granted from the Greek Research and Technology Network (GRNET) in the National HPC facility—ARIS—under project ID FLOWBB.

## References


1. Fischer, P., Lottes, J., Kerkemeier, S.: Nek5000 Web Page. https://nek5000.mcs.anl.gov (2008)
2. Koopman, G.H.: The vortex wakes of vibrating cylinders at low Reynolds numbers. J. Fluid Mech. **28**, 501–512 (1967)
3. Griffin, O.M.: The unsteady wake of an oscillating cylinder at low Reynolds number. J. Appl. Mech. **38**, 729–738 (1971)
4. Gioria, R.S., Jabardo, P.J.S., Carmo, B.S., Meneghini, J.R.: Floquet stability analysis of the flow around an oscillating cylinder. J. Fluids Struct. **25**(4), 676–686 (2009)
5. Peppa, S., Kaiktsis, L., Triantafyllou, G.S.: Numerical simulation of three-dimensional flow past a cylinder oscillating at the Strouhal frequency. J. Pressure Vessel Technol. Trans. ASME **137**(1), 011302 (2015)
6. Vandiver, J.K.: Drag coefficients of long flexible cylinders. In: Proceedings of the Offshore Technology Conference, Houston, TX, Paper No. 4490, pp. 405–414 (1983)
7. Kaiktsis, L., Triantafyllou, G.S., Özbas, M.: Excitation, inertia and drag forces on a cylinder vibrating transversely to a steady flow. J. Fluids Struct. **23**(1), 1–21 (2007)
8. Williamson, C.H.K., Roshko, A.: Vortex formation in the wake of an oscillating cylinder. J. Fluids Struct. **2**(4), 355–381 (1988)
9. Peppa, S., Triantafyllou, G.S.: Sensitivity of two-dimensional flow past transversely oscillating cylinder to streamwise cylinder oscillations. Phys. Fluids **28**(3), 037102 (2016)
10. Karniadakis, G.E., Sherwin, S.J.: Spectral/hp Element Methods for Computational Fluid Dynamics. Oxford University Press (2005)
11. Deville, M., Fischer, P.F., Mund, E.: High-Order Methods for Incompressible Fluid Flow. Cambridge University Press, Cambridge, UK (2004)
12. Williamson, C.H.K.: Vortex dynamics in the cylinder wake. Annu. Rev. Fluid Mech. **28**, 477–539 (1996)
13. Gioria, R.S., Meneghini, J.R., Aranha, J.A.P., Barbeiro, I.C., Carmo, B.S.: Effect of the domain spanwise periodic length on the flow around a circular cylinder. J. Fluids Struct. **27**(5–6), 792–797 (2011)
14. Maday, Y., Patera, A.T., Rønquist, E.M.: An operator-integration-factor splitting method for time-dependent problems: application to incompressible fluid flow. J. Sci. Comput. **5**(4), 263–292 (1990)

# Numerical Simulation of Oscillating Vibrating Flow Around Bodies

# Turbulent Backward-Facing Step Flow: Reliability Assessment of Large-Eddy Simulation Using ILSA


**Bernard J. Geurts, Amirreza Rouhi, and Ugo Piomelli**

**Abstract** Reliability assessment of large-eddy simulation (LES) of turbulent flows requires consideration of errors due to shortcomings in the modeling of sub-filter scale dynamics and due to discretization of the governing filtered Navier-Stokes equations. The Integral Length-Scale Approximation (ILSA) model is a pioneering sub-filter parameterization that incorporates both these contributions to the total simulation error, and provides user control over the desired accuracy of a simulation. The performance of ILSA, implemented as eddy-viscosity models, for separated turbulent flow over a backward-facing step is investigated here. We show excellent agreement with experimental data and with predictions based on other, well-established sub-filter models. The computational overhead is found to be close to that of a basic Smagorinsky sub-filter model.

**Keywords** Turbulence · Large-eddy simulation · ILSA modelling · Reliability

## 1 Introduction

Large-eddy simulation (LES) of turbulent flow has a long and rich history. During the 1960s first parameterizations, such as Smagorinsky's eddy-viscosity model [1]

B. J. Geurts (✉)
Multiscale Modeling and Simulation, Department of Applied Mathematics, University of Twente, P.O. Box 217, 7500 AE Enschede, Netherlands
e-mail: b.j.geurts@utwente.nl

Multiscale Physics of Energy Systems, Faculty of Applied Physics, Center for Computational Energy Research, Eindhoven University of Technology, P.O. Box 513, 5600 MB Eindhoven, Netherlands

A. Rouhi · U. Piomelli
Department of Mechanical and Materials Engineering, Queen's University, Kingston, ON K7L 4L9, Canada

A. Rouhi
Department of Mechanical Engineering, University of Melbourne, Victoria 3010, Australia



M. Braza et al. (eds.), *Advances in Critical Flow Dynamics Involving Moving/Deformable Structures with Design Applications*, Notes on Numerical Fluid Mechanics and Multidisciplinary Design 147,
https://doi.org/10.1007/978-3-030-55594-8_5

were proposed to capture the effects of localized turbulent motions on the large energy-carrying scales. The coarsening length-scale of choice was directly linked to the mesh-size in the computational grid, often chosen as the cube-root of the volume of a grid cell [2]. While coarsening is helpful in reducing the computational effort required for a simulation of a particular flow, it also introduces uncertainty regarding the accuracy of the results [3, 4]. Achieving a clear estimation and control of the level of uncertainty in the coarsened predictions, is a crucial pacing item in LES research. We review the recent ILSA proposal (Integral Length-Scale Approximation) which is a first framework that can address dynamic error control systematically, closely following [5, 6].

The computational grid for LES is often defined independent of the flow. Correspondingly, also the grid-based local coarsening length-scale is decoupled from the actual local flow. However, LES coarsening could in principle differ from location to location and from time to time, in response to local turbulence levels and variations in length- and time scales. Such would allow for lower resolution in regions of rather quiescent flow and higher resolution where required by the locally more detailed flow [7]. Recently, in Piomelli et al. [5] an alternative coarsening length-scale was put forward for LES, based on flow physics rather than on the grid scale. This idea was implemented in the form of an eddy-viscosity model based on the local integral length-scale. The model coefficient is specified with reference to the concept of 'sub-filter activity' as suggested in Geurts and Fröhlich [8]. The eddy-viscosity is such that an *a priori* user-defined measure for the error level can be maintained. Effective model parameters that implement this sub-filter activity level can be inferred computationally from exploratory coarser simulations, following the SIPI (Successive Inverse Polynomial Interpolation) error minimization [9]. Combined, ILSA is a first, complete formulation in which the issue of LES reliability for a particular flow is key.

In this paper we review the ILSA modeling strategy and discuss the development and testing of the new model for flow over a backward-facing step, showing that the new eddy-viscosity model compares closely with experimental data by Vogel and Eaton [10]. ILSA does not require the introduction of any *ad hoc* user-defined parameters, other than the target sub-filter activity, i.e., the desired level for the total simulation error. The ILSA model allows to separate the problem of *representing small-scale turbulent motions* in a coarsened flow model from that of *achieving accurate numerical resolution* of the solution. The formulation supports the notion of grid-independent LES, in which a prespecified reliability measure is used to determine the local coarsening length-scale. This is basic to achieving *a priori* error control.

The organization of this paper is as follows. In Sect. 2 we briefly review reliability issues in LES. Basic ILSA is presented in Sect. 3 in which the original 'global' ILSA and the 'local' ILSA extension are discussed. Section 4 presents results for turbulent backward-facing step flow, closely following [6]. Summarizing remarks are collected in Sect. 5.

## 2 Reliability Issues in Large-Eddy Simulation

In this section we briefly review the main components that make up the total simulation error in LES and discuss the error-landscape approach to visualize interacting error contributions. A standard formulation for LES assumes a spatial convolution filter with an effective width $\Delta$, coupling the unfiltered Navier-Stokes solution to the filtered solution. In this paper we work with incompressible flows, governed by conservation of mass and momentum respectively,

$$\partial_j \overline{u}_j = 0$$
$$\partial_t \overline{u}_i + \partial_j(\overline{u}_i \overline{u}_j) + \partial_i \overline{p} - \frac{1}{\mathrm{Re}} \partial_{jj} \overline{u}_i = -\partial_j(\overline{u_i u_j} - \overline{u}_i \overline{u}_j)$$

where the overbar denotes the filtered variable. Here, we use Einstein's summation convention and use $p$ for the pressure and $\boldsymbol{u}$ for the velocity field. Time is denoted by $t$ and partial differentiation with respect to the $j$th coordinate by the subscript $j$. Relevant length ($L$) and velocity ($U$) scales, and the constant density and kinematic viscosity ($\nu$) are used to make the equations dimensionless and define the Reynolds number $Re = UL/\nu$. On the left-hand side we observe the incompressible Navier-Stokes formulation in terms of the filtered variables. On the right hand side the filtered momentum equation has a non-zero contribution expressed in terms of the divergence of the sub-filter stress tensor

$$\tau_{ij} = \overline{u_i u_j} - \overline{u}_i \overline{u}_j$$

The sub-filter tensor expresses the central 'closure problem' in LES, as it requires both the filtered as well as the unfiltered representation of the solution. Since only the filtered solution is available in LES, the next step in modeling the coarsened turbulent flow is to propose a sub-filter model $M$ in terms of the filtered solution only. Numerous sub-filter models have been proposed for LES, among which eddy-viscosity models [3, 11] regularization models [12] and similarity models [13]. In this paper we restrict ourselves to eddy-viscosity models, in which the anisotropic part of sub-filter stress tensor is given by, where $S_{ij}$ denotes the rate of strain tensor of the filtered velocity field, i.e., the symmetric part of the velocity gradient, and $\nu_{sfs}$ is the sub-filter scale eddy viscosity.

A central premise of numerical simulation asserts that the solution to a given PDE problem should be obtained accurately and efficiently, while simultaneously, a close upper-bound for the error should be estimated. In the context of LES this not only implies a study of the effects of numerical discretization errors on the dynamics of the simulated solution, but also includes the role of the model for the sub-filter stress tensor as well as the interaction between these two basic sources of error [14–16]. However, in practice the computational costs of simulating a flow on $N^3$ grid points, using an explicit time-stepping method, scales $\sim N^4$ with $N$ the number of grid points along a coordinate direction. This cost implies a large role of the numerical

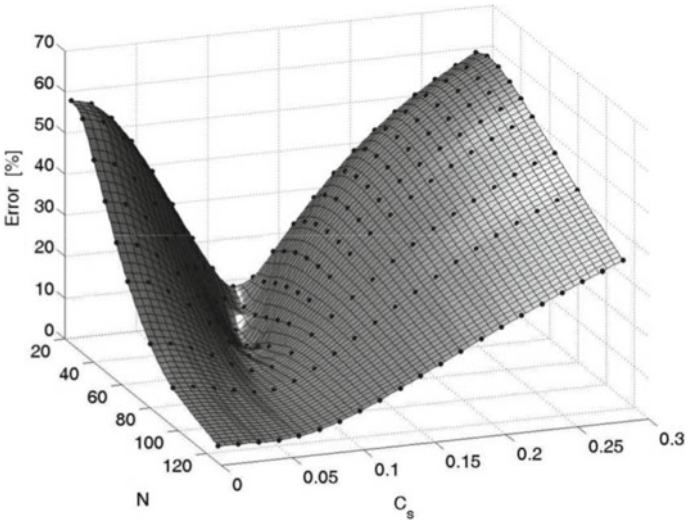


**Fig. 1** Error landscape for LES based on the Smagorinsky model applied to decaying homogeneous isotropic turbulence at a Taylor Reynolds number of 100. The error in the resolved enstrophy, relative to the DNS prediction, is shown as function of the spatial resolution $N$ and the Smagorinsky coefficient—reproduced with permission from Meyers et al. [18]. Each dot on the error-surface corresponds to a particular LES

method in capturing the actual LES solution [17]. Hence, at practically feasible, likely marginal resolution, both the selected sub-filter model as well as the adopted spatial discretization method can have a significant influence on the simulated dynamics. Together, these influences give rise to the total simulation error.

Since the modeling and discretization error effects can partially counteract each other [19–23] it is not straightforward to assess the overall simulation error in a given flow property. Instead, one can resort to a computational assessment of the simulation error for selected cases [24, 25]. This is known as the error-landscape approach. In Fig. 1 we show such an error-landscape for LES of homogeneous isotropic turbulence, based on the Smagorinsky model. The error is based on the relative deviation of the turbulent kinetic energy between, on the one hand, a particular LES (at given spatial resolution $N$ and value of the Smagorinsky coefficient $C_S$) and, on the other hand, the underlying direct numerical simulation. Each dot on the error-landscape surface denotes the error in a particular LES. At zero Smagorinsky coefficient, e.g., the LES corresponds to a 'no-model' or under-resolved simulation. We observe that the error decreases rapidly and smoothly with increasing spatial resolution, indicating convergence toward DNS predictions at high enough spatial resolution. Moreover, we notice that at fixed, coarse, spatial resolution $N$ and sufficiently large values of the Smagorinsky coefficients, also rather large errors arise. In between the 'no model' case and a very large $C_S$ there appears a minimum in which possible partial cancellation of modeling and discretization error effects is achieved optimally at that value of grid resolution $N$. This would yield the lowest total simulation error at the

corresponding computational cost. The optimal refinement strategy can be inferred by determining these minima as function of $N$. Knowledge about such error behavior can be used to classify errors due to numerical dissipation and sub-filter contributions [26]. Strictly speaking, the optimal refinement strategy can be inferred only after a database of LESs is collected—the optimal Smagorinsky coefficient at given spatial resolution is a quantity that currently cannot be predicted in advance theoretically [27].

A computational estimate of the optimal Smagorinsky coefficient at given spatial resolution can be obtained at modest additional cost using the SIPI method (Successive Inverse Polynomial Interpolation) [9]. At given $N$ this method takes error levels at three prior simulations using different $C_S$ values, and, via quadratic interpolation, progresses to converge $C_S$ to achieve the error minimum. Since the dependence of the optimal Smagorinsky coefficient on the spatial resolution is quite modest, one may proceed in two steps. First, at coarse resolution the optimal Smagorinsky coefficient is determined. Subsequently, at finer resolution, production simulations can be executed with this optimal coarse grid value. This approach is also basic to the original ILSA model to which we turn next.

## 3 ILSA—Integral Length-Scale Approximation

We review the length-scale definition for LES based on the resolved turbulent kinetic energy (TKE) and its dissipation. Rather than working with a grid-based length-scale, as in traditional LES, referring to sub-*grid* scales, we propose a flow-specific length-scale distribution defining the filter-width and hence refer to the LES approach as modelling the sub-*filter* scales.

The global ILSA model is an eddy-viscosity model in which the anisotropic part of the sub-filter stress tensor is given by $\tau_{ij}^a = -2\nu_{sfs}S_{ij}$ with turbulent eddy-viscosity defined as

$$\nu_{sfs} = (C_m\Delta)^2\left|\overline{S}\right| \equiv (C_mC_\Delta L)^2\left|\overline{S}\right| \equiv (C_kL)^2\left|\overline{S}\right|$$

where $C_k = C_mC_\Delta$ is referred to as the 'effective model coefficient', and the filter-width $\Delta$ is expressed as a fraction of the local integral length-scale, $\Delta = C_\Delta L$, inferred from

$$L = \frac{\langle K_{res}\rangle}{\langle \varepsilon_{tot}\rangle}$$

where the resolved turbulent kinetic energy (TKE) and total dissipation rate are given by

$$K_{res} = \frac{1}{2}\overline{u}_i'\overline{u}_i'; \quad \varepsilon_{tot} = 2\big(\nu + \nu_{sfs}\big)\overline{S}_{ij}'\overline{S}_{ij}'$$

in terms of resolved velocity fluctuations and the corresponding rate-of-strain tensor. Using the resolved TKE rather than the total one does not affect the estimated length-scale significantly [5, 28]. The choice to use the integral length scale $L$ implies that the local LES resolution adapts itself dynamically to the turbulence characteristics of the flow. The local grid resolution $h$ should at least resolve the integral length scale $L$, i.e., $L/h >> 1$. By selecting $h$ appropriately, an approximately grid-independent LES prediction may be obtained. Moreover, variations in $L$ automatically can be used to generate (adaptive) non-uniform grids on which to simulate the turbulent flow at hand [7].

Aside from the local integral length-scale $L$, a key ingredient toward the ILSA model is that adaptations in the effective model coefficient are made consistent with a measure toward explicit error control. This way, the effective model coefficient $C_k$ should be obtained in response to the local flow characteristics. For this purpose the concept of sub-filter activity [8] is used. This approach is conceptually related to the famous 'Pope 80% rule' [3] in which it is put forward that accurate LES requires the local filter-width to be such that the resolved turbulent kinetic energy is at least 80% of the total turbulent kinetic energy. Likewise, requiring a bounded sub-filter activity, we inherit a dynamic model response compliant with a desired level of error control.

The local ILSA model uses invariants of the sub-filter stresses directly. Following Rouhi et al. [6] we introduce

$$s_\tau = \left( \frac{\big\langle \tau_{ij}^a \tau_{ij}^a \big\rangle}{\Big\langle \big(\tau_{ij}^a + R_{ij}^a\big)\big(\tau_{ij}^a + R_{ij}^a\big) \Big\rangle} \right)^{1/2}$$

where the anisotropic part of the sub-filter tensor is denoted by $\tau_{ij}^a$ and the anisotropic part of the resolved stress tensor by $R_{ij}^a = \overline{u}_i'\overline{u}_j' - \overline{u}_k'\overline{u}_k'\delta_{ij}/3$. In case of an eddy-viscosity model the anisotropic sub-filter tensor $\tau_{ij}^a = -2\nu_{sfs}\overline{S}_{ij}$ with $\nu_{sfs} = \big(C_k L^2\big)\big|\overline{S}\big|$. This model implies

$$\begin{aligned}
\big\langle \tau_{ij}^a \tau_{ij}^a \big\rangle &= 4\big\langle \nu_{sfs} S_{ij} S_{ij} \big\rangle = \big\langle 2L^4 |S|^4 \big\rangle C_k^4 \equiv \chi_1 C_k^4 \\
\big\langle \tau_{ij}^a R_{ij}^a \big\rangle &= \big\langle -2\nu_{sfs} S_{ij} R_{ij}^a \big\rangle = -\big\langle 2L^2 |S| S_{ij} R_{ij}^a \big\rangle C_k^2 \equiv \chi_2 C_k^4
\end{aligned}$$

If we denote in addition $\big\langle R_{ij}^a R_{ij}^a \big\rangle \equiv \chi_3$ then we infer a fourth order polynomial equation governing the effective model coefficient as

$$\chi_1 \left(1 - \frac{1}{s_\tau^2}\right) C_k^4 + 2\chi_2 C_k^2 + \chi_3 = 0$$

from which the unknown coefficient $C_k$ can be obtained once the desired sub-filter activity is set to an appropriate value.

## 4 Local ILSA for Flow Over a Backward-Facing Step

In this section we illustrate the performance of the local ILSA model for turbulent flow over a backward-facing step at $Re_c = U_c h_s/\nu = 28{,}000$ based on the centerline velocity $U_c$ at the inlet ($x = 0$) and step height $h_s$. We compare results with the Lagrangian dynamic model [29], and show close agreement of local ILSA with experimental reference data by Vogel and Eaton [10]. We analyze the induced eddy-viscosity model on the computational grid and argue better numerical behavior in the ILSA model, contributing to the overall model performance. Figure 2: Structured grid for the backward-facing step flow on a coarse grid of $256 \times 100 \times 64$ grid points, clustered at characteristic locations in the domain, i.e., near the boundaries and shear layers inside the domain. All scales are normalized by the step height.

In Fig. 2 we show the computational grid used for the backward-facing step simulations. The height of the inflow channel is 4 step heights and the spanwise width is 3 step heights. The inflow length of the channel is 32 step heights and the velocity field at $x = -5h_s$ is recycled to the inflow located at $x = -32h_s$ to generate a well-developed turbulent inflow. At the outflow at $20h_s$ a convective boundary condition was adopted.

In Fig. 3 the mean flow statistics are shown at three spatial resolutions, comparing local ILSA with the Lagrangian dynamic model, with 'no model' and with experimental data. The LES results agree closely with each other and with the experimental data—only on the coarsest grid there is a slight difference between the local ILSA and Lagrangian dynamic model. This difference is most notable in the recovery region after the reattachment. The 'no model' option shows that the inclusion of a sub-filter model is beneficial for the accuracy of predictions.

The central model parameters of the local ILSA model are illustrated in Fig. 4. We compare the standard definition of the filter width (Fig. 4a) with the estimated integral scale $L$ (Fig. 4b). The local integral length-scale decreases considerably where the

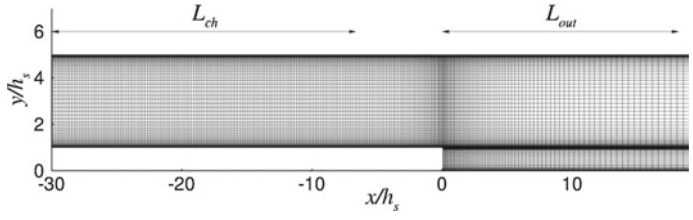


**Fig. 2** Structured grid for the backward-facing step flow on a coarse grid of $256 \times 100 \times 64$ grid points, clustered at characteristic locations in the domain, i.e., near the boundaries and intense shear layers inside the domain. All scales are normalized by the $h_s$ step height

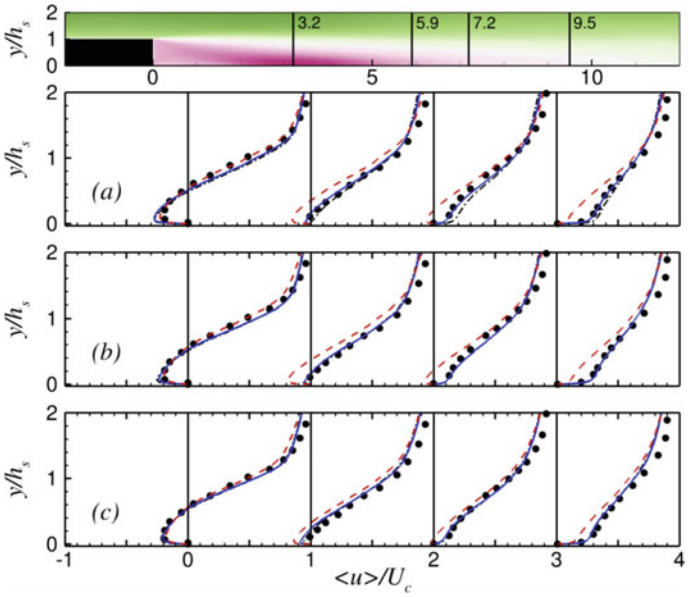


**Fig. 3** Mean velocity normalized by the centerline velocity at the inlet, determined at a number of locations downstream of the step on different grids: **a** 256 × 100 × 64 points, **b** 384 × 150 × 96 points, **c** 512 × 200 × 128 points. Experimental data [10] shown with full circles, Lagrangian dynamic model in dash-dot, no-model in dashed line and local ILSA in solid line (reproduced with permission from Rouhi et al. [6])

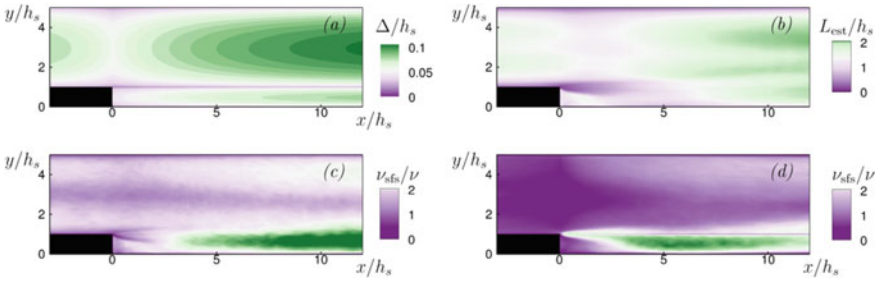


**Fig. 4** SFS quantities for the backward-facing step flow. **a** Filter size; **b** integral scale; **c** eddy viscosity, local ILSA model; **d** eddy viscosity, dynamic Lagrangian model. Intermediate grid, 384 × 150 × 96 points

flow has small scale features, i.e., in the boundary layers and near the shear layers. Away from these locations, $L$ increases as the typical scales that need resolving become larger. The structured character of the grid implies that a refined mesh is used in regions where the turbulent eddies are not small, for instance downstream of the step, $x/h_s \simeq 5$–$10$ and $y/h_s \simeq 1$. As a consequence, the Lagrangian eddy viscosity has an unphysical sharpness along the region where the grid is refined (Fig. 4d), which

is not observed when the local ILSA model is used (Fig. 4c). Such large variations in the local filter-width are linked to commutator errors [30, 31]. By allowing a smooth variation of the eddy-viscosity/filter-width, these commutator errors can largely be removed [32, 33].

## 5 Concluding Remarks

We discussed recent progress in the assessment of the reliability of LES predictions. The basic limitation in LES quality stems from an interplay between on the one hand effects of discretization errors and on the other hand modeling error. This can be clarified comprehensively in terms of a computed error-landscape in which the total simulation error is computed as function of spatial resolution and model coefficient. A key concept in dynamic error control for LES is 'sub-filter activity'. Adhering to a description that keeps the measure for the sub-filter activity near a pre-specified target value, allows some level of control over the dominant LES errors.

The ILSA model requires little extra computational overhead and yields close agreement with DNS and experimental reference material for backward-facing step flow. The main model innovation, implies using the local integral length scale to represent changes in the local flow physics. Much of the non-uniform variations in the turbulence properties is already reflected in changes in the integral length scale—the rest of the eddy-viscosity definition is less sensitive to flow details and was found to yield a natural adaptation of the sub-filter model to the flow.

The local ILSA model holds promise to be effective in LES also for wider classes of turbulent flow. Further studies to underpin this should include stronger variations in flow properties, including re-laminarization. Moreover, investigating the role of the target value for the sub-filter activity level on the reliability of the LES predictions and the convergence with spatial resolution are items of ongoing research toward a genuine error-bar for CFD.

## References

1. Smagorinsky, J.: General circulation experiments with the primitive equations. I. The basic experiment. Mon. Weath. Rev. **91**, 99–164 (1963)
2. Schumann, U.: Subgrid scale model for finite difference simulations of turbulent flows in plane channels and annuli. J. Comput. Phys. **18**, 376–404 (1975)
3. Pope, S.B.: Turbulent Flows. Cambridge University Press (2000). ISBN 978-0521598866
4. Geurts, B.J.: Elements of Direct and Large-Eddy Simulation. R.T. Edwards Inc. (2003). ISBN 978-1930217072
5. Piomelli, U., Rouhi, A., Geurts, B.J.: A grid-independent length scale for large-eddy simulations. J. Fluid Mech. **766**, 499–527 (2015)
6. Rouhi, A., Piomelli, U., Geurts, B.J.: Dynamic subfilter-scale stress model for large-eddy simulations. Phys. Rev. Fluids **1**(4), 044401 (2016)

7. Boersma, B.J., Kooper, M.N., Nieuwstadt, T.T.M., Wesseling, P.: Local grid refinement in large-eddy simulation. J. Eng. Math. **32**(2–3), 161–175 (1997)
8. Geurts, B.J., Fröhlich, J.: A framework for predicting accuracy limitations in large-eddy simulation. Phys. Fluids **14**(6), L41–L44 (2002)
9. Geurts, B.J., Meyers, J.: Successive inverse polynomial interpolation to optimize Smagorinsky's model for large-eddy simulation of homogeneous turbulence. Phys. Fluids **18**(11), 118102 (2006)
10. Vogel, J.C., Eaton, J.K.: Combined heat transfer and fluid dynamic measurements downstream of a backward-facing step. ASME J. Heat Transfer **107**(4), 922–929 (1985)
11. Germano, M., Piomelli, U., Moin, P., Cabot, W.H.: A dynamic subgrid-scale eddy viscosity model. Phys. Fluids A **3**(7), 1760–1765 (1991)
12. Geurts, B.J., Holm, D.D.: Regularization modeling for large-eddy simulation. Phys. Fluids **15**(1), L13–L16 (2003)
13. Bardina, J., Ferziger, J.H., Rogallo, R.S.: Improved subgrid scale models for large-eddy simulation. AIAA Paper 80-1357 (1980)
14. Geurts, B.J.: Balancing errors in LES, direct and large-eddy. Simulation **III**, 1–12 (1999)
15. Nicoud, F., Baggett, J.S., Moin, P., Cabot, W.H.: Large eddy simulation wall-modeling based on suboptimal control theory and linear stochastic estimation. Phys. Fluids **13**, 2968–2984 (2001)
16. Van der Bos, F., Van der Vegt, J.J.W., Geurts, B.J.: A multi-scale formulation for compressible turbulent flows suitable for general variational discretization techniques. Comput. Methods Appl. Mech. Eng. **196**(29–30), 2863–2875 (2007)
17. Geurts, B.J., Van der Bos, F.: Numerically induced high-pass dynamics in large-eddy simulation. Phys. Fluids **17**(12), 125103 (2005)
18. Meyers, J., Geurts, B.J., Sagaut, P.: A computational error-assessment of central finite-volume discretizations in large-eddy simulation using a Smagorinsky model. J. Comput. Phys. **227**(1), 156–173 (2007)
19. Meyers, J., Geurts, B.J., Baelmans, M.: Database analysis of errors in large-eddy simulation. Phys. Fluids **15**(9), 2740–2755 (2003)
20. Meyers, J., Meneveau, C., Geurts, B.J.: Error-landscape-based multiobjective calibration of the Smagorinsky eddy-viscosity using high-Reynolds-number decaying turbulence data. Phys. Fluids **22**(12), 125106 (2010)
21. Vreman, B., Geurts, B.J., Kuerten, H.: Discretization error dominance over subgrid terms in large eddy simulation of compressible shear layers in 2D. Commun. Numer. Methods Eng. **10**(10), 785–790 (1994)
22. Meyers, J., Sagaut, P., Geurts, B.J.: Optimal model parameters for multi-objective large-eddy simulations. Phys. Fluids **18**(9), 095103 (2006)
23. Geurts, B.J.: Interacting errors in large-eddy simulation: a review of recent developments. J. Turbul. N55 (2006)
24. Geurts, B.J.: How can we make LES fulfill its promise? In: Advances in LES of Complex Flows, pp. 13–32 (2002)
25. Geurts, B.J.: Mixing efficiency in turbulent shear layers. J. Turbul. **2**(17), 1–23 (2001)
26. Van der Bos, F., Geurts, B.J.: Computational error-analysis of a discontinuous Galerkin discretization applied to large-eddy simulation of homogeneous turbulence. Comput. Methods Appl. Mech. Eng. **199**(13–16), 903–915 (2010)
27. Klein, M., Meyers, J., Geurts, B.J.: Assessment of LES quality measures using the error landscape approach. In: Quality and Reliability of Large-Eddy Simulations, pp. 131–142 (2008)
28. Piomelli, U., Geurts, B.J.: A grid-independent length scale for large-eddy simulations of wall-bounded flows. In: Leschziner, M.A., Bontoux, P., Geurts, B.J., Launder, B.E., Tropea, C. (eds.) Proceedings of 8th International Symposium Engineering Turbulence Modelling and Measurements—ETMM8, pp. 226–231 (2010)
29. Meneveau, C., Lund, T.S., Cabot, W.H.: A Lagrangian dynamic subgrid-scale model of turbulence. J. Fluid Mech. **319**, 353–385 (1996)

30. Van der Bos, F., Geurts, B.J.: Commutator errors in the filtering approach to large-eddy simulation. Phys. Fluids **17**(3), 035108 (2005)
31. Vanella, M., Piomelli, U., Balaras, E.: Effect of grid discontinuities on large-eddy simulation statistics and flow fields. J. Turbul. **9** (2008)
32. Van der Bos, F., Geurts, B.J.: Lagrangian dynamics of commutator errors in large-eddy simulation. Phys. Fluids **17**(7), 075101 (2005)
33. Geurts, B.J., Holm, D.D.: Commutator errors in large-eddy simulation. J. Phys. A Math. Gen. **39**(9), 2213 (2006)

# Hydrodynamics of Cylinders Oscillating with Small Amplitude in Still Fluid or Free Stream


**Efstathios Konstantinidis and László Baranyi**

**Abstract** In the present study, we conducted numerical simulations of the two-dimensional viscous flow around a harmonically oscillating cylinder in a still fluid or transverse to a free stream at a Keulegan–Carpenter number of 0.5, a Stokes number of 200 and varying ratios of the free-stream velocity to the maximum oscillation velocity. The unsteady force in the direction of motion obtained from the simulations in still fluid is in excellent agreement with the analytical solutions of Stokes and Wang that are pertinent to attached flow around the cylinder. We demonstrate that the analytical solutions are valid also in separated flows occurring for corresponding cylinder oscillations transverse to a free stream for velocity ratios up to 2.0. At a velocity ratio of 5.0, the hydrodynamic force exhibits substantial deviations from the theoretical force due to the increased level of the fluctuations induced by the vortex shedding in the wake. These findings indicate that the 'inviscid potential force' due to the irrotational flow is embedded in the general viscous flow. However, we find that the hydrodynamic force in the streamwise direction exhibits fluctuations at twice the frequency of oscillation; interaction between the no-slip boundary condition and the potential of the irrotational flow around the cylinder seems likely to be the reason behind this phenomenon.

**Keywords** Flow-structure interaction · Unsteady flow · Laminar flow · Flow separation · Wake

E. Konstantinidis (✉)
Department of Mechanical Engineering, University of Western Macedonia, 50132 Kozani, Greece
e-mail: ekonstantinidis@uowm.gr

L. Baranyi
Department Fluid and Heat Engineering, University of Miskolc, Miskolc-Egyetemváros 3515, Hungary



M. Braza et al. (eds.), *Advances in Critical Flow Dynamics Involving Moving/Deformable Structures with Design Applications*, Notes on Numerical Fluid Mechanics and Multidisciplinary Design 147,
https://doi.org/10.1007/978-3-030-55594-8_6

## 1 Introduction

The design of structures involving moving and/or deformable members in a flow environment calls for a sound understanding of their interactions with the surrounding fluid. Several applications may be found in aeronautical, civil, mechanical, naval, and ocean engineering where flow-structure interaction can occur. Often, concepts such as added mass, fluid damping, or even fluid stiffness are incorporated in simplified models employed to predict the response of compliant structural members. In this context, a critical point on which there is some discussion among researchers is whether the hydrodynamic force acting on an oscillating structure can be segregated into distinct contributions due to the above fluid actions. For instance, a decomposition of the hydrodynamic force is often employed to justify the addition of the *virtual mass* (or *added mass*) to the mass of the structure in dealing with the equation of motion of a body undergoing vortex-induced vibration [11]. Our interest here is flows around oscillating bluff bodies, which are characterized by separation and unsteadiness even at low Reynolds numbers. In view of the complexity of unsteady separated flows, we will restrict our attention to two-dimensional flows around oscillating circular cylinders, for which few theoretical results and a rich literature exist.

The problem of an oscillating pendulum in still fluid was considered first by Stokes [13] who presented a solution assuming that the amplitude of oscillation is small and the flow is two-dimensional, laminar, and attached. Later, Wang [14] used the method of inner and outer expansions and also obtained analytical expressions for the stream function and the 'drag coefficient', which represents the dimensionless resistance force of the fluid to the cylinder motion. The total hydrodynamic force, $\boldsymbol{C} = \boldsymbol{C}_f + \boldsymbol{C}_p$, includes the contribution due to skin friction, $\boldsymbol{C}_f$, and due to pressure, $\boldsymbol{C}_p$. For a circular cylinder harmonically oscillating along an axis with amplitude $A$ and frequency $f$, with displacement given by $\xi(t) = A\cos(2\pi f t)$ as a function of time $t$, $C_f$ can be expressed as a series expansion in powers of $\beta^{-1/2}$,

$$C_f = \frac{2\pi^2}{K_C}\left\{\left[(\pi\beta)^{-1/2} + \frac{1}{4}(\pi\beta)^{-3/2}\right]\cos(2\pi\tau) + \left[(\pi\beta)^{-1/2} + (\pi\beta)^{-1} - \frac{1}{4}(\pi\beta)^{-3/2}\right]\sin(2\pi\tau)\right\}, \tag{1}$$

while $C_p$ can be expressed as

$$C_p = \frac{\pi^2}{K_C}\cos(2\pi\tau) + C_f, \tag{2}$$

where $\beta = fD^2/\nu$ is the Stokes number, $K_C = 2\pi A/D$ is the Keulegan–Carpenter number, $\tau = ft$ is the dimensionless time, $D$ is the diameter of the cylinder, and $\nu$ is the kinematic viscosity of the fluid. The forces have been normalized by $0.5\rho DU_{\max}^2$, where $U_{\max} = 2\pi fA$ is the maximum velocity of the cylinder.

Wang's solution differs from Stokes solution only in the $(\pi\beta)^{-3/2}$ terms and both yield very close results for practical purposes. Both solutions are valid in the limit of $K_C \ll 1$ and $\beta \gg 1$. It can be seen that $C_f$ has components opposing both the acceleration and velocity of the cylinder and that the pressure force includes a term equal to the skin friction. The first term of $C_p$ is the force "due to the inviscid, potential flow" and "can be identified as the drag caused by the 'virtual mass' of the cylinder" [14]. Thus, the effect due to the viscosity in the terms involving $\beta$ can be segregated from the contribution from the inertial effect due to the *virtual mass* under the said assumptions, i.e. that the flow remains two-dimensional, laminar, and unseparated. This may be also viewed as a decomposition of the flow into irrotational ('potential') and rotational ('vortex') components, i.e. $C = C_{inviscid} + C_{vortex}$ as discussed by Lighthill [8]. A key question is if such decomposition is meaningful and/or appropriate in more general viscous flows with separation.

The analytical solutions of Stokes and Wang provide the velocity and vorticity around an oscillating body in the entire flow domain and thereby the hydrodynamic forces. We will collectively refer to them as 'S–W theory', which is used as a reference case in the present study. In particular, we will verify the analytical result in Eqs. (1) and (2) against numerical solutions for a circular cylinder oscillating at low amplitude and high frequency in still fluid. At the same time, we will examine the effect of adding a free stream of constant velocity normal to the direction of oscillation on the flow field and on the hydrodynamic forces and thereby assess the range of validity of S–W theory. Our ultimate goal is to check whether the total hydrodynamic force can be decomposed into potential and vortex components and what is the appropriate potential of the flow associated with a cylinder oscillating transverse to a free stream in view of some recent theoretical analyses [6, 9].

## 2 Methodology

The full Navier–Stokes equations for incompressible flow in two dimensions were solved using an in-house code based on the finite difference method [1–3]. The equations are expressed in the velocity-pressure scheme in dimensionless form. The physical flow domain is bounded by two concentric circles with logarithmically-spaced cells in the radial direction. For the results reported in this paper, the outer radius of the physical domain is 160 times the radius of the cylinder in order to minimize numerical blockage effects and improve accuracy. The number of nodes in the final grid is 361 by 292 in the peripheral and radial directions, respectively. The physical domain is transformed into a rectangular computational domain with equi-spaced cells. The finite difference method is used for the solution of the governing equations in the transformed plane. Spatial derivatives are approximated by 4th order central differences except for the convective terms for which a 3rd order modified upwind scheme is used. The pressure Poisson equation is solved by the successive over-relaxation (SOR) method. The Navier–Stokes equations are integrated explicitly and continuity is enforced. The instantaneous force acting on the cylinder is computed

at each time step by suitable integration of the pressure and skin friction around the cylinder periphery. Initial tests for the dependence of the results on the grid resolution and time step indicated that the integrated pressure and shear stress forces converged to the third significant digit.

## 3 Results and Discussion

The results that will be presented in the following sections correspond to a cylinder oscillating with fixed parameters $K_C = 0.5$ and $\beta = 200$.

### *3.1 Instantaneous Flow Patterns and Distributions*

Figure 1 shows the flow patterns around the oscillating cylinder in terms of vorticity contours and streamlines for different values of the parameter $\gamma$, i.e. the ratio of the velocity of the free stream to the maximum velocity of the cylinder. The vorticity has been normalized by $D/U_{\max}$. The instantaneous fields shown in Fig. 1 correspond to the top-most position of the cylinder during its oscillation. For the case without the free stream, $\gamma = 0$, the flow remains attached and the vorticity is concentrated in onion layers of oppositely-signed vorticity around the cylinder whereas the rest of the flow is nearly irrotational. The superposition of a free stream transverse to the direction of oscillation causes the flow to separate from the sides of the cylinder and vortex shedding occurs in the wake ($\gamma = 1$, 2 and 5). It should be noted here that the Reynolds number based on the free stream velocity $Re = \gamma K_C \beta$ is above the threshold for the onset of vortex shedding. As $\gamma$ increases, the vorticity layers around the cylinder become thicker due to the increased generation of vorticity on the wall induced by the free stream. It should be mentioned that the frequency of cylinder oscillation is much higher than the frequency of vortex shedding under the prevailing conditions; thus, the vortex-wake patterns do not exhibit any strong synchronization with the oscillation of the cylinder. For all cases with and without the free stream, the vorticity at the back half of the cylinder surface is covered by a thin layer of positive vorticity. On the other hand, substantial differences can be observed in the distributions of vorticity at the front half of the cylinder surface for different $\gamma$ values.

It is known that the vorticity and the vorticity gradient on the wall determine the force exerted on the body [7, 12]. For example, the transverse hydrodynamic force $C_y$, i.e. in the direction of motion, can be calculated from the formula

$$C_y = -\frac{1}{Re}\int_0^{2\pi}\left[\left(\frac{\partial\omega}{\partial r}\right)_w - \omega_w\right]\cos\theta d\theta + \frac{\pi}{2}\ddot{y}, \tag{3}$$

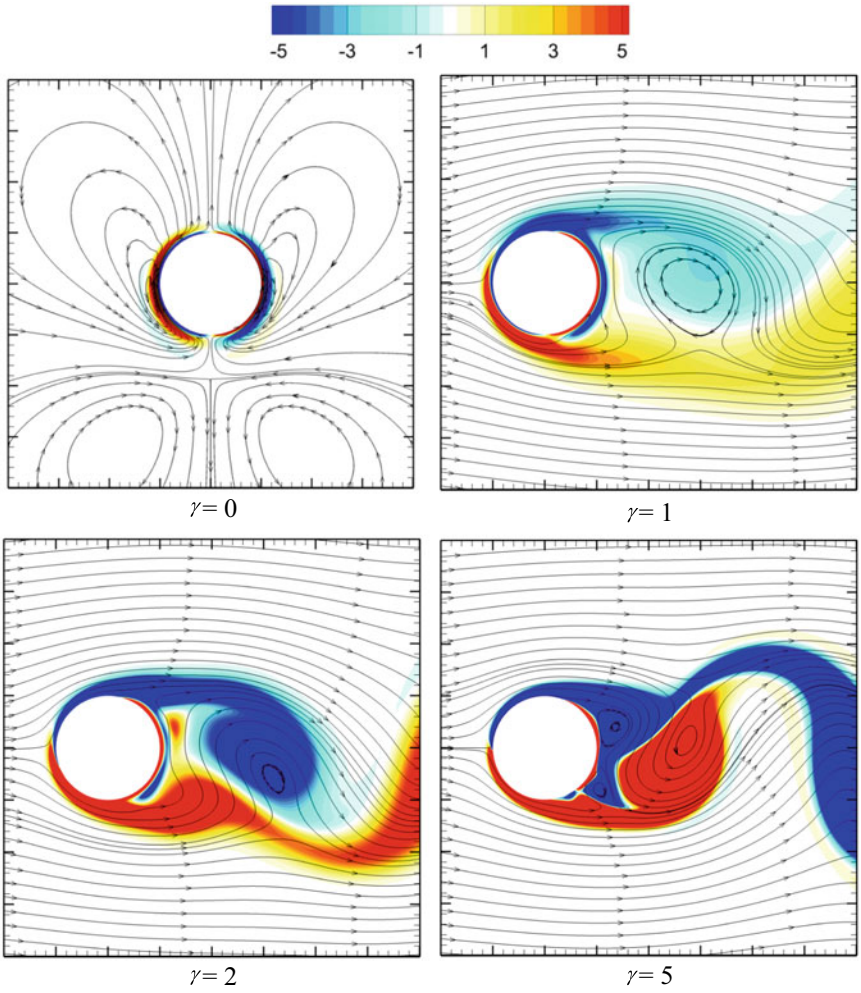


**Fig. 1** Iso-vorticity contours and streamlines around cylinders oscillating harmonically in a still fluid or transverse to a free stream ($K_C = 0.5$, $\beta = 200$). The length and velocity scales employed for normalization respectively are the cylinder diameter $D$ and the maximum velocity of the cylinder $U_{max}$, which are common for all cases shown

where $\omega$ is the vorticity, $r$ is the radial distance from the origin of the reference system, $\theta$ is the angle measured anticlockwise from the downstream $x$ direction, $\ddot{y}$ is the acceleration of the cylinder, and the subscript 'w' indicates values at the wall. The Reynolds number appearing in Eq. (3) is based on the maximum cylinder velocity and the diameter of the cylinder when other variables are normalized with the same scales. The first term in the integral is solely associated with the contribution of the pressure whereas the second term includes two equal contributions from pressure and shear stress (note that the contribution of the wall vorticity to the pressure force

does not appear in [7, 12], i.e. the second term in the integral differs by a factor of 2 here). From Eq. (3), it might be anticipated that $C_y$ is substantially affected by the addition of the free stream.

In Fig. 2, we examine the peripheral distributions of the wall vorticity $\omega_w$, the radial gradient of the vorticity at the wall $(\partial\omega/\partial r)_w$, and the pressure coefficient, $p$, around the cylinder. Generally, the magnitude of $(\partial\omega/\partial r)_w$ is nearly two orders of magnitude larger than $\omega_w$, which indicates that the integrated force $C_y$ is dominated by the pressure force. Furthermore, it can be seen that the velocity ratio $\gamma$ has a marked effect on the peripheral distributions of the wall vorticity and its radial gradient at the wall. It can be verified from Fig. 2 that the effect is more pronounced at the front half of the cylinder, $180° < \theta < 360°$. However, the distribution of the pressure coefficient $p$ is not too substantially affected except for the highest $\gamma = 5$ value. This illustrates that the net effect on the integrated force may be relatively weak despite the large changes in the distribution of vorticity and its radial gradient at the wall as a function of the velocity ratio $\gamma$.

### *3.2 Time-Histories of Forces*

Figure 3 shows the time histories of the hydrodynamic force in the $y$ direction, $C_y$, for different velocity ratios $\gamma$ computed from the numerical simulations in comparison to S–W theory. According to the theory, the force in the direction of oscillation depends only on $K_C$ and $\beta$, which remain the same for all cases shown ($K_C = 0.5$ and $\beta = 200$). It can be seen that the numerical results are in excellent agreement with S–W theory for the case of a cylinder oscillating in still fluid (Fig. 3a). For the other cases with the free stream, the time-history of $C_y$ is very similar to that in still fluid and in very good agreement with theory for $\gamma = 1$ (Fig. 3b), $C_y$ exhibits minor modulations from the regular theoretical oscillation for $\gamma = 2$ (Fig. 3c), whereas $C_y$ displays major deviations from theory for $\gamma = 5$ (Fig. 3d). The results shown in Fig. 3 confirm that the effect of the free stream on the integrated force is relatively weak for small values of the velocity ratio.

Figure 4 shows the time histories of the transverse force due to pressure, $C_{py}$. Comparing Figs. 3 and 4, we can see that the time histories of the pressure force are very similar to those of the total force and that the pressure force contributes approximately 90% of the total in all cases. Figure 4 also includes the theoretical forces due to the pressure as well as due to the 'inviscid potential flow'. The potential force comprises most of the pressure force in all cases except for the highest velocity ratio of $\gamma = 5$. In this case, there are substantial deviations between the potential and pressure forces, which might be attributed to the 'vortex force' (see Introduction). It is interesting to note that the vortex force must have a negative contribution when the total force becomes lower than the potential force over some finite periods (see Fig. 4d). The above observations contradict the hypothesis that the potential force depends on the velocity ratio as suggested in [6].

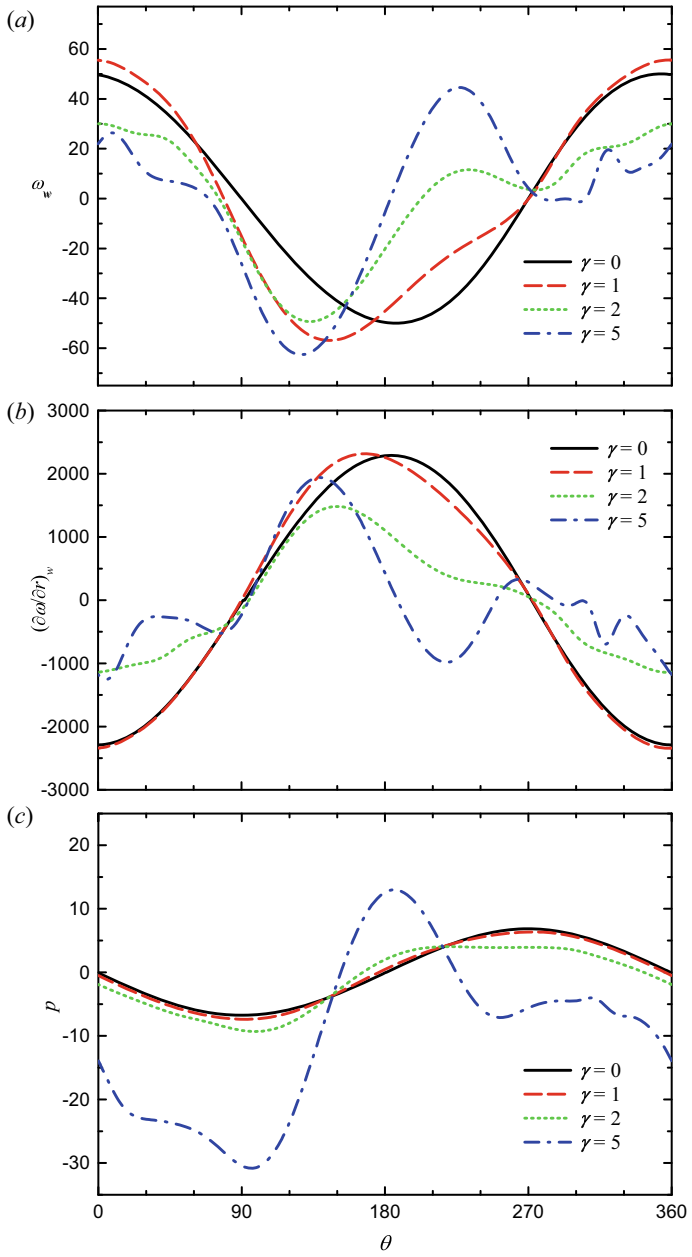


**Fig. 2** Peripheral distributions of the **a** normalized vorticity, **b** normalized vorticity gradient, and **c** pressure coefficient on the cylinder wall for different $\gamma$ values

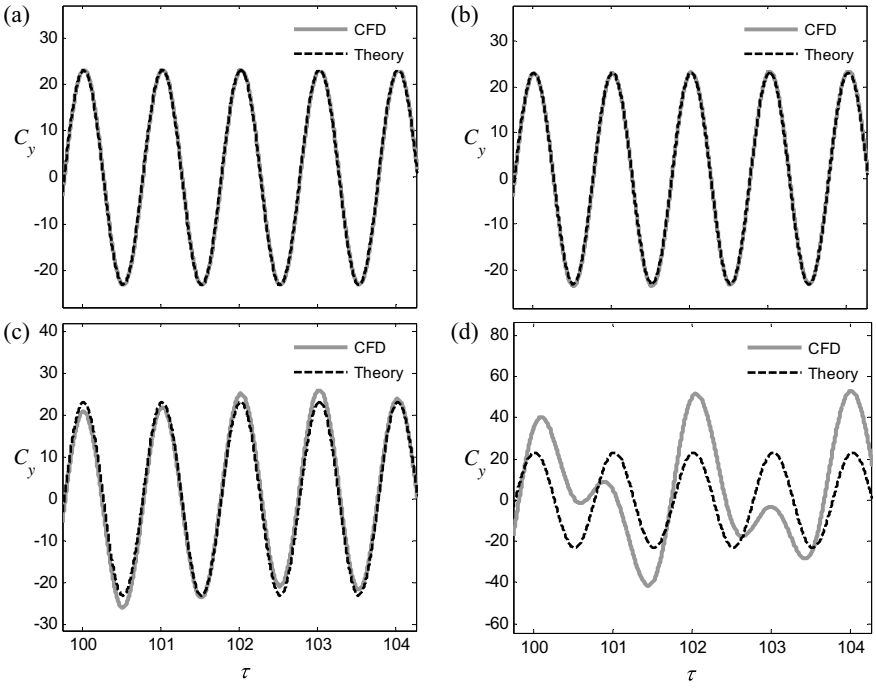


**Fig. 3** Time histories of the total force $C_y$ on a cylinder oscillating transverse to a free stream for **a** $\gamma = 0$, **b** $\gamma = 1$, **c** $\gamma = 2$, **d** $\gamma = 5$

The time-histories of the force in the streamwise $x$ direction, $C_x$, for different velocity ratios $\gamma$ are illustrated in Fig. 5. For the case without the free stream, there is no force acting in the direction transverse to the oscillation of the cylinder since the flow remains symmetrical with respect to the $y$ axis. On adding a free stream in the $x$ direction, a drag force arises due to the flow separation and the formation of a wake behind the cylinder as shown in Fig. 1. The unsteady flow in the wake due to vortex shedding induces fluctuations in $C_x$ as might be expected. The time-averaged mean drag increases with $\gamma^2$ since forces have been normalized by the maximum velocity of the cylinder. An interesting point is that the root-mean-square magnitude of the fluctuating drag also increases with $\gamma^2$ attaining values an order of magnitude higher than those for non-oscillating cylinders at corresponding Reynolds numbers (based on the free stream velocity).

It is clear from Fig. 5 that there is a component of the streamwise force at twice the oscillation frequency for the cases with the free stream. This component is evident and dominant at $\gamma = 1$ (Fig. 5b) but becomes masked at higher velocity ratios due to the increase in the magnitude of the force fluctuations at the vortex shedding frequency (Fig. 5c, d). An interesting question is whether this component is associated with changes solely in the vortex dynamics, or not. Since there is no component of the cylinder's acceleration in the streamwise $x$ direction, we hypothesize that the

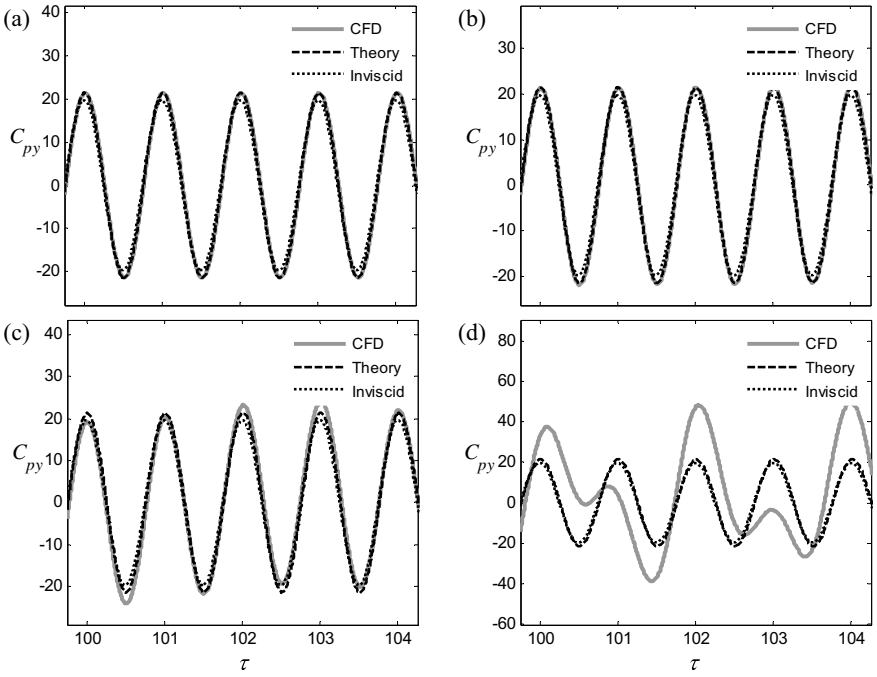


**Fig. 4** Time histories of the pressure force on a cylinder oscillating transverse to a free stream for **a** $\gamma = 0$, **b** $\gamma = 1$, **c** $\gamma = 2$, **d** $\gamma = 5$

component of $C_x$ at the oscillation frequency results through an interaction with the potential flow. This interaction can only be effected by the no-slip condition on the surface, which is not taken into account in the classical formulation of the 'inviscid potential flow' around a cylinder. Joseph et al. [5] have elaborated on the concept of 'viscous potential flow' in several cases but not including the present case of a circular cylinder undergoing harmonic oscillation transverse to a free stream. It should be noted that the formulation of the added mass in [6] allows for the enforcement of the no-slip condition on the cylinder wall.

In Fig. 6, we present spectra of the velocity fluctuations in the wake and the forces on the cylinder in order to exemplify the origin of the forces. Results are shown for the highest velocity ratio of $\gamma = 5$, which exhibits relatively more complex behaviour. The spectrum of the streamwise velocity displays a main peak that corresponds to the frequency of vortex shedding at a Strouhal number of 0.22 (note that in Fig. 6 the frequency axes have been normalized by $U_\infty/D$). There are several other minor peaks in the velocity spectrum that are integer combinations of the frequency of vortex shedding and the frequency of cylinder oscillation, which also appears as a distinct peak at 0.40. The $C_y$ spectrum has only two main peaks at the vortex shedding and oscillation frequencies. The spectrum of the component of the vortex force in the $y$ direction, computed as $C_{vortex,y} = C_y - C_{inviscid}$, is very similar to that of $C_y$,

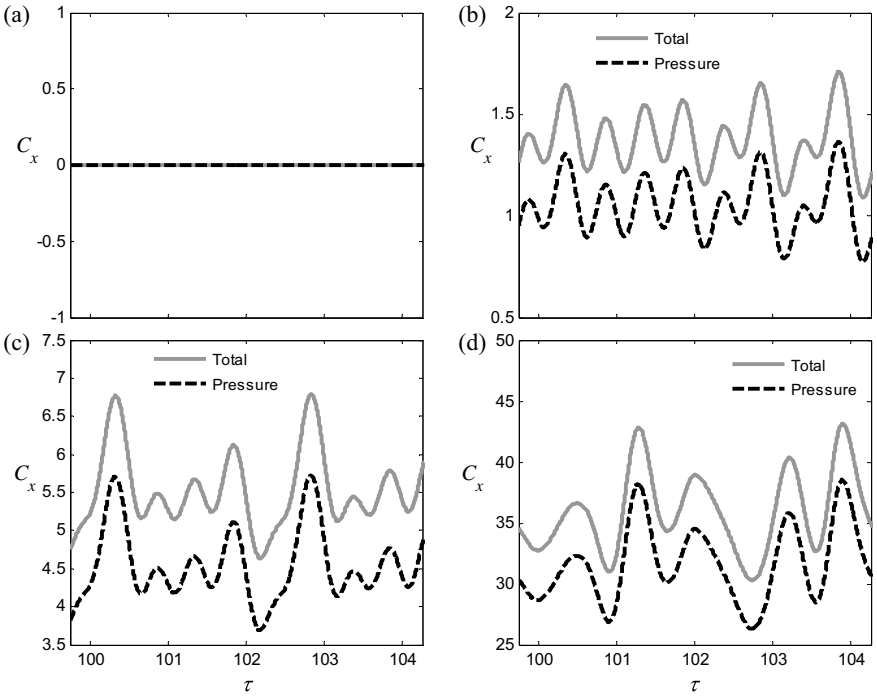


**Fig. 5** Time histories of the total streamwise force on a cylinder oscillating transverse to a free stream for **a** $\gamma = 0$, **b** $\gamma = 1$, **c** $\gamma = 2$, **d** $\gamma = 5$

indicating that the contribution from the inviscid potential flow is still embedded in the vortex force, i.e. potential and vortex components are not independent. On the other hand, the $C_x$ spectrum displays several distinct peaks that have been labelled on the plot. The most prominent peak appears at 0.44, which is twice the frequency of vortex shedding. This may be expected as alternating vortex shedding frequency at some frequency induces fluctuations in the drag force at twice that frequency. The other main peaks in the $C_x$ spectrum are integer combinations of the vortex shedding and oscillation frequencies. There is also a peak at 0.8 that corresponds to twice the oscillation frequency, which also indicates that the oscillation in the $y$ direction induces an additional component to the force in the $x$ direction. This issue deserves further consideration. It may be further examined using the decomposition developed by Chang [4] (see also [10]) which separates and quantifies the contributions of the potential flow and vortex flow to the force exerted on the cylinder. Some preliminary work along this direction, which is not included here due to space limitations, supports the argument that the classical formulation of the inviscid potential of the flow around the cylinder with slip velocity cannot account for the integrated force.

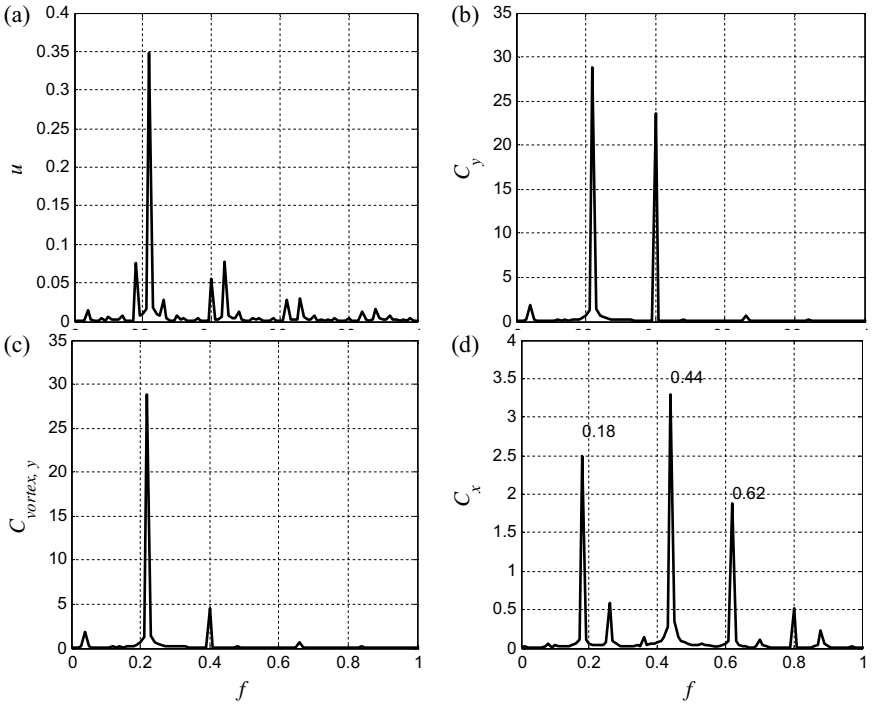


**Fig. 6** Spectra of **a** velocity fluctuations in the wake, $u$, **b** total transverse force, $C_y$, **c** vortex force, $C_{vortex,\ y}$, **d** streamwise force, $C_x$, for $\gamma = 5$, $K_C = 0.5$, and $\beta = 200$

## 4 Concluding Remarks

In the present study, we conducted numerical simulations of the two-dimensional viscous flow around a circular cylinder oscillating in a still fluid or transverse to a free stream at low amplitude and high frequency. We show that the unsteady force in the direction of motion agrees well with the analytical solutions of Stokes and Wang not only in attached flow around a cylinder oscillating in otherwise still fluid, the case for which the theory is valid, but also in separated flows for corresponding oscillations transverse to a free stream. This behaviour is clear at low values of the ratio of the free-stream velocity to the maximum oscillation velocity up to 2.0 but becomes masked at a velocity ratio of 5.0 due to the increasing contribution of the vorticity generated at the cylinder wall via the free stream. Finally, we found that the oscillation of the cylinder in the transverse direction induces an additional component to the force in the streamwise direction, which appears to be associated with the effect of the potential viscous flow around a circular cylinder oscillating in a free stream through the no-slip boundary condition.

**Acknowledgements** The second author gratefully acknowledges the support of the European Union and the Hungarian State, co-financed by the European Regional Development Fund in the framework of the GINOP-2.3.4-15-2016-00004 project, aimed to promote the cooperation between the higher education and the industry. The research was also supported by the EFOP-3.6.1–16-00011 "Younger and Renewing University—Innovative Knowledge City—institutional development of the University of Miskolc aiming at intelligent specialisation" project implemented in the framework of the Széchenyi 2020 program. The realization of these two projects is supported by the European Union, co-financed by the European Social Fund.

## References

1. Baranyi, L.: Computation of unsteady momentum and heat transfer from a fixed circular cylinder in laminar flow. J. Comput. Appl. Mech. **4**, 13–25 (2003)
2. Baranyi, L.: Lift and drag evaluation in translating and rotating non-inertial systems. J. Fluids Struct. **20**, 25–34 (2005)
3. Baranyi, L.: Numerical simulation of flow around an orbiting cylinder at different ellipticity values. J. Fluids Struct. **24**, 883–906 (2008)
4. Chang, C.C.: Potential flow and forces for incompressible viscous flow. Proc. R. Soc. Lond. A **437**, 517–525 (1992)
5. Joseph, D., Funada, T., Wang, J.: Potential Flows of Viscous and Viscoelastic Fluids. Cambridge University Press (2008)
6. Konstantinidis, E.: Added mass of a circular cylinder oscillating in a free stream. Proc. R. Soc. A **469**, 20130135 (2013)
7. Koumoutsakos, P., Leonard, A.: High-resolution simulations of the flow around an impulsively started cylinder using vortex methods. J. Fluid Mech. **296**, 1–38 (1995)
8. Lighthill, J.: Fundamentals concerning wave loading on offshore structures. J. Fluid Mech. **173**, 667–681 (1986)
9. Limacher, E., Morton, C., Wood, D.: Generalized derivation of the added-mass and circulatory forces for viscous flows. Phys. Rev. Fluids **3**, 014701 (2018)
10. Martín-Alcántara, A., Sanmiguel-Rojas, E., Fernandez-Feria, R.: On the development of lift and drag in a rotating and translating cylinder. J. Fluids Struct. **54**, 868–885 (2015)
11. Païdoussis, M.P., Price, S.J., de Langre, E.: Fluid-Structure Interactions: Cross-Flow-Induced Instabilities. Cambridge University Press (2011)
12. Shiels, D., Leonard, A., Roshko, A.: Flow-induced vibration of a circular cylinder at limiting structural parameters. J. Fluids Struct. **15**, 3–21 (2001)
13. Stokes, G.G.: On the effect of the internal friction of fluids on the motion of pendulums. Trans. Cambridge Philos. Soc. **9**, 8–106 (1851)
14. Wang, C.Y.: On high-frequency oscillating viscous flows. J. Fluid Mech. **32**, 55–68 (1968)

# Validation of Coupled CFD-CSM Methods for Vibration Phenomena in Nuclear Reactor Cores


**Angel Papukchiev, Peter Pandazis, Hristo Hristov, and Martina Scheuerer**

**Abstract** Today modern 3D computational fluid dynamics (CFD) and computational structural mechanics (CSM) codes are coupled to predict the interaction between fluids and solids. Within the scope of this work the multiphysics codes ANSYS CFX-MOR and ANSYS CFX-Mechanical are validated against the Vattenfall Rod Vibration Experiment data. The experimental setup consists of a Plexiglas test section with a slender stainless steel rod in the middle, which is pulled and then released. The calculated time dependent rod vibration amplitude in water and air environments with different fluid velocities is compared with measured data. The analyses show that the nature of the vibrations for the cases with flowing fluid is well predicted, while underestimation of the vibration amplitude and phase shift are observed in the cases with stagnant flow.

**Keywords** Vibration · Reactor core · Coupled CFD-CSM · Damping · Validation

## 1 Introduction

Under certain conditions flow-induced vibrations (FIV) might develop in nuclear power plant steam generators, reactor core, or other components. These phenomena could potentially damage some of the barriers for the safe enclosure of the radioactive inventory, and therefore, need to be analyzed carefully. In nuclear power plant (NPP) engineering, FIV analyses are mainly relevant for the design of the steam generator (SG) and the reactor core. The primary side of the SG consists of tube bundles, which are cooled by the secondary side water. In certain conditions, depending on fluid velocity, tube geometry and tube fixing amongst others, the secondary water may excite tube vibrations. As a consequence, repeating tube bending may lead to increased material fatigue and eventually damage [6, 12]. FIV may also occur in

A. Papukchiev (✉) · P. Pandazis · H. Hristov · M. Scheuerer
Gesellschaft für Anlagen- und Reaktorsicherheit (GRS) gGmbH, Boltzmannstraße 14, 85748 Garching, Germany
e-mail: angel.papukchiev@grs.de



M. Braza et al. (eds.), *Advances in Critical Flow Dynamics Involving Moving/Deformable Structures with Design Applications*, Notes on Numerical Fluid Mechanics and Multidisciplinary Design 147,
https://doi.org/10.1007/978-3-030-55594-8_7

reactor cores. Numerical investigations of fuel assembly vibrations in older VVER-440 reactor generation can be found in the literature [5]. The vibrations might be induced by pressure fluctuations in the control assembly channels and non-linear forces resulting from the mechanical contact of these elements with the channel walls. Earthquakes and loss-of-coolant accidents could also introduce external loads leading to structural vibrations in NPPs [7].

In the past the occurrence and the stability of FIV were investigated with the help of empirical correlations [2, 3]. Today modern 3D CFD programs are coupled with CSM tools to allow an accurate fluid structure interaction (FSI) analysis of FIV. Since this might be very expensive concerning CPU time, model order reduction (MOR) techniques are used to provide results at lower computational cost. ANSYS has developed such MOR and coupled it to the CFD program ANSYS CFX [1]. Within the scope of this work FSI simulations of the Vattenfall Rod Vibration Experiment [7–9] were performed and the results were compared with experimental data in order to validate these multiphysics programs.

## 2 Vattenfall Rod Vibration Experiment

### *2.1 Experimental Facility and Instrumentation*

The Vattenfall experimental facility consists of a closed piping loop with a square Plexiglas test section (80 mm × 80 mm), see Fig. 1. In the center of the test section a slender, rectangular stainless steel rod (cross section dimensions: 20 mm × 8 mm, and length L = 1500 mm with a fixed bottom-end and pinned top-end) is placed. A mechanism pulls the rod with a line fixed in its center. The line is then abruptly cut in a controlled and precise way by a sharp knife, which allows for a well-defined rod release. The free rod vibration constitutes to a large extent a harmonic, periodic

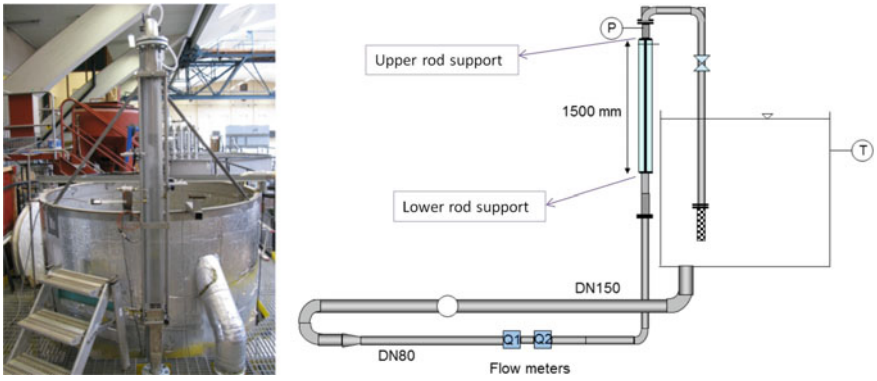


**Fig. 1** Vattenfall experimental facility

oscillation. This experiment was performed in air and water environments at different inlet mass flow rates and temperatures. Two laser distance meters are positioned at different heights on each side of the rod in order to verify the fundamental vibration mode. These measure the rod position as a function of time with a temporal resolution in the order of milliseconds and a spatial resolution of the order of 25 μm. The sampling frequency used was 1 kHz [8, 9].

### *2.2 Experimental Test Cases*

Four different test cases were performed in the experiment. Measurements in stagnant air and water were initially performed. In the subsequent two tests, the water bulk velocity at the inlet of the test section was set to be 1.0 m/s and then 3.0 m/s, see Table 1. Before each experiment the pulling mechanism displaced the rod center 10 mm away from its normal position. Several repetitions were performed for the same test case and test conditions, proving the repeatability of the experimental results [8].

## 3 CFD-CSM Multiphysics Simulation Methods

Two CFD-CSM multiphysics simulation methods were used for the vibration analyses in this work: ANSYS CFX-MOR and ANSYS CFX-Mechanical.

The goal of the MOR is to describe the static or dynamic responses of the mechanical system in a fast and accurate way. ANSYS has developed such model and coupled it to the CFD program ANSYS CFX. It is based on the mode-superposition method, which uses the natural frequencies and mode shapes generated from a modal analysis to characterize the dynamic response of a structure to transient or steady harmonic excitations [1]. Since the MOR model is a simplification of the mechanical system, it is important to remember that FSI simulations with ANSYS CFX-MOR are subject to some restrictions. The approach is valid for cases with linear dynamics and this implies moderate displacements, small strains, linear contacts and linear material behavior (no plasticity) [4].

**Table 1** Vattenfall experimental test cases

| Fluid | Bulk velocity (m/s) | Fluid temperature (°C) | Initial displacement (mm) |
|---|---|---|---|
| Air | 0 | 13.4 | 10 |
| Water | 0 | 11.3 | 10 |
| Water | 1 | 7.4 | 10 |
| Water | 3 | 11.6 | 10 |

For the second simulation approach ANSYS CFX and ANSYS Mechanical were coupled. In the current work the ANSYS Multi-field Solver (MFX), available for a large class of coupled analysis problems, is used. In the MFX solver, a "field solver" is each running instance of the different codes. These field solvers are coupled using stagger loops. The stagger loop allows for implicit coupling of the fields in the MFX solution. Within each step in the time step loop, the field solutions are repeated in a stagger loop until convergence is reached. In the presented analyses 5 stagger iterations were performed, and the total amount of ANSYS CFX iterations within one time step was around 50. The aforementioned restrictions, relevant for the ANSYS CFX-MOR approach do not apply here. Large displacements, strains and non-linear material behavior can be considered during FSI simulations with ANSYS CFX-Mechanical.

## 4 Modal Analysis with ANSYS Mechanical

Before the modal analysis with ANSYS Mechanical, the geometry and material data of the stainless steel rod were prepared for the structural program. The symmetric geometry allowed the utilization of a half rod model (in longitudinal direction). Approximately 9700 elements were used to generate an unstructured mesh for the 1500 mm long rod. Further refinement had no remarkable effect on the results. The lower end of the rod was fixed in $x$, $y$, $z$ directions, while the pinned, upper end of the rod was fixed only in $x$ and $y$ directions, thus allowing it to move in the axial $z$ direction.

The modal analysis was performed for six modes. The mode shapes, frequencies and the total mesh displacement for each node in $x$, $y$ and $z$ directions were extracted and used as input for ANSYS CFX-MOR code. For the current analysis the first mode is the most important one. This is due to the fact that the rod mainly vibrates in its first mode. The calculated natural frequency of *12.37 Hz* agrees well with the experimental result of *12.30 Hz*, as reported by Lundquist [9]. Table 2 provides information on the calculated eigenfrequencies.

**Table 2** Calculated eigenfrequencies

| Mode number | Calculated eigenfrequency (Hz) |
|---|---|
| First mode | 12.37 |
| Second mode | 40.09 |
| Third mode | 83.63 |
| Fourth mode | 142.97 |
| Fifth mode | 218.09 |
| Sixth mode | 308.96 |

# 5 Model Development and Boundary Conditions

## *5.1 CFD-CSM Model*

The CAD geometry of the complete test section, provided by Vattenfall (Fig. 2), was imported in DesignModeler in order to simplify the 3D model for the analyses. The geometry between the flow straightener and the upper rod support structure was extracted from the CAD model and then exported in the ICEM CFD meshing software. Because of the test section construction symmetry and in order to speed up the very expensive in terms of CPU time simulations, only half of the simplified geometry was meshed.

Good initial mesh quality is essential for the quality of the FSI results. During a FSI calculation mesh deformation might occur (like in the presented analyses). This directly affects the mesh quality during the simulation run by changing important mesh parameters (min. orthogonality angle, expansion factor, aspect ratio, etc.). For example, increasing the aspect ratio through mesh deformation might negatively affect the CFD solver convergence and lead to instability and other numerical issues. Therefore, the OECD CFD Best Practice Guidelines [11] were followed in the mesh generation process. A structured hexahedral mesh of the test section fluid domain was generated with ICEM CFD. This mesh was systematically refined and grid sensitivity studies were performed. The selected final mesh for the FSI simulations consisted of 276.540 elements (Fig. 3). The overall mesh quality is high: 62° min. orthogonality angle, expansion factor—2, and aspect ratio—3.

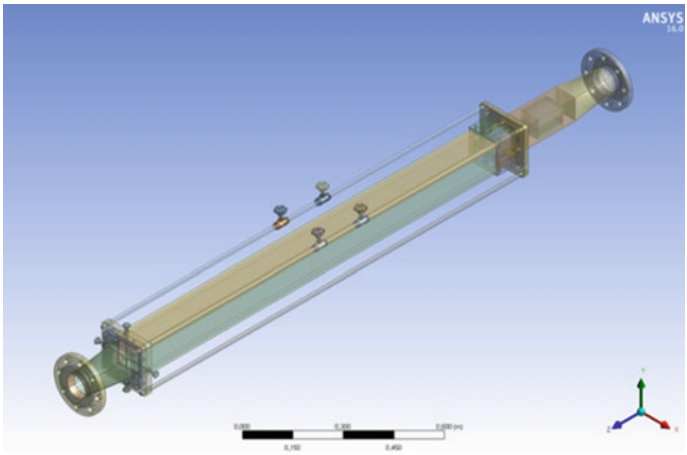


**Fig. 2** CAD model of the test section

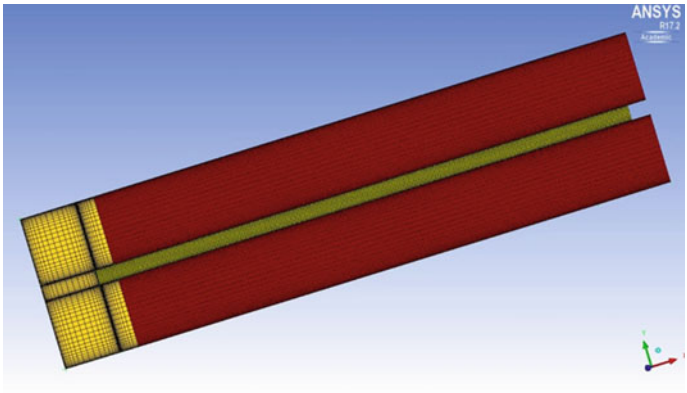


**Fig. 3** Numerical mesh of the simplified test section

### *5.2 Simulation Setup and Boundary Conditions*

For the CFD simulations IAPWS IF97 water material data were used from the ANSYS CFX material libraries. The CFD simulations were isothermal, because all Vattenfall experiments were performed at constant fluid temperatures. The vibrating rod was produced of stainless steel 304 [8]. For the discussed vibration simulations the most important rod material properties are the Young's modulus (193 GPa), the density (8000 kg/m$^3$), and the poisson ratio (0.3).

## 6 Simulation Results

### *6.1 Analysis*

At the beginning steady state calculations were performed with ANSYS CFX-MOR. In these the rod was pre-stressed and pulled to its initial displacement position. The results from the steady state calculations were then used for the initialization of the transient ANSYS CFX-MOR simulations, in which at $t = 0\ s$ the pre-stressed rod is abruptly released and starts to vibrate.

Figure 4, left, shows the velocity distribution in the CFD domain for the initial pre-stressed steady state ($t = 0\ s$) of the $u = 3\ m/s$ water case. Figure 4, right, represents the same parameter at the end of the simulation ($t = 3\ s$) when the rod stands still. In both figures the water flows in the positive $z$ direction (from right to the left). A flat velocity profile is specified at the test section inlet for two reasons: the first is the lack of measured inlet data; the second is the absence of the flow straightener in the

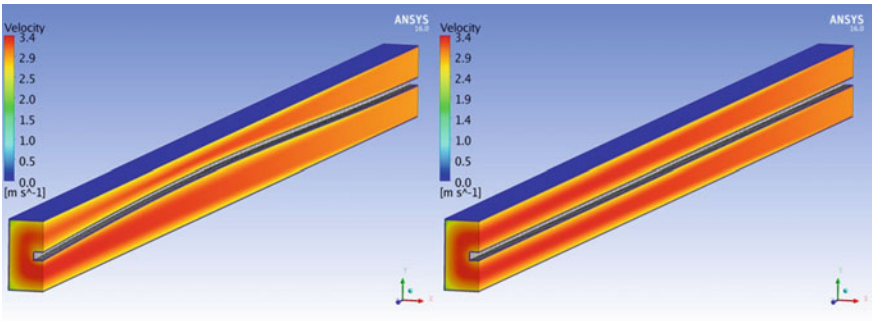


**Fig. 4** Velocity distribution in the CFD domain at $t = 0\ s$ (left) and $t = 3\ s$ (right)

CFD model, which is positioned several *cm* upstream the inlet. In both figures the maximum water velocity of approx. 3.4 m/s is reached at the test section outlet.

At the test section inlet, 5% turbulence intensity was specified for the cases with flowing water. The other initial and boundary conditions can be found in Table 1. For the numerical transport of the quantities (velocity, temperature, etc.) through the solution domain a High Resolution advection scheme was used. The SST turbulence model [10] was selected for the calculations. For the time discretization a Second Order Backward Euler scheme was chosen. Sensitivity studies on the time step size revealed strong dependence of the simulation results on the step size. It was found that it has significantly larger effect on the vibration amplitude than on the vibration frequency. The studies showed that reducing the time step size below 5E−5 s does not have noticeable impact on the numerical results, and hence, this value was used in the presented simulations. The highest RMS Courant number observed in all calculations was 0.1.

The simulation results are displayed as a time dependent vibration amplitude starting from the initial pre-stressed position and ending when the rod comes at rest. Three figures with the calculated rod vibration amplitude as a function of simulation time are shown for each case. This is done with different scales to allow direct and fair comparison with data. A very good agreement between measurement and experiment can be found for the water case with $u = 3\ m/s$ (see Figs. 5, 6 and 7). Not only the amplitude, but also the vibration frequency is predicted well by ANSYS CFX-MOR. Although simulation results almost overlap with data, small phase shifts can be observed in the second part of the results. The negligible phase shift is a result of the deviation of the predicted natural frequency ($12.37\ Hz$) from the experimental one ($12.30\ Hz$).

The next calculated experimental run was the $u = 1\ m/s$ water case (see Figs. 8, 9 and 10). The first part of the transient was predicted well by the coupled code (see Fig. 9), while after $t = 2\ s$ the vibration amplitude was underestimated. Although the absolute underestimation is just 0.3 mm, the predicted vibration amplitude (magenta line in Fig. 10) is lower by approx. 75% from the measured one. Additional studies

were performed to understand this deviation. Different boundary conditions, turbulence models, advection and transient schemes, symmetry assumptions, time step sizes, etc. were tested without any success. In a last try to improve the results, a mesh refinement procedure was carried out, although the used mesh (276.540 elements) proved to provide mesh independent results. It turned out that increasing the number of elements to 1.6 million had a significant influence on the vibration amplitude (orange line in Fig. 10) in the time frame $2.0 < t < 3.0$ *s*. The analysis reveals that the coupled simulations became mesh-sensitive for small vibration amplitudes cases and low physical damping. The new amplitude deviates from the experiment by less than 15% (0.06 mm). The mesh independence studies were performed for the $u = 3$ *m/s* case, and obviously, were not valid for the other cases. Further refinement could not improve the results for any of the experimental cases. Even a wall-resolved Large Eddy Simulation with Smagorinsky subgrid-scale model on a refined mesh (7 million elements, $y+ < 1$) did not show different vibration characteristics. Therefore, all forthcoming results, presented in Figs. 11, 12, 13, 14, 15 and 16, were produced with the 1.6 million mesh.

Figures 11, 12 and 13 show the results for the $u = 0$ *m/s* water case. In the first part of the transient ANSYS CFX-MOR correctly predicts the amplitude and the frequency of the rod vibration. With increasing simulation time the code starts to underestimate the rod displacement and hence the vibration amplitude. This is clearly seen in Fig. 13, which shows the time interval $2.5 < t < 3.0$ *s*. The predicted amplitude by ANSYS CFX-MOR is approx. 30% smaller than the measured value, but the absolute value of this underestimation is just 0.2 mm. It is important to mention, that in the late phase of the transient a slight phase shift develops, which is a result of the deviation between predicted and calculated natural vibration frequency.

Figures 14, 15 and 16 show the computational results for the air test case. The vibration amplitude and frequency are higher, compared to the water cases, because of the different air fluid properties, that lead to a different, smaller added mass effect. The significantly lower fluid density is responsible for the lower damping of the rod vibration, and therefore, shorter period. Although the first part of the experiment is well captured by ANSYS CFX-MOR (see Fig. 15), after $t = 2$ *s* the deviation between data and simulation increases. In Fig. 16 the phase shift at $t = 6$ *s* is almost half period and the amplitude is 25% (or ~1.5 mm) lower than the measured value.

ANSYS CFX-Mechanical simulations were performed only for this test case, because of two main reasons: the very high computation time needed (more than a month on 14 processors for 2.5 s simulation time) and the fact, that the air case appears to be the most challenging for prediction by the codes. The same ANSYS Mechanical and ANSYS CFX models were used, as with the simplified FSI approach. Unfortunately, the expensive coupled calculations with ANSYS CFX-ANSYS Mechanical ("MFX" curve) could not further improve the numerical results. The vibration amplitude is comparable to the ANSYS CFX-MOR one, the significant phase shift is also present.

Measured and calculated frequencies for all Vattenfall cases are shown in Table 3. An excellent agreement with data is observed, except for the air case.

**Table 3** Measured and predicted frequencies

| Case | Measured frequency (Hz) | Predicted frequency (Hz) |
|---|---|---|
| $u_{water} = 0$ m/s | 10.52 | 10.62 |
| $u_{water} = 1$ m/s | 10.64 | 10.63 |
| $u_{water} = 3$ m/s | 10.66 | 10.68 |
| $u_{air} = 0$ m/s | 12.17 | 12.51 |

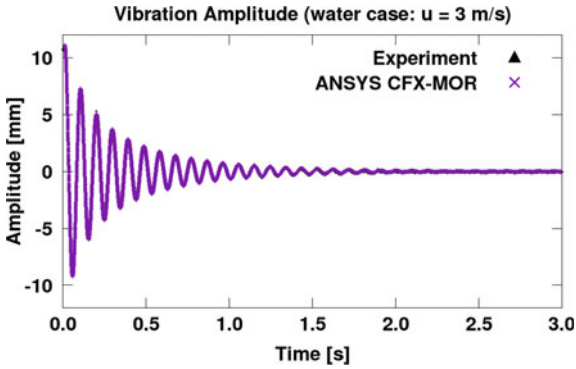


**Fig. 5** Vibration amplitude ($u_w = 3$ m/s), complete result

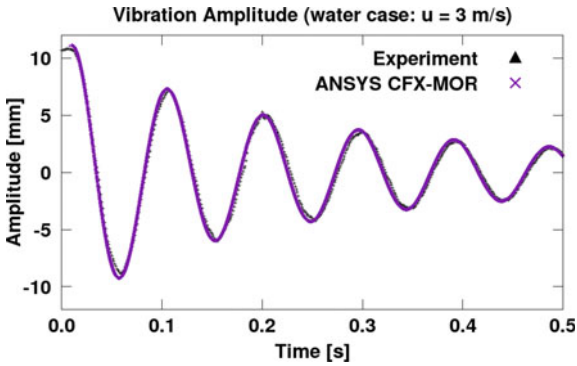


**Fig. 6** Vibration amplitude ($u_w = 3$ m/s), first part

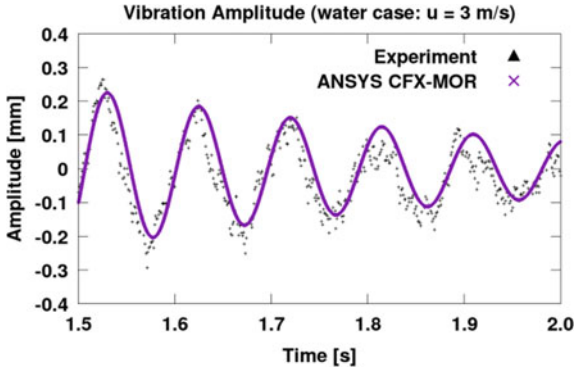


**Fig. 7** Vibration amplitude ($u_w = 3$ m/s), second part

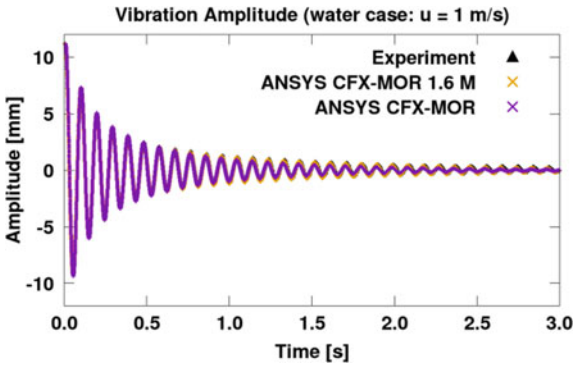


**Fig. 8** Vibration amplitude ($u_w = 1$ m/s), complete result

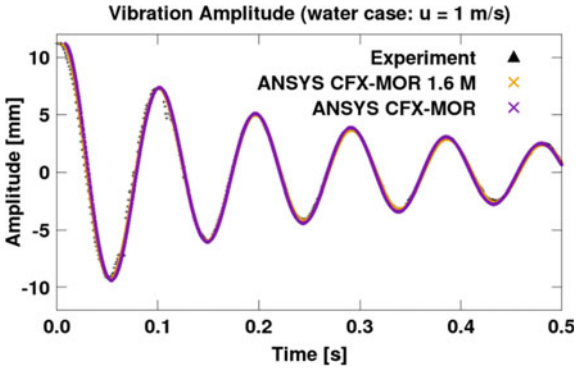


**Fig. 9** Vibration amplitude ($u_w = 1$ m/s), first part

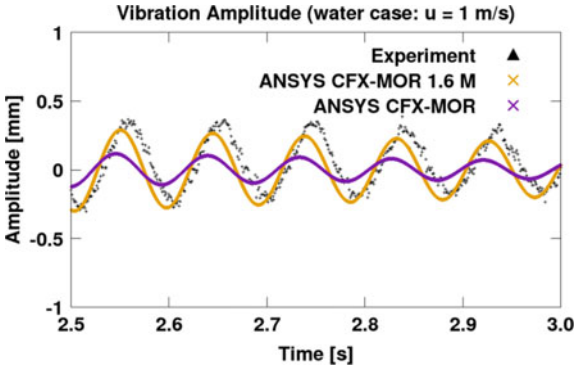


**Fig. 10** Vibration amplitude ($u_w = 1$ m/s), second part

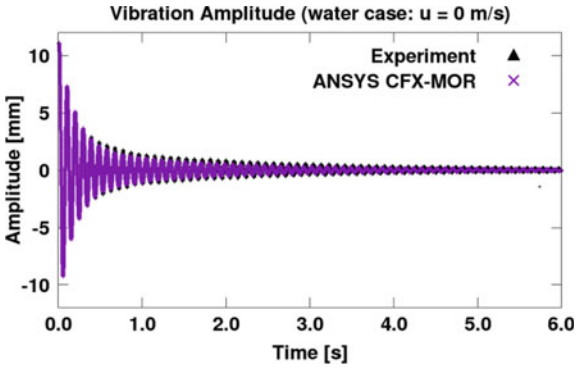


**Fig. 11** Vibration amplitude ($u_w = 0$ m/s), complete result

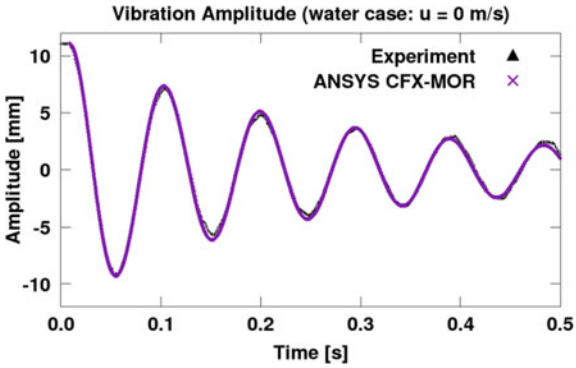


**Fig. 12** Vibration amplitude ($u_w = 0$ m/s), first part

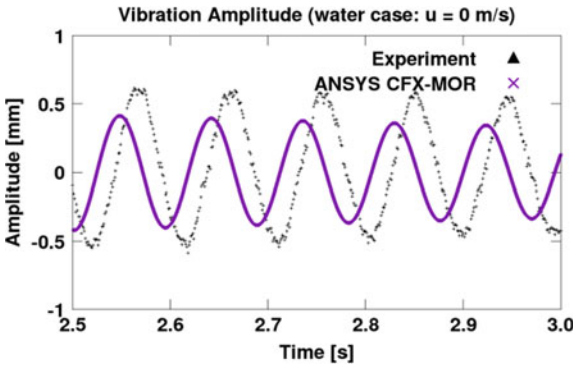


**Fig. 13** Vibration amplitude ($u_w = 0$ m/s), second part

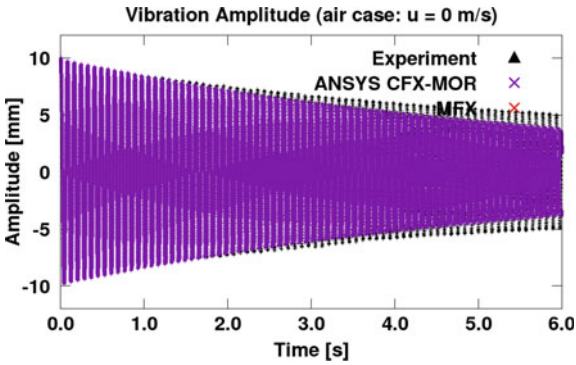


**Fig. 14** Vibration amplitude ($u_a = 0$ m/s), complete result

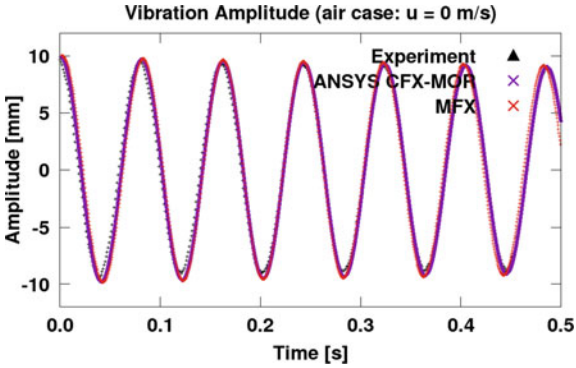


**Fig. 15** Vibration amplitude ($u_a = 0$ m/s), first part

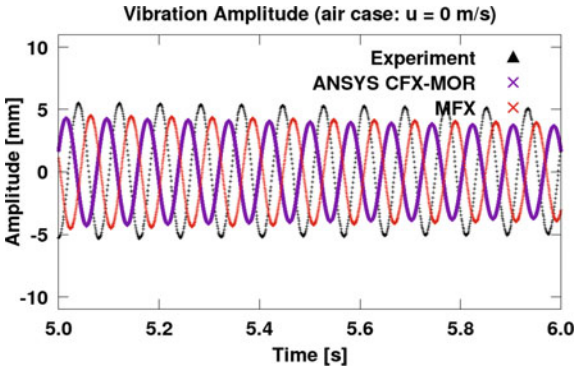


**Fig. 16** Vibration amplitude ($u_a = 0$ m/s), second part

## 6.2 Possible Explanations for the Observed Results

There might be several reasons for the damping overestimation, seen in Figs. 13, 14 and 16. The largest deviations observed are 30% (stagnant water case) and 25% (stagnant air case). The overall damping in the coupled simulation is the sum of the physical damping and the damping introduced by the code numerics. Important for the physical damping is the correct representation of the structural damping and the added mass effect. The structural damping may be considered as a sliding friction mechanism between molecular layers in the rod, in which the friction force is proportional to the displacement from the rest position [13]. The added mass effect represents the force acting on the moving steel rod as a consequence of the surrounding fluid acceleration/deceleration. The fundamental eigenfrequency of *12.37 Hz,* calculated with the modal analysis (ANSYS Mechanical), agrees very well with the measured one—*12.30 Hz.* Furthermore, in all simulations the same structural input data was used. These two facts lead to the conclusion, that the possible reason for the deviations should not be related to the structural part of the simulation. An incorrect representation of the added mass in stagnant flow conditions by the CFD code is more probable.

Another possible explanation might be too high numerical damping. Generally, the numerical damping should be very small compared to the physical. In the $u = 3$ *m/s* case the ratio between physical and numerical damping is significantly higher than in the $u = 0$ *m/s case*. Therefore, in a simulation with low physical damping the effect of the numerical damping on the vibration amplitude might become more obvious. On the other hand the air case has the lowest physical damping (very low fluid density, stagnant flow conditions) and the results deviate less from data, in comparison to the $u = 0$ *m/s* water case. It is important to emphasize, that for the water cases, the lower the physical damping, the larger the deviations from experimental data are (compare deviations in Figs. 7 and 13).

Other sources of uncertainty are the CFD boundary conditions. At stagnant flow conditions in- and outflow might occur at the test section boundaries as a result from the rod movement. Opening boundary conditions were specified at both boundaries and different combinations of boundary physical parameters (velocity-pressure; pressure-pressure) were tested. All efforts led to the presented results. Perhaps the piping with all bends and additional structures up- and downstream the test section also need to be modelled in order to get proper feedback at the test section boundaries. This, of course, needs larger modelling and CPU effort. The 3D simulations with stagnant fluid were also performed with a full model to check the influence of the symmetry assumption on the results, but no significant effects were observed.

Although the influence of the turbulence modelling on the results was already briefly discussed, it should be stressed out that the treatment of the turbulence in the stagnant fluid cases is challenging. Before the initiation of the vibration the fluid is at rest, and for such flow conditions the utilization of turbulence models is not appropriate. On the other hand, immediately after the rod release turbulence is

generated, which requires the use of a turbulence model. Neither LES, nor hybrid URANS-LES calculations could improve the results for the stagnant flow cases.

Finally, it was found that the simplifications introduced by the MOR approach do not affect the vibration parameters in the presented test cases. An extensive simulation of the air case with ANSYS CFX-Mechanical led to very similar numerical results. It required 5–6 times more CPU effort than the ANSYS CFX-MOR calculation.

## 7 Conclusions

The understanding of FIV is important for the safety evaluation of nuclear facilities. Such phenomena may lead to structural damage or component lifetime shortening. To analyze, predict, and avoid potential vibration problems, validated 3D advanced numerical tools based on CFD methods are required. GRS performed validation simulations with ANSYS CFX-MOR for four Vattenfall experiments. The air test case was simulated with ANSYS CFX-Mechanical. The analyses showed that ANSYS CFX-MOR predicts accurately the nature of the vibrations (amplitude, frequency, phase) for the cases with flowing water. The results for the cases with stagnant water and air agreed well with data only in the first transient part. Thereafter, the vibration amplitude is underestimated by the codes, which indicates an increased damping in the calculations. Moreover, a phase shift develops as a result from the difference between calculated and measured vibration frequency. Several possible reasons for the amplitude deviations were identified: incorrect prediction of the added mass effect in stagnant flow conditions by the codes; increased numerical damping in the simulations; lack of detailed boundary conditions. It was found that the simplifications introduced by the MOR approach do not affect the vibration parameters in these particular test cases. This simulation approach appeared to be quite more efficient than the fully coupled ANSYS CFX-Mechanical code system, that provided very similar results.

**Acknowledgements** The authors would like to acknowledge the kind support of Eric Lillberg from Vattenfall Sweden and Johannes Einzinger from ANSYS Germany. The work described in this contribution contains selected results of the research project no. RS1540 carried out on behalf of the German Federal Ministry for Economic Affairs and Energy (BMWi) in the framework of the reactor research program on the basis of a decision by the German Bundestag.

## References

1. ANSYS CFX 17.2 User's Manuals (2016)
2. Blevins, R.D.: Flow-induced vibration in nuclear reactors: a review. Prog. Nucl. Energy **4**, 25–49 (1979)
3. Blevins, R.D.: Formulae for Natural Frequency and Mode Shapes. Krieger Publishing Company, New York (1979).

4. Einzinger, J., Frey, Ch.: Bi-Directional Fluid-Structure Interaction with Model Order Reduction. ANSYS, Germany (2014)
5. Hollstein, F.: Berechnung von Neutronenflußdichteschwankungen in WWER-Druckwasserreaktoren infolge strömungsinduzierter Schwingungen. FZR-110 Report (1995)
6. Kotthoff, K., et al.: Erkenntnisse aus dem Ablauf ausländischer Vorkommnisse mit Dampferzeuger-Heizrohrbruch. GRS 1984. Technische Mitteilungen **77**, Nr. 1 (1984)
7. Lillberg, E., et al.: Tailored experiments for validation of CFD with FSI for nuclear applications. In: Proceedings of the NURETH-16 Conference, Chicago, USA, 30 Aug–4 Sept 2015
8. Lundquist, G., et al.: Validation of CFD with FSI: damping of free rod vibrations. In: Proceedings of the CFD4NRS-5 Workshop, Zurich, Switzerland, 11–13 Sept 2014
9. Lundquist, G., Angele, K.: Stavvibrationsförsök. Vattenfall Report, Report Number U 13:26 (2013)
10. Menter, F.: Two-equation eddy-viscosity turbulence models for engineering applications. AIAA J. **32**, 269–289 (1994)
11. OECD/NEA: Best Practice Guidelines for the Use of CFD in Nuclear Reactor Safety Applications. NEA/CSNI/R (2007)
12. Paidoussis, M.P.: Flow-Induced Vibrations in Nuclear Reactors, Practical Experience and State of Knowledge. Springer Verlag, Berlin/Heidelber/New York (1980)
13. Richardson, M., Potter, R.: Viscous vs. structural damping in modal analysis. In: 46th Shock and Vibration Symposium, San Diego, California, 21–23 Oct 1975

# Fluid Structure Interaction Arising in Aerodynamics and Flow Control

# Control of Cellular Separation Using Adaptive Surface Structures


**Michael G. C. Garland, Matthew Santer, and Jonathan F. Morrison**

**Abstract** The three-dimensional separation that gives rise to the formation of stall cells is shown to consist primarily of two discrete frequencies. The higher is the well known vortex shedding mode. However, at frequencies roughly ten times lower, the whole cell oscillates. Both features are clearly evident in both modal decomposition of the velocity field and surface pressure spectra.

**Keywords** Three-dimensional separation · Stall cells

## 1 Introduction

We report results from an experimental investigation of the three-dimensional separation produced by a high-lift aerofoil at moderate incidence, with constant section. Mean and time-resolved measurements are made using a NASA GA(W)-1 aerofoil with $AR = 6$ at $Re = 3.5 \times 10^5$. Surface oil visualisation and stereo Particle Image Velocimetry (PIV) are used to explore the flow field. The mean topology of the flow identifies characteristic spanwise periodic behaviour, "stall cells", along the surface of the model.

Analysis of the time-dependent surface pressure shows two distinct frequencies within the flow field. The higher frequency appears at a Strouhal number, $St \approx 0.2$, representative of vortex shedding, and the typical von Kármán vortex street. The lower frequency appears at $St \approx 0.02$, observed as a global fluctuation in stall-cell extent. This lower frequency is apparent in many separated flows (such as the "flapping" motion appearing in turbulent flow separating from a backward-facing step), but in the present context, does not appear to have been previously reported. It corre-

M. G. C. Garland · M. Santer · J. F. Morrison (✉)
Department of Aeronautics, Imperial College, London SW7 2AZ, UK
e-mail: j.morrison@imperial.ac.uk



M. Braza et al. (eds.), *Advances in Critical Flow Dynamics Involving Moving/Deformable Structures with Design Applications*, Notes on Numerical Fluid Mechanics and Multidisciplinary Design 147,
https://doi.org/10.1007/978-3-030-55594-8_8

lates with widely observed low-frequency unsteadiness in the wing loading around stall. While this mode is analogous to that observed in other types of separation, here the streamwise extent of the separation varies because the flow is separating from a curved surface rather than from a sharp edge; the width of the separated region also varies.

## 2 Experimental Setup

The following experiments are conducted in a closed-circuit wind tunnel with a working section of 1.38 m $\times$ 1.22 m $\times$ 3.0 m with a contraction ratio of 4.92:1. The air is driven through a four-bladed fan with a maximum free-stream velocity of approximately 40 $ms^{-1}$. The free-stream turbulence intensity is less than 0.1% at 25 $ms^{-1}$.

The model, Fig. 1, is suspended from a drag balance in the roof of the tunnel. The mechanical nature of the drag balance makes it unsuitable for measuring the unsteady forces, generated by separation from an aerofoil. However it does provide a suitable rigid mounting point. The model is mounted in the tunnel upside-down to allow laser access through glass panels of optical quality in the floor and side wall.

The PIV laser, cameras and optics are mounted on a 3-stage linear traverse. Once aligned, this allows the light sheet and cameras to move in the same frame of reference. This enables recording of data from planes near to the model for which it would otherwise not be possible to obtain an accurate calibration. The PIV equipment was used in two arrangements to obtain different fields of view. The light sheet may enter either through the side wall, parallel to the model, with cameras arranged underneath the tunnel as shown in Fig. 1, or through the tunnel floor, perpendicular to the model chord, with cameras mounted on either side of the working section. The overlapping field of view for the cameras is 178.6 mm $\times$ 133.7 mm (spanwise $\times$ streamwise) and each 32 $\times$ 32 interrogation window corresponds to 1.1 mm $\times$ 1.1 mm.

## 3 Key Results

### *3.1 Surface Skin Friction*

For a qualitative assessment of the skin-friction lines on the wing suction surface, oil flow visualisation was conducted at a range of incidences. The experiment was run at a free-stream velocity of 25 $ms^{-1}$ and the selected incidence angle until the paraffin evaporated, fixing the skin-friction patterns.

Figure 2 shows a typical series of surface flow patterns observed over the partially-stalled incidence range. The critical points have been marked, along with the local flow directions, in each image based on the observations made during of a number of

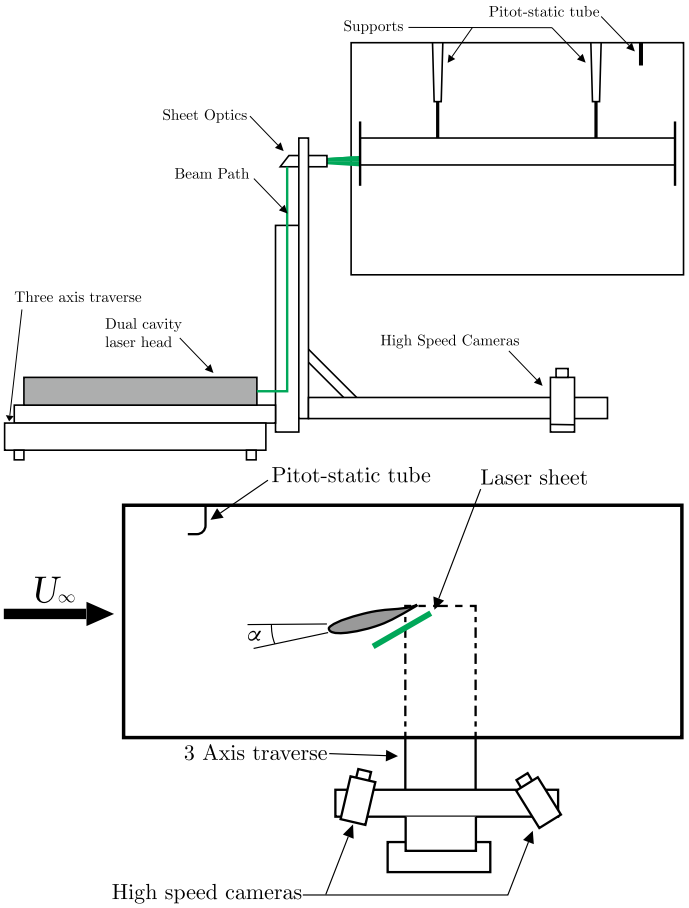


**Fig. 1** Experimental setup of the GA(W)-1 model in the Donald Campbell wind tunnel: top, downstream view; bottom, side view

experiments. A repeating series, consisting of two saddle points (marked S) and two counter-rotating foci (marked F), is observed at each incidence, indicating a periodic array of stall cells. In the regions between the Focus-Saddle-Focus structures, the undisturbed oil flow pattern is seen to continue farther along the chord toward the trailing edge than in the vicinity of the saddle point. This is particularly evident in Fig. 2e but can be observed in all cases and is indicative of regions of attached flow between the cells. As reported by previous authors the separated area within each cell is seen to increase with incidence angle.

At $\alpha = 12°$ and 16° the stall-cell positions were observed to switch between two stable states during a single run. Both states are repeatable and spatially offset by approximately half of the spanwise period. No characteristic time period was observed with each layout remaining steady for between approximately 2–30 s before

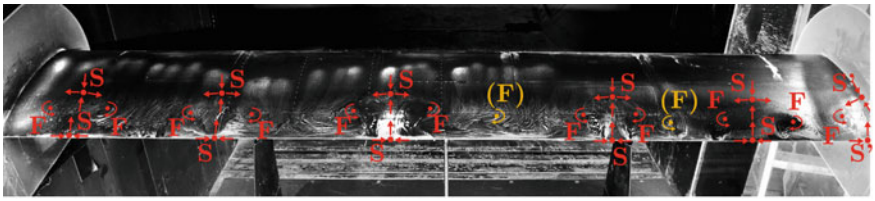


(a) 12°

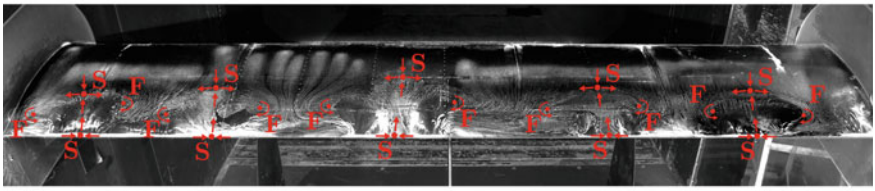

(b) 14°

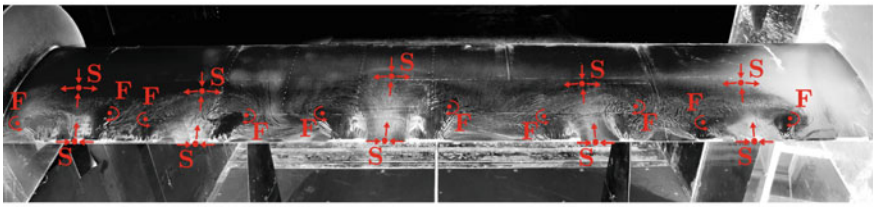

(c) 15°

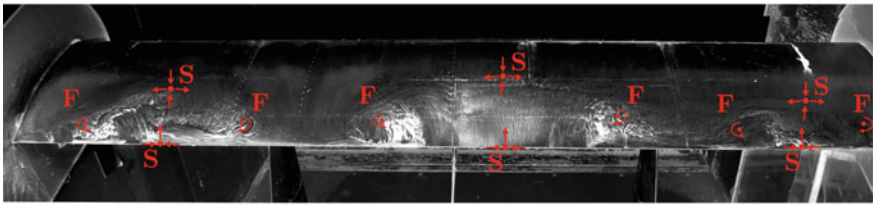

(d) 16°

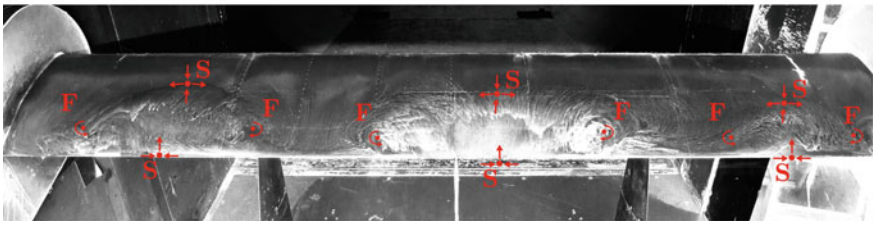

(e) 17°

**Fig. 2** Surface oil flow visualisation of the wall shear stress distribution for a NASA GA(W)-1 aerofoil at $Re \approx 3.5 \times 10^5$. Critical points are over-layed and distinguished between Saddles—S, and Foci—F

switching to the alternative topology. In Fig. 2a this is demonstrated by the isolated foci (marked in yellow) visible in the oil flow pattern.

## 3.2 Surface Pressure Spectra

Figure 3 shows the pre-multiplied energy spectra $St \cdot \Phi(St)$ distribution of surface pressure fluctuations against the corresponding Strouhal number, $St = fc\sin(\alpha)/U_\infty$. Data is presented from four spanwise positions with constant chordwise location $x/c = 0.74$, where $z_s = 0$ is the line of symmetry of the stall cell. The surface pressure was sampled at 500 Hz for 3600 s and is normalised by dynamic pressure.

While the surface pressure varies little throughout the separated region, the spectral density of the fluctuating component can be seen to vary between two distinct frequency ranges. At the centre of the cell, $z_s/c = 0$, a high-energy oscillation can be seen at frequency $St \approx 0.16$, the anticipated frequency range for von Kármán type vortex shedding. An additional oscillation is visible at a frequency an order of magnitude lower at $St \approx 0.02$, however this occurs with a significantly lower amplitude.

At measurement locations close to the edges of the cell, the magnitude of the peak at the shedding frequency decreases while that of the second, lower frequency, oscillation is seen to grow. At $z_s/c = 0.49$, the high frequency oscillation is no longer distinguishable while that at the lower frequency grows significantly. At $z_2/c = 0.63$, beyond the time-mean extent of the cell, the overall levels of fluctuation are reduced but a broad, low-frequency, signal is still visible in the spectrum. The presence of both signals within the pressure time-history at two widely separated frequencies

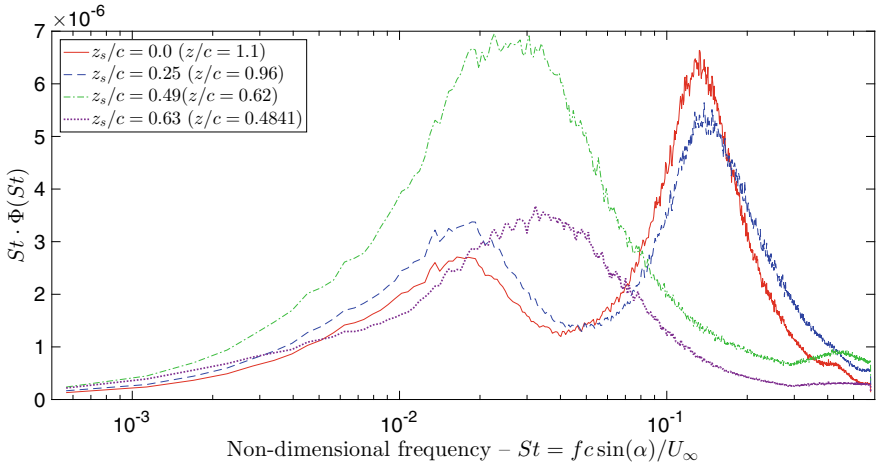


**Fig. 3** Surface pressure spectra from four spanwise positions across a stall cell, $Re = 3.5 \times 10^5$ and $\alpha = 15°$

and with varying amplitudes at $z_s/c = 0.0$ and at 0.25 indicates that the two features are independent of one another.

### 3.3 Modal Decomposition of Velocity Field

To identify velocity-field features that gives rise to the surface-pressure spectra described above, the fluctuating component of a number of velocity fields is examined by extraction of POD modes. A linear series of coefficients can be found by projecting the POD mode back onto the original vector field. In this way a time series of the relative weights of each mode may be examined in the frequency domain, so that the corresponding spectra may be calculated. The PIV frames and pressure data are sampled at the same frequency so that any features resolved by the pressure data should also be visible in the velocity data.

Decompositions have been conducted on several planes of importance within the flow field: two $(x, y)$-planes, those intersecting the saddle point and wall-normal foci, and one $(x, z)$-plane at $y_{TE} = 20$ mm. Here, data are examined for the first 10 POD modes calculated in the $(x, y)$-plane at $z_s/c = 0$. As expected, the greatest relative modal energy appears in the lowest mode, $m = 1$, for which it is approximately 30%. For higher modes, the relative modal energy decreases from 3% at $m = 2$ to 1% at $m = 6$.

Figure 4 shows the detail for the modes, $m = 1$ and then $m = 4, 5, 6$ energetic modes. For each, the vorticity distribution of the vector field for each POD mode is shown alongside the spectral content of the POD coefficients. The streamlines corresponding to the mean flow are overlaid on the vorticity contours to provide a visual reference.

In both streamwise/wall-normal planes, the most energetic modes are seen to act over the cell area. The modal coefficients relating to these large coherent variations are seen to occur at non-dimensional frequency $St \sim O(10^{-2})$. The exception to this trend is seen in mode $m = 2$ in plane $z_s/c = 0$ (not shown), where a narrow spike occurs at $St \approx 10^{-1}$. The energy in this mode is located near to the trailing edge of the aerofoil. Examination of the source images indicates that this is due to a fluctuating reflection of the laser sheet from the wing surface.

The energy content for the remaining modes is concentrated at higher frequencies, $St \sim O(10^{-1})$. The vector fields forming these modes contain coherent concentrations of vorticity with alternating sign which are significantly smaller than the mean stall cell. These are arranged along the shear layer separating the mean recirculating region and the free-stream. These structures are typical of von Kármán shedding from bluff body wakes and occur in the frequency range observed by previous authors.

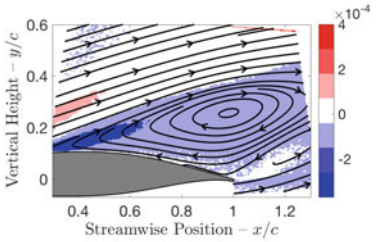


Vorticity distribution $m = 1$

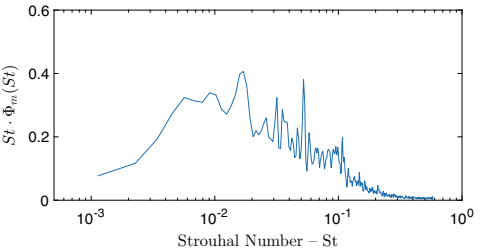


Frequency distribution $m = 1$

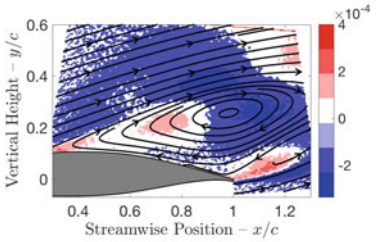


Vorticity distribution $m = 4$

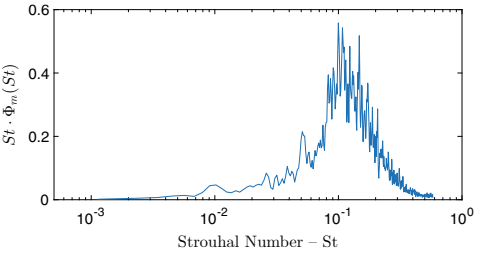


Frequency distribution $m = 4$

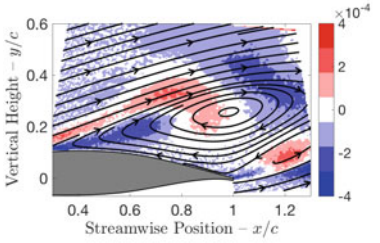


Vorticity distribution $m = 5$

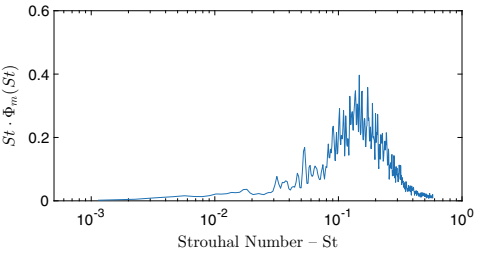


Frequency distribution $m = 5$

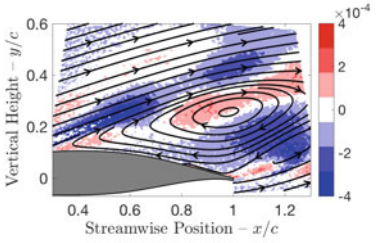


Vorticity distribution $m = 6$

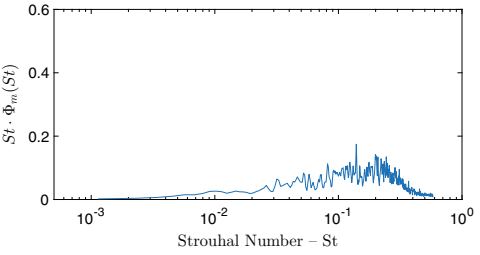


Frequency distribution $m = 6$

**Fig. 4** POD modes for $(x, y)$-plane at $z_s/c = 0$

## 4 Conclusions

We show that three-dimensional separation from a high-lift aerofoil (stall cells) comprises two discrete frequency ranges, one approximately ten times lower that normally associated with a vortex-shedding mode. This lower-frequency behaviour appears to arise as a wholesale oscillation of the stall cell. The full paper will compare the present results with the corresponding ones obtained when the surface is deformed using a point actuator comprising an adaptive device which is fully elastic in both deployment and reaction. While less effective than traditional non-retractable vortex generators, such a structure generates no parasitic drag when not required.

# Vibration Mechanism of Two Inline Cylinders


**Bin Qin, Md. Mahbub Alam, and Yu Zhou**

**Abstract** The paper presents an experimental investigation on flow-induced vibrations of two circular cylinders in tandem arrangement for spacing ratio $L/D = 1.2$–$6.0$ and reduced velocity $U_r = 3.8$–$47.8$, where $L$ is the cylinder center-to-center spacing and $D$ is the cylinder diameter. Both cylinders are allowed to vibrate in the cross-flow direction only. Extensive measurements are conducted to capture the cylinder vibration responses, surface pressures and flow fields using laser vibrometer, pressure scanner and PIV techniques. Four vibration regimes are identified based on the vibration characteristics and generation mechanism of the galloping vibration generated for the cylinders. Then the insight into the vibration generation in each regime is explored through an examination of the gap shear layer behaviour, vortex shedding process and pressure distribution around the cylinders. The gap vortices around the base surface of the upstream cylinder lead to the large vibration of the upstream cylinder. On the other hand, the gap shear layer interacts with the downstream cylinder which causes the change in the pressure distribution over the front and side surfaces, leading to the large vibration of the downstream cylinder.

**Keywords** Flow-induced vibration · Tandem arrangement · Shear layer · Vortices

## 1 Introduction

Multiple cylindrical structures are frequently involved in engineering applications. Two tandem circular cylinders is an excellent model to understand the fluid-structure interactions involved in multiple structures. Most of investigations have been performed on two fix-supported rigid circular cylinders. However, engineering structures are elastic and can be associated with violent vibrations. King and Johns

B. Qin · Md. M. Alam (✉) · Y. Zhou
Institute for Turbulence-Noise-Vibration Interaction and Control, Shenzhen Graduate School, Harbin Institute of Technology, Shenzhen, China
e-mail: alam@hit.edu.cn

Digital Engineering Laboratory of Offshore Equipment, Shenzhen, China



M. Braza et al. (eds.), *Advances in Critical Flow Dynamics Involving Moving/Deformable Structures with Design Applications*, Notes on Numerical Fluid Mechanics and Multidisciplinary Design 147,
https://doi.org/10.1007/978-3-030-55594-8_9

[1] performed experiments in a water tunnel on the free vibration of the two cylinders in two-degree-of freedoms ($L/D = 1.25$–$7.0$, $m^*\zeta = 0.051$), where $m^*$ is the mass ratio and $\zeta$ is the damping ratio. Zdravkovich [2] performed a study of two cylinder vibrations with $m^*\zeta = 50$ for $L/D = 4$. The vibration starts at $U_r \approx 50$ and ends with an amplitude of $1.7D$ at $U_r = 80$. Kim et al. [3] performed wind tunnel experiments on two tandem cylinders ($m^*\zeta = 0.65$), both free to vibrate laterally for $L/D = 1.1$–$4.2$ and $U_r = 1.5$–$26$. They observed different responses at different $L/D$. No cylinder vibrated at $1.1 \leq L/D < 1.2$ and $3.0 \leq L/D < 3.7$. Both cylinders vibrated violently at $1.2 \leq L/D < 1.6$ together with vortex excitation (VE). At $1.6 \leq L/D < 3.0$, VE was observed for both cylinders at $U_r$ smaller than that for a single isolated cylinder. At $L/D \geq 3.7$, each cylinder vibrated like an isolated cylinder. They, however, did not examine the flow structure and pressure distribution systematically; thus, the understanding of the fluid-structure interaction behind the observations was rather limited.

Despite the great progress made in the previous investigations, our understanding has yet to be greatly improved on the fluid-structure interactions involved in free vibrations on two elastic cylinders in crossflow. Many issues remain to be resolved. For example, do the amplitude of the two freely vibrating cylinders depend on each other? Under what conditions does the vibration amplitude of a cylinder overwhelm that of the other? How does the flow structure change during the vibrations? This work aims to address the above issues. A systematic experimental study is conducted on the fluid-structure interactions of two tandem cylinders that are free to vibrate laterally.

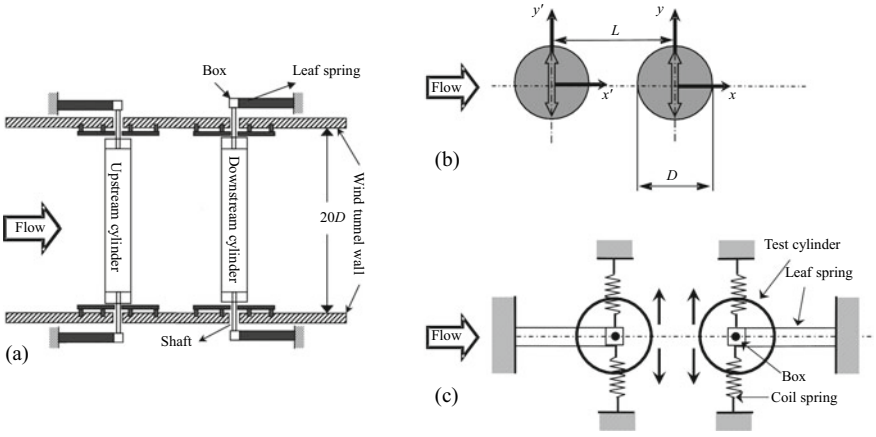


**Fig. 1** **a** Experimental setup, **b** definitions of symbols, **c** cylinder support system

## 2 Experimental Setup

Experiments were performed in a low-speed, closed-circuit wind tunnel. Figure 1 shows a schematic of the experimental setup. Both cylinders are with the diameter $D = 40$ mm, and length $l = 740$ mm. The mass ratio $m^*$ is 275. The cylinder center-to-center spacing ratios $L/D$ examined are 1.2, 1.5, 2.0, 2.5, 3.0, 4.0 and 6.0. As shown in Fig. 1, each cylinder may vibrate only laterally. End-plates are fitted on both sides of each cylinder to avoid interference/complexities caused by the cylinder support. The free-stream velocity $U_\infty$ is varied from 1.8 to 22.4 m/s, corresponding to $U_r = 3.8$–$47.8$ and Reynolds number $Re = 4.8 \times 10^3$–$6.0 \times 10^4$. The natural frequency $f_n$ is determined to be 0.0021 and the damping ratio $\zeta$ is estimated to be 11.72 Hz. Then, $m^*\zeta$ is found to be 0.58.

The flow-induced displacement signals $Y'$ and $Y$ of the upstream and downstream cylinders, respectively, are measured simultaneously using two laser vibrometers. A Dantec high-speed 2D PIV system is used to capture the flow in the gap of the cylinders and behind. The pressure around the cylinder surface was captured using a piezoresistive pressure scanner. The details of the pressure measurements can be found at Qin et al. [4].

## 3 Results and Discussions

### *3.1 Vibration Response*

Figure 2 shows the dependence of $A_u^*$ ($= A_u/D$), and $A_d^*$ ($= A_d/D$) on $U_r$ and $L/D$, where $A_u$ and $A_d$ are upstream and downstream cylinder displacement amplitudes respectively. At $L/D = 1.2$ (Fig. 2a), tiny humps for both cylinders at $U_r = 4.8$–$6.7$ represent VE. Beyond this $U_r$ range, a rapidly rising $A_u^*$ with an increase in $U_r$ indicates the occurrence of galloping (Fig. 2a). The $A_d^*$ is, however, more or less constant beyond the hump. Similar observations associated with the vibration responses are made at $L/D = 1.5$, $A_u^* > A_d^*$ for $U_r > 6.7$ (Fig. 2b). At $L/D = 2.0$, VE materializes at $U_r \approx 5.3$ and ends at $U_r \approx 9.1$, followed by no-vibrations of both cylinders up to $U_r \approx 21$. Galloping vibration emerges for $U_r > 21$, indicating that the responses of both cylinders display separated VE and galloping (Fig. 2c). Interestingly, $A_u^*$ is larger than $A_d^*$ at $21 < U_r < 33$, which follows the trends appearing at $L/D = 1.2$ and 1.5. The $A_d^*$ jumps at $U_r = 33$, becoming greater than $A_u^*$. At $L/D = 2.5$, VE appearing for both cylinders at $U_r = 6.5$–$7.2$, the downstream cylinder undergoes divergent violent galloping vibration at $U_r > 17.3$ whereas the upstream cylinder weakly vibrates, $A_u^* \leq 0.08$ (Fig. 2d), comparable to that in VE. A similar observation is made for $L/D = 3.0$ (Fig. 2e), with the downstream cylinder vibration becoming less violent ($A_d^* \leq 0.23$) than that at $L/D = 2.5$. At $L/D = 4.0$ in Fig. 2f and $L/D = 6.0$ (not shown), the downstream cylinder vibration is small, and the upstream cylinder has very small vibration.

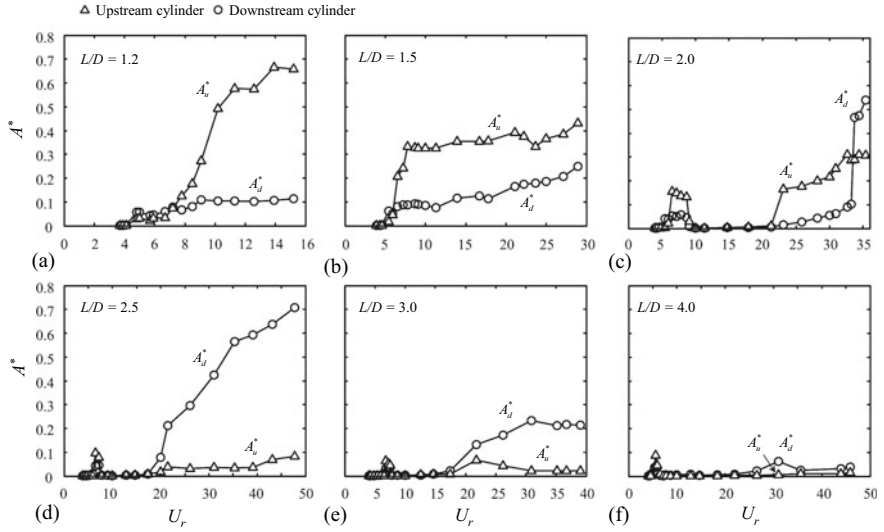


**Fig. 2** Dependence on $U_r$ of upstream- and downstream-cylinder vibration responses at **a** $L/D =$ 1.2, **b** 1.5, **c** 2.0, **d** 2.5, **e** 3.0 and **f** 4.0

Based on characteristics and generation mechanism of the vibration generated for the cylinders, the vibration responses can be classified into four regimes: Regime I ($L/D \leq 1.5$, $A_u^* > A_d^*$), Regime II ($1.5 < L/D < 2.5$, $A_u^* > A_d^*$ or $A_u^* < A_d^*$ depending on $U_r$), Regime III ($2.5 \leq L/D \leq 3.0$, $A_u^* < A_d^*$, with $A_u^*$ being small), and Regime IV ( $L/D > 3.0$, $A_u^*$ and $A_d^*$ being very small and small, respectively).

## *3.2 Galloping Vibration Generation Mechanism at Regime I*

The phase-averaged pressure coefficient $<C_P>$ distributions around both cylinders are superimposed with the phase-averaged vorticity structures at $L/D = 1.5$, $A_u^* = 0.3$ and $A_d^* = 0.07$ to explore the vibration mechanism of the large galloping vibration of the upstream cylinder, as shown in Fig. 3i–v. The correspondence between time instants and $Y'/D$ or $Y/D$ is given in Fig. 3vi. The $<C_P>$ is positive when pointing to the cylinder center, and a length of $D/2$ corresponds to $|<C_P>| = 1.0$. At instant (i), the upper shear layer of the upstream cylinder reattaches onto the front-side surface of the downstream cylinder, leading to a maximum $<C_P>$ (= 0.175) at $\theta$ = 56.25°, where $\theta$ is measured from the nominal front stagnation point. One part of the reattached flow passes over the upper surface of the downstream cylinder and the other part runs over the front surface, both causing negative pressure on the respective areas of the surface. For the upstream cylinder, the stagnation point occurs at $\theta = 0°$ where $<C_P> \approx 1$. Due to the rolling of the upper shear layer in the gap, a larger magnitude of negative pressure distributes around the upper-rear surface of

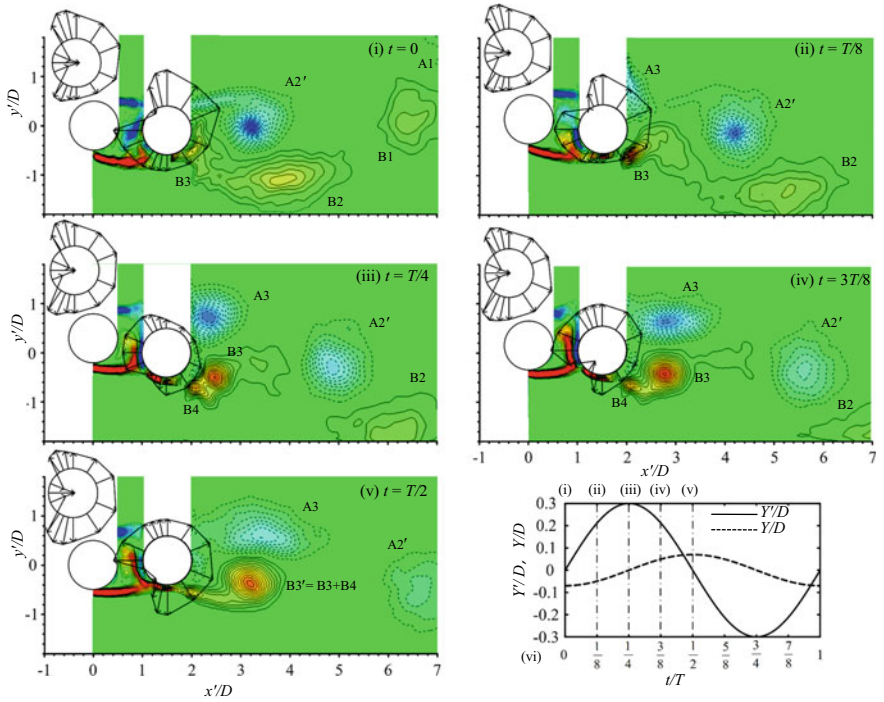


**Fig. 3** **i–v** Phase-averaged vorticity contours and pressure coefficient $<C_P>$ around cylinders in one-half cycle of the cylinder oscillation. The contour cut-off levels are $\pm 0.4$ and the increment is 0.4. **vi** Variations in $Y/D$ and $Y'/D$ where the time instants are specified by the dash-dotted lines corresponding to **i–v**. $L/D = 1.5$. $A_u^* = 0.3$ and $A_d^* = 0.07$

the upstream cylinder than the lower-rear surface. A shear layer shedding or growing is accompanied by a higher velocity and a lower pressure (Nishimura and Taniike [5], Alam [6]). Similarly, the rolling of the upper gap shear layer may cause more negative pressure than that of the lower shear layer for the upstream cylinder. As the upstream cylinder moves upward at instant (ii), the lower gap shear layer also rolls up with the pressure becoming more negative on the lower surface and less negative on the upper surface. When the upstream cylinder reaches the top and then goes down (instants iii, iv), the rolling of the lower gap shear layer, moving closer to the base of the upstream cylinder, generates pressure of a large negative value on the lower-rear surface. The pressure on the lower-rear surface turns into even more negative at instant (v) due to the strong rolling of the lower gap shear layer, along with that on the upper-rear surface becoming less negative. On the whole, the rolling of the gap shear layers, mainly affecting the pressure distribution on the side and rear surfaces of the upstream cylinder, contributes to the large vibration of the upstream cylinder.

The pressure pattern of the downstream cylinder seems more complicated. Due to the reattachment of the lower gap shear layer on the lower surface of the downstream

cylinder, the maximum pressure occurs at $\theta = 303.8°$ where $<C_P> = -0.13$, 0.48, and 0.13 for instants (iii), (iv) and (v), respectively. The complicated pressure pattern of the downstream cylinder arises from the interactions of the downstream cylinder with the gap shear layers as well as its own vortex shedding.

### 3.3 *Galloping Vibration Generation Mechanism at Regime III*

In order to excavate the physics why $A_u^* < A_d^*$ in regime III, the phase-averaged pressure coefficient $<C_P>$ distributions around both cylinders along with phase-averaged vorticity structures at $L/D = 2.5$ and $A_d^* = 0.6$ are shown in Fig. 4i–v. The $<C_P>$ distribution on the surface of the upstream cylinder does not change much between instants (i) and (v). The $<C_P>$ of the upstream cylinder decreases from 1.0 at $\theta = 0°$ (stagnation point) to the maximum negative value ($\approx -1$) at $\theta = 56.25°$, almost invariant on the rear surface. On the other hand, $<C_P>$ around the downstream cylinder surface at instant (i) is negative, with the maximum value ($<C_P> \approx -0.07$) appearing at $\theta \approx 67.5°$. The rolling of the lower reattached shear layer on the front

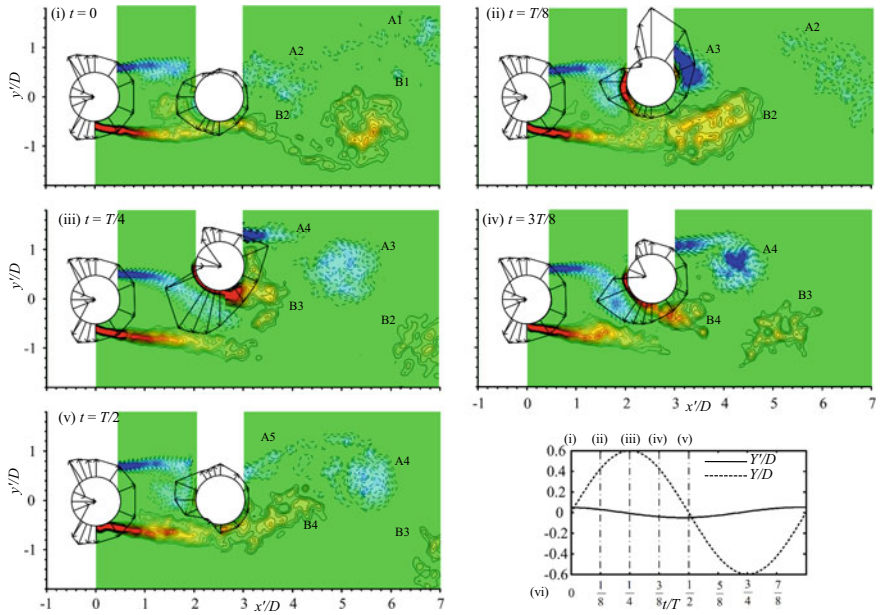


**Fig. 4** **i–v** Phase-averaged vorticity contours and pressure coefficient $<C_P>$ around cylinders in one-half cycle of the cylinder oscillation. The contour cut-off levels are $\pm 0.4$ and the increment is 0.4. **vi** Variations in $Y/D$ and $Y'/D$ where the time instants are specified by the dash-dotted lines corresponding to **i–v**. $L/D = 2.5$, $A_d^* = 0.6$

surface of the downstream cylinder gives rise to negative pressures at $\theta = -60° \sim 0°$, $<C_P> \approx -0.60 \sim -0.87$ (instant i). At instant (ii) where the cylinder is away from the centerline, the negative pressure on the front surface results from the rolling of the upper gap shear layer and from the boundary layer generated with positive vorticity. The boundary layer on the upper side and its separation and strong rolling beget the large negative pressure on the side surface with a maximum $<C_P> \approx -2.02$ at $\theta = 90°$. As the cylinder goes from instants (ii) to (iii), the pressure pattern changes dramatically, the highly negative pressure shifting from the upper side to the lower (minimum $<C_P> \approx -2.05$ at $\theta \approx 303.8°$). With the cylinder moving toward the centerline from instants (iii) to (iv), the maximum negative pressure region shifts from the lower side surface to the front surface, essentially ascribed to the change in the upper gap shear layer rolling (instants iii–v). Interestingly, it is the interaction between the gap shear layers and the downstream cylinder which causes largely the change in the pressure distribution over the front and side surfaces during the cylinder motion, leading to the large vibration of the downstream cylinder.

## 4 Conclusions

Based on characteristics and galloping vibration generation, the dependence of vibration and frequency responses on $L/D$ can be classified into four regimes, namely regime I ($L/D \leq 1.5$), regime II ($1.5 < L/D < 2.5$), regime III ($2.5 \leq L/D \leq 3.0$), regime IV ($L/D > 3.0$). Regime I is characterized by both cylinders experiencing galloping vibrations with $A_u^* > A_d^*$. In regime II, the galloping vibration is generated with $A_u^* > A_d^*$ at smaller $U_r$ but the opposite at larger $U_r$. In regime III, $A_d^* > A_u^*$ during galloping vibration. Regime IV features small vibration for the downstream cylinder and very small vibration for the upstream cylinder.

The $A_u^* > A_d^*$ occurring in regime I is connected to the reattached shear layer rolling very close to the base of the upstream cylinder, mainly affecting the pressure distribution on the side and rear surfaces of the upstream cylinder. The $A_d^*$ is also related to the gap shear layers and the upstream cylinder vibration. As $L/D$ increases, the reattachment of the gap shear layer occurs on the front surface of the downstream cylinder, the rolling being away from the upstream cylinder base, which leads to a radical pressure change largely occurring around the downstream cylinder. The $A_d^*$ thus overwhelms $A_u^*$ in regime III.

**Acknowledgements** Alam wishes to acknowledge the support given by the National Natural Science Foundation of China through grants 11672096 and 91752112.

## References

1. King, R., Johns, D.J.: Wake interaction experiments with two flexible circular cylinders in flowing water. J. Sound Vib. **45**, 259–283 (1976)
2. Zdravkovich, M.M.: Flow-induced oscillations of two interfering circular cylinders. J. Sound Vib. **101**, 511–521 (1985)
3. Kim, S., Alam, M.M., Sakamoto, H., Zhou, Y.: Flow-induced vibrations of two circular cylinders in tandem arrangement. Part 1: characteristics of vibration. J. Wind Eng. Ind. Aerodyn. **97**, 304–311 (2009)
4. Qin, B., Alam, M.M., Zhou, Y.: Two tandem cylinders of different diameters in cross-flow: flow-induced vibration. J. Fluid Mech. **829**, 621–658 (2017)
5. Nishimura, H., Taniike, Y.: Aerodynamic characteristics of fluctuating forces on a circular cylinder. J. Wind Eng. Ind. Aerodyn. **89**(7), 713–723 (2001)
6. Alam, M.M.: Lift forces induced by phase lag between the vortex sheddings from two tandem bluff bodies. J. Fluids Struct. **65**, 217–237 (2016)

# Experimental and Numerical Investigation of Steady Fluid Forces in Axial Flow on a Cylinder Confined in a Cylinder Array


**Aurélien Joly, Pierre Badel, Nicolas de Buretel de Chassey, Olivier Cadot, Alexandre Martin, Pierre Moussou, and Luc Pastur**

**Abstract** The goal of the paper is to investigate experimentally and numerically the Taylor-Lighthill-Païdoussis (TLP) model of fluid forces in axial flow, in the case of a flexible cylinder confined in a cylinder array. This model assumes that the local fluid forces depend only on the local angle, curvature, velocity and acceleration of the structure. The experimental setup consists of a wind tunnel with a test section of length 2m and of width 24cm, surrounding a square array of 3x3 cylinders with pitch-to-diameter ratio 1.33. The Reynolds number is about 100000. The central cylinder can be statically rotated or translated. The steady resultant fluid forces exerted on it are recorded using a 6-axis load cell. Experimental and numerical results are in good agreement. The TLP model performs well at predicting some of the forces measured. However, further investigation on the space distribution of these forces is needed to fully assess the performance of that model.

**Keywords** Fluid-structure interaction · Axial flow · Cylinder array

## 1 Introduction

Fluid-structure interaction plays a major role in the seismic design of fuel assemblies in pressurized water reactors. A fuel assembly consists of a 4 m high and 20 cm wide bundle of 17 × 17 fuel rods tied together by means of spacer grids. In order to extract the heat produced by the nuclear fuel, the assemblies are submitted to an axial flow of water, from bottom to top. Thus, the basic fluid-structure interaction case at stake

A. Joly (✉) · A. Martin · P. Moussou · L. Pastur
IMSIA UMR 9219, Palaiseau, France
e-mail: aurelien.joly@edf.fr

P. Badel · N. de Buretel de Chassey
EDF Lab Paris-Saclay, Palaiseau, France

O. Cadot
University of Liverpool, Liverpool, UK



M. Braza et al. (eds.), *Advances in Critical Flow Dynamics Involving Moving/Deformable Structures with Design Applications*, Notes on Numerical Fluid Mechanics and Multidisciplinary Design 147,
https://doi.org/10.1007/978-3-030-55594-8_10

here boils down to the transverse motion of a square array of cylinders submitted to an axial flow.

This case fits in the tradition of the study of slender, flexible structures in axial flow. This tradition is based on the early theoretical works by Taylor [20] and Lighthill [8] on slender fish locomotion. Later studies, most of which were related to the works of Païdoussis [11–13] and are reviewed in his recent book [14], were mainly dedicated to the instabilities arising in axial flow. However, experimental evidence on full-scale or downsized models of fuel assemblies have shown that, for the case of seismic loading in otherwise normal operating conditions (e.g. fluid velocity of about 5 m/s), the dominant fluid forces are of stabilizing nature. The experiments report above all a high fluid damping, which is proportional to the flow velocity (see e.g. [5]), but also a stiffening effect of the flow on the fuel assembly, i.e. an added stiffness [15].

Fluid damping has been the focus of some recent studies, for the case of a single cylinder oscillating in axial flow [4] as well as for a full-scale fuel assembly [10]. These studies, while making use of the traditional Taylor-Lighthill-Païdoussis model (TLP), also tackled its limits and suggested updates for the values of some coefficients used in the TLP equations.

Inspired by the approach developed in the 80s by Tanaka [17–19] for cross-flow vibrations of cylinder arrays, we focus here on the effects of a local geometrical disturbance of the array. The goal of this paper is thus to investigate experimentally and numerically the TLP model of fluid forces in axial flow, in the case of a cylinder confined in a cylinder array. After introducing the experimental setup as well as the numerical methods of the CFD model, we describe the TLP model and use it to make predictive estimations of the measured fluid forces. The experimental and numerical results are then given and compared to these predictions.

## 2 Experimental Apparatus and Numerical Model

### *2.1 A Wind Tunnel Test Rig*

The experimental setup consists of a wind tunnel with test section of length $L = 2\,\text{m}$ and width 24 cm surrounding a square array of $3 \times 3$ cylinders with pitch-to-

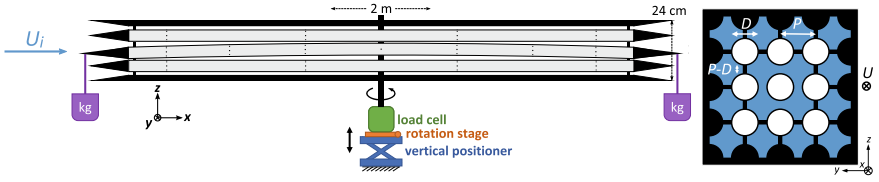


**Fig. 1** Experimental setup

**Table 1** Degrees of freedom of the central cylinder, corresponding tunable parameters and relevant fluid forces

| Degree of freedom | Parameter | Relevant fluid forces |
|---|---|---|
| Rotation | $\alpha_z$: yaw angle | $F_y$: horizantal lift, $F_x$: drag |
| Translation | $Z$: vertical displacement | $F_z$: vertical lift |

diameter ratio $P/D = 1.33$ (Fig. 1). The central cylinder has two degrees of freedom, corresponding each to a tunable parameter and a set of relevant fluid forces to be measured, see Table 1 and Fig. 2.

Thin-walled aluminium cylinders of diameter 4.5 cm and thickness 2 mm have been chosen, so as to minimise static deflection under their own weight. The walls of the test section are equipped with half cylinders, such that the developing boundary layers at the wall mimick the ones of a larger number of surrounding cylinders, see cross section in Fig. 1. The eight neighbour cylinders are supported at both ends via a grid of cylindrical elements of diameter 0.8 cm. The central cylinder is supported at its centre only, so as to enable resultant force measurements. The support has a diameter of 2.2 cm (green part in Fig. 2). In order to have a symmetric geometry, we added a similar rod on the top of the cylinder, without support function. Measurements are carried out both with and without that upper rod. The rotational and translational degrees of freedom are enabled by using highly precise rotation stage and vertical positioner.

The steady fluid forces exerted on the central cylinder are measured with an accuracy of $\pm 0.02$ N using an AMTI MC3A-100 6-axis load cell, by recording at a sample rate of 1 kHz and averaging over 30 s.

The mean velocity in the test section $U$ is calculated by multiplying the upstream velocity $U_i$, which is measured by means of a Pitot tube and a manometer, by the area ratio $4(P/D)^2/\left(4(P/D)^2 - \pi\right) \simeq 1.79$. $U$ can reach up to 32 m/s, which gives a maximum Reynolds number of $U D_h/\nu_{\text{air}} \simeq 110{,}000$, where the hydraulic diameter $D_h \simeq 5.14$ cm has been calculated as $D_h = D\left(4(P/D)^2 - \pi\right)/(P/D + \pi - 1)$. The turbulent intensity at the entrance of the test section upstream of the cylinders is about 0.5%. The incoming flow is not perfectly symmetric ($\pm 3\%$, the flow being slightly faster on the $y < 0$ side).

## 2.2 RANS Simulations

The numerical results presented here were obtained via RANS (Reynolds-averaged Navier–Stokes) simulations performed with Code_Saturne 4.0, an EDF in-house open CFD tool based on a collocated finite volume approach [1]. The code uses a centred scheme for the velocity and a simplec algorithm for the velocity-pressure coupling. We use a $k - \omega$ shear stress transport (SST) turbulence model and a two-

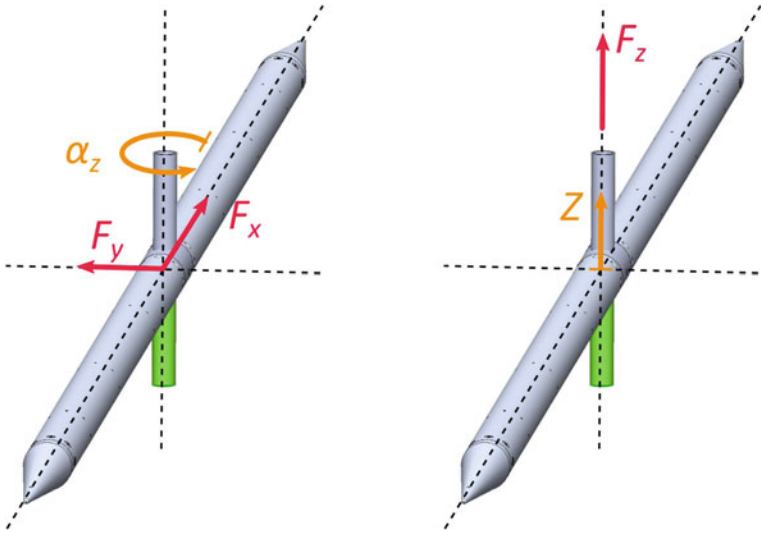


(a) Rotation. (b) Translation.

**Fig. 2** Degrees of freedom of the central cylinder, tunable parameters and relevant fluid forces

scale wall law, which was previously found to be well-suited to the prediction of the fluid force exerted upon a single cylinder in near-axial flow [4].

The fluid volume is discretized with a conform hexahedral mesh generated using the software SALOME 7.8.0 [16]. The geometry of the numerical model is identical to the one of the experiment, except for the supports of the cylinders (Fig. 1) and for some specificities of the test rig downstream of the cylinder array, which were in both cases not included in the numerical model. The resulting mesh is made up of 14 million cells, see Figs. 3 and 4. It is refined close to the walls. Cell sizes are adjusted according to the best practices for these types of flow and turbulence model, see Table 2 (the superscript $^+$ denotes non-dimensional values, using $\nu/u_*$ as a reference length, where $u_*$ is the shear velocity and $\nu$ the kinematic viscosity). The mesh is generated in the neutral configuration, where the central cylinder is at its original position. To deform the mesh according to the two degrees of freedom previously described (Fig. 2), we perform a solid mechanics computation on the fluid domain with Code_Aster 14.1 [2] with an imposed displacement on the central cylinder. We ensure that the cells at the wall keep their previously prescribed size by imposing the displacement on several mesh layers around the cylinders, see Fig. 5.

The time step was chosen such that the Courant–Friedrichs–Lewy condition CFL $< 1$ is met everywhere. We simulate 1.0 s of physical time with a total of 200,000 time steps. The maximum CFL is found at the cylinder tips and its value is 0.6. A constant and uniform velocity of 10 m/s is imposed at the inlet (Re $= 60{,}000$)

(a) Experimental model.

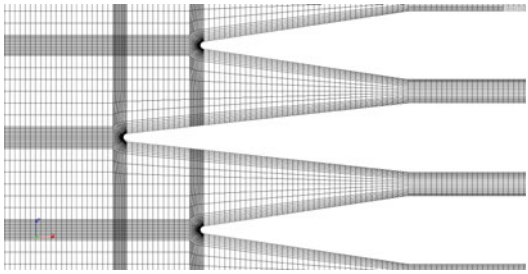

(b) Sliced mesh.

**Fig. 3** Side views

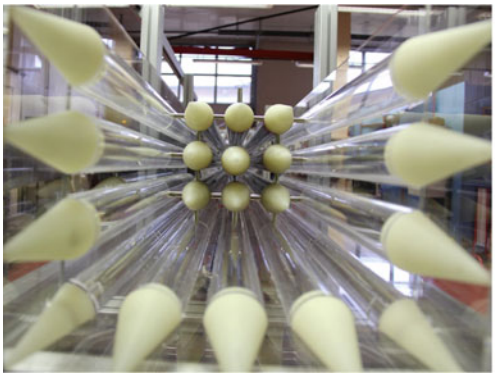

(a) Experimental model.

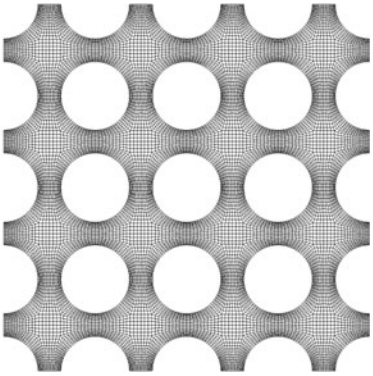

(b) Sliced mesh.

**Fig. 4** Front views

and a constant static pressure at the outlet. The sides of the domain and the cylinder walls are modelled as smooth walls.

The resultant fluid forces and moments are computed at each time step and then averaged over the last 0.1 s of the simulation, when the steady flow has clearly established.

**Table 2** Cell sizes at cylinder walls

| Dimension | Direction | Recommended value | Actual value |
|---|---|---|---|
| $\Delta r^+$ | Radial | 40–80 | 28–76 |
| $R\Delta\theta^+$ | Orthoradial | 100–200 | 105 |
| $\Delta x^+$ | Streamwise | 100–300 | 197 |

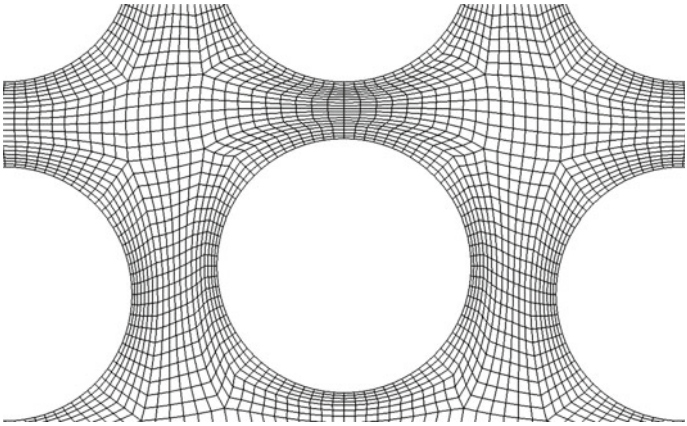

**Fig. 5** Sliced view of the mesh for the translational degree of freedom, with $Z = 5\,\text{mm}$

## 3 Taylor-Lighthill-Païdoussis Model of Fluid Forces

In this section, we describe the classical TLP model in the case of a flexible cylinder confined in a rigid cylinder array in axial flow. The cylinder is assumed to undergo Euler-like bending deformations. The longitudinal deformations are neglected. The transverse deflection (in $z$ direction) is denoted by $w(x, t)$, $x$ being in the main flow direction. In the following, $\dot{w} = \partial w/\partial t$ and $w' = \partial w/\partial x$.

The representation of the fluid forces introduced by Païdoussis [11] distinguishes between two main contributions: (1) the inviscid force, as introduced by Lighthill [8] and derived via a potential flow calculation in the frame of the slender-body approximation [7]; (2) the viscous force, using a model intuited by Taylor [20] and recently updated by Divaret et al. [4]. The inviscid force on a cylinder section is perpendicular to the deformed cylinder axis. It can in turn be decomposed into three terms (see e.g. [3]): the added mass term, proportional to the acceleration of the section $\ddot{w}$ and independent of the flow velocity; the Coriolis term, proportional to the rate of change of angle of incidence of the section $\dot{w}'$ and to the main flow velocity U; the centrifugal term, proportional to the cylinder curvature $w''$ and to the square of the main flow velocity. A major contribution of Lighthill consists in finding all these terms proportional to the inviscid added mass, in the assumption of potential flow:

$$\boldsymbol{f}_{\text{Lighthill}} = -\chi\rho S\left(\ddot{w} + 2U\dot{w}' + U^2 w''\right)\boldsymbol{n}, \tag{1}$$

where $\rho$ is the fluid density and $S$ the cylinder cross-section. $\boldsymbol{n} \simeq \boldsymbol{e}_z - w'\boldsymbol{e}_x$ is the normal unit vector of the deformed cylinder axis. The small $f$ stands for a local fluid force in N m$^{-1}$. The added mass coefficient $\chi$ is equal to 1 for a single unconfined circular cylinder. Moretti and Lowery [9] carried out experiments on a geometry similar to ours and found $\chi = 1.381$.

The viscous Taylor-Divaret force at low angles of incidence ($< 5°$) has a constant drag component and its lift component is a linear function of the local angle of incidence $w'$ and the local virtual angle of incidence $\dot{w}/U$:

$$\begin{aligned}\boldsymbol{f}_{\text{Taylor-Divaret}} =& \frac{1}{2}\rho U^2 D C_D \boldsymbol{e}_x \\ &-\frac{1}{2}\rho U^2 D c_L\left(w' + (1 + C_D/c_L)\,\frac{\dot{w}}{U}\right)\boldsymbol{e}_z.\end{aligned} \tag{2}$$

The slope $c_L = 0.10$ of the lift coefficient was determined experimentally by Divaret et al. [4] for a single unconfined cylinder. In a confined configuration, the drag coefficient $C_D$ can be calculated by estimating the shear stress $\tau = \rho U^2 \lambda_c/8$, where $\lambda_c$ is the friction coefficient. To evaluate it, we suggest to use Haaland's explicit formula [6]:

$$\frac{1}{\sqrt{\lambda_c}} = -1.8\log\left(\frac{6.9}{\text{Re}_{D_h}}\right). \tag{3}$$

For the geometry and Reynolds number range considered here, the resulting drag coefficient is:

$$C_D = \frac{\pi}{4}\lambda_c \simeq 0.014. \tag{4}$$

Two main assumptions underlie the expression of the Taylor-Divaret force given above (2):

1. 2–D fluid force assumption: the fluid force on a section of the deformed cylinder is the same as if that section was part of a long rigid cylinder with same angle of incidence and transverse velocity as the considered section;
2. quasi-steady assumption: the instantaneous velocity of the section is simply accounted for by introducing the virtual angle of incidence $\dot{w}/U$, as already mentioned.

The TLP-model described above, sometimes augmented by additional terms to account for specific phenomena, has been extensively used in order to predict instability thresholds in terms of flow velocity, be it buckling or flutter, and to estimate their characteristics (magnitude, frequency) [14]. This model has also allowed for a satisfying explanation of fluid damping on fuel assemblies [10]. In the next section, we will compare its predictions with experimental and numerical results for the case

of a stationary displaced cylinder. In that case, the time derivatives $\dot{w}$ and $\ddot{w}$ as well as the curvature $w''$ are zero, so that the local fluid force expression simplifies to:

$$\boldsymbol{f}(x) = \boldsymbol{f}_{\text{Taylor-Divaret}} = \frac{1}{2}\rho U^2 D \left(C_D \boldsymbol{e}_x - c_L w' \boldsymbol{e}_z\right), \tag{5}$$

## 4 Results and Discussion

Figure 6 shows the results. The displacement $Z$ is converted into equivalent angles by dividing it by the half length of the cylinder $L/2$. Forces are converted into fluid force coefficients by evaluating the following ratio:

$$C_i = \frac{F_i}{\frac{1}{2}\rho U^2 D L}, \tag{6}$$

where $i$ stands for $x$, $y$ or $z$. The symbol $\Delta$ on Fig. 6 means that the curves have been translated so that they fit together at zero angle or displacement. This allows for a better comparison of the results, since flow asymmetries in the experiment offset the values at zero.

The theoretical results (dashed blue lines, denoted *TLP model*) are obtained by integrating Eq. 5 over the whole span of the cylinder, yet ignoring the tapered ends. For the coefficients $C_D$ and $c_L$, we use the numerical values given in Sect. 3.

### *4.1 Rotation*

Figure 6 shows the evolution of the drag and lift coefficients when the cylinder is rotated. The drag remains fairly constant over the whole range of angle of incidence, which supports the assumption previously made (Eq. 2). As expected, the experimental drag is lower when the upper rod is removed. The numerical drag is coherent with the experimental results, since there is no supporting rod at all in the simulations. The drag predicted by Eq. 2 is much lower, which points out that the front and rear ends might have a non negligible contribution.

The linear trend of the lift predicted by the TLP model is well captured by all our tests (experimental with and without upper rod, numerical), illustrating how robust this behaviour is, with experimental values of $c_L$ ranging from 0.09 to 0.11 and a slightly higher CFD value (0.15).

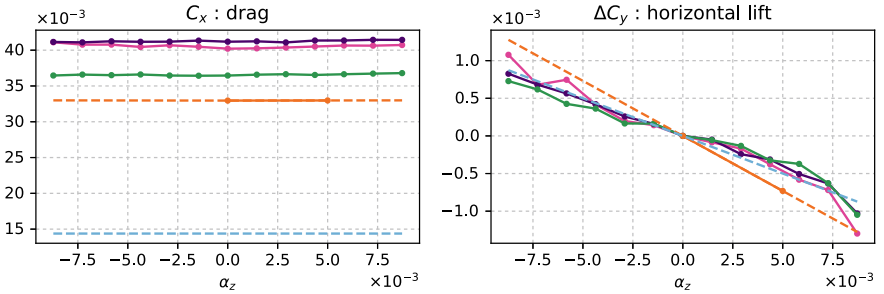


(a) Rotation.

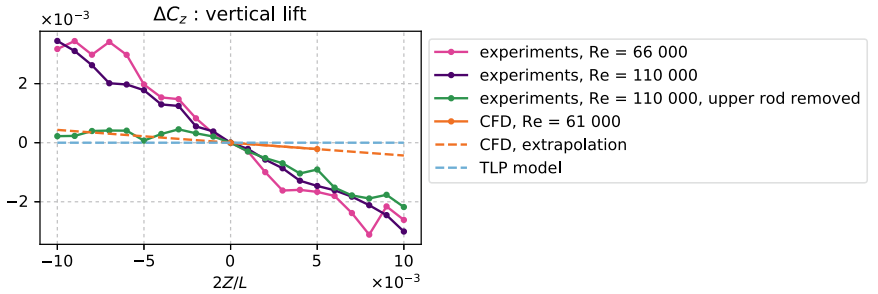


(b) Translation.

**Fig. 6** Fluid force results for the two degrees of freedom

## *4.2 Translation*

Figure 6 shows the evolution of the lift coefficient when the cylinder is translated. Early experimental results, with upper rod, suggested a positive fluid stiffness effect, the fluid force being opposed to the displacement. This would have been in agreement with experimental observations on a downsized model of a fuel assembly [15]. But it would have called for modifications of the TLP model, since the latter predicts zero force in this case. However, the symmetry of the curve is disrupted when the upper rod is removed (green line on Fig. 6). Moreover, the CFD results yield near-zero lift. Thus, the fluid stiffness effect observed in the present experiment is mainly caused by the supporting rods.

# 5 Conclusions

The global fluid forces on a confined cylinder in axial flow undergoing static rotation or translation have been studied both experimentally and numerically, with good agreement between the two approaches. The TLP model performs well in predicting

the drag and the lift in rotation. In order to further assess the TLP model, upcoming studies will investigate the case of a statically bended cylinder. The space distribution of the fluid forces in the CFD simulations will be compared to the predictions of the model. Similar results might be achieved experimentally by means of pressure measurements, with the challenge of having to measure tiny pressure differences.

## References


1. Archambeau, F., Méchitoua, N., Sakiz, M.: Code_saturne: a finite volume code for the computation of turbulent incompressible flows. Int. J. Finite Vol. **1** (2004)
2. Code_Aster. Open source finite element software. http://www.code-aster.org/
3. de Langre, E., Païdoussis, M.P., Doaré, O., Modarres-Sadeghi, Y.: Flutter of long flexible cylinders in axial flow. J. Fluid Mech. **571**, 371–389 (2007)
4. Divaret, L., Cadot, O., Moussou, P., Doaré, O.: Normal forces exerted upon a long cylinder oscillating in an axial flow. J. Fluid Mech. **752**, 649–669 (2014)
5. Flamand, J.C., Maguin, J.C., Mattei, A., Rigaudeau, J., Leroux, J.C.: Influence of axial coolant flow on fuel assembly damping for the response to horizontal seismic loads. In: Transactions SMiRT 11, vol. C (1991)
6. Haaland, S.E.: Simple and explicit formulas for the friction factor in turbulent pipe flow. J. Fluids Eng. **105**(1), 89–90 (1983)
7. Lighthill, M.J.: Mathematics and aeronautics. J. R. Aeronaut. Soc. **64**, 375–394 (1960)
8. Lighthill, M.J.: Note on the swimming of slender fish. J. Fluid Mech. **9**(2), 305–317 (1960)
9. Moretti, P.M., Lowery, R.L.: Hydrodynamic inertia coefficients for a tube surrounded by rigid tubes. J. Pressure Vessel Technol. **98**(3), 190–193 (1976)
10. Moussou, P., Guilloux, A., Boccaccio, E., Ricciardi, G.: Fluid damping in fuel assemblies. In: Proceedings ASME-PVP 2017 (2017)
11. Païdoussis, M.P.: Dynamics of flexible slender cylinders in axial flow. Part 1: theory. J. Fluid Mech. **26**(4), 717–736 (1966)
12. Païdoussis, M.P.: Dynamics of flexible slender cylinders in axial flow. Part 2: experiments. J. Fluid Mech. **26**(4), 737–751 (1966)
13. Païdoussis, M.P.: Dynamics of cylindrical structures subjected to axial flow. J. Sound Vib. **29**(3), 365–385 (1973)
14. Païdoussis, M.P.: Fluid-Structure Interactions: Slender Structures and Axial Flow, volu. 2, 2nd edn. Academic Press (2016)
15. Ricciardi, G., Bellizzi, S., Collard, B., Cochelin, B.: Fluid-structure interaction in a 3-by-3 reduced-scale fuel assembly network. Sci. Technol. Nucl. Install. (2010)
16. SALOME: Open source pre- and post-processing platform. http://www.salome-platform.org/
17. Tanaka, H., Takahara, S.: Fluid elastic vibration of tube array in cross flow. J. Sound Vib. **77**, 19–37 (1981)
18. Tanaka, H., Takahara, S., Ohta, K.: Flow-induced vibration of tube arrays with various pitch-to-diameter ratios. J. Pressure Vessel Technol. **104**, 168–174 (1982)
19. Tanaka, H., Tanaka, K., Shimizu, F., Takahara, S.: Fluidelastic analysis of tube bundle vibration in cross-flow. J. Fluids Struct. **16**, 93–112 (2002)
20. Taylor, G.I.: Analysis of the swimming of long and narrow animals. Proc. R. Soc. Lond. A **214**, 158–183 (1952)

# Numerical Investigation on the Thrust Performance of Bionic Motion Wing in Schools


**Gang Chen, Jiakun Han, Jinan Lv, Yang Zhang, and Chunlin Gong**

**Abstract** After billions of years of natural selection, creatures such as birds, insects and fish have developed excellent flight and mobility capabilities. Understanding on their movement mechanism can help us to develop new unmanned vehicles. It can also present reasonable explanations on biological evolution and morphological adaptability. In nature, birds and fishes often fly and swarm in schools. The phenomenon of biological clustering will be explained in the perspective of fluid mechanics. With the rapid development of computer technology, numerical study of biological motion has become the hot spot. The immersed-lattice Boltzmann method was used to study the biomimetic movement in Chinese Tianhe-II supercomputer. Based on the research of propulsion performance and vortex evolution of single bionic motion wing, multi-flapping wings in schools are numerically investigated. Triangle arrangements were employed to study overall propulsion performance and the unsteady flow mechanism. The influence of space distance of bionic motion wings in schools on thrust performance and vortex structure were analysed further. The numerical results show that the average thrust coefficients of the wings in schools are bigger than that of the single flapping wing. When the flapping wings are in triangular arrangement, the average thrust coefficient is related to the distance. The research on the motion mechanism of bionic wings and the way of bionics promotion will help to explore a new type of driving mode and provide the foundation for the development of bionic mechanisms.

**Keywords** Lattice-Boltzmann method · Immersed boundary method · Bionic motion wing · In schools · Vortex structure

G. Chen (✉) · J. Han · Y. Zhang
State Key Laboratory of Strength and Vibration for Mechanic Structures, School of Aerospace Engineering, Xi'an Jiaotong University, Xi'an 710049, China
e-mail: aachengang@xjtu.edu.cn

J. Lv
China Academy of Aerospace Aerodynamics (CAAA), Beijing 10000, China

C. Gong
School of Astronautics, Northwestern Polytechinical University, Xi'an 710072, China



M. Braza et al. (eds.), *Advances in Critical Flow Dynamics Involving Moving/Deformable Structures with Design Applications*, Notes on Numerical Fluid Mechanics and Multidisciplinary Design 147,
https://doi.org/10.1007/978-3-030-55594-8_11

## 1 Introduction

After billions of years of natural selection, creatures such as birds, insects and fish have developed excellent flight and mobility capabilities. Many studies dedicated to investigate thrust performance of bionic motion Wings [1–8]. In fact, many species in tend to swim and fly in the form of groups, known as schools. In nature, birds and fishes often fly and swarm in schools, the phenomenon of biological clustering will be explained in the perspective of fluid mechanics. Various schooling arrangements are observed in fish-swimming [9] that include line, diamond, triangular, and phalanx formations [10]. There are studies that each individual gains energetic benefits when they swim in schools [11–14]. Krause and Ruxton [15] found that living in schools can provide a number of costs and benefits to animals.

Research on bionic motions in schools generally uses experimental ways or numerical simulations. Experimentally, Webber et al. [16] measure the tail beat frequency and pressure to obtain the speed of the fish. Beal et al. [17] performed experiments to obtain a dead fish propelled in the wake of a bluff body. It's important to study this complex hydrodynamic phenomenon using advanced numerical techniques and computational resources. Weihs [18] observed that diamond pattern is more suitable for individuals in fish-schools by studied the hydrodynamic interaction between fish individuals using a three-dimensional non-stick flow model. However, many species didn't follow the diamond pattern in schools [19]. The swimming mechanisms of single fish and propulsion issues have been studied by Triantafyllou et al. [20], the main mechanism of propulsive force and transient force in oscillating flexible bodies and fins in water was determined, and the formation and control of large vortices were determined.

However, at present, most studies on the configuration adopt tandem model, in which case the influence of different parameters on the propulsion performance is studied. Akhtar et al. [21, 22] found that if the downstream fish swam to the back of another fish, it was not always affected by resistance. In this case, the downstream fish thrust to increase or decrease is considered to be related to the Strouhal number. Zheng et al. [23] simulated the flow field distribution of two tandem cylinders and use the flow field to provide information to analyse the pressure fluctuations in the cylinder and the far field. Therefore, in the present paper we pose the question whether the bionic motion wings in complex configuration is related to individual space distance. It is easy to explore the influence of parameters on the characteristics of flow field for numerical simulation. If finite volume or finite difference NS equations based on body-fitted mesh are used to solve dynamic boundary problems, it is necessary to regenerate the grid at every time step, which is time-consuming and inefficient.

Immersed boundary method was first proposed by Professor Peskin [24] to simulate blood flow in the heart in 1972. The immersed boundary method modulates the boundary into the force rather than boundary condition in the flow field, which the mesh need not re-mesh at each time step especially for biomimetic numerical simulations. Dong and Lu [25] used immersion boundary methods (IBM) to study the performance of two side-by-side undulating foils. Obviously, the development

of the Immersion Boundary (IB) method has made it possible to simulate the flow of bionic mobile boundary immersion bodies including fish and insects [26, 27]. Lattice Boltzmann method (LBM) is from lattice gas automaton, which is proposed by McNamara and Zanetti [27] and used in numerical simulation of hydrodynamics. The lattice Boltzmann method used a fixed Cartesian grid to simulate macroscopic and complex flows from the mesoscopic scale. It need not deal with coordinates from physical plane to computational plane and grid transformation problem. At the same time, the LBM method is easy to implement and naturally parallel which has received widespread attention and achieved accurate results in many areas [28–31]. Since both IBM and LBM use Cartesian grids, it is interesting to combine the two approaches to simulate complex unsteady flow problems. Feng and Michaelides [32, 33] proposed IB-LB method.

To gain deeper understanding and knowledge of fish-schooling mechanism, it is very important to study the performance of fish swarm in schools with new numerical method to save the computational resources. In this paper, we perform numerical simulation using the immersed boundary-lattice Boltzmann method for biomimetic movement in Chinese Tianhe-II supercomputer. Based on the research of propulsion performance and vortex evolution of single bionic motion wing, multi flapping wings in schools are numerically investigated. Triangle arrangement is employed to study overall propulsion performance and unsteady flow mechanism. This paper is organized as follow: Firstly, the IB-LBM numerical method is briefly introduced in Sect. 2; and our problems description and independence verification is obtained in Sect. 3. The influence of school configuration and its space distance on thrust performance was numerical investigated in Sect. 4; and Sect. 5 is conclusion.

## 2 Numerical Methodology and Solver Accuracy Validation

### *2.1 Numerical Method*

#### 2.1.1 Lattice Boltzmann Method

The lattice Boltzmann method uses a square or cube mesh to separate the fluid region into a series of grid points. The fluid is treated as fluid mass and can only move to the surrounding grid or remain stationary. The lattice Boltzmann equation describing the motion of fluid particles is as follows [34]:

$$f_i(\mathbf{x} + \mathbf{e}_i\delta t, \mathrm{t} + \delta t) - f_i(\mathbf{x}, t) = -\frac{1}{\tau}\left[f_i(\mathbf{x}, t) - f_i^{eq}(\mathbf{x}, t)\right] + \frac{3}{2}\omega_i \mathbf{f} \cdot \mathbf{e}_i \delta t \quad (2.1)$$

where $f_i$ is the particle density distribution function, $f_i{}^{eq}$ is the corresponding equilibrium state distribution function, $\delta t$ is the dimensionless relaxation time, $\mathbf{f}$ is the time step, $\tau$ is the fluid density, $\mathbf{e}_i$ is the particle velocity, $\omega_i$ is the weight coefficient,

$\mathbf{e}_i$ and $\omega_i$ are related to discrete density model. D3Q19 model is chosen in the paper. The centre point is position before fluid mass moves, and the remaining 18 points represent position where fluid mass may move at next time step. The fluid mass can also be stationary. So at next time step, the fluid possesses a total of 19 possible positions.

$$f_i^{eq} = \rho\omega_i\left[1 + 3\mathbf{e}_i \cdot \mathbf{u} + \frac{9}{2}(\mathbf{e}_i \cdot \mathbf{u})^2 - \frac{3}{2}\mathbf{u} \cdot \mathbf{u}\right] \tag{2.2}$$

Collision:

$$\widetilde{f}_i(\mathbf{x}, \mathrm{t} + \delta t) = f_i(\mathbf{x}, t) - \frac{1}{\tau}\left(f_i(\mathbf{x}, t) - f_i^{eq}(\mathbf{x}, t)\right) + \frac{3}{2}\omega_i \mathbf{f} \cdot \mathbf{e}_i \delta t \tag{2.3}$$

Streaming:

$$f_i(\mathbf{x} + \mathbf{e}_i\delta t, t + \delta t) = \widetilde{f}_i(\mathbf{x}, t + \delta t) \tag{2.4}$$

For the Lattice-Boltzmann equation with the external force, it can be reduced to the incompressible Navier-Stokes equations with force term by the Chapman-Enskog expansion method under the condition that the Mach number and the density are approximately constant.

### 2.1.2 The Immersed Boundary Method

In order to introduce the concept of the IBM, it is assumed that a flexible filament (denoted by $\Gamma$) is immersed in a two-dimensional incompressible viscous fluid (denoted by $\Omega$). The boundary of the flexible filament $\Gamma$ is denoted by Lagrangian coordinate $\boldsymbol{s}$, and the fluid area $\Omega$ is represented by Euler coordinates $\mathbf{x}$. The coordinates on the flexible filament can be expressed as: $\mathbf{x} = \mathbf{X}(\mathbf{s}, t)$. The entire systems of the immersed boundary method combined with the incompressible NS equations are listed below [35].

$$\rho\left(\frac{\partial \mathbf{u}}{\partial t} + \mathbf{u} \cdot \nabla\mathbf{u}\right) = -\nabla p + \mu\nabla^2\mathbf{u} + \mathbf{f} \tag{2.5}$$

$$\nabla \cdot \mathbf{u} = 0 \tag{2.6}$$

$$\mathbf{f}(\mathbf{x}, t) = \int_{\Gamma} \mathbf{F}(\mathbf{s}, t)\delta(\mathbf{x} - \mathbf{X}(\mathbf{s}, t))d\mathbf{s} \tag{2.7}$$

$$\frac{\partial \mathbf{X}}{\partial t} = \int_{\Omega} \mathbf{u}(\mathbf{x}, t)\delta(\mathbf{x} - \mathbf{X}(\mathbf{s}, t))d\mathbf{x} \tag{2.8}$$

$$\mathbf{F}(\mathbf{s}, t) = S(\mathbf{X}(\mathbf{s}, t), t) \tag{2.9}$$

where $p(x, t)$ is fluid pressure, $\rho$ is fluid density, $\upsilon$ is fluid viscosity, **F**(**s**, t) is concentrated force density at immersed boundary. **f**(**x**, t) is fluid force density. Equations (2.5) and (2.6) are incompressible viscous NS equations. Equation (2.7) shows the process of dispersing the concentrated force at the boundary into the surrounding fluid force density, $\delta(\mathbf{x} - \mathbf{X}(\mathbf{s}, t))$ is the Dirac delta interpolation function. Equation (2.8) is the process of interpolating velocity of the fluid mesh to the immersed boundary, which is essentially a slip-free boundary condition. Equation (2.9) corresponds to the process of determining the concentration force of a point on the boundary, and S is a function related to deformation.

Spring force [36] model and direct force model are suitable to deal with fluid-solid interaction motion. The object of this paper is numerical simulation of rigid active wing, so the virtual boundary model is chosen.

### 2.1.3 The Immersed-Boundary Lattice Boltzmann Method

The key to combine immersed boundary method and Lattice Boltzmann method is to add external force exerted by boundary to the Lattice Boltzmann equation. The complete equation can be described as:

$$f_i(\mathbf{x} + \mathbf{e}_i\delta t, t + \delta t) - f_i(\mathbf{x}, t) = -\frac{1}{\tau}\left(f_i(\mathbf{x}, t) - f_i^{eq}(\mathbf{x}, t)\right) + \Delta t\left(1 - \tfrac{1}{2\tau}\right)\omega_i\left[\frac{\boldsymbol{e}_i - \boldsymbol{u}}{c_s^2} + \frac{\boldsymbol{e}_i \cdot \boldsymbol{u}}{c_s^4}\right] \cdot \boldsymbol{f} \tag{2.10}$$

The penalty method is applied to compute the boundary force density. In this method, at time t, it can be assumed that the center of mass of rigid body is at **X**(t). The instantaneous body rotational matrix is **R**(t). Therefore, the position of a reference point may be determined by

$$\mathbf{X}_j^r(t) = \mathbf{X}(t) + \mathbf{R}(t)\left[\mathbf{X}_j^r(0) - \mathbf{X}(0)\right] \tag{2.11}$$

For the boundary point $X_j{}^t$ which is correspondent to the reference point $X_j{}^r$, it is slightly deformed by the fluid. When the reference point and the boundary point are not the same position, there occurs a displacement $\xi_j = X_j{}^t - X_j{}^r$, and a restoration $\mathbf{F}_j$ is generated that tends to restore the boundary point back to the reference point. It can be modelled by a linear spring relation.

$$\boldsymbol{F}_j = -k\xi_j \tag{2.12}$$

Then, the body force $\mathbf{f}(x, t)$ can be computed by Eq. (2.7) and the Lattice Boltzmann Eq. (2.1) can be solved.

In order to investigate the unsteady flows for three dimensional flapping wings, a three-dimensional parallel IB-LBM solver suitable for Chinese Tianhe-II supercomputer was developed from the two-dimensional IB-LBM algorithm as follows:

1. Initialize the fluid field.
2. According to Eqs. (2.7) and (2.9), compute the body force acting on the fluid mesh exerted immersed boundary.
3. Solve the lattice Boltzmann Eq. (2.10) to get new velocity field.
4. Interpolate from the neighbour fluid mesh to get the velocity of the immersed boundary.
5. The boundary position is updated.

### *2.2 Solver Accuracy Validation*

Figure 1 shows the comparison result of the flapping wing verification example. The rosy agreements have been obtained between the previously reported measurement and numerical simulation [37]. Therefore, provides a powerful platform for solving the problem of flapping wing unsteady flow mechanism and is broadly applicable to a variety of parameter research.

## 3 Problem Descriptions

### *3.1 3D Multi-bionic Wing Math Model*

The single math model of the flapping wing employed in this section is shown as in Fig. 2. The length along $x$-axis is 1 and the counterpart along $y$-axis is 2.55. The thickness of the wing along $z$-axis is 0.12.

Pitch-and-heave mode has been used widely in the simulation of fish and birds. The center of the wing heaves in the $z$-direction according to:

$$\mathrm{z(t)} = \mathrm{A_z}\sin(2\pi f t) \tag{3.1}$$

At the same time, the wing pitches about its center according to:

$$\theta(t) = \alpha_0 + A_\theta \cos(2\pi f t) \tag{3.2}$$

where $A_z$ is set as 0.5, the pitch-bias angle $\alpha_0$ is set as 0 and the pitch amplitude $A_\theta$ is $\pi/6$.The Strouhal number and Reynolds number are defined as, respectively:

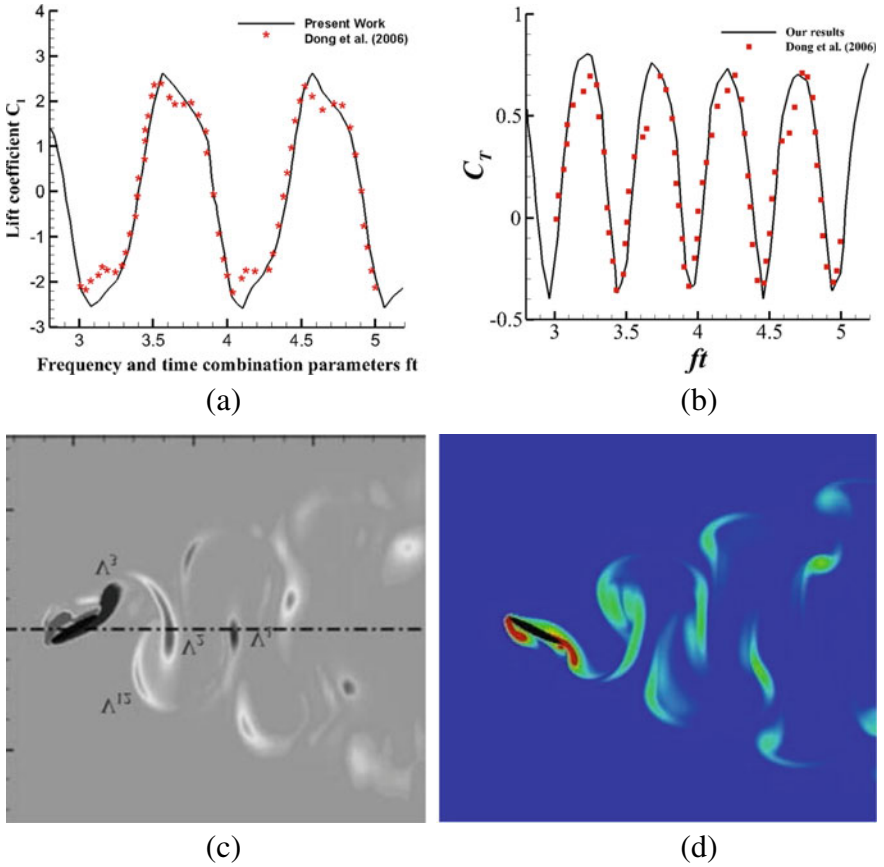


**Fig. 1** Variation of hydrodynamics forces with time. **a** Lift coefficient, **b** thrust coefficient. The asterisk scatter chart shows the result of Dong; the solid line is the calculation result of this article. The vorticity contour plot of flapping wing spread spanwise symmetry plane. **c** Dong [37], **d** Present work. We can find that the calculation results obtained are more obvious to receive flow information capture employing large-scale parallel compute

$$St = 2A_z f/U_\infty \qquad \mathrm{Re} = U_\infty L/\upsilon \tag{3.3}$$

where $f$ is flapping frequency which is set to 0.6 and L is the chord of the wing. The thrust and lift coefficients are defined as, respectively:

$$C_T = \frac{T}{0.5\rho U_\infty^2 A'}, \qquad C_L = \frac{L}{0.5\rho U_\infty^2 A'} \tag{3.4}$$

where T means the force in the streamwise direction, and L is the force in the z direction. $A'$ denotes twice the area of the ellipsoidal wing.

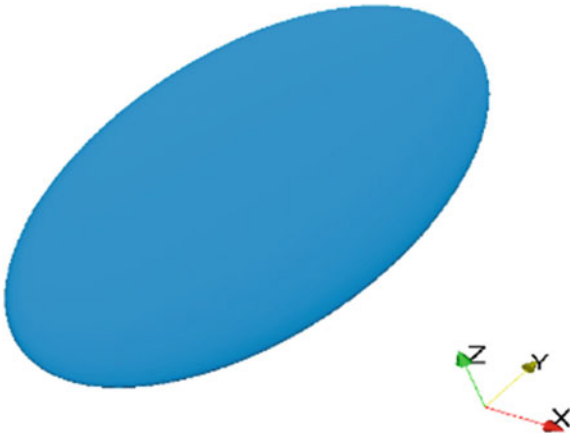


**Fig. 2** Typical ellipsoidal flapping wing model

The heave and pitch amplitude of the wing are 0.5 and $\pi/6$ respectively. The flapping frequency is 0.6. The Reynolds number is assigned to 200. The Strouhal number is equal to 0.6. The velocity of incoming fluid is 1. The detailed flow field calculation domain information is given in Fig. 3. The size of the fluid calculation domain is $18 \times 10 \times 10$. This choice of domain size was based on our experience with running test simulations on a number of different domains. The inlet side of the fluid on the left side adopts the boundary condition of velocity inlet; the outlet side of the fluid on the right side adopts the outflow boundary condition.

A simple schematic diagram for clearly representing their positions is shown in Fig. 4.

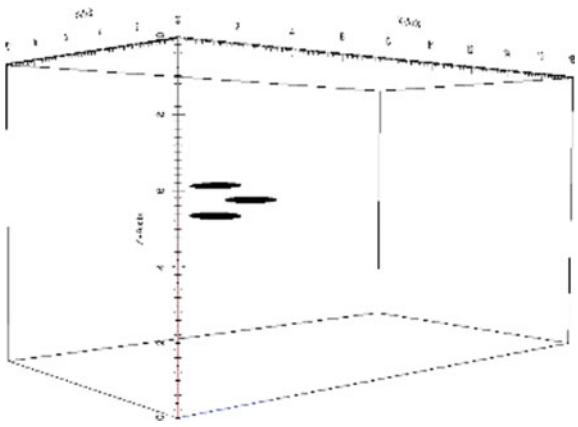

**Fig. 3** The flow field calculation domain

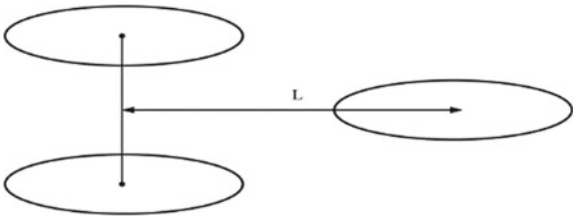


**Fig. 4** The flapping wings in triangle arrangement. When the flapping wing is located in the middle of its trajectory, the coordinate of the first and second wings are (5.0, 5.0, 5.0) and (5.0, 5.0, 4.5), respectively. Their centers remain constant when the distances L between the center of the third wing are 1.5, 2.0, 2.5

## *3.2 Grid Independence Validation*

The space step dx equals 0.033. The total mesh of fluid domain is 540 × 300 × 300, which is 48.6 million. It was treated as nominal grid. The overall grid size for this refined gird is 720 × 400 × 400 which amounts to about 115.2 million grid points. The overall gird size for this roughed gird is 450 × 250 × 250 which amounts to about 28.1 million. The time step dt equals 0.001.

Figure 5 shows a comparison of key dynamic quantities for the grid independence study carried out for the St = 0.6, Re = 200, $\varphi = \pi/2$ and $A\theta = \pi/6$ case. It is shown that the lift and trust force coefficients didn't change with the number of grid changed by comparing Fig. 5. Figure 6 shows the comparison of flow field vorticity cloud diagrams under the three grid states. It is shown that nominal grid and finer grid are basically consistent on the vorticity, which indicated the solver has a good convergence in the grid selection. The selected computational domain and the computational grid are justified.

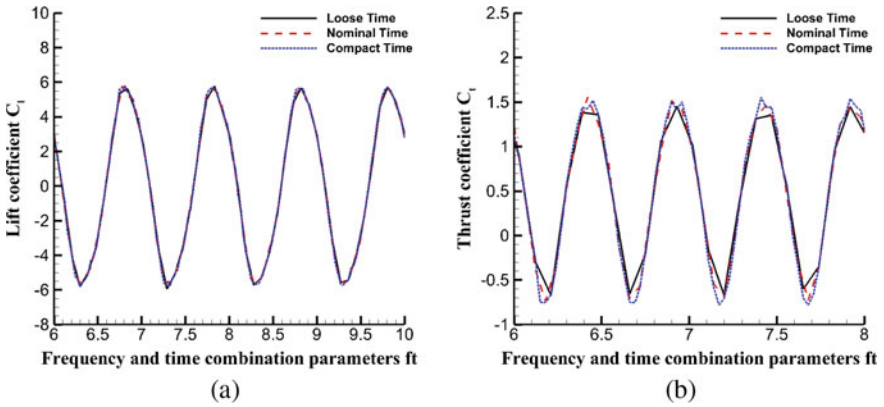


**Fig. 5** The hydrodynamics coefficients of flapping wings at different grid numbers for St = 0.6, Re = 200, $\varphi = \pi/2$ and $A\theta = \pi/6$ case. **a** Lift force coefficient. **b** Trust force coefficient

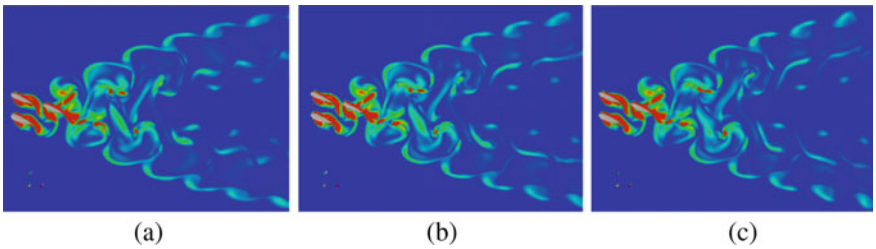


**Fig. 6** The vorticity contour plot of NACA0012 flapping wing spread spanwise symmetry plane under three different grids. **a** Coarse grid. **b** Nominal grid. **c** Finer grid

### *3.3 Time Independence Validation*

The same calculation model and kinetic parameters as in the previous section is chosen. To verify the time independence, we use identical normal grid but different time steps is dt = 0.0005, dt = 0.001 and dt = 0.0015, named as compact time, normal time and loose time respectively. Figure 7 shows the lift and thrust force coefficients under different time steps. From Fig. 7, it can be seen that lift and trust force coefficients are extremely similar with qualitative analysis. Figure 8 shows the comparison of flow field vorticity cloud diagrams under the three time steps. We can find that the obtained flow field information is the same as the problem described by the kinetic curve, which is shown that the solver has a good convergence in the time selection.

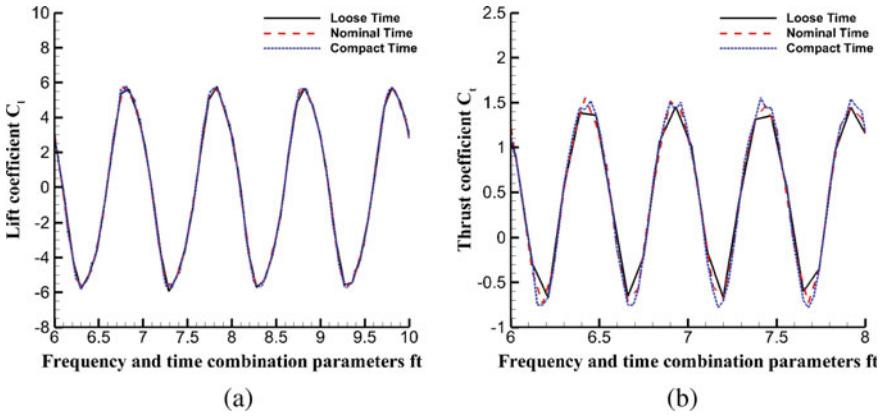


**Fig. 7** The hydrodynamics coefficients of flapping wings at different time steps for St = 0.6, Re = 200, $\varphi = \pi/2$ and $A\theta = \pi/6$ case. **a** Lift force coefficient. **b** Trust force coefficient

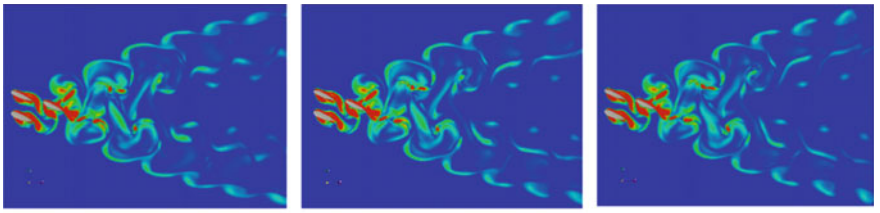


**Fig. 8** The vorticity contour plot of NACA0012 flapping wing spread spanwise symmetry plane under three different time steps. **a** Loose time. **b** Nominal time. **c** Compact time

## 4 Numerical Simulations and Discussions

In nature, birds and fish are always to hunt for foods in school. The phenomenon of biological clustering will be explained in the perspective of fluid mechanics. The schools' configurations in a triangle is employed to study their overall propulsion performance and unsteady flow mechanisms. The influence of the space of flapping wings in schools on thrust performance and vortex structure are analyzed in detail.

The lift coefficient for each wing at three different distances is given in Fig. 9. Single represents thrust coefficient of a single flapping wing. The time-averaging process of the lift curve. It is found that the thrust coefficient of one of the three flapping wings is larger than the one of the single flapping wing when the distance between center of leftmost wing and center of rightmost wing is 1.5. When the corresponding distances are 2 and 2.5, the thrust coefficient of one of three flapping wing is smaller than the one of the single wing. When the flapping wing is triangle arrangement, the thrust coefficient of wings located upper left and rightmost of the flapping wings are close to each other. The thrust coefficient of flapping wing located lower left is relatively large.

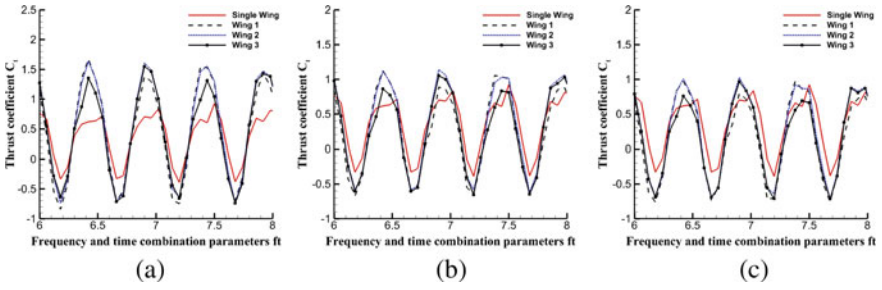


**Fig. 9** Wing 1, wing 2, wing 3 represent thrust coefficients of single flapping wing in school which are located at upper left, lower left and rightmost. **a** Thrust coefficients when the distance between wings is 1.5. **b** Thrust coefficients when the distance between wings is 2. **c** Thrust coefficients when the distance between wings is 2.5

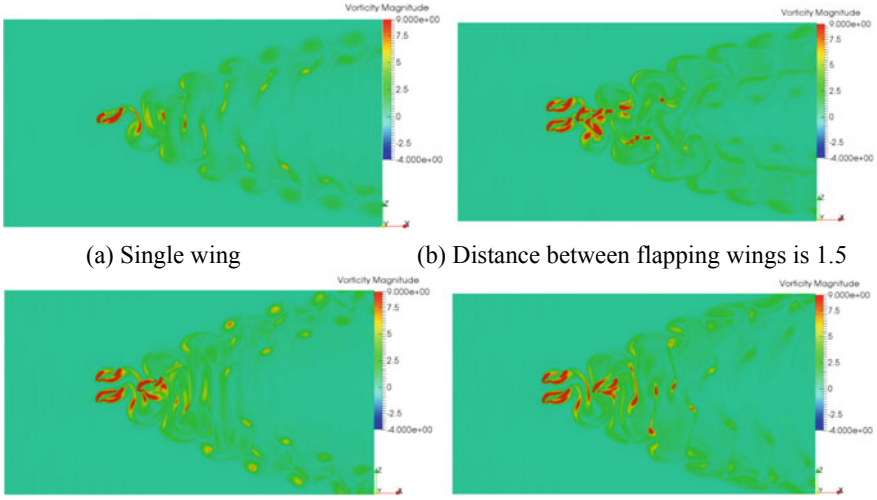


(a) Single wing (b) Distance between flapping wings is 1.5

(c) Distance between flapping wings 2.0 (d) Distance between flapping wings is 2.5

**Fig. 10** Vorticity contour of flapping wings at spanwise symmetry plane in triangle arrangement

The vorticity contour on spanwise symmetry plane of flapping wing is showed in Fig. 10. Figure 10a gives vorticity contour of single flapping wing under same conditions. When the distance between former and latter wing is small, vortex produced by former wing is separated by the downstream flapping wing, resulting in an increase in velocity and an enhanced effect on vortex of downstream flapping wing. The vortex is confined at a relatively small angle. The thrust coefficient increases with the distance when distance of centers of flapping wings is 1.5. When the distance of the centers of the flapping wing increases, vortex produced at former wings fall off at the leading edge of the latter wing. This will reduce the intensity of the downstream vortex, resulting in a decrease in thrust coefficient.

Figure 11 shows vortex structure of the flapping wings in wake zone. Figure 11a shows vortex structure of single flapping wing. The vortex rings are found in trailing area of flapping wings in group at different intervals. When the distance between the wings is 2 and 2.5, the length of vortex ring is smallest. At this time, the vortex induced by the first flapping wing diffuses to the surface of second flapping wing. Then it will be suppressed, resulting in a lower thrust coefficient. In contrast, when the distance between the leading edge and trailing edge is 1.5, the length along spanwise direction is smaller, which will lead to a larger thrust coefficient.

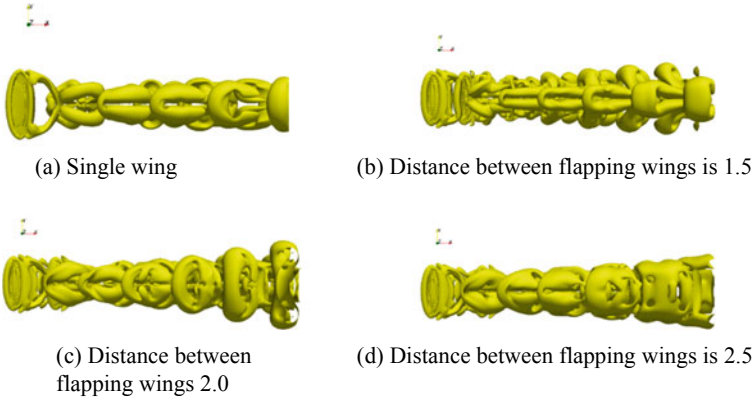

(a) Single wing

(b) Distance between flapping wings is 1.5

(c) Distance between flapping wings 2.0

(d) Distance between flapping wings is 2.5

**Fig. 11** Vortex structure identified by Q-criterion (Q = 0.1) in the wake zone of flapping wing

## 5 Conclusions

In this paper, three-dimension flapping wings are employed to investigate the influence of governing parameters instead of two-dimension one. For the elliptical flapping wing, the kinetic coefficient and the vortex structure of the flapping wing under different configurations are studied. We investigate the influence of space distance of bionic motion wings in schools on thrust performance and vortex structure. The numerical results show that the average thrust coefficients of the wings in schools are bigger than the one of single flapping wing, when the flapping wings are in triangle arrangements. Under different parameters of the triangular configuration, the thrust coefficient of the flapping wing on the lower left side is larger, and the average thrust coefficient on the upper left and right sides is smaller and similar. When the flapping wings are in triangular arrangement, the average thrust coefficient is related to the distance. The current work mainly focuses on the numerical study of rigid flapping wing under specified movement, which is of theoretical significance for the design of bionic aircraft or aircraft profile and controller.

**Acknowledgements** This work was supported by the National Natural Science Foundation of China (No. 11672225, 11511130053), the 111 project (B18040), the Basic Research foundations for the Central Universities (2014XJJ0126), and the Shanxi Province Natural Science Foundation of China (No. 2016JM1007). The authors will also acknowledge the Special Program for Applied Research on Super Computation of the NSFC-Guangdong Joint Fund (the second phase) under Grant No. U1501501 for providing Tianhe-II supercomputer resources.

## References


1. Buchholz, J.H.J., Smits, A.J.: On the evolution of the wake structure produced by a low-aspect-ratio pitching panel. J. Fluid Mech. **564**(1), 433–443 (2005)
2. Anderson, J.M., Streitlien, K., Barrett, D.S., et al.: Oscillating foils of high propulsive efficiency. J. Fluid Mech. **360**(360), 41–72 (1998)
3. Green, M.A., Smits, A.J.: Effects of three-dimensionality on thrust production by a pitching panel. J. Fluid Mech. **615**(615), 211–220 (2008)
4. Green, M.A., Rowley, C.W., Smits, A.J.: The unsteady three-dimensional wake produced by a trapezoidal pitching panel. J. Fluid Mech. **685**(7), 117–145 (2011)
5. Kang, C.K., Aono, H., Cesnik, C.E.S., et al.: Effects of flexibility on the aerodynamic performance of flapping wings. J. Fluid Mech. **689**(12), 32–74 (2011)
6. Harbig, R.R., Sheridan, J., Thompson, M.C.: Reynolds number and aspect ratio effects on the leading-edge vortex for rotating insect wing planforms. J. Fluid Mech. **717**(2), 166–192 (2013)
7. Hua, R.N., Zhu, L., Lu, X.Y.: Dynamics of fluid flow over a circular flexible plate. J. Fluid Mech. **759**, 56–72 (2014)
8. Dash, S.M., Lua, K.B., Lim, T.T., et al.: Enhanced thrust performance of a two dimensional elliptic airfoil at high flapping frequency in a forward flight. J. Fluids Struct. **76**, 37–59 (2018)
9. Fish, F.E.: Energetics of swimming and flying in formation. Comments Theor. Biol. **5** (1999)
10. Hemelrijk, C., Reid, D., Hildenbrandt, H., et al.: The increased efficiency of fish swimming in a school. Fish Fish. **16**(3), 511–521 (2015)
11. Herskin, J., Steffensen, J.F.: Energy savings in sea bass swimming in a school: measurements of tail beat frequency and oxygen consumption at different swimming speeds. J. Fish Biol. **53**(2), 366–376 (1998)
12. Svendsen, J.C., Skov, J., Bildsoe, M., et al.: Intra-school positional preference and reduced tail beat frequency in trailing positions in schooling roach under experimental conditions. J. Fish Biol. **62**(4), 834–846 (2003)
13. Johansen, J.L., Vaknin, R., Steffensen, J.F., et al.: Kinematics and energetic benefits of schooling in the labriform fish, striped surfperch *Embiotoca lateralis*. Mar. Ecol. Prog. **420**(6), 221–229 (2010)
14. Killen, S.S., Marras, S., Steffensen, J.F., et al.: Aerobic capacity influences the spatial position of individuals within fish schools. Proc. Biol. Sci. **279**(1727), 357–364 (2012)
15. Krause, J., Ruxton, G.D.: Living in groups. Behaviour **87** (2002)
16. Webber, D.M., Boutilier, R.G., Kerr, S.R., et al.: Caudal differential pressure as a predictor of swimming speed of cod (*Gadus morhua*). J. Exp. Biol. **204**(20), 3561–3570 (2001)
17. Beal, D.N., Hover, F.S., Triantafyllou, M.S., et al.: Passive propulsion in vortex wakes. J. Fluid Mech. **549**(549), 385–402 (2006)
18. Weihs, D.: Hydromechanics of fish schooling. Nature **241**(5387), 290–291 (1973)
19. Partridge, B.L., Pitcher, T.J.: Evidence against a hydrodynamic function for fish schools. Nature **279**(5712), 418 (1979)
20. Triantafyllou, M.S., Triantafyllou, G.S., Yue, D.K.P.: Hydrodynamics of fishlike swimming. Annu. Rev. Fluid Mech. **32**(32), 33–53 (2000)
21. Akhtar, I., Mittal, R., Lauder, G.V., et al.: Hydrodynamics of a biologically inspired tandem flapping foil configuration. Theoret. Comput. Fluid Dyn. **21**(3), 155–170 (2007)
22. Akhtar, I., Mittal, R.: A biologically inspired computational study of flow past tandem flapping foils (2005)
23. Zheng, Z.C., Yang, X., Zhang, N.: Flow/acoustic characteristics for flow over two tandem cylinders. In: ASME 2006 International Mechanical Engineering Congress and Exposition, pp. 115–124 (2006)
24. Peskin, C.S.: Flow patterns around heart valves. Lect. Notes Phys. **10**, 214–221 (1973)
25. Dong, G.J., Lu, X.Y.: Characteristics of flow over traveling wavy foils in a side-by-side arrangement. Phys. Fluids **19**(5), 99 (2007)
26. Wang, Z.J.: Dissecting insect flight. Annu. Rev. Fluid Mech. **37**(1), 183–210 (2005)

27. Mcnamara, G.R., Zanetti, G.: Use of the Boltzmann equation to simulate lattice gas automata. Phys. Rev. Lett. **61**(20), 2332 (1988)
28. Mahmoud, J., Mousa, F., Ali, R.D.A., et al.: Lattice Boltzmann simulation of melting phenomenon with natural convection from an eccentric annulus. Therm. Sci. **17**(3), 877–890 (2013)
29. Miguel, A.F.: Non-Darcy porous media flow in no-slip and slip regimes. Therm. Sci. **16**(1), 167–176 (2012)
30. Sajjadi, H., Gorji, M., Kefayati, G.H.R., et al.: Lattice Boltzmann simulation of turbulent natural convection in tall enclosures using Cu/water nanofluid. Therm. Sci. **19**(1), 66–66 (2015)
31. Tian, Z., Xing, H., Tan, Y., et al.: Reactive transport LBM model for $CO_2$ injection in fractured reservoirs. Comput. Geosci. **86**(C), 15–22 (2016)
32. Feng, Z.G., Michaelides, E.E.: The immersed boundary-lattice Boltzmann method for solving fluid–particles interaction problems. J. Comput. Phys. **195**(2), 602–628 (2004)
33. Feng, Z.G., Michaelides, E.E.: Proteus: a direct forcing method in the simulations of particulate flows. J. Comput. Phys. **202**(1), 20–51 (2005)
34. Succi, S.: The lattice Boltzmann equation—for fluid dynamics and beyond. Phys. Today **55**(12), 58–60 (2002)
35. Wu, J., Shu, C.: Implicit velocity correction-based immersed boundary-lattice Boltzmann method and its applications. J. Comput. Phys. **228**(6), 1963–1979 (2009)
36. Huang, W.X., Shin, S.J., Sung, H.J.: Simulation of flexible filaments in a uniform flow by the immersed boundary method. J. Comput. Phys. **226**(2), 2206–2228 (2007)
37. Dong, H., Mittal, R., Najjar, F.M.: Wake topology and hydrodynamic performance of low-aspect-ratio flapping foils. J. Fluid Mech. **566**(566), 309–343 (2006)

# Stress Analysis of Wind Turbine Tower Flange Using Fluid-Structure Interaction Method


**Myoungwoo Lee, Seok-Gyu Yoon, and Youn-Jea Kim**

**Abstract** There is growing interest and investment in the renewable energy industry with the goal of promoting eco-friendly growth globally. The proportion of wind power generation systems in the world's renewable energy market is kept continuously increased and is known as 21.9%. In order to reduce the fossil-fuel power generation capacity, many countries enlarge the investment of the wind power generation systems. As the size of blade enlarges, the installation cost decreases and then the power generation efficiency could be increased. However, as the sizes of the blade and tower are enlarged, the weight and the wind load of itself might be increased. Therefore, it is necessary to develop appropriate components and their build-up technology that can guarantee the structural safety of the wind turbine. In this study, the stress applied to the tower flange when the wind turbine is operating is numerically analyzed. In particular, optimal design value for the aspect ratio of the tower flange was obtained, using fluid-structure interaction (FSI) method. The lowest von Mises stress had an aspect ratio of $h_1/h_2 = 1.40$. Numerical analysis of local stress of the tower and flange was calculated using the commercial code ANSYS 18.1.

**Keywords** Wind tower · Tower flange · Fluid structure interaction analysis · von Mises stress

## 1 Introduction

Wind power generation, which is one of renewable energy generation technologies, is a technology to convert wind into electric power by using a wind turbine. In recent,

M. Lee · S.-G. Yoon
Graduate School of Mechanical Engineering, Sungkyunkwan University, Suwon 16419, Republic of Korea

Y.-J. Kim (✉)
School of Mechanical Engineering, Sungkyunkwan University, Suwon 16419, Republic of Korea
e-mail: yjkim@skku.edu



M. Braza et al. (eds.), *Advances in Critical Flow Dynamics Involving Moving/Deformable Structures with Design Applications*, Notes on Numerical Fluid Mechanics and Multidisciplinary Design 147,
https://doi.org/10.1007/978-3-030-55594-8_12

it is required to enlarge the tower in order to improve wind power generation efficiency. Increasing the size of the wind power generator not only increases the weight of itself but also increases the wind load, which is resulting in the problem of structural stability. In order to solve this problem, it is required to design element parts and securing manufacturing techniques. Especially the generator's tower flange is a crucial design element that connects between the towers and it plays an important role in securing the structural stability of the tower, so in-depth research should be conducted. Perelmuter and Yurchenko [1] proposed parametric optimization of wind turbine shell towers. They considered the minimum weight of the tower as an objective function. And they also set the shell diameter, thickness, and turbine installation height as design variables. Bazeos et al. [2] evaluated the structural stability by calculating the stress applied to the tower height by dynamic analysis such as seismic analysis, static analysis, and buckling analysis of 450 kW wind turbines. Murtagh et al. [3] presented an approach to investigate forced vibration response according to the wind speed of wind turbine tower and rotor assembly receiving wind load. Feliciano et al. [4] studied how the aerodynamic loading affects the structural responses of turbines tower under different thermal stability operating conditions. Jiang et al. [5] studied the optimization of the tower structure by measuring the residual stress according to the shape of the weld between the wind turbine tower and the lower flange. Ali et al. [6] studied a thermally stratified wind turbine array boundary layer using Lumley and barycentric maps. The interaction of the wind turbine atmospheric barrier layer was formalized. Cottina et al. [7] used the large eddy simulations to estimate the optimal scanning distance by creating realistic atmospheric flows and studied the influent turbulence as a function of wind farm and atmospheric stratification. Kragh et al. [8] studied the optimization of the yaw misalignment angle to lower the blade load induced by the wind shear.

In this study, the structural stability of a wind turbine flange was evaluated by one-way fluid-structure analysis. In the numerical analysis process, the wind loads and the blade dynamic loads according to the wind speed were considered and von Mises equivalent stress was calculated to evaluate the structural stability of the tower according to the flange shape. Based on the analysis results, a flange shape with stable structural characteristics was derived.

## 2 Numerical Analysis

### *2.1 Model Description*

In this study, a commercial 3 MW class wind turbine was used. Figure 1 showed the tower shell of a wind turbine and the flange model used for numerical analysis. The height of the tower is set to 104 m, and the basic shape of the tower flange is shown in Table 1. Structural stability was evaluated through von Mises equivalent stress evaluation of the flange using the fluid-structure coupled analysis method based on

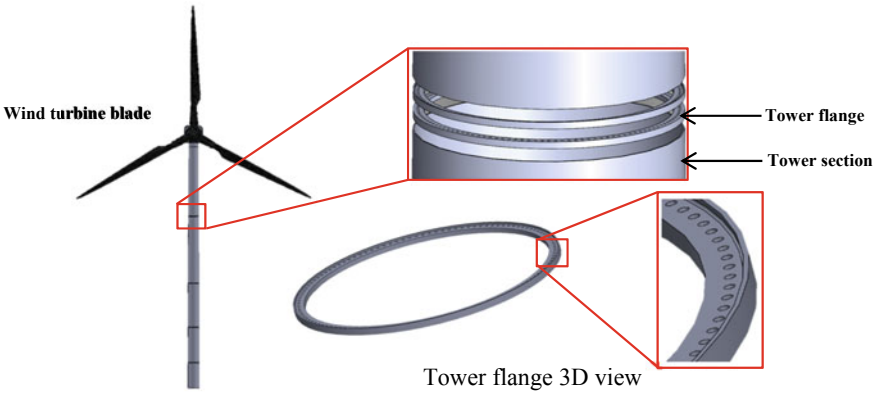


**Fig. 1** Reference model of the wind turbine

**Table 1** Reference model configuration of wind tower and flange

| | |
|---|---|
| Height of wind tower | 104 m |
| Diameter of turbine blade | 102 m |
| Outer diameter of flange | 3.850 m |
| Inner diameter of flange | 3.540 m |
| Outer height of flange ($h_1$) | 0.105 m |
| Inner height of flange ($h_2$) | 0.075 m |

the shape as shown in Fig. 2. The total area for the flow analysis is shown in Fig. 3. In order to minimize the influence of the interface, the width, height, and height were set to 150 m, 300 m, and 600 m, respectively, considering the blade diameter of 105 m. SM35C was selected as the material of the tower shell to withstand tension due to wind load and dynamic load by blade. The same material was chosen because

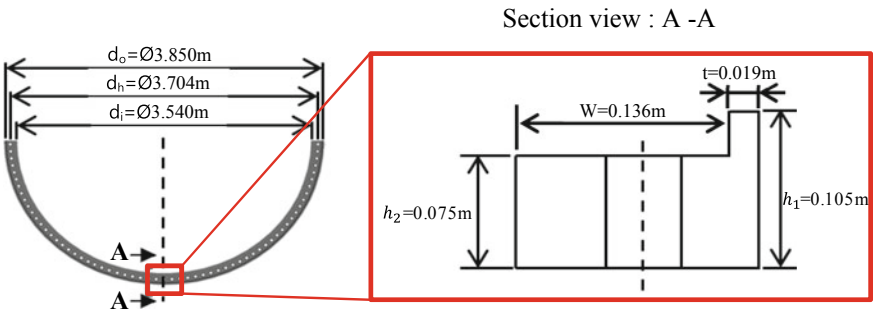


**Fig. 2** Reference model description of the tower flange

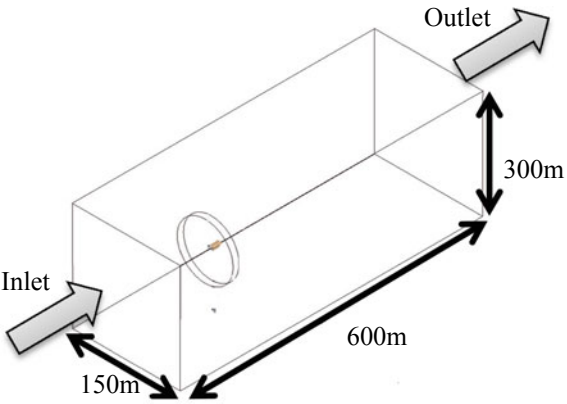


**Fig. 3** Flow domain of the wind turbine

the flange is connected by welding to the shell. Carbon-epoxy which is a synthetic fiber material with low density and high tensile strength was selected as the material of the blade, and physical property values are shown in Table 2.

## *2.2 Grid Systems*

Figure 4 showed the grid systems of the tower shell and flange created using ANSYS 18.1. In prticular, the grid systems of the flow region are mainly consisted with tetrahedral lattice systems. In the structural analysis, a hexahedral grid was applied

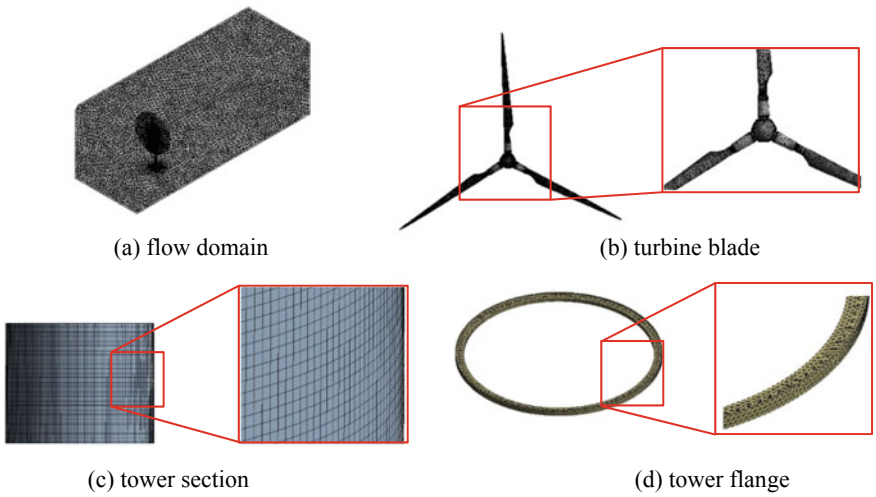


**Fig. 4** Grid systems applied in this study

to the blade as shown in Fig. 4b. The tower shell shown in Fig. 4c applied a tetrahedron grid system. The tower flange shown in Fig. 4d has a hexahedral grid to calculate the accurate convergence values applied by wind loads. The grid dependence test confirmed a constant wind pressure and von Mises stress with 700,000 elements in the flow regime and more than 950,000 elements in the wind tower shell.

## 3 One-Way Fluid-Structure Analysis

The continuity equation and the momentum equation are applied as the governing equations for calculating the pressure acting on the wind pressure area of the wind tower shell to determine the influence of the wind speed.

$$\frac{\partial \rho}{\partial t} + \frac{\partial (\rho u_i)}{\partial x_i} = 0 \tag{1}$$

$$\frac{\partial (\rho u_i)}{\partial t} + u_j \frac{\partial (\rho u_i)}{\partial x_j} = -\frac{\partial p}{\partial x_i} + \frac{\partial}{\partial x_i}\left[\mu \frac{\partial u_i}{\partial x_j} + \overline{\rho u_i u_j}\right] \tag{2}$$

The air is applied as working fluid and a uniform wind speed of 5 m/s applied to the inlet of the flow region. In addition, the dynamic load due to the revolutions per minute (10 RPM) of the blade was calculated and the results were applied to the structural analysis. Wind load due to wind pressure can be calculated as follows:

$$W = qCA \tag{3}$$

$$q = \frac{V^2}{30}\sqrt[4]{h} \tag{4}$$

where $W$ represents the wind load, can be calculated through the velocity pressure $q$, the wind force coefficient $C$, and the area $A$ under pressure. The velocity pressure $q$ can be calculated from the wind velocity $V$ and the height $h$ from the ground on the windward side. The SST (shear stress transport) turbulence model was applied. It has the advantages of a $k$-$\omega$ turbulence model that accurately predicts near-wall flow and a $k$-$\varepsilon$ turbulence model for general convection analysis. Therefore, it is useful to calculate the dynamic load due to the rotation of the turbine blades. The flow analysis was performed in a steady-state to reflect the effects of maximum instantaneous wind speed and blade rotation. The wind pressure distribution of the wind turbine calculated by reflecting the boundary conditions is shown in Fig. 5. Results showed that the maximum wind pressure was 3.98 kPa. The tower shell has a maximum wind pressure of 0.19 kPa, and it is observed that wind pressure is applied to a specific part due to the influence of the blade, not the wind pressure uniformly applied to the tower (Table 2).

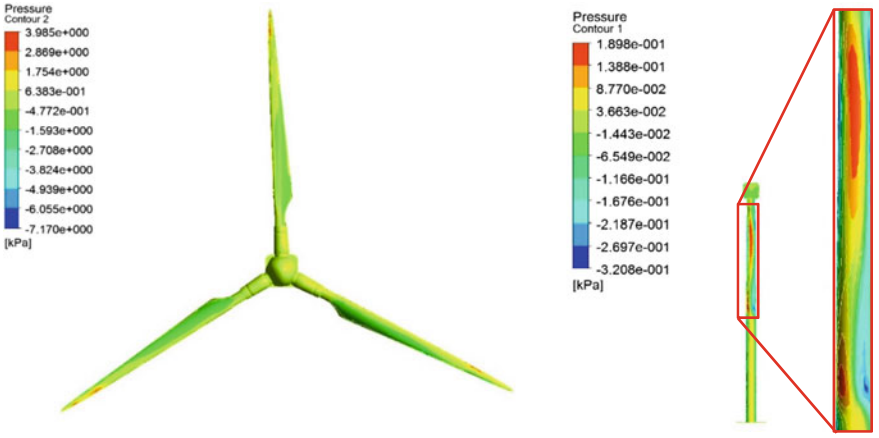


(a) Blade (b) Tower shell

**Fig. 5** Imported pressure applied to wind tower at blade rotation speed of 10 RPM

**Table 2** Material properties

| Material | SM35C | Carbon-epoxy |
|---|---|---|
| Density (kg/m$^3$) | 7850 | 1580 |
| Tensile strength (MPa) | 620 | 5360 |
| Poisson's ratio | 0.29 | 0.472 |
| Elastic modulus (GPa) | 205 | 138 |

## 4 Structural Stability Evaluation

In order to elucidate the stress applied to the flange, the von Mises stress can be evaluated and it can be calculated by the following equations:

$$\sigma_{vm} = \sqrt{\frac{(\sigma_1 - \sigma_2)^2 + (\sigma_2 - \sigma_3)^2 + (\sigma_3 - \sigma_1)^2}{2}} \tag{5}$$

$$\sigma_{vm} \leq \sigma_{yield} \tag{6}$$

Here $\sigma_{vm}$ indicates von Mises stress, which can be calculated through the triaxial principal stresses $\sigma_1$, $\sigma_2$ and $\sigma_3$. It can be judged that it breaks when the von Mises stress reaches the yield stress of the material. To perform the structural analysis, gravity conditions were applied to the tower shell and the flange, and the calculated wind pressure was applied by applying a fluid-solid surface to the outer surface area of the wind turbine subjected to wind pressure. As a result of the structural analysis, the region where the stress is concentrated through the von-Mises stress distribution was confirmed and shown in Fig. 6. In this study, case study is carried out by using

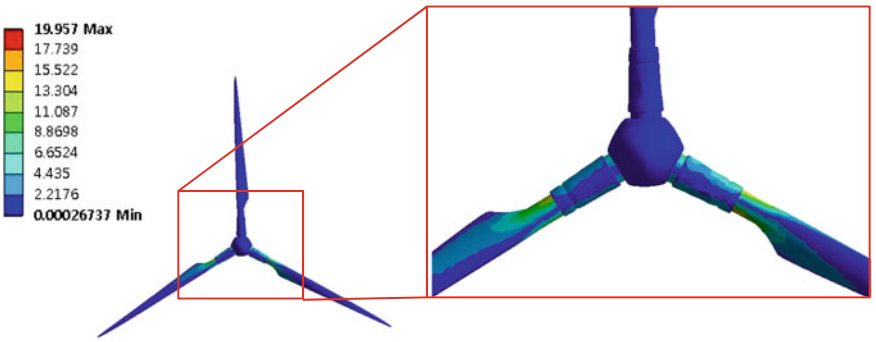


(a) wind turbine

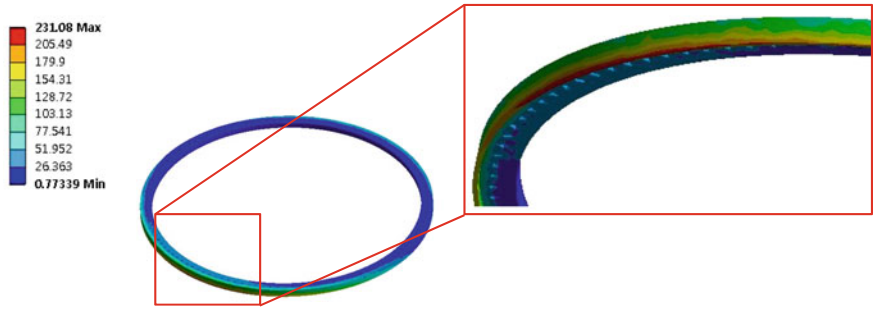


(b) upper tower flange

**Fig. 6** Von Mises distributions equivalent stress

aspect ratio ($h_1/h_2$), that is the height of outer diameter ($h_1$) and the height of inner diameter ($h_2$) of the flange as a design parameter, which is shown in Table 3. The aspect ratio was determined by changing the height of inner diameter ($h_2$), when the height of outer diameter ($h_1$) was fixed to the length of the basic model of the flange. When comparing the equivalent stress of von Mises stress between the upper part and the lower part of the flange, the upper part showed 226.37 MPa, and the lower part showed 231.08 MPa. Higher stresses were observed at the bottom flange than at the

**Table 3** Design parameters of tower flange for each case

| Case | Aspect ratio ($h_1/h_2$) |
|---|---|
| 1 | 1.24 |
| 2 | 1.33 |
| 3 | 1.36 |
| 4 | 1.40 |
| 5 | 1.44 |
| 6 | 1.48 |
| 7 | 1.61 |

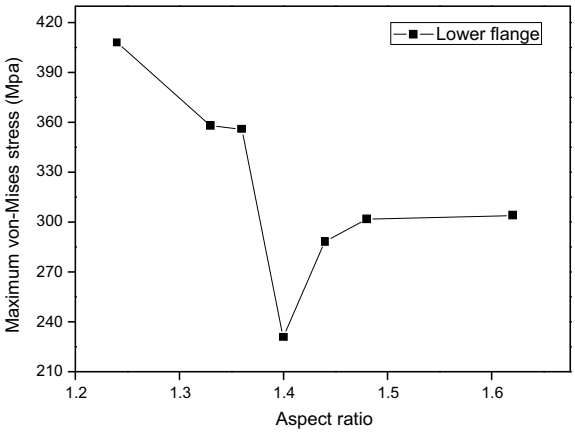


**Fig. 7** Maximum von Mises stress of tower flanges at wind speed of 5 m/s and blade rotation speed of 10 RPM

top flange. Figure 7 shows the von Mises equivalent stress acting on the lower flange when the inlet wind speed is 5 m/s. The flange aspect ratio was evaluated in the range of $h_1/h_2 = 1.2$–$1.6$. It is seen that the von Mises equivalent stress decreases as the aspect ratio increases. However, the von Mises equivalent stress increased when the aspect ratio was larger than $h_1/h_2 = 1.40$. Figure 8 shows the maximum deformation when the aspect ratio of flange is $h_1/h_2 = 1.40$. When the flange aspect ratio was $h_1/h_2 = 1.40$, the maximum von Mises stress value was lower than the yield stress of SM35C, and the maximum deformation amount was small. In hence, the flange aspect ratio with the most structural stability could be judged.

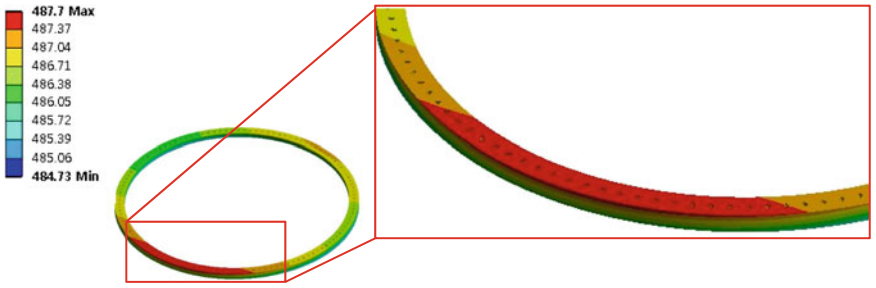


**Fig. 8** Total deformation of lower tower flange with aspect ratio of $h_1/h_2 = 1.40$

## 5 Conclusions

In this study, the shape of the tower flange connecting the tower shell in the wind turbine was confirmed by the fluid-structure analysis according to the wind speed and the dynamic load. The stress concentration was confirmed on the side of the center rather than on the center of the blade.

Through the case analysis according to the flange aspect ratios, the shape with low stress concentration was found. As a result of the numerical analysis, it was confirmed that the maximum von Mises stress had a lower stress value than that of the design material SM35C when the flange aspect ratio was $h_1/h_2 = 1.40$, and the maximum deformation amount was not large, respectively.

**Acknowledgements** This research was carried out by the research grant support (S-2017-2461-000) of the energy technology development project of Ministry of Industry and Commerce of Korea.

## References

1. Perelmuter, A., Yurchenko, V.: Parametric optimization of steel shell towers of high-power wind turbines. Procedia Eng. **57**, 895–905 (2013)
2. Bazeos, N., Hatzigeorgiou, G.D., Hondros, I.D., Karamaneas, H., Karabalis, D.L.: Static, seismic and stability analyses of a prototype wind turbine steel tower. Eng. Struct. **24**, 1005–1025 (2002)
3. Murtagh, P.J., Basu, B., Broderick, B.M.: Along-wind response of a wind turbine tower with blade coupling subjected to rotationally sampled wind loading. Eng. Struct. **27**, 1209–1219 (2005)
4. Feliciano, J., Cortina, G., Spear, A., Calaf, M.: Generalized analytical displacement model for wind turbine towers under aerodynamic loading. J. Wind Eng. Ind. Aerodyn. **176**, 120–130 (2018)
5. Jiang, W., Fan, Q., Gong, J.: Optimization of welding joint between tower and bottom flange based on residual stress considerations in a wind turbine. Energy **35**, 461–467 (2010)
6. Ali, N., Hamilton, N., Cortina, G., Calaf, M., Cal, B.: Anisotropy stress invariants of thermally stratified wind turbine array boundary layers using large eddy simulations. J. Renew. Sustain. Energy **10**, 013301 (2018)
7. Cortina, G., Calaf, M.: Turbulence upstream of wind turbines: a large-eddy simulation approach to investigate the use of wind lidars. Renew. Energy **105**, 354–365 (2017)
8. Kragh, K.A., Hansen, M.H.: Load alleviation of wind turbines by yaw misalignment. Wind Energy **17**, 971–982 (2014)

# The Dynamics of Bumblebee Wing Pitching Rotation: Measurement and Modelling


**Dmitry Kolomenskiy, Sridhar Ravi, Ru Xu, Kohei Ueyama, Timothy Jakobi, Thomas Engels, Toshiyuki Nakata, Jörn Sesterhenn, Marie Farge, Kai Schneider, Ryo Onishi, and Hao Liu**

**Abstract** Fluid-structure interaction of the flapping wings of a hovering bumblebee is considered. Kinematic reconstruction of the wing motion using synchronized high-speed video recordings is described, that provides the necessary input data for numerical modelling. Computational fluid dynamics (CFD) solver is combined with a dynamical model that describes the wing motion. Results of a high resolution numerical simulation are presented.

**Keywords** Flapping flight · Insect · Bumblebee · Wing · Fluid-structure interaction

D. Kolomenskiy (✉) · R. Onishi
Japan Agency for Marine-Earth Science and Technology (JAMSTEC), Yokosuka, Japan
e-mail: dkolom@gmail.com; dkolomenskiy@jamstec.go.jp

S. Ravi · T. Jakobi
School of Aerospace Mechanical and Manufacturing Engineering,
RMIT University, Melbourne, Australia

R. Xu · K. Ueyama · T. Nakata · H. Liu
Graduate School of Engineering, Chiba University, Chiba, Japan

R. Xu · H. Liu
Shanghai-Jiao Tong University and Chiba University International Cooperative Research Centre (SJTU-CU ICRC), Shanghai, People's Republic of China

T. Engels · M. Farge
LMD-CNRS, Ecole Normale Supérieure and PSL, Paris, France

T. Engels · J. Sesterhenn
ISTA, Technische Universität Berlin, Berlin, Germany

K. Schneider
Institut de Mathématiques de Marseille, CNRS, Aix-Marseille Université, Marseille, France



M. Braza et al. (eds.), *Advances in Critical Flow Dynamics Involving Moving/Deformable Structures with Design Applications*, Notes on Numerical Fluid Mechanics and Multidisciplinary Design 147,
https://doi.org/10.1007/978-3-030-55594-8_13

## 1 Introduction

Many insect species are skilful hovering fliers that can generate positive lift during both upstroke and downstroke. This ability is achieved by large pitching (feathering angle) rotations of the wings necessary for maintaining a positive kinematic angle of attack. Earlier research (e.g., [1, 2]) has shown that similar kinematic patterns can be produced by a wing with only up- and downstroke motion being prescribed, and elastic hinge attachment permitting passive pitching rotation. By construction, this model mimics dipteran wings, and serves as a mechanism for regulating the high-frequency flapping motion only using low-frequency control input [3]. It is logical to inquire whether this control strategy can be broadly used by all flying insects. In particular, it may be suitable for hymenopterans since their hindwings are connected to the forewings by hooks. To assess the accuracy of this hypothesis, we consider the hovering flight of a bumblebee *Bombus ignitus*. Our work consists of morphological measurements in order to quantify the geometrical and the inertial properties of the wings, construction of a kinematic model of the insect, free-flight measurement of the body posture and of the wing kinematics, and computational fluid dynamics (CFD) simulations. The objective of this paper is to describe the last two steps taking one selected flight of one individual bumblebee as an example. Statistical analysis of similar results obtained for multiple individuals is our current work in progress and it will be presented elsewhere.

Section 2 describes the process of three-dimensional reconstruction of the wing kinematics from synchronized video recordings. The outcome of it is the time evolution of the wing kinematic angles and the body attitude. Section 3 shows the results of a corresponding CFD simulation of the same flight. Conclusions are drawn in Sect. 4.

## 2 Kinematic Reconstruction

A hive (Mini Polblack, Koppert, Arysta LifeScience Asia, Japan) was maintained at Chiba University through May 2016. The bees were trained to fly through a tunnel with transparent ceiling. One end of the tunnel was connected to the hive and the other to the feeding area. In the duration of the experiment, the humidity was near to 80% and the temperature was maintained at about 22 °C. The test section in the flight tunnel was illuminated using lights. The video recordings of the hovering flight discussed in this paper were acquired using three synchronized high-speed cameras (FASTCAM SA3, Photron, Japan), equipped with CCTV lens (B2514D or B5014A, Pentax, Japan) at 2000 fps, but only two views were used in the present analysis. The image resolution was set to $1024 \times 1024$ pixels. The shutter speed was 1/7500 s. Sample frames from two cameras, with a zoom on the insect, are shown in Fig. 1. An extended description of the experiment and data acquisition setup can be found in [4].

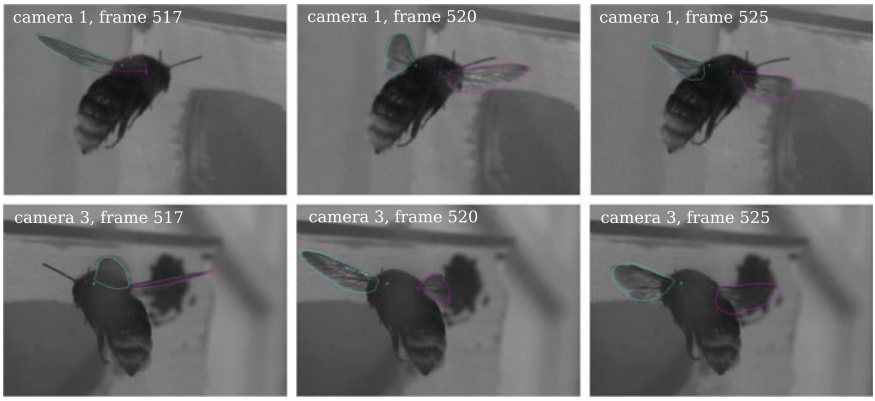


**Fig. 1** Sample frames from two synchronized video recordings: camera 1 (top row) and camera 3 (bottom row). Frames 517 and 520 correspond to downstroke, frames 525 correspond to upstroke. Theoretical rigid wing contour lines, shoulder points (plus signs) and body markers (dots) are superposed on the images

For kinematic analysis of the three-dimensional motion of the bumblebee body and flapping wings, we modified the open-source software DLTv5. The software is based on the direct linear transform method [5]. It is implemented in Matlab (MathWorks, Inc., USA). The modification mainly consists in introducing the same kinematic model as used in our CFD solver, FluSI [6]. Each forewing-hindwing pair is approximated as a single solid flat plate that can rotate about the hinge point at the shoulder, therefore its position with respect to the body is fully described with three angles. The body is also assumed rigid, therefore it is straightforward to relate the position of the shoulder points in the laboratory reference frame to the position of the center of mass and the three Euler angles of the body.

The video sequence selected for the present analysis corresponds to the hovering flight #6 in [7]. The body moves very little during the entire video. Nevertheless, this small motion should be taken into account when calculating the wing angles, because the latter are sensitive to movement of the hinges. Therefore, we first reconstructed the three-dimensional motion of the body. We selected three points that can be easily distinguished by morphological features. As shown in Fig. 1, point 1 is on the head between the antennae (red marker), point 2 is an abdominal pigmentation feature (green marker), and point 3 is the rear point of the abdomen (blue marker). Every 10th frame of total 1167 frames in each camera view were analyzed. The points were manually tracked and their coordinates in the laboratory reference frame reconstructed using DLTv5, the result being displayed in Fig. 2 (left). Figure 2 (right) shows the velocity magnitude of each point, calculated using central finite difference approximation. The velocity is no greater than $V_g = 0.023$ m/s, and the corresponding advance ratio is equal to $J = V_g/(2\Phi f R) = 0.0024$, where $f$, $\Phi$ and $R$ are the wingbeat frequency, amplitude, and the wing length, respectively. This small advance ratio is indicative of hovering.

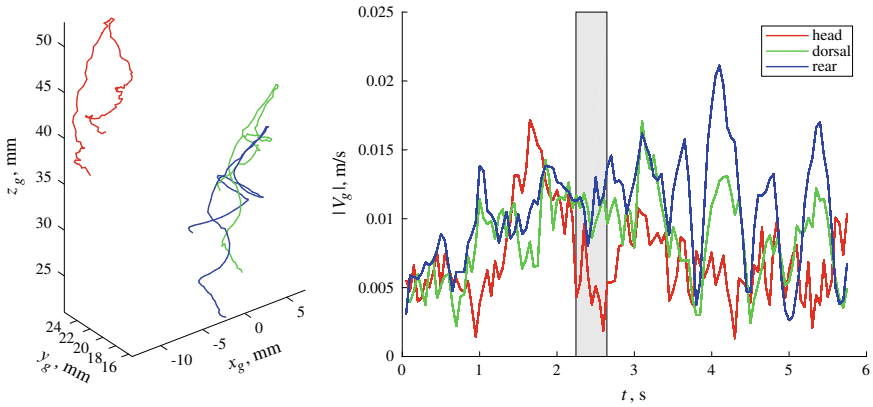


**Fig. 2** Left: trajectories of three points on the body—one on the head, one on the dorsal surface of the abdomen, and one on the rear end of the abdomen. Right: time evolution of the velocity magnitude of these points

The time sequence of almost 6 s is longer than required for digitization of the wing motion. We therefore select only a subsequence of 40 ms for the further analysis, which is shaded in Fig. 2 (right). The velocity in it is less than 0.015 m/s. During this short time interval, time-varying position of the three feature points in the laboratory reference frame is fit with cubic polynomials in order to filter out the digitization noise. In the body reference frame, relative position of different points (i.e., the shoulder hinges, the center of mass and the three selected morphological features) does not vary in time, therefore, it can be determined from prior morphological measurement or time-averaging over the duration of the entire flight sequence. Hence, after reconstructing the three-dimensional motion of the selected morphological feature points, we determine the motion of the entire body including the shoulder hinge points. The latter are shown in Fig. 1 with cyan and magenta plus signs.

As a next step, we track the wing tips, reconstruct the wing tip trajectories, convert them to the body reference frame and best-fit a plane, in the least-mean-square sense. The morphological stroke plane angle is determined as the angle between the normal to that plane and the body longitudinal axis. The stroke plane, in our definition, is inclined at the same angle to the body and passes through the shoulder hinge points, as shown in Fig. 3.

Finally, we determine the time evolution of the wing angles with respect to the stroke plane, see Fig. 3 for the definitions. The values of the positional angle $\phi$, the elevation angle $\theta$ and the feathering angle $\alpha$ are determined for the left and for the right wing separately, for every time frame. First approximation to $\phi$ and $\theta$ is calculated using the wing-tip coordinates relative to the hinge point. After that, the wing contour projection is superposed on the video image. It is drawn interactively as the values of $\phi$, $\alpha$ and $\theta$ are manually adjusted for the best visual fit. For this purpose, as for the subsequent CFD simulation, we use the archetypal contour constructed in

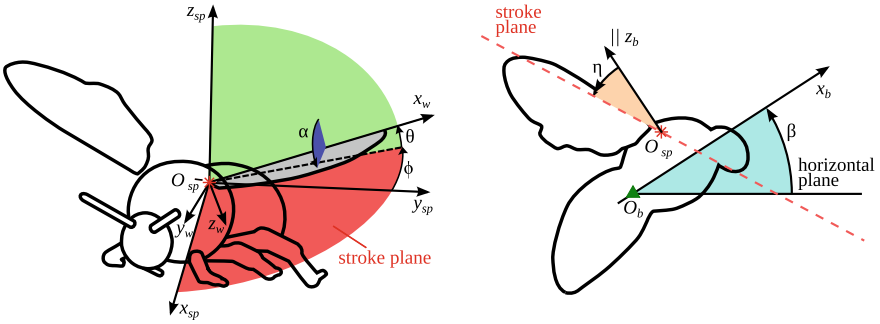


**Fig. 3** Definition of the wing positional angle $\phi$, feathering angle $\alpha$, elevation angle $\theta$, body angle $\beta$ and anatomical stroke plane angle $\eta$. $O_{sp}$ is one of the two shoulder points, $O_b$ is the body center of mass

[8], scaled with the wing length $R = 14.6$ mm determined from the video as the average distance between the shoulder and the wing tip. Example visualizations of this fit are shown in Fig. 1. The digitized left (resp., right) wing contour outline is shown with a cyan (resp., magenta) closed curve. Generally, the approximation is visually better during the downstroke (first two frames in a row) than during upstroke (last frame in a row), as the wing deformation is greater during upstroke.

The complete measured time sequences of the wing angles are displayed as markers in Fig. 4. The resolution of 13 points is high enough to describe the important repetitive features of the time profiles, such as the double negative peak of $\alpha$ during upstroke. The motion is nominally periodic, with small deviations that may be due to actuation, fluid-structure interaction and measurement errors. The next processing step consists in low-pass filtering the data at 450 Hz using the 4th order Butterworth filter and upsampling the result on a 100-times finer grid using spline interpolation. Thus we discard those points that produce unrealistically large accelerations. The resulting time profiles are shown with dotted and dashed lines that correspond to the left and the right wing, respectively.

From frequency analysis of $\phi(t)$ we find that the flapping frequency is equal to $f = 144.6$ Hz. We use this value to divide the sequences shown in Fig. 4 in cycles of length $T = 1/f = 6.92$ ms. In Fig. 5 (left), we plot the time evolution of $\phi$, $\alpha$ and $\theta$ during each cycle, with $t = 0$ corresponding to the beginning of downstroke. The original profiles are shown with thin faded lines. For every time instant $t$ during the cycle, we calculate the average of 4 subsequent wingbeats. The average time profiles are shown with thick bright lines in Fig. 5 (left), and thin bright lines in Fig. 5 (right). These time sequences are very close to periodic. There remains less than 10% difference between the angles of the left wing and those of the right wing, and we calculate their average. The result is plotted in Fig. 5 (right) using thick lines. Finally, Fourier analysis of these time sequences is performed. The time evolution of $\phi$, $\alpha$ and $\theta$ is described with less than 1% error using, respectively, 4, 5 and 4 harmonics. These coefficients are used as input data for the numerical simulation and analysis presented in the next section.

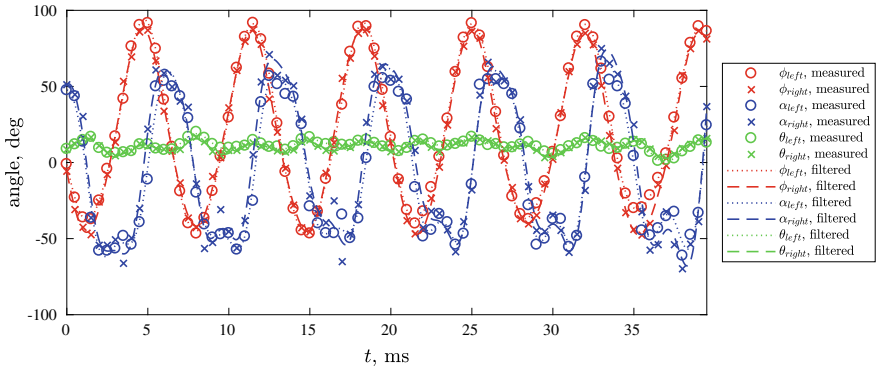


**Fig. 4** Time evolution of the wing kinematic angles. Markers show the raw data points obtained after digitizing each frame. Lines show the result of low-pass filtering and interpolation

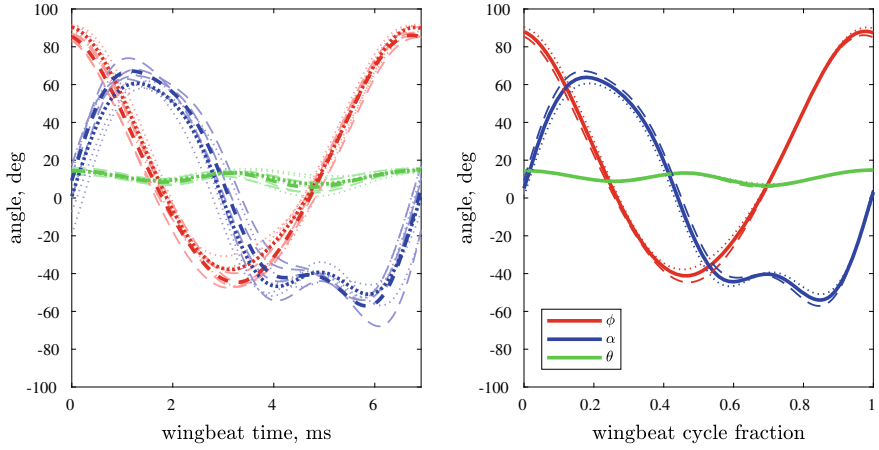


**Fig. 5** Left: Time evolution of the wing angles reduced to the time scale of one wingbeat (thin lines) and their average (thick lines). Right: average time profiles of the left and the right wing kinematics (thin lines) and the average of the two wings (thick lines), where the time is normalized by the wingbeat period $T$

## 3 Numerical Modelling

The fluid-structure interaction model of the flapping wings has been implemented using FluSI, a pseudo-spectral Navier–Stokes solver with volume penalization [6]. In the numerical simulation presented in this paper, the body of the bumblebee is fixed. The body shape is the same as in [9]. The shape of the wings is derived from the morphological measurements described in [8].

The positional angle $\phi(t)$ and elevation angle $\theta(t)$ of both wings are prescribed as periodic functions using Fourier coefficients, as described in the previous section. The feathering angle $\alpha(t)$ is determined from the following driven oscillator equation [2]:

$$\begin{aligned} I_{yy}\ddot{\alpha} &= M_{aero} - K(\alpha - \alpha_0) - C\dot{\alpha} \\ &+ I_{yy}\left[\frac{1}{2}(\dot{\phi}^2\cos^2\theta - \dot{\theta}^2)\sin 2\alpha - \ddot{\phi}\sin\theta - \dot{\phi}\dot{\theta}\cos\theta(1+\cos 2\alpha)\right] \\ &+ I_{xy}\left[\ddot{\phi}\cos\theta\cos\alpha + \ddot{\theta}\sin\alpha + \frac{1}{2}\dot{\phi}^2\sin 2\theta\sin\alpha - 2\dot{\phi}\dot{\theta}\sin\theta\cos\alpha\right], \end{aligned} \quad (1)$$

where $M_{aero}$ is the aerodynamic pitching moment. Positive $\theta$ is upwards. Typically, $\alpha$ is positive during downstroke and negative during upstroke. The moments of inertia are determined by integration of mass distribution in the $x_w - y_w$ plane of the wing, assuming that it is thin and flat, as follows:

$$I_{yy} = \int_{\Sigma_w} x_w^2 \mathrm{d}m_w, \qquad I_{xy} = \int_{\Sigma_w} x_w y_w \mathrm{d}m_w, \quad (2)$$

where $\Sigma_w$ is the wing surface, $\mathrm{d}m_w$ is the planar mass element of the wing, and $(x_w, y_w)$ are the coordinates of the element, see [8] for more detail. The aerodynamic pitching moment $M_{aero}$ is obtained by integrating the fluid forces acting on the wing. The shoulder hinge joint is modelled as a torsional spring with stiffness $K$, damping coefficient $C$ and neutral angle $\alpha_0$.

An example result of the numerical simulation is shown in Fig. 6. The parameters of the numerical simulation are as follows. The wing length is equal to $R = 14.6$ mm and the flapping frequency is $f = 144.6$ Hz, as described in the previous section. The wing beat amplitude that follows from Fig. 5 (right) is $\Phi = 129$ deg. Using the notation as in Fig. 3, the body angle is equal to $\beta = 47.8$ deg and the anatomical stroke plane angle is $\eta = 41$ deg. The elastic hinge model uses the stiffness $K = 2.52 \times 10^{-6}$ N m, damping $C = 0$ and neutral angle $\alpha_0 = -0.7$ deg. The wing moments of inertia are equal to $I_{yy} = 28.14 \times 10^{-12}\,\mathrm{kg\,m^2}$ and $I_{xy} = -0.70 \times 10^{-12}\,\mathrm{kg\,m^2}$.

Since the flapping motion started impulsively at the beginning of the numerical simulation, to avoid excessively large values of $M_{aero}$ at startup, the right-hand side of (1) was multiplied with a function smoothly varying from 0 to 1 during the time interval from 0.1 to 0.5 of the wingbeat period $T$. Therefore, the results of the simulation during the first wingbeat cycle are not physically significant. To reach quasi-periodic state of $\alpha(t)$ and the aerodynamic forces, the time span of the numerical simulation was set to $4T$.

In Fig. 6, gradations of grey are used to distinguish between the results that correspond to different wingbeat cycles in the numerical simulation. Time variation of $\alpha$ is almost the same during the last two cycles, see Fig. 6 (right). The r.m.s. distance is less than 11 deg with respect to $\alpha(t)$ obtained from the measurement described in the previous section (the blue line in Fig. 6). This value is of the same order of magnitude

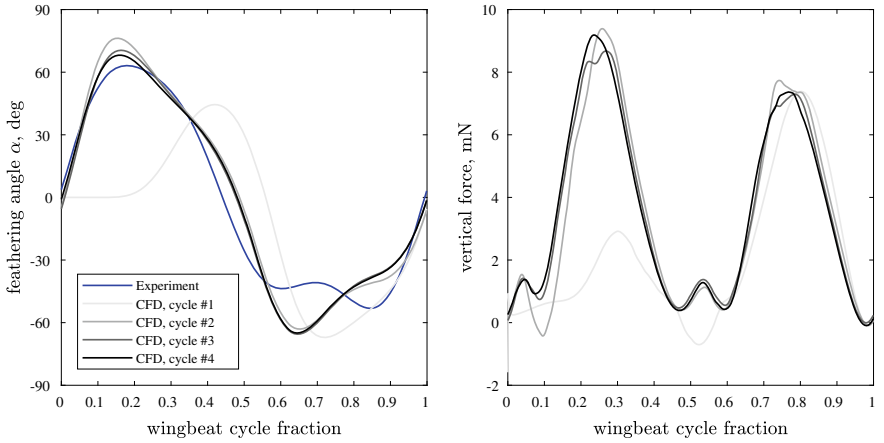


**Fig. 6** Left: time evolution of the feathering angle in the experiments and i the numerical simulation. Right: time evolution of the instantaneous aerodynamic vertical force

as the combined error of digitization, periodization, etc. The most obvious discrepancy is in the middle of upstroke when the model neglects wing deformation and, in particular, rotation of the hindwing relatively to the forewing. A more sophisticated deformable wing model may be necessary to reach better agreement in terms of $\alpha(t)$. Nonetheless, the agreement is reasonably good even using the present single-plate model, therefore, it is not surprising that the time-varying vertical force obtained from the model (Fig. 6 right) displays the double peak profile typical of hovering insects. The mean vertical force is large enough to support the body mass of 364 mg that is realistic for a bumblebee of this size.

## 4 Conclusions

In this paper, we discussed about application of a hinged-plate model to analyze pitching motion of flapping wings of a bumblebee during hovering. We described the methodology of kinematic reconstruction based on synchronized video recordings and presented an example of aerodynamic force calculation using CFD. In the model, the forewing and the hindwing are approximated by a one-piece rigid flat plate. Analysis of the video recordings suggests that the rigid wing contour can be adequately fit with outline of the real wing, despite some deformation of the latter. Numerical solution of the differential equation that governs the dynamics of the model, integrated with a Navier–Stokes solver, results in the wing pitching motion similar to that observed in the experiment. The r.m.s. error is less that 11 deg, and the discrepancy is essentially localized around the middle upstroke, when the flat wing approximation may fail. Nevertheless, the model successfully predicts the time

evolution of the lift force with two almost equal peaks, one during downstroke and the other during upstroke, that is typical of hovering insets wings. We found that the mean vertical aerodynamic force estimated from the numerical simulation is reasonably large to support the body weight.

**Acknowledgements** DK gratefully acknowledges financial support from the JSPS Grant-in-Aid 18K13693. TE, JS, MF, KS gratefully acknowledge financial support from the Agence nationale de la recherche (ANR Grant 15-CE40-0019) and Deutsche Forschungsgemeinschaft (DFG Grant SE 824/26-1), project AIFIT. This work was granted access to the HPC resources of IDRIS (Institut du Développement et des Ressources en Informatique Scientifique) under the allocation made by GENCI (Grand Équipement National de Calcul Intensif), project number A0022A01664.

## References

1. Ishihara, D., Horie, T., Niho, T.: An experimental and three-dimensional computational study on the aerodynamic contribution to the passive pitching motion of flapping wings in hovering flies. SIAM J. Sci. Comput. **9**(4), 046009 (2014)
2. Whitney, J.P., Wood, R.J.: Aeromechanics of passive rotation in flapping flight. Journal of Fluid Mechanics **660**, 197–220 (2010)
3. Beatus, T., Cohen, I.: Wing-pitch modulation in maneuvering fruit flies is explained by an interplay between aerodynamics and a torsional spring. Phys. Rev. E **92**(2), 022712 (2015)
4. Jakobi, T., Kolomenskiy, D., Ikeda, T., Watkins, S., Fisher, A., Liu, H., Ravi, S.:. Bees with attitude: the effect of gusts on flight dynamics. arXiv, 1802.03580 (2018)
5. Hedrick, T.L.: Software techniques for two- and three-dimensional kinematic measurements of biological and biomimetic systems. Bioinspiration Biomimet. **3**(3), 034001 (2008)
6. Engels, T., Kolomenskiy, D., Schneider, K., Sesterhenn, J.: A novel parallel simulation tool for flapping insect flight using a Fourier method with volume penalization. SIAM J. Sci. Comput. **38**(5), S3–S24 (2016)
7. Kolomenskiy, D., Ravi, S., Ueyama, K., Jakobi, T., Xu, R., Liu, H., Onishi, R., Engels, T., Schneider, K., Sesterhenn, J., Farge, M.: Bumblebee flight kinematics, Jan 2018. Dataset retrieved from: osf.io/2fked. Last Accessed on 16 May 2018
8. Kolomenskiy, D., Ravi, S., Xu, R., Ueyama, K., Jakobi, T., Engels, T., Nakata, T., Sesterhenn, J., Schneider, K., Onishi, R., Liu, H.: The dynamics of bumblebee wing pitching rotation: wing morphology and inertial properties. In: Proceedings of the 7th International Symposium on Aero Aqua Bio-mechanisms. ABMECH
9. Engels, T., Kolomenskiy, D., Schneider, K., Lehmann, F.-O., Sesterhenn, J.: Bumblebee flight in heavy turbulence. Phys. Rev. Lett. **116**(2), 028103 (2016)

# Transitional Flow Dynamics Past a Passively Flapping Airfoil in Gusty Flow


**Chandan Bose, Sayan Gupta, and Sunetra Sarkar**

**Abstract** This paper investigates the transitional flow dynamics behind a passively flapping airfoil supported by nonlinear springs in the presence of gusty inflow. The fluid-structure interaction (FSI) framework is composed of an incompressible Navier-Stokes solver weakly coupled with a two degree-of-freedom (dof) nonlinear structural model. The fluid-elastic system shows a rich bifurcation behavior in terms of successive Hopf bifurcations in uniform flow condition as the mean wind speed is increased. Presence of gusty fluctuations in the inflow makes the dynamics more complex through transitional states that we refer to as 'intermittency' between different dynamical states. A regular intermittent state between quasi-periodic dynamics and low amplitude aperiodic response has been observed when the FSI system is subjected to a time harmonic gust in terms of sinusoidal fluctuation. A parametric study has been carried out for various amplitudes and frequencies of the sinusoidal fluctuation to demarcate the transitional regimes. Thereafter, the system is subjected to random gusts modeled as Ornstein-Uhlenbeck process and 'on-off' and 'burst' type intermittent dynamics have been observed for long time-scale and short time-scale input fluctuations respectively. The intermittent states have been characterized through time series analyses tools and the corresponding flow-field dynamics has been investigated in detail.

**Keywords** Passive flapping · Fluid-structure interactions · Time harmonic gust · Ornstein-uhlenbeck process · Intermittent flow-field · On-off intermittency

C. Bose (✉) · S. Gupta
Department of Applied Mechanics, Indian Institute of Technology Madras, Chennai 600036, India
e-mail: cb.ju.1991@gmail.com

S. Sarkar
Department of Aerospace Engineering, Indian Institute of Technology Madras, Chennai 600036, India



M. Braza et al. (eds.), *Advances in Critical Flow Dynamics Involving Moving/Deformable Structures with Design Applications*, Notes on Numerical Fluid Mechanics and Multidisciplinary Design 147,
https://doi.org/10.1007/978-3-030-55594-8_14

## 1 Introduction

Of late, natural biological flyers have inspired the development of futuristic flapping wing micro aerial vehicles (MAVs), envisaged to perform a wide spectrum of missions including surveillance and environmental monitoring [1]. In this regard, the unsteady aerodynamics of rigid flapping wings in uniform flow condition is comparatively well explored in the literature [2, 3]. However, MAVs are highly susceptible to gusty flows due to their low inertia and low flight speed [4]. The performance of very light weight flapping wing MAVs can be significantly altered in the presence of gusty flow-field [5, 6]. Therefore, an appropriate understanding of aerodynamic performance of flapping wings subjected to gusty flows is crucial for the efficient design of bio-inspired man-made flapping devices.

The literature related to the effect of gust on the flapping wing aerodynamics is limited. Till date, researchers have mostly focused on quantifying the changes in the aerodynamic properties, such as lift and drag coefficients, in the presence of wind gust through computational fluid dynamics or experimental measurements. For instance, Lian and Shyy [7] observed that a flapping airfoil can significantly alleviate the impact of wind gust as compared to fixed airfoil, thus potentially benefiting the MAV design. Watkins et al. [5] reported that the wind gust made up of small scale eddies produce uneven lift distribution over a flapping wing, causing a rolling motion. On the other hand, gusts having large scale eddy motion cause pitch motion. Prater and Lian [8] inspected the effect of a sinusoidal gust on the cycle averaged lift force and the lift variation over a gust cycle. They also compared the force variations and increase in the force generation between stationary wings and flapping wings. Comparisons of aerodynamic performance were also made between different tandem wing configurations and a single wing in isolation in the presence of time harmonic gust. The above mentioned studies were carried out in the low Reynolds number regime. Recently, Jones and Yamaleev [9] considered turbulent flow conditions through an unsteady compressible Reynolds-averaged Navier-Stokes solver and reported that frontal gust significantly affects the instantaneous thrust generation by a flapping wing. In another recent study, Fisher et al. [10] carried out an experiment on a flapping flat plate wing in the presence of free-stream turbulence and measured the aerodynamic loads through pressure probes. They found that the average pressure distributions were significantly altered by turbulence and the variation in effective angle of attack was dominated by free-stream turbulence at low flapping frequencies.

Whereas most of these studies were confined to rigid wings, Shyy et al. [11] have compared the aerodynamic performance of rigid airfoils with that of flexible airfoils under gusty flows. They have reported that a flexible airfoil is able to maintain high lift to drag ratio as compared to a rigid airfoil. Thus, they concluded that flexibility can make the flapping flight gust tolerant. Nevertheless, the role of fluid-structure interaction in mitigating the effect of gust for flexible flapping wings is still an open-ended problem. Besides, the inclusion of flow fluctuations in the flapping wing aerodynamic models poses several computational challenges as the difference in the

gust frequency and the flapping frequency leads to a multi-scale problem. The fluid-elastic coupling adds to the computational difficulty. In most of these studies, the flow fluctuations were incorporated using a simplified model of time harmonic gust with a single frequency [7, 12, 13] and the flexibility was ignored. Very few studies [14–16] have considered a realistic gust model. While these studies investigated the quantitative change in the aerodynamic loads incurred by the wind gust, they do not study the gust induced transition in the system dynamics, the knowledge of which is essential for flight stability and control. In one of our recent study [17], stochastic bifurcation analysis of an elastically mounted airfoil subjected to random gust has been carried out in an inviscid fluid using a potential flow solver to avoid the massive computational cost associated with a N-S solver. The study revealed an interesting intermittent dynamics. To extend the understanding of the previous study in the presence of aerodynamic nonlinearity, this paper aims to examine the effect of fluctuating flow on the dynamical stability of a flexible flapping wing system using a high fidelity FSI framework since the coupled dynamics can be significantly altered due to the viscous separations in low Reynolds number regime.

The present study takes a detour from the conventional comparative analysis of aerodynamic loads generated by flapping wings in the absence and presence of wind gust and focuses on characterizing the dynamical transition that the system undergoes for different amplitudes and frequencies of the gusty fluctuation. This paper further aims to extend the understanding about the system stability in the presence of random gusts modeled as stochastic processes having either long or short time-scale fluctuations. Moreover, one of the main objectives of this paper is to explore the underlying flow physics to gain better insights into the transitional system dynamics. The rest of the paper is organized into three sections which discuss the governing equations and the computational methodology, the numerical results and the outcomes of this study.

## 2 Governing Equations and Computational Details

The structure is modeled as a chord-wise rigid NACA 0012 airfoil having translational and rotational springs to model the plunge and pitch degrees of freedom (dof) due to span-wise bending and torsional flexibility. The structural governing equations show the effect of geometric nonlinearity (large deformations) with a cubic nonlinear stiffness along pitch dof. The schematic diagram for the pitch-plunge 2-dof model is shown in Fig. 1.

The non-dimensionalized equations of motion for the pitch-plunge flapping wing model are [18],

$$h'' + x_\alpha \alpha'' + 2\,\zeta_h\,(\frac{\bar{\omega}}{U^*})\,h' + (\frac{\bar{\omega}}{U^*})^2\,h = \frac{1}{\pi\,\mu}\,C_l, \tag{1}$$

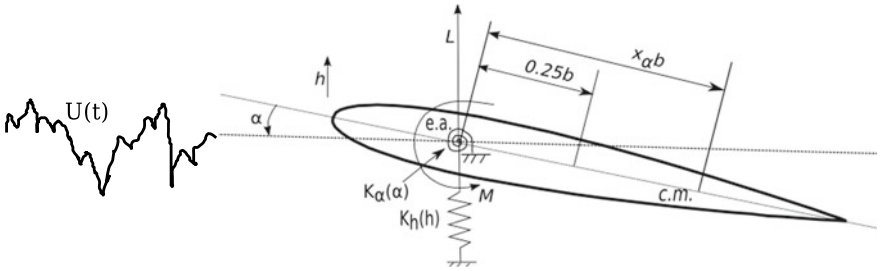


**Fig. 1** Schematic of airfoil in pitch and plunge degrees of freedom

$$\frac{x_\alpha}{{r_\alpha}^2}\, h'' + \alpha'' + 2\,\left(\frac{\zeta_\alpha}{U^*}\right)\alpha' + \left(\frac{1}{U^*}\right)^2 (\alpha + \beta_\alpha \alpha^3) = \frac{2}{\pi\,\mu\,{r_\alpha}^2}\, C_m. \tag{2}$$

The non-dimensional variables are defined as follows: $h = y/b$; $x_\alpha = S/mb$; $r_\alpha = \sqrt{I/mb^2}$; $U^* = U_\infty/b\omega_\alpha$; $\tau = U_\infty t/b$; $\bar{\omega} = \omega_h/\omega_\alpha$; $\mu = m/\pi\rho b^2$. Here, $b$ is the semi-chord, $r_\alpha b$ is the radius of gyration, $x_\alpha b$ is the distance between the center of mass and elastic center; $\omega_h$ and $\omega_\alpha$ are the uncoupled natural frequencies of plunge and pitch respectively; $\beta_\alpha$ determines the extent of non-linearity in the spring stiffness along the pitch degree of freedom; $U_\infty$ is the free-stream; $C_l$ and $C_m$ are the time varying lift and moment coefficients, which are computed using a N-S solver at each instant of time. The arbitrary Lagrangian Eulerian (ALE) formulation [19] has been opted for discretization of the N-S equation on a deformed mesh. The N-S equation is cast into the ALE form as [19],

$$\nabla.\vec{u} = 0, \tag{3}$$

$$\frac{\partial \vec{u}}{\partial t} + [(\vec{u} - \vec{u}^m).\nabla]\vec{u} = -\nabla p/\rho + \nu\nabla^2\vec{u}. \tag{4}$$

Here, $\vec{u}$ is the velocity of the flow, $\vec{u}^m$ is the grid point velocity, $p$ is the pressure, $\nu$ is the kinematic viscosity and $\rho$ is the fluid density. The simulations are performed using a finite-volume based open source CFD solver OpenFOAM® [20]. The simulation of the unsteady flow-field has been carried out over a rectangular computational domain ($21c \times 18c$) with the airfoil situated at a distance '$5c$' from the inlet ($c$ = chord length of the airfoil). A hybrid mesh with a combination of structured and unstructured grids containing a total of 82,372 grid points has been chosen after a mesh convergence test. The detailed computational methodology, grid independence test and the flow solver validation can be found in a recent study by the authors [21]. A partitioned approach based weak coupling method [22] has been adopted while coupling the unsteady flow solver with the structural model. The structural responses are obtained by numerically integrating Eqs. (1)–(2) using an explicit fourth-order Runge-Kutta method. The time step for integrating structural equations of motion is

**Table 1** Parameter values

| $b$ | $\beta_\alpha$ | $\bar{\omega}$ | $r_\alpha$ | $x_\alpha$ | $\mu$ | $\nu$ |
|---|---|---|---|---|---|---|
| 0.50 m | 3.00 | 0.80 | 0.50 | 0.25 | 5.00 | $0.05 \times 10^{-2}$ m$^2$/sec |

taken to be equal to that of the N-S solver. The computations have been performed with the parameter values mentioned in Table 1.

The fluctuating flow field can be represented as,

$$U(t) = U_\infty + U_g(t), \tag{5}$$

where $U_g(t) = A_g \sin(2\pi f_g t)$ is modeled as a sinusoidal fluctuation when the system is subjected to a time harmonic gust and $A_g$ and $f_g$ are the amplitude and frequency of the fluctuation. Alternatively, $U_g(t)$ could be modeled as an Ornstein-Uhlenbeck (O-U) process [23, 24] to represent a random gust. The O-U process is a stationary Gauss-Markov process and is defined by the following stochastic differential equation:

$$\mathrm{d}U_g(t) = -\Delta\omega U_g(t)\,\mathrm{d}t + \sqrt{\Delta\omega q}\,\mathrm{d}W(t), \tag{6}$$

where $W(t)$ is a Wiener process, $\Delta\omega$ and $q$ are noise parameters. The correlation function of the O-U process is given by,

$$\rho(t) = < U_g(t)U_g(0) > = q\exp(-\Delta\omega|t|). \tag{7}$$

The O-U process is simulated by numerically integrating the stochastic differential equation using the Euler-Maruyama method [25].

## 3 Results and Discussions

This paper is an extension of a recent study by the authors [26] in which the bifurcation behavior of the present system was studied in uniform flow condition ($Re = 1000$) considering the mean wind speed as the control parameter. In [26], the FSI system was seen to undergo two successive Hopf bifurcations at a very low solid to fluid added mass ratio ($\mu = 5$) - a supercritical Hopf bifurcation at $U^* = 1.1$ and a Neimark-Sacker bifurcation at $U^* = 1.8$. The first bifurcation leads to a stable limit-cycle oscillation (LCO) from a fixed-point (FP) response while the second one leads to the system transitioning to quasi-periodic (QP) oscillations; see the bifurcation diagram for plunge response in Fig. 2. Similar to the earlier study, the present analysis also chooses a low solid to fluid mass ratio ($\mu = 5$). The primary focus of the present paper is on understanding the changes manifested in the FSI dynamics as the incoming wind experiences temporal gusty fluctuations in terms of both time-harmonic and random gust.

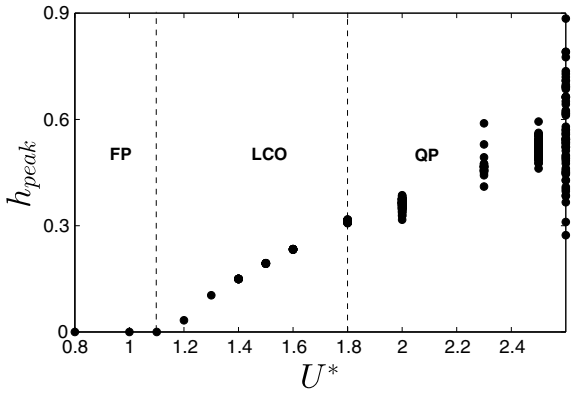


**Fig. 2** Bifurcation diagram of the plunge response in uniform flow condition

## *3.1 Effect of Time-Harmonic Gust*

The transitional dynamics of the system has been studied first in the presence of time-harmonic gust (a sinusoidal fluctuation is superimposed to the uniform free-stream velocity). Two different dynamical states present in the uniform flow condition, a FP response at $U^* = 1.0$ and a LCO response at $U^* = 1.3$, have been considered in this study to investigate the effect of time harmonic gust on the dynamical transition of the system. The system has been studied for normalized amplitudes, $A_g^*$ defined as $A_g/U_\infty$, equal to 15, 23 and 31% and frequencies lying in the range $0.05 - 2.0$ Hz.

Figure 3 presents the plunge response at the mean non-dimensional velocity $U_m^* = U_\infty/b\omega_\alpha = 1.0$, superimposed with a sinusoidal fluctuation having $A_g^* = 15\%$ and $f_g = 0.5$ Hz. It is observed that the system no longer gets attracted to the stable equilibrium point at zero as seen in the uniform flow condition; instead, the system experiences low amplitude aperiodic oscillations as can be seen in Fig. 3a. The broadband frequency components seen in the frequency spectra (Fig. 3b) along with the dominant peaks represent the aperiodic signature. Similar dynamics has been observed at the other amplitudes and frequencies considered in this paper.

An interesting course of transition has been observed in the system dynamics for different values of $f_g$ at $U_m^* = 1.3$. Figure 4 presents the time histories and the phase portraits of the plunge responses for different $f_g$ values at $A_g^* = 15\%$ and $U_m^* = 1.3$. The corresponding frequency spectra and the wavelet spectra are presented in Fig. 5. From the time history in Fig. 4a, it can be seen that the plunge response at $f_g = 0.1$ Hz is composed of two distinct dynamical states alternating periodically. In dynamical literature, the irregular hopping of the system between two distinct states of dynamics is defined as intermittency. It is to be noted that, in the presence of a time harmonic gust, the system alternates between two distinct dynamical states in a regular fashion and hence the phenomenon is termed as 'regular intermittency' in this paper. This is in contrast to the case when the system hops between two distinct states in an aperiodic manner. In this case, the regular intermittent transition takes place between quasi-periodic bursts and subsequent low amplitude aperiodic oscillations. The quasi-

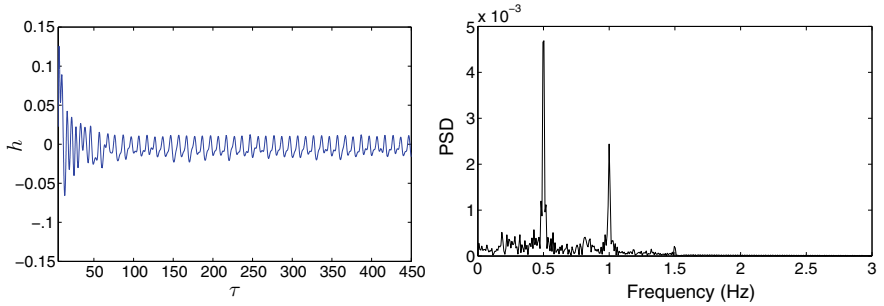


(a) Time history (b) Frequency Spectra

**Fig. 3** Plunge response at $U_m^* = 1.0$, $A_g^* = 15\%$ and $f_g = 0.5$ Hz

periodic nature can be confirmed from its toroidal phase-space; see Fig. 4b, as well as, from the incommensurate nature of the system frequency ($f_s$) and the gust frequency ($f_g$). As can be seen from the frequency spectra in Fig. 5a, the existing frequencies can be represented as a linear combination of $f_s$ and $f_g$, which is indicative of their incommensurate nature. A clear picture of this intermittent behavior can also be obtained through the temporal evolution of the frequency spectra in the wavelet spectra; see Fig. 5b. The regular intermittent transition between quasi-periodic bursts and the low amplitude aperiodic oscillations at low gust frequencies occurs because of the sinusoidal gust velocity crossing the second bifurcation limit in a periodic manner and spending sufficient time at each dynamical state. As $f_g$ is increased to 0.2 Hz., the stay-time in the low amplitude aperiodic state is seen to be significantly reduced and the quasi-periodic oscillations becomes dominant resulting in a denser toroidal structure in the phase-space; see Fig. 4c, d. This is also reflected in the wavelet spectra in Fig. 5d. As the value of $f_g$ is further increased, the intermittent states are seen to disappear paving way for a sustained quasi-periodic dynamics. This can be attributed to the fact that the system does not get sufficient time for transitioning to the other state and staying in that regime for sufficient time for the system dynamics to be manifested when the fluctuations are rapid (which implies short time scale fluctuations). Moreover, at $f_g = 1.5$, the system frequency locks in with the gust frequency resulting in period-1 behavior. The period-1 oscillation and the corresponding closed attractor can be seen from the time history and the phase-space respectively; see Fig. 4e, f. Figure 5e, f reveal the existence of a single dominant frequency in the frequency spectra and the wavelet spectra respectively. As $f_g$ is increased further, a fully developed quasi-periodic response is observed; see Fig. 4g, h. The presence of incommensurate frequencies is clearly seen in the frequency spectra as well as wavelet spectra (Figs. 5g, h). A parametric map with variation of parameters $A_g^*$ and $f_g$ is presented in Fig. 6 which denotes the set of different dynamical states observed in the system as described above. It is to be noted that the critical value of $f_g$ at which the quasi-periodic intermittent state disappears decreases as the amplitude of the sinusoidal gust increases.

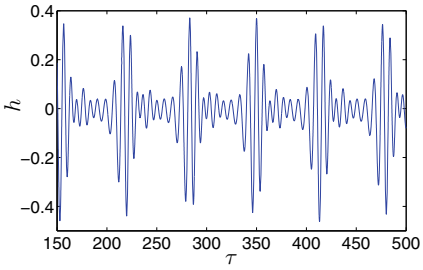


(a) Time history at $f_g = 0.1$ Hz.

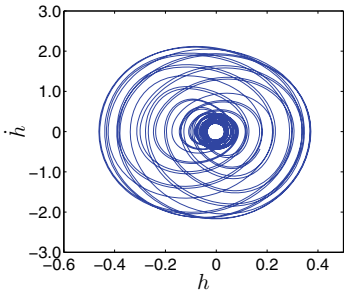


(b) Phase-space at $f_g = 0.1$ Hz.

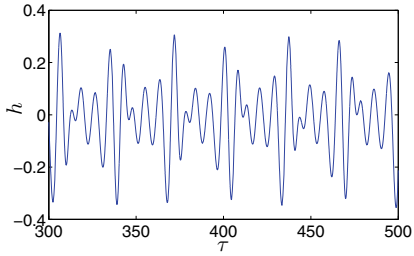


(c) Time history at $f_g = 0.2$ Hz.

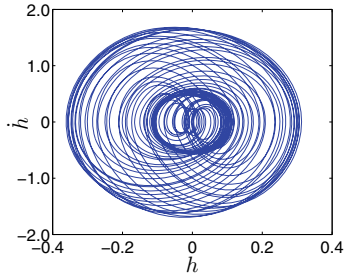


(d) Phase-space at $f_g = 0.2$ Hz.

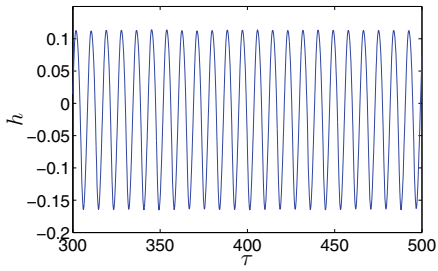


(e) Time history at $f_g = 1.5$ Hz.

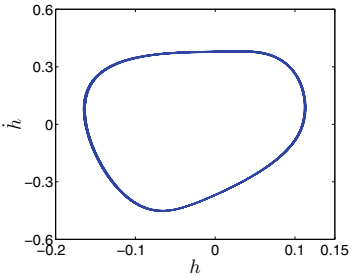


(f) Phase-space at $f_g = 1.5$ Hz.

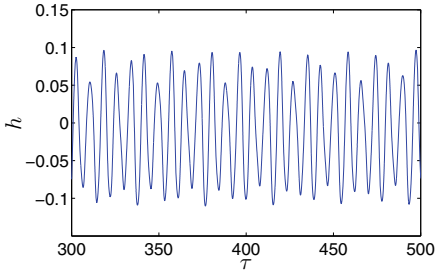


(g) Time history at $f_g = 2.0$ Hz.

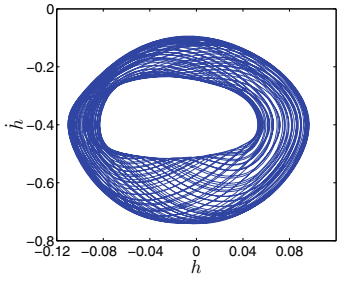


(h) Phase-space at $f_g = 2.0$ Hz.

**Fig. 4** Plunge response at $U_m^* = 1.3$, $A_g^* = 15\%$ and $f_g = 0.1$ Hz., 0.2 Hz., 1.5 Hz. and 2.0 Hz

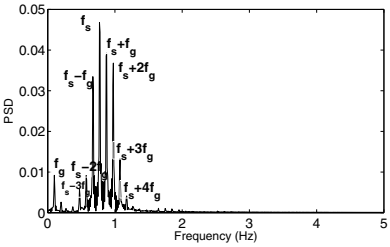


(a) Frequency spectra at $f_g = 0.1$ Hz.

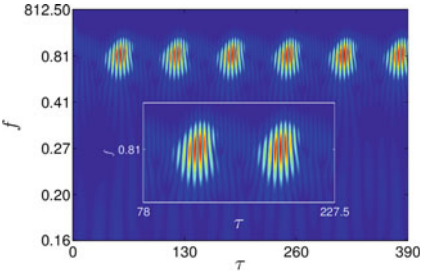


(b) Wavelet spectra at $f_g = 0.1$ Hz.

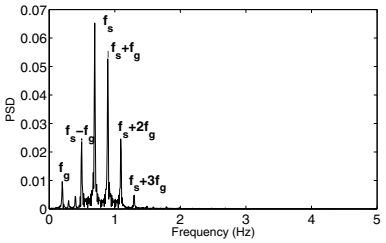


(c) Frequency spectra at $f_g = 0.2$ Hz.

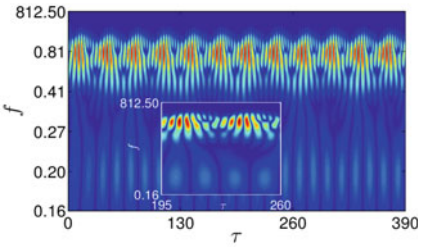


(d) Wavelet spectra at $f_g = 0.2$ Hz.

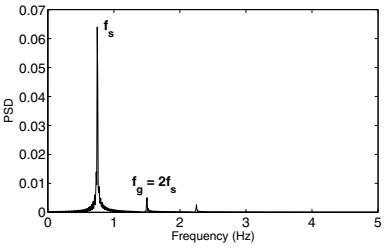


(e) Frequency spectra at $f_g = 1.5$ Hz.

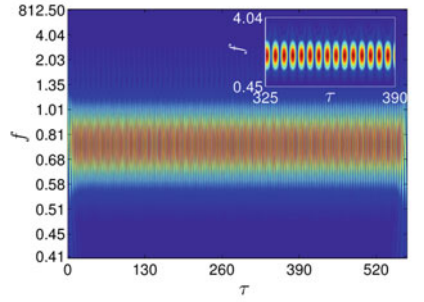


(f) Wavelet spectra at $f_g = 1.5$ Hz.

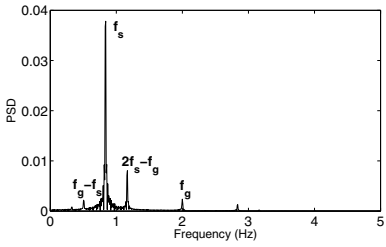


(g) Frequency spectra at $f_g = 2.0$ Hz.

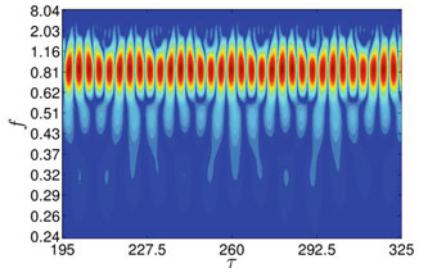


(h) Wavelet spectra at $f_g = 2.0$ Hz.

**Fig. 5** Time-frequency analysis of plunge response at $U_m^* = 1.3$, $A_g^* = 15\%$ and $f_g$ = 0.1 Hz., 0.2 Hz., 1.5 Hz. and 2.0 Hz

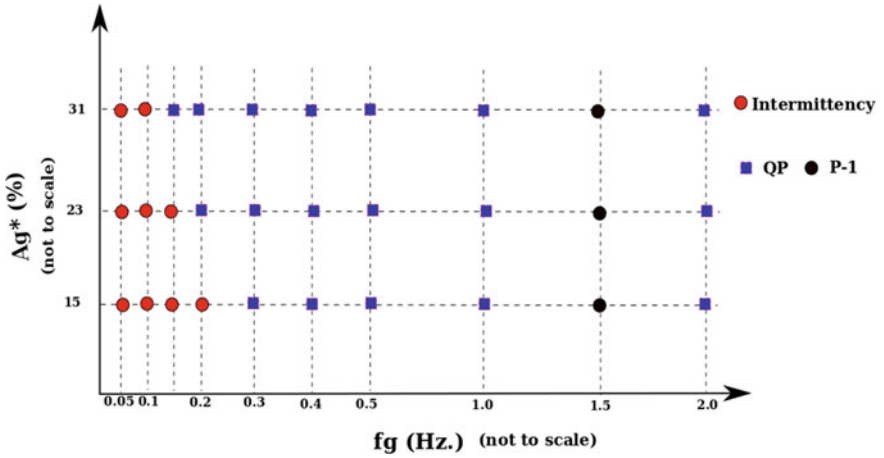


**Fig. 6** Parametric map of various dynamics of plunge response at $U_m^* = 1.3$

## *3.2 Intermittent Flow Dynamics*

The flow dynamics during the intermittent transition is discussed next in terms of the vortex evolution in the wake of the passively flapping airfoil in the temporal window of $\tau$ = 262.76 - 326.92 at $U_m^* = 1.3$, $A_g^* = 15\%$ and $f_g$ = 0.1 Hz. At $\tau$ = 262.76, the vorticity contour corresponds to the low amplitude oscillating state where the shear layers from the upper and lower surfaces of the airfoil are seen to shed past the airfoil trailing-edge undergoing a very low amplitude and low frequency oscillation; see Fig. 7a. As the airfoil motion approaches the higher amplitude quasi-periodic burst phase at $\tau$ = 279.14, the shear layers start oscillating with higher amplitude. Consequently, the shear layers become unstable and impinge on each other, resulting in a train of small vortex couples as can be seen from Fig. 7b. As the airfoil response enters the burst phase, it oscillates with even higher amplitude and frequency, which in turn increases the effective angle of attack, inducing vortex roll up in the leading edge. Secondary vortex structures are also seen to form over the airfoil surface. As a result, the small attached LEV convects towards the trailing edge and forms a couple with the secondary vortex structure, which gets separated from the trailing edge. It is to be noted that the phase of the vortex shedding changes slightly from one cycle to another resulting in loss of flow periodicity in line with the structural quasi-periodic oscillation. Thus, an oscillating wake pattern is observed, however, that changes by a small margin from one cycle to another at $\tau$ = 288.02; see Fig. 7c. Thereafter, as the airfoil approaches the end of the burst phase, the amplitude of the oscillation decreases and the corresponding system frequency also gets changed resulting in a transition in the wake pattern. At $\tau$ = 296.89, an interesting '4P' wake pattern is observed; see Fig. 7d. Further, the airfoil is again seen to enter the low amplitude aperiodic phase through a sharp transition resulting in a narrow width aperiodic wake

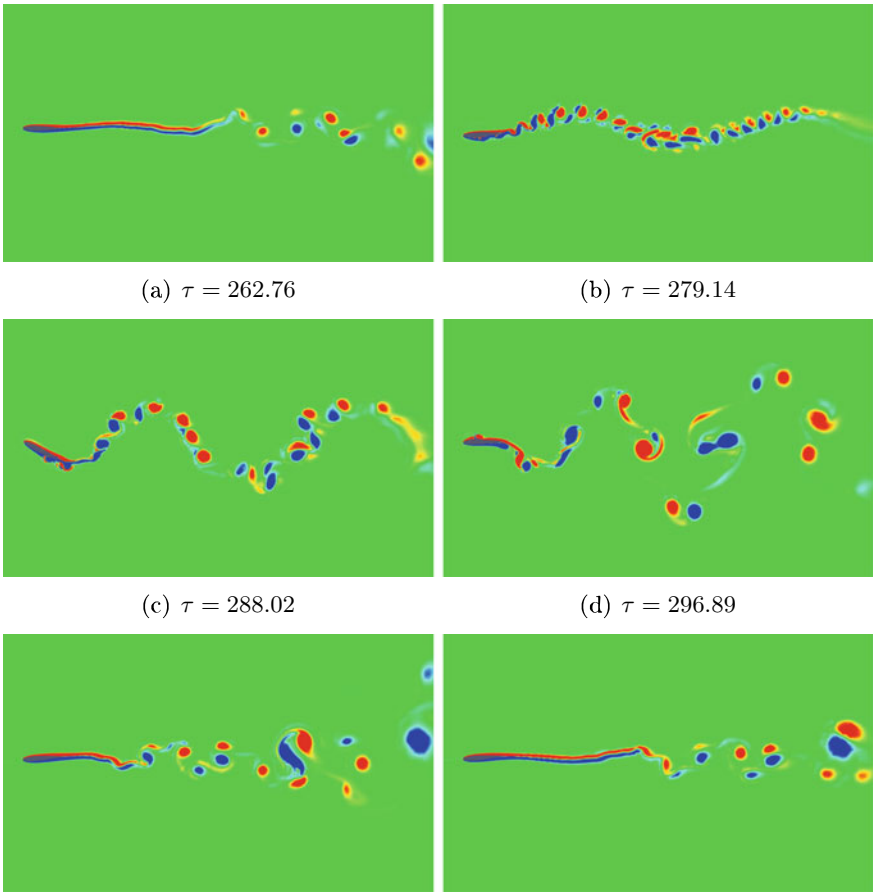

(a) $\tau = 262.76$ (b) $\tau = 279.14$

(c) $\tau = 288.02$ (d) $\tau = 296.89$

(e) $\tau = 320.78$ (f) $\tau = 326.92$

**Fig. 7** Intermittent flow dynamics at $U_m^* = 1.3$, $A_g^* = 15\%$ and $f_g = 0.1$ Hz

at $\tau$ = 320.75 (Fig. 7e) which is eventually carried away by the free-stream and the shear layers are again seen to be shedding from the airfoil surfaces at $\tau$ = 326.92 (Fig. 7f).

## *3.3 Effect of Random Gust*

To understand the effect of random gust on the FSI dynamics of the passively flapping wing, the system is subjected to two different time-scale gusts defined by O-U processes with different correlation lengths. Figure 8a shows the system exhibiting what is defined as 'on-off' type intermittency in the plunge response in the presence of a

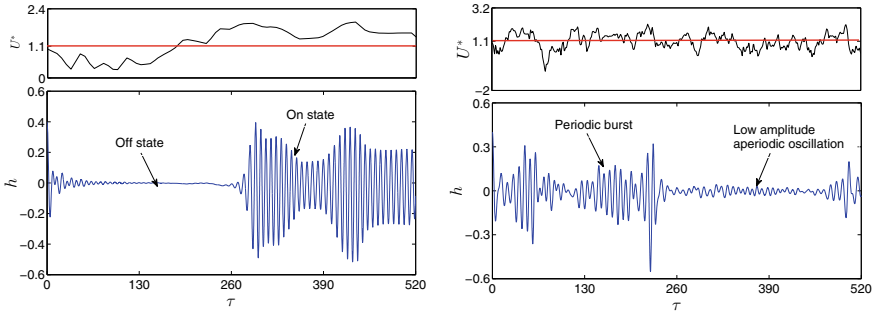


(a) On-off intermittency (b) Burst type intermittency

**Fig. 8** Intermittent plunge response in the presence of random gust

long-time scale random gust. Here, longer time scale fluctuations are generated by considering lower $\Delta\omega$ values in Eqs. 6 and 7. 'On-off' type intermittency is denoted by the irregular alteration between non-oscillatory state and modulated periodic state and is observed when the system is subjected to long time-scale random fluctuations. On the other hand, a 'burst' type intermittecy behavior is observed when the system is subjected to a short time-scale random gust (generated with higher $\Delta\omega$ value) and is denoted by irregular alteration between low amplitude aperiodic oscillations and bursts of periodic oscillations (Fig. 8b). Further studies are being carried out to understand the underlying flow-physics. Interested readers are directed to [27] for more discussions on the distinction between "on-off" and "burst" type intermittencies.

## 4 Concluding Remarks

The effect of time harmonic and random gust on the nonlinear FSI dynamics of a elastically mounted airfoil has been studied in this paper through a Navier-Stokes based high fidelity FSI solver. A regular intermittent transition has been observed between quasi-periodic bursts and low amplitude aperiodic oscillations in the presence of low frequency sinusoidal gusts (long time-scale). The intermittent states are seen to disappear as the frequency of the sinusoidal fluctuation is increased paving way for pure quasi-periodic and a frequency locked periodic states. The same transitional dynamics is also observed in the associated flow-field. Contrary to this behavior, on-off type and burst type intermittency have been observed in the presence of random gust with long and short time-scales of fluctuations, respectively.

## References


1. Jones, K., Platzer, M.: Bio-inspired design of flapping-wing micro air vehicles-an engineer's perspective. In: 44th AIAA Aerospace Sciences Meeting and Exhibit, p. 37 (2006)
2. Wang, Z.J.: Vortex shedding and frequency selection in flapping flight. J. Fluid Mech., **410**, 323–341 (2000)
3. Young, J., Lai, J.C.: Oscillation frequency and amplitude effects on the wake of a plunging airfoil. AIAA J. **42**(10), 2042–2052 (2004)
4. Chirarattananon, P., Chen, Y., Helbling, E.F., Ma, K.Y., Cheng, R., Wood, R.J.: Dynamics and flight control of a flapping-wing robotic insect in the presence of wind gusts. Interface Focus, **7**(1). 20160080 (2017)
5. Watkins, S., Milbank, J., Loxton, B.J., Melbourne, W.H.: Atmospheric winds and their implications for microair vehicles. AIAA J. **44**(11), 2591–2600 (2006)
6. Lian, Yongsheng, Shyy, Wei: Laminar-turbulent transition of a low reynolds number rigid or flexible airfoil. AIAA J. **45**(7), 1501–1513 (2007)
7. Lian, Y.: Numerical investigation of boundary effects on flapping wing study. In: 47th AIAA Aerospace Sciences Meeting including The New Horizons Forum and Aerospace Exposition, p. 539 (2009)
8. Russell Prater and Yongsheng Lian. Aerodynamic response of stationary and flapping wings in oscillatory low reynolds number flows. In: 50th AIAA Aerospace Sciences Meeting including the New Horizons Forum and Aerospace Exposition, p. 418 (2012)
9. Jones, M., Yamaleev, N.: The effect of a gust on the flapping wing performance. In: 50th AIAA Aerospace Sciences Meeting including the New Horizons Forum and Aerospace Exposition, p. 1080 (2012)
10. Fisher, Alex, Ravi, Sridhar, Watkins, Simon, Watmuff, Jon, Wang, Chun, Liu, Hao, Petersen, Phred: The gust-mitigating potential of flapping wings. Bioinspiration Biomimet. **11**(4), 046010 (2016)
11. Shyy, W.E.I., Jenkins, D., Smith, R.: Study of adaptive shape airfoils at low reynolds number in oscillatory flows. AIAA J. **35**(9), 1545–1548 (1997)
12. Williams, D., Buntain, S., Quach, V., Kerstens, W.: Flow field structures behind a 3d wing in an oscillating freestream. In: 39th AIAA Fluid Dynamics Conference, p. 3690 (2009)
13. Zhu, Jianyang, Jiang, Lin, Zhao, Hui, Tao, Bo, Lei, Bin: Numerical study of a variable camber plunge airfoil under wind gust condition. J. Mech. Sci. Technol. **29**(11), 4681–4690 (2015)
14. Golubev, V., Hollenshade, T., Nguyen, L., Visbal, M.: High-accuracy low-re simulations of airfoil-gust and airfoil-vortex interactions. In: 40th Fluid Dynamics Conference and Exhibit, p. 4868 (2010)
15. Raveh, D.E.: Gust-response analysis of free elastic aircraft in the transonic flight regime. J. Aircraft **48**(4), 1204–1211 (2011)
16. Bartels, R.: Developing an accurate cfd based gust model for the truss braced wing aircraft. In: 31st AIAA Applied Aerodynamics Conference, p. 3044 (2013)
17. Bose, C., Sarkar, S., Gupta, S.: Stochastic bifurcation analysis of an elastically mounted flapping airfoil. In: MATEC Web of Conferences, vol. 148, p. 08001. EDP Sciences (2018)
18. Lee, B.H.K., Jiang, L.Y.: Flutter of an airfoil with cubic restoring force. J. Fluids Struct. **13**, 75–101 (1999)
19. Ferziger, J.H., Peric, M.: Computational Methods for Fluid Dynamics, 3rd edn. Springer, Berlin (2002)
20. OpenFOAM. The Open Source CFD Toolbox User Guide. (2013)
21. Bose, Chandan, Badrinath, Sandeep, Gupta, Sayan, Sarkar, Sunetra: Dynamical stability analysis of a fluid structure interaction system using a high fidelity navier-stokes solver. Procedia Eng. **144**, 883–890 (2016)
22. Trimarchi, D.: Analysis of downwind sail structures using non-linear shell finite elements: wrinkle development and fluid interaction effects. Ph.D. thesis, University of Southampton, 2012

23. Graham, R., Schenzle, A.: Stabilization by multiplicative noise. Phys. Rev. A **26**(3), 1676 (1982)
24. Gillespie, D.T.: Exact numerical simulation of the ornstein-uhlenbeck process and its integral. Phys. Rev. E **54**(2), 2084 (1996)
25. Higham, D.J.: An algorithmic introduction to numerical simulation of stochastic differential equations. SIAM Rev. **43**(3), 525–546 (2001)
26. Bose, Chandan, Gupta, Sayan, Sarkar, Sunetra: Dynamical behavior of unsteady flowfield of an elastically mounted flapping airfoil. AIAA J. **56**(5), 2062–2069 (2018)
27. Venkatramani, J., Krishna Kumar, S., Sarkar, S., Gupta, S.: Physical mechanism of intermittency route to aeroelastic flutter. J. Fluids Struct. **75**, 9–26 (2017)

# Theoretical Aspects, Simulation and Reduced-Order Modelling of Fluid-Structure Interaction for Deformable Structures

# Using Multicompartmental Poroelasticity to Explore Brain Biomechanics and Cerebral Diseases


**John C. Vardakis, Liwei Guo, Dean Chou, and Yiannis Ventikos**

**Abstract** Numerical methods and simulations offer the prospect of improved clinically relevant predictive information, enabling more efficient use of resources for designing treatment protocols, risk assessment and urgently needed management of long term care systems for a wide spectrum of brain disorders. An extended poroelastic model of perfused parenchymal tissue coupled with separate workflows incorporating subject-specific meshes, permeability tensor maps and cerebral blood flow variability is outlined in this work. This consolidated pipeline is also used to provide subject-specific boundary conditions for the regions of the cerebroventricular volume responsible for cerebrospinal fluid (CSF) secretion, in addition to the exit sites which allow for the passage of CSF into the intricate drainage pathways of the brain. Subject-specific datasets used in the modelling of this paper were collected as part of a prospective data collection effort. Two cases were simulated involving one female cognitively healthy control (CHC) subject, and one female subject with mild cognitive impairment (MCI) undergoing a period of high activity. Results showed visibly reduced blood perfusion, clearance of CSF/interstitial fluid (ISF), CSF/ISF accumulation and drainage in the MCI case. Interestingly, peak aqueductal velocity was higher in the MCI case (1.80 cm/s compared to 0.35 cm/s).

**Keywords** Dementia · Multiple-network poroelastic theory · CFD · FEM

J. C. Vardakis
Institut national de la santé et de la recherche médicale (INSERM), Laboratory for Vascular Translational Science (U1148), Hôpital Bichat, Paris, France

L. Guo · Y. Ventikos (✉)
Department of Mechanical Engineering, University College London, Torrington Place, London WC17JE, UK
e-mail: y.ventikos@ucl.ac.uk

D. Chou
Department of Biomedical Engineering, National Cheng Kung University, Tainan City, Taiwan



M. Braza et al. (eds.), *Advances in Critical Flow Dynamics Involving Moving/Deformable Structures with Design Applications*, Notes on Numerical Fluid Mechanics and Multidisciplinary Design 147,
https://doi.org/10.1007/978-3-030-55594-8_15

## 1 Introduction

The epidemiologic transition succinctly refers to a process in which infectious, infant and maternal diseases are brought under manageable limits courtesy of advances in the healthcare sector which can to various degrees, be attributed to prolonged social and economic development. At the same time however, the increased mimicking of a western lifestyle, and its consequent behavioural model has led to chronic diseases taking over as the leading cause of mortality in every region of the world.

Brain disorders such as developmental and neurodegenerative diseases represent an enormous disease burden, not only in terms of human distress, but also economic cost. Dementias of the elderly correspond to a range of progressive, organic brain diseases that are characterized by problems of short-term memory, disturbances in language, psychological changes, psychiatric changes and lifestyle impairments [1]. Examples include Alzheimer's disease (AD) and Normal Pressure Hydrocephalus. In its early stage, AD may present itself as mild cognitive impairment (MCI), an intermediate state between normal ageing and dementia. Microscopically, the pathological features of AD are the extracellular deposition of amyloid-β peptide into plaques and the formation of intracellular tangles composed of hyperphosphorylated tau protein. Normal Pressure Hydrocephalus (NPH) may be broadly defined as the imbalance between production and circulation of cerebrospinal fluid within the brain (where a radiographically identifiable flow obstruction leading to this imbalance is not observed).

Dementias are exerting substantial pressures on society, through greater health expenditure arising from the specialised medical services (differential diagnosis for instance) required for such complex and overlapping pathologies. At the same time, medical expertise and evidence-driven policymaking and commissioning of services are increasingly evolving the definitive architecture of comprehensive long-term care, which incorporates diagnostic and medical continuing care services, family care, community care (whilst also considering cost containment strategies), relief opportunities and palliative end-of-life care.

Fluid-structure interaction (FSI), in most cases, involves a movable and/or deformable surface, as the part of a solid body that meets a fluid and is either displaced by the loads the fluid applies on it, or actively moves the fluid itself, or both. In this setting, the fluid can be external to the structure—an aircraft wing for example, or internal to the solid—like a dilating aorta. In all the scenarios discussed above, the "interface" i.e. the surface where the solid and the fluid come in contact, is defined in a deterministic manner.

In this work, we discuss a different topology for FSI: that of a poroelastic medium. If poroelasticity is viewed at the microscopic level, then there is no effective difference between an internal FSI setting: fluid is contained within a solid matrix (a set of communicating pores) and interacts with that matrix. However, when the number of pores, passages and conduits that the fluid occupies within the solid matrix is large, the microscopic view (and related direct simulation techniques) is of little use. In that case, an approach that gives us the capability to treat the two (or more)

phases of the problem (solid matrix and one or more fluid phases) in a statistically meaningful and computationally/theoretically tractable manner is needed. Poroelasticity fills this gap. In this case, the loads that the fluid applies to the solid are internal to the control volume and distributed across it. Therefore, for example, an increase in pressure at some point within the flow domain results in loading the solid matrix from within the control volume, with consequences in its strain field. Mass and momentum conservation equations for all phases are cast in a uniform context, flow is treated in a Darcian manner, and configurations with an arbitrary number of pores can be handled in an elegant and efficient manner. This class of methodologies, originally developed for groundwater engineering, is now being applied successfully to problems in biomedical engineering, since it seamlessly integrates the concept of extensive and microscale perfusion (with blood, but also other fluids) that is dominant in living tissue.

Modelling the transport of fluid within the brain, in a personalised manner and from first principles, is essential to help decipher some of the underlying mechanisms that are currently being investigated regarding diseases of the cerebral environment. In this work, it will be shown that using a multicompartmental poroelasticity model for perfused parenchymal tissue coupled with an automated image-based model personalization workflow and a subject-specific blood flow variability model, one may extract valuable insight [2] into the underlying mechanisms of the neurovascular unit. At the same time, the resulting solution fields from this multiporoelastic model can be used as the basis to provide subject-specific boundary conditions for computational fluid dynamics (CFD) models simulating the complex flow characteristics in important structures of anatomical significance in the brain, namely the cerebral ventricles.

## 2 Methodology

Poroelastic systems describe fluid flow through a porous medium coupled with deformation of the solid matrix. In this work, the matrix deformation obeys linear elasticity, whilst the percolating fluid is described by Darcy flow.

### *2.1 Multiple-Network Poroelastic Theory (MPET)*

The standard mathematical model for diffusive flow in an elastic porous medium is the diffusion-deformation model of poroelasticity proposed by Biot [3]. This is based on the coupling between the pore-fluid potential and the solid stress fields. An extension of Barenblatt's double-diffusion approach [4] and Biot's diffusion-deformation theory leads to the Barenblatt-Biot poroelastic model representing quadruple diffusion in elastic porous media. This model takes the following form:

$$-\nabla\cdot(\mathbb{C}:\varepsilon(u))+\sum_{j=1}^{A}\alpha_j\nabla p_j=f,$$

$$c_j\dot{p}_j+\alpha_j\nabla\cdot\dot{u}-\nabla\cdot\left(K_j\nabla p_j\right)+\sum_{i=1}^{A}\xi_{j\to i}\left(p_j-p_i\right)=h \tag{1a, b}$$

In the above formulation, for a given number of networks, $A\in\mathbb{N}$, the displacement of the solid skeleton is given by $u=u(x,t)$, whilst the fluid potentials for each respective compartment is given by $p_j=p_j(x,t)$, where $1\le j\le A$ for $x\in\Omega\subset\mathbb{R}^d$ $(d=1,2,3)$ and $t\in[0,T]$. $\alpha_j\in(0,1]$ is the Biot-Willis coefficient for each compartment which also satisfies $\phi\le\Sigma\alpha_j\le 1$, where $\phi$ is the total porosity, $c_j\ge 0$ is the storage coefficient, $K_j$ is the hydraulic permeability tensor defined by $K_j=\kappa_j/\mu_j>0$ (the ratio of the compartmental permeability to fluid viscosity), $\xi_{j\to i}$ are the intercompartmental transfer coefficients, $f=f(x,t)$ represents a body force and $h=h_j(x,t)$ represent additional compartment specific source terms. In this manuscript, $\varepsilon(u)$ is the small-strain tensor derived from the symmetric part of the gradient of the displacement $u$:

$$\varepsilon(u):=\frac{1}{2}\left(\nabla u+(\nabla u)^{\mathrm{T}}\right) \tag{2}$$

The elastic stiffness tensor, $\mathbb{C}$, defines a stress tensor $\sigma$ using Hooke's Law:

$$\sigma:=\mathbb{C}\varepsilon(u) \tag{3}$$

In this manuscript, we will assume an isotropic and homogeneous linear elastic medium with elasticity tensor, $\mathbb{C}$, defined by the identity:

$$\mathbb{C}:\varepsilon(u)=2\mu\varepsilon(u)+\lambda(\nabla\cdot u)\boldsymbol{I} \tag{4}$$

where $\boldsymbol{I}$ is the identity tensor, and $\mu$ and $\lambda$ are the Lamé moduli.

## 2.2 Three-Dimensional MPET Model for the Cerebral Environment

In this work, the MPET model was used to conduct mechanistic modelling of fluid transport through the brain parenchyma. Biologically, the solid matrix represents brain parenchyma and the communicating fluid phases considered are: an arterial network (a), an arteriole/capillary network (c), a CSF/ISF network (e) and a venous network (v) (see Fig. 1). This model allows for the simultaneous solutions of continuity and momentum conservation equations, in four interconnected fluid compartments, within a deformable solid matrix (the parenchymal tissue).

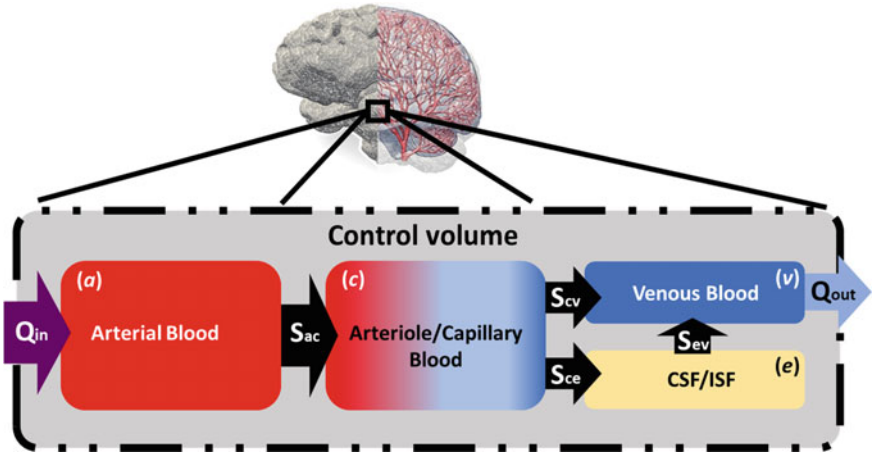


**Fig. 1** The four-compartment MPET model reflect the key fluid transport mechanisms in the brain tissue. Flow is prohibited between the CSF and the arterial network, whilst directional transfer exists between ($a$) and ($c$), ($c$) and ($v$), ($c$) and ($e$) and finally ($e$) and ($v$)

The MPET model uses the parenchymal tissue displacement ($u$), and the pore pressures of the four fluid compartments ($p_a, p_c, p_e, p_v$) as the primitive variables in the governing equations, which are given below:

$$
\begin{aligned}
&G\nabla^2 u + (G+\lambda)\nabla\varepsilon = \alpha_a \nabla p_a + \alpha_c \nabla p_c + \alpha_e \nabla p_e + \alpha_v \nabla p_v \\
&c_a \dot{p}_a + \alpha_a \nabla \cdot \dot{u} - \nabla \cdot (K_a \nabla p_a) = S_{c\to a} \\
&c_c \dot{p}_c + \alpha_c \nabla \cdot \dot{u} - \nabla \cdot (K_c \nabla p_c) = S_{a\to c} + S_{e\to c} + S_{v\to c} \\
&c_e \dot{p}_e + \alpha_e \nabla \cdot \dot{u} - \nabla \cdot (K_e \nabla p_e) = S_{c\to e} + S_{v\to e} \\
&c_v \dot{p}_v + \alpha_v \nabla \cdot \dot{u} - \nabla \cdot (K_v \nabla p_v) = S_{c\to v} + S_{e\to v}
\end{aligned}
\qquad \text{(5a–e)}
$$

The $s$ terms in Eq. (5b–e) define spatially varying source ($s_{ij} > 0$) or sink ($s_{ij} < 0$) densities (rate of fluid transfer between networks). More details can be found in Guo et al. [2]. Additional variables of practical interest, such as Darcy velocity and fluid content ($\zeta_e$) [1, 2, 5], are derived from primitive variables of the MPET system.

## 2.3 MPET Verification and Mesh Independence

The governing equations of the MPET system have been discretised using the finite element method and implemented into an in-house numerical code [6], which has been verified [7] against Terzaghi's [8] and Mandel's [9] problems. In addition to the verification, mesh dependence (12 meshes with total element numbers ranging from ~100 k to ~9 million) of the 3D MPET outputs (displacement, scalar pressures and

relevant filtration velocities from the four compartments) using a subject-specific brain geometry has been conducted [2].

## 2.4 Subject-Specific Datasets

The subject-specific datasets used in the modelling of this paper were collected as part of the VPH-DARE@IT project (www.vph-dare.eu), and prospective data collection was conducted at the Istituto di Ricovero e Cura a Carattere Scientifico (IRCCS) San Camillo, Lido di Venezia, Italy. The study includes a total of 103 people (50 cognitively healthy controls, age 71 $\pm$ 8 yr, and 53 with diagnosed MCI, age 75 $\pm$ 7 yr), and was approved by the joint ethics committee of the Health Authority Venice 12 and the IRCCS San Camillo (Protocol number 2014.08), and all participants gave informed consent prior to participation in the study. In this paper, one 68-year-old female CHC subject and one 62-year-old female MCI subject were chosen to conduct a preliminary analysis.

For each subject, several measurement modalities were collected: lifestyle questionnaires and neuropsychological tests, whole brain MR imaging (Turbo Field Echo T1 images were based on a $1.1 \times 1.1 \times 0.6$ mm$^3$ voxel resolution), clinical ultrasound flow imaging, portable Holter recordings of blood pressure, and actigraph measured activity levels, among others. Lifestyle information was collected by means of established questionnaires (CAIDE study [10]). Clinical ultrasound imaging comprised both carotid ultrasound and cardiac echography (Siemens Acuson X300PE and SC2000, Siemens Healthineers, Erlangen, Germany). Portable Holter devices (Cardioline walk200b, Cardioline S.p.A., Milan, Italy) measured both blood pressure and the electrocardiogram. Physical activity and sleep were measured using wrist-portable actigraph devices (MotionWatch 8, CamNtech Ltd, Cambridge, UK). For the Lido study cohort, T1-weighted and diffusion-weighted MR images were processed to create accurate 3D meshes and permeability tensor maps (PTMs) of the parenchyma; and Holter recordings and ultrasound flow measurements were used to generate boundary conditions of arterial blood flow. More details on the integration of these workflows is described in Guo et al. [2, 11].

## 2.5 Subject-Specific Boundary Conditions and Parameters

A subject-specific blood flow profile is used as the boundary condition (BC) for the arterial network of the MPET model at the cortical surface. A subject-specific characterization of 24-h blood flow variability is obtained through a combination of blood pressure measurements, clinical ultrasound flow measurements and mathematical modelling [12]. A lumped parameter circulation model (LPCM) [13] is used to simulate continuous arterial blood flow and translate spot measurements collected at 15 min intervals to continuous waveforms of arterial blood flow. Once the arterial

flow waveforms in the internal carotid artery (ICA) are obtained from the LPCM, they are coupled with another lumped parameter model for cerebral flow autoregulation [14]. The final output of this model is a 24-h prediction of middle cerebral artery flow. This is subsequently partitioned into the ICA blood to the left and right cerebrum, and the vertebral artery (VA) blood to the left and right cerebellum. These continuous waveforms are fed into the MPET modelling as BCs for the arterial compartment at the cortical surface, which is divided into four perfusion regions corresponding to the four waveforms. This allows for the total amount of arterial blood flow to be distributed across each perfusion region and applied as a Neumann condition [2] in the arterial compartment of the MPET model. In this paper, one specific measurement was chosen from the 24-h recording as indicative of the subject's high activity (e.g. exercise) identified by the highest peak values of arterial blood flow within 24 h.

The skull is assumed rigid (adult cases). For simplicity, this rigid BC is applied directly to the cortical surface. There are no displacement constraints at the ventricular wall, so it can expand or contract freely. For continuity of stresses, the pressure exerted by the CSF within the ventricles on the inner ependymal surface must balance the poroelastic stress in the parenchymal tissue [2, 5, 15]. A subject-specific blood flow profile is used as the BC for the arterial network at the cortical surface. Descriptions for the boundary conditions and parameters used in the MPET modelling framework can be found in previous studies [2, 5, 15].

The estimated diffusion tensor field and its associated principal eigenvectors were used to estimate permeability tensor maps (PTMs). The permeability map gives a heterogeneous and anisotropic permeability field (dimensionless permeability tensor scaled by the base permeability of the CSF/ISF compartment, $k_e$) to be applied within the parenchymal tissue. This PTM was used to further personalise the CSF/ISF compartment in the 3D MPET modelling [2, 11].

For the inlet and outlet BCs used in the CFD simulations, a personalised set of BCs arising from the Darcy filtration velocities of the MPET simulations (from the arteriole/capillary and CSF/ISF compartment) at the surface of the ventricles are applied to both the inlets and outlets in the cerebroventricular system. The inlet conditions are derived from the MPET output of the arteriole/capillary compartment (perfusion [2]), whilst the outlet conditions are derived from the CSF/ISF compartment (CSF/ISF clearance [2]). For the inlets, the filtration velocity of arteriole/capillary blood in the sites of the choroid plexuses of the lateral, third and fourth ventricle are assumed to coincide with portions of the walls of the cerebral ventricles. This assumption is adequate, since in the choroid fissures of the lateral ventricles, the choroid plexuses develop from the cisternae of the median walls, whilst in the third ventricle; they arise from the roof of those entities. In the fourth ventricle, the corresponding plexus is formed caudally and ventrally of the cerebellum [1]. The plexuses are supplied by the filtration velocity boundary condition representing the perfusion of arteriole/capillary blood at the different choroid plexus locations which are represented as surfaces (of representative sizes in the lateral, third and fourth ventricle) of varying curvature within the ventricular volume (see Fig. 2) that ultimately produce CSF filtrate. The boundary conditions at the outlets (CSF/ISF filtration velocity from the MPET simulations) are defined as patches in the fourth ventricle, specifically, at

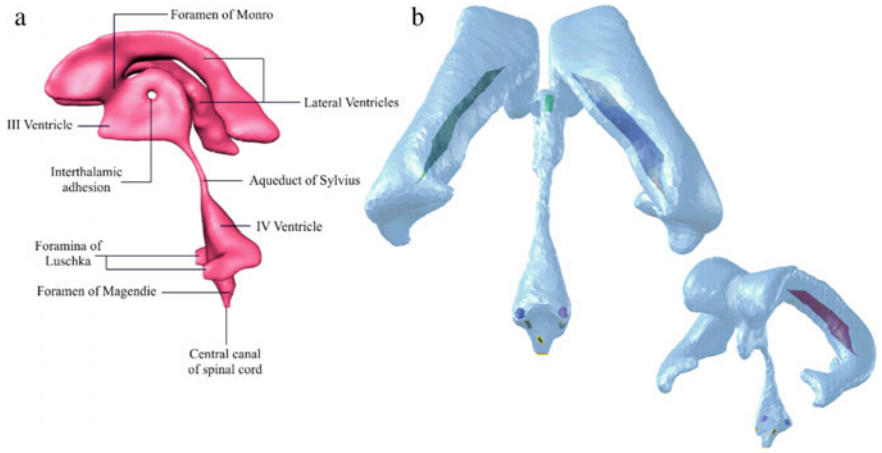


**Fig. 2** **a** The cerebroventricular system of a healthy volunteer. Obtained from Vardakis et al. [5]. No permission was required under the CC BY license agreement. **b** A depiction of the surface patches within a cerebroventricular volume of a patient with MCI. These surfaces represent the choroid plexus regions of the lateral, third, and fourth ventricle

the foramina of Magendie, the bilateral foramina of Luschka, and the central canal which lead the CSF to the surrounding subarachnoid space.

## *2.6 Cerebral Ventricles Volume Extraction and Discretization*

A fully automated workflow (see Fig. 3) has been developed to provide subject-specific meshes and PTMs for the MPET modelling. The tetrahedral meshes generated as part of the automated image-based modelling pipeline allowed for the extraction of the cerebroventricular surfaces. These were converted to Stereo Lithography (STL) files. To preserve key anatomical features such as the Sylvian aqueduct and impose features allied to the choroid plexus, subsequent smoothing of the STL files was conducted using the open-source modelling software, Blender (The Blender Foundation, www.blender.org). This software provides the user with powerful wire-frame, node-by-node, editing capabilities (such as smoothing) and in the process aids in improving the continuity of the required domains.

Flow through the cerebral ventricles is solved using the multiphysics software CFD-ACE+ (ESI Group, Paris, France) which is based on the finite volume approach, along with the Second-Order Upwind Scheme used for spatial differencing, algebraic multigrid scheme and the SIMPLEC pressure–velocity coupling. As in previous work by the authors [5], mesh generation for the 3D volumes was achieved via the use of CFD-VisCART (ESI Group, Paris, France), which is an unstructured adaptive Cartesian grid generation system. CFD-VisCART offers a projected single domain method tree-based data structure to generate Cartesian-based non-conforming grids.

The OmniTree data structure was used as it supports anisotropic grid adaptations [5]. Similarly, adequate discretization of the 3D ventricular domain is required to acquire fully resolved results (within a 5% band from what we considered as the fully converged solution). Grid independence analysis resulted in meshes of ~18 million and ~15 million cells for the cerebroventricular volume relating to the MCI and CHC case respectively.

## 3 Consolidated Modelling Pipeline for the Cerebral Environment

The MPET system gives rise to a generic model that simulates biomechanical behaviour of perfused tissue, and is personalized for individual subjects on three levels: cerebral geometries, and corresponding computational meshes, were extracted from structural MR images; spatial maps of CSF/ISF compartment permeability tensors were estimated from diffusion MR data; and arterial blood flow waveforms, used as cortical surface BCs, were derived from measurements of blood pressure, flow velocity and other inputs. The consolidated pipeline presented here was implemented on the MULTIX platform, developed within the VPH-DARE@IT project (see Fig. 3).

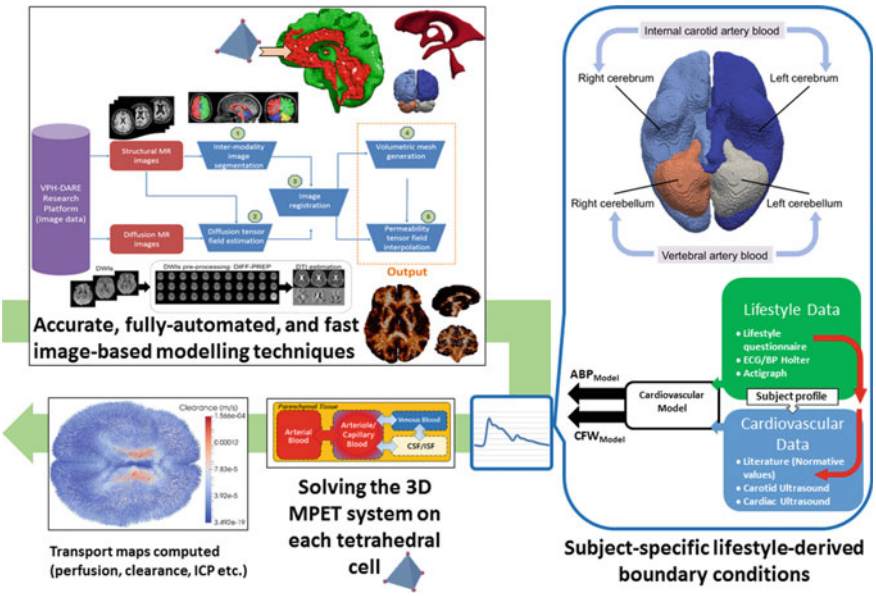


**Fig. 3** The consolidated pipeline that incorporates the 3D MPET solver itself, with image- and non-image-based model personalisation modules

## 4 Results and Discussion

As described in Sect. 2.4, the geometries and patient-specific boundary conditions allied to the parenchymal tissue and cerebroventricular volume of one 68-year-old CHC female control subject and one 62-year-old female MCI subject was used in the consolidated pipeline to conduct the MPET and CFD simulations. The parenchymal volumes of the two subjects are ~1014 ml and ~851 ml, whilst the cerebroventricular ventricular volumes are ~20 ml and ~36 ml respectively. The peak arterial flow rates during the period of high activity for the left and right ICA, and VA were 502, 470 and 122 ml/min for the CHC subject, and 334, 340 and 84 ml/min for the MCI subject.

Figure 4 depicts three solution fields arising from the MPET solver, namely clearance (Darcy velocity of CSF/ISF compartment), blood perfusion (Darcy velocity of capillary compartment), and CSF/ISF accumulation (positive values of fluid content, $\zeta_e$, of the CSF/ISF compartment). CSF/ISF clearance is reduced from around 56 to around 29 $\mu$m/s (a reduction of around 58%) in the MCI subject, whilst blood perfusion is reduced (from 0.31 to 0.15 mm/s) by over 50% for the same subject. Both CSF/ISF drainage ($\zeta_e < 0$) and accumulation ($\zeta_e > 0$) is lower in the MCI case. The solution fields also differ substantially in spatial morphology. The anisotropic nature of CSF/ISF fluid transport within the brain is accounted for via the subject-specific PTMs estimated from DT fields. A$\beta$ homeostasis is governed by production and clearance mechanisms [16]. Any subsequent imbalance in this homeostasis may result in excessive accumulation of cerebral A$\beta$, which is a known characteristic of AD [17].

Figure 5 depicts the velocity magnitude of CSF within the cerebroventricular system. A large increase in the peak velocity magnitude is witnessed between the

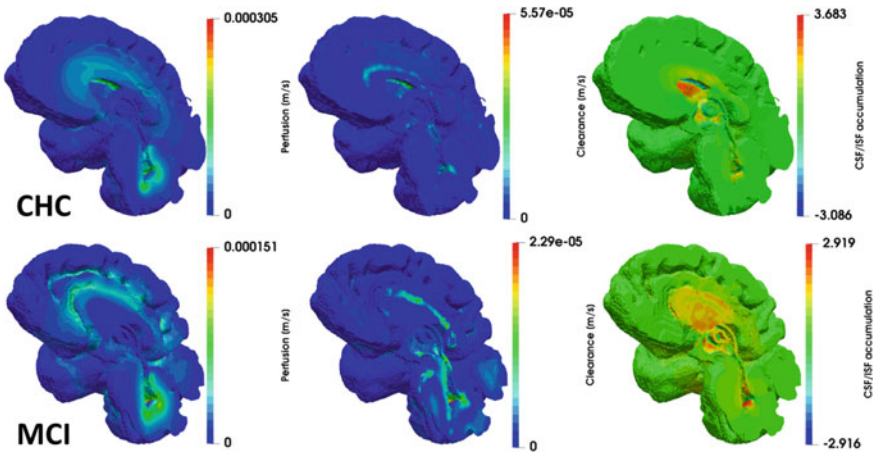


**Fig. 4** Midsagittal section depicting MPET results (blood perfusion, CSF/ISF clearance, and accumulation of CSF/ISF) of the CHC subject (top row) and MCI patient (bottom row). All results are acquired during a period of high activity

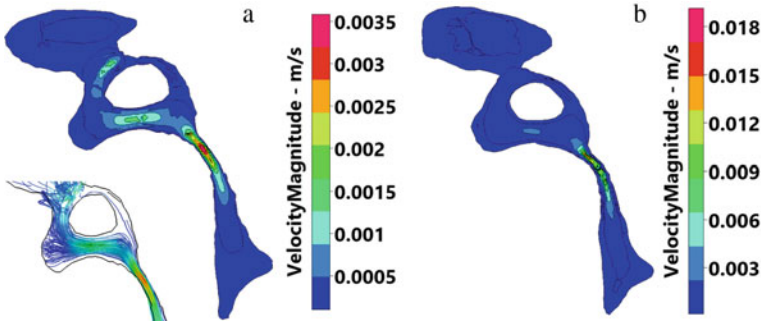


**Fig. 5** **a** Sagittal view of the aqueduct of Sylvius, lateral, third and fourth ventricles of the CHC subject. The contour lines denote velocity magnitude. A view of the velocity streamlines of the aqueduct of Sylvius and third ventricle is also shown. **b** Sagittal view of the aqueduct of Sylvius, lateral, third and fourth ventricles of the MCI subject. The contour lines denote velocity magnitude

CHC and MCI subject. The importance of considering the subject-specific boundary conditions at the choroid plexuses, in addition to the accurate assessment of CSF outflow velocities at the fourth ventricle is clear from the preliminary simulations considered thus far.

The consolidated pipeline presented in this work can integrate principles of solid and fluid mechanics and may aid in better understanding intricate hypotheses such as the role of chronic hypoperfusion in AD related disease progression, and the intricate mechanisms relating the role of repetitive and intensifying arterial pulsations (due to the increased stiffness of the arterial tree during ageing) on the underlying neuronal microstructure and glial function [18, 19]. A more detailed understanding of acute hydrocephalus is also possible, since the anatomically accurate cerebroventricular system and novel application of boundary conditions at all the choroid plexus sites can provide insight into the complicated nature of flow in the ventricles (and assist in its potential classification [20] between diseases). This makes investigations into aqueductal stenosis and fourth ventricle outlet obstruction possible, in addition to being able to predict if any symptoms can be alleviated via the use of shunting, endoscopic third or fourth ventriculostomy.

## 5 Conclusions

This paper outlines a recently developed consolidated pipeline that intertwines a 3D, finite-element based multiple-network poroelastic model of perfused parenchymal tissue, an image-based modelling pipeline and a subject-specific boundary condition model. Two cases were simulated, one involving a 68-year-old female control subject and one involving a 62-year-old female MCI case. Both cases were prescribed arterial boundary conditions relating to a period of high activity. The pipeline was also used to obtain personalised boundary conditions for the choroid plexus regions (sites

of production of CSF within the ventricles) in addition to the CSF exiting the cerebroventricular volume. CFD computations were subsequently run for the two cerebroventricular volumes to extend the state-of-the art capabilities of the consolidated pipeline.

**Acknowledgements** The work has been supported by the European Commission FP7 project VPH-DARE@IT (FP7-ICT-2011-9-601055). We would like to thank our collaborators in the consortium, namely Dr. T. Lassila, Dr. N. Ravikumar, Dr. A. Sarrami-Foroushani, Mr. Milton Hoz de Vila, Prof. Z. A. Taylor and Prof. A. F. Frangi from the University of Leeds for developing the models and workflows to generate subject-specific boundary conditions and extracting permeability tensor maps and meshes of the cerebroventricular system. We would also like to thank Dr. M. Mitolo from Policlinico S. Orsola e Malpighi in Bologna, and Prof. A. Venneri from the University of Sheffield for providing the clinical data allied to the subject-specific applications.

## References

1. Vardakis, I.C.: Multicompartmental poroelasticity for the integrative modelling of fluid transport in the brain. PhD thesis, Oxford University (2014)
2. Guo, L., Vardakis, J.C., Lassila, T., Mitolo, M., Ravikumar, N., Chou, D., Lange, M., Foroushani, A.S., Tully, B.J., Taylor, A.Z., Varma, S., Venneri, A., Frangi, A.F., Ventikos, Y.: Subject-specific multiporoelastic model for exploring the risk factors associated with the early stages of Alzheimer's disease. Interface Focus **8**(1) (2018)
3. Biot, M.A.: General theory of three-dimensional consolidation. J. Appl. Phys. **12**, 155–164 (1941)
4. Barenblatt, G.I., Zheltov, I.P., Kochina, I.N.: Basic concepts in the theory of seepage of homogeneous liquids in fissured rocks. J. Appl. Math. Mech. **24**, 1286–1303 (1960)
5. Vardakis, J.C., Tully, B.J., Ventikos, Y.: Exploring the efficacy of endoscopic ventriculostomy for hydrocephalus treatment via a multicompartmental poroelastic model of CSF transport: a computational perspective. PLoS ONE **8**(12) (2013)
6. Guo, L, Vardakis, J. C., Chou, D., Ventikos, Y.: A multiple-network poroelastic model for biological systems and application to subject-specific modelling of cerebral fluid transport. Int. J. Eng. Sci. **147**, 103204 (2020)
7. Guo, L., Vardakis, J.C., Chou, D., Ventikos, Y.: Development of a three-dimensional multicompartmental poroelastic model for the simulation of cerebrospinal fluid transport. In: Proceedings 12th World Congress on Computational Mechanics, Seoul, Korea (2016)
8. Terzaghi, K.: Erdbaumechanik auf bodenphysikalischer grundlage. F. Duticke, Vienna, Austria (1925)
9. Mandel, J.: Consolidation des sols (étude mathématique). Géotechnique **30**, 287–289 (1953)
10. Kivipelto, M., Ngandu, T., Laatikainen, T., Winblad, B., Soininen, H., Tuomilehto, J.: Risk score for the prediction of dementia risk in 20 years among middle aged people: a longitudinal, population-based study. Lancet Neurol. **5**, 735–741 (2006)
11. Vardakis, J. C., Guo, L., Peach, T. W., Lassila, T., Mitolo, M., Chou, D., Taylor, Z. A., Varma, S., Venneri, A., Frangi, A. F., Ventikos, Y.: Fluid–structure interaction for highly complex, statistically defined, biological media: Homogenisation and a 3D multi-compartmental poroelastic model for brain biomechanics. J. Fluids. Struct. **91** (2019)
12. Lassila, T., Di Marco, L.Y., Mitolo, M., Iaia, V., Levedianos, G., Venneri, A., Frangi, A.F.: Screening for cognitive impairment by model assisted cerebral blood flow estimation. IEEE Trans. Biomed. Eng. (2017)
13. Ursino, M.: Interaction between carotid baroregulation and the pulsating heart: a mathematical model. Am. J. Physiol. **275**(5 Pt 2), H1733–H1747 (1998)

14. Mader, G., Olufsen, M., Mahdi, A.: Modeling cerebral blood flow velocity during orthostatic stress. Ann. Biomed. Eng. **43**(8), 1748–1758 (2015)
15. Vardakis, J.C., Chou, D., Tully, B.J., Hung, C.C., Lee, T.H., Tsui, P.H., Ventikos, Y.: Investigating cerebral oedema using poroelasticity. Med. Eng. Phys. **38**, 48–57 (2016)
16. Ramanathan, A., Nelson, A.R., Sagare, A.P., Zlokovic, B.V.: Impaired vascular-mediated clearance of brain amyloid beta in Alzheimer's disease: the role, regulation and restoration of LRP1. Front. Aging Neurosci. **7** (2015)
17. Thomas, T., Miners, S., Love, S.: Post-mortem assessment of hypoperfusion of cerebral cortex in Alzheimer's disease and vascular dementia. Brain **138**(4), 1059–1069 (2015)
18. Stone, J., Johnstone, D.M., Mitrofanis, J., O'Rourke, M.: The mechanical cause of age-related dementia (Alzheimer's disease): the brain is destroyed by the pulse. J. Alzheimer's Dis. **44**(2), 355–373 (2015)
19. Levy Nogueira, M., Lafitte, O., Steyaert, J.M., Bakardjian, H., Dubois, B., Hampel, H., Schwartz, L.: Mechanical stress related to brain atrophy in Alzheimer's disease. Alzheimer's Dement. **12**(1), 11–20 (2016)
20. Stadlbauer, A., Salomonowitz, E., Riet, W., Buchfelder, M., Ganslandt, O.: Insight into the patterns of cerebrospinal fluid flow in the human ventricular system using MR velocity mapping. NeuroImage **51**, 42–52 (2010)

# The Shearing Mechanism Over a Deformed Surface of Breaking Waves


**S. G. Sajjadi and J. C. R. Hunt**

**Abstract** Surface wave breaking plays an important role in the coupling between the atmosphere and the ocean from local weather to global climate scales. In the absence of wave breaking, the dynamical and scalar transport between the atmosphere and oceans is through slow molecular diffusion and conduction processes. By contrast, when a wave breaks, the air–water surface typically experiences dramatic changes, with a water jets forming and plunging from the crest of the wave downwards into the water surface below the crest, which leads to air that is entrained in the ocean surface being transported in bubbly jets being submerged downwards into the ocean. Simultaneously water spray from the jet and from rising bubbles are ejected upwards into the air above the waves. We present an idealised computational study for initiation of the generation of a surface group of waves on a water surface, which is originally at rest, generated by a random distribution of normal pressure associated with the onset of a turbulent wind. Correlations between air and water motions are neglected and the water is assumed to be inviscid. It is found that groups of waves develop most rapidly by means of a resonance mechanism which occurs when a component of the surface pressure distribution moves at the same speed as the free surface wave with the same wave-number [similar to that of Phillips' (J. Fluid Mech. 2:417–445, 1957 [13]) mechanism]. It is shown that mostly the growth of groups of waves occurs in the principal stage of development and continues until the waves grow so high that non-linear effects become important. As waves become steep enough and break, they cause bubbles to be entrained and fragmented inside the breaking wave crest. This mechanism is a multi-phase application of shearing flow over a deformed water

S. G. Sajjadi—Deceased.

S. G. Sajjadi
Department of Mathematics, ERAU, Daytona Beach, FL, USA
e-mail: sajja8b5@erau.edu

J. C. R. Hunt (✉)
Earth Sciences, Gower St, London WC1E 6BT, UK

Trinity College, University of Cambridge, Cambridge, UK
e-mail: julian.hunt@ucl.ac.uk



M. Braza et al. (eds.), *Advances in Critical Flow Dynamics Involving Moving/Deformable Structures with Design Applications*, Notes on Numerical Fluid Mechanics and Multidisciplinary Design 147,
https://doi.org/10.1007/978-3-030-55594-8_16

surface, which occurs where waves are about to break, and is similar to other types of complex flows near walls and air–liquid surfaces.

**Keywords** Turbulence · Shearing mechanisms · Wave breakdown · Entrainment · Energy dissipation

## 1 Introduction

Breaking waves have great significance in the kinematics and dynamics of ocean waves and the air–sea boundary layers, and also to many other problems related to air–sea interactions [8]. Breaking waves transfer momentum and energy from waves to currents, and also to near-surface turbulence that leads to mixing within the surface layers of the ocean. Furthermore, heat and mass transfer are also enhanced by breaking waves (via gases and aerosols). These and other aspects of breaking have been reviewed by, for example, Banner and Peregrine [1], Melville [11], and Duncan [6]. Despite recent progress in measuring breaking waves in both field and laboratory studies, there are still major challenges to overcome for the experimentalist, the theoretician and the numerical modeller. Consequently even simple scaling arguments and limited measurements can be particularly valuable. In this paper, we present fine scale numerical simulations of wave breaking which in practice depend on the wave slope and its sharp crestedness (e.g. [3]) at the point of breaking. The simulations performed here also relate the kinematics to the dynamics of breaking waves. Most importantly, we demonstrate that the initial wave formation very rapidly leads to a wave group, and as more energy is transferred to them they grow and also become quite asymmetrical.

## 2 Theory

In this study, we follow the original theory posed by Phillips [13], which is briefly describe below. Here, we express the surface pressure fluctuations and surface elevation in terms of Fourier components. The pressure fluctuation $p$ and elevation $\eta$ are stationary random functions of position $\mathbf{x} = (\mathbf{x_1}, \mathbf{x_2})$ in the surface plane. Since now simple Fourier transforms do not exist, we invoke the theory of random functions (e.g. [2]) and define the Fourier-Stieltjes transform

$$\eta(\mathbf{x}, \mathbf{t}) = \int \mathbf{e}^{\mathbf{i}\kappa.\mathbf{x}}\, \mathbf{dA}(\kappa, \mathbf{t}) \tag{1}$$

with understanding that the integration is over all wave-numbers $\kappa$ in the plane. The two-dimensional instantaneous spectrum of the surface elevation

$$\Xi = \overline{\eta(\mathbf{x})\eta(\mathbf{x}+\mathbf{r})} \tag{2}$$

which tends to zero rapidly as $|\mathbf{r}| \to \infty$, thus its Fourier transform

$$\Phi(\kappa) = (2\pi)^{-2} \int \Xi(\mathbf{r}) \mathbf{e}^{-\mathbf{i}\kappa}.\mathbf{r}\, \mathbf{dr} \tag{3}$$

where $d\mathbf{r}$ represents $dr_1\, dr_2$ and the integration is taken over the surface with $\mathbf{x}$ kept fixed. The inverse transform of (3), the spectrum is given in terms of the Fourier-Stieltjes transform by

$$\Phi(\kappa, t) = \frac{\overline{dA(\kappa, t)\, dA^*(\kappa, t)}}{d\kappa_1\, d\kappa_2} \tag{4}$$

where $*$ represents the complex conjugate. Similarly expressions for the pressure fluctuations on the surface can be written as

$$p(\mathbf{x}, \mathbf{t}) = \int \mathbf{e}^{\mathbf{i}\kappa.\mathbf{x}}\, \mathbf{d}\varpi(\kappa, \mathbf{t}) \tag{5}$$

being related to the spectrum function $\Pi(\kappa, t)$ of the surface fluctuations by the expression

$$\begin{aligned} \Pi(\kappa, t) &= (2\pi)^{-2} \int \overline{p(\mathbf{x}, \mathbf{t}')\mathbf{p}(\mathbf{x}+\mathbf{r}, \mathbf{t}'+\mathbf{t})} e^{-i\kappa.\mathbf{r}}\, d\mathbf{r} \\ &= \frac{\overline{d\varpi(\kappa, t')\, d\varpi^*(\kappa, t'+t)}}{d\kappa_1\, d\kappa_2} \end{aligned} \tag{6}$$

which is a function of the wave-number $\kappa$ and time separation t. We shall assume the motion in the water is irrotational with $\phi$ being the velocity potential such that

$$\mathbf{u} = \nabla\phi \quad \text{and} \quad \nabla^{\mathbf{2}}\phi = \mathbf{0} \tag{7}$$

where $\mathbf{u}$ is the velocity vector. The surface dynamic boundary condition is given by

$$\frac{1}{\rho_w}\left\{p - T\left(\frac{\partial^2\eta}{\partial x_1^2} + \frac{\partial^2\eta}{\partial x_2^2}\right)\right\} = \left[\frac{\partial\phi}{\partial t}\right]_{z=0} - g\eta \tag{8}$$

In (8), $\rho_w$ is the water density, $T$ the surface tension at the interface, $g$ the acceleration due to gravity, $\eta$ the surface displacement, and $z$ is the vertical coordinate which is measured downwards from the undisturbed free surface. Re-writing Eq. (8) in a frame of reference moving with an arbitrary velocity $U$, we obtain

$$\frac{p}{\rho} = \left[\frac{\partial\phi}{\partial t} - U_i\frac{\partial\phi}{\partial x_i}\right]_{z=0} - g\eta + \frac{T}{\rho}\left(\frac{\partial^2\eta}{\partial x_1^2} + \frac{\partial^2\eta}{\partial x_2^2}\right) \tag{9}$$

The normal velocity of the surface $d\eta/dt$, or in the moving frame of reference may be expressed as

$$\left(\frac{\partial}{\partial t} - U_i \frac{\partial}{\partial x_i}\right)\eta = \left[\frac{\partial \phi}{\partial t}\right]_{z=0} = \int e^{i\kappa.\mathbf{x}}(dA' - i\kappa.\mathbf{U}\,\mathbf{dA}) \tag{10}$$

where prime represents time differentiation in the convected frame of reference. The irrotational motion in the water is obtained by solving for the velocity potentional $\phi$ through $\nabla^2\phi = 0$ subject to the boundary conditions that $\phi \to 0$ as $z \to \infty$, and that $\partial\phi/\partial z$ at $z = 0$ is given by (10). Phillips (1955) showed that the solution is

$$\phi = -\int e^{-\kappa z} e^{i\kappa.\mathbf{x}} \frac{dA' - i\kappa.\mathbf{U}\,\mathbf{dA}}{\kappa} \tag{11}$$

where $\kappa = |\kappa|$. Equation (9) can now be expressed in terms of the Fourier-Stieltjes transform as

$$\frac{d\varpi}{\rho} = -\left[\frac{\partial}{\partial t} - i\kappa.\mathbf{U}\right]^2 \frac{dA}{\kappa} - g\,dA - \frac{T}{\rho}\kappa^2\,dA \tag{12}$$

or

$$dA'' - 2in_1\,dA' - (n_1^2 - n_2^2)\,dA = -\frac{\kappa}{\rho}\,d\varpi(t), \tag{13}$$

where

$$n_1 = \kappa.U = \kappa U\cos\alpha, \qquad n_2 = (g\kappa + T\kappa^3/\rho)^{\frac{1}{2}} \tag{14}$$

Equation (13) describe the growth of each component of the surface elevation in terms of the corresponding component of the pressure distribution. Note that, the quantity $n_1$ represents the frequency, in radians per second, of a wave with wave-number $\kappa$ and speed $\mathbf{U}.\kappa/\kappa$ in the direction of the wind, and $n_2$ is the frequency of free surface of wavelength $2\pi/\kappa$. We next specify the convective velocity $U$ in order to determine the of component of the pressure field of wave-number $\kappa$. The numerical scheme that we adopted here to compute solutions is based on the projection approach developed by Bell et al. [5] and is described in detail in Sussman [16]. The second order Runge-Kutta method is used to advance the solution in time. A second order, slope limited, upwind finite difference scheme is used to discretize the nonlinear advective terms for wind flow above the waves.

## 3 Results

We consider homogeneous turbulence blowing over an otherwise flat sheet of water, and transferring energy exchange to small ripples as they begin to appear on the surface. At very early stages these ripples are linear. Most theories of wind generated waves (e.g. [4, 12]) consider this stage where the wave steepness $ka \ll 1$ and also assume that the waves are approximately steady. However, further input from wind to unsteady waves cause the surface waves to grow further (see, [14, 15]). At this waves stage waves form into groups and, as they become sharper, they form plunging breakers, which are also responsible for the generation of a sequence of large-scale coherent vortices. The main aim of this paper is to review the detailed studies of breaking waves, in particular the formation of water jets which plunge downwards into the surface, with the upwards ejection of spray and small eddies. We also consider the downwards transfer of energetic eddies of air into the ocean [9]. We compare our two-dimensional numerical simulation results, performed here on very fine grids, using a Large Eddy Simulation study of air entrainment under plunging breakers with

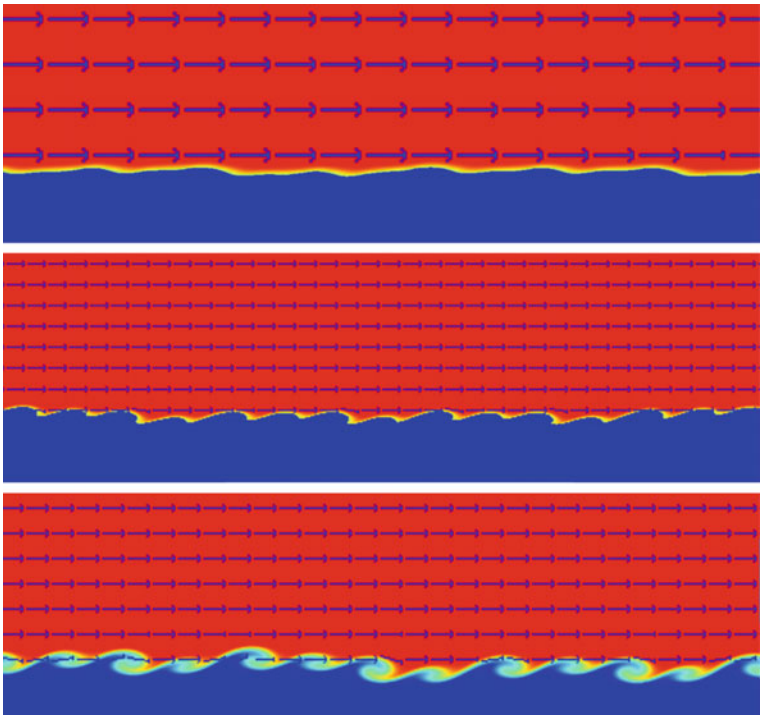

**Fig. 1** Time series for initial stages of wave formation by wind. Top: Unsteady waves growing and forming groups. Centre: Group of waves growing. Bottom: Group of unsteady wave steepening, becoming sharp crested, and begin to break

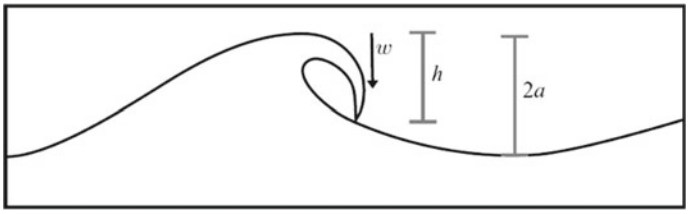


**Fig. 2** A definition sketch for a plunging wave before breaking. Here, $h$ is the height of the breaking region, $2a$ is the distance from the crest to the trough, and $w$ is the representative velocity scale (the vertical speed of the falling wave tip), taken from Drazen et al. [7]

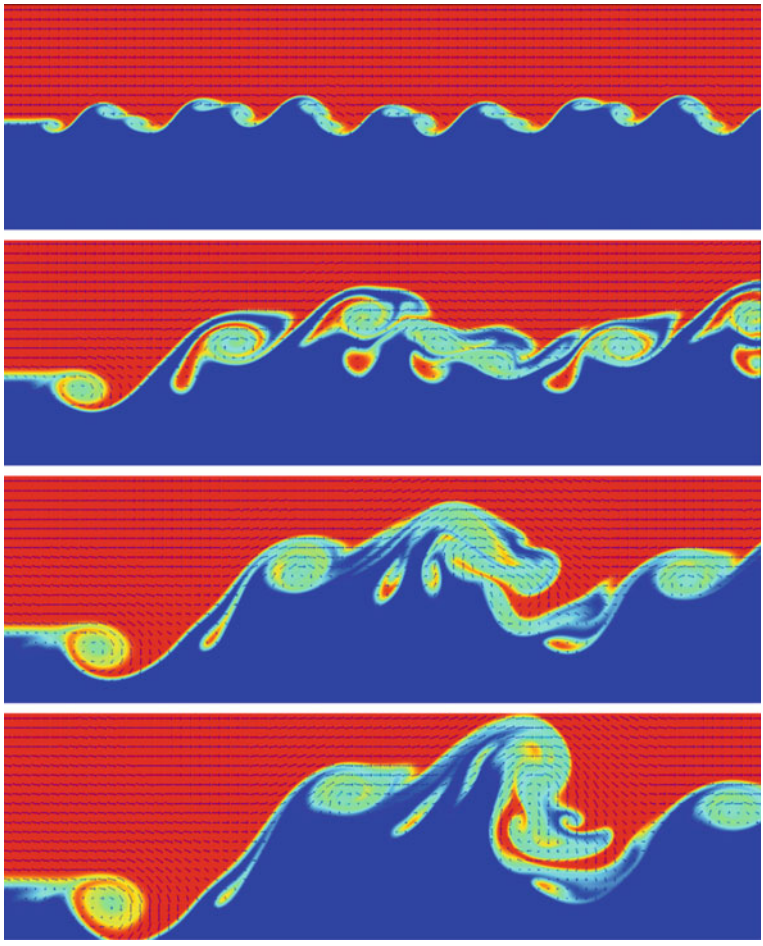

**Fig. 3** Time series for further growth of waves, showing as waves become steeper they break. The figures depict that bubbles are entrained and fragmented inside and below the breaking wave crest

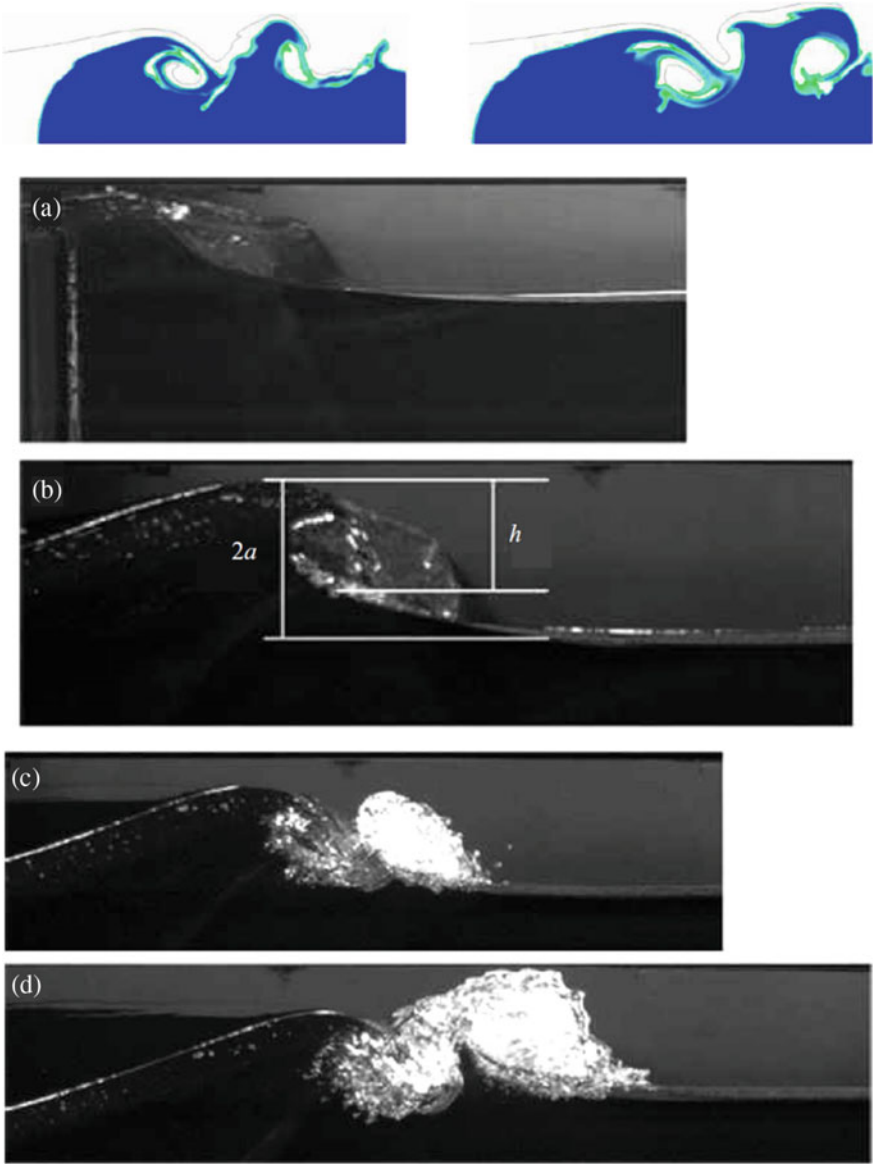


**Fig. 4** Top figure: Large Eddy Simulation of breaking waves showing similarities to present simulation (taken from Lubin et al. [10]). Bottom figure is a laboratory experiment showing close similarity with our simulation (taken from Drazen et al. [7])

those presented by Lubin et al. [10]. We demonstrate that the results are qualitatively similar. We remark that we have not adapted Lubin et al. [10] precisely for the Large Eddy Simulation conditions. (This, we shall do this in a later publication, since we have recently became aware of their paper). In this version of our paper we simply demonstrate some mathematical and the method used for numerical simulation for the air–sea interface which leads to generation and formation of wave breaking using essentially the Phillips [13] mechanism. In the following version, we shall present the full account. Here, we use our numerical tool to reproduce accurately the overturning motion, the splash-up occurrence and the dynamics generated under plunging breaking waves, where some of the complex features have been illustrated. The numerical results highlight the major role of the air entrainment phenomenon in the energy dissipation process. We have demonstrated the turbulence generation and air entrainment in our numerical simulations of breaking waves. We also have included a snap shots of a laboratory experiment by Drazen et al. [7] (Figs. 1, 2, 3 and 4).

## References

1. Banner, M.L., Peregrine, D.H.: Wave breaking in deep water. Annu. Rev. Fluid Mech. **25**, 373–397 (1993)
2. Batchelor, G.K.: The Theory of Homogeneous Turbulence. Cambridge University Press (1953)
3. Belcher, S.E., Vassilicos, J.C.: Breaking waves and the equilibrium range of wind-wave spectra. J. Fluid Mech. **342**, 377–401 (1997)
4. Belcher, S.R., Hunt, J.C.R.: Turbulent flow over hills and waves. Annu. Rev. Fluid Mech. **30**, 507–538 (1998)
5. Bell, J.B., Colella P., GLaz, H.M.: A second-order projection method for the incompressible Navier-Stokes equations. J. Comput. Phys. 85: 257–283 (1987)
6. Duncan, J.H.: Spilling breakers. Annu. Rev. Fluid Mech. **33**, 519–547 (2001)
7. Drazen, D.A., Melville, W.K., Lenain, L.: Inertial scaling of dissipation in unsteady breaking waves. J. Fluid Mech. **611**, 307–332 (2008)
8. Hunt, J.C.R., Sajjadi, S.G.: Mechanisms and modelling of wind driven waves. Proc. IUTAM **26**, 3–13 (2018)
9. Lixiao, L., Kareem, A., Xiao, Y., Hunt, J.C.R.: Turbulence spectra in typhoon boundary layer winds—a conceptual framework and field measurements at coastlines. Bound. Layer Meteorol. **154**, 243–263 (2015)
10. Lubin, P., Vincent, S., Abadie, S., Caltagirone, J.-P.: Three-dimensional large eddy simulation of air entrainment under plunging breaking waves. Coast. Eng. **53**, 631–655 (2006)
11. Melville, W.K.: The role of surface-wave breaking in air–sea interaction. Annu. Rev. Fluid Mech. **28**, 279–321 (1996)
12. Miles, J.W.: On the generation of surface waves by shear flows. J. Fluid Mech. **3**, 185–204 (1957)
13. Phillips, O.M.: On the generation of waves by turbulent wind. J. Fluid Mech. **2**, 417–445 (1957)
14. Sajjadi, S.G., Hunt, J.C.R., Drullion, F.: Asymptotic multi-layer analysis of wind over unsteady monochromatic surface waves. J. Eng. Math. **84**, 73–85 (2014)
15. Sajjadi, S.G., Hunt, J.C.R., Drullion, F.: Turbulent shear flows over monochromatic water waves; undulating or peaked and steady or unsteady. J. Fluid Mech. (2018) (to appear)
16. Sussman, M.: A second order coupled level set and volume-of-fluid method for computing growth and collapse of vapor bubbles. J. Comput. Phys. **187**, 110–136 (2003)

# Flag Flutter Close to a Free Surface: A Local Stability Analysis


**Jérôme Mougel and Sébastien Michelin**

**Abstract** A local stability analysis is performed to describe the effects of the free-surface on the stability of a flag-like flexible structure in a two-dimensional water channel. It is found that the free surface is at the root of a new instability arising from a resonance between free-surface waves and structural waves coupled with the flow referred to as *flag waves*. Interestingly the obtained instability may appear for lower reduced velocities than classical flutter. Additionally it is found that the free surface may affect significantly classical flutter threshold.

**Keywords** Fluid-structure interactions · Instability · Free surface waves · Flexible structures

## 1 Introduction

Thin flexible plates and membranes in a uniform flow become unstable when the destabilizing pressure forces overcome the stabilizing effects of structural bending rigidity. This mechanism, commonly referred to as flag flutter, has been extensively studied in the last decades (see [11] for a review). Most studies focus on the evolution of flutter velocity thresholds with the physical parameters of the problem such as the mass and aspect ratio of the flag [7]. Recently, confinement effects on flutter thresholds have been studied in the case of span-wise confinement [5, 6] and for lateral confinements [1, 3, 8, 12]. For the latter, it was demonstrated numerically using vortex sheet methods and analytically through an infinite flag model that lateral confinement increases instability regions of the flag [1]. Those predictions have been confirmed experimentally for a flag in ground effect [3]. The aim of the present paper

J. Mougel (✉)
Institut de Mécanique des Fluides de Toulouse (IMFT),
Université de Toulouse, CNRS, Toulouse, France
e-mail: jerome.mougel@imft.fr

S. Michelin
LadHyX—Département de Mécanique, Ecole Polytechnique—CNRS, 91128 Palaiseau, France



M. Braza et al. (eds.), *Advances in Critical Flow Dynamics Involving Moving/Deformable Structures with Design Applications*, Notes on Numerical Fluid Mechanics and Multidisciplinary Design 147,
https://doi.org/10.1007/978-3-030-55594-8_17

is to present a method to address the local stability of a flag close to a free surface. We focus our attention on the effect of the free surface on flag flutter thresholds and investigate potential additional free-surface induced instabilities. The paper is organized as follows. We first introduce the main assumptions, the corresponding equations and their non-dimensional counterparts. The fluid loading is then discussed before stability results are finally presented.

## 2 Problem Setting

Let us consider the stability of an infinitely long two-dimensional flag (i.e. with infinite span) aligned with a uniform flow of velocity $U$ of an inviscid fluid in a two-dimensional free-surface channel flow (Fig. 1). The flag immersion depth is noted $h$, the channel is assumed to be of infinite depth, and the streamwise and vertical coordinates are noted $x$ and $z$ respectively. The flow is assumed as two-dimensional and potential, with velocity potential $Ux + \phi(x, z, t)$, and the flag and free surface vertical displacements from there horizontal equilibrium state will be defined as $\eta_f(x, t)$ and $\eta_g(x, t)$ respectively. In this paper, subscript $f$ and $g$ respectively stand for *flag* and *gravity* and refer to flag and free surface quantities. The flag dynamics is modeled by the linear Euler-Bernoulli beam equation

$$\mu \frac{\partial^2 \eta_f}{\partial t^2} + B \frac{\partial^4 \eta_f}{\partial x^4} = -[p] \tag{1}$$

with $\mu$ the flag surface density, $B$ the bending rigidity per unit length in the spanwise direction, and $[p] = p(x, z = 0^+) - p(x, z = 0^-)$ the pressure jump across the flag.

The objective is now to obtain the pressure forcing on the structure and how it is impacted by free surface effects. Given the incompressible and potential flow assumptions, the hydrodynamic problem is fully described by the velocity potential perturbation $\phi$ which satisfies the two-dimensional Laplace equation

$$\Delta \phi = 0. \tag{2}$$

After solving this equation with boundary conditions detailed in Eqs. (4)–(7) the pressure field in the fluid domain is obtained from the linearized Bernoulli equation

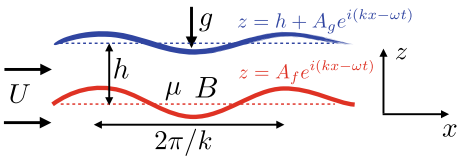


**Fig. 1** Sketch of the investigated two-dimensional configuration of a flag (red) in a uniform flow and confined by a free surface (blue).

$$p = -\rho \left( \frac{\partial}{\partial t} + U \frac{\partial}{\partial x} \right) \phi, \tag{3}$$

with $\rho$ the fluid density. Equation (3) eventually gives fluid loading in Eq. (1).

Linearized boundary conditions write

$$p = \rho g \eta_g \qquad \text{for } z = h, \tag{4}$$

$$\frac{\partial \phi}{\partial n} = \left( \frac{\partial}{\partial t} + U \frac{\partial}{\partial x} \right) \eta_g \qquad \text{for } z = h, \tag{5}$$

$$\frac{\partial \phi}{\partial n} = \left( \frac{\partial}{\partial t} + U \frac{\partial}{\partial x} \right) \eta_f \qquad \text{for } z = 0, \tag{6}$$

$$\phi = 0 \qquad \text{for } z \to -\infty, \tag{7}$$

where Eqs. (4)–(5) correspond to dynamic and kinematic boundary conditions on the free surface respectively, Eq. (6) to the kinematic boundary condition on the flag and Eq. (7) a condition of vanishing perturbation at infinity. Note that the dynamic boundary condition on the flag is already included in the beam equation (1).

Taking advantage of the invariance of the base flow in the stream-wise direction, wave like behaviors are considered in this direction under the normal mode decomposition

$$p(x, z, t) = \tilde{p}(z) e^{i(kx - \omega t)} \tag{8}$$

$$\phi(x, z, t) = \tilde{\phi}(z) e^{i(kx - \omega t)} \tag{9}$$

$$\eta_f(x, t) = A_f e^{i(kx - \omega t)} \tag{10}$$

$$\eta_g(x, t) = A_g e^{i(kx - \omega t)}. \tag{11}$$

In what follows, the wave number $k$ is fixed to a given real value, and the temporal stability of the system is studied. This approach has been successfully used in previous studies to estimate flag flutter thresholds ([9, 10] among others). Physically, the finite flag length would essentially fix the minimum wave number $k = 2\pi/L$ that can be supported by the flag, thereby relating the local analysis presented here to the stability of a finite flag. In the unbounded case, a more rigorous treatment of the flag finite length can be found in [7, 8], and increases significantly the complexity of the problem, requiring for example a proper description of the downstream wake of the flag and the upstream flow behaviour.

Using $L$, $L/U$, and $\rho L^3$ as typical scales for length, time and mass, we introduce the following non-dimensional variables

$$x^* = \frac{x}{L}, \qquad z^* = \frac{z}{L}, \qquad t^* = t \frac{U}{L}, \tag{12}$$

$$p^* = \frac{\tilde{p}}{\rho U^2}, \qquad \phi^* = \frac{\tilde{\phi}}{LU}, \qquad A_f^* = \frac{A_f}{L}, \qquad A_g^* = \frac{A_g}{L}, \tag{13}$$

as well as non-dimensional parameters governing the problem

$$M^* = \frac{\rho L}{\mu}, \qquad U^* = U\sqrt{\frac{\mu L^2}{B}}, \qquad \mathrm{Fr} = \frac{U}{\sqrt{gL}}, \qquad h^* = \frac{h}{L}, \tag{14}$$

where $M^*$ is a mass ratio, $U^*$ the reduced velocity based on bending stiffness, Fr the Froude number and $h^*$ a geometrical parameter corresponding to flag immersion depth. In addition, non-dimensional wave number $k^* = kL$ and frequency $\omega^* = \omega L/U$ will be used. In the remaining of the paper all results and equations are shown using non-dimensional variables. Stars will be omitted for $x$, $z$, $h$, $k$ and $\omega$.

The reduced velocity potential is introduced as $\phi_r = \phi^*/[-i(\omega - k)A_f^*]$. The associated set of non-dimensional linear equations reads

$$\frac{\partial^2 \phi_r}{\partial z^2} = k^2 \phi_r, \tag{15}$$

$$\frac{\partial \phi_r}{\partial z} = \mathrm{Fr}^2(\omega - k)^2 \phi_r, \quad \text{for } z = h, \tag{16}$$

$$\frac{\partial \phi_r}{\partial z} = 1, \quad \text{for } z = 0, \tag{17}$$

$$\phi_r = 0, \quad \text{for } z \to -\infty, \tag{18}$$

and the dispersion relation is obtained from the beam equation (1) as

$$-\omega^2 + \frac{1}{U^{*2}}k^4 - \frac{2M^*}{k}(\omega - k)^2 f(\omega) = 0, \tag{19}$$

with $f$ the normalized fluid loading function defined by

$$f(\omega) = -\frac{k}{2}[\phi_r], \tag{20}$$

where $[\phi_r] = \phi_r(z = 0^+) - \phi_r(z = 0^-)$. Function $f$ can be interpreted as the fluid loading exerted on the flag section normalized by the fluid loading in the unbounded case, i.e. when $h$ tends to infinity. In the two-dimensional case investigated here, the set of Eqs. (15)–(18) leads to an analytical expression for the fluid loading

$$f = \frac{\coth(kh)}{2}\left[\frac{1 - \frac{\mathrm{Fr}^2}{k}(\omega - k)^2 \tanh(kh)}{1 - \frac{\mathrm{Fr}^2}{k}(\omega - k)^2 \coth(kh)}\right] + \frac{1}{2}. \tag{21}$$

This fluid loading function is examined in various limit cases in the following section.

## 3 Analysis of Fluid Loading Function $f$

### 3.1 Unconfined Case (Large-h Limit)

The unconfined case corresponds to the limit where $h$ is large. In this case, solutions of Laplace equation (15) leading to vanishing values of $\phi_r$ for $z \to \pm\infty$ read

$$f = 1. \tag{22}$$

This result is consistent with the definition of $f$ proposed in the previous section. In the present unbounded case, the fluid loading can be interpreted as an added mass effect where $f = m_a k/2$, with $m_a = 2/k$ the non-dimensional added mass coefficient for a two-dimensional flag cross-section. Note however that the added mass coefficient is relative to the total acceleration of the flag as evidence by the factor $(\omega - k)^2$ in Eq. (19). This case is therefore more complex that a simple added mass effect of the form $m_a\omega^2$ which would only affect the frequency of the system and not it's stability.

### 3.2 Rigid Confinement (Small-Fr Limit)

In this section we study the fluid loading in the case of a flag in channel flow. This case corresponds to the small-Fr limit of the present study. The case $\mathrm{Fr} = 0$ indeed corresponds to a rigid free surface, i.e. a wall, where no penetration condition holds as can be seen from Eq. (16). In this limit Eq. (21) reads

$$f = \frac{\coth(kh)}{2} + \frac{1}{2}, \tag{23}$$

where each term of the above equation corresponds to the effect of the upper and lower fluid layers respectively. It is observed from (23) that the reduced fluid loading increases monotonically with the confinement parameter. Writing the fluid loading as $f = m_a k/2$ with $m_a$ the added mass coefficient, the classical trend of added-mass increase with the confinement is therefore recovered.

### 3.3 Free Surface Effects

An important result of the present paper corresponds to the expression of the fluid loading function given by Eq. (21) from which we now report small-Fr and large-Fr limits. The dependance upon the Froude number can be interpreted from free surface Eq. (16) which corresponds to a Robin boundary condition for finite values of Fr,

allowing to switch continuously from a Neumann boundary condition in the small-Fr limit, to a Dirichlet boundary condition in the large-Fr limit (if $\omega \neq k$).

In the small-Fr limit Eq. (21) tends to Eq. (23) and the free-surface behaves as a wall. Note that free-surface Eq. (16) indeed corresponds to a no-penetration condition for $\mathrm{Fr} = 0$.

The opposite limit of large-Fr which corresponds to a negligible effect of gravity (or a freely-deformable surface) leads to

$$f = \frac{\tanh(kh)}{2} + \frac{1}{2}. \tag{24}$$

In this limit, the fluid loading can also be interpreted as an added mass contribution with $f = m_a k/2$ as in the small-Fr limit. However, Eqs. (23) and (24) show that the contribution of the free upper surface to the fluid loading (its dependence with $h$) when $\mathrm{Fr} \gg 1$ is the inverse of that of an upper confining rigid wall ($\mathrm{Fr} \ll 1$). Interestingly the upper fluid layer contribution of Eq. (24) for small values of $kh$ leads to $m_a \sim h$ meaning that added mass corresponds to the mass of the upper fluid column in this limit for which the free surface is freely-deformable.

Function $f(\omega, k, \mathrm{Fr}, h)$ given by Eq. (21) is plotted as function of $Re(\omega)$ for other parameters fixed on Fig. 2. Note that $\omega$ is taken complex and so is $f$. It can be seen on the figure that strong variations of the fluid loading function is obtained in the vicinity of specific values of $Re(\omega)$ which correspond exactly to the classical two-dimensional surface wave solutions

$$\omega_g^{\pm} = k \pm \frac{1}{\mathrm{Fr}}\sqrt{k\tanh(kh)}. \tag{25}$$

This behaviour of the fluid loading is therefore associated to the presence of the free surface and its own dynamics.

On Fig. 2 small-Fr and large-Fr limits obtained for $f$ in Eqs. (23) and (24) respectively are also represented. Interestingly, the free surface is found to bear two kinds of behaviour outside the close vicinity of $\omega_g^{\pm}$. For frequencies inside the interval $[\omega_g^-, \omega_g^+]$ of width $2\sqrt{k\tanh(kh)}/\mathrm{Fr}$, the fluid loading $f$ is well approximated by the small-Fr limit predictions (i.e. rigid wall) given by Eq. (23). For frequencies outside the interval $[\omega_g^-, \omega_g^+]$, function $f$ is closer to the large-Fr limit predictions given by Eq. (24). This shows that for finite Fr the free surface can somehow be viewed as a band-pass filter.

## 4 Stability Results

In this section we solve the dispersion relation (19) with the fluid loading $f$ given by Eq. (20) as a function of $\omega(k, Fr, U^*, M^*, h)$. In the following the wave number $k$ is fixed to $2\pi$ as explained in Sect. 2, $M^* = 1$ and $h = 0.1$. We will focus on the

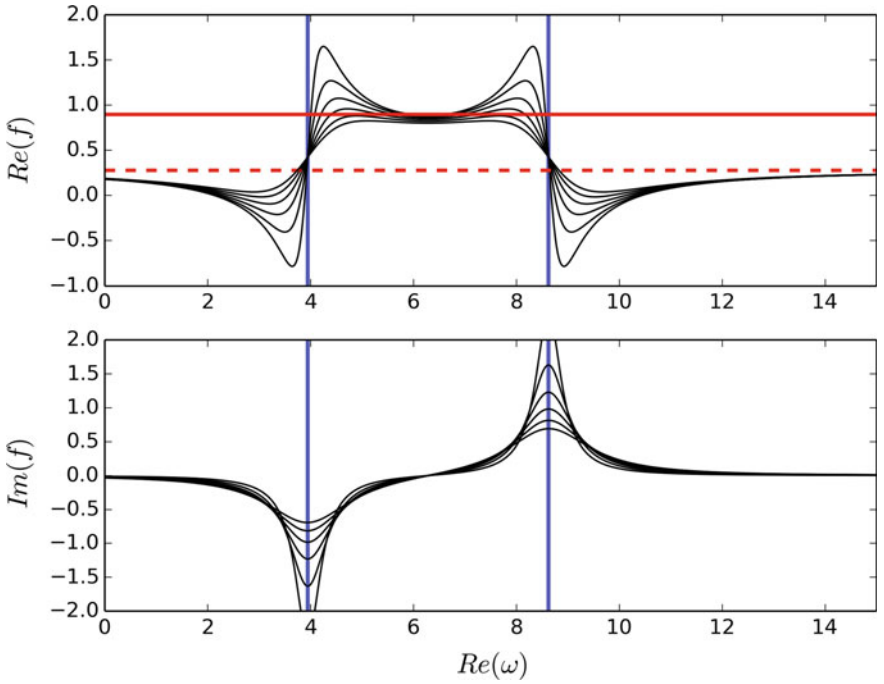


**Fig. 2** Evolution of $f$ as function of $Re(\omega)$ for Fr $= 0.8$ and $h = 0.1$. [black lines, Eq. (21)] complete case for $\omega_i = [0.3, 0.44, 0.58, 0.72, 0.86, 1]$; [red, Eq. (23)] small-Fr limit where the free surface corresponds to a wall; [dashed red, Eq. (24)] large-Fr limit, [vertical blue lines] solutions of the two-dimensional gravity wave dispersion relation $\omega_g^{\pm} = k \pm 1/\mathrm{Fr}\sqrt{k\tanh(kh)}$.

effects of $U^*$ and Fr on the frequency, $Re(\omega)$, and growth rate $Im(\omega)$ of the waves. Parameters for which $Im(\omega) > 0$ correspond to an unstable wave.

## 4.1 Confinement Versus Free Surface

Figure 3($a$) shows the evolution of the frequencies and growth rates with the reduced velocity $U^*$ for an unbounded flag [grey, $f$ given by Eq. (22)] and a confined flag [red, $f$ given by Eq. (23)]. For small values of reduced velocities (stiff flag), two neutral solutions (zero growth rate) with distinct frequencies are obtained and physically correspond to structural bending waves whose frequencies are modified by the flow. In the following these waves will be referred to as *flag waves*. When the reduced velocity is increased, the frequencies of those two flag waves are affected by the increasingly strong effect of fluid loading and eventually merge leading to a couple of complex conjugate solutions, one of which being unstable. This behaviour is identified as flag flutter and the smallest value of $U^*$ for which a positive growth

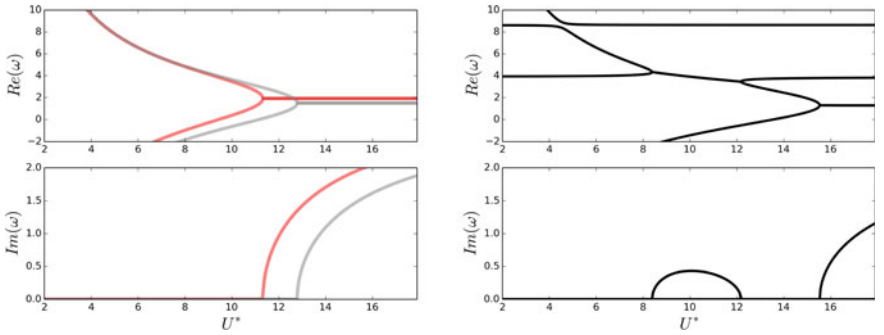


(a) Fr = 0 (b) Fr = 0.8

**Fig. 3** Real and imaginary parts of frequencies $\omega$ solution of the two-dimensional dispersion relations as function of reduced velocity $U^*$ for $k = 2\pi$, Fr = 0.8, $M^* = 1$ and $h = 0.1$. **a** (grey) unbounded flag; (red) confined flag (small-Fr limit). **b** (black) coupled problem for Fr = 0.8

rate is obtained defines the flutter threshold. The mechanism described above is qualitatively identical for both unbounded and bounded flags, but the presence of the wall reduces flutter threshold, in agreement with results reported in previous studies [1, 3, 4, 8].

Figure 3b shows stability results for the same parameter values as Fig. 3a but when a free-surface is considered with Fr = 0.8 (black lines). It is found that the free surface effect is more complex than a confinement effect for the investigated Froude number. In addition to a modification in flutter threshold (large $U^*$) a new unstable regime is obtained for values of the reduced velocity far below flutter threshold (around $U^*$) . The analysis of this new instability of interest is the focus of the following section.

## 4.2 *Free Surface-Induced Instability*

The set of Eqs. (15)–(20) can be written under the matricial form

$$\begin{bmatrix} D_g(\omega) & \frac{\mathrm{Fr}}{\sqrt{M^*}}\mathcal{C}(\omega) \\ \frac{\sqrt{M^*}}{\mathrm{Fr}}\mathcal{C}(\omega) & D_f(\omega) \end{bmatrix} \begin{bmatrix} A_g^* \\ A_f^* \end{bmatrix} = \begin{bmatrix} 0 \\ 0 \end{bmatrix} \tag{26}$$

with

$$D_g(\omega) = -1 + \frac{\mathrm{Fr}^2(\omega - k)^2}{k}\coth(kh), \tag{27}$$

$$D_f(\omega) = \omega^2 - \frac{1}{U^{*2}}k^4 + \frac{M^*(\omega - k)^2}{k}\left[\coth(kh) + 1\right], \tag{28}$$

and

$$\mathcal{C}(\omega) = -\frac{\mathrm{Fr}\sqrt{M^*}(\omega - k)^2}{k\sinh(kh)}. \tag{29}$$

One readily identifies $D_g(\omega) = 0$ as the classical dispersion relation for linear ocean waves in finite depth $h$ (whose two solutions are given by Eq. (25) and called *free surface waves*), and $D_f(\omega) = 0$ as the dispersion relation of an infinite flag with a one-sided confinement by a wall at a distance $h$ (whose two solutions are referred to here for clarity as *flag waves*). The present matricial form is convenient as it readily allows for physical interpretation. For large distances between the flag and the free surface, non-diagonal terms $\mathcal{C}(\omega)$ vanish and two uncoupled problems should be solved, namely the flag problem $D_f(\omega) = 0$ and the free surface problem $D_g(\omega) = 0$. $\mathcal{C}(\omega)$ should therefore be interpreted as a coupling term between the flag and the free surface.

The dispersion relation for the fully-coupled problem reads

$$D(\omega) \equiv D_g(\omega)D_f(\omega) - \mathcal{C}(\omega)^2 = 0. \tag{30}$$

and provides solutions $\omega$ as functions of the physical parameters of the problem. Solutions of coupled and uncoupled problems are superimposed on Fig. 4 (top) for the same parameter values as for Fig. 3. It is found that solutions of the uncoupled problems $D_g(\omega) = 0$ (blue lines) and $D_f(\omega) = 0$ (red lines) match the complete solution in specific parameter ranges. This identifies parameter for which the coupled problem essentially behaves as a free surface or as a confined flag. Note that the rigidly-confined flag and the complete problem show a good match for frequency values in the range $[\omega_g^-, \omega_g^+]$. This confirms results for the fluid loading obtained in Sect. 3. In addition, the interest of this analysis lies in the fact that interesting phenomena precisely occur for parameters where uncoupled problems have nearly the same frequency. The new instability attributed in the above to the presence of the free surface can therefore be interpreted as a resonance between a flag wave and a free surface wave. However why is only one resonance obtained whereas two uncoupled frequencies crossing occur, i.e. at $U^* \approx 4.5$ and $U^* \approx 9.2$? An interpretation for this phenomenon was originally proposed by Cairn [2] as explained below.

Let us assume that $kh \gg 1$ so that the coupling can be considered small. Under this assumption, $\coth(kh) \approx 1, \epsilon = 1/\sinh(kh) \ll 1$, and the dispersion relation given by Eq. (30) can be interpreted as a flag weakly coupled to the free surface. Let us consider solutions of the uncoupled case $\omega_g$ and $\omega_f$, and let us assume that parameters are such that the two uncoupled solutions have the same frequency, that is, we assume exact resonance which is defined by $\omega_g = \omega_f \equiv \omega_0$. We assume in addition that we are below flutter threshold so that those uncoupled solutions correspond to purely real frequencies, and search for solutions $\omega$ of the weakly-coupled problem as $\omega = \omega_0 + \delta\omega$ where $\delta\omega$ is a small correction of order $\mathcal{O}(\epsilon)$ due to coupling. The objective is to identify conditions for which the frequency correction has a positive imaginary part leading to an instability. Injecting the above decomposition for $\omega$ in Eq. (30) and proceeding to Taylor's series expansions we get at order $\mathcal{O}(\epsilon^2)$

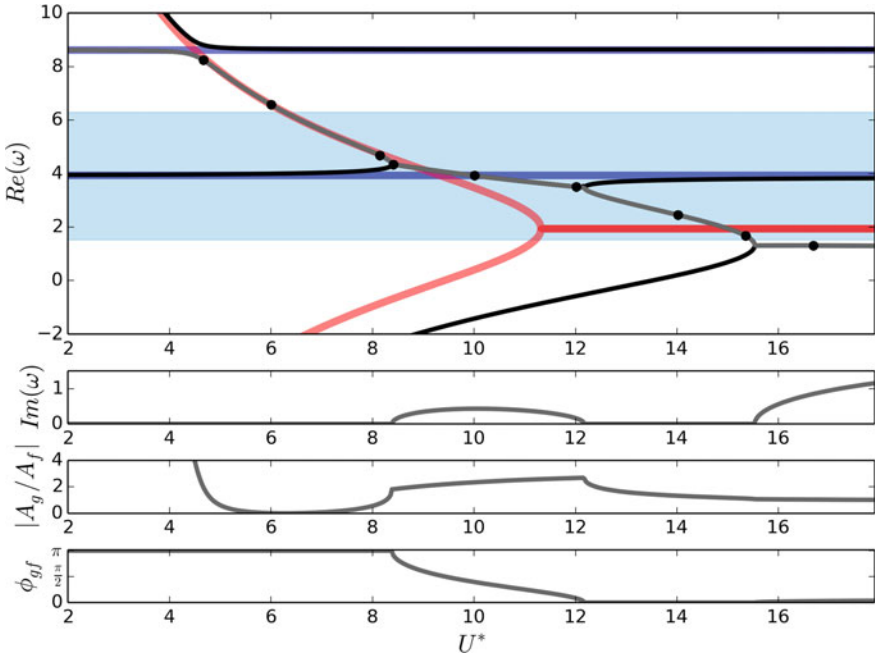


**Fig. 4** Frequencies and structural properties as function of reduced velocity $U^*$ for $k = 2\pi$, Fr $= 0.8$, $M^* = 1$, $h = 0.1$. (top) $Re(\omega)$ for both coupled [black and grey, $D(\omega) = 0$] and uncoupled [red, $D_f(\omega) = 0$; blue, $D_g(\omega) = 0$] problems. The grey line correspond to the path along which other quantities are tracked in the bottom panels. Pressure fields corresponding to black spots are shown on Figure 5. The blue shaded area corresponds to the frequency region given by Eq. (33). (bottom) Evolution of growth rate $Im(\omega)$, amplitude ratio $|A_g/A_f|$ and phase shift $\phi_{gf}$ following the grey path in the top panel

$$\delta\omega^2 \approx \frac{M^* \mathrm{Fr}^2 (\omega_0 - k)^4}{k^2 \left.\frac{\partial D_g}{\partial \omega}\right|_{\omega_0} \left.\frac{\partial D_f}{\partial \omega}\right|_{\omega_0}} \epsilon^2. \tag{31}$$

A necessary condition for instability is therefore

$$\left.\frac{\partial D_g}{\partial \omega}\right|_{\omega_0} \left.\frac{\partial D_f}{\partial \omega}\right|_{\omega_0} < 0, \tag{32}$$

which can be rewritten using Eqs. (27) and (28) for $kh \gg 1$ as

$$\frac{k}{1 + \frac{k}{2M^*}} < \omega_0 < k. \tag{33}$$

The frequency region corresponding to Eq. (33) is shown as the blue shaded region on Fig. 4. It is found that this criterium indeed allows to discriminate the crossing

between uncoupled waves which leads to an instability (that is the one occurring around $U^* \approx 9.2$). Note that instability condition given by Eq. (33) appears to be robust regarding the assumption $kh \gg 1$ which is not satisfied for parameters corresponding to Fig. 4 ($kh \approx 0.63$).

The conditions required for free-surface induced instability are therefore twofold: (1) a resonance between structural and gravity waves $\omega_0 = \omega_g = \omega_f$ and (2) a value of $\omega_0$ satisfying Eq. (33). In Cairn's terminology [2], this second condition means that the two waves at resonance should have opposite energy signs. In the present case, the surface wave should have negative energy (corresponding to a surface wave slower than base flow in this case) and the flag wave positive energy.

### 4.3 Mode Structure

We now propose to analyse the evolution in the structure of the waves solution of the coupled problem. Specifically, we focus on the relative amplitude and phase of the free surface and flag displacement for a given wave. From Eqs. (26), (27) and (29) amplitude ratio and phase shift are defined as follows

$$\frac{A_g}{A_f} = \left|\frac{A_g}{A_f}\right| e^{i\phi_{gf}} = \frac{\mathrm{Fr}^2(\omega - k)^2}{k \sinh(kh)\left[\frac{\mathrm{Fr}^2}{k}(\omega - k)^2 \coth(kh) - 1\right]}. \tag{34}$$

and can easily be obtained once $\omega$ is known (solution of the dispersion relation given by Eq. (19)). Equation (34) in the small-Fr limit directly leads to $A_g/A_f \sim 0$ in agreement with this rigid wall confinement limit. Conversely, the large-Fr limit leads to $A_g/A_f \sim 1/\cosh(kh)$, the amplitude of the free surface deformation being therefore in-phase with that of the flag and of the same magnitude for small immersions ($kh \ll 1$). This latter trend confirms the physical meaning of the large-Fr limit mentioned in Sect. 3, that is, a freely deformable free surface which follows flag's displacements.

On Fig. 4 we track the evolution of the relative amplitude and phase along the path represented as a grey line. The chosen path goes through the main features of interest identified in this study, namely the two regions where uncoupled frequencies cross (including the free surface-induced instability) and the classical flutter region for $U^* > 15.5$. Along this path, corresponding growth rate, amplitude ratio and phase shift between gravity and flag are represented on Fig. 5 (bottom). The pressure fields associated with specific values of the reduced velocity (shown in black dots) are also displayed on Fig. 5. For $U^* \in [2, 8.3]$ the chosen path for the coupled solution goes through the first crossing between the two uncoupled systems, by smoothly switching from a pure gravity wave ($A_f \approx 0$) to a pure flag wave ($A_g \approx 0$). The corresponding pressure fields are shown on Fig. 5 (first line) and confirm this analysis.

When the reduced velocity is further increased a second transition occurs around $U^* \approx 9.2$ and leads to a positive growth rate for the complete problem in the range

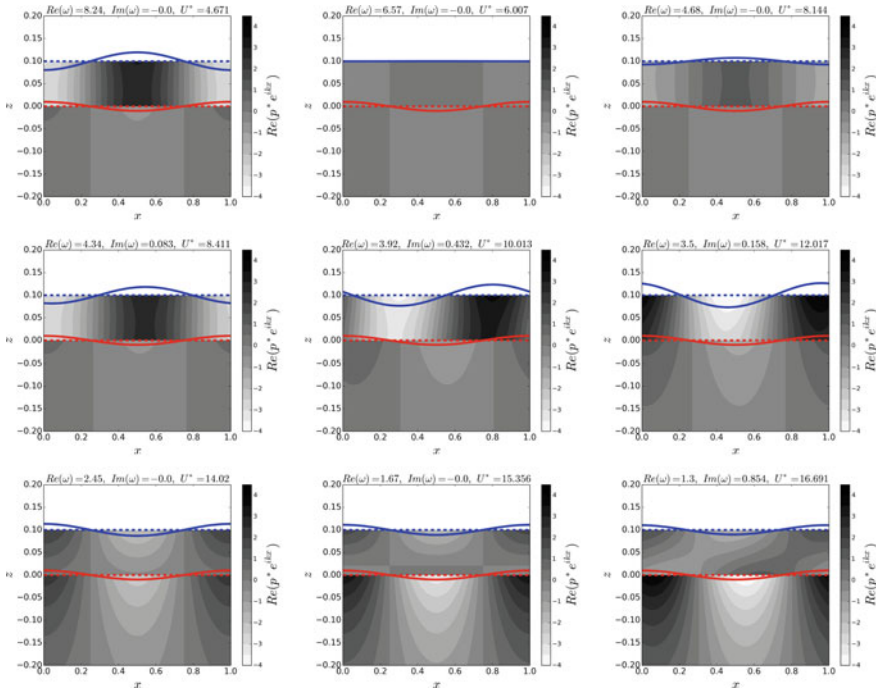

**Fig. 5** Pressure fields corresponding to black dots on Fig. 4. Blue (resp. red) lines correspond to reconstructed free surface (resp. flag) position. Dashed blue (resp. red) lines indicate mean free surface (resp. flag) locations. In this reconstruction of the linear perturbation, the amplitude of the normalized flag displacement is chosen as the reference.

$U^* \in [8.3, 12.1]$. The amplitude ratio in this frequency range remains close to 3 and the phase difference evolves monotonically from $\pi$ to 0 with $\pi/2$ corresponding to the maximum growth rate. The evolution of the mode structure along this unstable range can be seen on Fig. 5 (second line) where the above mentioned characteristics are recovered. Interestingly the main pressure contribution on the flag comes from the upper fluid layer in this reduced velocity range.

Further increase in reduced velocity leads to a stable area for $U^* \in [12.1, 15.5]$. As seen from Fig. 4 this zone quantitatively departs from the confined flag solution shown in red. This can be understood both from Fig. 2 where the fluid loading departs from the confined flag case outside the frequency range $[\omega_g^-, \omega_g^+]$, and from pressure field shown on Fig. 5 for $U^* \approx 14$ where important free surface deformations are obtained. In this range, free surface and flag are in phase with amplitudes of the same order, in agreement with the large-Fr limit discussed above when $kh \ll 1$.

Finally, large values of reduced velocities lead to flutter for $U^* > 15.5$. As already mentioned, flutter thresholds is higher than that obtained for the confined flag. Some clues for this trend obtained for $\mathrm{Fr} = 0.8$ can be found on Fig. 5 (for $U^* \approx 16.7$) as large values of the pressure acting on the flag essentially come from the lower fluid

layer. This means that the presence of the free surface attenuates the destabilizing pressure acting on the flag upper side and therefore leads to a larger flutter threshold. For $U^* > 15.5$ frequencies lie outside the range $[\omega_g^-, \omega_g^+]$ and we indeed recover the characteristics of the large-Fr limit (in the case $kh \ll 1$) i.e. waves in phase with similar amplitudes. The described change in velocity threshold can therefore be attributed to the added mass behaviour ($m_a \sim h$) obtained in this limit.

## 5 Conclusion

This work proposes a local stability analysis of a flexible flag-like structure in two-dimensional free surface channel flow. The influence of the free surface on fluid loading and stability of the flag has been presented. A two-fold effect of the free surface on the stability of the structure was found. The first effect corresponds to a modification of the flutter threshold. For $\mathrm{Fr} = 0.8$, flutter threshold was found for a larger reduced velocity than in the case of an unbounded flag. This trend is the opposite of confinement effects by a rigid wall reported in the literature and also reproduced in this paper (small-Fr limit). The second effect of the free surface is to lead to a new instability interpreted as a resonance with gravity surface waves. This latter free surface-induced instability has been investigated analytically allowing to establish simple instability conditions. Eventually, those two main features attributed to the presence of the free surface have been further studied through the evolution of the obtained mode structure as function of the reduced velocity.

Further analysis is however required to investigate in greater depth these peculiar features. This includes a more complete analysis of the effects of $M^*$, $h^*$ and Fr, as well as extensions of the present simple model to account for finite size effects of the flag in both streamwise and spanwise directions, the effect of internal tension, and the effect of a lower confining wall.

## References

1. Alben, S.: Flag flutter in inviscid channel flow. Phys. Fluids **27**(3), 033603 (2015)
2. Cairns, R.A.: The role of negative energy waves in some instabilities of parallel flows. J. Fluid Mech. **92**(1), 1–14 (1979)
3. Dessi, D., Mazzocconi, S.: Aeroelastic behavior of a flag in ground effect. J. Fluids Struct. **55**, 303–323 (2015)
4. Doaré O., Eloy, C.: The influence of channel walls on flag flutter. In: Flow Induced Vibration (2012)
5. Doaré, O., Mano, D., Ludena, J.C.B.: Effect of spanwise confinement on flag flutter: experimental measurements. Phys. Fluids **23**(11), 111704 (2011)
6. Doaré, O., Sauzade, M., Eloy, C.: Flutter of an elastic plate in a channel flow: confinement and finite-size effects. J. Fluids Struct. **27**(1), 76–88 (2011)
7. Eloy, C., Souilliez, C., Schouveiler, L.: Flutter of a rectangular plate. J. Fluids Struct. **23**(6), 904–919 (2007)

8. Guo, C.Q., Paidoussis, M.P.: Stability of rectangular plates with free side-edges in two-dimensional inviscid channel flow. J. Appl. Mech. **67**(1), 171–176 (2000)
9. Schouveiler, L., Eloy, C.: Coupled flutter of parallel plates. Phys. Fluids **21**(8), 081703 (2009)
10. Shelley, M., Vandenberghe, N., Zhang, J.: Heavy flags undergo spontaneous oscillations in flowing water. Phys. Rev. Lett. **94**(9), 094302 (2005)
11. Shelley, M.J., Zhang, J.: Flapping and bending bodies interacting with fluid flows. Ann Rev Fluid Mech **43**, 449–465 (2011)
12. Shoele, K., Mittal, R.: Flutter instability of a thin flexible plate in a channel. J. Fluid Mech. **786**, 29–46 (2016)

# FSI Simulation Using a Membrane Model: Inflation of Balloons and Flow Past Sails


**Mohd Furquan and Sanjay Mittal**

**Abstract** Interaction of thin membrane structures with an incompressible Newtonian fluid is numerically studied. A partitioned approach is utilized for solving the coupled fluid-structure equations. Material of the structure is assumed to follow the St. Venant-Kirchhoff's constitutive law. A simple, robust model for calculating the deformation of the membrane structure, proposed by Taylor et al. (Finite Element Analysis of Membrane Structures. Springer, The Netherlands, pp. 47–68, 2005, [7]), is utilized. Fluid flow is calculated using the SUPG/PSPG stabilized Petrov-Galerkin space-time finite element method. Fluid mesh is updated at each time step, to take into account the deformation of the domain, using pseudo-elastic mesh moving technique. The meshes for the fluid and the membrane have coincident nodes. This allows direct transfer of tractions and velocity between the fluid and the structure. First, inflation/deflation of a spherical balloon is considered for different values of elasticity and density ratio. The shape of an inflated balloon changes from nearly spherical to an elongated one as the value of elasticity is increased. The density ratio is observed to have negligible effect on the inflation rate. Uniform flow past a square piece of initially flat membrane with fixed edges is also studied. Reynolds number based on the edge length is 150. The membrane oscillations achieve a limit cycle in which the deformation of the membrane is similar to the first eigenmode of the structure.

**Keywords** FSI · Membrane · Balloons · Sails · Incompressible flow

## 1 Introduction

Several thin structural elements offer negligible resistance in bending. Such structures, like fabrics and thin rubber sheets, are often modelled in solid mechanics using membrane elements. These elements can support significantly large stretching force, but are unstable under compression. In many cases, the forces arise from a fluid

M. Furquan (✉) · S. Mittal
Department of Aerospace Engineering, Indian Institute of Technology Kanpur, Kanpur, India
e-mail: mfurquan@iitk.ac.in



M. Braza et al. (eds.), *Advances in Critical Flow Dynamics Involving Moving/Deformable Structures with Design Applications*, Notes on Numerical Fluid Mechanics and Multidisciplinary Design 147,
https://doi.org/10.1007/978-3-030-55594-8_18

flowing around the structure. Examples of systems where fluid-membrane interactions play a vital role include: fluttering flags, parachutes, safety airbags in vehicle, sailboats, balloons etc.

Due to its vast number of engineering applications, fluid-membrane interaction has been a subject of a number of FSI studies. A detailed literature survey will be beyond the scope of this paper, we however mention few important works. Tezduyar et al. [2, 5, 6] computed three-dimensional FSI of ring-sail parachutes in a number of configurations using stabilized space-time techniques. Saksono et al. [3] used a two-dimensional model with adaptive meshing to simulate the deployment of an air-bag. Sawada and Hisada [4] investigated the flapping of a two-dimensional flag model using interface tracking with ALE formulation. Although many researchers have demonstrated the capability of simulating fluid-membrane interactions, widespread application of these methods in unraveling the underlying physics, especially for three-dimensional problems, is yet to be seen. A number of factors are responsible for this situation including. The lack of a simple and robust membrane model which is easy to couple with a flow solver is one such problem. Usually, membranes are modelled using a specialization of shell theories. In this paper we avoid the complications of shell theories by using a simple triangular membrane element propose by Taylor et al. [7]. Another problem is the large deformation of membrane structures, which requires excessive adjustment to the fluid mesh. The problem can be avoided by using non-conforming fluid meshes along with interface capturing techniques. However, this approach suffers from poor resolution in the boundary-layer. In the present work, a boundary conforming fluid mesh is used, which is adjusted during each iteration to follow the interface.

## 2 Problem Formulation

In the present paper we consider two problems involving fluid-membrane interaction. The first problem consists of an initially spherical elastic balloon. A schematic of the computational domain is shown in Fig. 1a. The balloon is attached to a pipe of circular cross-section which supplies the fluid to inflate it. The fluid is incompressible Newtonian, while the membrane is nonlinear elastic. The material of the membrane follows St. Venant-Kirchhoff's constitutive law. The thickness of the membrane is neglected for the purpose of generating fluid meshes. This whole assembly is enclosed inside a cylindrical domain. The various geometric dimensions are indicated in Fig. 1a. The simulation begins with a spherical balloon. Stress-free condition is applied at the pipe inlet and at the external boundaries of the domain. A hydrostatic pressure gradient is specified in a region of the pipe to drive the fluid into the balloon. The influx of fluid causes the balloon to inflate.

The second problem consists of a rectangular elastic sail with all its edges fixed (Fig. 1b). The sail is held normal to the incoming flow. Schematic of the computational domain is shown in Fig. 1b, along with the boundary conditions. Also shown are the various dimensions relative to the edge length of the membrane. Free-slip and zero

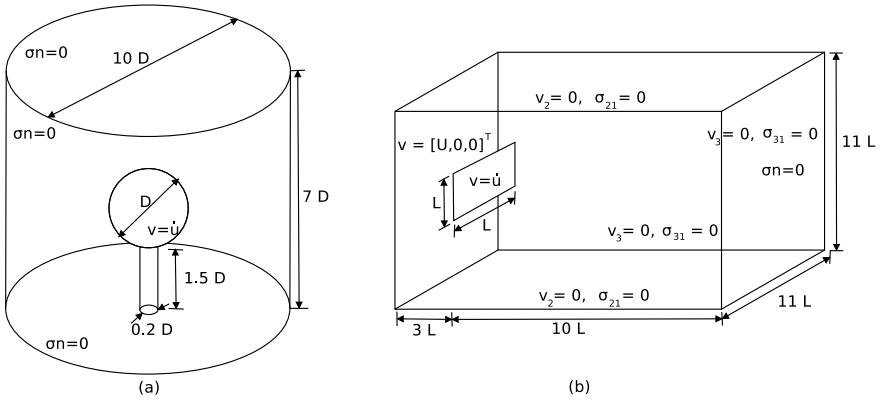


**Fig. 1** Schematics of the flow domain used for the computation of **a** inflation of a spherical balloon and **b** flow-induced vibration of a rectangular sail. The boundary conditions applied on the various boundaries of the domains are also indicated

normal velocity is enforced on the lateral boundaries, while stress free condition is applied on the outflow surface. As the incoming flow incidents on the sail, its fabric stretches and vibrates due to difference in pressure on the two sides.

## 3 Computational Method

In this work, a partitioned approach is applied to study the interaction of thin membrane structures with an incompressible Newtonian fluid. Fluid flow sub-problem is calculated using the Deforming Spatial Domain/Stabilized Space-time (DSD/SST) method proposed in [8, 9]. The formulation for DSD/SST, in a non-dimensionalized form, can be expressed as: given the initial velocity field $\mathbf{v}_0$, find $(\mathbf{v}^h, q^h) \in \left[\mathcal{H}^{1h}(Q_n)\right]^{n_{sd}+1}$, $n_{sd}$ is the number of space dimensions, satisfying $\mathbf{v}^h = \mathbf{g}$ on the Dirichlet part of the boundary $(\mathcal{P}_n)_g$, such that

$$\begin{aligned}
&\int_{Q_n} \mathbf{w}^h \cdot \left( \frac{\partial \mathbf{v}^h}{\partial t} + \mathbf{v}^h \cdot \nabla \mathbf{v}^h \right) dQ + \int_{Q_n} \frac{1}{2} \left( \nabla \mathbf{w}^h + \nabla \mathbf{w}^{h^{\mathsf{T}}} \right) : \sigma(p^h, \mathbf{v}^h)\, dQ \\
&+ \sum_{e=1}^{n_e} \int_{Q_n^e} \tau \left[ \frac{\partial \mathbf{w}^h}{\partial t} + \mathbf{v}^h \cdot \nabla \mathbf{w}^h - \nabla \cdot \sigma(q^h, \mathbf{w}^h) \right] \\
&\cdot \left[ \frac{\partial \mathbf{v}^h}{\partial t} + \mathbf{v}^h \cdot \nabla \mathbf{v}^h - \nabla \cdot \sigma(p^h, \mathbf{v}^h) \right] dQ \\
&+ \int_{Q_n} q^h \nabla \cdot \mathbf{v}^h dQ + \int_{\Omega_n} \mathbf{w}^{h+}_n \left( \mathbf{v}^{h+}_n - \mathbf{v}^{h-}_n \right) d\Omega = \int_{P_n} \mathbf{w}^h \cdot \mathbf{h}\, dP, \qquad (1)
\end{aligned}$$

for all $(\mathbf{w}^h, q^h) \in \left[\mathcal{H}^{1h}(Q_n)\right]^{n_{sd}+1}$ satisfying $\mathbf{w}^h = \mathbf{0}$ on $(\mathcal{P}_n)_g$. Here, $\mathbf{v}^h$ denotes the velocity, $p^h$ denotes the pressure, and $\sigma$ denotes the Cauchy's stress fields, all defined in a space-time domains $Q_n$. For the Newtonian, isotropic fluid $\sigma(p, \mathbf{u}) = -p\mathsf{I} + (\nabla\mathbf{v} + \nabla\mathbf{v}^{\mathsf{T}})/2\mathrm{Re}$, where Re is the Reynolds number for the flow. Also, $\mathbf{v}^{h\pm}_n = \lim_{\epsilon\to 0} \mathbf{v}^h(t_n \pm \epsilon)$ and $\mathbf{v}^{h-}_0 = \mathbf{v}_0$. $\Omega_n$ denotes the corresponding spatial domain, while $P_n$ represents the Neumann part of the boundary. The above formulation is equally valid for stationary as well as moving/deforming domains. It utilizes SUPG/PSPG stabilizations for the Navier-Stokes equation. The value of stabilization coefficient $\tau$ used in the present computations is given by: $\tau = 1/\sqrt{\left(\frac{2\|\mathbf{v}^h\|}{h^e}\right)^2 + \left(\frac{12}{h^{e^2}\mathrm{Re}}\right)^2}$, where $h^e$ is the minimum length of the element edges. Fluid mesh is updated at each time step, to take into account the deformation of the domain, using pseudo-elastic mesh moving technique [1]. The meshes for the fluid and membrane have coincident nodes. This allows direct transfer of tractions and velocity between the fluid and the structure.

Material of the structure is assumed to follow St. Venant-Kirchhoff's constitutive law. The problems considered include inflation and deflation of a balloon and the vibration of a sail-like structure in a fluid stream. A simple, robust model for calculating the deformation of the membrane structure, proposed by Taylor et al. [7], is used. The weak form for the membrane problem can be written using the principle of virtual-work:

$$\int_\Omega \delta\mathbf{x} \cdot m^*\mathbf{x}\, d\Omega + \int_\Omega \delta\mathsf{E} : \mathsf{S}\, d\Omega = \int_\Omega \delta\mathbf{x} \cdot \mathbf{f}\, d\omega\,, \tag{2}$$

where, $\mathbf{x}$ describes the current configuration of the membrane, $m^*$ denotes the density ratio of the structure to that of the fluid, $\mathbf{f}$ is the load on the membrane in global coordinate system. $\mathsf{E}$ and $\mathsf{S}$ are, respectively, the Green-Lagrange strain and the Second Piola-Kirchhoff stress tensors. As per the St. Venant-Kirchhoff's constitutive law:

$$\mathsf{S} = \mathrm{Ae}\left[\frac{\nu}{1-\nu^2}\mathrm{tr}(\mathsf{E}) + \frac{1}{1+\nu}\mathsf{E}\right], \tag{3}$$

where, $Ae = Eh/\rho_f U^2 D$ is the non-dimensionalized Young's modulus and $\nu$ is the Poisson's ratio.

The fluid and solid problems are solved together using a block-iterative coupling [8]. The load acting on the structure is obtained by solving the flow problem. In response, the membrane deforms due to these loads and alters the velocity and the shape of the interface. This alternate computations of fluid flow and structural deformation are carried out alternately, till convergence is achieved.

# 4 Results and Discussion

## 4.1 Inflation of a Balloon

The fluid mesh used for computations consists of 348,545 linear tetrahedral elements, while the membrane mesh consists of 13,220 linear triangles Fig. 2a. Fluid is fed through a pipe of circular cross-section attached to the balloon. A pressure gradient is specified in a portion of the pipe to generate an influx of fluid. This influx of fluid causes the balloon to inflate. The rate of inflation decreases with time and eventually the balloon asymptotically saturates to a fixed volume.

Two values of the density ratio $m^*$ of the structure to fluid are considered: 5 and 2.5. Characteristic velocity, $U$, of the fluid is chosen as the maximum velocity in the pipe alone due to the same pressure gradient. Reynolds number based on this velocity and initial balloon diameter D, is 40. Flexibility of the membrane is characterized by $Ae$, where is Young's modulus of the membrane. The value of $Ae$ is varied between 0.8 and 40. The balloons show shift from a spherical towards an elongated shape with increase in elasticity of the membrane. Fig. 2b shows a section through the center of the balloon with $m^* = 2.5$ and $Ae = 4$ after 1000 time units. Initial shape of the balloon is also indicated for comparison. The density ratio is observed to have no bearing on the inflation rate.

Deflation of balloons was studied by first inflating it for 1000 time units and then relieving the applied pressure gradient. The deflation starts with almost same rate as that of inflation but quickly decreases as the volume reduces. This is due small pressure gradient between the balloon and the pipe after the initial release.

## 4.2 Flow Past a Square Membrane

Uniform flow past a square piece of initially flat membrane, of density ratio 10 and $Ae = 5$, with fixed edges is studied. Fluid mesh consists of 74,488 linear tetrahedra, while the structure mesh used has 1040 linear triangles. Reynolds number based on the edge length $L$, is 150. Figure 2a shows an instantaneous pressure distribution for the case. Vortex shedding from the edges of the structure is clearly visible. Also shown, in Fig. 2b, is the time history of streamwise displacement of the center of the membrane. Initially, as the flow incidents on the membrane, the membrane bulges significantly on the downstream side. Later as the flow develops, unsteady forces acting on the membrane excite several modes of vibration. During this stage the membrane vibrates in a complicated pattern. Eventually, a limit cycle is achieved with a single dominant frequency of vibration. This coincides with a regular shedding of vortices from the edges of the membrane. The vibration pattern of the membrane also resembles its first eigenmode.

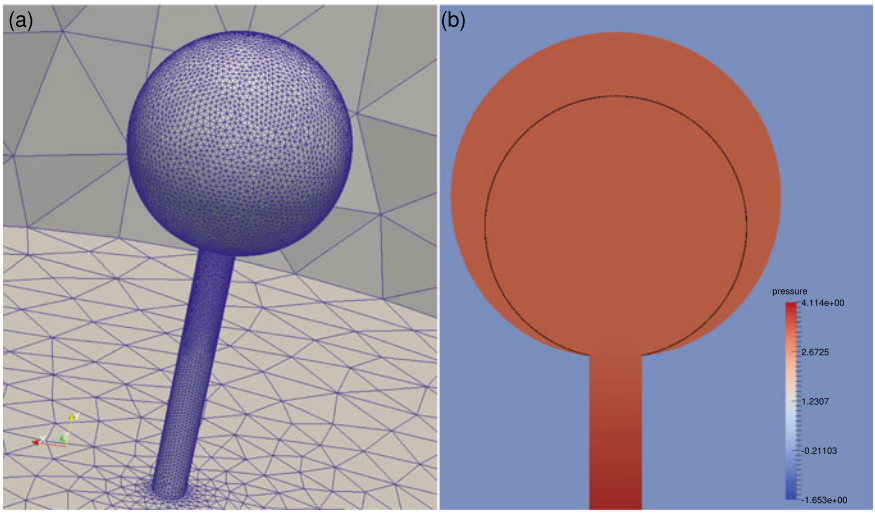


**Fig. 2** Inflation of an initially spherical balloon for $Re = 40$, mass ration 2.5 and $Ae = 4$: **a** a view of the surface mesh used, **b** a section through center of the balloon showing its shape after 1000 non-dimensional time units. Also indicated, using black curve, is the initial shape of the balloon

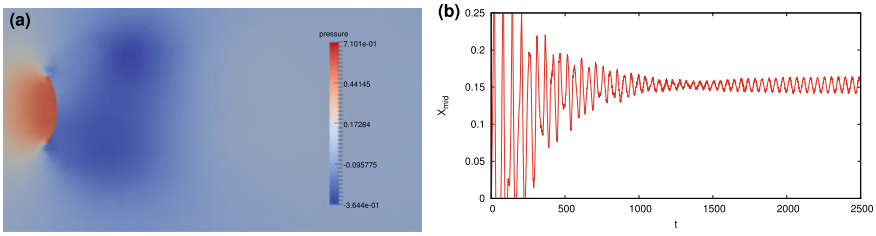


**Fig. 3** $Re = 150$ flow past a square membrane fixed normal to the flow: **a** mid-section of the flow field showing difference in pressure on two sides of the membrane, **b** time variation of the position of the mid-point of the membrane in the streamwise direction

## 5 Conclusion

A tool developed for studying fluid-membrane interactions is demonstrated. The tool uses a partitioned approach with SUPG/PSPG stabilizations for the fluid problem, coupled to a simple membrane model using linear triangles. Two fluid-structure interaction problems involving elastic membranes are studied. In the first problem, inflation of balloons is considered. The dependence of material parameters on shapes taken by the balloon during inflation is investigated. The second problem involves vibration of sail like structure in a fluid stream. For the chosen parameters, it is observed that the fluid-structure reaches a limit-cycle. During the limit cycle oscillations, the deformation of the membrane resembles the first eigenmode of the membrane vibration.

**Acknowledgements** Results presented in the present paper were computed using the High Performance Computing facility at Indian Institute of Technology Kanpur, established under the aegis of Department of Science and Technology, Government of India.

## References

1. Johnson, A.A., Tezduyar, T.E.: Mesh update strategies in parallel finite element computations of flow problems with moving boundaries and interfaces. Comput. Methods Appl. Mech. Eng. **119**(1), 73–94 (1994)
2. Kalro, V., Tezduyar, T.E.: A parallel 3d computational method for fluid-structure interactions in parachute system. Comput. Meth. Appl. Mech. Eng. **190**, 321–332 (2000)
3. Saksono, P.H., Dettmer, W.G., Peric, D.: An adaptive remeshing strategy for flows with moving boundaries and fluid-structure interaction. Int. J. Numer. Meth. Eng. **71**, 1009–1050 (2007)
4. Sawada, T., Hisada, T.: Fluid-structure interaction analysis of the two-dimensional flag-in-wind problem by an interface-tracking ale finite element method. Comput. Fluids **36**, 136–146 (2007)
5. Stein, R.B., Benney, R., Tezduyar, T., Potvin, J.: Fluid-structure interactions of a cross parachute: numerical simulation. Comput. Meth. Appl. Mech. Eng. **191**, 673–687 (2001)
6. Stein, R.B., Kalro, V., Tezduyar, T.E., Leonard, J., Accorsi, M.: Parachute fluid-structure interactions: 3-d computation. Comput. Meth. Appl. Mech. Eng. **190**, 373–386 (2000)
7. Taylor, R.L., Onate, E., Ubach, P.A.: Finite Element Analysis of Membrane Structures, pp. 47–68. Springer, The Netherlands (2005) (Chapter 4)
8. Tezduyar, T.E., Behr, M., Liou, J.: A new strategy for finite element computations involving moving boundaries and interfaces—the deforming-spatial-domain/space-time procedure: I. The concept and the preliminary numerical tests. Comput. Methods Appl. Mech. Eng. **94**(3), 339–351 (1992)
9. Tezduyar, T.E., Behr, M., Mittal, S., Liou, J.: A new strategy for finite element computations involving moving boundaries and interfaces—the deforming-spatial-domain/space-time procedure: II. Computation of free-surface flows, two-liquid FLO, and flows with drifting cylinders. Comput. Methods Appl. Mech. Eng. **94**(3), 353–371 (1992)

# Numerical Simulation on a Fixed Mesh for the Feedback Stabilization of a Fluid–Structure Interaction System with a Structure Given by a Finite Number of Parameters


**G. Delay, S. Ervedoza, M. Fournié, and G. Haine**

**Abstract** We study the numerical approximation of a 2d fluid–structure interaction problem stabilizing the fluid flow around an unstable stationary solution in presence of boundary perturbations. The structure is governed by a finite number of parameters and a feedback control law acts on their accelerations. The existence of strong solutions and the stabilization of this fluid–structure system were recently studied in [3]. The present work is dedicated to the numerical simulation of the problem using a fictitious domain method based on extended Finite Element [4]. The originality of the present work is to propose efficient numerical tools that can be extended in a simple manner to any fluid-structure control simulation. Numerical tests are given and the stabilization at an exponential decay rate is observed for small enough initial perturbations.

**Keywords** Fluid-structure interaction · DNS · Fictitious domain · XFEM · Control · Incompressible flow

## 1 Introduction

Critical flow dynamics involving moving/deformable structures with design applications has been receiving increasing attention from the scientific community. In the context of aeronautics, control flow by morphing remains a challenge [7] as well

G. Delay (✉) · S. Ervedoza · M. Fournié
Institut de Mathématiques, UMR 5219 Université Paul Sabatier, CNRS, Toulouse, France
e-mail: guillaume.delay@math.univ-toulouse.fr

S. Ervedoza
e-mail: sylvain.ervedoza@math.univ-toulouse.fr

M. Fournié
e-mail: michel.fournie@math.univ-toulouse.fr

G. Haine
Institut Supérieur de l'Aéronautique et de l'Espace, Toulouse, France
e-mail: ghislain.haine@isae.fr



M. Braza et al. (eds.), *Advances in Critical Flow Dynamics Involving Moving/Deformable Structures with Design Applications*, Notes on Numerical Fluid Mechanics and Multidisciplinary Design 147,
https://doi.org/10.1007/978-3-030-55594-8_19

on a comprehensive study of the physical problems as on a development of robust numerical methods [9].

## *1.1 Position of the Problem*

The question of how to design moving/deformable structures to control flow requires a rigorous justification of the process corresponding to study the following concepts.

- The modeling of the 2d fluid–structure model. In the present work, we consider a structure described by a finite number of parameters with a feedback control law acting on the acceleration of the structure, see [3].
- The well–posedness of the system. We refer to [3] for the proof of the existence and uniqueness of strong solution.
- The stabilizability of the continuous fluid–structure system. Under a unique continuation assumption for the eigenvectors of the adjoint system, a nonlinear feedback control is proposed to stabilize the whole fluid–structure system around a stationary solution at any chosen exponential decay rate for small enough initial perturbations, see [3]. The method reposes on the analysis of the linearized system and the feedback operator is given by a Riccati equation of small dimension (Reduced Order Model). This feedback control is able to stabilize the nonlinear semi-discrete controlled system.
- The semi-discretization in space of the infinite dimensional system. The stabilization of such a system must be studied even if the strategy is the same as the one used for the continuous problem. The justification is not straightforward and requires a specific proof for each new fluid–structure system. The numerical method retained for the discretization is the finite element method that can be used for complex geometry.
- The time evolution and numerical simulations. Beyond the well-known difficulties encountered to consider fluid–structure interactions to match the motion of the structure into the fluid (time evolution of the computational domain) [9], the contribution of the control control requires a specific attention.

## *1.2 Previous Work*

The continuous problem has already been studied in [3] and a similar approach to ours has been investigated in [8]. Other similar studies have already been led for the Navier–Stokes equations [1] and for a fluid–structure interaction problem [10]. This latter work is based on computations that are formulated into a fixed domain after a change of variables. However this mapping introduces nonlinear terms that are difficult to implement (introducing numerical errors) and involves a high computational time. In opposite, in the present work all computations are done in the

time dependent fluid domain. Preparatory work relating to this was done in a simpler situation where the control is governed by the fluid only and the deformation of the structure is located on small parts of its boundary [5]. This difficulty is addressed using a fictitious domain approach based on an extended finite element method. More precisely, the focus is on the so-called geometrically unfitted finite element methods where the solution of the PDE typically remains a standard finite element method, but the variational formulation is modified so that the constraints on the interface and boundaries can be integrated in the computation even if the mesh is not fitted to the geometry. In such approaches, the computational mesh used is independent of the physical domain. These methods are called CutFEM and can be viewed as particular XFEM methods, see [4].

### *1.3 Outline*

The outline of the paper is as follows. In Sect. 2, we present the setting of the problem that can be extended to more general system and we introduce the diffeomorphism that allows to model the deformation of the structure. In Sect. 3, we recall the principles to construct a feedback control law for the linear problem and give the synopsis of these ideas. In Sect. 4, the discretization of the fluid–structure system based on fictitious domain method is introduced before the presentation of the time evolution partitioned algorithm. Finally, in Sect. 5, numerical simulations with original treatment of the control are reported. We compare the results obtained with and without applying the control to the nonlinear fluid–structure system.

## 2 Setting of the Problem and Modelling of the Deformation

### *2.1 The Fluid–Structure Model*

The global domain represents a wind tunnel $\Omega \subset \mathbb{R}^2 = (0, L) \times (0, 1)$. Dirichlet boundary conditions are imposed on $\Gamma_i = \{0\} \times (0, 1)$ the inflow region, on $\Gamma_w = (0, L) \times \{0, 1\}$ the upper and lower walls ($\Gamma_D = \Gamma_i \cup \Gamma_w$) and Neumann conditions are retained on $\Gamma_{\mathrm{N}} = \{L\} \times (0, 1)$ the outflow region. We use a smooth approximation of a steering gear structure $S(\theta_1(t), \theta_2(t))$ depending on two parameters and the fluid fills the time evolving domain $\mathscr{F}(\theta_1(t), \theta_2(t)) = \Omega \backslash S(\theta_1(t), \theta_2(t))$.

Note that the structure can be viewed like an assembling of one solid $S_1$ tied to the fixed frame by a pivoting link $O$ and an other solid $S_2$ tied to solid $S_1$ by a pivoting link $P$. $S_1$ can be thought of as the aerofoil of a wing and $S_2$ as a steering gear such as an aileron.

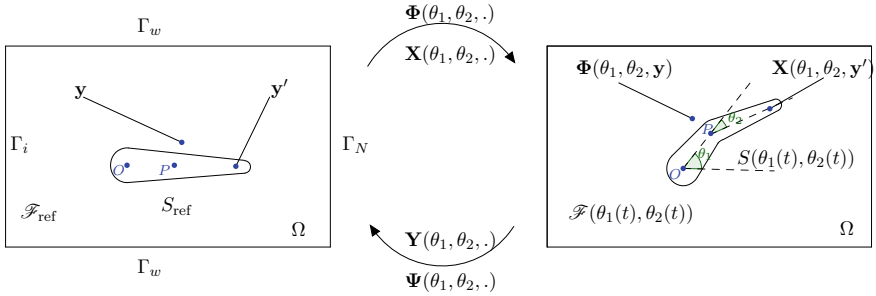


**Fig. 1** Real and reference structure configurations

The deformation of the structure is linked to its reference configuration $S_{\text{ref}}$ by a smooth diffeomorphism $\mathbf{X}(\theta_1, \theta_2, .)$ and we denote $\mathbf{Y}(\theta_1, \theta_2, .)$ its inverse, see Fig. 1.

The fluid is modeled by the incompressible Navier-Stokes equations. The equations of the structure are derived from a virtual work principle.

$$\begin{cases} \text{Find } (\theta_1(t), \theta_2(t)) \in \mathbb{D}_\Theta, \text{ such that} \\ \quad \forall \mathbf{w} \in \text{Vect}(\partial_{\theta_1}\mathbf{X}(\theta_1(t), \theta_2(t), .), \partial_{\theta_2}\mathbf{X}(\theta_1(t), \theta_2(t), .)), \\ \displaystyle\int_{S_{\text{ref}}} \rho \frac{\mathrm{d}^2}{\mathrm{d}t^2}(\mathbf{X}(\theta_1(t), \theta_2(t), \mathbf{y}))\cdot\mathbf{w}(\mathbf{y})\mathrm{d}\mathbf{y} \\ \quad \displaystyle+\int_{\partial S(\theta_1(t),\theta_2(t))} \sigma_F(\mathbf{u}, p)\mathbf{n}_{\theta_1,\theta_2} \cdot \mathbf{w}(\mathbf{Y}(\theta_1(t), \theta_2(t), \gamma_x))\mathrm{d}\gamma_x = 0, \end{cases}$$

where $\rho > 0$ is a constant modeling the mass per unit volume, $\mathbf{n}_{\theta_1,\theta_2}$ is the outward unitary normal to the fluid domain and $\sigma_F(\mathbf{u}, p) = -p\mathrm{I} + \nu(\nabla\mathbf{u} + \nabla\mathbf{u}^T)$, where $\nu$ is the viscosity of the fluid and $\mathbb{D}_\Theta$ is an admissible domain which is an open connected subset of $\mathbb{R}^2$. We denote $\mathbf{n}$ and $\mathbf{n}_{\theta_1,\theta_2}$ the outward unitary normals to $\Omega$ and to $\mathscr{F}(\theta_1(t), \theta_2(t))$, $\mathbf{f}_{\mathscr{F}}$ a source term, $\mathbf{u}^i$ a given inflow and $(.,.)_S$ the scalar product

$$(\boldsymbol{\phi}, \boldsymbol{\psi})_S = \int_{S_{\text{ref}}} \rho\boldsymbol{\phi}(\mathbf{y}) \cdot \boldsymbol{\psi}(\mathbf{y})\ \mathrm{d}\mathbf{y}.$$

We use the notations

$$Q_\theta^\infty = \bigcup_{t\in(0,\infty)} (\{t\} \times \mathscr{F}(\theta_1(t), \theta_2(t))), \quad \Sigma_\theta^\infty = \bigcup_{t\in(0,\infty)} (\{t\} \times \partial S(\theta_1(t), \theta_2(t))),$$
$$\Sigma_i^\infty = (0, \infty) \times \Gamma_i, \quad \Sigma_w^\infty = (0, \infty) \times \Gamma_w, \quad \Sigma_N^\infty = (0, \infty) \times \Gamma_N.$$

The resulting fluid–structure system reads for $t \in (0, T)$

$$
\begin{cases}
\dfrac{\partial \mathbf{u}}{\partial t} + (\mathbf{u}\cdot\nabla)\mathbf{u} - \operatorname{div}\sigma_F(\mathbf{u}, p) = \mathbf{f}_{\mathscr{F}}, & \text{in } Q_\theta^\infty,\\
\operatorname{div}\mathbf{u} = 0, & \text{in } Q_\theta^\infty,\\
\mathbf{u} = \dot\theta_1 \partial_{\theta_1}\mathbf{X}(\theta_1,\theta_2,\mathbf{Y}(\theta_1,\theta_2,.)) + \dot\theta_2\partial_{\theta_2}\mathbf{X}(\theta_1,\theta_2,\mathbf{Y}(\theta_1,\theta_2,.)), & \text{on } \Sigma_\theta^\infty,\\
\mathbf{u} = \mathbf{u}^i \text{ on } \Sigma_i^\infty, \quad \mathbf{u} = 0 \text{ on } \Sigma_w^\infty, \quad \sigma_F(\mathbf{u},p)\mathbf{n}(.) = 0 \text{ on } \Sigma_N^\infty,\\
\mathbf{u}(0,.) = \mathbf{u}_0(.), & \text{on } \mathscr{F}(\theta_{1,0},\theta_{2,0}),\\
\mathcal{M}_{\theta_1,\theta_2}\begin{pmatrix}\ddot\theta_1\\ \ddot\theta_2\end{pmatrix} = \mathbf{M_A}(\theta_1,\theta_2,-\sigma_F(\mathbf{u},p)\mathbf{n}_{\theta_1,\theta_2}) + \mathbf{M_I}(\theta_1,\theta_2,\dot\theta_1,\dot\theta_2)\\
\quad -k\begin{pmatrix}\theta_1\\ \theta_2\end{pmatrix} + \mathbf{h} + \mathbf{f_s},\\
\theta_1(0) = \theta_{1,0}, \quad \theta_2(0) = \theta_{2,0}, \quad \dot\theta_1(0) = \omega_{1,0}, \quad \dot\theta_2(0) = \omega_{2,0}, \quad \text{where}
\end{cases}
\tag{1}
$$

$$
\mathcal{M}_{\theta_1,\theta_2} = \begin{pmatrix} (\partial_{\theta_1}\mathbf{X}(\theta_1,\theta_2), \partial_{\theta_1}\mathbf{X}(\theta_1,\theta_2,.))_S & (\partial_{\theta_2}\mathbf{X}(\theta_1,\theta_2), \partial_{\theta_1}\mathbf{X}(\theta_1,\theta_2,.))_S \\ (\partial_{\theta_1}\mathbf{X}(\theta_1,\theta_2), \partial_{\theta_2}\mathbf{X}(\theta_1,\theta_2,.))_S & (\partial_{\theta_2}\mathbf{X}(\theta_1,\theta_2), \partial_{\theta_2}\mathbf{X}(\theta_1,\theta_2,.))_S \end{pmatrix} \in \mathbb{R}^{2\times 2},
$$

$$
\mathbf{M_I}(\theta_1,\theta_2,\dot\theta_1,\dot\theta_2) = \begin{pmatrix} -(\dot\theta_1^2\partial_{\theta_1\theta_1}\mathbf{X}(\theta_1,\theta_2,.) + 2\dot\theta_1\dot\theta_2\partial_{\theta_1\theta_2}\mathbf{X}(\theta_1,\theta_2,.) + \dot\theta_2^2\partial_{\theta_2\theta_2}\mathbf{X}(\theta_1,\theta_2), \partial_{\theta_1}\mathbf{X}(\theta_1,\theta_2,.))_S \\ -(\dot\theta_1^2\partial_{\theta_1\theta_1}\mathbf{X}(\theta_1,\theta_2,.) + 2\dot\theta_1\dot\theta_2\partial_{\theta_1\theta_2}\mathbf{X}(\theta_1,\theta_2,.) + \dot\theta_2^2\partial_{\theta_2\theta_2}\mathbf{X}(\theta_1,\theta_2), \partial_{\theta_2}\mathbf{X}(\theta_1,\theta_2,.))_S \end{pmatrix} \in \mathbb{R}^2,
$$

$$
\mathbf{M_A}(\theta_1,\theta_2,-\sigma_F(\mathbf{u},p)\mathbf{n}_{\theta_1,\theta_2}) = \begin{pmatrix} \displaystyle\int_{\partial S(\theta_1,\theta_2)} -\sigma_F(\mathbf{u},p)\mathbf{n}_{\theta_1,\theta_2}\cdot\partial_{\theta_1}\mathbf{X}(\theta_1,\theta_2,\mathbf{Y}(\theta_1,\theta_2,\gamma_x))\,\mathrm{d}\gamma_x \\ \displaystyle\int_{\partial S(\theta_1,\theta_2)} -\sigma_F(\mathbf{u},p)\mathbf{n}_{\theta_1,\theta_2}\cdot\partial_{\theta_2}\mathbf{X}(\theta_1,\theta_2,\mathbf{Y}(\theta_1,\theta_2,\gamma_x))\,\mathrm{d}\gamma_x \end{pmatrix} \in \mathbb{R}^2,
$$

$\mathbf{u}_0(.), \theta_{1,0}, \theta_{2,0}, \omega_{1,0}, \omega_{2,0}$ are initial data and $\mathbf{h} \in \mathrm{L}^2(0,T;\mathbb{R}^2)$ is a control modelling a force acting on the structure, $k > 0$ is a constant used to introduce a damping and $\mathbf{f_s}$ is a constant force that constraints the structure to be in a given reference position. In the sequel, we denote $\mathbf{M_I}(\theta_1,\theta_2,\dot\theta_1,\dot\theta_2) = \mathbf{M_I}(t)$ and $\mathbf{M_A}(\theta_1,\theta_2,-\sigma_F(\mathbf{u},p)\mathbf{n}_{\theta_1,\theta_2}) = \mathbf{M_A}(t)$. For $T > 0$ small enough, under some compatibility conditions for the initial data, there exists a strong solution to the problem (1), see [3].

## 2.2 *The Diffeomorphisms Used to Model the Deformation of the Structure Given by a Finite Number of Parameters*

### 2.2.1 The Diffeomorphism X

We consider that every fibre of matter stays normal to the mid–line in every configuration. Hence the deformation of the structure is given by the deformation of the mid–line.

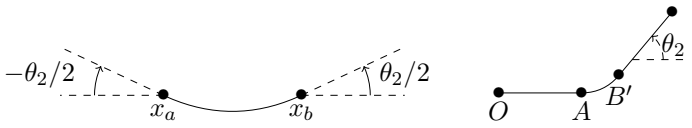


(a) (b)

**Fig. 2** **a** The parabola $f(x)$, **b** the deformation of the mid–line

***The deformation of the mid–line***. In the non–deformed configuration, the mid–line goes from $\ell = 0$ to $\ell = 1$. Let $x_a < x_b$ be in $(0, 1)$, we want the mid–line to be at rest in $(0, x_a)$ and be a straight line of slope $\theta_2$ (the first parameter to characterize the structure) in $(x_b, 1)$ and we consider on $(x_a, x_b)$ the parabola

$$f(x) = \frac{\tan(\theta_2/2)}{x_b - x_a}(x - x_c)^2 - \tan(\theta_2/2)\frac{x_b - x_a}{4}, \quad \text{with } x_c = (x_a + x_b)/2,$$

such that we have a $\mathscr{C}^1$ curve on $[0, 1]$, see Fig. 2a. The next step is to rotate this parabola around $(x_a, 0)$ with an angle $\theta_2/2$, to prolong it on the left hand-side by $y = 0$ and on the right by a straight line of slope $\theta_2$. This will give the desired deformation for the mid–line, see Fig. 2b, the point $B' = (x_{B'}, y_{B'})^T = (x_a + (x_b - x_a)\cos(\theta_2/2), (x_b - x_a)\sin(\theta_2/2))^T$.

The mid–line is then given by the parametric representation $\ell \to (g_x(\ell), g_y(\ell))^T$ where

$$g_x(\ell) = \begin{cases} \ell \\ x_a + (\ell - x_a)\cos(\frac{\theta_2}{2}) - f(\ell)\sin(\frac{\theta_2}{2}) \\ x_{B'} + (\ell - x_b)\cos\theta_2 \end{cases}$$

$$g_y(\ell) = \begin{cases} 0 & \text{if } \ell \le x_a, \\ (\ell - x_a)\sin(\frac{\theta_2}{2}) + f(\ell)\cos(\frac{\theta_2}{2}) & \text{if } \ell \in (x_a, x_b), \\ y_{B'} + (\ell - x_b)\sin\theta_2 & \text{if } \ell \ge x_b. \end{cases}$$

***Deformation of the structure***. In the sequel, $\mathbf{y} = (y_1, y_2)$ denotes the Lagrangian coordinates and $\mathbf{N}(\ell) = \begin{pmatrix} N_x(\ell) \\ N_y(\ell) \end{pmatrix} = \begin{pmatrix} -g_x'(\ell) \\ g_y'(\ell) \end{pmatrix}$ is normal to the mid–line. We define the following diffeomorphism $\tilde{\mathbf{X}}(\theta_2, \mathbf{y}) = \left(g_x(y_1) + y_2\frac{N_x(y_1)}{|\mathbf{N}(y_1)|}, g_y(y_1) + y_2\frac{N_y(y_1)}{|\mathbf{N}(y_1)|}\right)^T$.

***The rotation of the deformed structure***. We get the final diffeomorphism $\mathbf{X}$ after a rotation $\mathrm{R}_{\theta_1}$ of angle $\theta_1$ (the second parameter to characterize the structure) around the center $O$, see Fig. 3, $\mathbf{X}(\theta_1, \theta_2, \mathbf{y}) = R_{\theta_1}\tilde{\mathbf{X}}(\theta_2, \mathbf{y})$ where $\mathrm{R}_{\theta_1} = \begin{pmatrix} \cos\theta_1 & -\sin\theta_1 \\ \sin\theta_1 & \cos\theta_1 \end{pmatrix}$.

***Deformation of the profile's boundary***. We consider a reference configuration for the structure $S_{\text{ref}} = S(0, 0)$. The boundary of this structure is described by two parametric functions: $\boldsymbol{\gamma}^+(\ell)$ for the extrados and $\boldsymbol{\gamma}^-(\ell)$ for the intrados. The boundary

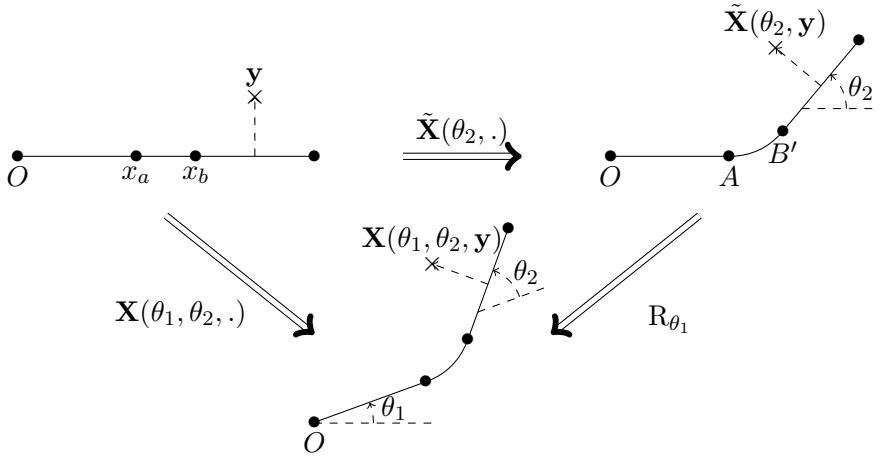


**Fig. 3** The diffeomorphisms $\mathbf{X}$ and $\tilde{\mathbf{X}}$

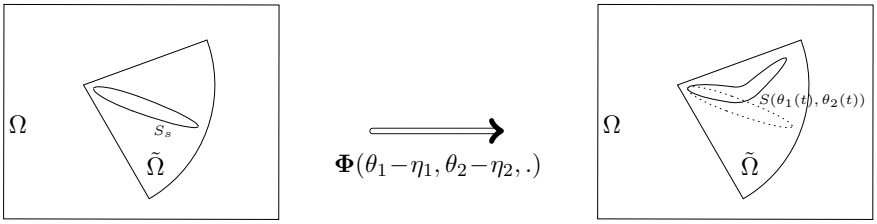


**Fig. 4** The diffeomorphism $\Phi$

of $S(\theta_1(t), \theta_2(t))$ is then described by the two parametric functions $\mathbf{X}(\theta_1, \theta_2, \boldsymbol{\gamma}^+(\ell))$ and $\mathbf{X}(\theta_1, \theta_2, \boldsymbol{\gamma}^-(\ell))$, where

$$\mathbf{X}(\theta_1, \theta_2, \boldsymbol{\gamma}^+(\ell)) = \begin{pmatrix} \cos\theta_1 & -\sin\theta_1 \\ \sin\theta_1 & \cos\theta_1 \end{pmatrix} \begin{pmatrix} g_x(\gamma_x^+(\ell)) + \gamma_y^+(\ell)\frac{N_x(\gamma_x^+(\ell))}{|\mathbf{N}(\gamma_x^+(\ell))|} \\ g_y(\gamma_x^+(\ell)) + \gamma_y^+(\ell)\frac{N_y(\gamma_x^+(\ell))}{|\mathbf{N}(\gamma_x^+(\ell))|} \end{pmatrix}, \tag{2}$$

and the expression of $\mathbf{X}(\theta_1, \theta_2, \boldsymbol{\gamma}^-(\ell))$ is the analogy. In the sequel, for numerical tests, we consider the case of an elliptic symmetric reference domain, see Fig. 4.

Its boundary is given by the functions

$$\begin{cases} \boldsymbol{\gamma}^+(\ell) = (\ell, \gamma_2^+(\ell)), \\ \boldsymbol{\gamma}^-(\ell) = (\ell, -\gamma_2^+(\ell)), \end{cases} \quad \text{where } \gamma_2^+(\ell) = \begin{cases} b\sqrt{1 - \left(\frac{\ell - x_a}{x_a}\right)^2} & \text{if } \ell \in [0, x_a], \\ b\sqrt{1 - \left(\frac{\ell - x_a}{1 - x_a}\right)^2} & \text{if } \ell \in ]x_a, 1]. \end{cases} \tag{3}$$

This explicit expression allows us to construct a set of ordered points to describe the structure's profile.

**Remark 2.1** The framework presented can be used for more general geometries.

### 2.2.2 The Diffeomorphism Φ

We consider a stationary configuration $S_s = S(\eta_1, \eta_2)$. Let $\tilde{\Omega} \subset \Omega$ be a smooth domain such that for every $(\theta_1, \theta_2) \in \mathbb{D}_\Theta$, we have $S(\theta_1, \theta_2) \subset \tilde{\Omega}$. Let $(\theta_1, \theta_2) \in \mathbb{D}_\Theta$, see Fig. 4 and we consider $\mathbf{s}_{\theta_1,\theta_2}$ the solution to

$$\begin{cases} \Delta \mathbf{s}_{\theta_1,\theta_2} = 0 & \text{in } \tilde{\Omega}\backslash S_s, \\ \mathbf{s}_{\theta_1,\theta_2} = \mathbf{X}(\eta_1 + \theta_1, \eta_2 + \theta_2, \mathbf{Y}(\eta_1, \eta_2, .)) - \mathrm{Id} & \text{on } \partial S_s, \\ \mathbf{s}_{\theta_1,\theta_2} = 0 & \text{on } \partial\tilde{\Omega}. \end{cases} \tag{4}$$

We define the diffeomorphism Φ by

$$\begin{aligned} &\forall (\theta_1, \theta_2) \in \mathbb{D}_\Theta, \quad \forall \mathbf{y} \in \Omega, \\ &\Phi(\theta_1, \theta_2, \mathbf{y}) = \begin{cases} \mathbf{X}(\eta_1 + \theta_1, \eta_2 + \theta_2, \mathbf{Y}(\eta_1, \eta_2, \mathbf{y})) & \text{if } \mathbf{y} \in S_s, \\ \mathbf{y} + \mathbf{s}_{\theta_1,\theta_2}(\mathbf{y}) & \text{if } \mathbf{y} \in \tilde{\Omega}\backslash S_s, \\ \mathbf{y} & \text{if } \mathbf{y} \in \Omega\backslash\tilde{\Omega}. \end{cases} \end{aligned} \tag{5}$$

and verify that

$$\partial_{\theta_j}\Phi(\theta_1, \theta_2, \mathbf{y}) = \begin{cases} \partial_{\theta_j}\mathbf{X}(\eta_1 + \theta_1, \eta_2 + \theta_2, \mathbf{Y}(\eta_1, \eta_2, \mathbf{y})) & \text{if } \mathbf{y} \in S_s, \\ \partial_{\theta_j}\mathbf{s}_{\theta_1,\theta_2}(\mathbf{y}) & \text{if } \mathbf{y} \in \tilde{\Omega}\backslash S_s, \\ 0 & \text{if } \mathbf{y} \in \Omega\backslash\tilde{\Omega}, \end{cases} \tag{6}$$

where $\partial_{\theta_j}\mathbf{s}_{\theta_1,\theta_2}$ is solution to

$$\begin{cases} \Delta(\partial_{\theta_j}\mathbf{s}_{\theta_1,\theta_2}) = 0 & \text{in } \tilde{\Omega}\backslash S_s, \\ \partial_{\theta_j}\mathbf{s}_{\theta_1,\theta_2} = \partial_{\theta_j}\mathbf{X}(\eta_1 + \theta_1, \eta_2 + \theta_2, \mathbf{Y}(\eta_1, \eta_2, .)) & \text{on } \partial S_s, \\ \partial_{\theta_j}\mathbf{s}_{\theta_1,\theta_2} = 0 & \text{on } \partial\tilde{\Omega}. \end{cases}$$

## 3 Stabilization of the Linear Problem

In order to construct a linear feedback law that is easy to compute and able to locally stabilize the nonlinear fluid–structure problem with any exponential decay rate, we follow a strategy summarized in six following steps, we refer to [1] for more details

*Step 1:* We write the equations in the fixed domain $\mathscr{F}_s = \Omega\backslash S(0, 0)$ using the change of variable $\mathbf{u}_{ref}(\mathbf{y}) = \mathrm{cof}(\nabla\Phi(\theta_1, \theta_2, \mathbf{y}))^T \mathbf{u}_h \circ \Phi(\theta_1, \theta_2, \mathbf{y})$. We

linearize the resulting system around a stationary solution to the fluid–structure problem $(\mathbf{u_s}, p_s, \eta_1, \eta_2, 0, 0)^T$ and then we define the matrix formulation of the linear discretized problem with Lagrange multipliers.

*Step 2:* We give a reformulation of the finite dimensional linear system after elimination of the Lagrange multipliers from the equations by using a projector which plays a similar role to the Leray projector (for the infinite dimensional system).

*Step 3:* The construction of the linear feedback law based on previous steps is numerically difficult to compute. To overcome this difficulty we study the relationships between the eigenvalue problems (initial problem and projected problem).

*Step 4:* We define the projected systems associated to the unstable part of the spectral decomposition. Stabilization of the unstable part is sufficient to stabilize the whole system.

*Step 5:* We define the linear feedback law $\mathbf{h}$ by solving an Algebraic Riccati Equation of small dimension (Optimal control problem on Reduced Order Model).

*Step 6:* We stabilize the nonlinear system using $\mathbf{h}$ defined on the linear system.

At the end of the process, we have constructed the matrix $\mathbf{K}$ such that the feedback law $\mathbf{h}$ is given by the relation

$$\mathbf{h} = \mathbf{K}(\mathbf{z} - \mathbf{z_s}) \tag{7}$$

where $\mathbf{z} = (\mathbf{u}_{ref}, \theta_1, \theta_2, \omega_1, \omega_2)^T$ and $\mathbf{z_s} = (\mathbf{u_s}, \eta_1, \eta_2, 0, 0)^T$. Note that the feedback is defined in a fixed reference configuration $\mathscr{F}_s$, so $\mathbf{z}$ must be known on $\mathscr{F}_s$ at each time step.

In *Step 1*, writing the equations in the fixed domain, introduces some additional nonlinear terms (geometrical terms) that must be linearized and must be taken into account in the definition of the feedback. We refer to the paper [3] for the expression of that terms. Contrary to previous works, the numerical simulations are based on fictitious domain method that does not require to consider those additional terms. In our knowledge this strategy in control theory is new and powerful.

## 4 The Discretization and Time Evolution of the Fluid–Structure System

This section presents the approximation of the coupled problem (1). To take into account the Dirichlet boundary conditions of the fluid on $\Gamma_D$ and at the interface between the fluid and the structure, we introduce $\boldsymbol{\lambda}$ a Lagrange multiplier defined by $\boldsymbol{\lambda} = (\boldsymbol{\lambda}_\mathrm{s}, \boldsymbol{\lambda}_\mathrm{i}, \boldsymbol{\lambda}_\mathrm{w})^T$. We introduce finite-dimensional subspaces $V_h \subset V = \mathbf{H}^1(\mathscr{F}(\theta_1, \theta_2); \mathbb{R}^2)$ for the velocity, $Q_h \subset Q = \mathrm{L}^2(\mathscr{F}(\theta_1, \theta_2))$ for the pressure, $W_h \subset W = \mathbf{H}^{-1/2}(\partial S(\theta_1, \theta_2)) \times \mathbf{H}^{-1/2}(\Gamma_\mathrm{D})$ for the multipliers.

Find $(\theta_1, \theta_2, \omega_1, \omega_2) \in H^2(0,T;\mathbb{D}_\Theta) \times H^1(0,T;\mathbb{R}^2)$
and $(\mathbf{u}, p, \boldsymbol{\lambda}) \in H^1_{loc}((0,\infty); V_h) \times L^2_{loc}((0,\infty); Q_h) \times L^2_{loc}((0,\infty); W_h)$ such that

$$\begin{cases} \displaystyle\int_{\mathscr{F}(\theta_1,\theta_2)} \frac{\partial \mathbf{u}}{\partial t} \cdot \mathbf{v} + (\mathbf{u}\cdot\nabla)\mathbf{u}\cdot\mathbf{v} + \frac{\nu}{2}(\nabla\mathbf{u} + \nabla\mathbf{u}^T) : (\nabla\mathbf{v} + \nabla\mathbf{v}^T) - p\mathrm{div}\ \mathbf{v}\ \mathrm{d}\mathbf{x} \\ \quad + \displaystyle\int_{\Gamma_D \cup \partial S(\theta_1,\theta_2)} \boldsymbol{\lambda}\cdot\mathbf{v}\ \mathrm{d}\gamma_x = 0, \\ \displaystyle\int_{\mathscr{F}(\theta_1,\theta_2)} q\mathrm{div}\ \mathbf{u}\ \mathrm{d}\mathbf{x} = 0, \\ \displaystyle\int_{\Gamma_D \cup \partial S(\theta_1,\theta_2)} \mathbf{u}\cdot\boldsymbol{\mu}\ \mathrm{d}\gamma_x = \int_{\Gamma_i} \mathbf{u}^i \cdot \boldsymbol{\mu}\ \mathrm{d}\gamma_x \\ \quad + \displaystyle\int_{\partial S(\theta_1,\theta_2)} \sum_j \omega_j \partial_{\theta_j}\mathbf{X}(\theta_1,\theta_2,\mathbf{Y}(\theta_1,\theta_2,\gamma_x))\cdot\boldsymbol{\mu}\ \mathrm{d}\gamma_x, \end{cases}$$

for every $(\mathbf{v}, q, \boldsymbol{\mu}) \in V_h \times Q_h \times W_h$ and

$$\begin{cases} \mathcal{M}_{\theta_1,\theta_2}\begin{pmatrix}\dot\omega_1\\ \dot\omega_2\end{pmatrix} = \left(\displaystyle\int_{\partial S(\theta_1,\theta_2)} \boldsymbol{\lambda}\cdot\partial_{\theta_j}\mathbf{X}(\theta_1,\theta_2,\mathbf{Y}(\theta_1,\theta_2,\gamma_x))\ \mathrm{d}\gamma_x\right)_{j=1,2} + \mathbf{M_I}(\theta_1,\theta_2,\omega_1,\omega_2) \\ \quad -k\begin{pmatrix}\theta_1\\ \theta_2\end{pmatrix} + \mathbf{h}, \\ \omega_1 = \dot\theta_1, \\ \omega_2 = \dot\theta_2. \end{cases} \tag{8}$$

In what follows, $\Delta t$ denotes the time-step length, $t_n = n\Delta t$ for $n \in \mathbb{N}$. First, we discuss the discretization based on a fictitious domain method for the fluid equations (Navier-Stokes) [4]. The approximation of the structure equations is realized by a backward finite difference scheme. In this section, we describe the algorithm which is of partitioned type to prescribe the time evolution. The location of the interface is governed by a level-set. Finally, we present an original treatment of the feedback that must be done into the reference configuration. Specific manipulations must be done to obtain an efficient algorithm.

## *4.1 Fluid Approximation: Unfitted Extended Finite Element Method with Lagrange Multipliers*

We define a background mesh covering $\Omega$. The interface between the fluid and the solid can arbitrary cut this mesh, see for instance Fig. 5 where different zones are highlighted.

We use Lagrange multipliers to enforce the Dirichlet boundary conditions. We define a triangulation $\mathcal{T}_h$ of $\Omega$ and a background finite element method with $\mathbb{P}_2$–$\mathbb{P}_1$–$\mathbb{P}_1$ Taylor–Hood elements for the velocity, the pressure and the multipliers respectively,

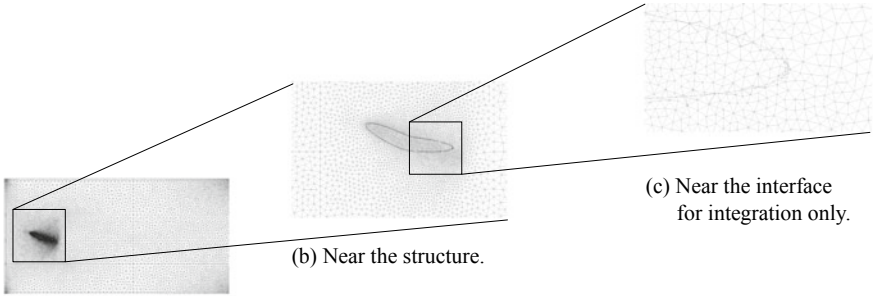


**Fig. 5** The fictitious domain

$$\begin{aligned}
\widetilde{V}_h &= \{\mathbf{u}_h \in \mathscr{C}^0(\Omega) \ \text{ with } \ \mathbf{u}_{h|T} \in (\mathbb{P}_2(T))^2, \quad \forall T \in \mathcal{T}_h\},\\
\widetilde{Q}_h &= \{p_h \in \mathscr{C}^0(\Omega) \ \text{ with } \ p_{h|T} \in \mathbb{P}_1(T), \quad \forall T \in \mathcal{T}_h\},\\
\widetilde{W}_h &= \{\boldsymbol{\lambda}_h \in \mathscr{C}^0(\Omega) \ \text{ with } \ \boldsymbol{\lambda}_{h|T} \in (\mathbb{P}_1(T))^2, \quad \forall T \in \mathcal{T}_h\}.
\end{aligned}$$

The basis functions that are considered in the sequel are traces of the background basis functions of $\widetilde{V}_h$, $\widetilde{Q}_h$ and $\widetilde{W}_h$. The traces are taken over the fluid domain $\mathscr{F}(\theta_1, \theta_2)$ for the basis functions of the velocity and the pressure and on the interface $\partial S(\theta_1, \theta_2)$ for the Lagrange multipliers. More precisely, we consider the following natural discretizations of $V$, $Q$ and $W$ spaces,

$$V_h^n = \widetilde{V}_{h|\mathscr{F}(\theta_1^n,\theta_2^n)}, \quad Q_h^n = \widetilde{Q}_{h|\mathscr{F}(\theta_1^n,\theta_2^n)}, \quad W_h^n = \widetilde{W}_{h|\partial S(\theta_1^n,\theta_2^n)}.$$

The fluid domain $\mathscr{F}(\theta_1^n, \theta_2^n)$ and the interface $\partial S(\theta_1^n, \theta_2^n)$ depend on the parameters of the structure $(\theta_1^n, \theta_2^n)$, hence this dependence occurs also on the trace spaces. That is why we have used the superscript $n$ on these spaces.

Similarly to XFEM, where the shape functions of the finite element space is multiplied with an Heaviside function, this corresponds here to the multiplication of the shape functions with the characteristic function of the fluid domain.

An approximation of the problem (8) can be easily given replacing the continuous functions $\mathbf{u}, p, \boldsymbol{\lambda}$ by the discrete ones $\mathbf{u}_h, p_h, \boldsymbol{\lambda}_h$. However it is known that it is not sufficient to recover the correct solution. Even if the equations are integrated only over the physical domain, to obtain stable discretizations, the approximation spaces must be carefully chosen or a stabilization term must be added to ensure an inf-sup condition. In the present work, we add the term

$$-\gamma_0 h \int_{\partial S(\theta_1,\theta_2)} (\boldsymbol{\lambda}_h + \sigma_F(\mathbf{u}_h, p_h)\mathbf{n}_{\theta_1,\theta_2}) \cdot (\boldsymbol{\mu}_h + \sigma_F(\mathbf{v}_h, q_h)\mathbf{n}_{\theta_1,\theta_2}) \, \mathrm{d}\gamma_x, \tag{9}$$

with a mesh–independent constant $\gamma_0 > 0$. It results a stable and optimally convergent approximation (in particular for the multiplier $\boldsymbol{\lambda}$) provided any mesh element $T$ is cut by the interface in a certain way so that $\mathscr{F}(\theta_1, \theta_2) \cap T$ is a big enough portion of $T$.

If for some elements, this is not the case, the method can be still cured by replacing the approximating polynomial in such "bad elements" by the polynomial extended from adjacent "good elements". In the stabilization term (9), the variables $\mathbf{u}$ and $p$ are considered under this "robust reconstruction" and we specify this writing $\widehat{\mathbf{u}}$ and $\widehat{p}$ in the approximations. In practice, the assumptions required to ensure robustness of the method are satisfied if the mesh is sufficiently refined near the interface, see [4]. We denote $(\mathcal{U}_k)$, $(\mathcal{P}_k)$, $(\mathcal{W}_k)$ the basis functions of $V_h^{n+1}$, $Q_h^{n+1}$, $W_h^{n+1}$ respectively and $\mathbf{U}$, $\mathbf{P}$, $\Lambda$ are the coefficients of $\mathbf{u}_h$, $p_h$, $\boldsymbol{\lambda}_h$ in those basis. We realize a finite element approximation of the problem (8) where first order Euler finite difference in time is used. Note that the problem is formulated on $\mathscr{F}(\theta_1^{n+1}, \theta_2^{n+1})$ and we have to solve the following linear system for the fluid

$$(M^{n+1} + \Delta t A^{n+1})\mathbf{Z}^{n+1} = \Delta t \mathbf{F}^{n+1} + M^{n+1}\mathbf{Z}^n, \tag{10}$$

where those vectors and matrices are given by

$$M^{n+1} = \begin{pmatrix} M_{\mathbf{uu}} & 0 & 0 \\ 0 & 0 & 0 \\ 0 & 0 & 0 \end{pmatrix}, \quad A^{n+1} = \begin{pmatrix} A_{\mathbf{uu}} & A_{\mathbf{u}p} & A_{\mathbf{u}\boldsymbol{\lambda}} \\ A_{\mathbf{u}p}^T & A_{pp} & A_{p\boldsymbol{\lambda}} \\ A_{\mathbf{u}\boldsymbol{\lambda}}^T & A_{p\boldsymbol{\lambda}}^T & A_{\boldsymbol{\lambda}\boldsymbol{\lambda}} \end{pmatrix},$$

$$\mathbf{Z} = \begin{pmatrix} \mathbf{U} \\ \mathbf{P} \\ \Lambda \end{pmatrix} \quad \text{and} \quad \mathbf{F} = \begin{pmatrix} 0 \\ 0 \\ F_{\boldsymbol{\lambda}} \end{pmatrix}, \quad \text{with}$$

$$(M_{\mathbf{uu}})_{jk} = \int_{\mathscr{F}(\theta_1^{n+1}, \theta_2^{n+1})} \mathcal{U}_j \cdot \mathcal{U}_k \, \mathrm{d}\mathbf{x}, \quad (A_{pp})_{jk} = -\gamma_0 h \int_{\partial S(\theta_1^{n+1}, \theta_2^{n+1})} \widehat{\mathcal{P}_j}\widehat{\mathcal{P}_k} \, \mathrm{d}\gamma_x,$$

$$\begin{aligned}(A_{\mathbf{uu}})_{jk} = &\int_{\mathscr{F}(\theta_1^{n+1}, \theta_2^{n+1})} (\mathbf{u}_h^n \cdot \nabla)\mathcal{U}_k \cdot \mathcal{U}_j + \frac{\nu}{2}(\nabla \mathcal{U}_j + \nabla \mathcal{U}_j^T) : (\nabla \mathcal{U}_k + \nabla \mathcal{U}_k^T) \, \mathrm{d}\mathbf{x} \\ &-\nu^2 \gamma_0 h \int_{\partial S(\theta_1^{n+1}, \theta_2^{n+1})} (\nabla \widehat{\mathcal{U}_j} + \nabla \widehat{\mathcal{U}_j}^T)\mathbf{n}_{\theta_1,\theta_2} \cdot (\nabla \widehat{\mathcal{U}_k} + \nabla \widehat{\mathcal{U}_k}^T)\mathbf{n}_{\theta_1,\theta_2} \, \mathrm{d}\gamma_x,\end{aligned}$$

$$\begin{aligned}(A_{\mathbf{u}p})_{jk} = &-\int_{\mathscr{F}(\theta_1^{n+1}, \theta_2^{n+1})} \mathcal{P}_k \mathrm{div}\, \mathcal{U}_j \, \mathrm{d}\mathbf{x} \\ &+\nu\gamma_0 h \int_{\partial S(\theta_1^{n+1}, \theta_2^{n+1})} \widehat{\mathcal{P}_k}\mathbf{n}_{\theta_1,\theta_2} \cdot (\nabla \widehat{\mathcal{U}_j} + \nabla \widehat{\mathcal{U}_j}^T)\mathbf{n}_{\theta_1,\theta_2} \, \mathrm{d}\gamma_x,\end{aligned}$$

$$\begin{aligned}(A_{\mathbf{u}\boldsymbol{\lambda}})_{jk} = &-\int_{\Gamma_D \cup \partial S(\theta_1^{n+1}, \theta_2^{n+1})} \mathcal{U}_j \cdot \mathcal{W}_k \, \mathrm{d}\gamma_x \\ &-\nu\gamma_0 h \int_{\partial S(\theta_1^{n+1}, \theta_2^{n+1})} \mathcal{W}_k \cdot (\nabla \widehat{\mathcal{U}_j} + \nabla \widehat{\mathcal{U}_j}^T)\mathbf{n}_{\theta_1,\theta_2} \, \mathrm{d}\gamma_x,\end{aligned}$$

$$(A_{p\boldsymbol{\lambda}})_{jk} = \gamma_0 h \int_{\partial S(\theta_1^{n+1}, \theta_2^{n+1})} \widehat{\mathcal{P}_j}\mathbf{n}_{\theta_1,\theta_2} \cdot \mathcal{W}_k \, \mathrm{d}\gamma_x,$$

$$(A_{\boldsymbol{\lambda}\boldsymbol{\lambda}})_{jk} = -\gamma_0 h \int_{\partial S(\theta_1^{n+1}, \theta_2^{n+1})} \mathcal{W}_j \cdot \mathcal{W}_k \, \mathrm{d}\gamma_x,$$

$$\begin{aligned}(F_{\boldsymbol{\lambda}})_k = &\int_{\Gamma_i} \mathbf{u}^i \cdot \mathcal{W}_k \, \mathrm{d}\gamma_x \\ &+ \int_{\partial S(\theta_1^{n+1}, \theta_2^{n+1})} \sum_j \omega_j^{n+1} \partial_{\theta_j} \mathbf{X}(\theta_1^{n+1}, \theta_2^{n+1}, \mathbf{Y}(\theta_1^{n+1}, \theta_2^{n+1}, \gamma_x)) \cdot \mathcal{W}_k \, \mathrm{d}\gamma_x.\end{aligned}$$

### 4.2 Structure Approximation

We use a Finite Difference scheme to approximate the velocity and the displacement of the structure

$$\begin{cases} \begin{pmatrix} \theta_1^{n+1} \\ \theta_2^{n+1} \end{pmatrix} = 2 \begin{pmatrix} \theta_1^{n} \\ \theta_2^{n} \end{pmatrix} - \begin{pmatrix} \theta_1^{n-1} \\ \theta_2^{n-1} \end{pmatrix} + \Delta t^2 \mathcal{M}^{-1}_{\theta_1,\theta_2} \left( \mathbf{M_A}(t^n) + \mathbf{M_I}(t^n) + \mathbf{h} - k \begin{pmatrix} \theta_1^{n} \\ \theta_2^{n} \end{pmatrix} \right), \\ \begin{pmatrix} \omega_1^{n+1} \\ \omega_2^{n+1} \end{pmatrix} = \begin{pmatrix} \omega_1^{n} \\ \omega_2^{n} \end{pmatrix} + \Delta t \mathcal{M}^{-1}_{\theta_1,\theta_2} \left( \mathbf{M_A}(t^n) + \mathbf{M_I}(t^n) + \mathbf{h} - k \begin{pmatrix} \theta_1^{n} \\ \theta_2^{n} \end{pmatrix} \right). \end{cases} \tag{11}$$

### 4.3 Coupling Scheme

We use a partitioned approach, see [2, 6], which means that we treat the update with two sequential steps: a fluid step and a structure step. At each time step we do the following procedure

1. Compute **h** (if the control is applied)
2. Compute $(\theta_1^{n+1}, \theta_2^{n+1}, \omega_1^{n+1}, \omega_2^{n+1})$ with the structure step (11).
3. Update the fluid domain $\mathscr{F}(\theta_1^{n+1}, \theta_2^{n+1})$ and finite element spaces $V_h^{n+1}$, $Q_h^{n+1}$, $W_h^{n+1}$ (new definition near the interface).
4. Assembling the matrices $M^{n+1}$, $A^{n+1}$ and $F^{n+1}$ in (10).
5. Compute $(\mathbf{u}_h^{n+1}, p_h^{n+1}, \boldsymbol{\lambda}_h^{n+1})$ with the fluid step (10).
6. Compute the next time step $\Delta t$ such that only one row of elements can be crossed by the structure, i.e. $\Delta t = cfl \times \dfrac{h}{V_{\max}}$, where $h$ is the characteristic mesh-size, $V_{\max}$ is the maximum velocity of the structure and $cfl \in (0, 1)$.

### 4.4 Fictitious Points and Level-Set Update

During the time-marching procedure, difficulties arise near the interface. Indeed, the field variable at the time level $t^{n+1}$ can become undefined near the interface since there was no fluid flow at the time level $t^n$ ($S(\theta_1^{n+1}, \theta_2^{n+1}) \neq S(\theta_1^n, \theta_2^n)$ for the solid and $\mathscr{F}(\theta_1^{n+1}, \theta_2^{n+1}) \neq \mathscr{F}(\theta_1^n, \theta_2^n)$ for the fluid). In other words, some degrees of freedom for the fluid part which are not considered at the time level $t^n$ must be taken into account at the time level $t^{n+1}$.

**Level–set function and integration method over the cut elements**. The matrices in (10) are computed via an integration over $\mathscr{F}(\theta_1, \theta_2)$ and $\partial S(\theta_1, \theta_2)$. These integration methods need a well–defined interface $\partial S(\theta_1, \theta_2)$ and a method to integrate functions over the cut elements. The interface is defined as the null level of a level–set function

and the integration over the cut cells is done by dividing those cells into sub–cells, see Fig. 5c, (QHULL library). Note that the level–set is defined by a set of discrete ordered points located on the position of the interface which is known explicitly according to the parameters $\theta_1$, $\theta_2$ and the diffeomorphism $\mathbf{X}$, see (2). The distance to the level–set is computed by searching the two points that minimize the distance and by taking the projection on the segment defined by those two points. In order to reduce the computational cost of this method, at each time step, we compute the distance to the level–set only for the mesh nodes that are needed, i.e. the nodes near the interface. This drastically reduces the computational cost.

**Treatment of the fictitious points**. When solving (10) we need $\mathbf{U}^n$, the coordinates of $\mathbf{u}_h^n$ in the basis of the space $V_h^{n+1}$ while it is known in $V_h^n$. Even if the computation is realized only on the fluid domain, we affect values for the velocity in each degree of freedom of the background mesh. In the fluid domain, the values come from the resolution of the Navier-Stokes equations at the time level $t^n$ while the values in the structure come from the velocity of the structure

$$\boldsymbol{u}_{str}^n(\mathbf{x}) = \omega_1^n \partial_{\theta_1} \mathbf{X}(\theta_1^n, \theta_2^n, \mathbf{Y}(\theta_1^n, \theta_2^n, \mathbf{x})) + \omega_2^n \partial_{\theta_2} \mathbf{X}(\theta_1^n, \theta_2^n, \mathbf{Y}(\theta_1^n, \theta_2^n, \mathbf{x})).$$

In practice, for each nodes $\mathbf{y}_i$ of the mesh in the reference configuration $S_{ref}$, we compute $\mathbf{x}_i = \mathbf{X}(\theta_1^n, \theta_2^n, \mathbf{y}_i)$ and $\partial_{\theta_j}\mathbf{X}(\theta_1^n, \theta_2^n, \mathbf{y}_i)$ to determine the velocity $\boldsymbol{u}_{str}^n(\mathbf{x}_i)$. Considering this set of velocity values we can approximate $\boldsymbol{u}_{str}^n(\mathbf{x})$ in any point $\mathbf{x}$ (using a weighted arithmetic mean). Indeed, we do not have any explicit expression for $\mathbf{Y}(\theta_1, \theta_2, \mathbf{x})$.

**Remark 4.1** For efficiency, the node $\mathbf{y}_i$ retained to compute $\boldsymbol{u}_{str}^n(\mathbf{x})$ are reduced to the ones located near the structure's boundary in $S_{ref}$.

## 4.5 Computation of the Feedback Control in the Actual Domain

The main originality of our work compared with other stabilization studies is that the simulation is run in the actual domain $\mathscr{F}(\theta_1, \theta_2)$ instead of the reference domain $\mathscr{F}_s$ corresponding to the configuration of the stationary solution. However, the feedback matrix $\mathbf{K}$ has been computed in $\mathscr{F}_s$ (see Sect. 3), then to apply the feedback control (7) given by $\mathbf{h} = \mathbf{K}(\mathbf{z} - \mathbf{z_s})$, we need the value of the velocity $\mathbf{u}_{ref}$ at any time iteration in the reference configuration $\mathscr{F}_s$. In order to get the value of $\mathbf{u}_{ref}$, for every node $\mathbf{y}$ of the mesh on $\mathscr{F}_s$, we use the relation

$$\mathbf{u}_{ref}(\mathbf{y}) = \mathrm{cof}(\nabla \Phi(\theta_1, \theta_2, \mathbf{y}))^T \mathbf{u}_h \circ \Phi(\theta_1, \theta_2, \mathbf{y}).$$

For each node $\mathbf{y}$, we compute the corresponding point $\mathbf{x} = \Phi(\theta_1, \theta_2, \mathbf{y})$ in the computational domain $\mathscr{F}(\theta_1, \theta_2)$. Then we obtain the value of $\mathbf{u}_h(\mathbf{x})$ by interpolation

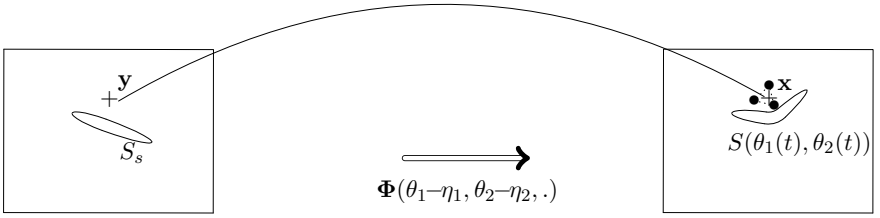


**Fig. 6** Interpolation to compute the velocity in the fixed domain

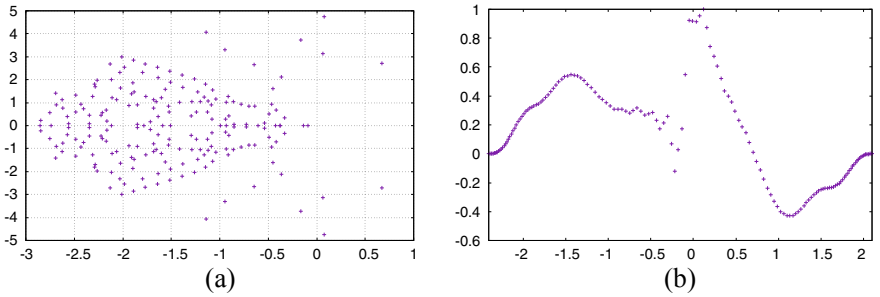


**Fig. 7** **a** Spectrum of the linearized problem, **b** Inflow perturbation $\sigma(\psi^1, p^1)\mathbf{n}.\mathbf{n}$

using the velocity computed on $\mathscr{F}(\theta_1, \theta_2)$ at each time step. We can conclude by multiplying by the transposed cofactor of the Jacobian matrix of $\Phi$ given by (6).

To sum up, the feedback is simply based on $\Phi$ numerically defined as an extension of $\mathbf{X}$ into the fluid domain and that can be obtained by solving a Poisson problem formulated on a small domain defined around the structure (see the sector in Fig. 4).

## 5 Numerical Results

We consider the configuration illustrated in Fig. 1 with $\Omega = (-1.0, 8.0) \times (y_{\min}, y_{\max})$ where $y_{\min} = -2.4, y_{\max} = 2.1$ and the structure domain is given by (3) with the point $O$ located in $(0, 0)$. The initial position of the structure is $(\eta_1, \eta_2) = (-25°, 0)$, the initial inflow boundary datum is given by a Poiseuille profile $\mathbf{u}^i(x_2) = \frac{6U_m}{(y_{\max}-y_{\min})^2}(-x_2^2 + (y_{\max} + y_{\min})x_2 - y_{\max}y_{\min})$, where $U_m$ is the mean speed of the inflow datum. The Reynolds number $\mathcal{R}e = \frac{cU_m}{\nu}$, where $c = 1$ is the chord of the profile, is taken as $\mathcal{R}e = 300$. In the sequel, we use $U_m = 1$ and $\nu = \frac{1}{300}$. The initial state of the fluid is computed as the stationary state associated to the datum $\mathbf{u}^i$. We consider on $\Gamma_i$ an inflow boundary perturbation $\mathbf{u}(\mathbf{x}) = \mathbf{u}^i + \beta_p g(\mathbf{x}) e^{-30(t-0.3)^2}$, where $\beta_p > 0$ is a coefficient that represents the intensity of the perturbation (here we take $\beta_p = 0.5$), $g(\mathbf{x}) = (\sigma(\psi^1, p^1)\mathbf{n}.\mathbf{n}, 0)^T$ for $\psi^1$ and $p^1$ computed as the real part of an eigenvector associated to the most unstable eigenvalue of the adjoint problem introduced to

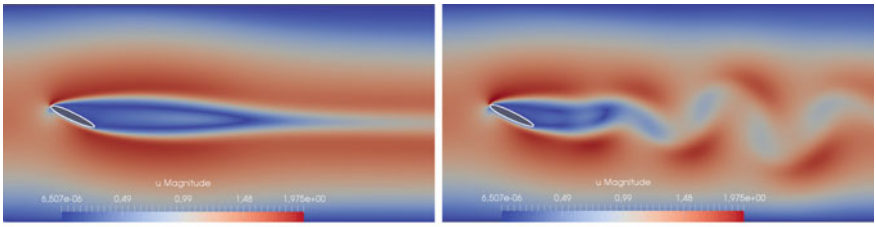


**Fig. 8** **a** Stationary solution (t = 0 s), **b** perturbated solution (t = 12 s) for $Re = 300$

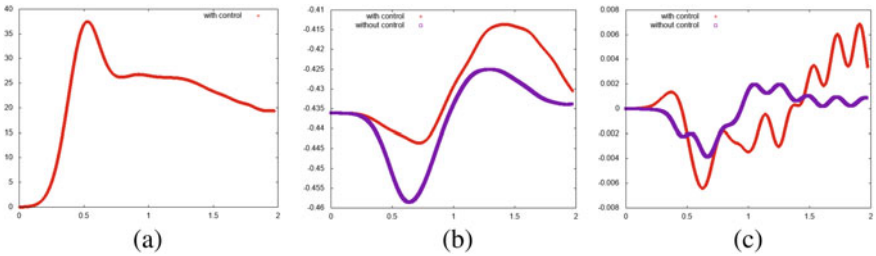


**Fig. 9** **a** Evolution of $\|\mathbf{u} - \mathbf{u_s}\|_2$ and **b** Evolution of $\theta_1$ and **c** $\theta_2$ with and without control

define $\mathbf{K}_\delta$ (the vector $\sigma(\psi^1, p^1)\mathbf{n}$ was normalized). Such perturbation is one of the most destabilizing normal boundary perturbations for the fluid [1]. The parameters of the structure are given by $\rho = 5$ and $k = 12$.

The numerical computations are led on a triangular mesh of 35,731 cells locally refined near the boundary, near the structure and near the wake of the structure (see Fig. 5a). We use the finite element spaces and the time stepping process defined above. The total number of degrees of freedom is equal to 153,880 at the initial time and varies according to the number of elements that are discarded.

We run two simulations, one in open loop and the other one in closed loop. In that way, we can observe the efficiency of the feedback control. The results are shown in Fig. 9 and confirm the good behavior of the method.

## References

1. Airiau, C., Buchot, J.-M., Dubey, R.K., Fournié, M., Raymond, J.-P., Weller-Carlo, J.: Stabilization and best actuator location for the Navier-Stokes equations. SIAM J. Sci. Comput. **39**(5), B993–B1020 (2017)
2. Burman, E., Fernández, M.A.: An unfitted Nitsche method for incompressible fluid-structure interaction using overlapping meshes. Comput. Methods Appl. Mech. Eng. **279**, 497–514 (2014)
3. Delay, G.: Etude d'un problème d'interaction fluide–structure: modélisation, analyse, stabilisation et simulation numérique. Ph.D. thesis. Université de Toulouse (2018)

4. Fournié, M., Lozinski, A.: Stability and optimal convergence of unfitted extended finite element methods with Lagrange multipliers for the Stokes equations. Lect. Notes Comput. Sci. Eng. **121**, 143–182 (2018)
5. Fournié, M., Morrison, J.: Fictitious domain for stabilization of fluid-structure interaction. IFAC Pap. OnLine **50**(1), 12301–12306 (2017)
6. Fernández, M., Mullaert, J.: Convergence and error analysis for a class of splitting schemes in incompressible fluid–structure interaction. IMA J. Numer. Anal. **36**(4), 1748–1782 (2016)
7. Gomez, J.C., Garcia, E.: Morphing unmanned aerial vehicles. Smart Mater. Struct. **20**, 103001–1030171 (2011)
8. Heinkenschloss, M., Sorensen, D.C., Sun, K.: Balanced truncation model reduction for a class of descriptor systems with application to the Oseen equations. SIAM J. Sci. Comput. **30**(2), 1038–1063 (2008)
9. Hou, G., Wang, J., Layton, A.: Numerical methods for fluid-structure interaction. A review. Commun. Comput. Phys. **4**, 609–644 (2012)
10. Ndiaye, M.: Stabilisation et simulation de modèles d'interaction fluide–structure. Ph.D. thesis. Université de Toulouse (2016)

# Studying the Transition in the Flow Around a Cylinder Using a Low Dimensional Model and Sensitivity Analysis


**G. Patino, R. Gioria, J. A. P. Aranha, and J. R. Meneghini**

**Abstract** This work focuses on the representation of the two-dimensional flow around a cylinder using a reduced model. The reduced model will be constructed by the projection of the incompressible flow equations into an appropriate orthonormal basis, built from the most energetic Fourier modes plus a disturbance of the mean flow pointing in the direction of the greatest eigenvalue growth rate. The Fourier modes are obtained through snapshots of the temporal simulation, and the optimal disturbance is calculated using sensitivity analysis to base flow modifications. The temporal dynamics as well as the hydrodynamic forces are calculated in the reduced space and compared with the results of the physical space showing a significant similarity. The addition of the mean flow disturbed by the sensitivity to base flow modifications aids to build a base flow that has a nonzero growth rate, allowing to describe the saturation path of the system in an appropriate way.

**Keywords** Landau equation · Reduced space · Sensitivity analysis · Stability

G. Patino (✉) · J. A. P. Aranha · J. R. Meneghini
Department of Mechanical Engineering, NDF,
University of Sao Paulo, 05508 -030 Sao Paulo, Brazil
e-mail: gustavopatino@usp.br

J. A. P. Aranha
e-mail: japaran@usp.br

J. R. Meneghini
e-mail: jmeneg@usp.br

R. Gioria
Department of Mining and Petroleum Engineering, NDF,
University of Sao Paulo, 05508 -030 Sao Paulo, Brazil
e-mail: rafaelgioria@usp.br



M. Braza et al. (eds.), *Advances in Critical Flow Dynamics Involving Moving/Deformable Structures with Design Applications*, Notes on Numerical Fluid Mechanics and Multidisciplinary Design 147,
https://doi.org/10.1007/978-3-030-55594-8_20

## 1 Introduction

In the present work, a low dimensional model is constructed to simulate the two-dimensional flow around a cylinder at different Reynolds numbers. The reduced models are relevant to understand the main physical processes exhibited by the system, studied in a space with few degrees of freedom. Numerical results have shown that many complex flows exhibit low dimensionality [1, 2]. Different approximations of reduced models have been proposed for flow around cylinders, many of them focused on studying the primary wake transition. Next to the primary transition or Hopf bifurcation, the system presents a vortex shedding dynamics which can be described using Galerkin methods [3]. The Galerkin methods are appropriate to obtain relevant physical information such as: the temporal dynamics of the system, the exchange of energy between small and large scales [4] and understand the physical mechanisms involved in the transition. They are also a good alternative to develop 2D global stability analysis with low computational cost. The size and properties of the Galerkin models depend on the choice of the expansion modes in the Galerkin approximation. These modes must satisfy the incompressibility condition and the boundary conditions. [5] constructed a reduced space based on the hierarchy of the most energetic scales of the fluid, resulting in the construction of spaces with few modes. [6] built a nicely reduced hierarchical model for the incompressible flow around a cylinder at low Reynolds numbers. The model is based on a Karhunen-Loeve decomposition of the numerical solution and incorporates a disturbed mode representing a correction of the mean flow. [6] finds that the inclusion of the mean flow correction improves the resolution of the transient dynamics from the onset of the vortex shedding to the Von Karman periodic flow, and can be even enhanced by enriching the space with the linear stability modes of the system. The full Galerkin model proposed by [6] is constructed based on the mean flow, a fluctuation formed by the linear stability modes calculated using the steady solution of the Navier Stokes equation and a shift-mode obtained from the correction of the mean flow after a Gram-Schmidt orthonormalization technique. Although the reduced space of [6] works very well for the studied Reynolds numbers, it has the difficulty of being linked with the steady flow and the solution of the linear stability problem around it, a presumption that is not appropriate in our archetypal since we intend to model the flow around a cylinder using an asymptotic expansion which restricts the linear growth rate of the perturbation to be a very small number for any number of Reynolds. The original mean flow can not consider in the construction of the Galerkin model because the transition time between the fixed point of the model and the limit cycle is enormous, given that the system is linearly stable to infinitesimal perturbations [7]. Bearing in mind the idea of [6], we propose a new model defined using the mean flow plus an optimal pertubation of it. The optimization criterion would be to determine the optimum direction in which the most unstable eigenvalue tends to have the greatest linear growth, following the sensitivity theory to estructutal modifications developed by [8]. In the present work, the base of the reduced space will be constructed using a Fourier modes decomposition of the numerical solution plus a perturbation of the mean flow using sensitivity to base flow modifications. The

temporal dynamics and the hydrodynamic forces are calculated in the reduced space and compared with the results of the physical space showing a significant similarity.

## 2 Theoretical Formulation of the Reduced Model

An appropriate definition for the fixed point is essential when building a reduced model. The most natural approach would be to define the fixed point as the stationary solution of the NSE $\mathbf{U}_{st}$. This fixed point was efficiently used by [6] to model the transient dynamics in a Galerkin model, however it is not appropriate for us given that we intend to model the flow around a cylinder using an asymptotic expansion of the Navier Stokes equations, forcing the growth rate of a perturbation $\sigma$ to be a small value. $\sigma \ll 1$ is only satisfied at Reynolds numbers near to the bifurcation point Re $\approx 47$, but it fails for larger Reynolds numbers. The mean flow is not a good candidate either, since the system has practically a zero growth rate, making the transient solution to take a long time in the path of leaving the equilibrium point and reaching the limit cycle. Our idea is to slightly disturb the mean flow in an optimal direction defined by the sensitivity to base flow modifications, in this way we preserve the condition of non null $\sigma$ with $\sigma \ll 1$ for arbitrary Reynolds numbers, allowing to define a Landau path in a reduced space manifold. The optimization criterion will be to determine the optimum direction in which the most unstable eigenvalue tends to have the greatest linear growth. Obviously, the path of the transient solution in the manifold of the physical space and the manifold of the reduced space will be different, however the final state (the limit cycle) will be the same in both spaces. Taking this into account, our model would fail to reproduce the hydrodynamic variables during the transition, but would reproduce adequately these variables in a developed flow.

### *2.1 Fourier Modes Decomposition*

Considering the ansatz

$$\mathbf{U}(t) = \mathbf{U}_p + \mathbf{U}_0(t) \tag{1}$$

into the Navier-Stokes equations, we can approximate the flow by the finite Fourier expansion

$$\mathbf{U}_0(t) = (\mathbf{U}_m - \mathbf{U}_p) + \sum_{\alpha=1}^{N} (\mathbf{U}_\alpha e^{i\alpha\omega_s t} + c.c) \tag{2}$$

where $\mathbf{U}_m$ represents the mean flow, $\mathbf{U}_p$ is a particular solution to be defined in the next section and $\mathbf{U}_\alpha$ are the $N$ first Fourier modes and $c.c$ the complex conjugate.

The Fourier coefficients are expressed as

$$\mathbf{U}_{\alpha cos} = \frac{2}{T}\int_{t_0}^{t_0+T} \mathbf{U}(t)\cos(\omega_\alpha t)\,dt \tag{3}$$

$$\mathbf{U}_{\alpha sin} = \frac{2}{T}\int_{t_0}^{t_0+T} \mathbf{U}(t)\sin(\omega_\alpha t)\,dt \tag{4}$$

In this study the Fourier modes are calculated from 256 snapshots evenly distributed over a simulation period.

Figures 1 and 2 show the cosine component of the first two Fourier modes. Fourier odd modes are antisymmetric in relation to $x$ axis

$$\begin{aligned} u(x,-y) &= -u(x,y) \\ v(x,-y) &= v(x,y) \end{aligned} \tag{5}$$

while the even modes are symmetric

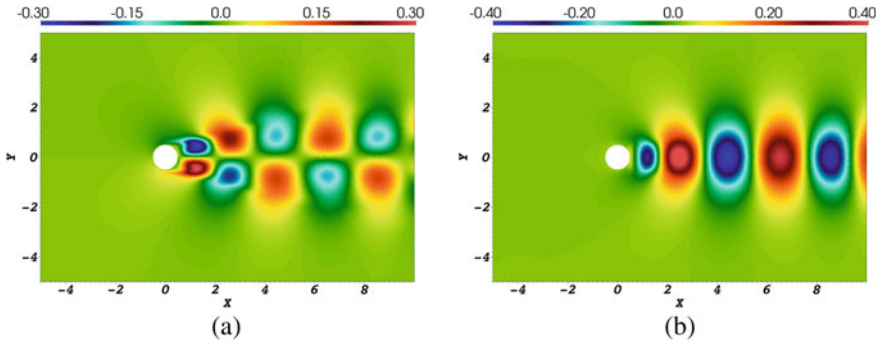


**Fig. 1** **a** $u$ component of $\mathbf{U}_{\alpha cos}$, $\alpha = 1$ . **b** $v$ component of $\mathbf{U}_{\alpha cos}$, $\alpha = 1$ , Re $= 100$

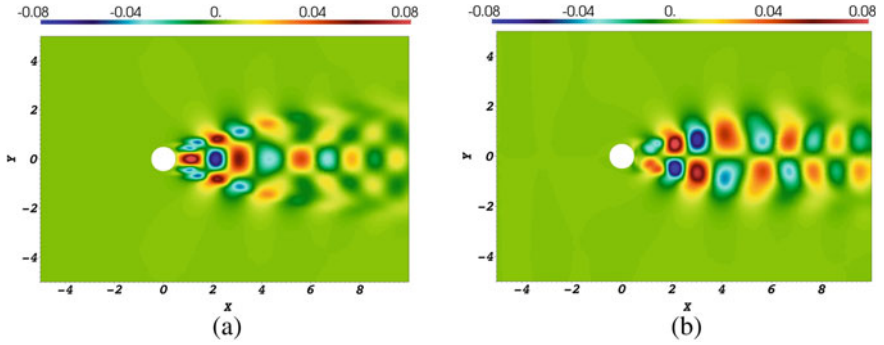


**Fig. 2** **a** $u$ component of $\mathbf{U}_{\alpha cos}$, $\alpha = 2$ . **b** $v$ component of $\mathbf{U}_{\alpha cos}$, $\alpha = 2$ , Re $= 100$

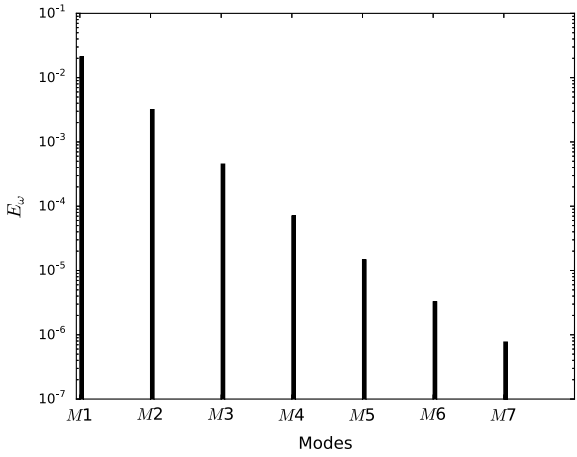


**Fig. 3** Energy of the first non null frequency fourier modes. Re = 100

$$\begin{aligned} u(x,-y) &= u(x,y) \\ v(x,-y) &= -v(x,y) \end{aligned} \tag{6}$$

Given that the basis of the reduced space is constructed using Fourier modes, it is essential to define the number of Fourier modes required to set the reduced space with enough degrees of freedom, so that the dynamic and stability properties in the original physical space are well defined. Calculating the energy of the Fourier modes $E_\omega$ as $E_\omega = \int_\Omega \mathbf{U}_\alpha^2 \, d\Omega$, we can deduce from the behavior of the energy in function of the modes for Re = 100 (Fig. 3) that the energy decays abruptly in the higher frequency modes. A similar behavior can be observed from the scale of the velocities in Figs. 1 and 2 were the second Fourier mode has already a much smaller magnitude than the first one, consequently, 10 Fourier modes ($N = 10$) can be defined as an appropriate measure in the construction of the reduced space.

## 2.2 Calculation of the Sensitivity Field $\hat{\mathcal{E}}$

The sensitivity to base flow modifications is defined as [8]

$$\mathcal{S} = -\nabla \mathbf{U}_e^H \cdot \mathbf{U}_{ae} + \nabla \mathbf{U}_{ae} \cdot \mathbf{U}_e^* \tag{7}$$

with $\mathbf{U}_{ae}$ the adjoint field associated to the most unstable mode $\mathbf{U}_e$ resulting of the linear stability analysis around the mean flow. The sensitivity field shows the regions where the most unstable eigenvalue is more susceptible to suffer alterations. This field is not solenoidal by construction, therefore the solenoidal component of $\mathcal{S}$ must be obtained in order to satisfy the condition of zero divergence in the NSE. Assuming that $\mathcal{S}$ is a complex entity $\mathcal{S} = \widehat{\mathcal{R}} + i\widehat{\mathcal{C}}$ and has a solenoid and gradient components,

we have

$$\begin{aligned} \widehat{\mathcal{R}} &= \widehat{\mathcal{R}}_s + \widehat{\mathcal{R}}_g \\ \widehat{\mathcal{C}} &= \widehat{\mathcal{C}}_s + \widehat{\mathcal{C}}_g \end{aligned} \tag{8}$$

where the gradient components can be calculated from a Poisson equation for a potential function. Let us assume the base flow modification field $\hat{\mathcal{E}}$ given by the linear combination of the auxiliary fields $\hat{\mathcal{E}}_\sigma$, $\hat{\mathcal{E}}_\omega$

$$\hat{\mathcal{E}} = \alpha\hat{\mathcal{E}}_\sigma + \beta\hat{\mathcal{E}}_\omega \tag{9}$$

with $\hat{\mathcal{E}}_\sigma$ defined as the auxiliary field which represents only variations in the eigenvalue growth rate and not in the frequency, and $\hat{\mathcal{E}}_\omega$ the field defined as the auxiliary field which represents variations in the frequency and not in the growth rate. Both fields are represented in the space generated by the vectors $\widehat{\mathcal{R}}_s$, $\widehat{\mathcal{C}}_s$.

$$\begin{aligned} \hat{\mathcal{E}}_\sigma &= \cos(\theta_\sigma)\widehat{\mathcal{R}}_s + \sin(\theta_\sigma)\widehat{\mathcal{C}}_s \\ \hat{\mathcal{E}}_\omega &= \sin(\theta_\omega)\widehat{\mathcal{R}}_s + \cos(\theta_\omega)\widehat{\mathcal{C}}_s \end{aligned} \tag{10}$$

$\cos(\theta_\sigma)$, $\sin(\theta_\sigma)$, $\sin(\theta_\omega)$, $\cos(\theta_\omega)$ are arbitrary coefficients given by the projection of $\hat{\mathcal{E}}_\sigma$, $\hat{\mathcal{E}}_\omega$ in the base vectors $\widehat{\mathcal{R}}_s$, $\widehat{\mathcal{C}}_s$. In order to calculate these coefficients, we consider the variation of the most unstable eigenvalue given by the projection of $\hat{\mathcal{E}}$ onto the sensitivity field $\hat{\mathcal{S}}$

$$\Delta\lambda = \Delta\sigma + i\Delta\omega = (\widehat{\mathcal{R}}_s + i\widehat{\mathcal{C}}_s) \cdot \hat{\mathcal{E}} \tag{11}$$

Using the definition of $\hat{\mathcal{E}}_\sigma$ one has

$$\begin{aligned} \Delta\sigma &= \| \widehat{\mathcal{R}}_s \|^2 \cos(\theta_\sigma) + \widehat{\mathcal{R}}_s^T \cdot \widehat{\mathcal{C}}_s \sin(\theta_\sigma) \\ \Delta\omega &= 0 \end{aligned} \tag{12}$$

which allows to calculate the angle $\theta_\sigma$ as

$$\tan\theta_\sigma = \frac{-\widehat{\mathcal{R}}_s \cdot \widehat{\mathcal{C}}_s}{\| \widehat{\mathcal{C}}_s \|^2}$$

In a similar way the angle $\theta_\omega$ can be calculated as

$$\tan\theta_\omega = \frac{-\widehat{\mathcal{R}}_s \cdot \widehat{\mathcal{C}}_s}{\| \widehat{\mathcal{R}}_s \|^2}$$

Therefore the variation in the eigenvalue is done by

$$\begin{pmatrix} \Delta\sigma \\ \Delta\omega \end{pmatrix} = \begin{pmatrix} \|\widehat{\mathcal{R}}_s\|^2 & \widehat{\mathcal{R}}_s^T \cdot \widehat{\mathcal{C}}_s \\ \widehat{\mathcal{R}}_s^T \cdot \widehat{\mathcal{C}}_s & \|\widehat{\mathcal{C}}_s\|^2 \end{pmatrix} \begin{pmatrix} \alpha \\ \beta \end{pmatrix} \tag{13}$$

The eigenvalues of the matrix in Eq. (13) represent the intensity of the perturbation and the eigenvectors the respective directions. The optimum mean flow perturbation is given by the eigenvalue of greater value in Eq. (13) and its eigenvectors define the optimal direction of growth in $\sigma$.
It must be guaranteed that the mean flow perturbation is much smaller than the mean flow itself. For this purpose we normalize the field $\hat{\mathcal{E}}$ using the standard norm

$$\| \hat{\mathcal{E}} \|_1 = \| \mathbf{U}_m \|_1 \tag{14}$$

with $\| \mathbf{U}_m \|_1^2 = \mathbf{U}_m^{\mathcal{H}} \cdot \mathbf{D} \cdot \mathbf{U}_m$ (being $\mathbf{D}$ the diffusion matrix). The norm 1 has been chosen since it does not depend on the domain size used in the discretization of the physical domain. With this in mind the perturbation is defined as

$$\mathbf{U}_p = \mathbf{U}_m + \delta\widehat{\mathcal{E}} \tag{15}$$

where $\delta$ is an arbitrarily small number. The sensitivity mode $\hat{\mathcal{E}}$ points in the direction of greatest variation of the most unstable eigenvalue and since the mode was normalized according to the Eq. (14), the magnitude of the disturbance remains defined by the factor $\delta$. This factor is arbitrary because its function is to disturb the mean flow allowing a route for the saturation, however, it should not be close to 1. Different values of $\delta$ influence the time that the system takes to leave the particular solution $\mathbf{U}_p$ and fall into the saturated solution, but it not must affect the limit cycle. As an example in these simulations a value $\delta = 0.05$ was chosen.

## 2.3 Building the Reduced Space

Solving the linear stability problem around the particular solution $\mathbf{U}_p = \mathbf{U}_m + \delta\hat{\mathcal{E}}$ we obtain the complex mode $\widehat{\mathbf{U}}_{mod}$ whose real and imaginary part are used to enrich the space generated by the $\mathbf{U}_\alpha$ fourier modes. The vectors used in the construction of the base for the reduced space $J_f$ are then

$$\begin{aligned} &\mathbf{J}_f = [\mathbf{U}_\alpha, \text{Real}(\widehat{\mathbf{U}}_{mod}), \text{Imag}(\widehat{\mathbf{U}}_{mod})] \\ &\alpha = 1, 2, \ldots .N \end{aligned} \tag{16}$$

The base of the reduced space is built using a Gram-Schmidt procedure beginning with the first fourier mode. In this way the base of the new reduced space will be the

orthonormal system $\mathbf{T}$ constructed from the vectors Eq. (16) and the Gram-Schmidt procedure

$$\mathbf{T} = [\mathbf{T}_1, \ldots \mathbf{T}_{N+2}] \tag{17}$$

Considering that the transformation between the reduced space and the physical space is done by

$$\mathbf{U}_0(t) \cong \mathbf{T} \cdot \mathbf{q} \tag{18}$$

with $\mathbf{q}$ the degrees of freedom in the reduced space calculated from the solution of the NSE in the reduced space. The dynamic NSE equations in the reduced space can be derived from the projection of the NSE in the physical space into the reduced space $J_f$ using the base $\mathbf{T}$.

## 2.4 Hydrodynamic Fields and Forces

Knowing the dynamic solution in the reduced space and the base $\mathbf{T}$, the velocity field in the physical space can be calculated from the transformation $\mathbf{U}(t) \cong \mathbf{T} \cdot \mathbf{q} + \mathbf{U}_p$ with $\mathbf{U}_p = \mathbf{U}_m + \delta\mathcal{E}$. In Fig. 4 we see the velocity field reassemble from the reduced space. It is notorious the similarity between the fields, considering that the velocity field in Fig. 4b was obtained from the direct solution of NSE in a rich physical space with more than 50000° of freedom and the reduced space only has 22. In the other side, the pressure field can be obtained directly from the NSE. Applying the divergence operator in the Navier Stokes equation yields to a discrete Poisson equation for the pressure. In Fig. 5 we see the pressure field obtained from the reduced space in comparison with the pressure in the physical space. Again the similarity between the fields is remarkable. These results allow to infer that the hydrodynamic forces

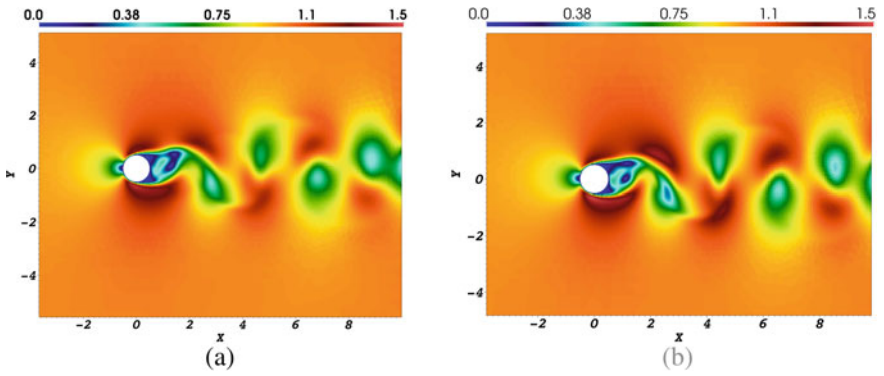


**Fig. 4** Velocity fields Re = 200. **a** Velocity calculated using the dynamic solution in the reduced space. **b** Velocity calculated from the solution of the NSE in the physical space

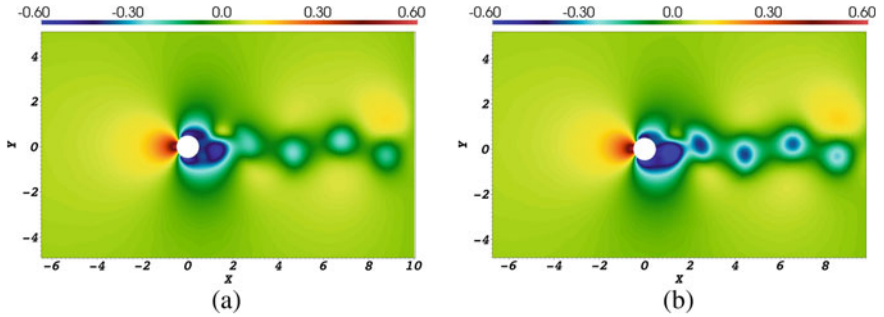


**Fig. 5** Pressure fields Re = 200. **a** Pressure calculated using the dynamic solution in the reduced space. **b** Pressure calculated from the solution of the NSE in the physical space

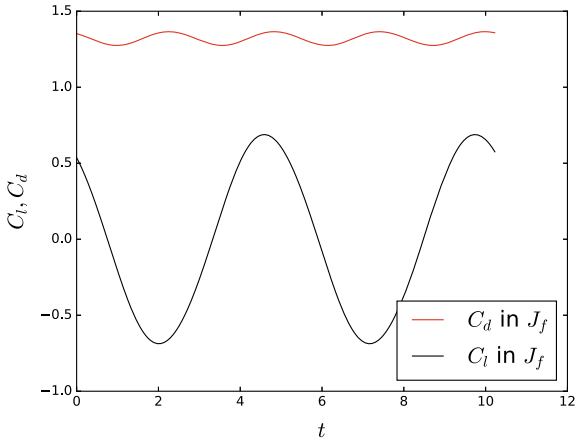


**Fig. 6** Hydrodynamic forces calculated using the dynamic solution in the reduced space. Re = 200

acting on the cylinder using the solution in the reduced space must be similar to the forces in the physical space, as can be corroborated in Fig. 6 when compared with the forces in the physical space reported by [9, 10]. The forces on the cylinder are obtained from the integration of the stress tensor over the entire cylinder surface.

## 3 Conclusion

In the present work a guideline for the construction of an appropriate reduced model is given to simulate the flow around a cylinder for different Reynolds numbers. The trial bases were constructed based on hierarchical modes extracted from a temporal simulation of the NSE following a Fourier decomposition plus the mean flow disturbed by the sensitivity to base flow modifications mode. In this context, and taking advantage of the energy flow from the lower frequency modes to the higher ones,

the reduced model was built with a base of just 10 Fourier modes plus the sensitivity mode. The reduced space constructed allows to obtain accurately several dynamic properties such as: vortex shedding frequency, hydrodynamic forces, pressure and velocity fields.

## References

1. Deane, A.E., Kevrekidis, I.G., Karniadakis, G.E., Orszag, S.A.: Low-dimensional models for complex geometry flows: application to grooved channels and circular cylinders. Phys. Fluid A Fluid Dyn. **3**(10), 2337–2354 (1991)
2. Ma, X., Karamanos, G.-S., Karniadakis, G.E.: Dynamics and low-dimensionality of a turbulent near wake. J. Fluid Mech. **410**, 29–65 (2000). https://doi.org/10.1017/S0022112099007934
3. Rempfer, Dietmar: Low-dimensional modeling and numerical simulation of transition in simple shear flows. Annu. Rev. Fluid Mech. **35**(1), 229–265 (2003)
4. Noack, Bernd R., Eckelmann, Helmut: A low-dimensional galerkin method for the three-dimensional flow around a circular cylinder. Phys. Fluids **6**(1), 124–143 (1994)
5. Ma, Xia, Karniadakis, George E.M.: A low-dimensional model for simulating three-dimensional cylinder flow. J. Fluid Mech. **458**, 181–190 (2002). https://doi.org/10.1017/S0022112002007991
6. Noack, Bernd R., Afanasiev, Konstantin, Morzynski, Marek, Tadmor, Gilead, Thiele, Frank: A hierarchy of low-dimensional models for the transient and post-transient cylinder wake. J. Fluid Mech. **497**, 335–363 (2003). https://doi.org/10.1017/S0022112003006694
7. Barkley, D.: Linear analysis of the cylinder wake mean flow. EPL Euro. Lett. **75**(5), 750 (2006)
8. Marquet, Olivier, Sipp, Denis, Jacquin, Laurent: Sensitivity analysis and passive control of cylinder flow. J. Fluid Mech. **615**, 221–252 (2008). https://doi.org/10.1017/S0022112008003662
9. Henderson, R.D.: Details of the drag curve near the onset of vortex shedding. Phys. Fluids **7**, (1995)
10. Norberg, C.: Fluctuating lift on a circular cylinder: review and new measurements. J. Fluids Struct. **17**(1), 57–96 (2003)

# Reduced Order Modeling for Plasma Aeroelastic Control of Airfoils in Cascade: Dynamic Mode Decomposition


**P. Neumann, V. Motta, L. Malzacher, T. D. Phan, R. Liebich, D. Peitsch, and G. Quaranta**

**Abstract** A dynamic mode decomposition is carried out for the flow field of a compressor cascade with plasma actuators employed for aeroelastic control. Numerical assessments carried out in previous works have shown that alternate triggering of pressure side/suction side actuators installed at the trailing edge of the blades can effectively reduce vibratory loads and enlarge the flutter boundaries of a linear compressor cascade. With the twofold aim of having an in depth understanding of the flow physics associated to plasma actuation and of developing an optimized control law for the actuators, the dominant structures of the pressure field are extracted via a dynamic mode decomposition. The decomposition is conducted on the actuated and non actuated pressure fields at several inter blade phase angles. The fundamental effects of plasma actuations on the flow field, and in turn on the blade loading, are identified and discussed. The procedure allows to get an useful picture of the main fluid mechanic phenomena associated to plasma aeroelastic control on turbomachinery bladings.

**Keywords** Reduced order modeling · Dynamic mode decomposition · Plasma actuation · Aeroelastic control

## 1 Introduction

The demand for lighter and more efficient aero engines is continuously growing. To face these challenges, compressors with increasingly larger pressure ratio per stage have been designed. Natural consequences of these solutions are increasing risks of

P. Neumann · V. Motta (✉) · L. Malzacher · D. Peitsch
Technische Universität Berlin, Str. des 17. Juni 135, 10623 Berlin, Germany
e-mail: valentina.motta@tu-berlin.de

T. D. Phan · R. Liebich
Technische Universität Berlin, Marchstr. 12–14, 10587 Berlin, Germany

G. Quaranta
Politecnico di Milano, via La Masa 34, Milano, MI 20156, Italy



M. Braza et al. (eds.), *Advances in Critical Flow Dynamics Involving Moving/Deformable Structures with Design Applications*, Notes on Numerical Fluid Mechanics and Multidisciplinary Design 147,
https://doi.org/10.1007/978-3-030-55594-8_21

fatigue and flutter phenomena on compressor blades. Degradations in aerodynamic and aerostructural response are also encountered on pulsed detonation engines, currently under study within the Collaborative Recearch Center 1029 of Technische Universität Berlin[1]. Several solutions have been proposed to control flow separation and minimize pressure losses arising on these novel configurations [1–6]. Among the conceived approaches, plasma actuators seem to be very promising, thanks to their lightness and to their almost negligible intrusiveness in the flow [7]. Whereas the control of the aerodynamic performance of heavily loaded blades has been widely investigated, the aeroelastic feasibility problems of these new designs have not been thoroughly pursued so far. In previous works, the authors showed numerically that plasma actuators may be successfully employed as virtual control surfaces to reduce vibration [8, 9] and to enlarge the flutter boundaries [10, 11] on a linear compressor cascade. With the ultimate aim of designing optimal open- and closed-loop control architectures, it is necessary to develop an appropriate reduced order model (ROM) for the clean—i.e. non-actuated—and the plasma-equipped cascade, capable to reproduce accurately the unsteady behavior of the blades. In this work—carried out within the Collaborative Research Centre 1029 of TU Berlin—a dynamic mode decomposition (DMD), first proposed in [12], is developed. The decomposition is applied on the flow field issued by the computational fluid dynamic (CFD) assessments detailed in [8–11]. The capability of the proposed ROM in reproducing the most relevant flow dynamics is highlighted. A further advantage of the dynamic mode decomposition is the possibility of getting an insight into the flow physics associated to this novel concept of active aeroelastic control. This paper is structured as follows. The numerical model and selected CFD results are presented in Sect. 2. A brief overview on the theoretical aspects and on the formulation of the dynamic mode decomposition is provided in Sect. 3. The results achieved by applying the DMD on the clean and actuated cascade are reported in Sect. 4. Concluding remarks are given in Sect. 5.

## 2 Computational Fluid Dynamic Assessments

### *2.1 Baseline Flow with and Without Plasma Actuation*

The DMD is applied on the numerically simulated flow field of a linear compressor cascade. The cascade resembles the aeroelastic test rig of the Chair of Aero Engines at TU Berlin [13]. The two-dimensional cascade features NACA 65 series airfoils, with a chord length of 0.15 m and a pitch-to-chord ratio of 0.75. Experimental tests showed that the flow can be considered as two-dimensional, for the investigated range of freestream conditions and for the small amplitude blade oscillations taken under consideration [13]. Thus, a 2D CFD-model is applied.

[1] Substantial efficiency increase in gas turbines through direct use of coupled unsteady combustion and flow dynamics, https://www.sfb1029.tu-berlin.de/menue/sfb_1029/parameter/en/.

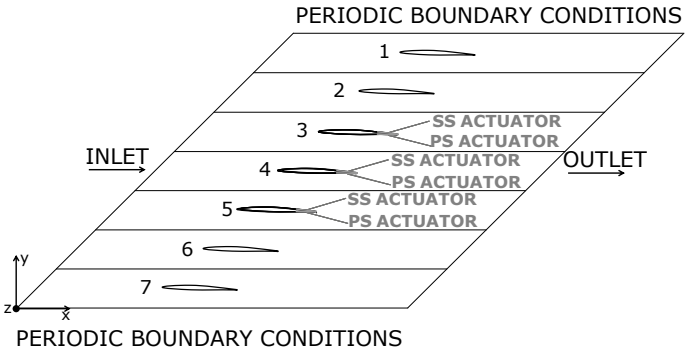


**Fig. 1** Sketch of the computational geometry for the linear cascade

The cascade is modeled with 7 blades and periodic boundary conditions on the top and on the bottom, as shown in Fig. 1. At the inlet, the freestream velocity is imposed, whereas at the outlet a pressure value of 101,325 Pa is defined. For the actuated case, plasma actuators are modelled on the rear side of the three central blades, on the suction side (SS) and pressure side (PS). For the numerical simulations the finite volume solver Ansys CFX is employed. The advection terms are solved with a high resolution scheme, whereas a second order backward scheme is applied for the transient terms. The flow is assumed as fully turbulent, and the system of RANS equations is closed with the SST k-$\omega$ turbulence model. The mesh is designed with a refinement at the blade surface walls resulting in an $y^+$ value close to 1. The incompressible flow simulations are conducted with Reynolds numbers of ∼195,000 and ∼350,000. The temperature is set to 20 °C and the reference pressure to 101,325 Pa.

The plasma actuators are implemented on the rear side of the blades on the suction side (SS) and pressure side (PS) as a 10 mm wide and 0.1 mm thick actuation area, see Fig. 2. The plasma actuation is implemented as a body force, directed against the freestream direction and with a force magnitude consistent to [14, 15]. Actuating against the freestream causes the development of low-speed recirculating flow areas. This yields an increase in static pressure, which is maximum in the actuator area and which—for subsonic flows—propagates upstream up to the leading edge. Therefore, PS actuation will yield effects comparable to those of a flap-like device deflected downward. That is lift and nose down pitching moment will be increased [9, 16]. Conversely, SS actuation will provide effects comparable to those of a trailing edge spoiler, that is lift and nose-down pitching moment will be decreased [9, 16].

The reliability of the numerical computations has been shown in Refs. [8–11], where space and time convergence studies, as well as comparison with experimental data, are reported.

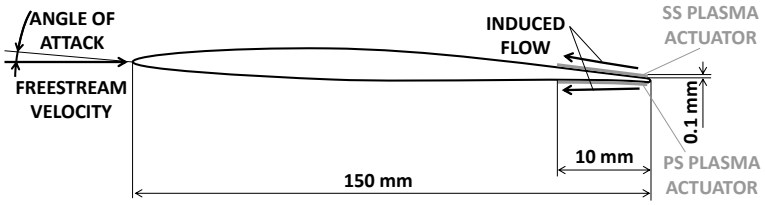


**Fig. 2** Sketch of the blade section with the plasma actuators

## *2.2 Reference Numerical Results with and Without Plasma Actuation*

The unsteady flow simulations are carried out for several traveling wave modes. A traveling wave mode, first introduced by Lane [17], describes the specific blade motion of tuned rotors. It is a widely employed representation of structure-induced pressure waves propagating along a turbomachinery annulus. According to the traveling wave mode formulation, blades oscillate with same frequency and amplitude, but with a constant and uniform phase shift between two adjacent blades, referred to as Inter Blade Phase Angle (IBPA). Each of the modes generates a specific set of traveling waves. Traveling wave pitch modes—about the mid-chord are considered in this work. Indeed experimental tests carried out on the cascade under consideration have highlighted that the purely torsional pitch mode is the most unstable, whereas the bending mode is far from the instability threshold [18]. Specifically the blade mean angle of attack and the oscillation amplitude are set to 2° and 1°, respectively. The reduced frequency based on the semi-chord is k = 0.4597. This specific value of the reduced frequency has been selected, because it is the one at which flutter was detected experimentally on the considered cascade [18].

It's worth remarking that steady simulations show a different efficiency of the suction side actuation and the pressure side actuation [8]. To balance this out the SS actuation force is set to 450 mN/m and the PS actuation force is set to 225 mN/m. Notice that the applied increase in the SS body force is still compliant with modern plasma actuators, see e.g. [19].

The dynamic actuation is set to maximize the aeroelastic stability, i.e. the net flow of energy transferred from the blade to the flow. To this aim, and consistently with the recommendations of [20], SS plasma is triggered during the upstroke phase—nose moving upward—of the pitching cycle. On the other hand, PS plasma is triggered during the downstroke phase. Figure 3 sketches the triggering of PS and SS actuation relative to the time history of the moment coefficient and to the blade motion. The light gray area highlights the operating window of the SS actuation. On the other hand, the dark gray area shows the operating window of the PS actuation.

Figure 4 (top) shows TE details of the velocity magnitude field during an oscillation cycle of a traveling wave mode simulation. The velocity is made dimensionless with the freestream velocity. The central blade of the cascade is displayed. PS actu-

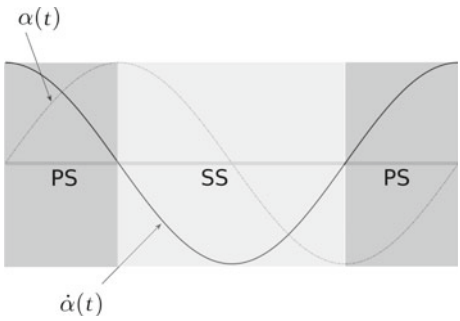


**Fig. 3** Sketch of PS and SS actuation triggering with respect to the blade motion $\alpha(t)$ and of its time derivative $\dot{\alpha}(t)$

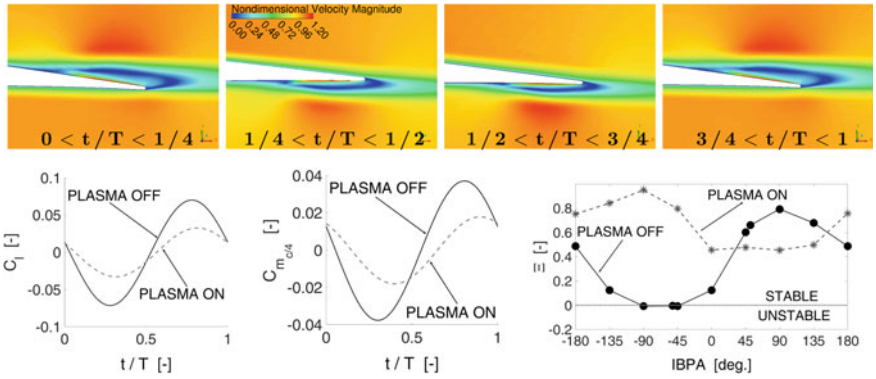


**Fig. 4** Top: TE detail of velocity magnitude, normalized by the freestream velocity, over the oscillation cycle; plasma actuation on. Bottom left and bottom middle: time history of lift and moment coefficient oscillations without and with actuation. Bottom right: aerodynamic damping versus IBPA with and without plasma. Re $\sim 1.9 \times 10^5$; IBPA = -51.43 deg.; $\alpha = 2 + \sin 2\pi f\, t + 4 \times \text{IBPA}\pi/180$ deg.; f = 19.17 Hz, T = 1/f; PS body force: 225 mN/m; SS body force: 450 mN/m

ation generates the expected recirculating flow areas during the downstroke phase, with a consequent increase in the blade loading relative to the clean counterpart. The opposite occurs during the upstroke phase [10, 11]. The oscillatory loads obtained with and without actuation are displayed in Fig. 4 (bottom left and bottom middle). The reduction in the unsteady lift and moment peaks enabled by alternate PS/SS actuation is clearly visible. Beneficial effects on the blade aeroelastic stability provided by unsteady plasma actuation are also obtained. Figure 4 (bottom) shows the non-dimensional aerodynamic work—defined as aerodynamic damping Ξ in [10, 11]—versus the IBPA, with and without actuation.

With the ultimate aim of developing an actuation law which maximizes the effectiveness of the control for the different operating regimes of the compressor, large scale optimization studies need to be performed. Indeed an effective feed-forward or

feed-back architecture has to operate with different flow velocities, vibration amplitudes, measurement uncertainties, dead times, coupled modes, switch of control law in dependecy of the most urgent problem (stability or forced vibrations).

Yet tremendous rises of computational burden would occur when performing CFD-based optimization studies of actuation laws. Within this framework is appears useful to build up a reduced order model which allows to rapidly evaluate the performance of the aeroelastic control system, whilst reproducing correctly the dominant physical phenomena of the flow field. In this work the dynamic mode decomposition will be applied to the pressure fields of the clean and actuated case. It will be shown that the model is capable to retain the most important flow dynamics and can therefore be used to compute accurately and rapidly the unsteady airloads on the clean and actuated cascade. Moreover the dynamic mode decomposition allows to have an useful picture of the physical phenomena associated to the alternate PS/SS plasma actuation first proposed by the authors in [8–11].

## 3 Overview on the Dynamic Mode Decomposition

Proper orthogonal decomposition (POD) has been and still is widely used to extract the main structures of complex flows, see e.g. [21–23]. Specifically, orthogonal structures are extracted, by computing the correlation matrix of flow field snapshots. The coherent structures, ranked according to the energy content, can be extracted by diagonalizing the computed correlation matrix. However, because the modes and the eigenvalues are computed on a second order statistics—i.e. the correlation matrix—the phase information is lost [22, 24]. In fact the phasing information and the knowledge of the dynamic temporal evolution of flows is of fundamental importance when dealing with aeroelastic problems, oscillating airfoils in general, and localized self sustained oscillations [9–11, 25–28]. In particular the spatial POD modes are not temporarily independents and each of them is often contaminated by other uncorrelated structures. Due to this impurity, especially the higher order modes may lack of physical meaningfulness.

In order to overcome these limitations Schmid [12] and Rowley [29] introduced the dynamic mode decomposition (DMD), in which the dynamic modes are extracted by applying the Koopman operator to the flow snapshots, without recurring to any statistical indicator. Compared to the POD, the modes are temporally—yet not spatially—orthogonal. Therefore the DMD allows to identify correctly the dynamic evolution of the system, as the misleading coupling of temporal modes is avoided. The DMD is based on the fitting of the data sequence with a high order polynomial, which is meant to approximate the temporal evolution of the system. The fitting polynomial is an infinite dimension space containing also the dynamics of the dataset, i.e. of the flow. It is proved that the eigenfunctions of a properly selected subspace of the fitting polynomial are a realistic representation of the dynamic response of the system under consideration [29]. A brief overview on the DMD algorithm is given hereinafter. For more details, please refer to Refs. [12, 29].

The flow field—e.g. velocity, vorticity, pressure—retrieved with numerical computations or particle image velocimetry surveys can be collected into a matrix containing temporally equidistant snapshots. This matrix can be written as $\boldsymbol{V}_1^N = \{\boldsymbol{v}_1, \boldsymbol{v}_2, \ldots, \boldsymbol{v}_N\}^{N\text{x}M}$, being $N$ the number of recorded time steps and $M$ the number of sample points within a snapshot. If the collected ensemble is enough large to approach the system dynamics asymptotically, it is possible to employ a constant mapping $\boldsymbol{A}$ for relating one snapshot $(j)$ to the following one $(j+1)$. Therefore it is possible to write:

$$\boldsymbol{v}_{j+1} = \boldsymbol{A}\boldsymbol{v}_j, \tag{1}$$

where $\boldsymbol{A}$ is the same for $j = 1, 2, \ldots, N-1$. The eigenvalues of $\boldsymbol{A}$ can be computed by defining the Krylov sequence and by performing an Arnoldi iteration on the resulting matrix. By adopting this approach, the matrix $\boldsymbol{V}_1^{N-1}$ which subtracts the last snapshot from the original data matrix can be expressed as $\boldsymbol{V}_1^{N-1} = \{\boldsymbol{v}_1, \boldsymbol{A}\boldsymbol{v}_1, \boldsymbol{A}^2\boldsymbol{v}_1, \ldots, \boldsymbol{A}^{N-2}\boldsymbol{v}_1\}$. Therefore one gets:

$$\boldsymbol{A}\boldsymbol{V}_1^{N-1} = \boldsymbol{A}\boldsymbol{V}_2^N, \tag{2}$$

being $\boldsymbol{V}_2^N = \{\boldsymbol{v}_2, \boldsymbol{v}_3, \ldots, \boldsymbol{v}_N\}$. The matrix $\boldsymbol{A}$ maps the flow at the time step $j$ into the flow at the time step $j+1$. The operation of the matrix $\boldsymbol{A}$ can be seed also as a shifting temporally the flow field at the time step $j$ to the time step $j+1$. Ultimately $\boldsymbol{A}$ can be interpreted as the state transition matrix of a generic dynamic system. Consistently, the eigenvalues of the mapping matrix $\boldsymbol{A}$ will provide information on the dynamic behavior of the flow field. The matrix $\boldsymbol{A}$ is associated to the governing equations and therefore can't be computed directly from the snapshots. Consequently a finite-dimensional matrix $\boldsymbol{S}$ approximating $\boldsymbol{A}$ is employed. Specifically equation (2) is expressed as:

$$\boldsymbol{A}\boldsymbol{V}_1^{N-1} = \boldsymbol{A}\boldsymbol{V}_2^N = \boldsymbol{V}_1^{N-1}\boldsymbol{S} + \boldsymbol{r}\boldsymbol{e}_{N-1}^{\text{T}} \approx \boldsymbol{V}_1^{N-1}\boldsymbol{S}, \tag{3}$$

being $\boldsymbol{S}$ a companion approximating matrix and $\boldsymbol{r}$ the residual [12, 30]. The matrix $\boldsymbol{S}$ is computed by performing a least square minimization of Eq. (3) with respect to $\boldsymbol{r}$. The eigenfunctions of $\boldsymbol{S}$ are known to approximate the counterparts of the reference matrix $j$th. As a consequence, performing a global stability analysis on the matrix $\boldsymbol{S}$, provides an approximation of the actual flow dynamics contained in $\boldsymbol{A}$. The $j$th equation of eigenvalue problem for $\boldsymbol{S}$ reads:

$$\boldsymbol{S}\boldsymbol{y}_j = \mu_j \boldsymbol{y}_j, \tag{4}$$

where $\mu_j \in \mathbb{C}$ approximates one of the eigenvalues of $\boldsymbol{A}$. Recalling Ref. [30], physically more meaningful information can be retrieved by computing the logarithmic decrement associated to $\mu_j$, i.e. $\omega_j = \log \mu_j / \Delta t = \Re(\omega_j) + \text{i}\,\Im(\omega_j) = \omega_j^r + \text{i}\,\omega_j^i$—being $\Delta t$ the time step amplitude. The real part of $\mu_j$ sets the time rate of growth/decay for the $j$th mode of the flow quantity under consideration. On the other hand, the imaginary part of $\omega_j$ quantifies the phase velocity of the $j$th mode

under consideration. The $j$th spatial mode $\Phi_j$ of the flow quantity collected $\boldsymbol{V}_1^{N-1}$ is computed as: $\Phi_j = \boldsymbol{V}_1^{N-1}\boldsymbol{y}_j$. That is, based on Eq. (3) the modes are retrieved by projecting the flow field data onto the eigenvalues of $\boldsymbol{S}$. As a result, the flow field reconstructed with isolated dynamic modes can be expressed as:

$$\mathbf{V}_1^{N-1}(x, y, t) = \sum_{j=1}^{N-1} \Phi_j(x, y)\, a_j(t), \tag{5}$$

where $a_j$ takes the form

$$a_j = \mathrm{e}^{\omega_j^r + \mathrm{i}\,\omega_j^i}. \tag{6}$$

Starting from the seminal works of Refs. [12, 29] the DMD has been effectively applied to several problems, including e.g. the flow past cylinders [22], the near-wake flow of a Gurney flap [30], turbulent cavity flows [24] or shallow flows [31].

In this work the DMD is applied to the pressure field of the central passage of the aforementioned compressor cascade, sketched in Fig. 1, with and without plasma actuators. The results are discussed in the following section.

## 4 Results

The DMD is computed for the pressure field in the central passage of the cascade. Four different IBPAs are taken under consideration, namely, $-90°$, $-51°$, $-45°$ and $+51°$. These specific negative values are considered, as the cascade is aeroelastically instable for IBPA in the range $\sim [-120, \ -30]°$. One additional positive IBPA is considered, for completeness. It's worth remarking that, according to the convention adopted in this work, negative IBPAs indicate a pressure wave traveling from the pressure side of a blade to the suction side of the adjacent blade. Conversely, for positive IBPAs the pressure wave travels from the suction side of a blade to the pressure side of the neighboring wave. The clean configuration, as well as the plasma-equipped blade actuated to the sketch of Fig. 3, are considered. It appears useful to recall that the dynamic mode decomposition is performed for the blades oscillating about the mid-chord, according to a traveling wave pitch mode. The mean angle of attack, the oscillation amplitude and the reduced frequency are 2°, 1° and 0.4597, respectively. The Reynolds number is ∼195,000.

The first four modes are extracted from the pressure fields obtained with CFD simulations. For brevity reasons exclusively the most relevant results are shown. The pressure modes for an IBPA +51° for the clean configuration and for an IBPA of −51° for the clean and actuated case are depicted in Figs. 5, 6 and 7. The spacial modes are normalized against the maximum singular value of the matrix mode. The temporal mode spectra obtained on the clean and actuated cascade for an IBPA of −51° are shown in Fig. 8. The mode spectra for the other IBPAs have an analogous behaviour. The spectra for mode 1 are not reported, as this mode represents the steady-state

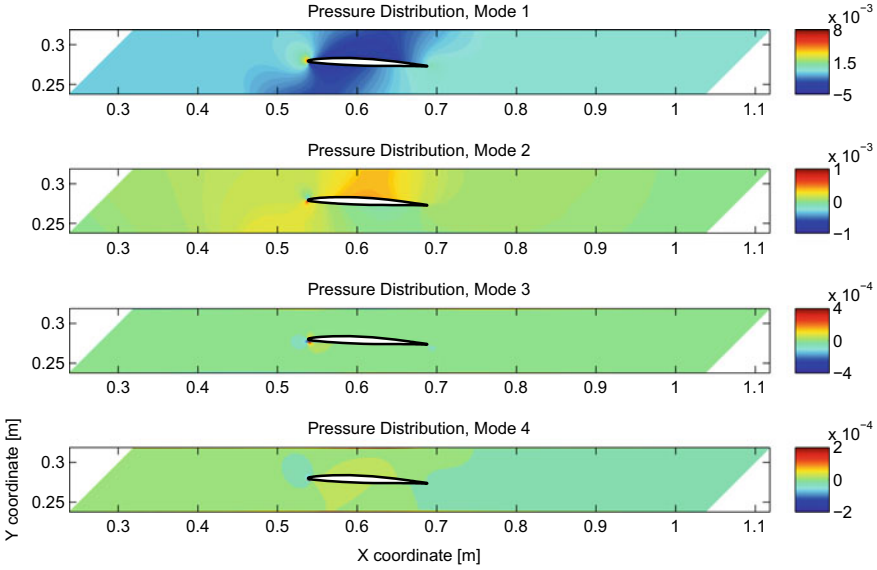


**Fig. 5** Normalized spatial modes of pressure field on the central stage of the cascade; plasma off; IBPA = 51°

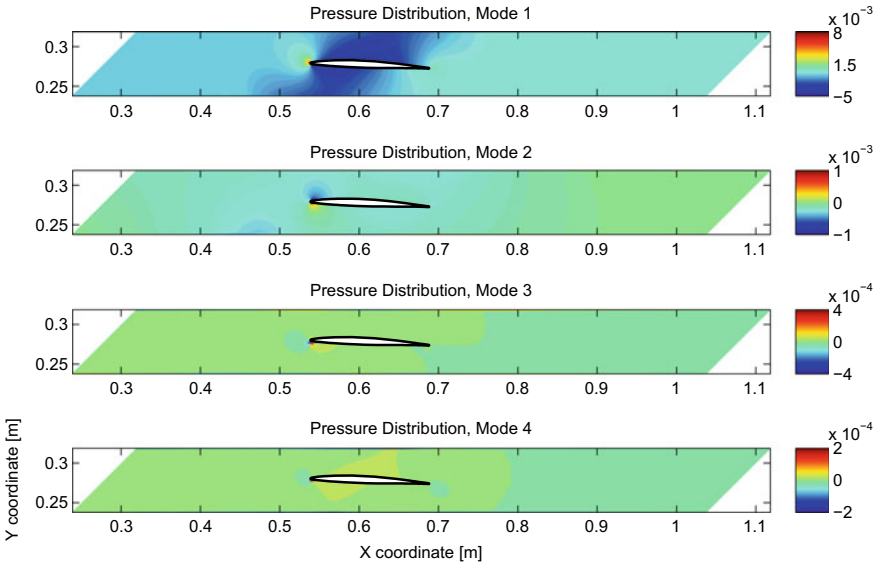


**Fig. 6** Normalized spatial modes of pressure field on the central stage of the cascade; plasma off; IBPA = −51°

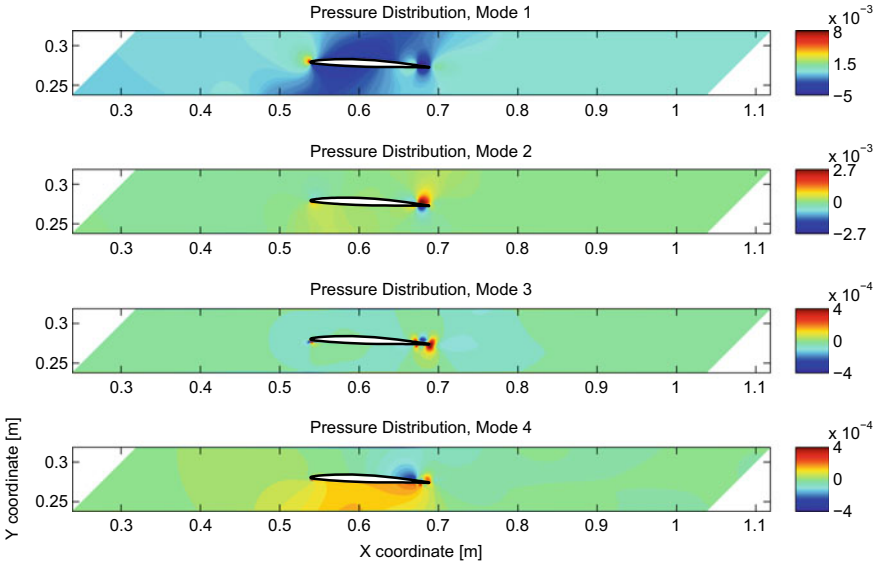


**Fig. 7** Normalized spatial modes of pressure field on the central stage of the cascade; plasma on; IBPA = −51°

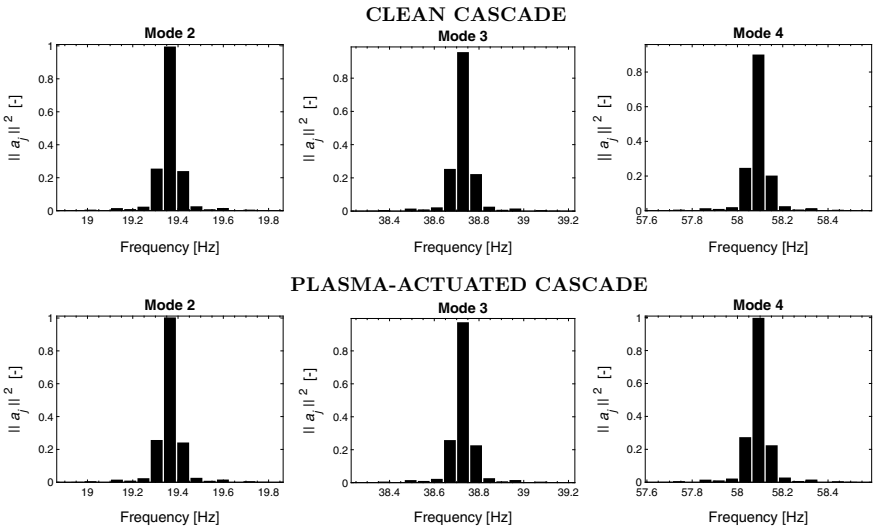


**Fig. 8** Power spectral density of the temporal pressure modes on the central stage of the cascade; IBPA = −51°

behaviour, and its frequency is therefore zero. The spectra of the temporal modes, plotted in terms of their power spectral density, they capture correctly the oscillation frequency of the blades and its integer multiples. Specifically, the spectrum of mode 2 has a peak at ∼19 Hz, i.e. at the frequency of oscillation. The spectrum of the 3rd mode has a peak at a frequency of∼38 Hz, which is indeed the double of the oscillation frequency. The spectrum of the 4th mode has a frequency of ∼57 Hz, i.e. three times the oscillation frequency.

The first spacial mode represents the mean pressure field. It is nearly identical for all IBPAs in the clean case, as well for all IBPAs in the actuated case. The effects of the actuation are clearly visible on the 1st mode of the pressure distribution, see Fig. 7. In comparison with the non actuated case, low pressure fields in the actuation areas with accompanying upstream high pressure fields are seen. The second spacial pressure modes in Figs. 5 and 6 show the modal pressure distributions corresponding to the travelling wave modes. They differ therefore for every calculated IBPA. Mode 2 in the actuated case shows clearly the alternating regions of recirculating flow areas. The modes change with to the clean case is highest near the actuation area but also seen in the overall pressure distribution. Not only the actuation on the blade itself, but also the actuation on the adjacent blades influences the overall spacial pressure fields. The effect of plasma actuation is also observable for all the higher modes at each of the IBPAs. The actuation leads to a significant increase in the spacial pressure amplitudes for all modes except mode 1. These higher amplitudes are especially, but not solely, located in the actuation area. With increasing mode number the spacial pressure mode amplitudes are decay rapidly.

## 5 Conclusions

A dynamic mode decomposition is applied to the unsteady pressure field generated by a linear compressor cascade oscillating according to traveling wave pitch modes. Results from computational fluid dynamic simulations are used as a reference for the decomposition. The central blades of the cascade are equipped with pairs of trailing edge plasma actuators located on the pressure side and on the suction side, respectively. An alternate triggering of pressure side/ suction side actuators allows to enhance remarkably the aeroelastic stability of the cascade.

The spacial pressure distributions issued by the dynamic mode decomposition show that the actuation causes high pressure alterations in the actuation area. Furthermore the actuation influences the overall pressure modes. Here the role of the adjacent blade actuation is clearly visible. Another expected effect observed for all the considered spacial modes is the increase in flow energy due to actuation. It is found that indeed the flow dynamics can be correctly reproduced by a small number of modes, without the need of involving the high frequency small spacial scale dynamics computed by numerical simulations. The advantages of the applied decomposition are twofold. On one hand, the projection of the flow dynamics onto a space with a reduced number of degrees of freedom, enables to perform large scale

optimization studies for the actuation law, without recurring to time and resource consuming numerical simulations. On the other hand, the dynamic mode decomposition allows for getting an insight into the most relevant flow patterns. Therefore the applied dynamic mode decomposition can be successfully used for performing large scale optimization studies on the actuation parameters and in turn maximize the benefits of plasma actuation for aeroelastic control on turbomachinery bladings.

**Acknowledgements** The authors gratefully acknowledge the support of the Deutsche Forschungsgemeinschaft (DFG) as part of collaborative research center CRC 1029 "Substantial efficiency increase in gas turbines through direct use of coupled unsteady combustion and flow dynamics".

## References

1. Tiedemann, C., Heinrich, A., Peitsch, D.: New Linear High Speed Compressor Stator Cascade, A., for Active Flow Control Investigations. In: 6th AIAA Flow Control Conference, 25–28, : New Orleans, p. 2012. USA, LA, USA, New Orleans, LA (2012)
2. Matejka, M., Popelka, L., Safarik, P., Nozicka, J.: Influence of active methods of flow control on compressor blade cascade flow. In: ASME Turbo Expo, 9–13 June 2008, Berlin, Germany, Number GT2008-51109 (2008)
3. Trávníček, Z., Cyrus, V, Šimurda, D., Luxa, M., Lukač, J., Kordik, J.: Experimental investigation of the compressor cascade under an active flow control. In: EPJ Web of Conferences, 45, (2013)
4. Hammer, S., Phan, D.T., Peter, J., Werder, T., Meyer, R., Liebich, R., Thamsen, P.U.: Active flow control by adaptive blade systems in periodic unsteady flow conditions. In: Active Flow and Combustion Control, 10–12. Berlin, p. 2014. Berlin, Germany (2014)
5. Monner, H.P., Huxdorf, O., Riemenschneider, J., Keimer, R.: Design and manufacturing of morphing fan blades for experimental investigations in a cascaded wind tunnel. In: 23rd AIAA/AHS Adaptive Structures Conference, 5–9 Jan 2015, Kissimmee, FL, USA
6. Phan, D.T., Springer, P., Liebich, R.: Numerical investigation of an elastomer-piezo-adaptive blade for active flow control of a nonsteady flow field using fluid-structure interaction simulations. J. Turbomach. 139, 091004–1–091004–10 (2017)
7. De Giorgi, M.G., Pescini, E., Marra, F., Ficarella, A.: Experimental and numerical analysis of a micro plasma actuator for active flow control in turbomachinery. In: Proceedings of ASME Turbo Expo 2014: Turbine Technical Conference and Exposition, Number GT2014-25337, Düsseldorf, Germany. American Society of Mechanical Engineers, 16–20 June 2014
8. Motta, V., Malzacher, L., Neumann, P., Peitsch, D.: Numerical assessment of virtual control surfaces for compressor blades. In: AIAA Aviation Forum, Denver, COL, USA. American Institute of Aeronautics and Astronautics, 5–9 June 2017
9. Motta, V., Malzacher, L., Peitsch, D.: Numerical assessment of virtual control surfaces for load alleviation on compressor blades. MDPI (2018)
10. Motta, V., Malzacher, L., Peitsch, D.: Numerical investigation of virtual control surfaces for vibration control on compressor blades. In: International Forum on Aeroelasticity and Structural Dynamics, Como, Italy, 25–28 June 2017
11. Motta, V., Malzacher, L., Peitsch, D.: Numerical investigation of virtual control surfaces for aeroelastic control on compressor blades. J. Fluids Struct. **81**, 617–637 (2018). August
12. Schmid, P.J.: Dynamic mode decomposition of numerical and experimental data. J. Fluid Mech. **656**, 5–28 (2010)
13. Malzacher, L., Geist, S., Peitsch, D., Hennings, H.: A low speed compressor test rig for flutter investigations. In: Proceedings of ASME Turbo Expo, : Turbomachinery Technical Conference

and Exposition, 12–16 June 2016, Seoul, South Korea, Number GT2016-57960, p. 2016. Seoul, South Korea (2016)
14. Akcayoz, E., Huu, D.V., Mahallati, A.: Controlling corner stall separation with plasma actuators in a compressor cascade. J. Turbomach. **138**(8) (2016)
15. Corke, T.C., Post, M.L., Orlov, D.M.: SDBD plasma enhanced aerodynamics: concepts, optimization and application. Prog. Aerospace Sci. **43**(7–8), 193–217 (2007)
16. Motta, V., Zanotti, A., Gibertini, G., Quaranta, G.: Numerical assessment of an L-shaped Gurney flap for load control. In: Proceedings of the Institution of Mechanical Engineers, Part G: Journal of Aerospace Engineering **138** (2016)
17. Lane, F.: System mode shapes in the flutter of compressor blade rows. J. Aeronaut. Sci. **23**(1), 54–66 (1956)
18. Sachs, W.: Windkanal für instationäre Gitter (WiG), Messstrecke für instationäre Gitter (MiG). Phase 1: Bau und InbetriebnahmeWindkanal für instationäre Gitter (WiG). Technical report, DLR (1990)
19. Zhang, H., Yu, X., Liu, B., Wu, Y., Li, Y.: Control of corner separation with plasma actuation in a high-speed compressor cascade. Appl. Sci. **7**(5), 465–480 (2017)
20. Zanotti, A., Grassi, D., Gibertini, G.: Experimental investigation of a trailing edge L-shaped tab on a pitching airfoil in deep dynamic stall conditions. Proce. Inst. Mech. Eng. Part G J. Aerosp. Eng. **228**(12), 2371–2382 (2014)
21. Berkooz, G., Holmes, P., Lumley, J.L.: The proper orthogonal decomposition in the analysis of turbulent flows. Ann. Rev. Fluid Mech. **25**(1), 539–575 (2011)
22. Zhang, Q., Liu, Y., Wang, S.: The identification of coherent structures using proper orthogonal decomposition and dynamic mode decomposition. J. Fluids Struct. **49**, 53–72 (2014)
23. Jodin, G., Motta, V., Scheller, J., Duhayon, E., Döll, C., Rouchon, J.-F., Braza, M.: Dynamics of a hybrid morphing wing with active open loop vibrating trailing edge by time-resolved piv and force measures, minor review in progress. J. Fluids Struct. (2017)
24. Seena, A., Sung, H.J.: Dynamic mode decomposition of turbulent cavity flows for self-sustained oscillations. Int. J. Heat Fluid Flow **32**, 1098–1110 (2011)
25. Carta, F.O.: An analysis of the stall flutter instability of helicopter rotor blades. J. Am. Helicopter Soc. **12**(4), 1–18 (1967)
26. Motta, V., Guardone, A., Quaranta, G.: Influence of airfoil thickness on unsteady aerodynamic loads on pitching airfoils. J. Fluid Mech. **774**, 460–487 (2015)
27. Motta, V., Quaranta, G.: A comparative assessment of vibration control capabilities of a L-shaped Gurney flap. Aeronaut. J. **120**(1233), 1812–1831 (2016)
28. Keerthi, M.C., Shubham, S., Kushari, A.: Aerodynamic influence of oscillating adjacent airfoils in a linear compressor cascade. AIAA J. **55**(12), 4113–4126 (2017)
29. Rowley, C.W., Mezić, I., Bagheri, S., Schlatter, P., Hanningson, D.S.: Spectral analysis of nonlinear flows. J. Fluid Mech. **641**, 115–127 (2009)
30. Pan, C., Yu, D., Wang, J.: Dynamical mode decomposition of gurney flap wake flow. Theor. Appl. Mech. Lett. **1**(1) (1993)
31. Higham, J.E., Brevis, W., Keylock, C.J.: Implications of the selection of a particular modal decomposition technique for the analysis of shallow flows. J. Hydraul. Res. (2018)

# Dynamic Behavior of Leading Edge Vortex and Vorticity on Suction Surface of a Heaving Elastic Airfoil


**Masaki Fuchiwaki**

**Abstract** The flow field around an elastic moving body has attracted attention in recent years and can be modeled as a coupled problem between the fluid and structure (fluid/structure interaction, FSI). Many studies have been carried out on the flow field around an elastic moving body using experimental and numerical approaches. However, the impact of elastic deformation on the vortices generated in the vicinity of the wall and the dynamic behavior of micro scale vortices have not been clarified sufficiently. The present study investigates the dynamic behavior of the leading-edge vortex and the vortices that form on the suction surface of a heaving elastic airfoil via FSI simulation using ANSYS 16.1/ANSYS CFX 16.1. The growth of the leading-edge vortex of the elastic airfoil is slightly delayed compared to that of the rigid airfoil due to the effective angle of attack. Moreover, the small effective angle of attack for the elastic airfoil strengthens the leading-edge vortex and delays its growth. Vorticity with clockwise rotation grows in the vicinity of the wall due to elastic deformation. This vorticity mainly consists of a strong rotational component.

**Keywords** Vortex · Airfoil · Unsteady flow · Fluid structure interaction

## 1 Introduction

Many studies on the flow field around moving airfoils, such as pitching airfoils, heaving airfoils, and airfoils that exhibit a combination of pitching and heaving motions, have been carried out using experimental and numerical approaches. These flow fields are a typical example of unsteady flow and have thus attracted attention. These studies have focused on the formation and growth of vortices produced by the body, the development, dynamic behavior, and structure of these vortices, as well as the relationship between vortex flow and the characteristics of dynamic fluid forces [1–5]. The present authors have previously qualitatively and quantitatively

M. Fuchiwaki (✉)
Kyushu Institute of Technology, 680-4 Kawazu, Iizuka 8208502, Japan
e-mail: futiwaki@mse.kyutech.ac.jp



M. Braza et al. (eds.), *Advances in Critical Flow Dynamics Involving Moving/Deformable Structures with Design Applications*, Notes on Numerical Fluid Mechanics and Multidisciplinary Design 147,
https://doi.org/10.1007/978-3-030-55594-8_22

characterized vortex structures that form in the wake of a rigid airfoil with pitching [6], heaving [7], and a combination of both motions [8].

The flow field around an elastic moving body has recently attracted attention from the viewpoint of insect flight, aquatic animal swimming, and the development of micro air vehicles. The flow field around an elastic body can be modeled as a coupled problem between the fluid and structure (fluid/structure interaction, FSI), with a series of phenomena, motions, structural deformations, and the generation, growth, and development of vortices repeated continuously. Many studies have been carried out on the flow field around an elastic moving body. Heathcote et al. [9, 10] visualized the wake of a heaving airfoil with a thin plate that elastically deforms on its trailing edge, measured the dynamic forces, and clarified the influence of the thin plate's elasticity on the flow field and thrust properties. In another study, they also measured the thrust acting on the elastic airfoil, which deforms elastically in the span direction, and also performed particle image velocimetry measurements [11]. Fuchiwaki et al. [12] applied a heaving motion to a moving elastic airfoil and studied the vortex structure of the wake and the nature of the dynamic thrust acting on the airfoil. Kurinami et al. [13] reported that the dynamic thrust acting on a heaving airfoil depends strongly on the Strouhal number, which is proportional to the maximum amplitude at the trailing edge of the airfoil. The above studies used numerical simulations. Gordnier et al. [14] investigated the effects of the angle of attack and the Reynolds number on a flow field by varying the oscillation of a thin elastic plate at low Reynolds numbers. They reported that the oscillation of such a plate causes the stall angle to change and reduces the Reynolds shear stress. Furthermore, the relationship between elastic deformation and the flow field was examined. Young [15] experimentally and numerically demonstrated that the elastic deformation of the blade of a marine propeller can reduce vibration and noise without reducing propeller efficiency. Fuchiwaki et al. [16] performed a fluid structural interaction simulation of the flow field around an elastic heaving airfoil using ANSYS/ANSYS-CFX and clarified the relationship between three key parameters, namely Strouhal number $St$, Reynolds number $Re$, and bending stiffness $K$, to elucidate the nature of the dynamic forces acting on an elastic airfoil as a function of these three dimensionless parameters. Fuchiwaki et al. defined the new quantity $St^2/K$ and showed that the characteristics of dynamic forces depend on this quantity [16]. These results provide insight into the macroscale vortex structure and the dynamic forces acting on the elastic moving airfoil. However, the impact of elastic deformation on the vortices generated in the vicinity of the wall and the dynamic behavior of microscale vortices have not been clarified sufficiently.

The present study investigates the dynamic behavior of the leading-edge vortex and the vortices that form on the suction surface of a heaving elastic airfoil via FSI simulation using ANSYS 16.1/ANSYS CFX 16.1. The impact of elastic deformation on the dynamic behavior of the leading-edge vortex and vortex growth in the vicinity of the wall are also examined.

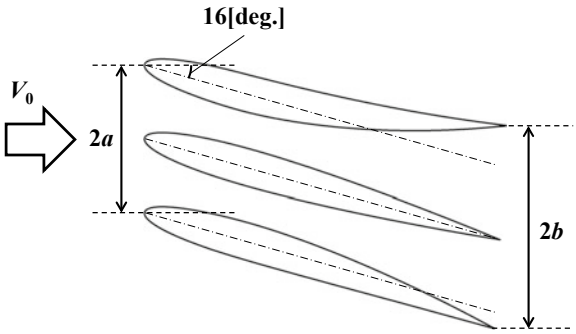


**Fig. 1** Airfoil configuration and its elastic deformation in our fluid structure interaction simulation

## 2 Fluid Structure Interaction Simulation

### *2.1 Airfoil Model*

The rigid and elastic airfoils used in the numerical simulation are NACA0010 airfoils. The chord length $c$ of the airfoils is 60 mm and the Reynolds number based on the chord length is 4000. The elastic airfoil consists of a rigid part (front quarter) and an elastic part (remaining section), as shown in Fig. 1. The Young's modulus and density of the elastic part are $E = 0.06$ MPa and $\rho = 1143$ kg/m$^3$, respectively. The heaving motion expressed in Eq. (1) was applied to the quarter-chord axis of the airfoil. The Strouhal number, given by Eq. (2), is a function of the maximum trailing edge amplitude (0.3 in this study). The flapping frequency, the main flow velocity, and the heaving amplitude were 0.833 Hz, 0.067 m/s, and 0.0012 m, respectively. The bending stiffness $K$ is defined in Eq. (3).

$$y = a \sin(2\pi f t) \tag{1}$$

$$St = \frac{2af}{V_0} \tag{2}$$

$$K = \frac{EI_G}{0.5\rho V_0^2 A c^2} \tag{3}$$

### *2.2 Fluid Structure Interation Simulation*

In the present study, a numerical simulation of the flow field around an elastic airfoil under heaving motion was performed via a fluid structure coupled analysis using ANSYS 16.1 and ANSYS-CFX 16.1. For the fluid, the governing equations are the equations of continuity (Eq. 4) and the Navier-Stokes equation (Eq. 5), and the finite

volume method (FVM) is used for discretization. For the structural part, the governing equations are the constitutive equations given by Eq. (6) and the finite element method (FEM) is used for discretization. In the analysis region, shown in Fig. 2, the leading edge, trailing edge, and airfoil surface are set to $2c$, $10c$, and $3c$, respectively, for chord length $c$ in the vertical direction. The depth in the spanwise direction of the airfoil is set to $c/12$. Figures 3 and 4 show the computational grid of a flow field around an elastic airfoil and the structure of the elastic airfoil, respectively. Tables 1 and 2 show the computational conditions for the fluid and rigid parts, respectively. The height of the first lattice point is approximately 0.02% of the chord length $c$. A pressure-transmitting boundary and displacement data are defined for the airfoil surface.

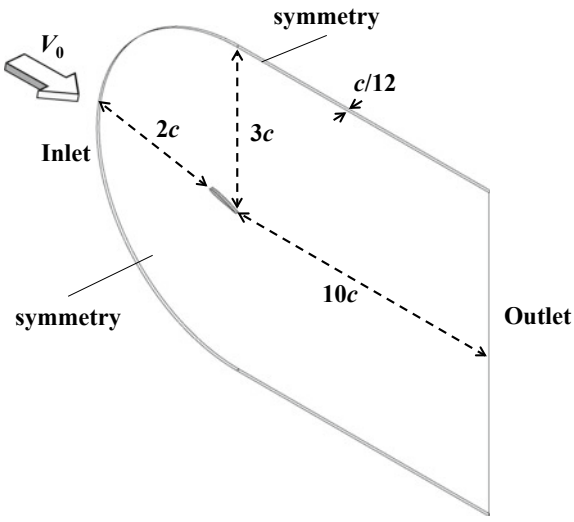


**Fig. 2** Computational domain for our fluid structure interaction simulation using ANSYS 16.1 and ANSYS-CFX 16.1

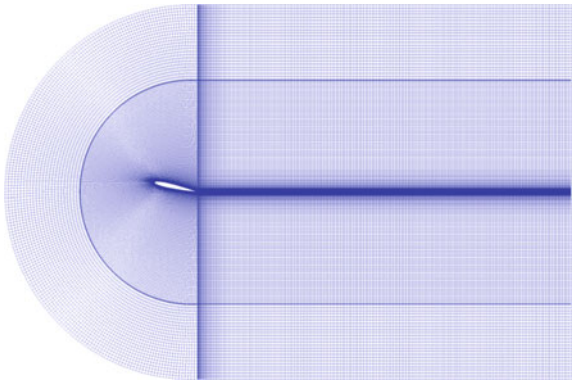

**Fig. 3** Computational grid of a flow field around an elastic heaving airfoil

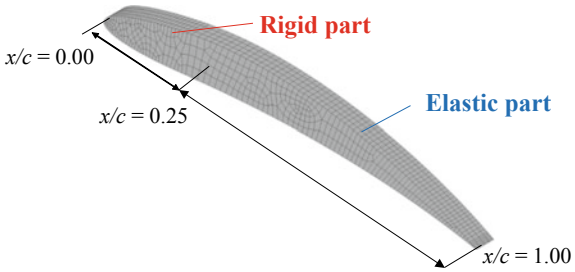


**Fig. 4** Computational grid of a structure on an elastic heaving airfoil

**Table 1** Computational conditions for fluid part

| Fluid | Water |
|---|---|
| Main flow | 0.067 (m/s) |
| Outlet | 0.0 (Pa) |
| Wall | Non-slip |
| Turbulence | $k$-$\omega$ |
| $y^+$ | $y^+ < 5$ |
| Nodes | 369,000 |
| Mesh | Hexa |
| Time step $t$ | 0.01 (s) |
| Total time | $10 \times T$ |

$$\nabla \bullet U = 0 \tag{4}$$

$$\rho \frac{\partial U}{\partial t} + U \bullet \nabla U = -\nabla P + \mu \nabla^2 U \tag{5}$$

$$[M]\ddot{X} + [C]\dot{X} + [K]X = F \tag{6}$$

In the proposed method, the interaction between the fluid and structure is considered in a bi-directional coupling simulation. A decoupled solver referred to as the

**Table 2** Computational conditions for structure part

| Material | Silicone |
|---|---|
| Elastic model | Neo-Hookean |
| Young's modules | 0.08 (MPa) |
| Poisson ratio | 0.45 |
| Density | 1043 (kg/m$^3$) |
| Nodes | 8273 |
| Mesh | Hexa |

weak coupled method, for which the governing equations of the fluid and structural regions are calculated independently, is used. Although this method has problems related to calculation time, convergence, and mapping of the interface data, the governing equations are calculated precisely. Therefore, the physical quantities related to the fluid structure interface can be transferred adequately. As a result, actual phenomena related to fluid and structural regions can be treated rigorously.

The coupling analysis includes four regions, namely the fluid analysis region, the interpolation region from the wall pressure in the fluid to pressure load data in the structure, the structural analysis region, where pressure loads are used as the initial values, and the mesh movement solution region, where the interpolation obtained from structural displacements is used. The calculations for these four regions are performed in order; each iteration of the four calculations is referred to as a step. The inner iterations of the fluid and the structure and the coupling iteration between the fluid and structure are defined as $N_{\mathrm{Fluid}}$, $N_{\mathrm{Structure}}$, and $N_{\mathrm{Coupling}}$, respectively. The total number of iterations for one step can be expressed as $N_{\mathrm{Coupling}} \times (N_{\mathrm{Fluid}} + N_{\mathrm{Structure}})$. Since the simulation requires a very long time, each step is divided into $N_{\mathrm{Coupling}}$ iterations implicitly. A convergent solution for complex phenomena, such an elastic body moving due to the dynamic forces generated by deformations, can thus be obtained.

## 3 Results and Discussion

### *3.1 Dynamic Behaviors of Leading Edge Vortex*

Figures 5 and 6 show the vorticity contours around the leading edge of the heaving rigid and elastic airfoils, respectively, representing the dynamic behavior of the leading-edge vortex. The figures show results obtained at $t/T = 0.33$, 0.42, and 0.50, which correspond to the near centers of the heaving motion from the bottom dead position, moving upward from the center of the heaving motion, and the top dead position, respectively. Blue and red in Figs. 5 and 6 indicate vorticity rotation in the clockwise and counterclockwise directions, respectively.

For both airfoils, the leading-edge vortex rolls up at $t/T = 0.42$. The reattachment of the leading-edge vortex can be clearly seen. This phenomenon was observed in the flow field around a pitching airfoil in our previous studies [6]. Maresca et al. [17] found that a heaving rigid airfoil exhibited the same dynamic behavior. These results indicate that the separation on the heaving elastic airfoil may be controlled by the leading-edge vortex that rolls up from the elastic airfoil. A comparison between the results of the rigid and elastic airfoils indicates that the growth of the leading-edge vortex on the elastic airfoil is slightly delayed compared to that on the rigid airfoil ($t/T = 0.42$ vs. 0.50). The maximum vorticity of the leading-edge vortex on the elastic airfoil at the top dead position was $-144.57\ \mathrm{s}^{-1}$, which is larger than that of the rigid airfoil ($-123.12\ \mathrm{s}^{-1}$). This is due to the small effective angle of attack of the

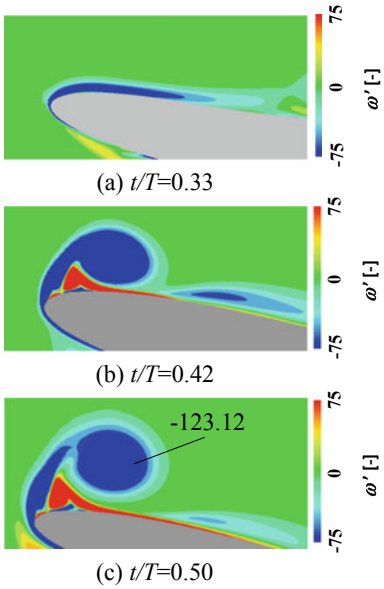


**Fig. 5** Vorticity contours around the leading edge of the heaving rigid airfoil

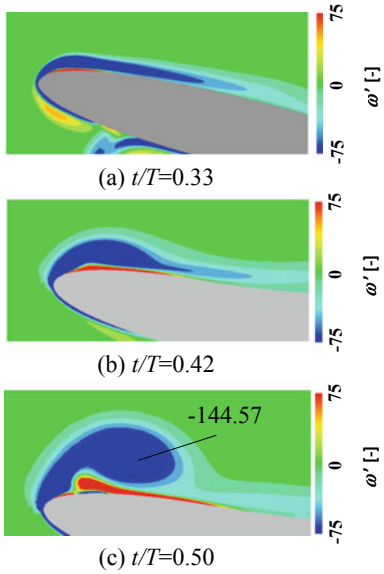


**Fig. 6** Vorticity contours around the leading edge of the heaving elastic airfoil

elastic airfoil. Figure 7 shows the effective angles of attack of the rigid and elastic airfoils at $St = 0.3$. Red and black lines show the results for rigid and elastic heaving airfoils, respectively. The effective angles of attack are defined in Eqs. (7) and (8), respectively.

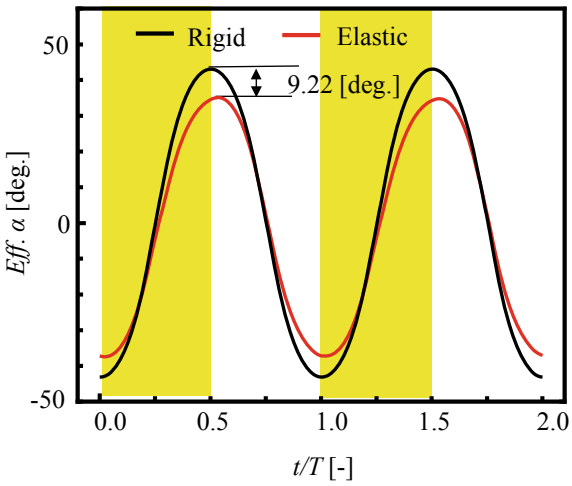


**Fig. 7** Effective angles of attack of the rigid and elastic airfoils at $St = 0.3$

$$\alpha_{eff} = \tan^{-1}\left(\frac{-V_{LE}}{V_0}\right) - \varphi \tag{7}$$

$$\alpha_{eff} = \tan^{-1}\left(\frac{-V_{LE}}{V_0}\right) - \alpha_{ela} - \varphi \tag{8}$$

The effective angle of attack of the elastic airfoil is delayed and smaller compared to that of the rigid airfoil. The minimum effective angles of attack for the two airfoils are almost the same, but there is a difference (9.22°) between the maximum effective angles of attack. These results indicate that the small effective angle of attack for the elastic airfoil strengthens the leading-edge vortex and delays its growth.

## *3.2 Growth of Vorticity in Vicinity of Wall*

Figures 8 and 9 show the vorticity distributions in the vicinity of the wall of the heaving rigid and elastic airfoils, respectively. The figures show results obtained at $t/T = 0.6, 0.7, 0.8, 0.9$, and 1.0. Figure 10 shows the corresponding elastic deformations of the elastic airfoil. Blue in Figs. 8 and 9 represents vorticity rotation in the clockwise direction.

Vorticity with clockwise rotation grows in the vicinity of the wall for both airfoils. The range of vorticity is larger and the vorticity region is thicker for the elastic airfoil compared to those for the rigid airfoil. These differences are clear at $t/T = 0.8$. That is, when the elastic deformation becomes large from $t/T = 0.7$ to $t/T = 0.8$, the vorticity with clockwise rotation becomes wider and thicker. We previously reported that vortices with strong vorticity roll up from the trailing edge of the elastic airfoil

and that these vortices form a vortex street with high vorticity [12, 13]. These vortices are formed by the vorticity in the vicinity of the wall due to large elastic deformation.

Figures 11 and 12 show the Q-criterion in the vicinity of the wall of the rigid and elastic airfoils, respectively. The figures show results obtained at $t/T = 0.6$, 0.7, 0.8, 0.9, and 1.0.

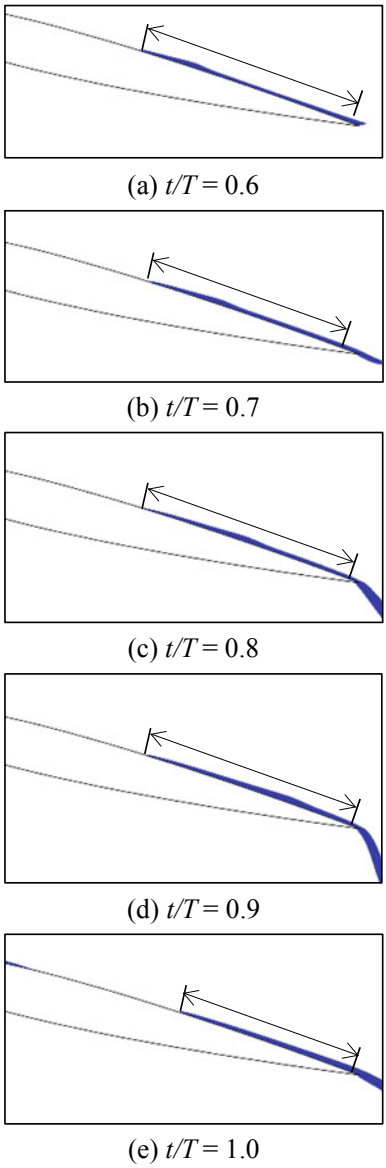

(a) $t/T = 0.6$

(b) $t/T = 0.7$

(c) $t/T = 0.8$

(d) $t/T = 0.9$

(e) $t/T = 1.0$

**Fig. 8** Vorticity distributions in the vicinity of the wall of the heaving rigid airfoil

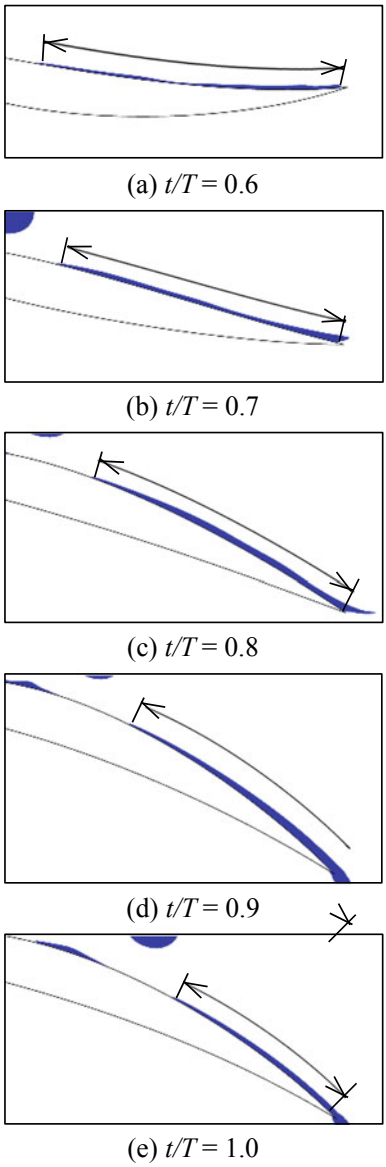


**Fig. 9** Vorticity distributions in the vicinity of the wall of the heaving elastic airfoil

For the rigid airfoil, the Q-criterion does not detect vorticity in the vicinity of the wall, as shown in Fig. 11. For the elastic airfoil, it detects vorticity in the vicinity of the wall. The range of the Q-criterion is almost the same as that of the vorticity with clockwise rotation, as shown in Fig. 9. Moreover, the thickness of the Q-criterion becomes much higher at the trailing edge. Based on the results in Figs. 8, 9, 11, and 12, it is found that vorticity with clockwise rotation grows in the vicinity of the wall

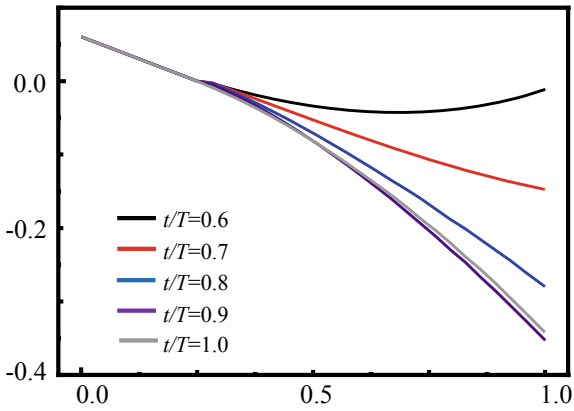


**Fig. 10** Elastic deformations of the elastic airfoil at $St = 0.3$

due to elastic deformation and it mainly consists of a strong rotational component. The vortices roll up in the wake and form a vortex street with high vorticity [12, 13].

## 4 Conclusions

The dynamic behavior of the leading-edge vortex and the vorticity that forms on the suction surface of a heaving elastic airfoil were investigated via FSI simulation using ANSYS 16.1/ANSYS CFX 16.1. The impact of elastic deformation on the dynamic behavior of the leading-edge vortex and the growth of vorticity in the vicinity of the wall were examined.

The growth of the leading-edge vortex of the elastic airfoil is slightly delayed compared to that of the rigid airfoil due to the effective angle of attack. Moreover, the small effective angle of attack for the elastic airfoil strengthens the leading-edge vortex and delays its growth. Vorticity with clockwise rotation grows in the vicinity of the wall due to elastic deformation. This vorticity mainly consists of a strong rotational component.

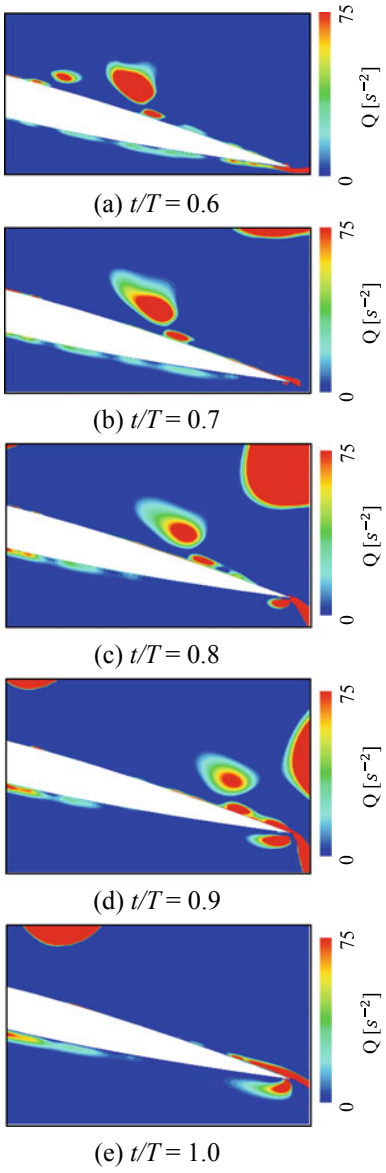


**Fig. 11** Q-criterion in the vicinity of the wall of the rigid airfoil

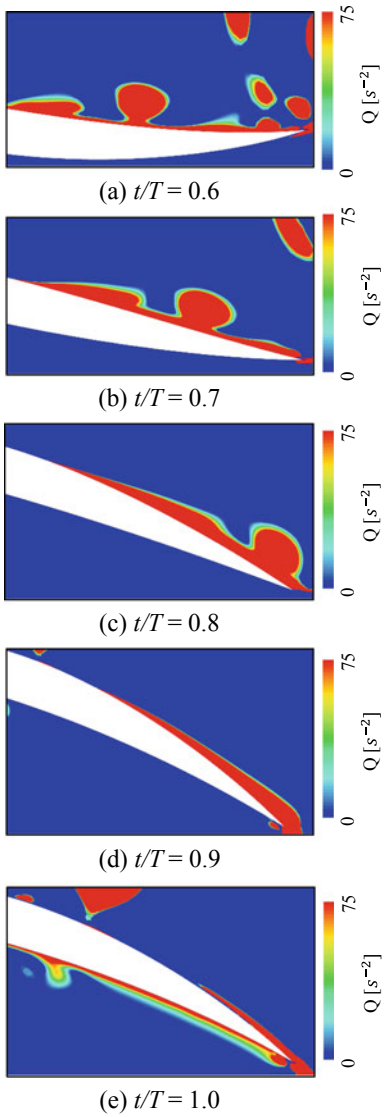


**Fig. 12** Q-criterion in the vicinity of the wall of the elastic airfoil

**Acknowledgements** This work was supported by JSPS KAKENHI Grant Number 17K06161.

## References

1. Lai, J.C.S., Platzer, M.F.: Jet characteristics of a plunging airfoil. AIAA J. **37**(12), 1529–1537 (1999)

2. Fuchiwaki, M., Tanaka, K.: Two-dimensional structure of the wake behind a pitching airfoil with higher non-dimensional pitching rate. J. Vis. **4**(4), 323–329 (2001)
3. Ramamurti, R., Sandberg, W.: Simulation of flow about flapping airfoils using finite element. J. Exp. Biol. **210**, 881–896 (2001)
4. Hover, F.S., Haugsdal, O., Triantafyllou, M.S.: Effect of angle of attack profiles in flapping foil propulsion. J. Fluid Struct. **19**, 37–47 (2004)
5. Guerrero, J.E.: Wake signature of finite-span flapping rigid wings. High Perform. Comput. Sci. Eng. **10**, 407–427 (2011)
6. Fuchiwaki, M., Tanaka, K.: Arrangement and dynamic behavior of vortices from a pitching airfoil. JSME Int. J. B Fluids Therm. Eng. **43**(3), 443–448 (2000)
7. Fuchiwaki, M., Tanaka, K.: Wake structure and dynamic thrust of an unsteady airfoil. In: ASME Fluids Engineering Division Summer Meeting, FEDSM2005-77473 (2005)
8. Fuchiwaki, M., Tanaka, K., Nakashima, M.: Characteristics of dynamic thrust on an unsteady airfoil in pitching and heaving motions. In: ASME/JSME 5th Joint Fluids Engineering Conference, FEDSM2007-37222 (2007)
9. Heathcote, S., Martin, D., Gursul, I.: Flexible flapping airfoil propulsion at zero freestream velocity. AIAA J. **42**(11), 2196–2204 (2004)
10. Heathcote, S., Gursul, I.: Flexible flapping airfoil propulsion at low Reynolds numbers. AIAA J. **45**(5), 1067–1079 (2007)
11. Heathcote, S., Wang, Z., Gursul, I.: Effect of spanwise flexibility on flapping wing propulsion. J. Fluid Struct. **24**, 183–199 (2008)
12. Fuchiwaki, M., Kurinami, T., Tanaka, K.: Detailed wake structure behind an elastic airfoil. J. Fluid Sci. Technol. **4**(2), 391–400 (2009)
13. Kurinami, T., Fuchiwaki, M., Tanaka, K.: Vortex flow developed in the vicinity of a wall of an elastic heaving airfoils and its wake structure. J. Fluid Sci. Technol. **6**(4), 562–574 (2011)
14. Gordnier, R.E., Demasi, L.: Implicit LES simulations of a flapping wing in forward flight. In: ASME Fluids Engineering Summer Meeting, FEDSM 2013-16540 (2013)
15. Young, Y.L.: Fluid–structure interaction analysis of flexible composite marine propellers. J. Fluid Struct. **24**, 799–818 (2008)
16. Fuchiwaki, M., Nagata, T., Tanaka, K.: Dynamic forces acting on elastic heaving airfoils based on the bending stiffness considerations. In: ASME 2014 4th Joint US-European Fluids Engineering Division Summer Meeting Collocated with the ASME 2014 12th International Conference on Nanochannels, Microchannels, and Minichannels, FEDSM2014-21302 (2014)
17. Maresca, C., Favier, D., Rebont, J.: Experiments on an aerofoil at high angle of incidence in longitudinal oscillations. J. Fluid Mech. **92**(4), 671–690 (1979)

# Studying Sound Production in the Hole-Tone Configuration Using Compressible and Incompressible Global Stability Analyses


**R. Longobardi, D. Fabre, P. Bonnefis, V. Citro, F. Giannetti, and P. Luchini**

**Abstract** We study the jet passing through two successive circular holes, also known as hole-tone configuration. Such flow is relevant to many applications like human whistling, wind instruments and tea kettles. Recently, Fabre et al. [1] investigated this flow configuration adopting a global stability approach, showing that the whistling is linked to a purely incompressible instability of the jet between the two holes. In this work, we focus our attention on a little different and more realistic geometry, known as birdcall configuration, consisting into two successive holes in curved thick plates. Although the whistle is related to compressible phenomena, the incompressible approach can provide some useful information, at least in the region near the hole, where, in some conditions, the flow can be considered incompressible. We thus initially perform a purely incompressible stability approach. We identify the critical conditions, the global frequencies and discuss the structure of the resulting global eigenmodes. In order to reintroduce and evaluate compressible effects, which can be relevant into the cavity between the two holes, we model the cavity as a Helmholtz resonator and couple it to the incompressible simulation. Finally, a full compressible stability analysis is performed in order to check the accuracy of these simplified approaches in term of critical conditions, global frequencies and structure of the modes.

**Keywords** Instability · Compressible · Whistle · Birdcall

R. Longobardi (✉) · V. Citro · F. Giannetti · P. Luchini
DIIN, Universitá Degli Studi di Salerno, Via Giovanni Paolo II, 84084 Fisciano, SA, Italy
e-mail: rlongobardi@unisa.it

R. Longobardi · D. Fabre · P. Bonnefis
IMFT, Université de Toulouse, CNRS, Allée Camille Soula, 31400 Toulouse, France



M. Braza et al. (eds.), *Advances in Critical Flow Dynamics Involving Moving/Deformable Structures with Design Applications*, Notes on Numerical Fluid Mechanics and Multidisciplinary Design 147,
https://doi.org/10.1007/978-3-030-55594-8_23

## 1 Introduction

It is known that the flow passing through two circular holes in thick plates, also known as hole-tone configuration, gives rise to a whistle tone and this situation is encountered in various practical situations, such as human whistling, wind instruments or tea kettles. Such kind of problems attracted the interest of numerous acoustic researches such as Helmholtz [2], Rayleigh [3] and Bouasse [4], which investigated the problem majorly from an acoustic point of view, namely without considering the existence of a mean flow and its dynamics. More recently Henrywood and Agarwal [5] investigated the hole-tone configuration from an experimental point of view, identifying two regimes: at low velocities the whistle frequency is selected by the cavity between the two holes whereas at high speed regimes the jet dynamics is more relevant in the frequency selection process. Recently, Fabre et al. [1] studied this problem by using an incompressible analysis thanks to the assumption of acoustically compact holes: they assumed the wavelength of the sound wave greater than the characteristic length scales of the cavity and holes. In particular, they used the global approach to compute the stability characteristics of the flow system. They found that the frequency selection is triggered by the hydrodynamic regime, although the whistle is related to compressible phenomena.

In this paper we study a more realistic geometry, namely the *birdcall configuration* (more details about the geometry are given in Sect. 2). We investigate the whistling properties of this flow configuration using a global stability analysis. In particular, the main objectives of the paper can be summarized as follows:

(i) Characterization of the incompressible (hydrodynamic) mechanism; we apply the classical global stability approach to the Navier-Stokes system, showing the existence of various unstable branches.
(ii) Modeling the effect of compressibility by assuming the cavity as an Helmholtz resonator; we impose a complex spring-like impedance boundary condition on the upper wall of the cavity.
(iii) Validation of the model by using a full compressible stability analysis.

## 2 Geometry Configuration and Governing Equations

The birdcall configuration is a more realistic evolution of the classical hole-tone one. It consists in two successive holes in thick curved plates with the two diameters of similar dimensions. Figure 1 shows the geometry considered in this paper and an example of the mesh used for the computations. This geometry models a real whistle shown in the upper right corner of Fig. 1. In the actual case, the first hole is greater than the second one, whereas the thickness is considered the same for both the plates. More details about the geometrical parameters of the birdcall are reported in Table 1. The birdcall connects two open spaces, whose dimensions are taken sufficiently large in order to guarantee domain size independent results. The mean flow moves from

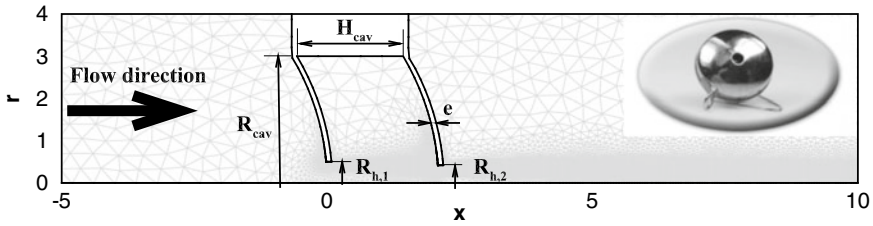


**Fig. 1** Sketch of the birdcall configuration, frame of reference and definition of the main geometrical parameters. An example of computational mesh is also reported in light gray. An example of the real configuration used in this paper is depicted in the upper right corner of the figure

**Table 1** Geometrical parameters of the birdcall. The labels are referred to the one reported in Fig. 1. All the quantities are non-dimensionalized using the diameter of the first hole

| $R_{cav}$ | $H_{cav}$ | $R_{h,1}$ | $R_{h,2}$ | $e$ |
|---|---|---|---|---|
| 3 | 2 | 0.5 | 0.42 | 0.1 |

left to right driven by a pressure difference and it is constrained to pass through the holes, forming a recirculation region into the cavity and free shear layers into the cavity and past the second hole.

Here, we present the theoretical framework for the compressible Navier-Stokes equations: the incompressible formulation can be retrieved just taking the limit $Ma \to 0$. In particular, we assumed an ideal gas with a Prandtl number $Pr = \mu c_p/\kappa$ equal to 0.7, where $c_p$ is the constant specific heat, $\kappa$ is the thermal conductivity and $\mu$ is the dynamic viscosity. Moreover, we suppose that the viscosity and the thermal conductivity don't change with the temperature [6]. Under these assumptions, the compressible Navier-Stokes equations can be written as:

$$\left.\begin{aligned} \partial_t \rho + \mathbf{u}\cdot\nabla\rho + \rho\nabla\cdot\mathbf{u} &= 0 \\ \rho\partial_t\mathbf{u} + \rho\mathbf{u}\cdot\nabla\mathbf{u} + \nabla p - \frac{1}{Re}\nabla\cdot\tau(\mathbf{u}) &= \mathbf{0} \\ \rho\partial_t T + \rho\mathbf{u}\cdot\nabla T + (\gamma-1)\rho T\nabla\cdot\mathbf{u} - \gamma(\gamma-1)\frac{Ma^2}{Re}\tau(\mathbf{u}):\mathbf{d}(\mathbf{u}) - \frac{\gamma}{Pr\,Re}\nabla^2 T &= 0 \\ \rho T - 1 - \gamma Ma^2 p &= 0 \end{aligned}\right\}, \tag{1}$$

where $\gamma$ is the ratio of specific heats (here equal to 1.4), $\rho$ and $T$ are respectively the density and the temperature, $\mathbf{d}(\mathbf{u}) = \frac{1}{2}\left(\nabla\mathbf{u} + \nabla\mathbf{u}^T\right)$ is the strain tensor and $\tau(\mathbf{u}) = [2\mathbf{d}(\mathbf{u}) - \frac{2}{3}(\nabla\cdot\mathbf{u})\mathbf{I}]$ is the stress tensor per unit viscosity. The velocity vector is defined as $\mathbf{u}(x, r, t) = (u_x, u_r)$ where $x$ and $r$ represent the axial and radial coordinates whereas $u_x$ and $u_r$ are respectively the axial and radial velocity components. The equations are non dimensionalized using the diameter of the first hole as length scale, the mean velocity into the first hole $U_m$ as velocity scale and the internal density $\rho_{in}$ and temperature $T_{ext}$ as density and temperature references; the dimensionless

pressure, following Fani et al. [7], is defined as $\frac{p - p_{ext}}{\rho_{in} U_m^2}$. As direct consequence of these choices, the Reynolds number $Re$ and Mach number $Ma$ are defined as:

$$Re = \frac{2R_{h,1}\rho_{in}U_m}{\mu} = \frac{2\dot{m}}{\mu\pi R_{h,1}}, \quad Ma = \frac{U_m}{\sqrt{\gamma RT_{ext}}}$$

where $R$ is the ideal gas constant and $\dot{m}$ the mass flow rate across the first hole. System (1) has to be completed by suitable boundary conditions. In particular, we assume no-slip and adiabatic conditions on the solid walls and appropriate conditions on the axis (see Fabre et. al. [8] for more details). The flow is forced to move through the holes by a pressure jump; thus, we should impose a given pressure on both inlet and outlet. Since the pressure jump is not known a priori, we prefer to impose velocity at the inlet as in Fabre et al. [8]. In particular, we impose the asymptotical Stokes solution provided by Harrison [9] with the density equal to its reference value $\rho_{in}$. The inlet mass flow rate is chosen in order to have a unitary mean velocity into the first hole in the incompressible case; then, we use the same mass flow rate also for the compressible simulation. On the other side, we impose the reference value of the temperature $T_{ext}$ and no stress boundary conditions at the outlet. In this way, the pressure jump across the two holes is automatically provided by the solution of the system (1).

## 3 Global Stability Approach

The main hypothesis of this work is that sound emissions are related to self-sustained oscillations caused by an instability of the flow. Here we use the global stability approach to shade light on this mechanism since it is largely applied in literature to explain self-sustained instabilities [10] of various flow configurations, such ad jets and wakes [11]. In order to tackle the problem, we decompose the total flow field into a steady base flow and a time harmonic perturbation, namely:

$$q(\mathbf{x}, t) = Q_B(\mathbf{x}) + \varepsilon q'(\mathbf{x}) exp(\sigma t), \tag{2}$$

with $\varepsilon \ll 1$. Inserting the ansatz (2) into the Navier-Stokes equations and linearizing, we obtain two sets of PDEs; in particular, we find that the base flow is described by the steady state Navier-Stokes equations whereas the perturbation is governed by the Linearized Navier-Stokes Equations (LNSE). Imposing suitable boundary conditions to the LNSE, we are left with a generalized eigenvalue problem. The arising leading complex eigenvalue $\sigma$ provides important information about the dynamic evolution of the system: if $\Re(\sigma) < 0$ the system is asymptotically stable whereas $\Re(\sigma) > 0$ indicates a system asymptotically unstable. The imaginary part of the eigenvalue, namely $\Im(\sigma) = \omega$, is the frequency of the global mode.

### 3.1 Incompressible Analysis

In the limit of $Ma = 0$, the dynamic evolution of the flow is well described by the incompressible Navier-Stokes equations. As mentioned in the introduction, one of the our aim is to use the incompressible limit ($Ma = 0$) to characterize the dynamics of the birdcall. In this case, system (1) is reduced to the standard incompressible Navier-Stokes equations. As described above, introducing the flow decomposition (2) into the governing equations and linearizing, we obtain two problems. The resulting eigenvalue problem can be written as follow:

$$\left.\begin{array}{r} \nabla \cdot \mathbf{u}' = 0 \\ \sigma \mathbf{u}' + (\mathbf{U}_B \cdot \nabla)\mathbf{u}' + (\mathbf{u}' \cdot \nabla)\mathbf{U_B} + \nabla \mathbf{p}' - \dfrac{\mathbf{1}}{Re}\nabla^{\mathbf{2}}\mathbf{u}' = 0 \end{array}\right\}. \tag{3}$$

This system of equations is completed by imposing a zero velocity on the walls, appropriate boundary conditions on the axis [8] and free-stress boundary conditions both at inlet and outlet.

### 3.2 Modeling the Effect of Compressibility of the Cavity in an "Augmented Incompressible Approach"

The aim of this section is to include the effect of the compressibility by using a simple model coupled to the incompressible equations. In particular, the main hypothesis of this model is that the geometry is acoustically compact, namely the main geometrical parameters of the birdcall (diameter and distance between the two holes) result to be much smaller than the acoustic wavelength: under this hypothesis, in fact, we can retain that the flow is locally incompressible, leading to a constant value of the pressure inside the cavity (and also of the density since we are in the incompressible regime). If the pressure is constant, we can model the cavity as an Helmholtz resonator [12]: in this case we take into account of the compressibility effect imposing a spring-like impedance boundary condition on the upper wall of the cavity rather than a no slip one. The variation of the mass into the cavity can be written, in dimensional form, as [13]:

$$\partial_{t^d} m^d_{cav} = -\rho^d Q^d_{cav} \tag{4}$$

where $m^d_{cav} = \rho^d V^d_{cav}$ and $Q^d_{cav}$ are respectively the mass of the fluid inside the cavity and the flow rate outgoing from the cavity, whereas $V^d_{cav}$ is the volume of the cavity. Note that the superscript $""^d$ refers to dimensional quantities. For an adiabatic and isoentropic thermodynamical system, pressure and density are linked through the following relation:

$$p^d_{cav} = {c^d_0}^2 \rho^d_{cav}, \tag{5}$$

where $c_0^{d\,2}$ is the speed of sound. Using the isoentropic condition (5) in equation (4), applying the non dimensionalization of the variables, and using the Fourier transform for the time derivative, the following equation is obtained:

$$\sigma p_{cav} + \frac{1}{\chi_c} Q_{cav} = 0 \quad \text{with} \quad \chi_c = V_{cav} Ma^2. \tag{6}$$

The coefficient $\chi_c$ can be defined as a compressibility parameter and it is clear that the compressibility effects are influenced both by the Mach number and the volume of the cavity. The unknown terms $p_{cav}$ and $Q_{cav}$ are the augmented variables and they are linked with the incompressible unknown terms through:

$$\left.\begin{aligned} p_{cav} &= \frac{1}{S_{cav}} \int_{S_{cav}} p' \mathrm{d}S \\ Q_{cav} &= \int_{S_{cav}} \mathbf{u}' \cdot \mathbf{n} \mathrm{d}S \end{aligned}\right\}, \tag{7}$$

where $S_{cav}$ is the surface of the upper wall of the cavity. Coupling Eqs. (6) and (7) with the incompressible linearized Navier-Stokes system (3), a generalized eigenvalue problem is obtained: its solution provides information about the stability of the augmented system with the modeled compressibility.

### 3.3 Full Compressible Approach

We also use the full compressible stability analysis in order to check the accuracy of the results obtained with the two previously described approaches. The system of equations governing the stability of the compressible flow reads as:

$$\left.\begin{aligned} \sigma\rho' + \mathbf{U}_B \cdot \nabla\rho' + \mathbf{u}' \cdot \nabla\rho_B + \rho_B \nabla \cdot \mathbf{u}' + \rho' \nabla \cdot \mathbf{U}_B &= 0 \\ \sigma\rho_B \mathbf{u}' + \rho' \mathbf{U}_B \cdot \nabla \mathbf{U}_B + \rho_B \mathbf{u}' \cdot \nabla \mathbf{U}_B + \rho_B \mathbf{U}_B \cdot \nabla \mathbf{u}' + \nabla p' - \frac{1}{Re} \nabla \cdot \tau(\mathbf{u}') &= \mathbf{0} \\ \sigma\rho_B T' + \rho' \mathbf{U}_B \cdot \nabla T_B + \rho_B \mathbf{u}' \cdot \nabla T_B + \rho_B \mathbf{U}_B \cdot \nabla T' + & \\ +(\gamma - 1)\left(\rho' T_B \nabla \cdot \mathbf{U}_B + \rho_B T' \nabla \cdot \mathbf{U}_B + \rho_B T_B \nabla \cdot \mathbf{u}'\right) + & \\ -\gamma(\gamma - 1)\frac{Ma^2}{Re}\left[\tau(\mathbf{u}') : \mathbf{d}(\mathbf{U}_B) + \tau(\mathbf{U}_B) : \mathbf{d}(\mathbf{u}')\right] - \frac{\gamma}{Pr\,Re} \nabla^2 T' &= 0 \\ \rho' T_B + \rho_B T' - 1 - \gamma Ma^2 p' &= 0 \end{aligned}\right\}. \tag{8}$$

## 4 Numerical Methods

We use the finite element method implemented in the open source code FreeFem++ [14] (http://www.freefem.org/) in order to solve the various problems of this paper. The unknown terms have been discretized using a triangular unstructured mesh,

generated by the built-in Bamg routine. We use classical Taylor–Hood elements ($P2-P2-P1$) for the incompressible equations. On the other hand, in the compressible case, we adopt $P2$ elements for the velocity and $P1$ for the other variables, namely pressure, density and temperature. After having obtained the variational formulations of the various problems, matrices of the arising discrete systems have been assembled by FreeFem++ libraries. The nonlinear equations for the base flow have been solved using a classical Newton method: at each iterative step the matrix inversion has been performed using the parallel MUMPS library. As far as the stability problems are concerned, we first use ARPACK library in order to localize the eigenvalues in the complex plain; then, the leading ones have been followed using the inverse iteration algorithm in order to have cheapest computations. In the compressible computation, in order to avoid the unphysical reflections of the acoustic waves from the inflow and outflow boundaries, we use a sponge zone technique combined with a grid stretching in order to assorbe and dissipate the acoustic waves (for more details see Rowley et al. [15]).

## 5 Results

### *5.1 Incompressible Results*

In this section, we report results obtained in the incompressible regime. In particular, Fig. 2 shows the growth rates and the frequencies of the most unstable eigenvalues as function of the Reynolds number. We find the existence of four unstable branches quantized in frequency, which is almost constant with the Reynolds number. At low Reynolds numbers, the dynamic is driven by the first branch ($B1$), with a frequency of $\omega \approx 3.3$; as the Reynolds number increases, the growth rates of the second ($B2$) and then with the third ($B3$) branch become dominant with frequencies respectively of $\omega \approx 5.5$ and $\omega \approx 7.7$. The fourth unstable branch ($B4$), on the other hand, is characterized by a frequency of $\omega \approx 10.2$, and never becomes dominant in term of the growth rate respect to the other ones, almost in the range of Reynolds numbers investigated. Figure 3 depicts the structure of the pressure for the four unstable branches at their critical Reynolds numbers. First, it is possible to observe that at low frequencies the spatial structure of the global modes extends for a longer distance from the birdcall. Secondly, the four different unstable branches are characterized by very different structures between the two holes. The first branch is characterized by one pressure node between the two holes, the second one by two pressure nodes and so on: this means that there is a direct link between the frequency quantization and the pressure oscillations between the two holes [16].

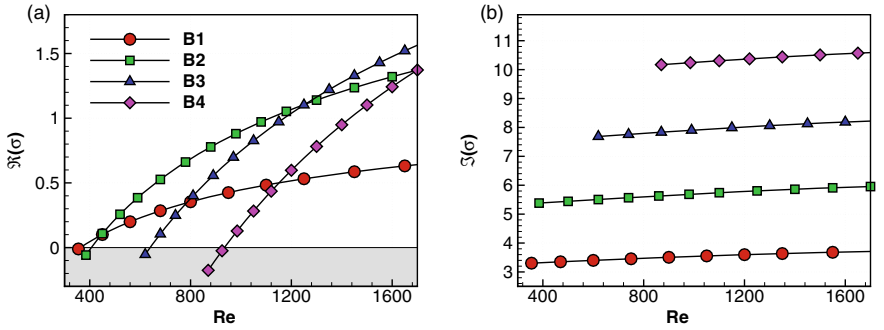


**Fig. 2** **a** Growth rate and **b** frequency of the most unstable modes as function of $Re$. The stable region, namely $\Re(\sigma) < 0$ is filled in gray

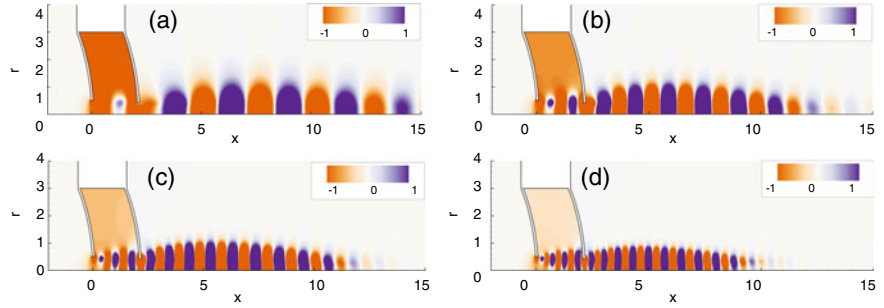


**Fig. 3** Real part of the pressure ($\Re(p')$) for the four unstable branches at the critical Reynolds number: **a** $Re = 363$, $\omega \approx 3.3$; **b** $Re = 406$, $\omega \approx 5.4$; **c** $Re = 639$, $\omega \approx 7.7$; **d** $Re = 934$, $\omega \approx 10.2$

## 5.2 *Effect of Compressibility*

Once characterized the incompressible dynamics, we investigate the effect of the compressibility of the flow. In particular, we compare the full compressible results with the one obtained using the Helmholtz resonator augmented model described in Sect. 3.2, in order to validate it and discuss its range of validity. Figure 4 depicts the growth rates and the frequencies obtained using the augmented model and the full compressible approach at $Ma = 0.05$, within the incompressible results: even if the Mach number is very low, the compressibility seems to have a considerable effect on such kind of flow configuration, as already observed by Yamouni et al. [6]. In particular, we can see that compressibility has a destabilizing effect on the first two unstable branches, in opposition to what happens in the compressible wakes [17]. Moreover, compressible effects tends to reduce the frequency of the unstable modes and this effect is as strong as the frequency gets larger. As can be noted from numerical results, the model well predicts both the growth rates and the frequencies of the unstable modes for the lower branches, namely the branch $B1$ and $B2$, whereas it gives less accurate results for the higher ones. In Fig. 5 we report the comparison

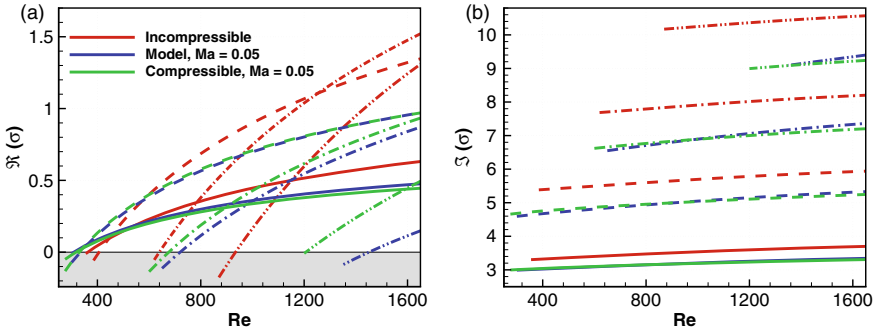


**Fig. 4** **a** Growth Rate and **b** frequency of the most unstable modes as function of $Re$. The red lines are the incompressible results, the blu lines are the model's results whereas the green lines are the full compressible results, both computed at $Ma = 0.05$. The first branch $B1$ is reported with full lines, the second branch $B2$ with dashed lines, the third branch $B3$ with dash–dot lines and the fourth branch $B4$ with dash–double dot lines. The stable region, namely $\Re(\sigma) < 0$ is filled in gray

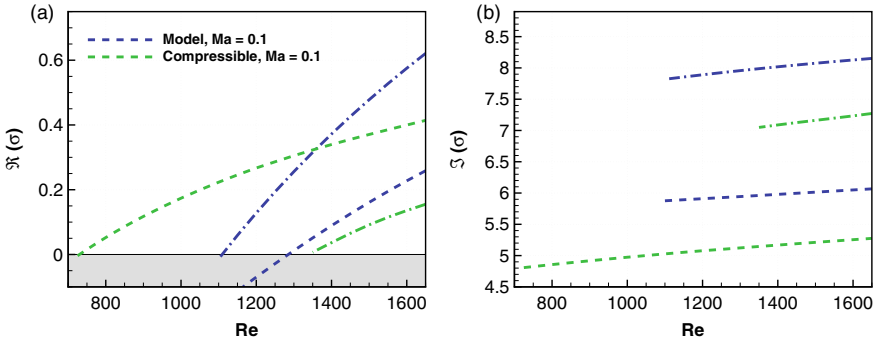


**Fig. 5** Same of Fig. 4 but for $Ma = 0.1$. In these figures we omit the incompressible results

between the model and compressible results at $Ma = 0.1$. We can observe that we don't find any unstable eigenvalues belonging to the branch $B1$, almost in the range of Reynolds number investigated. Moreover, as far as the other branches goes, it easy to note that the model is not able to predict the results of the full compressible simulations.

The prediction capability of the model is strictly related to the acoustic wavelength:

$$\lambda_{ac} = \frac{2\pi}{\omega}\frac{1}{Ma}. \tag{9}$$

In fact, the main hypothesis of the model is the local incompressibility of the flow, meaning that the acoustic wavelength must be greater than the characteristic length-scale of the considered geometry. However, from Eq. (9) it is easy to verify that the acoustic wavelength decreases when the Mach number and the frequency increase

and this explains why the model fails at high frequencies and larger Mach numbers. For the geometry considered in this paper, the greater characteristic lengthscale is the diameter of the cavity, namely $D_{cav} = 2R_{cav}$ (see Fig. 1; Table 1). Numerical simulations confirm that the model is able to provide accurate results until $\lambda_{ac} > 2D_{cav} = 12$ for the geometry considered here: if such relation does not hold, the acoustic waves are able to penetrate into the cavity and the pressure cannot be considered constant anymore contradicting the hypothesis of the model.

Finally, in Fig. 6, we depict the real part of the pressure of the global modes computed using the compressible equations. In particular, in Fig. 6a we report $\Re(p')$ for $Re = 800$, $Ma = 0.05$ and $\omega \approx 4.95$, a case where the model returns good results, as it is possible to verify from Fig. 4. In particular, it is possible to observe that the acoustic waves, propagating into the far field as spherical waves, have a wavelength equal to $\lambda_{ac} \approx 25$, so that the relation of validity of the model is respected. In Fig. 6a it is also shown the zoom of the near field, with a different color scale, showing the same pressure patterns already observed for the incompressible mode and a constant pressure into the cavity. In Fig. 6b, instead, we report $\Re(p')$ for $Re = 1400$, $Ma = 0.1$ and $\omega \approx 7.1$. In this case, the acoustic wavelength is equal to $\lambda_{ac} \approx 8.85$ and the model is outside its range of validity, as it is possible to verify from Fig. 5. Here, we can observe that pressure is not constant anymore into the cavity. Moreover, also the acoustic directivity seems to change when the acoustic wave is able to penetrate into the cavity, as largely reviewed by Yamouni et al. [6].

### 5.3 An Example of Practical Application

In this last paragraph we try to set up a real experiment, that is the next step of our research. In the previous paragraph, we varied both the Reynolds and the Mach numbers independently, in order to test the augmented model and define its range of validity. Actually, if we want to simulate a real situation, this is not true, since the Reynolds and Mach numbers result to be linked, as shown by Fabre et al. [18]. In particular, the Mach number results to be proportional to the Reynolds number:

$$Ma = \frac{U_m^d}{c_0^d} = \underbrace{\frac{\nu^d}{D_{h,1}^d c_0^d}}_{K_p} Re. \tag{10}$$

In order to simulate the experiment, we use the measures of a real birdcall depicted in the upper right corner of Fig. 1. In particular, the dimensional diameter of the first hole results to be equal to $D_{h,1}^d = 3\,mm$ whereas the air temperature is hypothesized to be $T^d = 300K$: the other properties of the air have been obtained from a standard table, leading to a value of $K_p \approx 1.5 \cdot 10^{-5}$. The range of Reynolds number investigated here is $Re \in [300 - 1650]$ leading to a range of Mach number $Ma \in [0.004 - 0.025]$. The use of the model rather than the full compressible simulation is here justified,

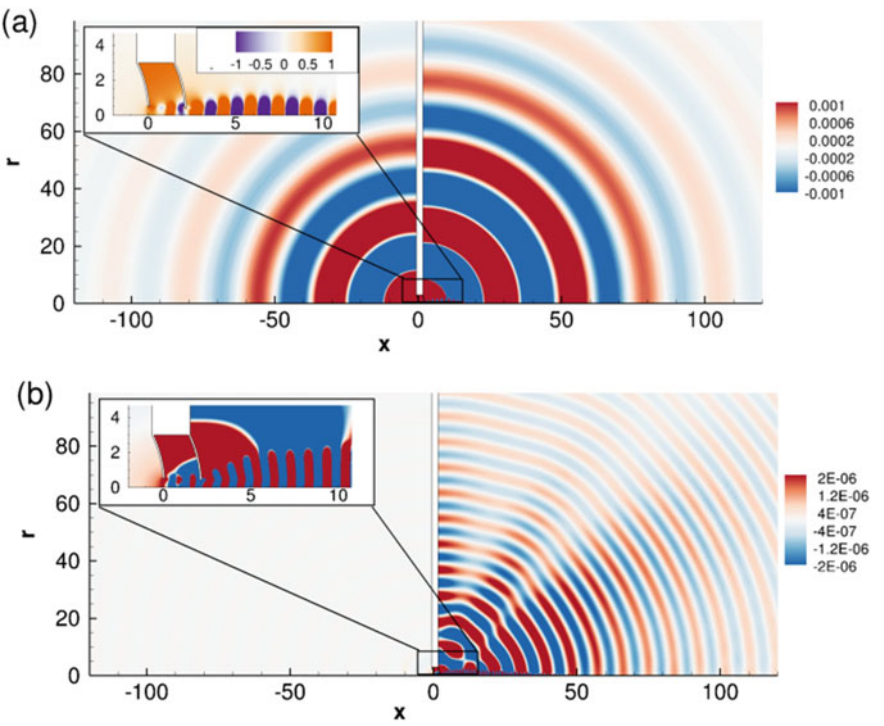


**Fig. 6** Real parto of the pressure global modes $\Re(p')$ for: **a** $Re = 800$, $Ma = 0.05$ and $\omega \approx 4.95$; **b** $Re = 1400$, $Ma = 0.1$ and $\omega \approx 7.1$

at least for this specific geometry, by three main statements: first, the higher Mach number is small enough to have a good accuracy of the model, as demonstrated in the previous section; secondly, the full compressible simulation at very low Mach numbers can result very expansive since the acoustic wavelength grows, requiring very big domains with very long sponge zones; finally, the model has a very fast computation respect to the full compressible case, since we don't need sponge regions. In Fig. 7 we report the comparison between the incompressible results and the one obtained with the augmented model. One can note that for the first two lower branches results are very slowly affected by compressibility, both in term of growth rate and frequency and the incompressible approximation is able to give good results. On the other hand, the effects of the compressibility are larger for the branches three and four. However, for all the unstable branches, we can observe two common features: (1) the compressibility has a destabilizing effect for this flow configuration; (2) the frequency is usually smaller than it is in the incompressible case. This effect is more enhanced when the Reynolds (and consequently the Mach number) increases.

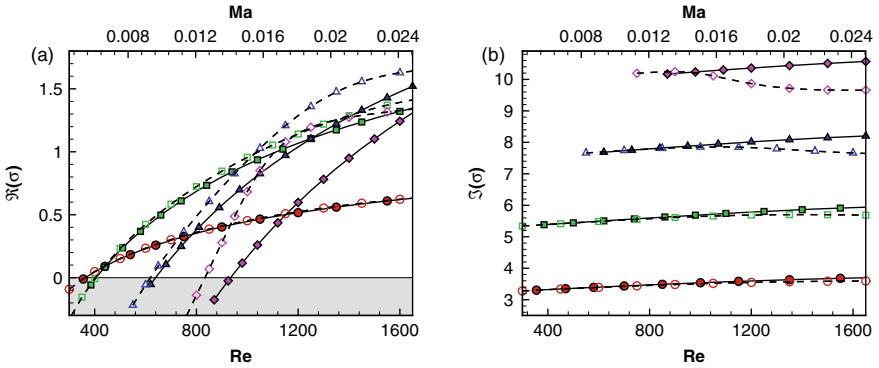


**Fig. 7** **a** Growth Rate and **b** frequency of the most unstable modes as function of *Re* and *Ma*. The legend is the same of Fig. 2: the full symbols with solid lines are the incompressible results whereas the empty symbols connected by dashed lines are the compressible augmented ones. The stable region, namely $\Re(\sigma) < 0$ is filled in gray

## 6 Conclusions

In this paper we investigate the whistling properties of a birdcall using the global stability approach. In particular, we first use a full incompressible approach in order to characterize the dynamic of such kind of flow configuration. We find four unstable branches which are quantized in frequency. The associate pressure field of the leading global modes shows pressure oscillations between the two holes and such pattern is conserved along each branch: in fact the first branch has only one pressure node, the second one is characterized by two pressure nodes and so on.
Once the incompressible dynamic has been characterized, we have considered the effect of the flow compressibility. In particular, we have first modeled the cavity between the two holes as an Helmholtz resonator. Then, we have performed a full compressible stability analysis in order to test the model and figure out the range of validity of both the incompressible approximation and the augmented model. We have found that the compressibility has an important effect on the stability of such kind of system, in term of both growth rate and frequency: in general, the compressibility reduces the frequency of the global modes, for almost all low Mach numbers investigated.

Numerical results have shown that the model is able to give accurate results only when the acoustic wavelength is greater that two cavity diameters, namely $\lambda_{ac} > 2D_{cav}$, almost for the configuration investigated in this paper.

The last part of the paper, finally, is about a practical application: in fact we have simulated a real experiment, in which the Reynolds and Mach number are proportional through a parameter that is function of the real geometry and air conditions. We have considered the effect of the compressibility using the model since the relation of validity is respected. We have found that, in a real experiment, the incompressible

approximation gives good results for low Reynolds (and Mach) numbers and low frequencies, whereas the effect of compressibility is relevant at higher frequencies and Reynolds (and Mach) numbers.

## References


1. Fabre, D., Bonnefisa, P., Charru, F., Russo, S., Citro, V., Giannetti, F., Luchini, P.: Application of Global Stability Approaches to Whistling Jets and wind Instruments. In Proc, ISMA (2014)
2. Helmholtz, H.: The theory of sound. Nature **17**(430), 237 (1878)
3. Lord Rayleigh. The theory of sound, 1945
4. Bouasse, H.: Instruments à vent. Impr, Delagrave (1929)
5. Henrywood, R.H., Agarwal, A.: The aeroacoustics of a steam kettle. Physics of fluids **25**(10), 107101 (2013)
6. Yamouni, S., Sipp, D., Jacquin, L.: Interaction between feedback aeroacoustic and acoustic resonance mechanisms in a cavity flow: a global stability analysis. J. Fluid Mech. **717**, 134–165 (2013)
7. Fani, A., Citro, V., Giannetti, F., Auteri, F.: Computation of the bluff-body sound generation by a self-consistent mean flow formulation. Phys. Fluids **30**(3), 036102 (2018)
8. Fabre, D., Longobardi, R., Bonnefis, P., Luchini, P.: The acoustic impedance of a laminar viscous jet through a thin circular aperture. J. Fluid Mech. Under Rev
9. Harrison, W.J.: The pressure in a viscous liquid moving through a channel with diverging boundaries. Proc. Cambridge Phil. Soc. **19**, 307–312 (1919)
10. Citro, V., Giannetti, F., Pralits, J.O.: Three-dimensional stability, receptivity and sensitivity of non-newtonian flows inside open cavities. Fluid Dyn. Res. **47**(1), 015503 (2014)
11. Citro, V., Tchoufag, J., Fabre, D., Giannetti, F., Luchini, P.: Linear stability and weakly nonlinear analysis of the flow past rotating spheres. J. Fluid Mech. **807**, 62–86 (2016)
12. Bonnefis, P.: Etude theorique et numerique d'un jet sifflant. Master's thesis, IMFT (2014)
13. Fry, B.: Etude theorique, numerique et experimentale d'un jet sifflant. Master's thesis, IMFT, UPMC, 2016
14. Hecht, F.: New development in freefem++. J. Numer. Math. **20**(3–4), 251–265 (2012)
15. Rowley, C.W., Colonius, T., Basu, A.J.: On self-sustained oscillations in two-dimensional compressible flow over rectangular cavities. J. Fluid Mech. **455**, 315–346 (2002)
16. Matsuura, K., Nakano, M.: A throttling mechanism sustaining a hole tone feedback system at very low mach numbers. J. Fluid Mech. **710**, 569–605 (2012)
17. Meliga, P., Sipp, D., Chomaz, J.M.: Effect of compressibility on the global stability of axisymmetric wake flows. J. Fluid Mech. **660**, 499–526 (2010)
18. Fabre, D., Marragou, S., Longobardi, R., Lo Jacono, D., Bonnefis, P., Fry, B., Citro, V., Giannetti, F., Luchini, P.: The whistling jet instability: Experimental investigation and global stability modelling of a bird- call. Ercoftac Sig. 33, La certosa di Pontignano (Siena),19-21 June 2017

# Rotating Effects, Fish Motion, Swimmers, Energy Harvesting

# Simultaneous Energy Harvesting Using Dual Piezo-Solar Devices


**Mostafa R. A. Nabawy, Jorge Silva-Leon, Joseph O'connor, Andrew Kennaugh, Andrea Cioncolini, and Alistair Revell**

**Abstract** This paper aims to develop a novel concept for energy harvesting via flexible inverted flags combining photovoltaic cells with piezoelectric material. Using technology currently available off-the-shelf, we have built dual piezo-solar harvesters made of polyvinylidene fluoride (PVDF) piezoelectric elements combined with mini solar panels of different sizes. Dynamics and power generation experimental measurements were collected for the flags when simultaneously subjected to both wind and light sources. This allowed for an improved understanding of the effect of adding the solar panels on the motion and power generation characteristics. Additionally, flapping amplitude and frequency responses are confirmed using a lattice Boltzmann-immersed boundary numerical method. Results indicate a significant improvement in the capability of energy harvesting compared to isolated single piezoelectric devices. As such, we anticipate a significant impact of dual piezo-solar energy harvesting devices on a range of applications where remote power generation is needed.

**Keywords** Energy harvesting · Dynamics · Piezoelectric · Solar · Fluid structure interaction · Lattice Boltzmann

M. R. A. Nabawy · J. Silva-Leon · J. O'connor · A. Kennaugh · A. Cioncolini · A. Revell (✉)
Department of Mechanical, Aerospace and Civil Engineering, The University of Manchester, Manchester M1 3BB, UK
e-mail: alistair.revell@manchester.ac.uk

M. R. A. Nabawy
Aerospace Engineering Department, Faculty of Engineering, Cairo University, Giza 12613, Egypt

J. Silva-Leon
Facultad de Ingeniería en Mecánica y Ciencias de la Producción, Escuela Superior Politécnica del Litoral, ESPOL, Campus Gustavo Galindo Km 30.5 Vía Perimetral, P.O. Box 09-01-5863, Guayaquil, Ecuador



M. Braza et al. (eds.), *Advances in Critical Flow Dynamics Involving Moving/Deformable Structures with Design Applications*, Notes on Numerical Fluid Mechanics and Multidisciplinary Design 147,
https://doi.org/10.1007/978-3-030-55594-8_24

## 1 Introduction

Energy harvesting is the process of reusing wasted energy from a system to generate useful power. Within small scale applications, piezoelectric devices are recognized as one of the most promising solutions to convert wasted energy into electricity. Energy harvesting from base vibrations/excitation using piezoelectric elements has received most of the attention (e.g. [1–4]); however, the interest in energy harvesting from wind excitation has also increased significantly. Whilst the literature contains a remarkable number of theoretical and numerical studies (e.g. [5–11]), for compactness, we will only focus herein on experimental contributions which are consistent with the approach adopted in our present study.

Among the different configurations used for energy harvesting from wind excitation, the inverted cantilever flag configuration (clamped downstream) has recently received more attention due to its inherent more unstable nature compared to the usual upstream-clamped cantilever. This idea sparked several fundamental studies on the motions and dynamics of inverted flags (e.g. [12–14]). In particular, Kim et al. [12] performed an experimental study on the dynamics of an inverted flag made of polycarbonate in wind and water tunnels (set up in a way that the sheet does not bend due to gravity). They focused on identifying the modes of motion and compared them with conventional flag configurations. The inverted flag showed the following modes as the wind speed was increased: (1) straight (vibrates), (2) large-amplitude flutter, (3) fully deflected to one side (vibrates). Notably, the motion amplitude was much larger than that achieved in conventional flag configurations. Moreover, the inverted flag required less flow velocity for achieving a self-excited motion compared to conventional flags.

Cossé et al. [13] reported on the effects of angle of attack and aspect ratio on the inverted flag dynamics. For the aspect ratio study, they found that there is a critical height under which the flag does not enter into the flapping mode when increasing the wind speed. As the height of the flag is increased, the range of wind speed at which the flag flaps becomes wider. For the angle of attack study, they found that at 0° the transition to the flapping mode occurred abruptly. When oriented at 10°, the transition occured gradually. At 20° the transition occurred earlier (lower wind speed) but reached lower amplitudes compared to the other cases of smaller angles of attack. Most recently, an array of PVDF (polyvinylidene fluoride) elements in an inverted flag configuration was considered [14]. The effect of the flag's geometric parameters on the flapping behaviour and power generation was investigated. Moreover, the work demonstrated the capability of harvesting energy from the ambient wind to power a temperature sensor.

Several experimental studies considering energy harvesting from wind excitation using other configurations have also been presented. For example, a PVDF flapping-leaf taking an 'L' shape has been reported [15, 16]. An *array* of PVDF elements mimicking artificial grass has also been proposed [17]. Notably, within these wind excitation energy harvesting experiments the used piezoelectric material was PVDF.

This is because of its favourable flexibility, robustness and power generation characteristics. Vatansever et al. [18] confirmed this through investigating the effect of material selection on the harvested power of polymer based harvesters utilising PVDF versus ceramic based harvesters when subjected to side wind or rain drop excitations. At a wind speed of 10 m/s, they showed that the PVDF based harvester has a power density that is at least 16 times higher than that of unimorph and bimorph ceramic based harvesters.

The combined energy harvesting from piezoelectric and solar devices has not been considered seriously. To the best of our knowledge, this concept has only been touched upon by Erturk and Delporte [19] but for a cantilever piezoelectric-solar membrane in a still fluid where from in-air measurements they were able to obtain enough energy for providing thrust for a 'mechanical fish'. However, the capabilities of this synergetic configuration are yet to be explored for an inverted cantilever flag located in a flowing fluid. Moreover, since generation from a single piezoelectric device is expected to be low, a novel approach would be to embed the piezoelectric flag with photovoltaic cells, and harvest energy from both wind and solar sources within the same device. As such, the primary research objective of this work is to investigate the potential for the simultaneous harvesting of energy from both piezoelectric and solar elements during dynamic operation of an inverted-flag device.

## 2 Materials and Methods

### *2.1 Piezo-Solar Harvesters*

The configuration of a piezoelectric harvester embedded with photovoltaic panels (so-called "piezo-solar") is shown in Fig. 1a. The proposed piezo-solar harvester is typically made of a number of flexible PVDF piezoelectric elements with two mini solar panels attached at the tips—one on each side. The PVDF elements used are

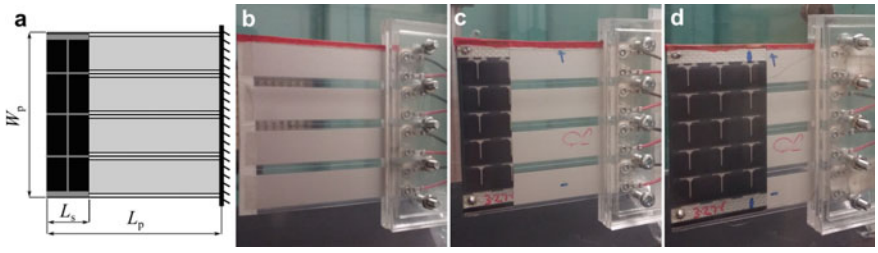


**Fig. 1** Configuration of the piezo-solar flags used in this study. A flag is made of four flexible PVDF elements and two mini solar panels attached to both sides at the tip. **a** The dimensions used to describe the geometry of a flag. **b–d** The three flags investigated in this study—no solar ($CR = 0$), half solar ($CR = 0.32$) and full solar ($CR = 0.64$) respectively

supplied from TE Connectivity-model LDT2-028K/L [20]. The maximum dimensions for one PVDF element are 73 mm × 16 mm × 0.205 mm (length × width × thickness). The PVDF properties including density, Young's modulus and Poisson's ratio are 1780 kg/m$^3$, 3 GPa and 0.34, respectively [21]. The mini solar panels used are supplied from Powerfilm, and are capable of generating 22 mA @ 3 V [22]. The mass of one complete solar panel is 0.7 g and has dimensions of 64 mm × 36.5 mm × 0.2 mm (width× length× thickness).

The configuration of an inverted flag can be mainly described with three variables, Fig. 1a. The first variable is a dimensional one and is selected as the overhang length of the flag (length from the fixed support to the free tip, $L_p$). The two other variables are non-dimensional variables and these are selected as the flag aspect and coverage ratios. The aspect ratio, *AR*, is the flag's length to width ratio, $AR = L_p/W_p$, whereas the coverage ratio, *CR*, is the ratio of the solar panel area to the total area of the PVDF elements. For our purposes, the flags are sized so that the total width of the PVDF elements is equal to the width of a solar panel; hence, the coverage can be expressed as $CR = L_s/L_p$.

In the current study, our focus is directed towards understanding the effect of the coverage ratio, *CR*, on the flag dynamics and hence power generation. As such, the flag overhang length, $L_p$, and aspect ratio, *AR*, are fixed. Here we use an $L_p$ value of 57 mm and an *AR* value of 0.9. The coverage ratios, *CR*, investigated herein are 0 (so-called "No Solar"), 0.32 (so-called "Half Solar"), and 0.64 (so-called "Full Solar"). The configurations of the three flags investigated are shown in Figs. 1b–d.

## 2.2 Experimental Setup

The experimental set-up of the present study is shown in Fig. 2. The wind tunnel used is an open-circuit with octagonal cross section (height and width of 350 mm). The velocity profile across the wind tunnel is uniform to within 1%, whilst the turbulence intensity is on average 0.6% within the range of free stream velocities from 1.5 to 30 m/s of interest here. The boundary layer extended less than 5 mm from the walls of the wind tunnel at the lowest speed setting employed. The flags were clamped downstream to a vertical pole located at half width of the test section, thus leaving free the upstream side of the flag (i.e. inverted flag configuration). The fixation of the harvesters was achieved using a mounting system manufactured from laser cut acrylic. The flag mount was designed to hold the flag in a sandwich arrangement with a pair of acrylic plates acting as a clamp to hold the flag itself. LED lights were located on both sides of the wind tunnel test section, perpendicular to the rest position of the flag (aligned to the flow direction). The light intensity at the flag was set to 1.8k Lux measured with a portable light meter. The ambient conditions during the tests were 293 K and 1 atm.

We applied contactless, in-house developed, experimental capabilities for the optical tracking of flexible structures in flow [23, 24] in order to characterize the dynamic response of the devices to a range of conditions. At each wind speed the

motion of the flag was recorded via a digital camera (LUMIX DMC-FZ200) at 200 frames per second, located on top of the wind tunnel. In order to help with the detection of the shapes of flags, a thin red paper tape was added to the upper border of the harvesters (Fig. 1). The videos were post-processed with the Image Processing Toolbox in Matlab (www.mathworks.com). The position of the flag at each instant was defined by the angle described between the free and the fixed end. Locally, the flags possess a variable curvature when deflected, therefore our definition of the angular position gives a representative measure of the whole flag. The frequency of motion was then obtained by applying a FFT to the time series of the angular position.

The power generated from the piezo-solar harvesters was collected and processed through LabVIEW 2017 and the data was gathered through a National Instruments NI-USB-6225 external DAQ device. In order to collect the data from the individual solar and piezo devices, separate circuits were built using prototyping breadboards that allowed circuit changes to be made quickly. The same basic circuitry was used for both devices; however, due to the different electrical outputs of the individual devices the individual circuits differed. Note that the voltage measurement range of the DAQ device was limited to $\pm 10$ V, whereas the voltage output of the piezo devices exceeded that. Hence, to provide a voltage that could be measured a number of equal value resistors were used in series and the voltage drop across one of them was used to measure both the current through the circuit and the total voltage drop, by multiplying the individual voltage drop by the number of resistors. For the solar panels, the same

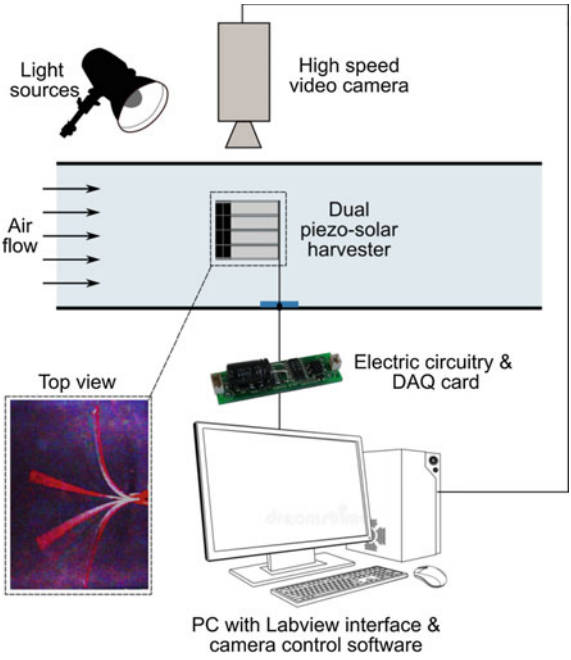


**Fig. 2** Experimental set-up used to characterise the dynamics and power generation from the flags subjected to wind and light sources

circuitry principle was adopted, but with the voltage output being less than 10 V only 2 resistors were needed, one to provide a voltage drop for the current measurement and another potentiometer to provide the correct load to maximise the power output.

The data acquisition program was written as a VI in LabVIEW 2017 using the standard DAQ-mx library. This program gathered, saved and displayed the data with some processing to allow an immediate impression of the power generated to be seen and to allow the load resistance to be set to give the highest power output. The sampling rate was set at 1000 samples per second to allow sufficient resolution of data through a flapping cycle for any particular flapping characteristics, e.g. hysteresis, to be seen.

## *2.3 Numerical Solver*

Numerical simulations are employed to allow detailed analyses of the flow-structure interactions. A partitioned approach is adopted, whereby the fluid and structural dynamics are handled via their own separate field solvers. The lattice Boltzmann method [25], an alternative to traditional Navier-Stokes-based CFD solvers, is employed to solve the fluid dynamics. The main advantage of this approach is its amenability to parallel implementation, as well as the regular square lattice which aids with the solver coupling. A corotational finite element method is adopted to solve the structural dynamics. Nonlinear large deformations are handled via a Newton-Raphson iteration scheme and second-order time integration is achieved via the implicit Newmark scheme.

The immersed boundary method [26] is used to couple the separate field solvers. This approach allows the fluid and structure to be solved on their own separate grids and dictates the transfer of information between them. This simplifies meshing and facilitates large deformations of the structure. To ensure stability, a block Gauss-Seidel coupling scheme is adopted [27], whereby the field solvers are iterated over within the time step until the interface conditions are satisfied. To accelerate the convergence of these iterations, a dynamic relaxation factor is used to relax the displacements of the structure after each iteration [27].

The strongly coupled fluid-structure interaction model is capable of handling the large nonlinear deformations associated with the inverted flag configuration. Euler-Bernoulli beam elements are used to model the structure, which limits the present model to structures with large length-to-thickness ratios. However, for the present case, this is an acceptable assumption. The variation in thickness across the flag, associated with the presence of the solar panel, is accounted for in the structural solver. However, the immersed boundary, which is the geometry that the fluid ‘sees’, is represented as a line. This means the variation in thickness is not accounted for in the fluid solver. However, it is unlikely that this will have a significant impact on the resulting flow field.

The numerical simulations were set up to match the experimental conditions. However, to reduce computational expense, the kinematic viscosity was increased by

three orders of magnitude, thus decreasing the Reynolds number proportionally. This simplification has been used in multiple previous works for similar problems whilst still capturing the main characteristics of the instability [28, 29]. Furthermore, since the deformation is mainly two-dimensional, 2D simulations were deemed appropriate. To promote the onset of any instabilities, the flag was initialised with a small transverse displacement (1% of its length). After the initial transient, the simulations were run for approximately 20 flapping periods.

# 3 Results

## *3.1 Flag Dynamics*

Flapping dynamics results obtained from wind tunnel measurements for the piezo-solar harvester configurations are shown in Fig. 3. The presence of Limit-Cycle Oscillations (LCO) is evident at a good range of speeds. At conditions exhibiting this dynamical state, the flapping is a symmetrical large-amplitude motion, and the flag is bent from one side to the other in a sustained fashion. In fact, the angular position time series showed a sinusoidal waveform. The tip mass effect of the solar panels on the harvester dynamics is evident from Fig. 3. It can be seen that adding the solar panels allowed larger angular span for the same wind speeds within the LCO window. The added mass also reduced the required wind speed for onset of vibration and for large-amplitude motion. The maximum angular spans were 172° and 187° at 9.4 and 9 m/s for the No Solar and Full Solar cases, respectively. In all cases, flags cease flapping at around 10 m/s. Finally, as expected, the frequency of oscillation within the limit cycle window decreased from around 6.9 Hz to 4.7 Hz with the increase of tip mass.

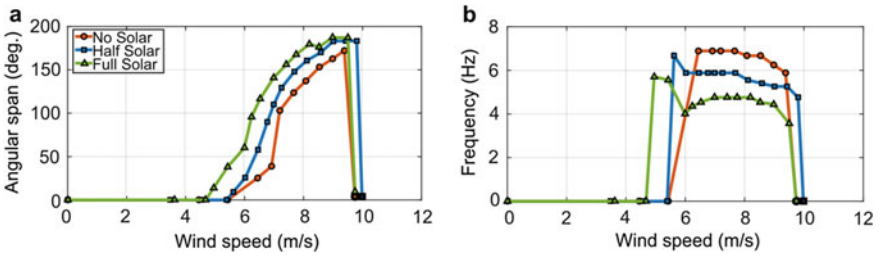


**Fig. 3** Dynamics of inverted flags. **a** Angular span of motion versus air flow speed. **b** Frequency of the flags versus air flow speed

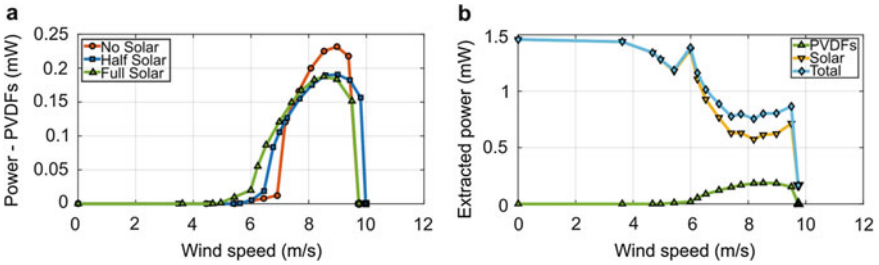


**Fig. 4** Power generation from inverted flags under wind excitation. **a** RMS power generated from the 4 PVDF elements. **b** Illustration of the expected total extracted power from the harvester including the contributions from the 4 PVDF elements and the 2 full solar panels @1.8k Lux

## *3.2 Power Generation*

Figure 4 shows the power generated from the flags under investigation. Optimal load resistances that allow peak power generation were identified. Note that the power values for the PVDF elements are calculated based on the root mean square (RMS) value of the measured voltage. On the other hand, the solar power levels shown are the average values of power generated. Noticeably, Fig. 4b shows that the power generation from the solar panels decreases within the LCO window. This is due to the non-uniform lighting exposure during the flapping excursions as well as the possible flickering from the LED lights. A representation of the total power generation is also shown in Fig. 4b. This is based on addition of the RMS power value from the PVDF elements to the average power value from the solar panels. Within the LCO window, it could be seen that the total power generation from the harvester is enhanced due to the extra power boosting from the solar panels.

## *3.3 Numerical Simulations*

Figure 5 compares the flapping angular span and frequency from the numerical simulations against the experimental measurements for both the No Solar and Full Solar cases. Overall, the agreement is good; the location and extent of the instability is predicted reasonably well by the numerical model and the amplitudes and frequency are comparable. However, there is a noticeable difference in the critical flow velocity, particularly for the No Solar case. This can possibly be explained by 3D effects in the experiment, due to the finite span of the flag, which have been shown to increase stability in the conventional flag configuration [30]. Furthermore, the numerical model does not capture the initial dynamic mode exhibited at low flow velocities in the Full Solar case. The shift in frequency measured in the experiment in this region suggests a different driving mechanism for the instability, compared to the flapping motion exhibited at higher flow velocities. This can possibly be explained by

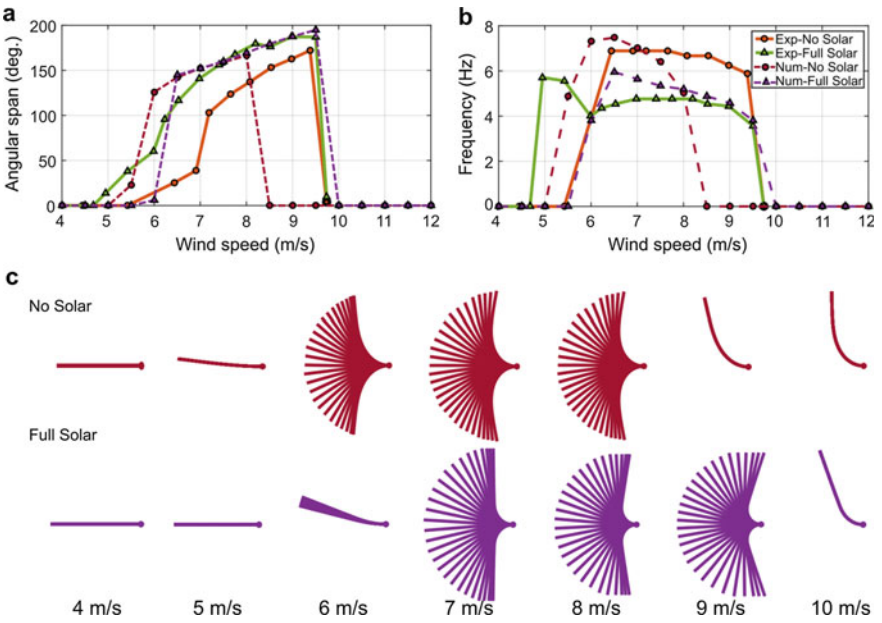


**Fig. 5** Comparison of numerical solver results against experimental measurements. **a** Angular span motion versus air flow speed. **b** Frequency of the flags vs air flow speed. **c** Example flapping profiles from numerical simulation at various wind speeds

the discontinuity in the geometry due to the solar panels; whilst the structural solver accounts for this discontinuity, the fluid solver does not. However, further work is required in this area to fully understand the onset of this higher frequency motion and why it is not captured by the numerical model.

Figure 5c also shows the flapping profiles of the flag for both the No Solar and Full Solar cases. Whilst the critical flow velocity for each state is different between the two cases, both exhibit a transition from a static zero-deflection state, through small-amplitude and large-amplitude flapping states, and finally a large-deflection static state. Furthermore, in the Full Solar case, the bending deformation is localised towards the root of the flag, with very little bending towards the tip (due to the stiffening effect of the solar panels). This will have implications in terms of power generation from the PVDFs in this region, and may explain the lower power output from the PVDF elements within the Full Solar configuration seen in Fig. 4a.

## 4 Discussion and Conclusions

The dual piezo-solar harvester presented herein proved to be an attractive concept and allowed for a noticeable advancement in the performance of flexible inverted flag

harvesters. The addition of solar panels to the flexible piezoelectric PVDF elements enabled two main features. First, the solar panels acted as tip masses; hence, they widened the operational range of the PVDF elements allowing more controllability on the characteristics of flapping motion: It was shown that the inclusion of solar panels of different sizes had an effect on the flapping amplitudes and frequencies of operation which in turn had a direct effect on the power generation characteristics of the flag. Second, the solar panels—being themselves a device for energy harvesting—allowed for boosting the amount of power that could be generated from a flag without significant concerns on volume or cost.

To assess the performance of the presented concept, Table 1 provides a comparison against other concepts available in the literature. Note that for convenience, the comparison here is only limited to previous studies that employed PVDF elements within a wind tunnel set-up. However, the layout of the flag against the flow varies from one case to another. It could be seen that the power density of our 4 PVDF elements alone is relatively high. More importantly, the addition of the solar panels proved to be an efficient way to boost the power density of the device. Clearly, for the lab set-up conditions measured in this study there was a noticeable improvement in power density; however, if a 100% sun condition is assumed, the power density jumps to unprecedented levels where the contribution from the solar panels becomes dominant.

There is potential for more improvements within the current concept to achieve better performance. For example, inclusion of a substrate (e.g. metal shim) would

**Table 1** Comparison of power generation and wind speed for harvester concepts relying on PVDF elements

| Configuration | PVDF | Power density ($mW/cm^3$) | Wind speed (m/s) | Ref. |
|---|---|---|---|---|
| Long sample—side flow | LDT4-028K/L | 0.16 | 10 | [18] |
| L shape device—cross flow | LDT2-028K/L | 0.871 | 8 | [16] |
| Artificial grass; 6 PVDFs as an inline array one behind the other—side flow | LDT2-028K/L | 0.0051 | 7 | [17] |
| Inverted flag—4 PVDFs stacked beside each other (no solar) | LDT2-028K/L | 0.27 | 8.5 | Current |
| Inverted flag—4 PVDFs stacked beside each other with 2 solar panels @ 1.8k Lux | LDT2-028K/L | 0.48 | 8.5 | Current |
| Inverted flag—4 PVDFs stacked beside each other with 2 solar panels @ 100% sun | LDT2-028K/L | ~79 | Not relevant | Current |

decrease the observed hysteresis effects. A drawback of the piezo/solar flag paradigm is a memory effect (nonlinearity) which prevents the flag to resume its flapping motion whenever it has been deflected totally to one side at high wind speeds. It was observed that these flags resumed their flapping motion only after having reduced enough the wind speed, nearly down to the critical onset of flapping motion. This results in a diminished window of operative wind speeds. However, adding a metallic substrate to the flag is expected to minimise these hysteresis effects. Moreover, addition of a metal substrate can allow more flexibility in controlling the flag aspect ratio through increasing the length of the flag in a more systematic fashion. Note that the current study showed the possibility of controlling the dynamics of the flags using different solar panel sizes. However, we anticipate a wider controllability of the operation window of these flags through varying the aspect ratio.

In summary, results on flapping dynamics show that the dual piezo-solar flag is capable of exhibiting limit-cycle oscillations, and preliminary measurements of produced power indicate a significant improvement in the capability of energy harvesting compared to isolated single piezo-devices. Hence, we anticipate crossover impact of dual piezo-solar energy harvesting devices within a range of sectors where remote power is needed (e.g. for autonomous sensing, smart structures etc.).

**Acknowledgements** The financial support of BAE Systems is gratefully acknowledged. The technical support of Amir Rezai and Matthew Stevens from BAE Systems-Air is gratefully acknowledged.

## References

1. Erturk, A., Inman, D.J.: An experimentally validated bimorph cantilever model for piezoelectric energy harvesting from base excitations. Smart Mater. Struct. **18**, 025009 (2009)
2. Renno, J.M., Daqaq, M.F., Inman, D.J.: On the optimal energy harvesting from a vibration source. J. Sound Vib. **320**, 386–405 (2009)
3. Stanton, S.C., Erturk, A., Mann, B.P., Inman, D.J.: Nonlinear piezoelectricity in electroelastic energy harvesters: modeling and experimental identification. J. Appl. Phys. **108**, 074903 (2010)
4. Abdelkefi, A., Najar, F., Nayfeh, A.H., Ayed, S.B.: An energy harvester using piezoelectric cantilever beams undergoing coupled bending–torsion vibrations. Smart Mater. Struct. **20**, 115007 (2011)
5. Doaré, O., Michelin, S.: Piezoelectric coupling in energy-harvesting fluttering flexible plates: linear stability analysis and conversion efficiency. J. Fluids Struct. **27**, 1357–1375 (2011)
6. Michelin, S., Doaré, O.: Energy harvesting efficiency of piezoelectric flags in axial flows. J. Fluid Mech. **714**, 489–504 (2013)
7. Hobeck, J.D., Inman, D.J.: A distributed parameter electromechanical and statistical model for energy harvesting from turbulence-induced vibration. Smart Mater. Struct. **23**, 115003 (2014)
8. Nabawy, M.R.A., Crowther, W.J.: Dynamic electromechanical coupling of piezoelectric bending actuators. Micromachines **7**, 12 (2016)
9. Nabawy, M.R.A., Parslew, B., Crowther, W.J.: Dynamic performance of unimorph piezoelectric bending actuators. Proc. Inst. Mech. Eng. I: J Syst. Control Eng. **229**, 118–129 (2015)
10. Shoele, K., Mittal, R.: Flutter instability of a thin flexible plate in a channel. J. Fluid Mech. **786**, 29–46 (2016a)

11. Shoele, K., Mittal, R.: Energy harvesting by flow-induced flutter in a simple model of an inverted piezoelectric flag. J. Fluid Mech. **790**, 582–606 (2016b)
12. Kim, D., Cossé, J., Huertas Cerdeira, C., Gharib, M.: Flapping dynamics of an inverted flag. J. Fluid Mech. **736**, R1 (2013)
13. Cossé, J., Sader, J., Kim, D., Huertas Cerdeira, C., Gharib, M.: The effect of aspect ratio and angle of attack on the transition regions of the inverted flag instability. In: Proceedings of the ASME 2014 Pressure Vessels & Piping Conference. Anaheim, California, USA, PVP2014-28445 (2014)
14. Orrego, S., Shoele, K., Ruas, A., Doran, K., Caggiano, B., Mittal, R., Kang, S.H.: Harvesting ambient wind energy with an inverted piezoelectric flag. Appl. Energy **194**, 212–222 (2017)
15. Li, S., Lipson, H.: Vertical-stalk flapping-leaf generator for wind energy harvesting. In: Proceedings of the ASME 2009 Conference on Smart Materials, Adaptive Structures and Intelligent Systems. Oxnard, California, USA (2009)
16. Li, S., Yuan, J., Lipson, H.: Ambient wind energy harvesting using cross-flow fluttering. J. Appl. Phys. **109**(2011), 026104 (2011)
17. Hobeck, J.D., Inman, D.J.: Artificial piezoelectric grass for energy harvesting from turbulence-induced vibration. Smart Mater. Struct. **21**, 105024 (2012)
18. Vatansever, D., Hadimani, R.L., Shah, T., Siores, E.: An investigation of energy harvesting from renewable sources with PVDF and PZT. Smart Mater. Struct. **20**, 055019 (2011)
19. Erturk, A., Delporte, G.: Underwater thrust and power generation using flexible piezoelectric composites: An experimental investigation toward self-powered swimmer-sensor platforms. Smart Mater. Struct. **20**, 125013 (2011)
20. https://www.te.com/commerce/DocumentDelivery/DDEController?Action=srchrtrv&DocNm=LDT_with_Riveted_Leads&DocType=DS&DocLang=English
21. Deivasigamani, A., McCarthy, J. M., John, S., Watkins, S., Coman, F.: Investigation of asymmetrical configurations for piezoelectric energy harvesting from fluid flow. In: Proceedings of the ASME 2014 Conference on Smart Materials, Adaptive Structures and Intelligent Systems. New port, Rhode Island, USA (2014)
22. https://www.powerfilmsolar.com/custom-solutions/oem-solar-panels/oem-solar-panels-product-page/oem-solar-panels/sp3-37
23. Silva-Leon, J., Cioncolini, A., Filippone, A.: Determination of the normal fluid load on inclined cylinders from optical measurements of the reconfiguration of flexible filaments in flow. J. Fluids Struct. **76**, 488–505 (2018)
24. Silva-Leon, J., Cioncolini, A., Filippone, A., Domingos, M.: Flow-induced motions of flexible filaments hanging in cross-flow. Exp. Therm. Fluid Sci. **97**, 254–269 (2018)
25. Chen, S., Doolen, G.: Lattice Boltzmann method for fluid flows. Annu. Rev. Fluid Mech. **30**, 329–364 (1998)
26. Mittal, R., Iaccarino, G.: Immersed boundary methods. Annu. Rev. Fluid Mech. **37**, 239–261 (2005)
27. Kuttler, U., Wall, W.A.: Fixed-point fluid-structure interaction solvers with dynamic relaxation. Comput. Mech. **43**, 61–72 (2008)
28. Zhu, L., Peskin, C.: Simulation of a flapping flexible filament in a flowing soap film by the immersed boundary method. J. Comput. Phys. **179**, 452–468 (2002)
29. Ryu, J., Park, S., Kim, B., Sung, H.: Flapping dynamics of an inverted flag in a uniform flow. J. Fluids Struct. **57**, 159–169 (2015)
30. Eloy, C., Souilliez, C., Schouveiler, L.: Flutter of a rectangular plate. J. Fluids Struct. **23**, 904–919 (2007)

# Hydrokinetic Energy Conversion Using a Single-Cylinder Nonlinear Oscillator in Flow Induced Oscillations


**M. M. Bernitsas and H. Sun**

**Abstract** In 2006, the Marine Renewable Energy Laboratory of the University of Michigan introduced a new concept for horizontal Marine Hydrokinetic (MHK) energy conversion using alternating-lift. The Converter, nicknamed VIVACE, utilizes alternating-lift based on cylinders on elastic support responding in FIO (Flow Induced Oscillations) and particularly Vortex Induced Vibrations (VIV), galloping, and their coexistence. Over a decade of research using 1–4 oscillators in tandem and staggered arrangements, with smooth and rough cylinders, and linear and nonlinear springs and dampers have produced a power envelope showing high power-to-volume density and efficiency in MHK energy conversion as well as slow-flow onset. This paper focuses on: (i) Single-cylinder Converter. (ii) Various nonlinear oscillator models with displacement-adaptive stiffness and velocity-adaptive damping. (iii) Systematic variation of parameters for energy harnessing. (iv) Identifying flow domains where each nonlinear effect enhances MHK energy conversion. Experiments were conducted for $20{,}000 < \mathrm{Re} < 120{,}000$, a subset of the TrSL3 flow regime.

**Keywords** Hydrokinetic energy · Vortex induced vibrations · Galloping · Nonlinear oscillator

## 1 Introduction

Horizontal Marine Hydrokinetic energy is clean, renewable, abundant, and worldwide available in rivers, currents, and tides [5]. In 2006, the Marine Renewable Energy Laboratory (MRELab) of the University of Michigan introduced a new

M. M. Bernitsas (✉) · H. Sun
Marine Renewable Energy Laboratory, Naval Architecture and Marine Engineering, University of Michigan, 2600 Draper Rd, Ann Arbor, MI 48109-2145, USA
e-mail: michaelb@umich.edu

H. Sun
e-mail: sunhai2009@gmail.com



M. Braza et al. (eds.), *Advances in Critical Flow Dynamics Involving Moving/Deformable Structures with Design Applications*, Notes on Numerical Fluid Mechanics and Multidisciplinary Design 147,
https://doi.org/10.1007/978-3-030-55594-8_25

concept—the VIVACE (VIV for Aquatic Clean Energy) Converter as an alternative to turbines [2–4]. VIVACE utilizes FIO to passively generate alternating lift to harness MHK energy. This should be contrasted to two concepts: (a) Turbines, which use steady lift passively to harness MHK energy. (b) Fish, which use alternating lift actively to propel efficiently in water. The Converter is an Alternating-Lift Technology (ALT) based on cylinders on elastic end-supports responding in FIO. Typically, these phenomena (VIV and galloping) are destructive and suppressed in engineering applications. VIVACE enhances flow induced oscillations and controls the motion of its oscillating cylinders to generate mechanical and subsequently electrical energy from MHK.

Since 2006, research in a dedicated facility using a large channel, with a bias-free controller to emulate linear and nonlinear oscillators, laser broad field-of-view flow-visualization with a high-speed camera and PIV, validated computational fluid dynamics, extensive data post-processing, and energy conversion has established the Converter's performance [5, 17, 19–21]. In this paper, results are summarized and presented with recent findings. Envelopes of harnessed MHK power show the benefits of each nonlinearity and parameter.

Altering the natural frequency and damping of an oscillator helps maximizing the harnessed power. Findings in the literature show: (i) Nonlinearities can modify the natural frequency [1, 11]. (ii) The harnessed power can be enhanced using nonlinear stiffness in the TrSL3 flow regime where the upper VIV branch is fully extended [13, 20]). (iii) Nonlinear stiffness can even expand the upper branch in low Reynolds numbers ($2{,}000 < \mathrm{Re} < 10{,}000$; TrSL2 regime) [14]. (iv) A bi-stable oscillator can provide better performance compared to a linear oscillator in terms of energy extracted from a generic wider vibration spectrum [8].

The aim of the VIVACE Converter is to: (a) Maximize the power generated at a given velocity by enhancing FIO. (b) Maintain simplicity by using passive control to not adversely affect FIO. (c) Start at low flow-velocity since turbines require a minimum of 4 knots ($\approx$2m/s) while typical currents are slower than 3 knots and rivers are slower than 2 knots. (d) Remain environmentally compatible by using alternating-lift like fish. (e) Use one or more nonlinear oscillators [5].

This paper focuses on a single-cylinder nonlinear-oscillator to maximize the Converter's power by changing the nonlinear stiffness function and the nonlinear damping function and their parameters. The model and experimental facilities are described in Sect. 2 and the mathematical model in Sect. 3. Results are presented and discussed in Sect. 4 and conclusions are drawn at the end.

## 2 Physical Model and Nonlinear Oscillator

1. **LTFSW Channel**: All tests were conducted in the Low Turbulence Free Surface Water (LTFSW) Channel, in the MRELab of the University of Michigan (Fig. 1). The LTFSW Channel recirculates 10,000 gallons of fresh water at speed up to 1.4m/s using an impeller powered by a 20 HP induction motor. The turbulence

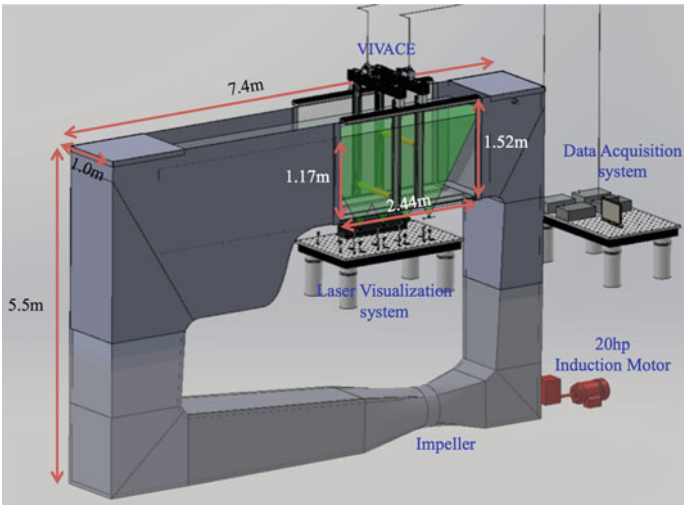


**Fig. 1.** The low turbulence free surface water channel and a VIVACE system (MRELab)

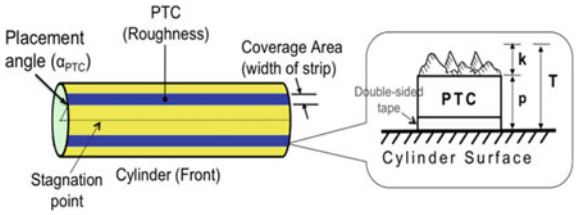


**Fig. 2.** Passive turbulence control (PTC) on cylinder [7]

**Table 1** PTC parameters (Sandpaper P60)

| | | |
|---|---|---|
| Strip placement angle | $\alpha_{PTC}$ [degree] | 20 |
| Angular coverage of strip | $\theta$ [degree] | 16 |
| Sand paper + tape thickness | $P$ [mm] | 0.587 |
| Average grit height | $k$ [mm] | 0.26 |
| Total thickness of strip | $T = P + k$ [mm] | 0.847 |

intensity normalized by the free-stream velocity was reported at 0.095% [5]. The test section is 2.44 m long and 1.0 m wide, made of transparent plexi-glass enabling visualization of the flow past cylinders using two 5 W argon lasers and aluminum oxide particles of 100 μm. For this study, the water depth at the test-section was set at 1.17 m and the maximum flow velocity was limited to 1.35 m/s for safety against the galloping instability.

2. **Cylinder and turbulence stimulation**: Distributed roughness in the form of sandpaper strips was introduced and extensively studied experimentally [2–5, 7, 12] and numerically [9, 10, 22] in the MRELab. It was termed Passive Turbulence

Control (PTC) and this study resulted in a most valuable tool, the *PTC-to-FIM Map* [15, 16]. As shown in Fig. 2, PTC consists of a pair of straight roughness strips attached symmetrically to the surface of the cylinder. According to the *PTC-to-FIM Map,* the location of the roughness strips determines the response FIO of the cylinder. The placement angle, $\alpha_{PTC} = 20°$, is measured in degrees with respect to the forward stagnation point to the upstream edge of the roughness strip. Based on the results of previous studies [7, 15, 16] on PTC, sandpaper with commercial roughness designation P60 and width of 12.7 mm, which covers 16° on each side of the 88.9 mm diameter cylinder, was used in this study. Table 1 shows the PTC details in this study.

The total PTC thickness is about equal to the boundary layer thickness. The robustness of the *PTC-to-FIM Map* was studied by Park et al. [16] defining not only the PTC coverage requirement in the direction of the flow but also the hierarchy of dominance of the zones where PTC is applied. PTC has a major impact on the energy conversion and the efficiency of the Converter.

3. **Vck system**: The second generation of Virtual spring and damping system (Vck), which is based on an open loop of the position-speed tracking control, was developed by Sun et al. [18]. It was found that the viscous damping of the oscillator is highly nonlinear, not as modeled in classical vibration textbooks. The purpose of Vck is to emulate the physical springs and dampers of the oscillator without including the hydrodynamics in the closed control loop, which would bias the FIO phenomenon being measured (Fig. 3).
4. **Nonlinear oscillator emulated by Vck**: The Vck controller implements any mathematical form—linear or nonlinear—and its parameter values for damping and stiffness. This is done after extensive system identification to eliminate the system damping so the model is mathematically accurate.

   (i) *Displacement-adaptive stiffness of the oscillator*: In the VIV region, the cylinder needs soft spring in order to initiate VIV earlier. Higher spring stiffness, however, results in higher natural frequency and higher power harnessed in the upper branch [5]. Galloping, on the other hand, is an instability where, as the stiffness decreases, the oscillation amplitude increases resulting in higher energy harnessing [7, 19].

   (ii) *Velocity-adaptive harnessing damping:* In galloping, the cylinder oscillates near its natural frequency. *A/D*, on the other hand, reduces with damping. Thus, the oscillation speed of the cylinder is decided by the damping and the stiffness/mass or its natural frequency. At lower damping, the cylinder oscillates at higher *A/D*, resulting in faster oscillations but lower converted power. At high damping, the cylinder does not have enough speed to support harnessing power, because the FIO is being suppressed. In the VIV region, frequency increases from the initial branch, not changing significantly as the damping changes. Actively adjusting the damping compensates for the low oscillation speed at the end of the oscillation. Thus, adaptive damping can also lead to higher power in VIV, albeit smaller then in galloping.

Based on (i) and (ii) above, the following nonlinear systems have been tested: (I) Three displacement-adaptive nonlinear stiffness functions (soft-hard, hard-soft, and cubic; Fig. 4a–c.) (II) Velocity-adaptive harnessing damping with linear stiffness (Fig. 4d).

## 3 Mathematical Model

The linear oscillator is modeled assuming its response to be purely sinusoidal (one frequency of oscillation $f_{osc}$) with the cylinder in VIV or galloping [19]. To convert hydrokinetic energy to mechanical energy in the oscillator and subsequently electrical energy, additional damping is introduced into the system. The mechanical power in VIVACE with linear harnessed damping is:

$$P_{converted} = \frac{1}{T_{osc}} \int_0^{Tox} 4\pi m_{osc} \zeta_{total} y^2 f_n dt = 8\pi^3 m_{osc} \zeta_{total} (A f_{osc})^2 f_n \tag{1}$$

where part is dissipated in system friction and part is harnessed by the generator

$$P_{dissipated} = 8\pi^3 m_{osc} \zeta_{structure} (A f_{osc})^2 f_n \tag{2}$$

$$P_{harness} = 8\pi^3 m_{osc} \zeta_{harness} (A f_{osc})^2 f_n \tag{3}$$

and fn is the natural frequency of the oscillator in quiescent water.

**Power harnessed by the nonlinear oscillator**: To make consistent comparison between linear and various nonlinear oscillators, the harnessed power can be calculated by averaging the instantaneous harnessed power. For a linear system, since Eqs. (2) and (3) depend explicitly on the mass $m_{osc}$, power can be calculated via the recorded amplitude and the frequency of oscillation. For both linear and nonlinear damping, power can be recast as follows:

$$P_{harness}(t) = c_{harness} \dot{y}(t) \dot{y}(t) \tag{4}$$

and

$$P_{dissipated}(t) = c_{structure} \dot{y}(t) \dot{y}(t) \tag{5}$$

where, $\dot{y}(t)$ is the oscillation speed of the cylinder as measured by the Vck system. Equations (4) and (5) do not depend on the specific way the added mass is calculated or even the value of the added mass explicitly. For a detailed derivation of the above equations, the reader is referred to [19]. The harnessed efficiency is measured off the Betz limit, which is the theorical maximum energy that can be extracted from an

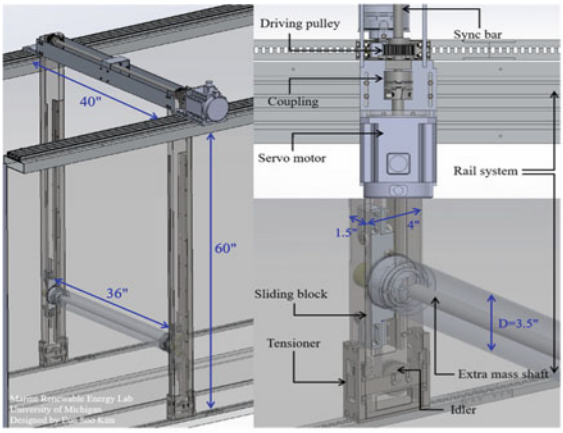


**Fig. 3.** VIVACE Converter with $V_{ck}$: **a** 3D drawing for the converter models. **b** Servo motor with the Vck shaft. **c** One-cylinder converter with Vck mounted in the LTFSW Channel (top view)

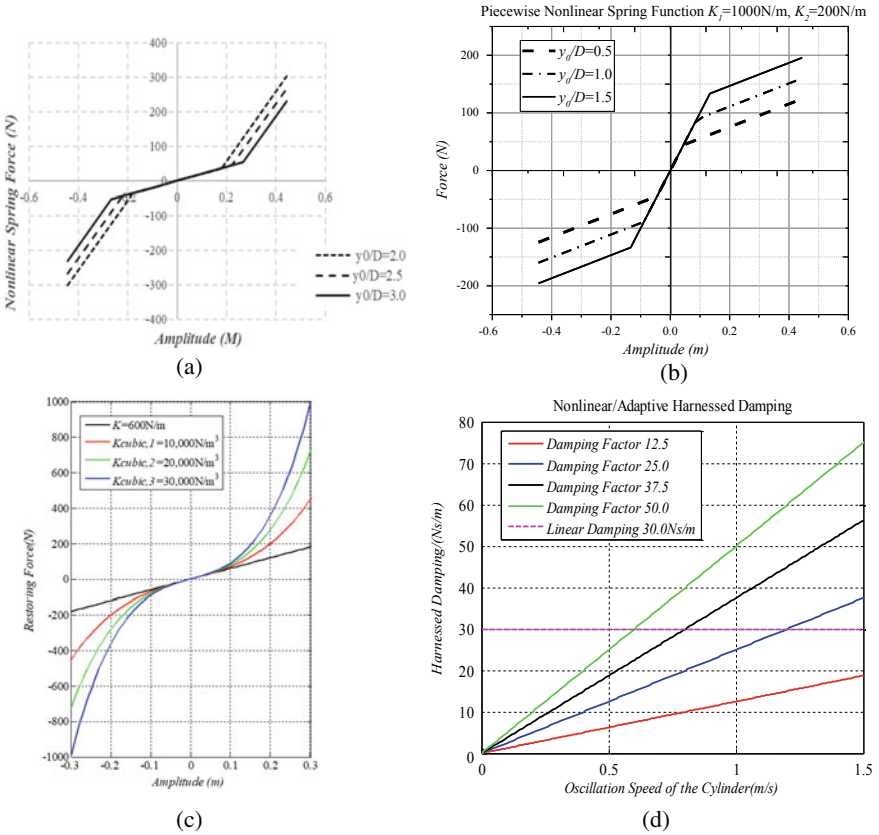


**Fig. 4.** Nonlinear stiffness and damping functions: **a**, **b** Piecewise stiffness [13, 20], **c** Cubic stiffness [21], **d** Adaptive harnessing damping [20]

open flow and is equal to 59.26% (=16/27) [6].

$$\eta_{harness}(\%) = \frac{100 \cdot P_{harness}}{P_{fluid}(Betz - Limit)} \tag{6}$$

where

$$P_{Fluid} = \frac{1}{2}\rho U^3(2A_{\max} + D)L \tag{7}$$

## 4 Results and Discussion

The main response characteristics of the Converter are amplitude, frequency, power, and efficiency. Those are compared next for all four nonlinear oscillators.

### *4.1 Response of Converter with Noinlinear Oscillators*

1. **Amplitude response**: The amplitude ratio *A/D* of all the nonlinear stiffness/damping functions (Fig. 4) is shown in Figs. 5, 6, 7 and 8 for PTC-cylinders. The amplitude *A* is calculated by averaging the absolute values of the 30 highest positive and 30 highest negative peaks in 60 s of running time past the transient of the channel. The mean deviation is denoted by vertical error bars.

   (i) *In the VIV region* ($Re < 78{,}000$), the soft-hard model initiates oscillation at much lower flow velocity and has wider upper branch compared to the hard-soft model. As the harnessing damping increases, the *A/D* range becomes narrower for both stiffness functions. This is more obvious in the hard-soft model. Both functions exhibit wider vibration ranges compared to linear stiffness. The lower branch becomes less obvious as the hard-soft oscillator extends its first segment $K_2 = 1{,}000$ N/m, which is also the case as the harnessing damping decreases. For the hard-soft function, there is no lower branch. Higher stiffness/natural frequency shifts the entire VIV region to higher flow velocity.
   The cubic stiffness function oscillator has the advantages of both piecewise functions: (a) As parameter $K_{cubic,n}$ increases, the width of the VIV upper branch decreases. (b) As damping increases, the upper branch width also decreases. The former is attributed to the higher equivalent natural frequency $f_n$, which for a given $m^* = m_{osc}/m_d$ has the effect of shifting the regions of VIV to higher flow velocities. This results in the extension of the upper branch [19]. In this case, near the equilibrium position, the restoring force is relatively low. The impact of stronger nonlinearity $K_{cubic,3}$ has an effect similar to higher linear stiffness as the flow velocity increases, which can extend to the end of the upper branch. As the nonlinearity $K_{cubic,n}$ increases, albeit the amplitude increase, the range decreases.
   As the adaptive damping parameter increases, the width of both the upper branch and the initial branch remains unchanged for all stiffness *K* values tested. The overall harnessing damping $c_{harness}$ is varied with the oscillation speed of the oscillator. That is, the higher $c_{harness}$ is not applied until the cylinder reaches higher speeds. As a result, the width of the VIV branches is not affected as opposed to the linear viscous damping oscillators.

   (ii) *In transition* ($78{,}000 < Re < 89{,}000$) between VIV and galloping, for the soft-hard stiffness functions, increasing of damping $c_{harness}$ shrinks the VIV range and delays the onset of galloping separating VIV from galloping. In

this region, which includes all three sub-ranges, VIV lower branch, transition, onset of galloping, the amplitude drops dramatically and random oscillatory patterns appear as expected. Consequently, the error bars become significantly higher in this region (Figs. 5, 6, 7 and 8). On the other hand, the amplitude of the hard-soft function shows less of a drop for the same additional damping, due to the first high-stiffness segment.
The stronger nonlinearity $K_{cubic,3}$ shows a similar response to higher linear-stiffness cylinders [19], where, at lower damping, the amplitude rises in the lower branch to transition. At higher damping, transition occurs at lower oscillation amplitude and frequency. The adaptive damping model, bridges transition for all the damping factors and all stiffness values.

(iii) *Galloping* occurs at 89,000 < *Re* for the three nonlinear stiffness functions and 80,000 < *Re* for the adaptive damping model. Adaptive damping initiates galloping at lower flow speed than the fixed linear viscous damping oscillator. Thus, although the VIV region shifts to higher flow velocity as the base linear-stiffness increases, the initiation velocity remains the same. In the cubic-stiffness oscillator, the response is not the same as the typical galloping response of linear-stiffness oscillators, where the galloping amplitude increases substantially, especially at lower damping ratios. *A/D* reaches a steady higher value for soft-hard stiffness, which is understandable since the higher stiffness segment essentially serves as a "bumper". *A/D* of the hard-soft nonlinear stiffness increases with flow speed.
In summary, from the energy harnessing point of view, the velocity-proportional adaptive damping has impressive advantages: the VIV range is not shrunk, the VIV to galloping transition is minimized, and the galloping onset is not delayed with damping increase.

2. **Frequency response**: Four different nonlinear parameters result in a total for 48 sets of experiments conducted. Only selective results in the form of frequency spectra are used to show the features of all FIV regions (Figs. 9, 10, 11 and 12). The results are presented in dimensional form because the natural frequency changes between models and a frequency ratio cannot be defined. The frequency spectrum is calculated for each cylinder by FFT (Fast Fourier Transform) of the time history after exclusion of the end-transients.

**Frequency spectra for PTC-cylinder for four noinlinear oscillator models**
The following observations can be made:

(i) *In VIV*, the frequency spectra of the four nonlinear oscillators follow the typical FIO response. The $f_{osc}$ (Hz) increases as the flow velocity increases to the end of the upper branch to about $1.4 f_{osc}$. The soft-hard and adaptive models initiate FIO at a lower $U$ than the other functions. The first due to lower stiffness, and the second due to low damping at mean position (low speed).

(ii) *In transition*, all but the soft-hard nonlinear oscillators tested exhibit stable oscillation pattern, as opposed to the linear oscillator [19]. Specifically, for the

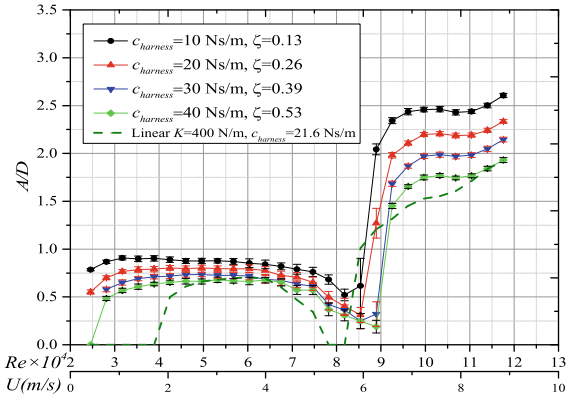


(a)

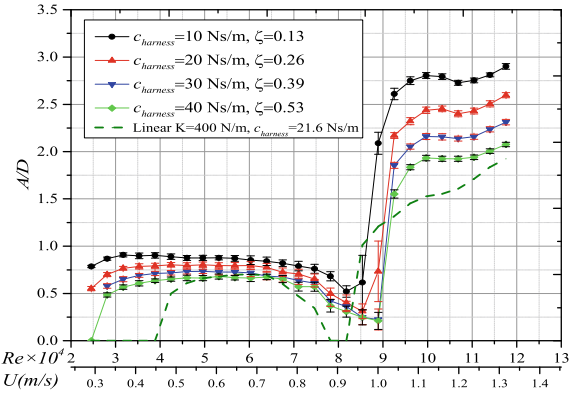


(b)

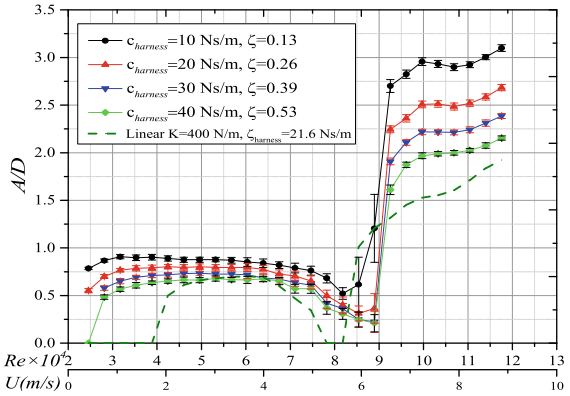


(c)

**Fig. 5.** Amplitude ratio for soft-hard stiffness, $y_0/D =$ 2.0 (**a**), 2.5 (**b**), 3.0 (**c**), $K_1 =$ 200 N/m, $K_2 = 1000$ N/m, $c_{harness} = 10$–40 Ns/m

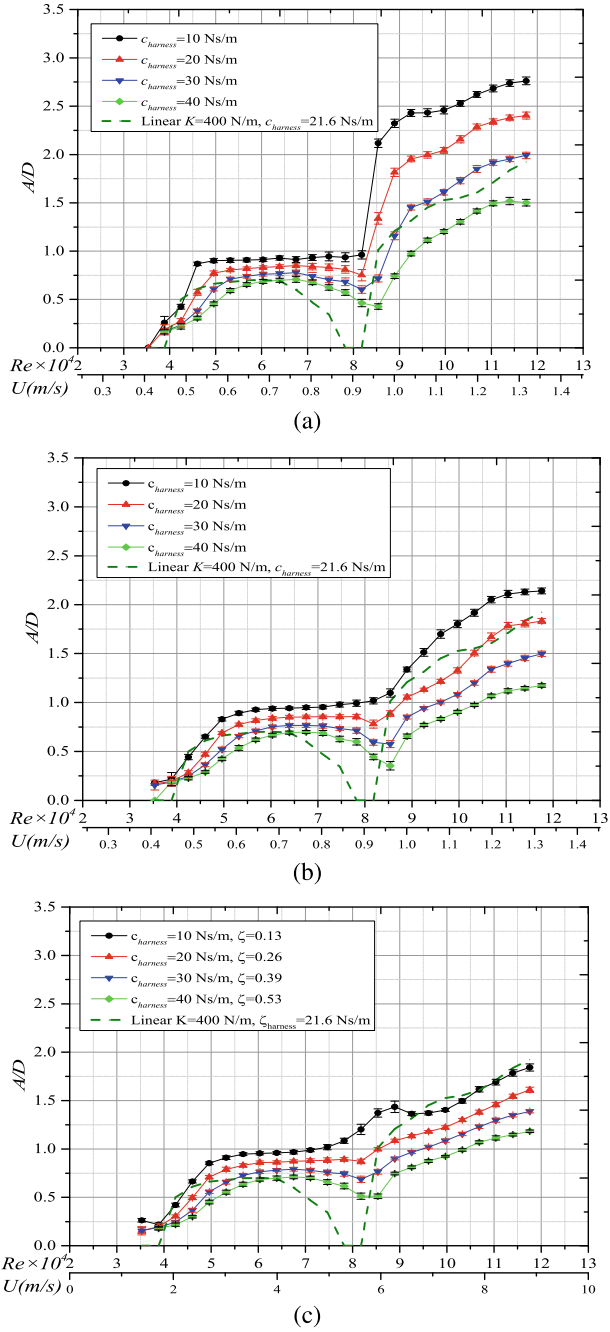


**Fig. 6.** Amplitude ratio for hard-soft stiffness, $y_0/D = 0.5$ (**a**), 1.0 (**b**) and 1.5 (**c**), $K_1 = 1000$ N/m, $K_2 = 200$ N/m, $c_{harness} = 10$–40 Ns/m

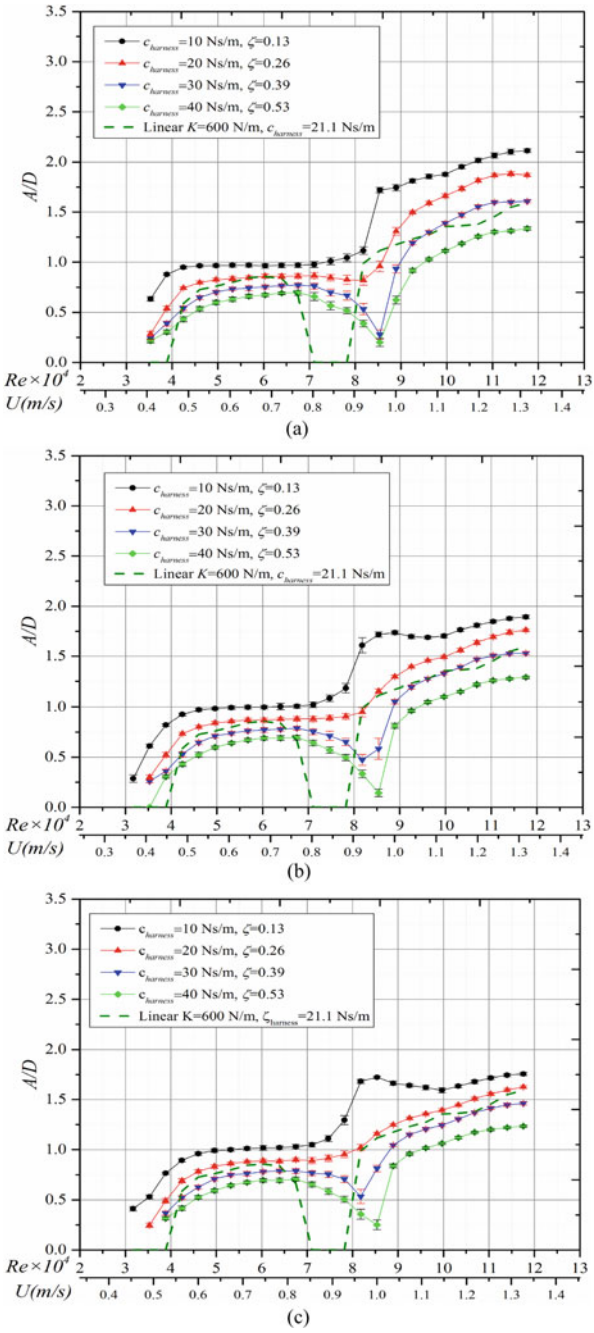


**Fig. 7.** Amplitude response for cubic stiffness $K_{cubic}$ = 10,000, 20,000, 30,000 N/m$^3$ (**a**, **b**, **c**, respectively); $c_{harness}$ = 10–40 Ns/m

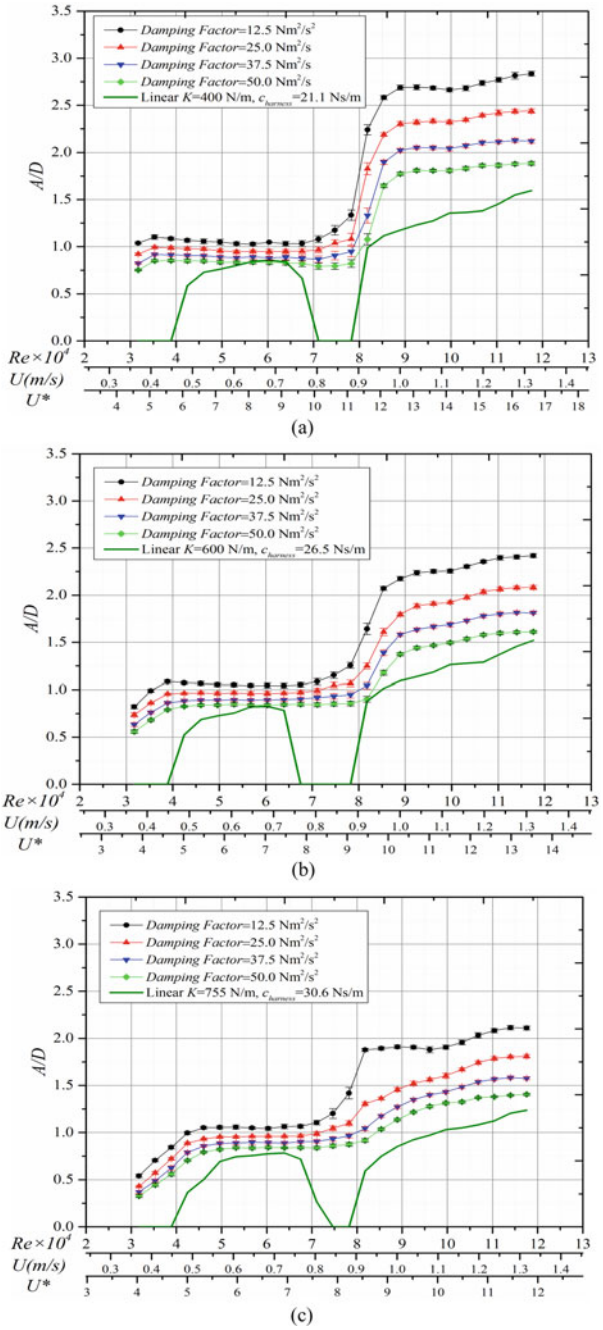


**Fig. 8.** Amplitude response for adaptive damping, $K = 400$, 600, 800 N/m (**a**, **b**, **c**, respectively); damping factor = 12.5–40 $Nm^2/s^2$

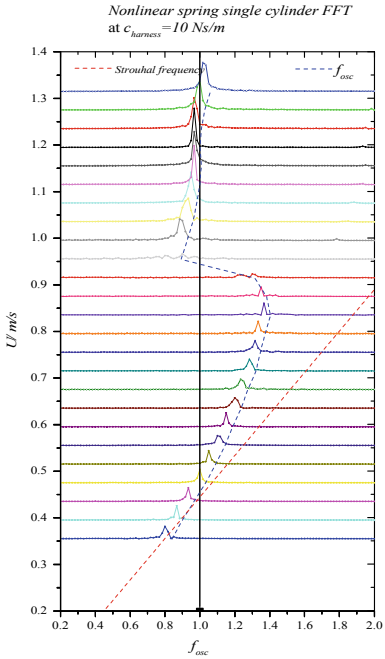


**Fig. 9.** Soft-hard spring: $K_1$ = 200 N/m and $K_2$ = 1000 N/m

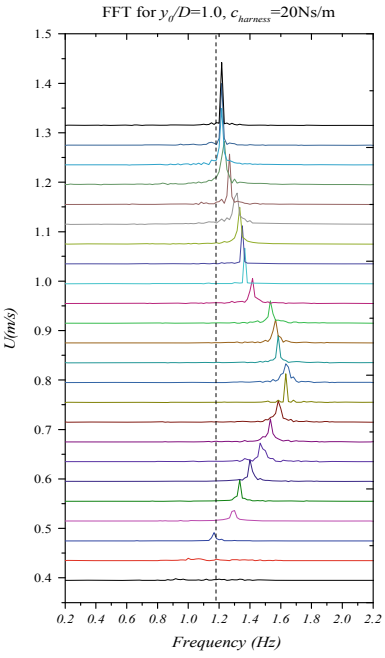


**Fig. 10.** Spring-function with $y_0/D$ = 1.0; 20 Ns/m

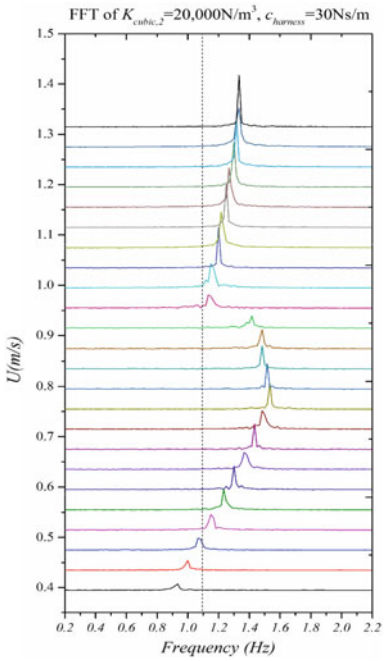


**Fig. 11.** $K_{cubic} =$ 20,000 N/m$^3$ and $c_{harness} =$ 30 Ns/m

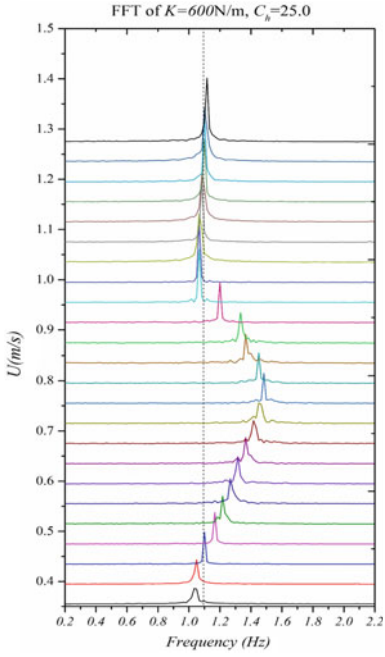


**Fig. 12.** Adaptive damping $c_h = 25$ Ns$^2$/m$^2$, K = 600 N/m

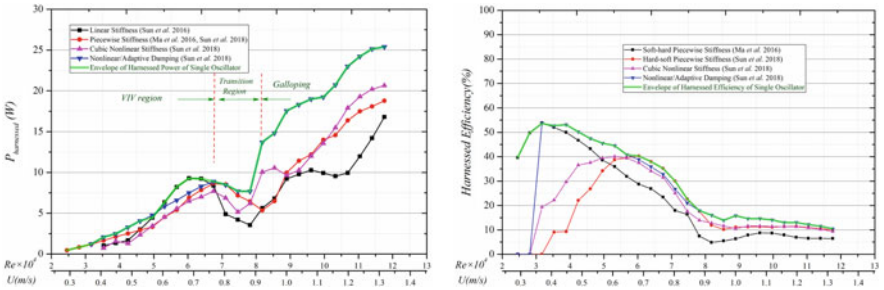


**Fig. 13.** Envelope of harnessed power and efficiency of single-cylinder Converter based on four nonlinear and the classical linear oscillator; $m^* = 1.343$

adaptive damping and hard-soft models, $f_{osc}$ is stable. Adaptive damping initiates oscillations more smoothly because the additional damping is proportional to the cylinder speed. For the hard-soft stiffness, the stiffer first segment delays the onset of the VIV lower branch; as a result, the drop in transition is mitigated at the expense of a shorter VIV initial branch.

(iii) In galloping, typically, the oscillation frequency in the galloping region is close to the linear natural frequency of the cylinder in water. This applies to the nonlinear models as well. The frequency of the nonlinear stiffness cylinder is strongly related to *A/D*, which can be observed from the initial galloping to fully developed galloping. For instance, in Fig. 11, the frequency increases from 1.11 to 1.31 Hz as the oscillation amplitude increases sweeping. In Fig. 10, the frequency decreases from 1.41 to 1.18 Hz.

## *4.2 Harnessed Power and Efficiency*

The optimal power and the efficiency of the four nonlinear oscillators are shown in Fig. 13 and compared to the linear oscillator and the power envelope.

(i) *In the initial branch to upper branch*, the soft-hard stiffness oscillator has the highest efficiency at 40–54%, where the amplitude starts at a lower flow velocity (0.274 m/s, $Re = 24{,}000$). As *Re* increases, the efficiency of the adaptive damping oscillator exceeds the nonlinear stiffness oscillators and into the upper branch. At $Re = 57{,}000$, the first high segment of the piecewise stiffness engages and has the highest efficiency. The total efficiency of single-cylinder VIVACE starts dropping due to the increased *A/D* in the denominator of Eq. (7).

(ii) *In transition to galloping and fully developed galloping*, the adaptive damping oscillator exhibits the optimal efficiency and higher harnessed power by 40–70%. Typically [19], the efficiency of a PTC-cylinder in fully developed galloping is around 10% and has a decreasing trend. The adaptive-damping oscillator has efficiency of 11–15%. This represents a big improvement in

power harnessing. Note that the power and efficiency optima do not coincide because the denominator in Eq. (7) is amplitude-dependent as defined by Eq. (8). This establishes the superiority of the adaptive damping oscillator. Proper balance between the cylinder speed and the harnessing damping results in higher harnessed power in galloping. Since galloping is not self-limiting like VIV, the mechanical power of the oscillator is determined by the cylinder speed.

## 5 Conclusions

The flow induced oscillations and the hydrokinetic power conversion capacity of a single, rigid, circular cylinder with passive turbulence control, on springs were investigated experimentally using four nonlinear and the classical linear oscillator models. Three displacement-adaptive stiffness models and one velocity-adaptive damping model were tested with several parameters. Experiments were conducted in the TrSL3 flow regime (24,000 < Re < 120,000, 0.274 m/s < $U$ < 1.315 m/s). The following conclusions can be drawn:

(a) The power envelope of a single-cylinder MHK energy Converter based on FIO (VIV/galloping) and the five models was generated. It shows ranges of oscillator nonlinearities enhancing MHK energy harnessing.
(b) Alternating lift provides an environmentally compatible way of harnessing MHK energy even from flows as low as 0.343m/s. Nonlinear (piecewise-linear) stiffness initiates VIV at even lower flow velocity (0.274m/s), and the onset of fully developed galloping occurs earlier for soft-hard springs.
(c) The instantaneous natural frequency of the oscillator with nonlinear cubic springs changes with the oscillation amplitude. The cubic restoring force increases the Converter's power by up to 78.6% compared to linear oscillators.
(d) Velocity-proportional, adaptive-damping coefficient initiates VIV even earlier and bridges the gap in harnessed power and efficiency in transition from VIV to galloping (0.85 m/s < $U$ < 1.0 m/s) for all the spring stiffness $K$ values tested. The nonlinear-adaptive damping coefficient yields a 128% increase in power compared to the linear (constant) damping oscillator.
(e) In galloping, the nonlinear adaptive damping increases the harnessed power by 51–95%.

**Acknowledgements** This research was funded by the Cooperative Agreement No. DE-EE0006780 between Vortex Hydro Energy and the U.S. Department of Energy; and the National Nature Science Foundation of China (No. 51609053). The MRELab is a subcontractor through the University of Michigan.

## References


1. Barton, D.A., Burrow, S.G., Clare, L.R.: Energy harvesting from vibrations with a nonlinear oscillator. J. Vib. Acoust. **132**(2), 021009 (2010)
2. Bernitsas, M.M., Raghavan, K., Ben-Simon, Y., Garcia, E.M.H.: VIVACE (Vortex Induced Vibration Aquatic Clean Energy): a new concept in generation of clean and renewable energy from fluid flow. In: OMAE 2006; and J Offshore Mech. Arctic Eng. **130**(2008), 041101-15 (2006)
3. Bernitsas, M.M., Raghavan, K.: Fluid motion energy converter. United States Patent and Trademark Office, Patent# 7,493,759 B2 issued on February 24 (2009)
4. Bernitsas, M. M., Raghavan, K.: Enhancement of vortex induced forces and motion through surface roughness control. US Patent & Trademark Office, Pat.#8,047,232B2, Nov 1 (2011)
5. Bernitsas, M.M.: Harvesting energy by flow included motions, Chap. 47. In: Dhanak, M.R., Xiros, N.I. (eds.) Springer Handbook of Ocean Engineering. Springer, Berlin. ISBN 978-3-319-16648-3, pp. 1163–1244 (2016)
6. Betz, A.: Das Maximum der theoretisch möglichen Ausnützung des Windes durch Windmotoren. Zeitschrift für das gesamte Turbinenwesen **26**, 307–309 (1920)
7. Chang, C.C., Kumar, A.R., Bernitsas, M.M.: VIV and galloping of single circular cylinder with surface roughness at $3 \times 10^4 \leq \mathrm{Re} \leq 1.2 \times 10^5$. Ocean Eng. **16**(38):1713–1732 (2011)
8. Cottone, F., Vocca, H., Gammaitoni, L.: Nonlinear energy harvesting. Phys. Rev. Lett. **102**(8), 080601 (2009)
9. Ding, L., Bernitsas, M.M., Kim, E.S.: 2-D URANS vs. Experiments of flow induced motions of two circular cylinders in tandem with passive turbulence control for 30,000<*Re*<105,000. Ocean Eng. **72**(1), 429–440 (2013)
10. Ding, L., Zhang, L., Kim, E.S., Bernitsas, M.M.: 2D-URANS vs. experiments of flow induced motions of multiple circular cylinders with passive turbulence control. J. Fluids Struct. **54**, 612–628 (2015)
11. Ibrahim, R.A.: Recent advances in nonlinear passive vibration isolators. J. Sound Vib. **314**(3–5), 371–452 (2008)
12. Kim, E.S., & Bernitsas, M.M.: Performance prediction of horizontal hydrokinetic energy converter using multiple-cylinder synergy in flow induced motion. Appl. Energy **170**, 92–100 (2016)
13. Ma, C., Sun, H., Nowakowski, G., Mauer, E., Bernitsas, M.M.: Nonlinear piecewise restoring force in hydrokinetic power conversion using flow induced motions of single cylinder. Ocean Eng. **128**(2018), 1–12 (2016)
14. Mackowski, A.W., Williamson, C.H.K.: An experimental investigation of vortex induced vibration with nonlinear restoring forces. Phys. Fluids **25**(8), 087101. 1e19 (2013)
15. Park, H.R., Kumar, R.A., Bernitsas, M.M.: Enhancement of flow induced motions of rigid circular cylinder on springs by localized surface roughness at $3\times10^4 \leq \mathrm{Re} \leq 1.2 \times 10^5$. Ocean Eng. **72**(1), 403–415 (2013)
16. Park, H.R., Kim, E.S., Bernitsas, M.M., Sensitivity to zone covering of the map of passive turbulence control to flow-induced motions for a circular cylinder at 30,000 < Re < 120,000. J. Offshore Mech. Arctic Eng. **139**(2): 021802-021802-6 (2017). https://doi.org/10.1115/1.4035140
17. Raghavan, K., Bernitsas, M.M.: Experimental investigation of reynolds number effect on vortex induced vibration of rigid cylinder on elastic supports. Ocean Eng. **38**(2011), 719–731 (2011)
18. Sun, H., Bernitsas, M.P., Kim, E.S., Bernitsas, M.M., Virtual spring-damping system for fluid induced motion experiments. J. OMAE ASME Trans. **137**, 1, 061801, (2015)
19. Sun, H., Kim, E.S., Nowakowski, G., Mauer, E., Bernitsas, M.M.: Effect of mass-ratio, damping, and stiffness on optimal hydrokinetic energy conversion of a single, rough cylinder in flow induced motions. Renew. Energy **99**, 936–959 (2016)
20. Sun, H., Ma, C., Bernitsas, M.M.: Hydrokinetic power conversion using flow induced vibrations with nonlinear (piecewise-linear) springs. Energy **143**, 1085–1106 (2018)

21. Sun, H., Ma, C., Bernitsas, M.M.: Hydrokinetic power conversion using flow induced vibrations with cubic restoring force. Energy. https://doi.org/10.1016/j.energy.2018.04.065 (2018)
22. Wu, W., Bernitsas, M.M., Maki, K.J.: 2D-URANS simulation versus experimental measurements of flow induced motion of circular cylinder with passive turbulence control at 30,000 < Re < 120,000. In: OMAE 2011 Paper #50293, Rotterdam, The Netherlands, June 19–24, 2011. J. Offshore Mech. Arctic Eng. **136**(4) (2014)

# Synergistic Flow Induced Oscillations of Multiple Cylinders in Harvesting Marine Hydrokinetic Energy


**H. Sun and M. M. Bernitsas**

**Abstract** Power-to-volume density is a critical metric for all renewable energy technologies. Harnessing Marine Hydrokinetic (MHK) energy using a single linear or nonlinear oscillator with a cylinder in Flow Induced Oscillations (FIO) has proven to be an efficient and environmentally compatible method. MHK power harnessing by two rigid, circular, tandem cylinders on end-springs for Reynolds number $3 \times 10^4 \leq Re \leq 1.2 \times 10^5$ with spacing, damping, and stiffness as parameters is investigated experimentally. The objective is to identify optimal parameter combinations where the cylinders, in close-proximity, undergo synergistic FIO harnessing more power than they would individually. The spring-damper controller $V_{ck}$, developed in the Marine Renewable Energy Laboratory (MRELab), enables embedded computer-controlled change of viscous-damping and spring-stiffness for fast and precise oscillator realization. Experimental results for amplitude response, energy harvesting, and efficiency are presented and discussed. Center-to-center spacing of 1.57, 2.0, 2.57 diameters, harnessing damping ratio $0.00 < \zeta_{harness} < 0.24$, and spring stiffness 200 N/m $< K <$ 1200 N/m are tested. Limited results are presented for three cylinders. The main conclusions are: (1) For the tested parameters, two cylinders harness 2.56–7.5 times the power of a single cylinder; the corresponding efficiency ratio is 2.0–6.68. (2) The MHK power harnessed by the upstream cylinder is increased by up to 100%, affected by the downstream cylinder. (3) The MHK power harnessed by the downstream cylinder and its FIO benefit less by the interaction as the spacing becomes smaller. (4) Power-to-volume density increases by nearly two orders of magnitude.

**Keywords** Hydrokinetic energy harnessing · Synergistic flow-induced oscillations · Vortex induced vibrations · Galloping · Tandem spacing · Virtual spring-damping

H. Sun (✉) · M. M. Bernitsas
Marine Renewable Energy Laboratory, Naval Architecture & Marine Engineering, University of Michigan, 2600 Draper Rd, Ann Arbor, MI 48109-2145, USA
e-mail: sunhai2009@gmail.com



M. Braza et al. (eds.), *Advances in Critical Flow Dynamics Involving Moving/Deformable Structures with Design Applications*, Notes on Numerical Fluid Mechanics and Multidisciplinary Design 147,
https://doi.org/10.1007/978-3-030-55594-8_26

## 1 Introduction

Rigid cylinders on elastic supports in transverse flows can be excited in Flow Induced Oscillations (FIO), thus, converting Marine Hydrokinetic (MHK) energy to mechanical in oscillators. VIV, galloping, and their coexistence are implemented in the VIVACE Converter mechanics [1, 2]. Interactions between cylinders affect FIO and energy harnessing. Spacing between cylinders in FIO affects directly the critical metric of power-to-volume ratio, which is the Achilles heel of all renewable energy technologies [2]. Fish in schools move effortlessly by proper placement in the wake of fish ahead of them [3–5]. VIVACE is being developed to achieve optimal FSI (Fluid-Structure Interaction) among cylinders in a school to perform as a 3-D converter instead of a point, line, or area-absorber. That is, instead of separating oscillators by 10–20 diameters to minimize interference, they are placed closely to increase FIO and MHK energy harnessing via synergy. Systematic experiments show that power increase and space reduction increase the critical metric by nearly two orders of magnitude.

The effects of spacing, linear stiffness, and linear viscous damping on a Converter with two tandem-cylinders, both oscillating in FIO, to attain higher MHK power, are studied experimentally. In most prior VIV studies of two rigid, circular, tandem cylinders, the 1st cylinder was stationary to measure the wake interference effects on the trailing (2nd) cylinder in VIV [6, 7]. Additional linear damping on the oscillators, changes their FIO. Previous work in the MRELab has established harnessing of MHK energy by a single cylinder with turbulence stimulation and a single smooth cylinder using linear viscous damping as parameter experimentally [1–3, 8] and numerically [9]. For two cylinders, experimentally [10, 11] and numerically [12], damping was proven to be an important factor in changing their FIO and harnessed power. In addition, hydrodynamic interactions, such as shielding and oscillation patterns [13], also depend on the spring stiffness, spacing, and damping ratios of the cylinders as they affect amplitude and frequency response. The present study focuses on two oscillating rigid circular cylinders in tandem, in steady uniform, two-dimensional flow, with spacing $L/D = 1.57$, 2.0 and 2.57, where each value results in different kind of interference. Specifically, interference may result in FIO response of the two cylinders as: (1) A single bluff body with no gap flow even though there are vortices between the cylinders. (2) Intermittent gap flow causing in-phase motion with some lag. (3) Intermittent gap flow causing out-of-phase motion. (4) Interference similar to that between two stationary cylinders. Limited multi-cylinder FIO results are presented.

The physical model and controller are presented in Sect. 2 and the mathematical model in Sect. 3. Results are presented and discussed in Sect. 4 and conclusions are drawn at the end.

## 2 Physical Model and the Virtual Controller

Details of the physical model, the Low Turbulence Free-Surface Water (LTFSW) channel, and the cylinder turbulence stimulation are provided in [9]. Physical change of $K$ and $c$ requires extensive time for calibration and validation of the oscillator prior to conducting experiments. As time progresses, fatigue results in change of physical parameters. In the MRELab, the $V_{ck}$ controller was developed to emulate the springs and dampers. The critical issues in development of the $V_{ck}$ system in the MRELab are [14, 15]:

1. The hydrodynamic lift-force is not included in the closed control loop. Including it would bias the FIO phenomenon being measured and produce incorrect results for converted power due to the phase-shift introduced between lift-force and cylinder velocity. That is, load cells are not used in the loop to measure the lift force, calculate the displacement from the differential equation, and force the displacement at the next time step. The latter approach has been used in VIV experiments as early as 1997 [11] and recently in [16, 17].
2. The MERLab developed the 1st generation $V_{ck}$ in 2008–2010 [13] and the 2nd in 2013 [15]. The controller force in the $V_{ck}$ model is expressed as:

$$F_{controller} = F_{nonlinear\_damping} - c_{virtual}\dot{y} - K_{virtual}y \tag{1}$$

where, $F_{controller}$ is the force applied by the virtual system, $F_{nonlinear\_damping}$ is the total nonlinear damping force; $K_{virtual}$ and $c_{virtual}$ are the virtual spring and linear viscous damping parameters. Any nonlinear function can be realized [8]. The process is lengthy and must be repeated for each oscillator separately. The stiffness part of $V_{ck}$ is simple involving determination of the torque-rotation relation to establish the $K_{virtual}$ relation. The damping system identification, though, is lengthy as structures seldom have damping in the classical textbook relation of linear viscous damping [9, 15]. The identified system damping is then subtracted from the system through the controller. Figure 1 shows the free decay test results for $K_{\text{virtual}} = 800$ N/m and 600 N/m after subtracting the nonlinear system damping and adding mathematically linear damping. With the $V_{ck}$, a perfectly linear viscous damping is implemented. A resistor bank is used to dissipate the generated power. After subtracting the nonlinear damping, the oscillator with the $V_{ck}$ system showed good agreement with the ideal (emulated; also called cyber-physical [17]) oscillator (Fig. 1). Nonlinear adaptive damping was used in [9].

The features of the Converter model are summarized in Table 1. In the current model design, the linear motion mechanism was brought under water, providing a realistic model. The whole linear motion system, which consists of the end sliding-blocks, one timing-belt and pulleys, is fitted inside of a 38 mm wide slender tube. Figure 2 shows a two cylinder model with $V_{ck}$ mounted in the LTFSW channel.

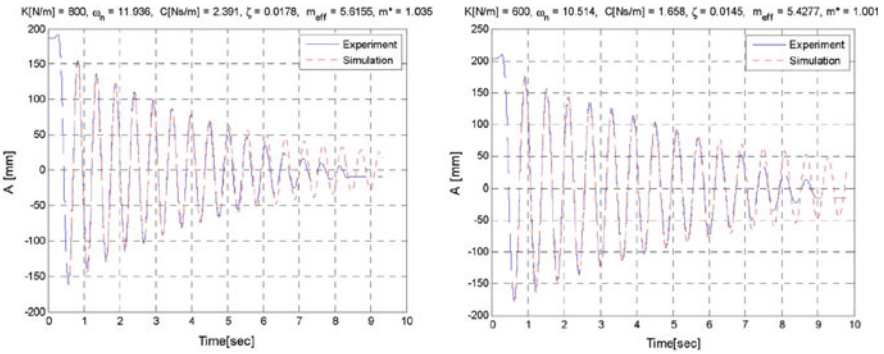


**Fig. 1** Free decay tests (FDT) for $V_{ck}$ at $K_{virtual} = 600$ and 800 N/m [15]


**Fig. 2** Two-oscillator Converter with $V_{ck}$ in the LTFSW Channel

**Table 1** Specifications of experimental model converter

| Mass ratio | Aspect ratio | Maximum amplitude | Longitudinal distance |
|---|---|---|---|
| $0.634 \leq m^* \leq 2$ | $L/D = 10.07$ | $A_{max}/D_{3.5''} = 5.5$ | $1.429 \leq d/D_{3.5''} \leq 6.0$ |

## 3 Mathematical Model

The fluid power through the area swept by the cylinders is:

$$P_{Fluid} = 0.5\rho_{water}U^3(2A_{\max} + D)L_c \tag{2}$$

where, $A_{max}$ is the largest amplitude among all cylinders in a multi-cylinder converter. $P_{Fluid}$ appears in the denominator of the efficiencies defined by Eqs. 2 and 3. It depends on the cylinder response, unlike propellers or wind turbines where the flow area is determined by the fixed geometry of the area swept by the blades. The Betz limit is the theoretical maximum power that can be extracted from an open flow and is equal to 59.26% (=16/27). Based on the Betz limit and the power formula in [9], the power conversion efficiency $\eta_{convert}$, and power harness efficiency $\eta_{harness}$ become:

$$\eta_{convert}(\%) = \frac{P_{convert}}{P_{Fluid} \times Betz\ Limit} \times 100 \tag{3}$$

$$\eta_{harness}(\%) = \frac{P_{harness}}{P_{Fluid} \times Betz\ Limit} \times 100 \tag{4}$$

Commercial scale wind turbines achieve efficiency of 75–80% of the Betz limit.

## 4 Results and Discussion

A series of experiments were conducted to measure the flow induced oscillations of two cylinders in tandem with the parametric ranges in Table 2: Spring-stiffness 400 N/m $\leq K \leq$ 1200 N/m; damping ratio $0 \leq \zeta_{harness} \leq 0.24$; longitudinal center-to-center spacing ratio (*L/D*) values of 1.57, 2.0 and 2.57; mass ratio $m^*$ of 1.343. Stiffness $K$ is accurate in form and value and exact as they are defined by the calibrated motor-torque and its relation to rotation. That is, the $K$ value is not subjected to

**Table 2** Particulars of two cylinders in tandem

| | Test sets |
|---|---|
| *L/D* (spacing) | 1.57, 2.0, 2.57 |
| $k$ (N/m) | 400,600, 800, 1000, 1200 |
| Temperature (°C) | 18.5–20.5 |
| $\mu$ (N s/m$^2$) | 1.004E−03 |
| $\upsilon$ (m$^2$/s) | 9.940E−07 |
| $\rho$ (kg/m$^3$) | 999.729 |
| $D$ (m) | 0.0889 |
| $Lc$ (m) (length) | 0.895 |
| $m_{displacement}$ (kg) | 5.425 |
| $m_{oscillation}$ (kg) | 7.286 |
| $m_{added}$ (kg) | 5.425 |
| $\zeta_{structure}$ | 0.020 |
| $f_{n,water}$ | 0.97–1.67 |

fabrication error or degradation in time due to fatigue. Similarly, $\zeta_{harness}$ *and* $\zeta_{total}$ are exact as explained in the discussion on $V_{ck}$. The flow velocity, Reynolds number, and reduced velocity range is 0.35 m/s $\leq U \leq$ 1.35 m/s, 30,000 $\leq Re \leq$ 120,000, and 2.92 $\leq U^* \leq$ 15.33, respectively. The upstream and downstream cylinders are set to be identical adjusted by two independent $V_{ck}$ controllers. In this research, the $\zeta_{harness}$ and $\zeta_{structure}$ are adjusted precisely to each mass and stiffness.

## *4.1 Harnessed Power and Efficiency of the Two-Cylinder Converter*

(1) *Harnessed power*: Figs. 3, 4 and 5, show the test-results for harnessed power for the three tested spacing values of *L/D* = 1.57, 2.01, 2.57, respectively. The flow velocity and Reynolds number, are proportional, and are the two x-axes. The reduced velocity *U** is not shown, because it depends on *K*. In Figs. 6, 7, 8, 9, 10 and 11, the response of the two oscillators and power and efficiency are shown for the optimal design, for each spacing. Tables 3, 4 and 5 show the power and the ratio of synergistic versus single cylinder power output. In Figs. 6, 7, 8, 9, 10 and 11, *K* is constant enabling adding *U** to the x-axis. The following observations are made:

(a) In general, power in the flow increases with the cube of the flow velocity. In the three *L/D* values tested, however, the harnessed power exhibits drops and jumps. Specifically: (1) In VIV, ($3.5 \times 10^3 < Re < 6 \times 10^4$ for *L/D* = 1.57; $3.5 \times 10^3 < Re < 7.8 \times 10^4$ for *L/D* = 2.01, 2.57), the harnessed power increases with flow velocity. Higher spring stiffness results in higher

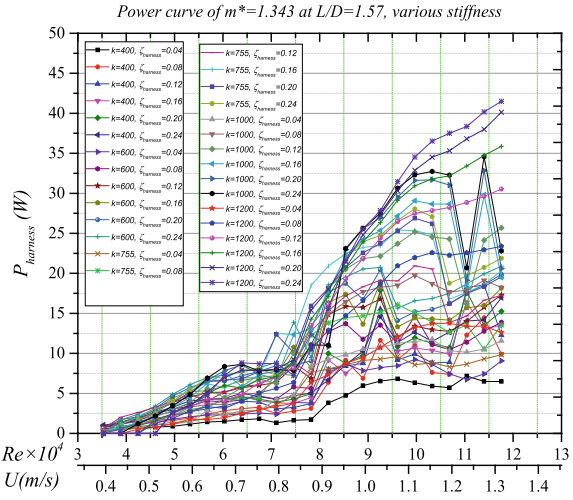


**Fig. 3** Harnessed power at *L/D* = 1.57

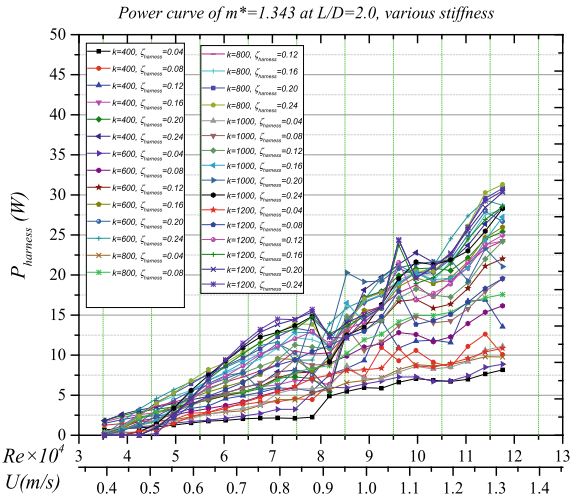


**Fig. 4** Harnessed power at $L/D = 2.01$

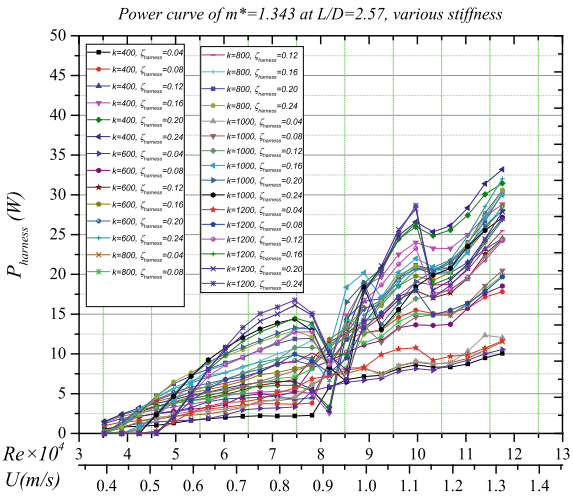


**Fig. 5** Harnessed power at $L/D = 2.57$

power harnessed at the VIV upper branch. Lower stiffness results in higher harnessed power at the VIV lower branch. (2) The first drop in power occurs in transition from VIV to galloping (Figs. 3, 4 and 5: $7.2 \times 10^4 < Re < 8 \times 10^4$ for $L/D = 1.57$; $7.8 \times 10^4 < Re < 8.7 \times 10^4$ for $L/D = 2.01$ and 2.57). The power drop is obvious at $L/D = 2.57$ (Fig. 5), which is consistent with the single-cylinder case. As the spacing increases, the oscillatory response approaches that of the isolated cylinder [10]. Figs. 3, 4 and 5 show that higher damping cases of two cylinders exhibit gaps in the transition region, while the lower damping cases do not. (3) In galloping, changes in harnessed power occur at $Re \cong 1.05 \times 10^5$ for $L/D = 2.01$ and

2.57. The harnessed power drops and then increases steadily (Figs. 4 and 5). At closer spacing, the drop occurs at lower stiffness ($K < 600$ N/m) (Fig. 3). At the higher stiffness ($K = 1200$ N/m), though, power increases without a drop (Fig. 3).

(b) As damping increases, a point is reached where a gap appears between the end of VIV and the beginning of galloping. This is due to two factors. Higher damping results in delay of galloping onset and in reduced amplitude and range of VIV. The flow velocity and corresponding Reynolds number of the gap between VIV and galloping in harnessed power increases as *L/D* decreases, being, $Re \sim 6.8 \times 10^4$, ~$7.8 \times 10^4$, ~$8.2 \times 10^4$ for *L/D* = 1.57, 2.01, 2.57, respectively.

(c) In VIV, power exhibits a local maximum at the end of the upper branch, being $P_{harness}$ = 12.49w, 14.88w, 16.75w at *L/D* = 1.57, 2.01, 2.57, respectively. That is, the optimal harnessed power increases as the spacing increases due to the decrease in optimal *K*. In low spacing, the interference between the two cylinders has a negative effect on the harnessed power affecting the oscillation patterns [13].

(d) In galloping, the local maximum is at the highest velocity since galloping is not self-limiting and it is an instability phenomenon. The optimal harnessed power is $P_{harness}$ = 41.50w, 31.30w, 33.20w for *L/D* = 1.57, 2.01, 2.57, respectively. As spacing decreases, the optimal power harnessed by the two cylinders increases. At each specific *L/D,* power increases nearly linearly with the flow velocity. This is counter-intuitive since flow power increases with the cube of the velocity. The dependence of FSI on *K* explains this.

(e) The optimal harnessed and converted power occur at the highest velocity with different configuration. The optimal pairs for *(L/D, K)* are: (1.57, 1200 N/m), (2.01, 800 N/m) (2.57,400 N/m). That is, as spacing increases, the highest harnessed power is achieved with low spring stiffness/natural frequency.

(f) Jumps and drops occur in the harnessed power in galloping. Specifically, at *L/D* = 1.57, in the fully developed galloping range (90,000 < *Re*), the harnessed power shows unstable trends at most of the $\zeta_{harness}$ expect at $\zeta_{harness}$ = 0.04 (lowest) and 0.24 (highest); both points show stable harnessed power, due to the close spacing and interaction between the cylinders. At *L/D* = 2.01 and 2.57, the harnessed power in galloping, however, shows a stable trend in harnessed power, expect at higher stiffness values. Variations in the harnessed power occur at $1.05 \times 10^5 < Re < 1.15 \times 10^5$ at *L/D* = 1.57 and $1.1 \times 10^5 < Re < 1.15 \times 10^5$ at *L/D* of 2.01 and 2.57. In our experiments, at lower spacing, the cylinders move as one single bluff body for most cases; at higher spacing (2.57), the vortex and gap-flow in between the cylinders may have a positive effect ($K = 400$ N/m, $\zeta_{harness}$ = 0.24), or a negative effect ($K = 1200$ N/m, $\zeta_{harness} = 0.24$) on the harnessed power. The oscillatory response of the systems that generate optimal power for each spacing and their respective *K* and $\zeta_{harness}$ are considered next.

### 4.2 Oscillatory Response, Power and Efficiency of the Optima

Figures 3, 4 and 5 show that, when placing the two tandem cylinders closer, the optimal harnessed power occurs at higher spring stiffness $K$. Tables 3, 4 and 5 present the converted power and the ratio of power generated by the two tandem cylinders in FIO synergy to a single cylinder for the three spacing values in transition to fully developed galloping. Those are $K = 1200$ N/m, 800 N/m and 400 N/m at $L/D = 1.57$, 2.01 and 2.57, respectively. The harnessed power and the efficiency of the upstream

**Table 3** Harnessed power by two tandem cylinders and single cylinder: $L/D = 1.57$, K = 1200 N/m

| $U$ (m/s) | Converted power (W) | | | | Ratio | Efficiency (%) | | Ratio |
|---|---|---|---|---|---|---|---|---|
| | 1st Cyl | 2nd Cyl | Synergy | Isolate | | Synergy | Isolate | |
| 0.95 | 17.43 | 5.94 | 23.37 | 5.36 | 4.36 | 34.25 | 12.35 | 2.77 |
| 1.03 | 20.73 | 9.41 | 30.14 | 8.01 | 3.76 | 33.49 | 12.13 | 2.76 |
| 1.15 | 24.7 | 14.86 | 39.56 | 9.29 | 4.26 | 30.84 | 9.83 | 3.14 |
| 1.19 | 25.85 | 14.78 | 40.63 | 10.59 | 3.84 | 28.37 | 9.79 | 2.90 |
| 1.27 | 26.92 | 16.6 | 43.52 | 15.02 | 2.90 | 25.11 | 10.31 | 2.44 |
| 1.31 | 26.56 | 18.41 | 44.97 | 17.71 | 2.54 | 24.05 | 10.54 | 2.28 |

**Table 4** Harnessed power by two tandem cylinders and single cylinder: $L/D = 2.01$, $K = 800$ N/m

| U (m/s) | Converted power (W) | | | | Ratio | Efficiency (%) | | Ratio |
|---|---|---|---|---|---|---|---|---|
| | 1st Cyl | 2nd Cyl | Synergy | Isolate | | Synergy | Isolate | |
| 0.95 | 12.25 | 2.56 | 14.81 | 3.77 | 3.93 | 27.48 | 8.2 | 3.35 |
| 1.03 | 16.57 | 2.73 | 19.3 | 6.48 | 2.98 | 24.44 | 8.63 | 2.83 |
| 1.15 | 17.81 | 4.35 | 22.16 | 9.33 | 2.38 | 19.58 | 7.65 | 2.56 |
| 1.19 | 19.57 | 4.86 | 24.43 | 10.01 | 2.44 | 18.83 | 7.6 | 2.48 |
| 1.27 | 24.8 | 7.8 | 32.6 | 12.29 | 2.65 | 18.58 | 6.96 | 2.67 |
| 1.31 | 26.62 | 7.29 | 33.91 | 13.4 | 2.53 | 17.12 | 6.12 | 2.80 |

**Table 5** Harnessed power by two tandem cylinders and single cylinder: $L/D = 2.57$, $K = 400$ N/m

| U (m/s) | Converted power (W) | | | | Ratio | Efficiency (%) | | Ratio |
|---|---|---|---|---|---|---|---|---|
| | 1st Cyl | 2nd Cyl | Synergy | Isolate | | Synergy | Isolate | |
| 0.95 | 9.41 | 4.35 | 13.76 | 1.02 | 13.49 | 14.96 | 2.24 | 6.68 |
| 1.03 | 15.05 | 7.45 | 22.5 | 6.12 | 3.68 | 15.87 | 6.13 | 2.59 |
| 1.15 | 18.11 | 9.35 | 27.46 | 8.49 | 3.23 | 12.98 | 5.53 | 2.35 |
| 1.19 | 18.67 | 9.64 | 28.31 | 9.6 | 2.95 | 11.97 | 5.47 | 2.19 |
| 1.27 | 21.94 | 12.08 | 34.02 | 12.84 | 2.65 | 11.17 | 5.45 | 2.05 |
| 1.31 | 22.69 | 13.27 | 35.96 | 13.65 | 2.63 | 10.63 | 5.18 | 2.05 |

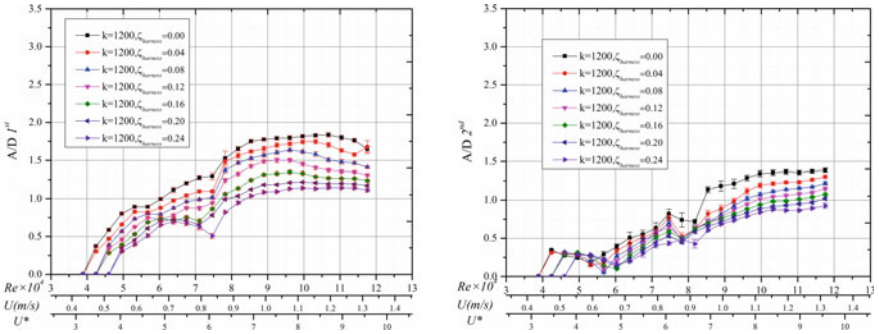


**Fig. 6** Amplitude *A/D* upstream (1st) and downstream (2nd) cylinders: K = 1200 N/m, m* = 1.343, L/D = 1.57

(1st), the downstream (2nd), and the isolated cylinder are also shown. In addition, the harnessed power, efficiency of the upstream and downstream cylinder and the isolated cylinder are also listed. The ratio values prove the benefit of synergy in a tandem configuration. Specifically:

(a) At low spacing $L/D = 1.57$, in the VIV initial branch and transition region, the harnessed power and efficiency are not on par with the rest of spacing ratios. The downstream cylinder performs better at $L/D = 1.57$ than other *L/Ds*. However, the harnessed power is considerably lower than the isolated cylinder until the flow velocity increases to the initiation of galloping for all three spacing values.

(b) At higher spacing $L/D = 2.01$ and 2.57, in VIV and transition, the upstream cylinder performs better overall compared to the isolated cylinder in terms of power. At the closest spacing $L/D = 1.57$, the interaction between cylinders causes lower harnessed power in the upper branch at $K = 1200$ N/m. In the VIV lower branch to transition, the power of the pair is redistributed from to the 2nd cylinder.

(c) In transition to galloping and in galloping, the harnessed efficiency increases considerably as the spacing ratio decreases. For instance, at $Re = 89{,}000$, the efficiency is 16% at $L/D = 2.57$ and increases to 35% at $L/D = 1.57$. This is partially due to the higher stiffness cylinder resulting in higher frequency and lower amplitude ratio. In galloping at higher spacing $L/D = 2.57$, the upstream cylinder shows an enhancement in power, and the rear one is lower than that of L/D = 2.01. The overall performance is better at 2.57. At lower spacing $L/D = 1.57$, the power and efficiency show intense interactions due to cylinder proximity. Specifically, at $9.5 \times 10^4 < Re < 1.07 \times 10^5$, the power drop is around 50% for both cylinders; the efficiency remains relatively stable and slowly decreases as the flow velocity increases due to amplitude increase, which affects the swept area.

(d) The most important conclusions are that: (i) Two cylinders in tandem, in synergistic FIO, can generate 2.56–7.5 times the power of an isolated cylinder in FIO. (ii) As the spacing of the two cylinders decreases, the optimal configuration has

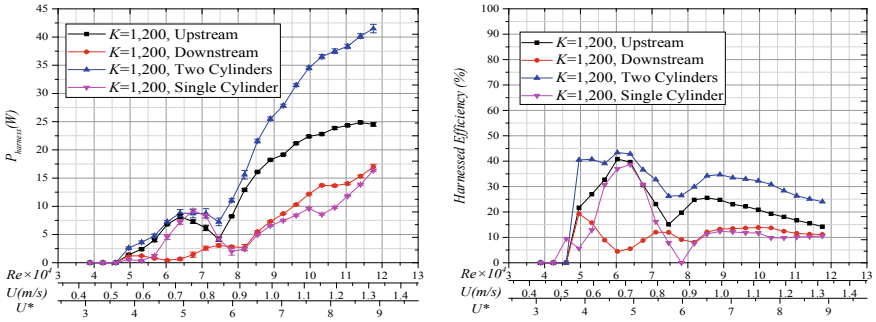


**Fig. 7** Power and efficiency for upstream (1st) and downstream (2nd) cylinders compared to single cylinder: $K = 1200$ N/m, $m^* = 1.343$, $L/D = 1.57$, $\zeta_{harness} = 0.24$

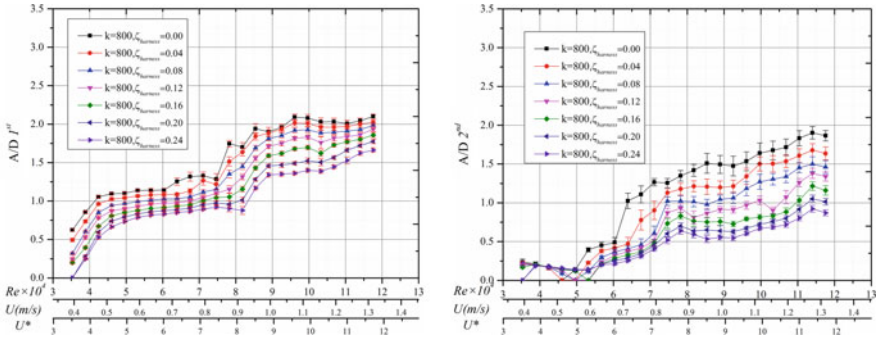


**Fig. 8** Amplitude *A/D* upstream (1st) and downstream (2nd) cylinders: K = 800 N/m, m* = 1.343, L/D = 2.01

increasing stiffness K. This is similar to fish in schools; when the school moves faster, fish reduce spacing and increase their body oscillation frequency.

## *4.3 Multiple Cylinders*

To test the potential of beneficial synergy of multiple cylinders in a VIVACE Converter, three and four cylinders in tandem tests have been conducted with multiple $V_{ck}$ systems. Only selective cases and results are shown in Fig. 12 for harnessed power for three cylinders and damping ratios $\zeta_{harness} = 0.16, 0.20, 0.24$. Comparisons between the single isolated cylinder and three cylinders are shown in Tables 6, 7 and 8.

Cylinder synergy and important observations are identified in two regions:

(a) $30{,}000 \leq Re \leq 85{,}000$: VIV and transition ranges.

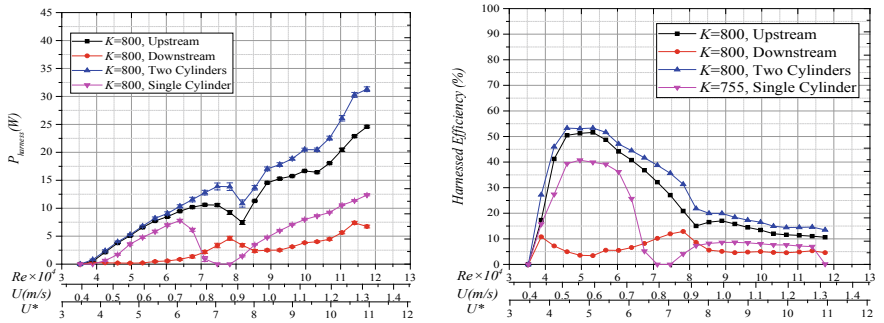


**Fig. 9** Power and efficiency for upstream (1st) and downstream (2nd) cylinders compared to single cylinder: $K = 800$ N/m, $m^* = 1.343$, $L/D = 2.01$, $\zeta_{harness} = 0.24$

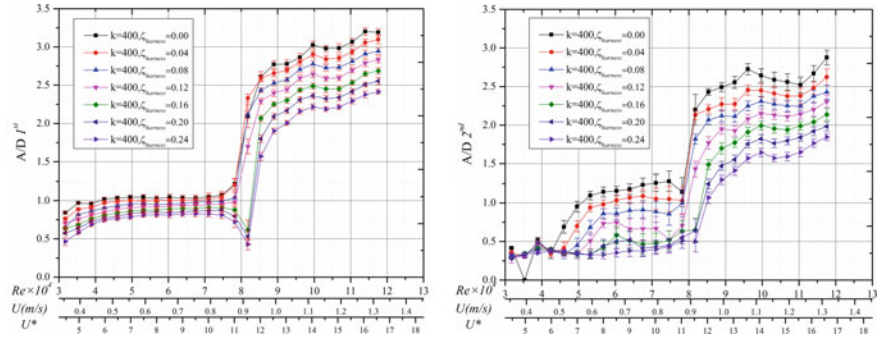


**Fig. 10** Amplitude *A/D* (1st) and downstream (2nd) cylinders: K = 400 N/m, m* = 1.343, L/D = 2.57

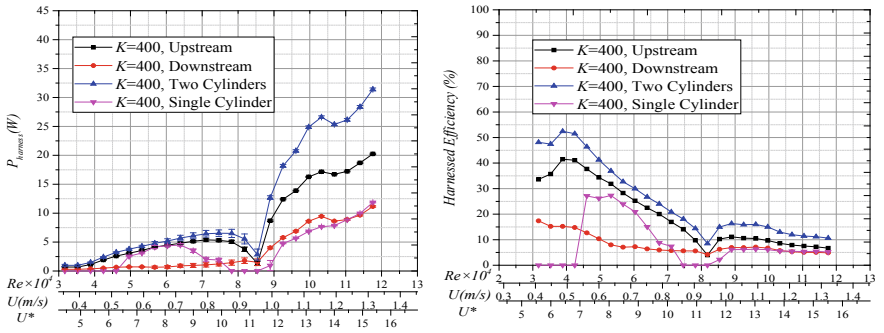


**Fig. 11** Power and efficiency for upstream (1st) and downstream (2nd) cylinders compared to single cylinder: $K = 400$ N/m, $m^* = 1.343$, $L/D = 2.57$, $\zeta_{harness} = 0.24$

- The harnessed power increases linearly with the flow velocity. Compared to a single cylinder, power generation by multiple cylinders initiates at lower Re.
- Aside from ceasing oscillation for a single cylinder in transition from VIV to galloping, increasing $\zeta_{harness}$ does not increase the harnessed power by much in the cases tested because amplitudes decrease as the damping increases.
- In the lower branch, the harnessed power for multiple cylinders does not drop as in a single cylinder. The harnessed power is 330% for three tandem cylinders and 300% for two tandem cylinders higher than a single cylinder.
- Compared to the power of two tandem cylinders, the power of three cylinders does not have an obvious drop in the lower branch, where, the power of a single isolated cylinder drops significantly at higher $\zeta_{harness}$.

(b) $85{,}000 \leq Re$: galloping range.

- At the initial galloping range, the synergistic FIO of multiple cylinders greatly enhances the harnessed power, as shown in Tables 6, 7 and 8. The onset of galloping is decided by the damping of the oscillator.
- In all the damping values tested, the power of three tandem cylinders is more than three times that of the single cylinder.
- At the last flow velocities tested, the power of three cylinders drops. The amplitude of the third cylinder decreases.

## 5 Conclusions

Flow induced oscillations and hydrokinetic power conversion capacity of two and three rigid, circular cylinders in tandem, with passive turbulence control [12, 13, 18], placed on end-springs, were investigated experimentally, for $0.00 < \zeta_{harness} < 0.24$, $3 \times 10^4 < Re < 1.2 \times 10^5$, $K = 400$–$1200$ N/m, and center-to-center spacing of 1.57, 2.01 and 2.57 diameters. The Reynolds number range falls in the TrSL3, high-lift, flow regime. The following conclusions can be drawn.

1. In the galloping range, the converted power by the two-cylinder Converter was between 2.56 and 7.5 times the power of a single cylinder for the parametric values tested.
2. The harnessed power by the three-cylinder Converter also shows beneficial synergistic FIO. For the tested values of cylinder spacing, three cylinders harnessed power between 3.36 and 5.82 times the power of a single cylinder.
3. In VIV, the power enhancement in multiple cylinder FIO is minimal and not worth the cost of designing a multi-cylinder Converter.
4. Both in transition from VIV to galloping and in galloping, the power increase due to the synergy between the two cylinders comes from the lead cylinder, which benefits from the presence of the downstream cylinder. In transition both cylinders benefit from the interaction regardless of the spacing ratio.

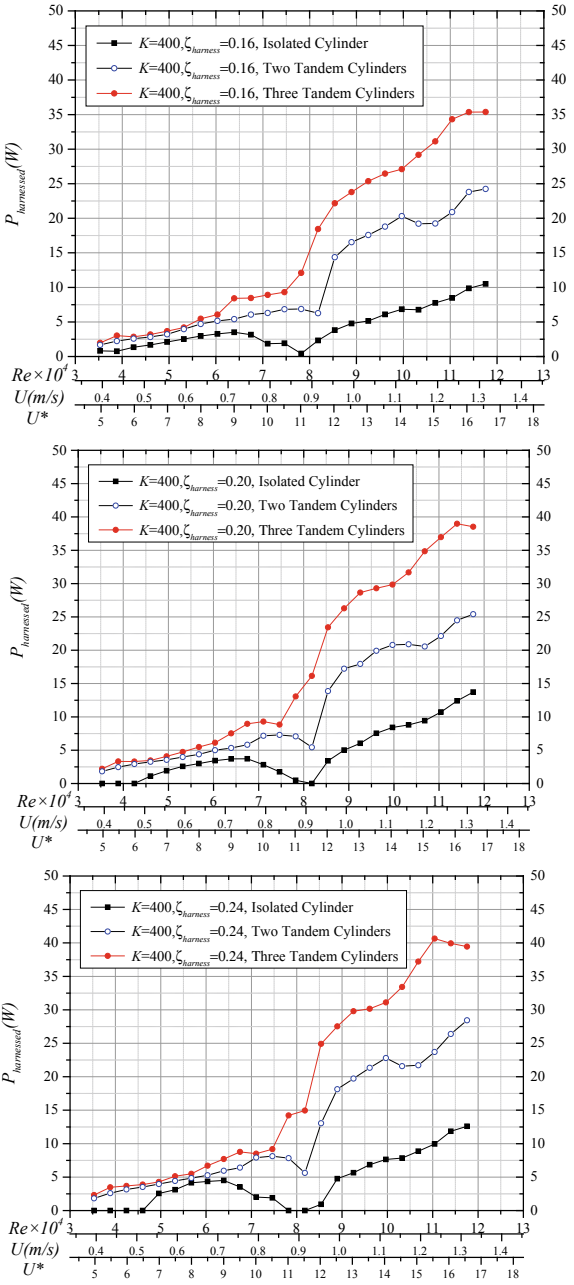


**Fig. 12** Harnessed power of single isolated, two, and three tandem cylinders at $K = 400$ N/m, $m^* = 1.343$ and $L/D = 2.01$

**Table 6** Comparison of tandem cylinders to isolated cylinder $\zeta_{harness} = 0.16$

| $U$ (m/s) | Harnessed power (W) | | | Ratio two to single Isolated | Ratio three to isolated |
|---|---|---|---|---|---|
| | Single | Two | Three | | |
| 0.85 | 3.83 | 14.36 | 22.17 | 3.77 | 5.82 |
| 1.03 | 5.14 | 17.58 | 25.36 | 3.42 | 4.93 |
| 1.15 | 6.76 | 20.31 | 29.18 | 3.00 | 4.31 |
| 1.19 | 7.75 | 19.20 | 31.13 | 2.48 | 4.01 |
| 1.23 | 8.47 | 19.24 | 34.32 | 2.27 | 4.05 |
| 1.27 | 9.85 | 20.89 | 35.36 | 2.12 | 3.59 |

**Table 7** Comparison of tandem cylinders to isolated cylinder $\zeta_{harness} = 0.20$

| $U$ (m/s) | Harnessed power (W) | | | Ratio two to Isolated | Ratio Three to Isolated |
|---|---|---|---|---|---|
| | Single | Two | Three | | |
| 0.85 | 3.40 | 13.86 | 23.43 | 4.07 | 6.88 |
| 1.03 | 6.03 | 17.94 | 28.66 | 2.97 | 4.74 |
| 1.15 | 8.79 | 20.71 | 31.68 | 2.36 | 3.60 |
| 1.19 | 9.42 | 20.88 | 34.86 | 2.22 | 3.70 |
| 1.23 | 10.73 | 20.55 | 36.96 | 1.91 | 3.44 |
| 1.27 | 12.41 | 22.13 | 38.99 | 1.78 | 3.14 |

**Table 8** Comparison of tandem cylinders to isolated cylinder $\zeta_{harness} = 0.24$

| $U$ (m/s) | Harnessed power (W) | | | Ratio two to isolated | Ratio three to isolated |
|---|---|---|---|---|---|
| | Single | Two | Three | | |
| 0.85 | 0.94 | 13.04 | 24.91 | 13.85 | 26.46 |
| 1.03 | 5.65 | 19.73 | 29.79 | 3.49 | 5.26 |
| 1.15 | 7.84 | 22.79 | 33.41 | 2.90 | 4.26 |
| 1.19 | 8.86 | 21.58 | 37.22 | 2.43 | 4.19 |
| 1.23 | 9.95 | 21.70 | 40.65 | 2.18 | 4.08 |
| 1.27 | 11.85 | 23.70 | 39.93 | 1.99 | 3.36 |

(5) The highest efficiency reached in this set of tests is 63% of the Betz limit for converted power. It occurs at center-to-center spacing between the two cylinders of 2.57 diameters and spring stiffness $K = 400$ N/m.
(6) As the spacing of the two cylinders decreases, the optimal configuration requires increased stiffness $K$. This is similar to fish in schools; when the school moves faster, fish reduce spacing and increase body oscillation frequency.

**Acknowledgements** This research was funded by the Cooperative Agreement No. DE-EE0006780 between Vortex Hydro Energy and the U.S. Department of Energy; and the National Nature Science

Foundation of China (No. 51609053). The MRELab is a subcontractor through the University of Michigan.

## References

1. Bernitsas, M.M.: Harvesting energy by flow included motions. In: Dhanak, M.R., Xiros, N.I. (eds.) Ch#47, Springer Handbook of Ocean Engineering. Springer, Berlin (2016)
2. Bernitsas, M.M., Raghavan, K., Ben-Simon, Y., Garcia, E.M.H.: VIVACE (vortex induced vibration aquatic clean energy): a new concept in generation of clean and renewable energy from fluid flow. In: OMAE 2006; J. Offshore Mech Arctic Eng. ASME Tran, Nov. 2008 **130**(4), 041101–15 (2006)
3. Sun, H., Ma, C., Kim, E.S., Nowakowski, G., Mauer, E., Bernitsas, M.M.: Hydrokinetic energy conversion by two rough tandem-cylinders in flow induced motions: effect of spacing and stiffness. Renew. Energy **107**, 61–80 (2017)
4. Wolfgang, M.J., Anderson, J.M., Grosenbaugh, M.A., Yue, D.P.K., Triantaphyllou, M.S.: Near body flow dynamics in swimming fish. Exp. Biol. **202**, 2303–2327 (1999)
5. Liao, J.C., Beal, D.N., Lauder, G.V., Triantafyllou, M.S.: Fish exploiting vortices decrease muscle activity. Science **302**(5650), 1566–1569 (2003)
6. Assi, G.R.S., Meneghini, J.R., Aranha, J.A.P., Bearman, P.W., Casaprima, E.: Experimental investigation of flow-induced vibration interference between two circular cylinders. J. Fluids Struct. **22**(6), 819–827 (2006)
7. Chen, S.S.: A review of flow induced vibration of two circular cylinders in crossflow. J. Pressure Vessel Technol. **108**, 382–393 (1986)
8. Sun, H., Kim, E.S., Nowakowski, G., Mauer, E., Bernitsas, M.M.: Effect of mass-ratio, damping, stiffness on optimal hydrokinetic energy conversion of a single, rough cylinder in flow induced motions. Renew. Energy **99**, 936–959 (2016)
9. Bernitsas, M.M., Sun, H.: Hydrokinetic energy conversion using a single-cylinder nonlinear oscillator in flow induced oscillations. In: IUTAM Symposium on Critical Flow Dynamics Involving Moving/Deformable Structures with Design Applications, 18–22 June, Santorini, Greece (2018)
10. Kim, E.S., Bernitsas, M.M.: Performance prediction of horizontal hydrokinetic energy converter using synergy of multiple cylinders in flow induced motion. Appl. Energy **170**, 92–100 (2016)
11. Zdravkovich, M.M.: Flow Around Circular Cylinders, vol. 1, Achenbach, E. (ed.). Oxford University Press, Oxford (1997)
12. Ding, L., Zhang, L., Kim, E.S., Bernitsas, M.M.: 2D-URANS vs. Experiments of flow induced motions of multiple circular cylinders with passive turbulence control. J. Fluids Struct. **54**, 612–628 (2015)
13. Lan, K., Sun, H., Bernitsas, M.M.: Two Tandem cylinders with passive turbulence control in FIV: relation of oscillation patterns to frequency response. J. OMAE **140**, 031801 (2018)
14. Lee, J.H., Xiros, N., Bernitsas, M.M.: Virtual damper-spring system for VIV experiments and hydrokinetic energy conversion. J. Ocean Eng. **38**(5), 732–747 (2011)
15. Sun, H., Bernitsas, M.P., Kim, E. S., Bernitsas, M.M.: Virtual spring-damping system for fluid induced motion experiments. J. Offshore Mech. Arctic Eng. ASME **137**(1), 061801 (2015)
16. Hover, F.S., Techet, A.H., Triantafyllou, M.S.: Forces on oscillating uniform and tapered cylinders in crossflow. J. Fluid Mech. **363**(1), 97 (1998)
17. Mackowski, A.W., Williamson, C.H.: Developing a cyber-physical fluid dynamics facility for fluid-structure interaction studies. J. Fluids Struct. **27**(5), 748–757 (2011)
18. Ding, L., Zhang, L., Chang, C.C., Bernitsas, M.M.: Numerical simulation and experimental validation for energy harvesting of single-cylinder VIVACE converter with passive turbulence control. Renew. Energy **85**, 1246–1259 (2016)

# Flapping Foil Hydrokinetic Turbine: From a Strongly Coupled FSI Solver to the Experiment in a Confined Channel


**Leandro Duarte, Nicolas Dellinger, Guilhem Dellinger, Abdellah Ghenaim, and Abdelali Terfous**

**Abstract** At a time of reframing the classic large-scale energy production and networks, several devices have been designed to fully exploit the hydroelectric potential all around the world. One of those promising micro-hydro concepts is the bio-inspired flapping foil harvester, based on the aeroelastic oscillations emerged from the fluid-structure interactions of an elastically mounted airfoil and a uniform fluid flow. With the aim of better understanding the dynamics of a fully-passive flapping foil turbine in low-speed water flows, a 2D model has been implemented and validated within open-source toolboxes. This model has shown to be capable of reproducing accurately the self-sustained oscillations of the foil by means of a strongly coupled fluid-structure solver, leading the design of a reduced scale prototype for parametric study in a free surface water channel. The first experimental tests showed that a self-sustained oscillations regime exists under a wise choice of the structural parameters and that is highly sensitive to the position of the elastic axis center and the pitching stiffness. In addition, it has been found that a significant amount of dry friction present on both degrees of freedom limits considerably the prototype's performance, which led to the design of an active compensation strategy.

**Keywords** Flapping foil · Hydrokinetic turbine · Fluid-structure interaction · Renewable energy

## 1 Introduction

The positive net exchange of energy from a fluid flow to a rigid obstacle leading to aeroelastic oscillations is typically dealt with in a predictive manner in order to avoid its adverse effects on structure stability. However, over the last few decades,

L. Duarte (✉) · N. Dellinger · G. Dellinger
ICube Laboratory, Fluid Mechanics Team, 2 rue Boussignault, 67000 Strasbourg, France
e-mail: leandro.duarte@unistra.fr

A. Ghenaim · A. Terfous
Institut National des Sciences Appliquées, 24 bd de la Victoire, 67000 Strasbourg, France



M. Braza et al. (eds.), *Advances in Critical Flow Dynamics Involving Moving/Deformable Structures with Design Applications*, Notes on Numerical Fluid Mechanics and Multidisciplinary Design 147,
https://doi.org/10.1007/978-3-030-55594-8_27

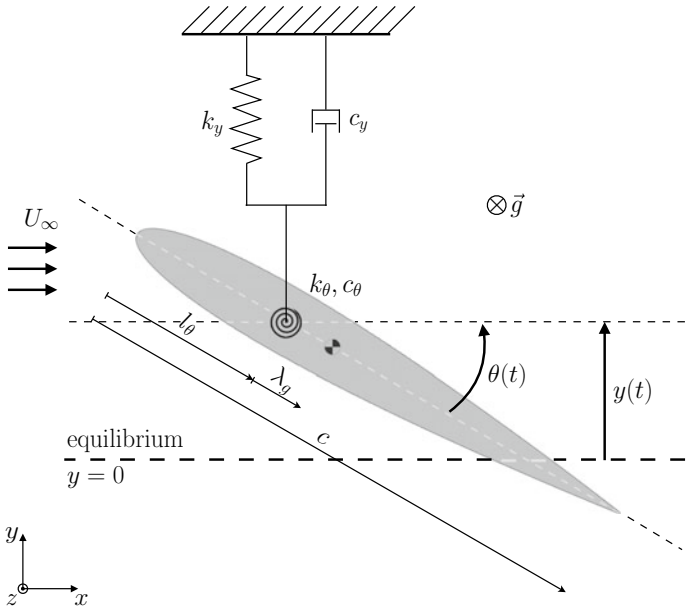


**Fig. 1** 2D schematic model of a fully-passive flapping foil [2]

mechanisms based on such phenomena have been found to be a promising novel hydrokinetic energy harvester. Besides reaching efficiencies not very far from the theoretical Betz limit of 59% for flow energy harvesters, the concept of a bio-inspired flapping foil turbine has the advantages of being environment-friendly, structurally robust and deployable in low-speed shallow waters, unlike the widely employed rotating turbines [5].

Since the application of flapping foils to extract energy from uniform flows was first proposed in the 80s, a growing number of researches on this matter have been reported. Among the most significant contributions, we may cite the stability analysis performed by Peng and Zhu [3] leading to the identification of the different oscillation regimes and the numerical study conducted by Veilleux, and Dumas [4] suggesting an optimized configuration for a fully-passive flapping foil.

In order to investigate the feasibility of such fully-passive flapping foil turbine, just as depicted in Fig. 1, an intensive research project has been conducted at ICube Laboratory of Strasbourg. This novel concept consists of an elastically mounted airfoil of chord length $c$, allowing a translational ($y(t)$) and a rotational ($\theta(t)$) rigid body motions, with springs and dampers for both degrees of freedom. The rotational axis is distant $l_\theta$ from the leading edge. Put vertically to interact with an uniform flow, this system is supposed—under a wise choice of its parameters—to perform self sustained oscillations, harvesting the kinetic energy out of the flow.

Numerical simulations have been performed within OpenFOAM, an open source computational fluid dynamics toolbox. Along with a finite volume method for the

incompressible Navier-Stokes equations, a second order solver based on the leapfrog integration is used to solve for the rigid body motion of the foil. This FSI segregated solver being implemented with a strong coupling between the fluid and the solid solvers, no added mass instability has been observed when simulating cases with a mass ratio of about 1. Through this we should be able to perform a numerical optimisation in a less restricted parametric space, including cases of a lightweight foil.

In the absence of experimental data for a fully-passive flapping foil turbine, a prototype has been recently designed and partially installed in the free surface water channel at the INSA of Strasbourg. The first test campaign was conducted in order to characterise the viscous and dry friction present in the heaving motion of the foil, so that we could estimate the amount of kinetic energy harvested from the flow. Besides, the friction coefficients measured being slightly too high, a real-time compensation through a closed-loop control of an actuator has been implemented for the future tests.

## 2 The Numerical Modeling

Simulations of fluid-structure interactions between a uniform flow and a fully-passive flapping foil have been performed through a boundless 2D numerical model implemented within OpenFOAM. Firstly, a CFD model to simulate the flow around a fixed aerodynamic profile has been built, tested and validated against NASA experimental data for the static stall and the theoretical Strouhal frequency of vortex shedding. Secondly, a second order solver for the rigid body motion of the foil has been coupled to the CFD solver, along with a morphing mesh technique to reproduce the oscillations described by the flapping foil.

### *2.1 Main Features of the CFD Model*

The Navier-Stokes equations for an incompressible viscous flow around an aerodynamic profile are solved by means of a finite volume discretisation. The mesh is structured, filling up a circular fluid domain 50 times longer than the aerodynamic profile at its centre (Fig. 2). Standard inlet and outlet boundary conditions are applied to the external bounds of the domain, while a smooth wall is set over the foil. Intended for flow regimes with a Reynolds number of about $10^5$, turbulence is modelled through a RANS approach. Both the one-equation Spalart-Allmaras and the two-equations SST k-$\omega$ models were tested.

This CFD model has been validated against experimental data for the static stall of a NACA0012 foil. Despite a relatively early stall, the CFD results with a SST k-$\omega$ turbulence model showed to be in good agreement with the experimental data, being thus held for future simulations. The model has also been validated with respect to the Strouhal number for the vortex shedding frequency downstream a stalled foil [2].

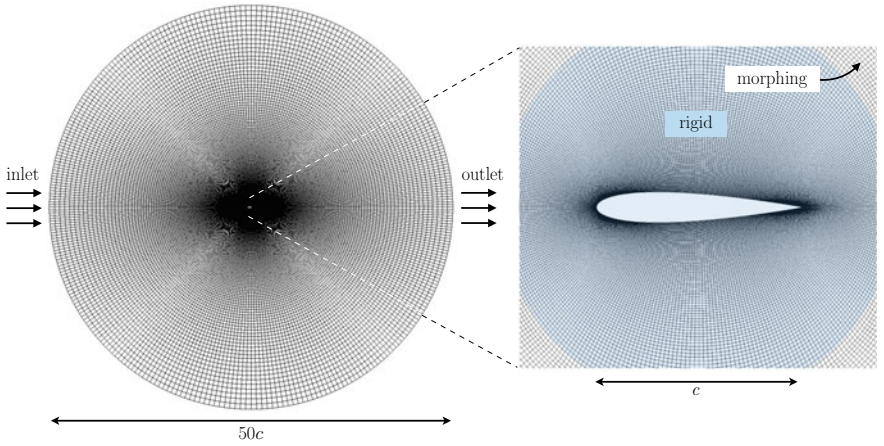


**Fig. 2** Structured 2D mesh around the foil. Details on the rigid zone close to the foil and the outlying morphing zone. Adapted from [2]

## 2.2 Fluid-Structure Coupling

The equations of motion for the elastically mounted flapping foil can easily be derived from a Lagrangian formulation. They correspond to those for a 2 DOF second order system with a term related to the static imbalance and the aerodynamic lift force and pitching moment:

$$\begin{cases} m_y\ddot{y} + c_y\dot{y} + k_y y + m_\theta \lambda_g(\dot{\theta}^2 \sin\theta - \ddot{\theta}\cos\theta) = F_y \\ I_\theta\ddot{\theta} + c_\theta\dot{\theta} + k_\theta\theta + m_\theta\lambda_g\ddot{y}\cos\theta = M_z \end{cases} \tag{1}$$

These equations are numerically solved by means of a second order solver, integrated to the previous CFD model. The architecture of the FSI solver is illustrated in Fig. 3. At the beginning of a new time step, the pressure field calculated by the CFD solver at the previous iteration is integrated over the foil surface to obtain the aerodynamic forces. To these we add the mechanical forces applied by the springs and dampers and we calculate the acceleration of the foil. From the acceleration, the velocity and position are obtained by an implicit leapfrog integration. For the heaving motion, this scheme can be written as follows:

$$\begin{aligned} \dot{y}_{i+1} &= \dot{y}_i + \tfrac{\Delta t}{2}(\ddot{y}_{i+1} + \ddot{y}_i) \\ y_{i+1} &= y_i + \tfrac{\Delta t}{2}(\dot{y}_{i+1} + \dot{y}_i) \end{aligned} \tag{2}$$

where $i$ corresponds to the current PIMPLE iteration and $\Delta t$ to the time step.

The mesh is then moved to adjust the new position of the foil and the fluid solver is called to recalculate the momentum and pressure fields. The updated fluid solution

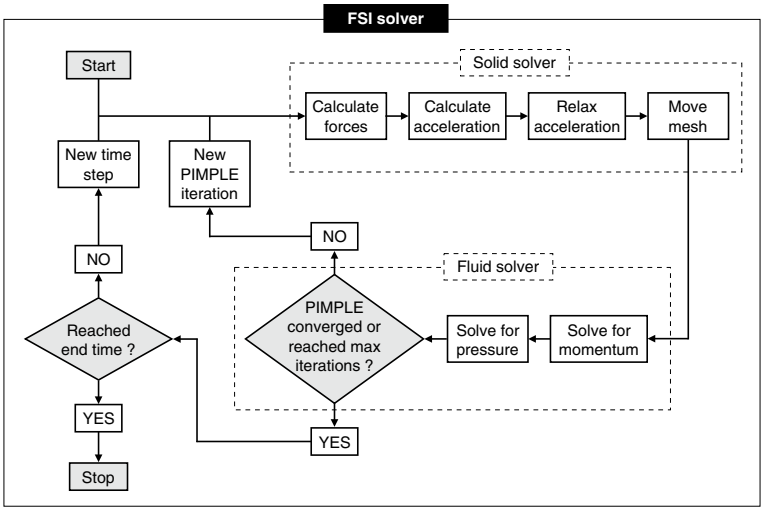


**Fig. 3** Flow chart of the FSI solver

is then repassed iteratively to the solid solver until convergence is reached before moving to the next time step.

The strong coupling between fluid and solid solvers through the update of the mesh on each of the multiple subiterations $i$ make the FSI solver insensitive to the well-known added mass instability [1]. As a matter of fact, the staggered character of the FSI solver introduce some sort of holes in the fluid grid after moving the mesh. Filling these holes greatly affects the pressure field and may propagate instabilities all over the domain. In the current FSI solver, this is avoided through a reduction of the time lag between the fluid and the solid solvers. In addition, relaxation of the acceleration is needed to damp the foil motion in the intermediate subiterations in order to reach a converged solution via a stable way in every time step.

The added mass instability arises when the ratio between the solid and fluid densities $\rho_s/\rho_f$ approaches 1, which is the case for a lightweight flapping foil designed for water flows, purpose of this study.

## *2.3 Numerical Results*

Numerical simulations have been conducted with the aim of testing the FSI solver in terms of its capacity to deal with highly coupled systems with a density ratio close to 1 without presenting any added mass instability issue. To do so, a baseline case

**Table 1** Structural parameters and flow conditions of the baseline case adapted from [4]

| | | |
|---|---|---|
| Reynolds number | $Re$ | $10^5$ |
| Flow velocity | $U_\infty$ | 0.5 m/s |
| Fluid density | $\rho_F$ | $10^3$ kg/m$^3$ |
| Chord length | $c$ | 0.2 m |
| Pitching axis location | $l_\theta$ | 0.667 m |
| Heaving mass | $m_y$ | 63.9 kg |
| Heaving stiffness | $k_y$ | 289.5 Nm |
| Heaving damper | $c_y$ | 97.5 Ns/m |
| Pitching inertia | $I_\theta$ | 0.146 kgm$^2$ |
| Pitching stiffness | $k_\theta$ | 0 |
| Pitching damper | $c_\theta$ | 0.501 Nms/rad |

has been adapted from a previous CFD study [4]. Its structural parameters and flow conditions are presented in Table 1. In spite of the relevance of the results presented in that study, the weakly coupled FSI solver proposed cannot be extended to the case of a lightweight flapping foil. As a mater of fact, no simulations have been performed with a mass ratio under 10 due to added mass instabilities.

Starting from this baseline case we could investigate the effect of reducing the mass ratio on the self-sustained oscillations described by the flapping foil. Besides the mass ratios, stiffness and damping have also been reduced by the same factor so that the natural frequency and the damping ratio remained constant. The results are presented in Fig. 4.

Figure 4a shows the limit-cycle oscillations described by the foil in the baseline case. Reducing the inertia of the system by a factor of 2, the response observed in Fig. 3b shows higher amplitudes for both heaving and pitching. Apart from this amplification, an even lighter foil with mass ratios of 5 or 3 reveals a loss of regularity in the motion pattern. The two consecutive strokes to the same direction observed in Fig. 3c, d suggest the existence of a regime with two attractors. This should be further investigated once the same behaviour has already been reported in the literature [3].

In spite of the major successes achieved on implementing a strongly coupled FSI solver, the CFD results have still not been validated against experimental data since no experimental work has been reported iso far n the literature on this matter.

## 3 Fully-Passive Flapping Foil Prototype

In the absence of experimental data for a fully-passive flapping foil turbine, a prototype has been recently designed and installed in the free surface water channel at the INSA of Strasbourg aiming for an experimental study of the main structural parameters of the system and its influence on the performance of the turbine.

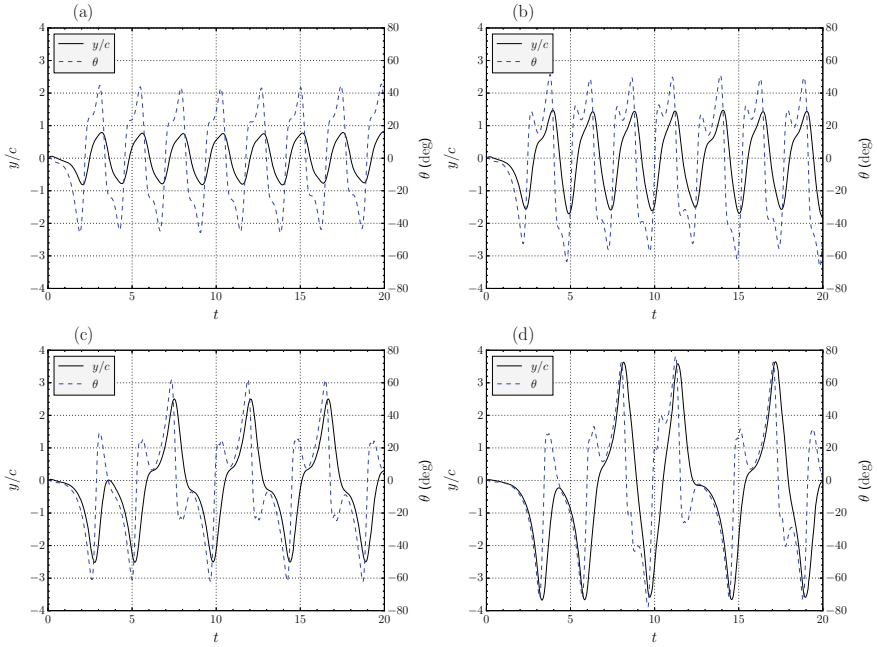


**Fig. 4** Numerical results for the heaving position by chord length $y/c$ and the pitching angle $\theta$ of the flapping foil for **a** a baseline case with $\rho_s/\rho_f = 15$, **b** $\rho_s/\rho_f = 7$, **c** $\rho_s/\rho_f = 5$ and **d** $\rho_s/\rho_f = 3$

## *3.1 Experimental Setup*

Figure 5 presents a front view of the real device built and mounted inside the channel. The fully passive flapping foil prototype consists of symmetric NACA0015 wing made out of a 3D printer. A pitching shaft is mounted on its upper edge with a sliding connection allowing the elastic axis to be accurately positioned in a wide range on the chord line. The shaft casing is then mounted on the heaving rail through a linear bearing carriage. Belt pulley transmission links the heaving motion to a DC servomotor which is intended for applying a viscous friction to model the electric generator.

During the first tests performed with a baseline configuration, self-sustained oscillations emerged under a fine adjustment of the parameters. It was observed that the stability of the system is highly dependent on the position of the elastic axis and the pitching stiffness, a slight change in one of them leading to a completely different regime. At present, a sensibility study on these parameters is being performed in order to draw the characteristic responses of the system, aiming for a validation with the stability analysis conducted by Peng and Zhu [3] suggesting the existence of 4 different regimes.

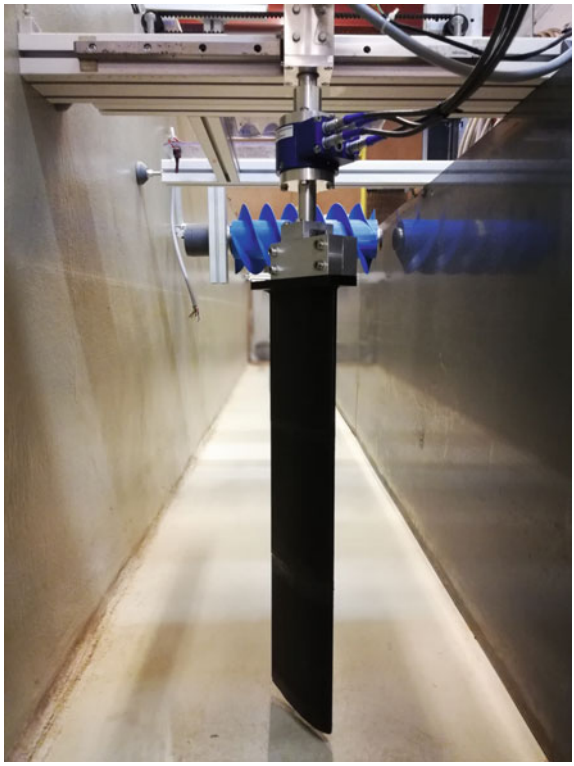

**Fig. 5** Experimental fully-passive flapping foil prototype

The relatively low heaving speed described by the prototype reveals a poor harvesting performance for the baseline case, which reinforces the idea that a parametric optimisation is needed. We could still try to quantify the energy harvested by the prototype at this stage, that would be equal to the amount of energy dissipated by friction at the heaving slide link.

## *3.2 Friction Characterisation*

The forces resisting the relative motion between the linear bearing carriage slide and the heaving rail are of two kinds: dry friction, emerging from the lateral motion of solid surfaces in contact, and viscous friction, due to the lubrication of the bearing.

In order to quantify these friction forces, a step response identification method has been applied. Neglecting air resistance, the heaving velocity response $v(t)$ to a step force $F_M$ exert by the DC servomotor is the solution of the following differential equation:

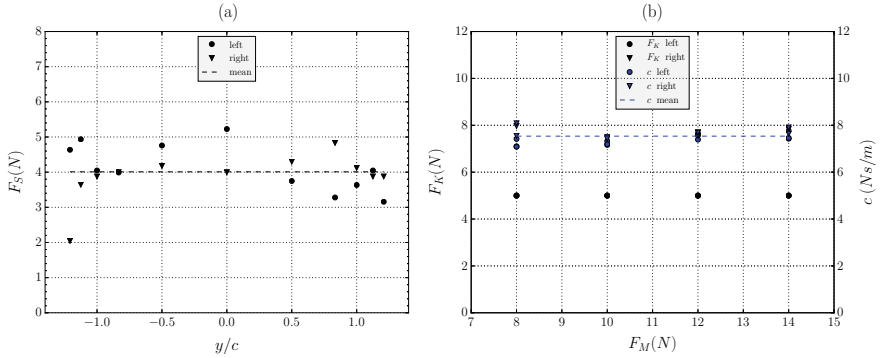


**Fig. 6** Experimental results for the friction forces involved in the heaving motion of the prototype: **a** static dry friction $F_S$ for different heaving positions $y/c$ and **b** kinetic dry friction $F_K$ and viscous friction coefficient $c_y$ for different values of step force $F_M$

$$\frac{m}{c_y}\dot{v} + v = \frac{F_M - F_K}{c} \tag{3}$$

where $m$ the heaving mass, $c_y$ the viscous friction coefficient and $F_K$ the kinetic dry friction. Considering a stationary initial condition $v_0 = 0$, Eq. (3) admits an exponential solution as follows:

$$v(t) = \frac{F_M - F_K}{c}\left(1 - e^{-\frac{c_y}{m}t}\right) \tag{4}$$

From this, the friction characterisation tests performed consisted of submitting the heaving system at rest to a step force $F_M$ and measuring the heaving velocity $v(t)$ described by the foil while crossing the rail. An optimization method was then applied to find the values of $c_y$ and $F_K$ that ensure the best fit between the measured points and the exponential solution given by Eq. (4). The value of the kinetic dry friction $F_K$ was constrained to be smaller than the maximum value of the previously measured static dry friction $F_S$, which is simply the minimum force required to enable heaving motion. Results are presented in Fig. 6.

Despite a slight dispersion of the forces measured depending on the heaving position and the direction of the motion as depicted in Fig. 6a, the average value of about 4N for the static dry friction is quite representative. Figure 6b shows an even smaller dispersion for the kinetic dry friction $F_K$ and the viscous coefficient $c_y$ for the different step forces $F_M$, with average values of about 5 N and 7.5 Ns/m, respectively.

Knowing the friction forces involved in the heaving motion is essential not only to estimate the harvesting performances of the turbine but also to improve the numerical model of the system by correcting the viscous friction coefficient $c_y$ and eventually adding a dry friction term $-F_K \mathrm{Sgn}\,(\dot{y})$.

Dry and viscous friction are also present in the pitching motion. Even if they do not impact directly on the harvesting performances of the system, they are a key parameter for the self-sustained oscillations regime to be achieved. According to [4], the pitching dry friction must not exceed 40% of the viscous friction, otherwise the system becomes stable and no limit-cycle oscillations will emerge out of it. For this reason, a similar test campaign has been conducted in order to characterise the friction forces involved in the pitching motion of the prototype, preliminary results suggesting a kinetic dry friction moment $M_K = 3.94 \times 10^{-2}$ Nm and a viscous friction coefficient $c_z = 2.53 \times 10^{-3}$ Nms/rad.

## 4 Conclusions and Perspectives

The fully-passive flapping foil hydrokinetic turbine is a novel promising concept which tends to be a suitable solution for harvesting low current shallow waters, extending the exploitable hydroelectric potential and improving the share of renewables in electricity. Since the idea was first raised, many theoretical and numerical studies have been conducted with the aim of better understanding the feasibility of such a hydrokinetic harvester. The present work brings considerable contributions on this matter, notably in terms of the strongly coupled FSI solver and the design of a reduced-scale prototype.

Through the implementation of an implicit solver for the foil motion, along with multiple exchanges between the fluid and solid solvers and relaxation of the acceleration in the subiterations, the numerical FSI model is capable of simulating systems with strong fluid-structure interactions. Numerical results issued by this model have guided the design of a fully-passive flapping foil prototype, the first to the knowledge of the authors. The first experimental tests provided evidence of self-sustained oscillations in a harvest regime, despite the high amount of dry friction present in both heaving and pitching motions. At present, a control technique is being developed to allow a real-time compensation of not only friction forces but also inertia and stiffness, which will enable a parametric experimental study of the system aiming to maximise its harvesting performance.

**Acknowledgements** This research project is supported by University of Strasbourg, ICube laboratory and INSA of Strasbourg. We would like to show our gratitude to our colleagues from the lab who provided insight and expertise that greatly assisted the research.

## References

1. Chow, J.H., Ng, E.Y.K.: Strongly coupled partitioned six degree-of-freedom rigid body motion solver with aitken's dynamic under-relaxation. Int. J. Naval Archit. Ocean Eng. **8**(4), 320–329 (2016)

2. Duarte, Leandro, Dellinger, Nicolas, Dellinger, Guilhem, Ghenaim, Abdellah, Terfous, Abdelali: Flapping foils as efficient hydrokinetic turbines: first steps in CFD modelling. Int. J. Hydropower Dams **25**, 94–99 (2018)
3. Peng, Z., Zhu, Q.: Energy harvesting through flow-induced oscillations of a foil. Phys. Fluids **21**(12), 123602 (2009)
4. Veilleux, J.-C., Dumas, G.: Numerical optimization of a fully-passive flapping-airfoil turbine. J. Fluids Struct. **70**, 102–130 (2017)
5. Xiao, Q., Zhu, Q.: A review on flow energy harvesters based on flapping foils. J. Fluids Struct. **46**, 174–191 (2014)

# Machine Learning of Dynamics with Applications to Flow Control and Aerodynamic Optimization


**Steven L. Brunton**

**Abstract** The optimization and control of fluid systems, such as a wing in a high-speed flow, is a central challenge in modern engineering. Turbulent fluids are characterized by high-dimensionality, strong nonlinearity, multiscale physics, and short time scales, all of which confound feedback flow control. One of the primary challenges for effective turbulence control is associated with the computational complexity and latency required to make a control decision, which may introduce unacceptable time-delays and destroy robust performance. Similarly, optimization may require several iterations involving experimental or high-performance computing resources, for example to modify the shape of an airfoil for beneficial lift and drag properties. Thus, considerable effort has gone into developing efficient reduced-order models that capture only the most relevant flow features needed to manipulate and control the system [6]. Increasingly, data-driven methods and machine learning are dominating the reduced-order modeling, optimization, and control landscapes. In this paper, leading and emerging methods are discussed and compared in the context of the optimization and control of fluids. A number of dichotomies will be explored, including the low-data and large-data limits, the challenges of combinatorially large search spaces, and the derivation of parsimonious model descriptions of dominant fluid behaviors.

**Keywords** Machine learning · Dynamical systems · Nonlinear dynamics · System identification · Flow control

## 1 Introduction

Reduced order models that capture essential flow physics are necessary for the overarching goals of optimization and flow control. Working flows are at the heart of several trillion dollar industries, e.g., security, energy, transportation, health, and there is a tremendous potential to benefit from improved optimization and control

S. L. Brunton (✉)
Department of Mechanical Engineering, University of Washington, Seattle, WA 98115, USA
e-mail: sbrunton@uw.edu



M. Braza et al. (eds.), *Advances in Critical Flow Dynamics Involving Moving/Deformable Structures with Design Applications*, Notes on Numerical Fluid Mechanics and Multidisciplinary Design 147,
https://doi.org/10.1007/978-3-030-55594-8_28

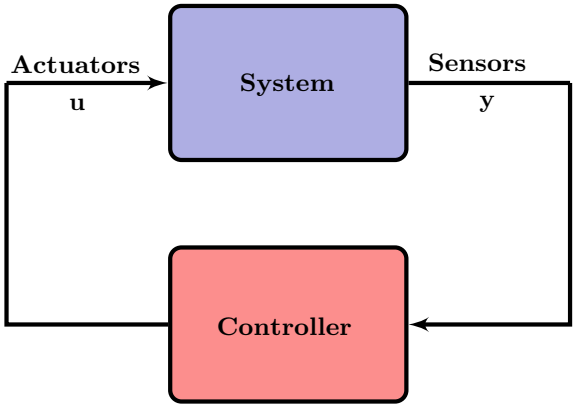


**Fig. 1** In the standard control framework machine learning may be used (1) to develop a model of the system, (2) to learn a controller, or (3) to identify effective sensors and actuators

algorithms. However, fluids are governed by nonlinear physics and exhibit multi-scale behavior that require expensive high-dimensional representations; these many degrees of freedom make optimization and control particularly challenging. Fortunately, machine learning encompasses a rapidly growing set of techniques for high-dimensional nonlinear optimization that leverages the increasing wealth of data available in nearly every field. The field of fluid dynamics, in particular, is generating unprecedented amounts of data due to advances in computational fluid dynamics and experiments, along with cheaper computers and storage. Thus, machine learning is currently redefining what is possible in the modeling, optimization, and control of complex systems in fluid dynamics. This review will explore a handful of the many data-driven techniques to model fluids for optimization and control. In particular, we will explore how machine learning is being used to develop reduced order models for optimization and control. In addition, machine learning is being used to directly learn effective controllers, bypassing the modeling step. More extensive reviews of flow control and modal analysis may be found in [6, 59]. An overview of some of the potential uses of machine learning for modeling and control are shown in Fig. 1.

## *1.1 The Big Data and Small Data Limits*

Fluid dynamics is one of the original "big-data" sciences, consistently pushing the frontiers of computation, storage, and data-processing algorithms for decades [47]. Fluid simulations and experiments often generate tremendous amounts of data, which is necessary to capture the multi-scale nature of turbulence. Ironically, because of the expense and complexity of these simulations and experiments, it is often challenging to explore parameter spaces for optimization and control, resulting in very limited samples for parametric studies. It is critical to recognize these two extremes, as there are various techniques in machine learning that are tailored to both the big-data and small-data limits.

### *1.2 Combinatorially Large Optimizations*

Many practical problems of interest may result in combinatorially hard optimizations that do not scale well to large systems. For example, the optimal placement of a few sensors and actuators is combinatorially hard, as it would require trying every combination to determine the best placement [34]. However, emerging techniques in sparse optimization are systematically making broad classes of combinatorial problems tractable.

### *1.3 Parsimonious Models and Physics*

Many of the impressive demonstrations of machine learning have been demonstrated on static tasks, such as image or scene labeling. In these applications, raw classification performance is generally the highest priority. However, when applying machine learning to physical systems, it is often desirable to have models that are *interpretable* and that *generalize*, such as Newton's laws of motion. Thus, it is essential to extend machine learning techniques to be able to enforce known constraints, symmetries, and conservation laws. There is also an increasing emphasis on *parsimonious* models for physics, relying on the ubiquitous observation that the simplest model is often the correct one.

## 2 Machine Learning for Flow Modeling and Discovery

Model reduction and system identification are well-established fields of mathematical physics and engineering, with long histories in fluid dynamics. Reduced-order models have long been used to accelerate optimization and enable low-latency control, and this is especially important in fluid systems where the dynamics are particularly high-dimensional and timescales may be quite short. Machine learning and modern methods in regression and optimization are currently re-defining the scope of what is possible in model discovery and modeling of fluids. Here, we will explore a handful of promising approaches to model dynamical systems from data, such as fluid systems.

### *2.1 Linear Models*

Linear models are by far the most simple to work with, because of the wealth of analytic and closed-form solutions for linear optimization and control problems. Thus, linear modeling of fluid flows is an important field of research, despite the inherent strong nonlinearity of many flows. The dynamic mode decomposition (DMD) [24,

52, 55, 64] is a particularly useful linear modeling framework, in which it is possible to identify dominant spatio-temporal coherent structures and a linear model for how they evolve in time. The DMD modes are physically interpretable, and the low-order model is efficient to work with. Because DMD is framed as a linear regression, there have been many innovations and extensions [50, 69]. DMD also benefits from a strong connection to nonlinear dynamical systems via the Koopman operator [36, 37, 52].

## 2.2 Sparse and Parsimonious Models

In many situations, the behavior of a flow is fundamentally nonlinear and must be modeled accordingly. Recently, the sparse identification of nonlinear dynamics (SINDy) [7] has provided an interpretable and data-driven technique to obtain differential equation models for nonlinear systems, including fluids [32, 33]. The SINDy framework uses sparse regression in a library of candidate nonlinear functions to identify the fewest terms in an ODE that are required to explain the data, resulting in a parsimonious model with a handful of physically relevant interaction terms. It has been shown that these models have increased flexibility and may provide more accurate predictions than standard Galerkin projection. In addition, it is possible to directly enforce known constraints and symmetries [32], as SINDy models are based on an iteratively thresholded least-squares regression scheme. Recent work has shown that SINDy models may be identified directly on physically realizable sensor measurements [33], such as lift and drag, which has the potential to overcome the well-known issue of mode deformation that challenges traditional Galerkin projection onto proper orthogonal decomposition modes. SINDy has since been extended to identify PDE models [53, 54], and is able to identify the Navier-Stokes equations from data [53].

In addition to SINDy, there are many other powerful nonlinear modeling techniques, such as NARMAX [4, 17, 57, 70]. Other leading methods include the use of Gaussian process priors to infer ODEs from noisy data [51]. In addition, the viewpoint of parsimony was taken earlier in the seminal work of Bongard and Lipson [5] and Schmidt and Lipson [56], where genetic programming was used to identify models of physical systems.

## 2.3 Neural Networks

Recently, neural networks and deep learning have demonstrated remarkable performance on some of the most challenging machine learning tasks where large labeled training datasets are available. Neural networks are essentially very sophisticated curve-fitting techniques that leverage a wealth of historical data for interpolation. They are generally not effective for extrapolation, but with increasingly vast datasets,

it may be possible to obtain training data that sufficiently spans the space of possible future measurements.

Neural networks have long been used in fluid modeling [21, 26–28, 38, 48, 65], and larger datasets and more powerful computers are driving renewed interest. In particular, deep learning has been recently leveraged to great advantage for turbulence closure models [25, 29–31, 35, 45, 58, 62, 63, 66–68]. This is one of the grand challenge problems in turbulence, and it is increasingly likely that machine learning will dramatically improve our ability to develop sub-grid-scale models.

### *2.4 Other Emerging Approaches*

There are many other leading approaches that are leveraging modern data science for flow modeling towards optimization and control. Network theory has recently been introduced to model fluids [40, 41, 60], based on powerful techniques developed in graph theory and network science. Cluster-based methods have also been used for reduced order modeling [2, 19], based on powerful clustering algorithms from machine learning.

## 3 Machine Learning for Optimization and Control

In addition to developing models that may then be used for optimization and control, it is possible to use machine learning directly to optimize and control without a proxy model. For example, early applications of genetic algorithms in flow control involved parameter optimization in open-loop control [39], wake control and drag reduction [14], turbulent channel control [22], and drag reduction of linked bodies [16], to name a few key applications. More recently, genetic programming has been used to design nonlinear controllers for fully turbulent systems, including boundary layers, mixing layers, and jets [6, 11].

Directly using machine learning to design controllers is appealing, as painstakingly identified reduced-order fluid models may change after control is applied. Instead, directly parameterizing and exploring the control space may result in effective control laws, regardless of our ability to model the resulting phenomena. It is also important to note that control design is often formulated by an optimization problem that is constrained by the dynamics or physics of the system. Thus, machine learning, which constitutes a collection of powerful nonlinear optimization techniques based on data, is well positioned to advance nonlinear flow control.

### 3.1 Optimization

Optimization is generally an iterative procedure, and for fluid systems it is often desirable to minimize the number of iterations, as these typically require expensive simulations or experiments. Evolutionary algorithms have long been used in fluid dynamics for optimization, as they provide an effective method to explore a high-dimensional search space [8, 14, 16, 23]. Early efforts used evolutionary algorithms for parameter optimization in open-loop control [39]. This approach was applied to jet mixing [23], wake control and drag reduction [14, 49], optimization of noisy combustion processes [8], and drag reduction of linked bodies [16]. This method was also applied in a combustion experiment to tune the parameters of $\mathcal{H}_\infty$ controllers [18].

### 3.2 Control

Machine learning control based on genetic programming [11] has recently emerged as a technique to control strongly nonlinear experimental flows [6, 10, 13, 15, 43, 44]. Genetic programming is an optimization procedure inspired by biological evolution, where the structure of a function is determined using genetic operations that imitate biological replication, mutation, and cross-over. Genetic programming control has been used effectively to manipulate macroscopic quantities of interest, such as drag, lift, and mixing in a wealth of experiments, including a generalized mean-field model [12], the mixing layer with pulsed actuation jets on the splitter plate [44], the backward facing step controlled by a slotted jet [13, 15], and and a turbulent separated boundary layer [13].

There are many other machine learning control strategies, including neural networks and reinforcement learning. Neural networks have long been used, for example in opposition control [27]. In addition, reinforcement learning has been used for flow control [46] and flight control of UAVs [1, 3, 9, 20, 42, 61].

**Acknowledgements** I am grateful for discussions with Bing Brunton, Eurika Kaiser, Petros Koumoutsakos, Nathan Kutz, Jean-Christophe Loiseau, and Bernd Noack on related topics. I would like to acknowledge support from the Air Force Office of Scientific Research (AFOSR FA9550-18-1-0200).

## References

1. Abbeel, P., Coates, A., Quigley, M., Ng, A.Y.: An application of reinforcement learning to aerobatic helicopter flight. In: Advances in Neural Information Processing Systems, pp. 1–8 (2007)
2. Amsallem, D., Zahr, M.J., Farhat, C.: Nonlinear model order reduction based on local reduced-order bases. Int. J. Numer. Methods Eng. **92**(10), 891–916 (2012)

3. Andrew Bagnell, J., Schneider, J.G.: Autonomous helicopter control using reinforcement learning policy search methods. IEEE International Conference on Robotics and Automation **2**, 1615–1620 (2001)
4. Billings, S.A.: Nonlinear System Identification: NARMAX Methods in the Time, Frequency, and Spatio-Temporal Domains. Wiley, New York (2013)
5. Bongard, J., Lipson, H.: Automated reverse engineering of nonlinear dynamical systems. Proc. Nat. Acad. Sci. **104**(24), 9943–9948 (2007)
6. Brunton, S.L., Noack, B.R.: Closed-loop turbulence control: progress and challenges. Appl. Mech. Rev., **67**, 050801–1–050801–48 (2015)
7. Brunton, S.L., Proctor, J.L., Kutz, J.N.: Discovering governing equations from data by sparse identification of nonlinear dynamical systems. Proc. Nat. Acad. Sci. **113**(15), 3932–3937 (2016)
8. Buche, D., Stoll, P., Dornberger, R., Koumoutsakos, P.: Multiobjective evolutionary algorithm for the optimization of noisy combustion processes. IEEE Trans. Syst. Man Cybernet. Part C Appl. Rev. **32**(4), 460–473 (2002)
9. Cory, R., Tedrake, R.: Experiments in fixed-wing UAV perching. In: Proceedings of the AIAA Guidance, Navigation, and Control Conference, pp. 1–12 (2008)
10. Debien, A., von Krbek, K.A.F.F., Mazellier, N., Duriez, T., Cordier, L., Noack, B.R., Abel, M.W., Kourta, A.: Closed-loop separation control over a sharp edge ramp using genetic programming. Experim Fluids **57**(3), 40 (2016)
11. Duriez, T., Brunton, S.L., Noack, B.R.: Machine Learning Control: Taming Nonlinear Dynamics and Turbulence. Springer (2016)
12. Duriez, T., Parezanović, V., Cordier, L., Noack, B.R., Delville, J., Bonnet, J.-P., Segond, M., Abel, M.: Closed-loop turbulence control using machine learning. arXiv preprint arXiv:1404.4589 (2014)
13. Duriez, T., Parezanovic, V., Laurentie, J.-C., Fourment, C., Delville, J., Bonnet, J.-P., Cordier, L., Noack, B.R., Segond, M., Abel, M., Gautier, N., Aider, J.-L., Raibaudo, C., Cuvier, C., Stanislas, M., Brunton, S.L.: Closed-loop control of experimental shear flows using machine learning. 7th Flow Control Conference AIAA Paper 2014-2219 (2014)
14. Fukagata, K., Kern, S., Chatelain, P., Koumoutsakos, P., Kasagi, N.: Evolutionary optimization of an anisotropic compliant surface for turbulent friction drag reduction. J. Turbul. **9** (2008)
15. Gautier, N., Aider, J.-L., Duriez, T., Noack, B.R., Segond, M., Abel, M.: Closed-loop separation control using machine learning. J. Fluid Mech. **770**, 442–457 (2015)
16. Gazzola, M., Vasilyev, O.V., Koumoutsakos, P.: Shape optimization for drag reduction in linked bodies using evolution strategies. Comput. Struct. **89**(11), 1224–1231 (2011)
17. Glaz, B., Liu, L., Friedmann, P.P.: Reduced-order nonlinear unsteady aerodynamic modeling using a surrogate-based recurrence framework. AIAA J. **48**(10), 2418–2429 (2010)
18. Hansen, N., Niederberger, A.S.P., Guzzella, L., Koumoutsakos, P.: A method for handling uncertainty in evolutionary optimization with an application to feedback control of combustion. IEEE Trans. Evol. Comput. **13**(1), 180–197 (2009)
19. Kaiser, E., Noack, B.R., Cordier, L., Spohn, A., Segond, M., Abel, M., Daviller, G., Osth, J., Krajnovic, S., Niven, R.K.: Cluster-based reduced-order modelling of a mixing layer. J. Fluid Mech. **754**, 365–414 (2014)
20. Kim, J.H., Jordan, M.I., Sastry, S., Ng, A.Y.: Autonomous helicopter flight via reinforcement learning. In: Advances in Neural Information Processing Systems, pp. 799–806 (2004)
21. Knaak, M., Rothlubbers, C., Orglmeister, R.: A Hopfield neural network for flow field computation based on particle image velocimetry/particle tracking velocimetry image sequences. Int. Conf. Neural Netw. **1**, 48–52 (1997)
22. Koumoutsakos, P.: Active Control of Turbulent Channel Flow. Ctr, Stanford (1997)
23. Koumoutsakos, P., Freund, J., Parekh, D.: Evolution strategies for automatic optimization of jet mixing. AIAA J. **39**(5), 967–969 (2001)
24. Kutz, J.N., Brunton, S.L., Brunton, B.W., Proctor, J.L.: Dynamic Mode Decomposition: Data-Driven Modeling of Complex Systems. SIAM (2016)
25. Kutz, J.N.: Deep learning in fluid dynamics. J. Fluid Mech. **814**, 1–4 (2017)

26. Labonté, G.: A new neural network for particle-tracking velocimetry. Experim. Fluids **26**(4), 340–346 (1999)
27. Lee, C., Kim, J., Babcock, D., Goodman, R.: Application of neural networks to turbulence control for drag reduction. Phys. Fluids **9**(6), 1740–1747 (1997)
28. Liang, D., Jiang, C., Li, Y.: Cellular neural network to detect spurious vectors in PIV data. Exp. Fluids **34**(1), 52–62 (2003)
29. Ling, J., Jones, R., Templeton, J.: Machine learning strategies for systems with invariance properties. J. Comput. Phys. **318**, 22–35 (2016)
30. Ling, J., Kurzawski, A., Templeton, J.: Reynolds averaged turbulence modelling using deep neural networks with embedded invariance. J. Fluid Mech. **807**, 155–166 (2016)
31. Ling, J., Templeton, J.: Evaluation of machine learning algorithms for prediction of regions of high Reynolds averaged Navier Stokes uncertainty. Phys. Fluids **27**(8), 085103 (2015)
32. Loiseau, J.-C., Brunton, S.L.: Constrained sparse Galerkin regression. J. Fluid Mech. **838**, 42–67 (2018)
33. Loiseau, J.-C., Noack, B.R., Brunton, S.L.: Sparse reduced-order modeling: sensor-based dynamics to full-state estimation. J. Fluid Mech. **844**, 459–490 (2018)
34. Manohar, K., Brunton, B.W., Nathan Kutz, J., Brunton, S.L.: Data-driven sparse sensor placement. IEEE Control Syst. Mag. **38**(3), 63–86 (2018)
35. Maulik, R., San, O.: A neural network approach for the blind deconvolution of turbulent flows. *arXiv preprint* arXiv:1706.00912 (2017)
36. Mezić, I.: Spectral properties of dynamical systems, model reduction and decompositions. Nonlinear Dyn. **41**(1–3), 309–325 (2005)
37. Mezic, I.: Analysis of fluid flows via spectral properties of the Koopman operator. Ann. Rev. Fluid Mech. **45**, 357–378 (2013)
38. Milano, M., Koumoutsakos, P.: Neural network modeling for near wall turbulent flow. J. Comput. Phys. **182**(1), 1–26 (2002)
39. Müller, S.D., Milano, M., Koumoutsakos, P.: Application of machine learning algorithms to flow modeling and optimization. Ann. Res. Briefs, pp. 169–178 (1999)
40. Nair, A.G., Taira, K., Brunton, S.L.: Networked oscillator based modeling and control of unsteady fluid flows. Submitted J, Fluid Mech (2017)
41. Nair, A.G., Taira, K.: Network-theoretic approach to sparsified discrete vortex dynamics. J. Fluid Mech. **768**, 549–571 (2015)
42. Ng, A.Y., Coates, A., Diel, M., Ganapathi, V., Schulte, J., Tse, B., Berger, E., Liang, E.: Autonomous inverted helicopter flight via reinforcement learning. In: Experimental Robotics IX, pp. 363–372. Springer (2006)
43. Parezanovic, V., Cordier, L., Spohn, A., Duriez, T., Noack, B.R., Bonnet, J.-P., Segond, M., Abel, M., Brunton, S.L.: Frequency selection by feedback control in a turbulent shear flow. J. Fluid Mech. **797**, 247–283 (2016)
44. Parezanovic, V., Laurentie, J.-C., Duriez, T., Fourment, C., Delville, J., Bonnet, J.-P., Cordier, L., Noack, B.R., Segond, M., Abel, M., Shaqarin, T., Brunton, S.L.: Mixing layer manipulation experiment–from periodic forcing to machine learning closed-loop control. J. Flow Turbul. Combust. **94**(1), 155–173 (2015)
45. Parish, E.J., Duraisamy, K.: A paradigm for data-driven predictive modeling using field inversion and machine learning. J. Comput. Phys. **305**, 758–774 (2016)
46. Pivot, C., Mathelin, L., Cordier, L., Guéniat, F., Noack, B.R.: A continuous reinforcement learning strategy for closed-loop control in fluid dynamics. In: 35th AIAA Applied Aerodynamics Conference, pp. 3566 (2017)
47. Pollard, A., Castillo, L., Danaila, L., Glauser, M.: Whither Turbulence and Big Data in the 21st Century?. Springer (2016)
48. Poloni, C., Giurgevich, A., Onesti, L., Pediroda, V.: Hybridization of a multi-objective genetic algorithm, a neural network and a classical optimizer for a complex design problem in fluid dynamics. Comput. Methods Appl. Mech. Eng. **186**(2), 403–420 (2000)
49. Poncet, P., Cottet, G.-H., Koumoutsakos, P.: Control of three-dimensional wakes using evolution strategies. Comptes R. Mecan. **333**(1), 65–77 (2005)

50. Proctor, J.L., Brunton, S.L., Nathan Kutz, J.: Dynamic mode decomposition with control. SIAM J. Appl. Dyn. Syst. **15**(1), 142–161 (2016)
51. Raissi, M., Perdikaris, P., Em Karniadakis, G.: Inferring solutions of differential equations using noisy multi-fidelity data. J. Comput. Phys. **335**, 736–746 (2017)
52. Rowley, C.W., Mezić, I., Bagheri, S., Schlatter, P., Henningson, D.S.: Spectral analysis of nonlinear flows. J. Fluid Mech. **645**, 115–127 (2009)
53. Rudy, S.H., Brunton, S.L., Proctor, J.L., Kutz, J.N.: Data-driven discovery of partial differential equations. Sci. Adv. **3**(e1602614) (2017)
54. Schaeffer, H.: Learning partial differential equations via data discovery and sparse optimization. In: Proceedings of Royal Society A, vol. 473, p. 20160446. The Royal Society (2017)
55. Schmid, P.J.: Dynamic mode decomposition of numerical and experimental data. J. Fluid Mech. **656**, 5–28 (2010)
56. Schmidt, M., Lipson, H.: Distilling free-form natural laws from experimental data. Science **324**(5923), 81–85 (2009)
57. Semeraro, O., Lusseyran, F., Pastur, L., Jordan, P.:. Qualitative dynamics of wavepackets in turbulent jets. *arXiv preprint* arXiv:1608.06750 (2016)
58. Singh, A.P., Medida, S., Duraisamy, K.: Machine-learning-augmented predictive modeling of turbulent separated flows over airfoils. AIAA J. **55**(7), 2215–2227 (2017)
59. Taira, K., Brunton, S.L., Dawson, S., Rowley, C.W., Colonius, T., McKeon, B.J., Schmidt, O.T., Gordeyev, S., Theofilis, V., Ukeiley, L.S.: An overview. To appear in AIAA J, Modal Anal Fluid Flows (2017)
60. Taira, K., Nair, A.G., Brunton, S.L.: Network structure of two-dimensional decaying isotropic turbulence. J. Fluid Mech. **795**, R2 (2016)
61. Tedrake, R., Jackowski, Z., Cory, R., William Roberts, J., Hoburg, W.: Learning to fly like a bird. In: 14th International Symposium on Robotics Research. Lucerne, Switzerland (2009)
62. Tracey, B., Duraisamy, K., Alonso, J.: Application of supervised learning to quantify uncertainties in turbulence and combustion modeling. AIAA Paper **259**, 2013 (2013)
63. Tracey, B., Duraisamy, K., Alonso, J.J.: A machine learning strategy to assist turbulence model development. AIAA Paper **1287**, 2015 (2015)
64. Tu, J.H., Rowley, C.W., Luchtenburg, D.M., Brunton, S.L., Kutz, J.N.: On dynamic mode decomposition: theory and applications. J. Comput. Dyn. **1**(2), 391–421 (2014)
65. Wang, D.H., Liao, W.H.: Modeling and control of magnetorheological fluid dampers using neural networks. Smart Mater. Struct. **14**(1), 111 (2004)
66. Wang, J.-X., Wu, J.-L., Xiao, H.: Physics-informed machine learning approach for reconstructing Reynolds stress modeling discrepancies based on DNS data. Phys. Rev. Fluids **2**(3), 034603 (2017)
67. Wang, J.-X., Wu, J.-L., Ling, J., Iaccarino, G., Xiao, H.: A comprehensive physics-informed machine learning framework for predictive turbulence modeling. arXiv preprint arXiv:1701.07102 (2017)
68. Wang, Z., Xiao, D., Fang, F., Govindan, R., Pain, C.C., Guo, Y.: Model identification of reduced order fluid dynamics systems using deep learning. Int. J. Numer, Methods Fluids (2017)
69. Williams, M.O., Kevrekidis, I.G., Rowley, C.W.: A data-driven approximation of the Koopman operator: extending dynamic mode decomposition. J. Nonlinear Sci. **6**, 1307–1346 (2015)
70. Zhang, W., Wang, B., Ye, Z., Quan, J.: Efficient method for limit cycle flutter analysis based on nonlinear aerodynamic reduced-order models. AIAA J. **50**(5), 1019–1028 (2012)

# Compressibility Effects in Fluid-Structure Interaction

# Effect of Frozen Turbulence Assumption on the Local Blades Vibration on the Choke Flutter Instability in Transonic UHBR Fan


**Pierre Duquesne, Stéphane Aubert, Quentin Rendu, and Pascal Ferrand**

**Abstract** The choke flutter can lead to the failure of fan or compressor blade in turbojet engines. Choke flutter appears when a strong shock-wave chokes the blade to blade channel. In UHBR fan, choke flutter appears at part speed regimes and at low or negative incidence. In this paper, the choke flutter instability is analyzed based on the resolution of time-Linearised Reynolds-Averaged Navier-Stokes on a 2D blade to blade extraction of an Ultra High Bypass Ratio (UHBR) fan named ECL5v1. An analytical motion of rotation of the airfoil around its leading edge, without the deformation of the blade surface is imposed to a typical choke flutter fan operating condition. For a selected Inter Blade Phase Angle (90°) and selected reduced frequency (0.15), choke flutter instability happens. The blade vibration is decomposed in a large set of subsection to determine the main local flutter sources. This paper aims to analyze the effect of the turbulence modelling on the position of the main local flutter sources and on the work exchange along the blade. Two cases are considered, with the frozen turbulence assumption or with the linearization of the turbulence model. The results locate the main local flutter sources at the same position, with the same work exchange direction but with a modulation of the work exchange magnitude. Amplification or restriction of the magnitude seems to be linked to the steady flow phenomena around both the excitation source and the receptor.

**Keywords** Frozen turbulence · Choke flutter · LURANS · UHBR fan · Transonic flow

P. Duquesne (✉) · S. Aubert · Q. Rendu · P. Ferrand
Université de Lyon, ECL, LMFA UMR CNRS 5509,
36 av. Guy de Collongue, 69134 Ecully, France
e-mail: pierre.duquesne@ec-lyon.fr



M. Braza et al. (eds.), *Advances in Critical Flow Dynamics Involving Moving/Deformable Structures with Design Applications*, Notes on Numerical Fluid Mechanics and Multidisciplinary Design 147,
https://doi.org/10.1007/978-3-030-55594-8_29

# 1 Introduction

The choke flutter can lead to the failure of fan or compressor blade in turbojet engines. Choke flutter appears when a strong shock-wave chokes the blade to blade channel. In UHBR fan, choke flutter appears at part speed regimes (typically 80 Nn) and at low or negative incidence (high mass flow, low total pressure ratio). The steady flow is subsonic upstream and downstream of the blade row and supersonic in the blade to blade channel. A strong shock-wave chokes the channel from the suction side to the pressure side.

This paper is the continuity of previous works on a specific case of UHBR fan named ECL5v1. The choke flutter instability is analyzed based on the resolution of time-Linearised Reynolds-Averaged Navier-Stokes on a 2D blade to blade extraction. An analytical motion of rotation of the airfoil around its leading edge, without the deformation of the blade surface (i.e. a rigid body motion), is imposed to a typical choke flutter fan operating condition. For a selected Inter Blade Phase Angle (IBPA = 90°) and selected reduced frequency (0.15), choke flutter instability happens [4]. In [1], for the same test-case, the blade vibration is decomposed in a large set of subsection to determine the main local flutter sources. The analysis reveals few zones of important work exchange. The exchange induce by the motion of two side by side small zones near the trailing edge on the pressure side lead the overall stability. The direction of the work exchange is different for each zone depending on the phase. The suspected phenomenon, the same in both cases, is the amplification of backward pressure waves at the shock wave. Another couple of sources located on each side of the shock-wave on the suction side has a significant contribution to the overall work exchange. Vibration of these points induce a supplementary motion of the separation bubble and the shock wave.

In the previous works the $k$-$\omega$ turbulence model is Linearised, the main goal of this paper is to apply the same methodology on a set of calculation with the frozen turbulence assumption and compare these results and the results obtain without this assumption.

# 2 Numerical Methods

## *2.1 Steady RANS Solver*

The compressible RANS solver Turb'Flow is used in this work to compute the 2D steady flow in a 90% height blade to blade channel. This solver relies on vertex centred finite volume method on multi-block structured grids [8].

Convective fluxes are obtained through upwind scheme of Roe [6] with Monotonic Upstream-centred Scheme for Conservative Laws (MUSCL) interpolation of third order [9]. The interpolation order is reduced in strong gradient zones according to Harmonic Cubic Upwind Interpolation (H-CUI) limiter. Diffusive fluxes are

obtained through central interpolation of conservative variables. The pseudo time discretisation relies on backward Euler with CFL = 20 and local time step to speed up the convergence. The linear problem arising from the implicit method is solved through GMRES iterative method [7].

The flow is considered fully turbulent and the $k$-$\omega$ turbulence model of Wilcox [11] has been used. At the wall $\omega$ value is extrapolated to be assumed infinite.

## 2.2 Time-Linearised URANS Solver

The Linearised RANS (LRANS) solver Turb'Lin is used to compute the harmonic flow around the steady state. This solver has been previously validated on transonic separated flows [3, 5]. The solution is obtained in the frequency domain by solving the linear system. Spatial discretisation relies on Jameson et al. [2] centred scheme with linearised pressure sensor.

## 2.3 Aeroelasticity

The complex amplitude of displacement $\widetilde{\delta \mathbf{x}}$ and velocity $\widetilde{\mathbf{V}}$ is imposed at each node of the blade mesh to model the blades oscillation. The steady position of the blade is chosen as the phase origin. This yields

$$\Re(\widetilde{\delta \mathbf{x}}) = 0 \quad ; \quad \Im(\widetilde{\mathbf{V}}) = 0 \tag{1}$$

The interblade phase angle (IBPA) $\sigma$ is modelled through quasi-periodic boundary conditions in azimuthal direction

$$\widetilde{\boldsymbol{q}}(\boldsymbol{x_b} + \boldsymbol{g}) = \widetilde{\boldsymbol{q}}(\boldsymbol{x_b}) e^{j\sigma} \tag{2}$$

where $\widetilde{\boldsymbol{q}}$ is the complex amplitude of conservative variable fluctuations, $\boldsymbol{x_b}$ the domain boundary and $\boldsymbol{g}$ the interblade pitch.

The work $\mathcal{W}$ extracted by the flow from the structure is written according to the convention of Verdon [10].

$$\mathcal{W} = \int_0^T \left[ -\widetilde{Ps}(\mathbf{x}, t) * \mathbf{S}(\mathbf{x}, t) \right]^t \cdot \widetilde{\mathbf{V}}(\mathbf{x}, t) \mathrm{d}t \tag{3}$$

where $\widetilde{Ps}$ is the instantaneous static pressure, $\mathbf{S}$ the vector associated to the instantaneous surface, oriented towards the structure, and $\widetilde{\mathbf{V}}$ the instantaneous velocity vector associated to the blade displacement.

In frequency domain, neglecting second order terms, the only contribution to the unsteady work is, for a rigid body motion,

$$\Re(\,{}^1\widetilde{Ps})\,\mathbf{S}\cdot\Re(\,{}^1\widetilde{\mathbf{V}}) \tag{4}$$

where ${}^1\widetilde{Ps}$ and ${}^1\widetilde{\mathbf{V}}$ are the complex amplitude of first harmonic of static pressure and velocity vector, respectively. Thus only the real part of fluctuating static pressure contributes to the stability of the fluid-structure interaction.

The damping coefficient is then obtained by the integral of the extracted work normalized by the maximal vibrating kinetic energy along the blade surface

$$\zeta = \frac{1}{4\pi}\frac{\int\int_\Omega \mathcal{W}\mathrm{d}\Omega}{\mathcal{U}} \tag{5}$$

where $\Omega$ is the fluid-structure contact interface and $\mathcal{U}$ the maximal vibrating kinetic energy of the blade given by

$$\mathcal{U} = \frac{1}{2}\rho\omega S_B \tag{6}$$

where $\rho$ is the blade material density, $\omega$ the vibration pulsation and $S_B$ the total blade surface.

Superposition principle induced by the linearisation of RANS equation leads to the equality between the unsteady flow generated by the vibration of the whole blade and the vibration of each surface mesh node. The blade vibration can thus be decomposed in an arbitrary number of zones $N$ and the global damping coefficient can be computed by the sum of the damping coefficient associated to each vibration. Formally,

$$\zeta = \sum_i^N \zeta_i \quad ; \quad \zeta_i = \frac{1}{4\pi\mathcal{U}}\int\int_\Omega \Re(\,{}^1\widetilde{Ps_i})\,\mathbf{S}\cdot\Re(\,{}^1\widetilde{\mathbf{V}})\mathrm{d}\Omega \tag{7}$$

where $\widetilde{Ps_i}$ represents the pressure fluctuations generated by the motion of zone $i$. To avoid even-odd decoupling, the blade is decomposed into pairs of adjacent mesh nodes. Each computation consists in the vibration of two adjacent nodes: first calculation is computed with the motion of the first and second mesh nodes, next calculation by the motion of the third and fourth nodes, etc. The equality of the global damping coefficient, and its repartition along the chord, for the entire blade vibration and the result of the sum of the motion of each node has been checked. This decomposition strategy has some subtleties: the distance between adjacent nodes is not constant, to compare the contribution of each nodes association the extracted work need to be normalized by the length between the two points. The set of calculations includes 828 L-URANS calculations (half with the calculated turbulence in 424 positions and half with the frozen turbulence assumption at the same positions). All these calculations are based on the same 2D steady state calculation.

### 2.4 Frozen Turbulence Assumption

With the frozen turbulence assumption, the turbulence variables are fixed in time at their steady values, this assumption means that the characteristic time of the turbulence evolution is very slow comparatively to the blade vibration characteristic time (here 300 Hz). In opposition, without the frozen turbulence assumption, the turbulence model is also Linearised and turbulence variables are calculated in each time step. Physically, that corresponds to consider that the turbulence reacts without delay to the fluctuation of the flow. In previous papers, because of the separated flows the turbulence model has linearised [1, 3, 5].

## 3 Studied Configuration

### 3.1 UHBR Fan

The chosen test case is the Ultra High Bypass Ratio (UHBR) fan ECL5v1. The ECL5 design goals are to generate selected aeroelastic and aerodynamic instabilities, including the choke flutter at part-speed regime, remaining representative of future transonic UHBR fan. The operating range of the ECL5v1 fan, issues from numerical simulations, is plotted in Fig. 1 for three different rotational speeds (nominal speed Nn = 10 450 rpm).

The energetic method allows to decompose 3D blade in a sum of 2D airfoils. Most of the extracted work is generated close to the tip due to high levels of both blade velocity and pressure fluctuations. Therefore a 2D blade to blade channel mesh has been extracted at 90% of ECL5v1 height to run the aeroelastic study. At this height the blade surface shows thin, highly staggered blades with low camber, which is typical of transonic fan tip airfoils.

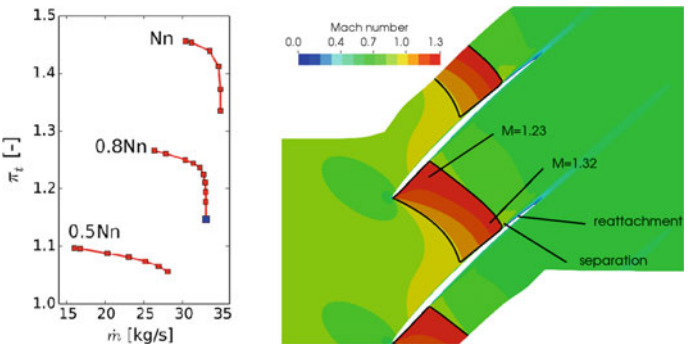


**Fig. 1** Left: operating range of ECL5v1—choked operating point in blue. Right: steady relative Mach number for choked flow

Choke flutter is associated with negative incidence and strong shock-wave choking the interblade channel. It appears for part-speed regime, typically around 80% of the nominal rotational speed. For the aeroelastic study, the operating point showing the highest massflow on 0,8 Nn speed characteristic line is thus chosen (in blue in Fig. 1).

### *3.2 Steady Flow*

The mesh used for both steady and unsteady computations has been obtained through a convergence study. It consists in 106 007 points with $y^+ < 1$ for the first layer of cells close to the blade surface. Total pressure, total temperature and azimuthal velocity are imposed at the upstream boundary and the static pressure at downstream boundary. The boundary conditions of the 2D-steady flow calculation are set to preserve the shock-wave position from the 3D calculation. The steady relative Mach number associated with the choked flow is plotted in Fig. 1.

Looking at the leading edge zone, negative incidence can be seen as well as a supersonic region choking the interblade channel and terminated by a strong shock-wave. On the pressure side, the maximal Mach number is 1.23 and the boundary layer is attached to the blade downstream of the shock-wave. On the suction side, the Mach number reaches 1.32 which leads to the separation of the boundary layer downstream of the shock-wave. The separation is closed and the reattachment point is located 8.3% of chord downstream of the separation point.

### *3.3 Modeshape*

In this study, the chosen mode shape consists in a rotation of the airfoil around its leading edge without the deformation of the blade surface (i.e. a rigid body motion). This mode shape is representative of the first 3D torsion mode of the blade where the transonic flutter is observed. Motion of adjacent blades can present a phase shift called interblade phase angle or IBPA (frequency and mode shape remain identical between blades). The IBPA is by convention positive when the wave propagates in the same direction as the rotor speed and negative otherwise. The reduced frequency, for turbomachinery aeroelastic study, represents the ratio between the time of flight of a fluid particle along the chord and the time of a vibration period. In this work based on previous study, the IBPA is set at 90° and the reduced frequency is low at 0.15. The damping coefficient obtained is negative. In the paper convention the work exchange is from the blade to the fluid so this case presents a choke flutter instability.

A sketch of three adjacent blades position during the vibration cycle is plotted in Fig. 2. For each blade, colours correspond to different instants (−T/4, 0, T/4). Vibration amplitude and interblade distant are modified for illustration purpose. The

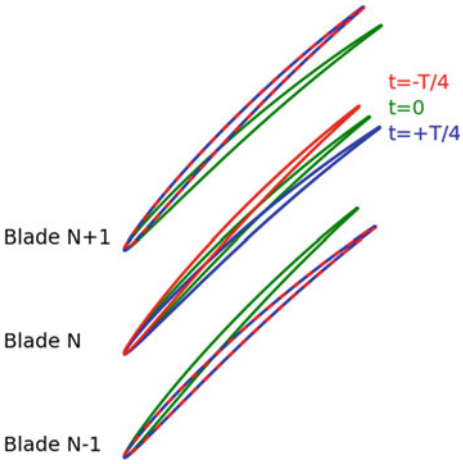


**Fig. 2** Sketch of the vibration of three adjacent blades at three different instants, airfoil colours show the different instants: −T/4, 0, T/4. Vibration amplitude and interblade distant are modified for illustration purpose

effective solidity (spacing/chord ratio) is 1.37. The out of phase blades vibration induces different passage section for adjacent interblade channels (see the same instant for the two channels in Fig. 2). This area fluctuation leads to strong velocity fluctuations.

## 4 Effect of Frozen Turbulence Assumption

### *4.1 Effect on the Total Damping Coefficient*

The total damping coefficient $\zeta$ (calculate with Eq. 5) is negative, which corresponds to the blade vibration amplification (flutter case), independently of the frozen turbulence assumption use. The damping coefficient magnitude is smaller, but in the same order of magnitude, for the frozen turbulence case. The damping coefficient difference between both cases is similar to the difference when another turbulence model is Chosen. In this sense the frozen turbulence assumption has a restricted effect on the prediction of the damping coefficient.

The work exchange, normalized by the maximal vibrating kinetic energy and element surface, along the chord is plotted in Fig. 3 for the calculated turbulence case (blue line) and for the frozen turbulence case (dashed red). The smaller damping coefficient for the frozen turbulence case is induced by a smaller work exchange downstream to the shock-wave. The work exchange reduction is more important on the suction side in particular in the flow separation bubble zone. This result suggests that the effect of the frozen turbulence assumption is concentrated on the flow separation bubble that is consistent with the importance of viscous effects in this type of secondary flow. The flow downstream the shock wave is indirectly impacted

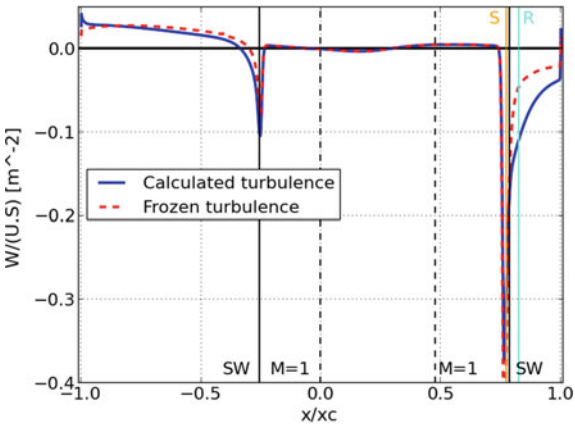


**Fig. 3** Extracted normalized work along blade chord for calculated or frozen turbulence (leading edge at x/xc = 0, pressure side: x/xc < 0, suction side: x/xc > 0). Separation, reattachment, sonic line and shock-wave positions are represented by vertical lines labeled S, R, M = 1 and SW respectively

by the effect on the flow separation bubble and the flow upstream is not affected, protected by the strong shock-wave which chokes the interblade channel.

## *4.2 Effect on Main Flutter Source*

To determine the main flutter sources, the sum of the work along the chord is performed for the individual motion of each point. Results for both sets of calculations are represented in Fig. 4, the case with calculated turbulence on the left and with the frozen turbulence assumption in the middle. The right side of Fig. 4 shows the enlargement of the trailing edge in both cases. The colours correspond to the work around the airfoil for the motion of the segment at this position. Here, the work is normalized by the length of the moving segment to determine main flutter sources without the effect of the segment length. Colour scale has been restricted for presentation purpose due to local high values near the trailing edge. In Fig. 4, the supersonic zone is delimited by black lines and the position of the separation point and reattachment point are reported by (S) and (R) respectively.

The global repartition pattern of the flutter sources is similar between both sets of calculations: the overall stability is induced by few localized excitation sources with high intensity near the trailing edge. The stabilizing or destabilizing aspect of main local sources have the same direction in both cases. Four particular zones have been selected because of their high contribution to stability in a restricted area. In addition to having the same stabilizing or destabilizing behaviour, main flutter sources with or without calculated turbulence have the same size. These zones are listed in Table 1 and reported in Fig. 4 with a reference letter (A,B,C,D).

In both set of calculations zones are the same. The A-zone is located on the pressure side near (but not at) the trailing edge. The vibration of this small zone, less than 0.1% of the total airfoil length, induces the largest part of the negative

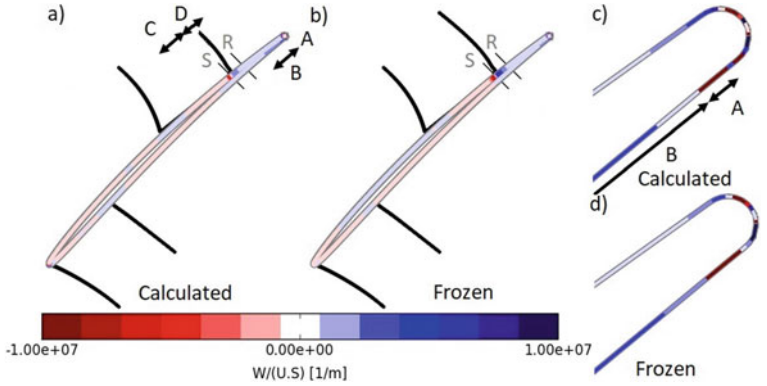


**Fig. 4** Normalized work on the airfoil, sonic line is in black, (S) and (R) are respectively separation and reattachment points, selected zones are referred by A, B, C, D. Left airfoil represents results for calculated turbulence, middle figure for frozen turbulence assumption and the trailing edge enlargement at right

**Table 1** Selected region name, work (−:destabilizing, +:stabilizing) for calculated and frozen turbulence, the percentage in bracket is the work contribution induce by the segment motion in the destabilizing part of the work (or stabilizing case dependent) and the zone length versus the airfoil length

| Zone name | Calculated $\mathcal{W}/\mathcal{U}.10^{-3}$ | Frozen $\mathcal{W}/\mathcal{U}.10^{-3}$ | Zone length (% of chord) |
|---|---|---|---|
| *A* | − 11.5 (56%) | − 7.9 (44%) | 0.1 |
| *B* | + 8.5 (44%) | + 5.7 (32%) | 5 |
| *C* | − 3.6 (17%) | − 6.1 (34%) | 4 |
| *D* | + 3.1 (16%) | + 6.1 (34%) | 2 |
| Airfoil | − 1.4 | − 0.3 | |
| Sum $\mathcal{W}/\mathcal{U} < 0$ | − 20.6 | − 18 | |
| Sum $\mathcal{W}/\mathcal{U} > 0$ | + 19.2 | + 17.7 | |

(destabilizing) work. The vibration of the zone just upstream the A-zone on the pressure side (B-zone) induces a large part of the positive (stabilizing) work. Even if B-zone is larger than the A-zone, it is small (4.2% of the total airfoil length). The stabilizing work induced by the motion of the B-zone cannot compensate for the large amount of destabilizing work induced by the motion of the A-zone : the cumulative work of A and B-zones is negative (destabilizing). On the suction side, most of the contribution on the stability is again induced by the motion of points located near the trailing edge. The C-zone is just upstream the shock-wave and the D-zone downstream. D-zone corresponds to the flow separation bubble (between the separation and the reattachment point). The separation point is the border between C and D zones and corresponds to an inversion of the work exchange. C zone induces negative (destabilizing) work instead of D-zone that induces positive (stabilizing)

work. The proportion to the contribution to the stabilizing work and the destabilizing work induced by both zones are similar.

The frozen turbulence assumption impact magnitude of all flutter sources but in different ways. The frozen turbulence assumption tends to predict smaller work exchange for zones A and B and larger work exchange for zones C and D. For example, the contributions of zone C on the total destabilizing work is twice when frozen turbulence assumption is used (from 17 to 34%). The same effect can be observed for zone D and in the same time contributions of zones A and B decrease. Despite that, the pressure side flutter sources always lead the global stability. The balance between zone A and B is smaller when using frozen turbulence assumption but always negative (destabilizing) and larger than other sources. In comparison, the couple zone C and zone D tend to cancel their effect mutually in both cases. Due to this result, the next analysis is focused on the work exchange induced by the motion of a point of A and B zone only.

### *4.3 Effect on the Stability Induced by Pressure Side Zones*

Figure 5 presents the extracted work along the blade chord for the motion of the most destabilizing point from A-zone (in red) and for the motion of the most stabilizing point from B-zone (in green). Solid line and dashed lines represent results

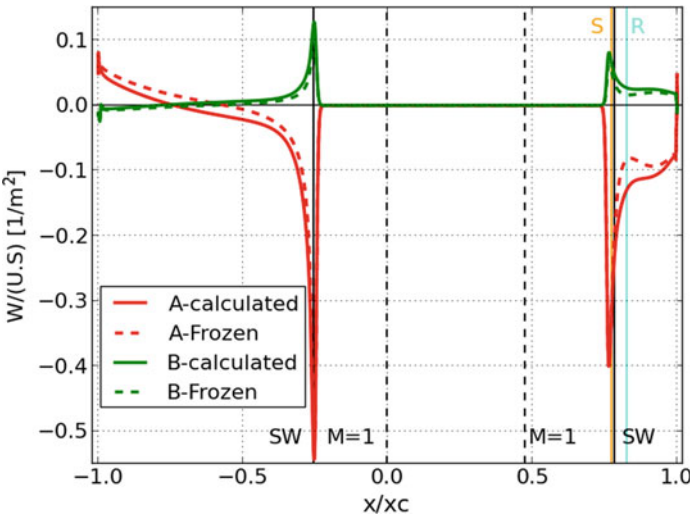


**Fig. 5** Normalised extracted work along blade chord produced by the motion of a point in zone A and B (leading edge at x/xc = 0, pressure side: x/xc < 0, suction side: x/xc > 0). Separation, reattachment, sonic line and shock-wave positions are represented by vertical lines noted S, R, M = 1 and SW respectively. Solid and dashed line for calculated and frozen turbulence respectively

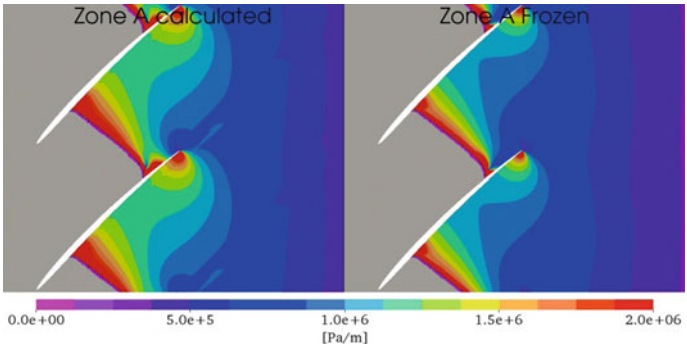


**Fig. 6** Pressure fluctuation modulus induces by the motion of the most destabilizing point in A-zone. Calculated and frozen turbulence respectively at left and right

for calculated turbulence and frozen turbulence cases respectively. The two selected points are close together and on the pressure side downstream the shock-wave near the trailing edge. As is postulated in [1], backward pressure waves generated by the motion of a point in zone A or B travel upstream in the blade to blade channel up to the shock-wave. When the backward pressure waves reach the shock-wave their amplitude increased. The amplification of the pressure fluctuation induces more work exchange. Results for frozen turbulence assumption shows a more stabilizing behaviour downstream the shock-wave in particular in the flow separation bubble.

The pressure fluctuation modulus for the motion of a point in zone A with or without frozen turbulence assumption is presented in Fig. 6 (the pressure fluctuation modulus for a point in zone B has the same pattern with a smaller amplitude). At the excitation source, the pressure fluctuation produced by the motion of the segment is larger with the frozen turbulence assumption, but as shown in Fig. 6, pressure fluctuation is smaller in the neighbourhood of the source. The frozen turbulence tends to reduce the propagation of the pressure waves. Also, the frozen turbulence reduces the interaction of the pressure wave with the flow separation bubble and leads to smaller pressure fluctuations in this region. This observation tends to confirm the hypothesis that the higher pressure fluctuation gradient on the suction side is explained by the interaction with the flow separation bubble as formulated in [1]. The frozen turbulence assumption seems to lead to smaller pressure fluctuations where viscous effects are important.

The direction of the work exchange seems to be linked to the phase of the excitation source. The phase mapping of the motion of a point in A zone (destabilizing) and in B zones (stabilizing) have similar pattern but with a 180° phase shift. The frozen turbulence assumption has no effect on the phase shift. The representation of turbulence plays here a minor part. The direction of the work exchange is not sensitive to the viscous effect and the mechanism of amplification of the pressure wave at the shock-wave appears mainly like a potential effect.

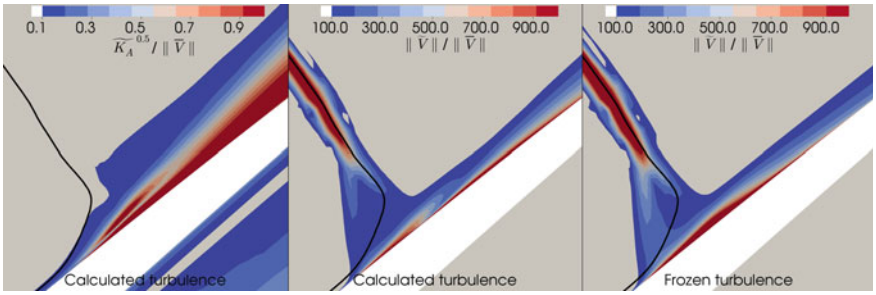


**Fig. 7** Squared normalized turbulent kinetic energy fluctuation modulus induces by the motion of the most destabilizing point in A-zone for calculated turbulence at left. Normalized velocity fluctuation modulus induces by the same point for calculated and frozen turbulence respectively in the middle and at right. Black lines represent the steady shock-wave

In Fig. 7 the square root of the turbulent kinetic energy fluctuation modulus and the velocity fluctuation modulus, both normalized by the averaged velocity norm, are represented. The map of the turbulent kinetic energy fluctuation modulus is not represented for the frozen turbulence, as by definition this one is null everywhere. Due to the small displacement assumption in the Linearised calculation, the fluctuation values don't correspond to the real fluctuation but are scaled for a unitary displacement.

As shown in Fig. 7, the velocity fluctuation is more prominent at the shock-wave and in the flow separation bubble in both cases. The velocity fluctuation at the shock wave is relatively similar with or without frozen turbulence assumption. Contrary to inside and near the flow separation bubble, the velocity fluctuation is more important and more uniform in the case of the frozen turbulence. At the same positions, the turbulent kinetic energy fluctuates when the turbulence is not frozen. In the case of the frozen turbulence assumption, the fluctuation of the total energy can only be redirected to the term of pressure fluctuation and velocity fluctuation. In the case of the calculated turbulence, the term of the turbulence can absorb a part of the energy fluctuation. Therefore the turbulence (when calculated at each time) acts like a damper in the boundary layer and limit the velocity fluctuation. Even if the turbulence fluctuation is three orders of magnitude smaller than velocity fluctuation they have a non-negligible effect on the work exchange induced by the vibration of the A-zone.

## 5 Conclusions

The choke flutter in an Ultra High Bypass Ratio fan is analyzed using a time-Linearised Reynolds-Averaged Navier-Stokes equation solver on a 2D blade to blade extraction at 90% height. Two cases for the $k$-$\omega$ turbulence model are considered:

with the turbulence quantities calculated at each time step or using the frozen turbulence assumption. A vibrating decomposition method based on the superposition principle is performed on each surface mesh node to identify the main sources of the work exchange between the flow and the blade.

In both cases, with and without frozen turbulence assumption, the damping coefficient and the position of most intense destabilizing sources and stabilizing sources are similar. The overall stability is leading by two couples of stabilizing/destabilizing sources. The first couple is downstream of the shock-wave near the trailing edge on pressure side. The vibration of this zone induces backward travelling pressure waves, which propagates upstream up to the shock-wave. The next couple is on the suction side in the neighborhood of the interaction between the shock-wave and the flow separation. The destabilizing source is just upstream the shock-wave and the stabilizing source correspond to the flow separation bubble. For both couples of sources, the stability direction is linked to the phase, stabilizing sources and destabilizing sources have a phase shift of 180°.

The frozen turbulence assumption plays on the amplitude of these two couples of sources. With the frozen turbulence assumption, the main source on the pressure side has a smaller work exchange and, in opposition, the work exchange is more intense for the main source on the suction side. The frozen turbulence has more effect where the viscous effects are important in the flow dynamics (i.e. in the flow separation bubble). Analysis of turbulent kinetic energy fluctuations and velocity fluctuations of the most destabilizing zone (A-zone) reveals that the turbulence acts like a damper in the boundary layer and limits the velocity fluctuation when turbulence is calculated at each time step. The small proportion of total energy absorbed by the turbulence has a non-negligible impact on the work exchange. This test-case shows an example of the importance to calculate the turbulence at each time step, in particular when flow phenomena are driven by viscous effects.

## References

1. Duquesne, P., Rendu, Q., Ferrand, P., Aubertm, S.: Local contribution of blades vibration on the choke flutter instability in transonic UHBR fan. In: 53rd 3AF International Conference on Applied Aerodynamics. Salon de Provence, France (2018)
2. Jameson, A., Schmidt, W., Turkel, E.: Numerical solution of the Euler equations by finite volume methods using Runge Kutta time stepping schemes. In: *14th Fluid and Plasma Dynamics Conference*. American Institute of Aeronautics and Astronautics, Palo Alto (1981)
3. Philit, M., Ferrand, P., Labit, S., Chassaing, J.-C., Aubert, S., Fransson, T.: Derivated turbulence model to predict harmonic loads in transonic separated flows over a bump. In: 28th International Congress of Aeronautical Sciences. Brisbane, Australia (2012)
4. Rendu, Q., Aubert, S., Ferrand, P.: Influence of reduced frequency on choke flutter instability in transonic UHBR fan. In: International Forum on Aeroelasticity and Structural Dynamics, Como, Italy (2017)
5. Rendu, Q., Philit, M., Labit, S., Chassaing, J.-C., Yannick, R., Aubert, S., Ferrand, P.: Time-linearized and harmonic balance Navier-Stokes computations of a transonic flow over an oscillating bump. In: 11th International Symposium on Unsteady Aerodynamics, Aeroacoustics and Aeroelasticity of Turbomachines. Stockholm, Sweden (2015)

6. Roe, P.L.: Approximate Riemann solvers, parameter vectors, and difference schemes. J. Comput. Phys. **43**(2), 357–372 (1981)
7. Saad, Y., Schultz, M.: GMRES: A generalized minimal residual algorithm for solving non-symmetric linear systems. SIAM J. Sci. Stat. Comput. **7**(3), 856–869 (1986)
8. Smati, L., Aubert, S., Ferrand, P., Massão, F.: Comparison of numerical schemes to investigate blade flutter. In: Unsteady Aerodynamics and Aeroelasticity of Turbomachines, pp. 749–763. Springer, Dordrecht (1998)
9. Van Leer, B.: Towards the ultimate conservative difference scheme. V. A second-order sequel to Godunov's method. J. Comput. Phys. **32**(1), 101–136 (1979)
10. Verdon, J.: Linearized unsteady aerodynamic theory. In: AGARD Manuel on Aeroelasticity in Axial-Flow Turbomachines, Vol. 1. Unsteady Turbomachinery Aerodynamics. Advisory Group for Aerospace Research and Development, Neuilly-sur-Seine (France) (1987)
11. Wilcox, D.C.: Reassessment of the scale-determining equation for advanced turbulence models. AIAA J. **26**(11), 1299–1310 (1988)

# Numerical and Experimental Investigations of Buffet on a Diamond Airfoil Designed for Space Launcher Applications


**Jéromine Dumon, Yannick Bury, Nicolas Gourdain, and Laurent Michel**

**Abstract** The capability to reuse space launchers for new missions requires to better understand flow phenomena in the transonic regime, such as buffet, and its interaction with the structure. Indeed, the mechanical integrity of the launcher can be compromised by shock/boundary layer interactions, that induce lateral forces responsible for plunging and pitching moments. This work reports some numerical and experimental investigations about the aerodynamic and aero-elastic behavior of a diamond airfoil, designed for microsatellite-dedicated launchers, with a particular interest for the fluid/structure interaction during buffeting. Experiments have been conducted, based on Schlieren visualizations, and compared with numerical predictions obtained with unsteady RANS and Large-Eddy Simulation. Finally, the effect of buffeting on the composite aileron is studied by solving the equation of the dynamics, showing that the aerodynamic response of the airfoil tends to damp the structural displacement, and thus limit the effect of buffeting.

**Keywords** Buffet · URANS · LES · Wind tunnel test · Fluid structure interaction · Composite

J. Dumon (✉) · Y. Bury · N. Gourdain
Department of Aerodynamics, Energetic and Propulsion, ISAE-SUPAERO, University of Toulouse, Toulouse, France
e-mail: jeromine.dumon@isae.fr

Y. Bury
e-mail: yannick.bury@isae.fr

N. Gourdain
e-mail: nicolas.gourdain@isae.fr

J. Dumon · L. Michel
Institut Clément Ader (ICA), CNRS-INSA-ISAE-Mines Albi-UPS, University of Toulouse, Toulouse, France
e-mail: laurent.michel@isae.fr



M. Braza et al. (eds.), *Advances in Critical Flow Dynamics Involving Moving/Deformable Structures with Design Applications*, Notes on Numerical Fluid Mechanics and Multidisciplinary Design 147,
https://doi.org/10.1007/978-3-030-55594-8_30

## 1 Introduction

Microsatellite-dedicated launchers, for which payload is lower than 50 kg, are of paramount importance for future space missions. Among the difficulties encountered for the design of such launchers, the aero-elastic behavior of the ailerons in transonic regimes still remains nowadays partly unknown. Such ailerons are originally designed to provide stability to the launcher, especially when lateral winds are experienced. The PERSEUS' project (French acronym for Academic and Scientific European Student project for Space research) is an initiative of CNES, the French Space Agency, to promote the emergence of innovative technical solutions for space launchers. The present work takes place in the frame of the development of SERA (Supersonic Experimental Rocket ARES) series launchers (Fig. 1).

To improve the stability of the rocket, SERA is equipped with three ailerons, composed of diamond airfoils made in composite material. With the objective to increase their reliability in turbulent transonic flows, it is necessary to better understand the interaction between the unsteady flow, including shock induced flows, and the composite walls. Moreover, such information is relevant in the context of reusable launchers, where the number of cycles that can be accomplished by the aileron must be accurately predicted.

It is thus necessary to predict the loads induced by the buffeting, to ensure that structure components and subsystems possess adequate strength, stress and fatigue margins in regard to the structural dynamic response. Buffeting is a well-known instability, that occurs in the transonic regime. Buffet is characterized by fluctuating pressures resulting from flow-induced turbulence, flow separation, wake effects, and shock oscillations. The interaction between the shock wave and the separated

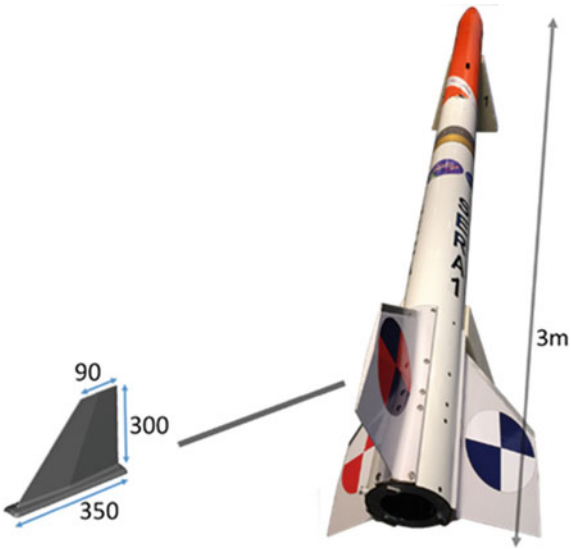


**Fig. 1** Global view of the SERA launcher and details of the aileron shape and dimensions (mm)

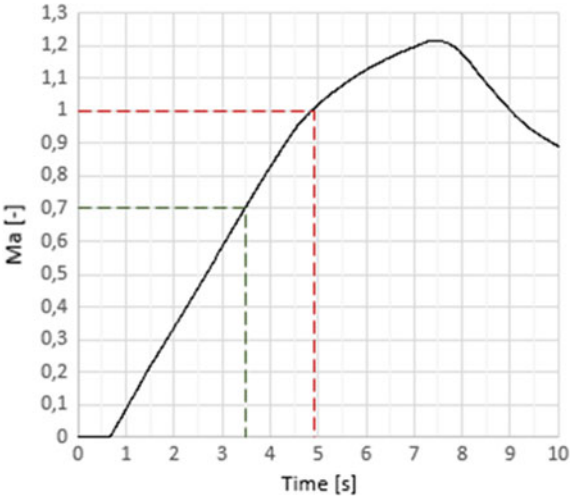


**Fig. 2** Evolution of the Mach number, as recorded during a typical flight of the SERA rocket

boundary layer causes the inception of instabilities responsible for a self-sustained periodic motion of the shock over the surface of the airfoil. In a typical flight of a SERA rocket, the transonic regime occurs during less than two seconds during its atmospheric phase as shown in Fig. 2.

Transonic buffet is observed in many aeronautical applications, including internal flows (e.g. compressor passages) and external flows (e.g. aircraft wings). This phenomenon has been extensively studied, see for example the works of Percey and Rao [13], Tijdeman [16] and Lee [10], thanks to experimental campaigns on reference geometries [8, 11] or numerical simulations [4, 14, 15]. Based on this extensive knowledge, it has been possible to delay or alleviate buffeting in such geometries [5–7]. Unfortunately, the detailed mechanisms that are responsible for the buffet inception and its dynamics are still debated. Moreover, contrary to classical supercritical profiles for civil aircraft, there is a lack of studies for diamond airfoils, adapted to supersonic flows, which are the target of this work.

The first part of this paper deals with the experimental and numerical methods that have been used to study buffet. In a second part, aerodynamic data are compared and analyzed, in order to highlight some of the mechanisms related to buffet for a non-moving airfoil. In the last part of the paper, numerical simulations are conducted, considering a moving airfoil, that dynamically responds to aerodynamic forces. Finally, some conclusions and perspectives are drawn.

## 2 Methods

### 2.1 Experimental Setup

The ISAE-SUPAERO transonic wind tunnel has a 130mm-by-80-mm rectangular slotted test section. It is powered by four vacuum pumps and provides flow Mach numbers ranging from $0.7 \pm 0.05$ to $1.3 \pm 0.1$. Here the Mach number is determined from the stagnation pressure $P_i$ and the test section static pressure P according to Eq. 1, with Ma the Mach number and $\gamma$ the heat capacity ratio.

$$\frac{P}{P_i} = \left(1 + \frac{\gamma - 1}{2} Ma^2\right)^{-\frac{\gamma}{\gamma - 1}} \tag{1}$$

Time-resolved Schlieren visualizations are recorded using a high speed Photron camera. Two sets of data can be recorded: (1) $704 \times 512$ pixels' image with an acquisition frequency of 20,000 frames per second or (2) a $512 \times 272$ pixels' image with an acquisition frequency of 50,000 frames per second. (see Fig. 3 for a global view of the experimental setup). However, Schlieren technique intrinsically integrates 3D information into a 2D image. This complicates the analysis of the images when the flow naturally exhibits 3D structures, and is responsible for a hard-to-quantify inaccuracy.

The aileron dimensions are 80mm in span and 50mm in chord, with a symmetric diamond shape (Fig. 3). Its thickness is equal to 12% of the chord, corresponding to 6 mm thick. Such dimensions, with the Mach numbers considered in this work, correspond to a Reynolds number of about 700,000. The mock-up is fixed on one of the transparent glass window of the wind tunnel test section (Fig. 3), on a rotating device allowing to change the angle of attack of the aileron. The 0° angle is determined on the basis of the Schlieren images revealing the symmetric distribution of the shock waves on both sides of the WT model. The accuracy of the aerodynamic angle is estimated at 0.5° via post processing images of calibration targets. The angle of attack can be set from −2° to 2° by steps of 0.5°.

In order to determine the potential occurrence of a coupling between the characteristic frequencies of the flow (in particular with the oscillating shock waves) and

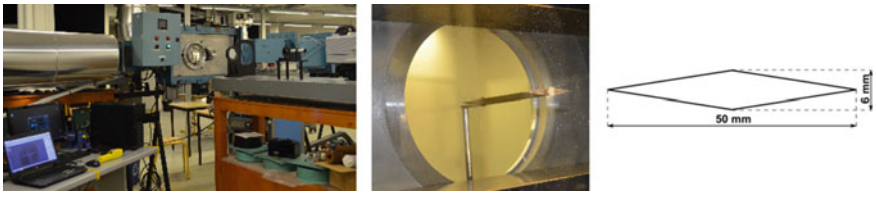


**Fig. 3** (Left) Global view of the wind tunnel and Schlieren test bench and a detailed view of the wind tunnel model of the aileron in the test section, (right) schematic view and dimensions of the wind tunnel aileron

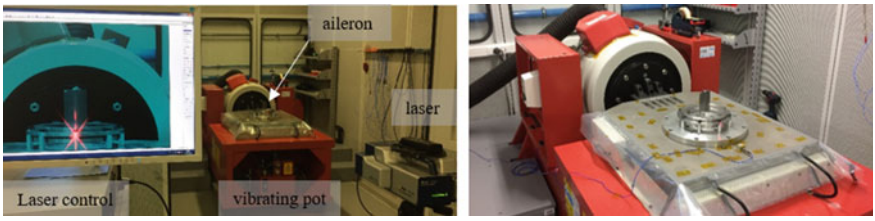


**Fig. 4** Close view of the vibrating pot (right) and details of the laser scanner used for the modal analysis (left)

a specific vibratory frequency of the aileron, a modal analysis is conducted on a vibrating pot (Fig. 4). The setup of the aileron on the vibrating pot is chosen similar to its setup in the wind tunnel model (Fig. 3), taking into account both the fixing beam of the aileron to the wind tunnel structure and the window in close contact with the aileron. The modal analysis reveals three main natural frequencies $f_1 = 196\,\text{Hz}$, $f_2 = 226\,\text{Hz}$ and $f_3 = 850\,\text{Hz}$. The frequency $f_3$ is associated with the fixation of the window to the vibrating pot, $f_1$ and $f_2$ correspond to the two first flexion modes of the aileron.

The predicted aerodynamics frequencies are away of the above-mentioned structural frequencies, which ensures that (i) the potential occurrence of pressure fluctuations on the surface of the aileron due to the buffeting phenomenon and to other flow unsteadinesses during the wind tunnel tests will not be induced or enhanced by the structural deformation of the aileron, (ii) the aileron will not experience severe deformation promoted by the aerodynamic excitation and its coupling with the structural deformation of the model under resonant effects.

On the basis of the time-resolved Schlieren visualizations, a spectral analysis of the shock oscillation is proposed, based on a three-step process: (i) a one pixel-height sensor line is selected in the oscillation area (Fig. 5—left), (ii) a time series of the grey level signal is then extracted (Fig. 5—right), (iii) the Power Spectral Density (PSD) of this signal can be computed (if the signal is periodic).

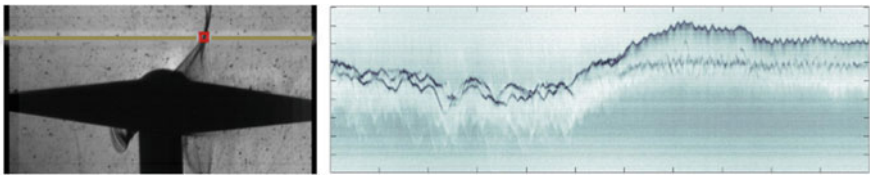

**Fig. 5** Description of the image processing-based frequency analysis, relying on the selection of a one pixel-height sensor line (left), where grey level associated with the position of the shock wave on the image is observed as a function of the time (right, time in abscissa, position in ordinate, see more details of the signal extraction procedure in the Results section)

## 2.2 Numerical Setup

This section presents the numerical analysis, led with unsteady Reynolds Averaged Navier Stokes (RANS) and Large Eddy Simulation (LES) approaches, considering the operating conditions of the wind tunnel (including wind tunnel walls). As the zone located downstream of the shock wave is subsonic, it is expected that perturbations generated in the boundary layer and in the close wake of the aileron travel upstream and impact the shock development in the zone of the lambda-shaped shock pedestal, especially as the expected buffeting results from an interaction between separated boundary layer and the shock wave.

The numerical model used in the URANS approach is purely two dimensional, in order to reduce computational time effort, corresponding to the section of the aileron (Fig. 3). The dimensions of the computational domain are similar to those of the wind tunnel test section (130mm high and 30 chords long). The center of the model is positioned 10 chords downstream of the inlet of the domain. For the LES computations, the 2D section of the actual wind tunnel model is extruded in the spanwise direction, with a span corresponding to 25% of the chord, in order to ensure uncorrelated turbulence.

The URANS simulations are performed using STAR-CCM+ v11.02. The $k-\omega$ SST-Menter turbulence model [12] is used for modeling the turbulence. A compressible solver is is used with a second order Runge-Kutta scheme for the time discretization. The spatial discretization of the convective fluxes is performed by a third-order MUSCL scheme. Regarding the grid, an unstructured polyhedral 2D mesh is generated with StarCCM+, based on prism layers close to the airfoil walls and polyhedral cells in the rest of the computational domain. The size of the mesh is highly refined close to the aileron surface, and in the zone where the shock waves are expected to develop. The prism layers were set on the aileron and wall surfaces to better capture the flow gradients in the boundary layer. The size of the first layer was chosen to impose y+ $< 0.5$ on the aileron surfaces. A grid convergence study was performed, based on the evolution of both drag and lift coefficients, showing that a 1 Million cell mesh is sufficient to ensure convergence on the efforts while capturing the buffeting phenomenon.

LES computations are performed using the CharLESX solver [2], which solves the spatially filtered compressible Navier-Stokes equations using a finite volume formulation on unstructured hexahedral meshes. A fourth-order central scheme is used for the computation (2nd order on stretched volumes as in the present study). An explicit third-order Runge-Kutta (RK3) scheme is used for time integration with the Vreman subgrid-scale (SGS) model [17]. The approach relies on the combination of a non-dissipative centered numerical scheme and an essentially non-oscillatory (ENO) second-order shock-capturing scheme, with a shock sensor [2]. Two grid strategies have been considered. The first one relies on a wall-modelling approach, with $y^+ \approx 15$, $x^+ \approx 30$ and $z^+ \approx 50$, leading to a 30 million cells grid. The second method relies on a wall resolved approach [9], with $y^+ \approx 1$, $x^+ \approx 30$ and $z^+ \approx 20$, that leads to a 120 million cells grid. Beyond the mesh size reduction, the main

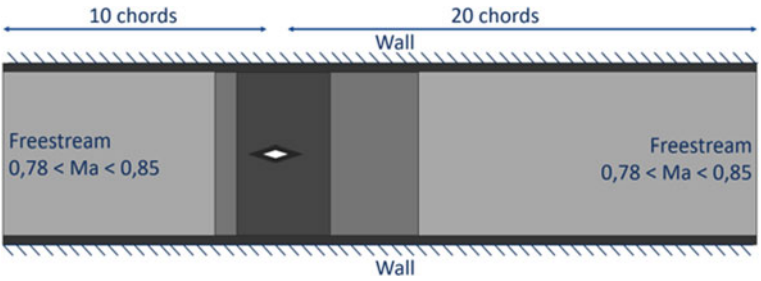


**Fig. 6** Schematic of the computational domain, mesh grid refinement as a function of grey levels and boundary conditions

interest with the wall-modelling approach is the possibility to increase the time step by a factor of 10 in contrast to the wall resolved approach. Indeed, the cost ratio here between wall resolved and wall modelling approaches is around 40.

As shown in Fig. 6, for URANS, the inlet and outlet flow conditions are modelled as freestream and the walls are considered as adiabatic with a no-slip condition. For LES, total pressure and temperature are imposed at the inlet, static pressure at the outlet, and walls are considered as adiabatic with a no-slip condition.

The spectral analysis presented in the experimental section is applied for the numerical data on the density gradient captures. Moreover, aerodynamic loads (drag and lift) are analyzed in order to highlight the link between loads and the position of shock waves, using Fast Fourier Transform (FFT).

## 3 Analysis of Results

### *3.1 At Wind Tunnel Conditions*

Shock wave and separated boundary layer oscillations are observed in both experimental and numerical simulations (Fig. 7).

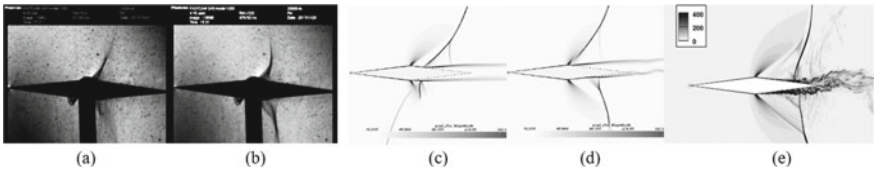


**Fig. 7** Schlieren visualizations (**a**, **b**), instantaneous iso contours of density gradient (**c**, **d**—URANS results) at 2 distinct instants and instantaneous density gradient, showing dissymmetric shock waves (**e**—wall-model LES) , revealing the oscillations of the shock waves associated with the buffeting phenomenon

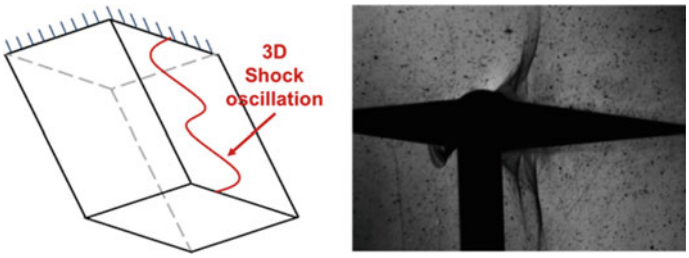


**Fig. 8** 3D supposed shock wave visualization on the aileron confronted to the 2D Schlieren vizualisation (more visible on the animated sequence)

The analysis of the Schlieren-based data shows an aperiodic three-dimensional, time-varying deformation of the shock wave in the spanwise direction (Fig. 8).

A secondary oscillation of the shock wave is observed in both numerical and experimental data: the local boundary layer separation induces an oblique weak shock wave in front of the strong shock wave, resulting in a classical delta shaped pedestal. While the dominant frequency results from the interaction between the strong shock wave and the boundary layer separation, the secondary oblique shock wave also oscillates due to the local periodic flow separation in front of the strong shock wave.

While numerical data are strictly periodic, experimental data exhibit a chaotic behavior. Two states can be distinguished in this chaos: the "delta state" and the "flag state" (Fig. 9). The delta state (Fig. 9 upper right) is a state where a sinusoidal oscillation of the shock is clearly observed. To be more precise, both the oblique weak shock wave and the strong shock wave oscillate at the same frequency. For this state the flow can reasonably be considered as two dimensional. The flag state (Fig. 9 down right) corresponds to phases of the flow when the shock deforms in the spanwise direction, in the manner of a wind-flapping flag. At this stage of the study, the detailed analysis of this specific unstable state is however compromised by the lack of experimental data. In particular, due to the 2D spatial integration of the Schlieren technique, it can't be confirmed if it is or not periodic. When the shock wave is experiencing the delta state, it is positioned closer to the trailing edge than when it is experiencing the flag state (Fig. 9 left). Finally, a third state, hereafter denoted "flying state" can also be transiently observed as the shock wave tends to travel, but fails to, from the "delta state" to the "flag state" mean positions. Figure 10 depicts the temporal evolution of the shock wave states and of their transitions from the flag state—number 1 in the figure—to the delta state—number 4 in the figure—and reversely, and the transient occurrence of the "flying state"—number 3 in the figure.

With an angle of attack (2°), both flag and delta states are present. But contrary to a zero angle of attack, the scenario doesn't switch alternatively from one state to the other state. The flag state is present on the suction side of the aileron and the delta state on the pressure side.

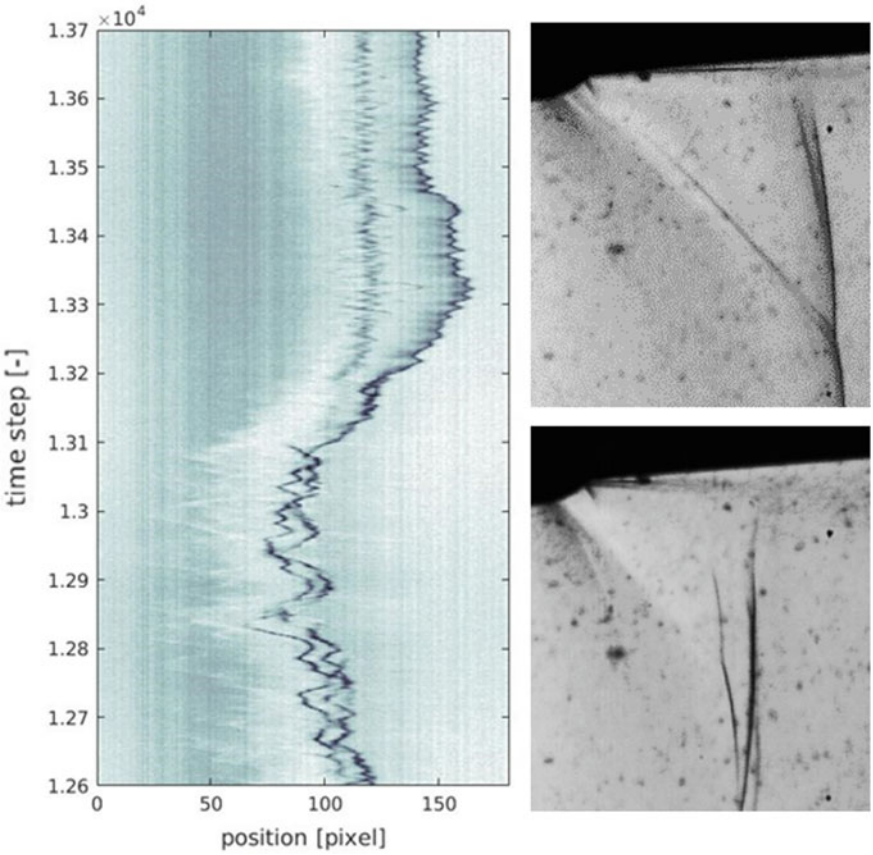


**Fig. 9** Shock position signal (upper left image, time step = 1/60,000 s) illustrating delta (upper right schlieren image) and flag (lower right image) states

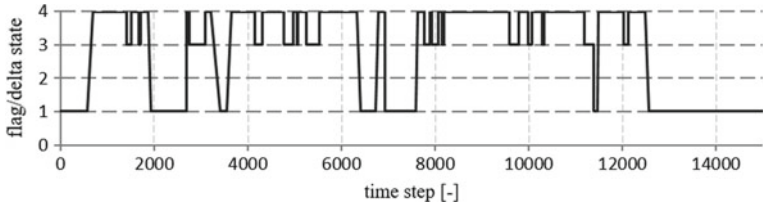


**Fig. 10** Temporal history of the shock state changes (time step = 1/60,000 s)

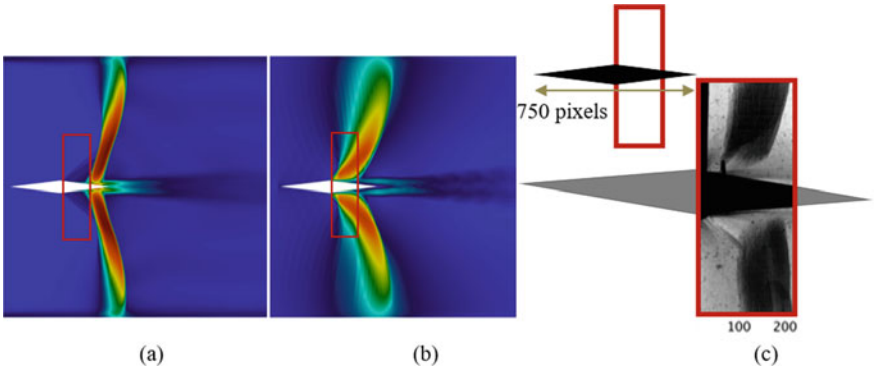


**Fig. 11** Shock magnitude oscillation for LES (**a**), URANS (**b**) and wind tunnel test (**c**)

The frequency of the shock oscillation is evaluated to f = 620 Hz (URANS) and f = 310 Hz (LES) with the spectral analysis. However, the results should be considered with caution for LES due to the limited amount of time available. As mentioned, the analysis of the Schlieren-based data remains difficult due to the presence of a three-dimensional, time-varying deformation of the shock wave in the spanwise direction.

However, the delta state is completely periodic, as revealed by the extraction of the shock wave displacement as a function of time on the Schlieren images (Fig. 10). An oscillating frequency of 4,7kHz is determined for the delta states. However, the oscillating phenomenon observed in numerical results differs from the experiment. More investigations have to be lead for a best understanding.

Figure 11a, b depicts the density standard deviation fields based on the LES and URANS computations. Figure 11c shows cumulated density gradient fields based on time resolved Schlieren images obtained in the wind tunnel. These two complementary post-processing approaches provide similar information on the displacement amplitude of the shock wave experiencing the buffeting effect.

The magnitude of the shock wave oscillations varies depending on the method used (LES, URANS or wind tunnel tests). It is worth to mention that the angle of attack in the experimental setup is not exactly zero, as revealed by a non-strictly symmetric distribution of the shock wave footprint. Relatively to the wind tunnel results, the amplitude of the shock wave oscillations is better predicted with LES than with URANS. However, the mean position of the shock is better predicted with URANS than with LES. The shock position is greatly dependant on the boundary layer thickness on the lateral walls for a given Mach number, which is a difficult parameter to predict.

The aerodynamic loads are unsteady due to the shock oscillations, as shown in Fig. 12. Indeed, the lift and drag oscillations are driven by the buffeting phenomenon. The FFT in Fig. 12 highlights a fundamental peak at 516 Hz and its harmonics. The Strouhal number, based on the upstream velocity and the chord, is equal to 0.089.

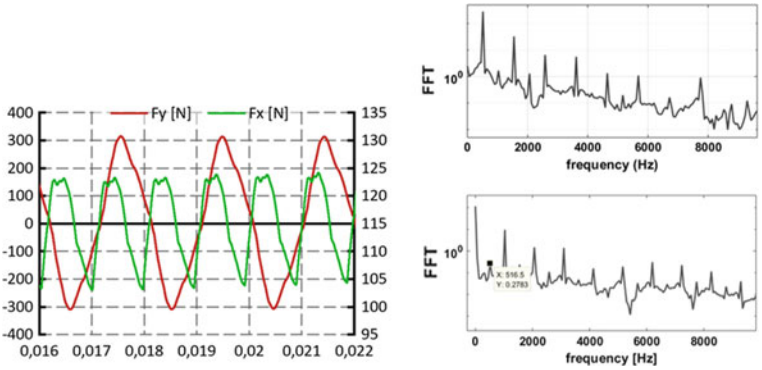


**Fig. 12** Aerodynamics efforts (left: lift, right: drag) as a function of time (s) (URANS results) (left) and FFT of lift (up right) and drag (down right) from the URANS simulation

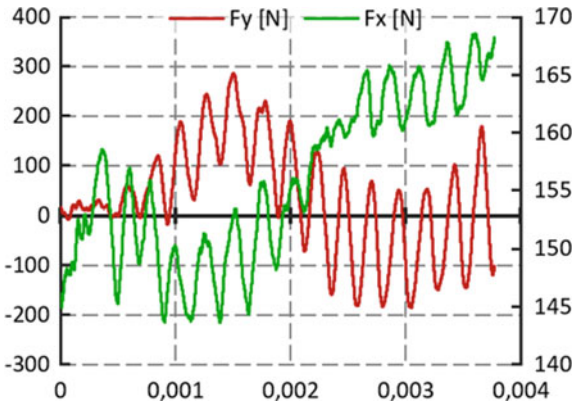


**Fig. 13** Aerodynamics efforts (left: lift, right: drag) as a function of time (s) (LES results. Note that the transient phase of the computation is still not fully completed, as only the first buffeting period has been computed yet)

The analysis of load signals is not straightforward. Interestingly enough, correlations between instantaneous flow fields and lift signals reveal that the instant at which the lift is null does not correspond to the instant where the shock waves are symmetric on both sides of the airfoil. This behavior is explained by the dynamics of the shock wave, which is different depending on its direction of displacement (upstream or downstream). This shock dynamic is thus associated with both lift and drag signals which are not sinusoidal, which in turn explains why the zero lift is not achieved when the positions of the shocks are symmetric. This analysis also shows that the drag frequency is twice the lift frequency.

The lift and drag predicted with the wall-resolved LES are shown in Fig. 13. Only one period of the shock oscillation has been simulated at the moment, which is insufficient to fully analyze the spectral content of the signal. However, these results highlight two main frequencies: one low frequency associated to buffeting and one higher frequency, related to the oblique shock oscillation. The magnitude order in terms of lift and drag are similar to URANS predictions.

### 3.2 *Influence of Reynolds and Mach Numbers*

To complete the numerical simulations, a study has been performed at Reynolds conditions close to the ones encountered by the SERA rocket at real dimensions. The URANS approach is used with the same methodology, as previously described. The 2D geometry considered here is based on a slice of the real aileron, at mid-span of the real swept aileron. At this location, the chord of the airfoil is 200mm and the relative thickness is 12% of the chord (Fig. 14).

The numerical simulations are performed for several Mach numbers so that the transonic range is entirely covered, from Ma = 0.77 to Ma = 0.83. Figure 14 depicts three instants of the simulation which allows to identify buffeting thanks to the shock wave and the boundary layer oscillations.

Buffeting is observed for Mach numbers ranging from 0.78 to 0.81. As illustrated in Fig. 15, the normalized frequency of buffeting is constant, corresponding to a Strouhal number (based on upstream velocity and axial chord) of 0.083, which is still very close to the Strouhal number reported for the 1:4th scaled model-based URANS computations. The amplitude of oscillations increases as a function of the the Mach number.

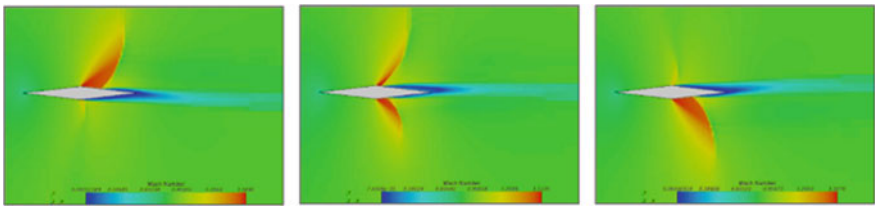

**Fig. 14** Instantaneous flow fields colored with Mach number isocontours, at three different instants of the buffeting period

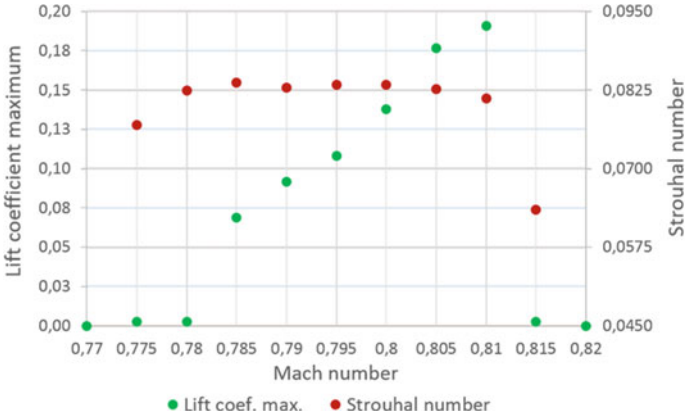


**Fig. 15** Lift coefficient and Strouhal number evolution with respect to the Mach number

## 4 Fluid Structure Interaction: Impact of Buffeting on Aileron

The objective is now to study the effect of aerodynamic forces on the dynamic response of the profile. As a first approximation, only rigid movements of the aileron are considered, such as bending and torsion, as shown in Fig. 16a. The 3D aileron is reduced to its 2D extruded shape. The bending is modeled by a pure vertical translation in the plane while the torsion is modeled by a rotation in the plane, as in in Fig. 16b.

The aileron is made of a sandwich composite material. The core is an epoxy foam and the skin is a carbon laminate. The aileron is considered as a beam with a thin web cross section. Moments of inertia are then calculated geometrically, for a diamond cross section of diagonals equal to 220 and 12.5 mm, with a 1 mm thick web corresponding to the laminate skin. The Young's modulus E and the shear modulus G are material properties, determined by the Classical Laminate Theory [3]. The stiffness results are presented in Table 1.

The dynamic response of the aileron is driven by the fundamental equation of dynamics. The ideal solution is to simulate the solid displacement in a fully coupled way with the flow. However, the large difference between the characteristic times of the fluid and the solid makes this approach impracticable in the present case. The method relies thus on a separation between the numerical simulation of the flow and the resolution of the aileron dynamics. As a first step, only flapping is considered, that is driven by (2):

$$M\ddot{x} + D\dot{x} + Kx = \sum F_A \tag{2}$$

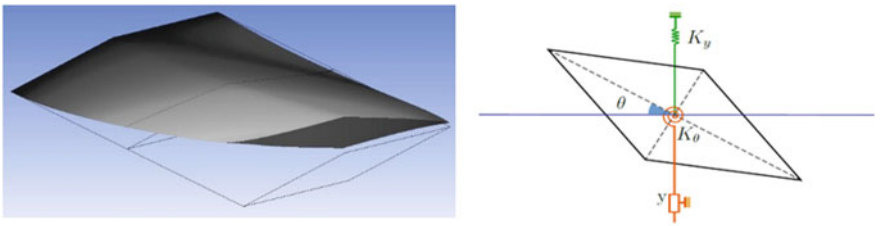


**Fig. 16** Example of the **a** aileron deformation (bending and torsion) and **b** 2D modelling

**Table 1** Estimation of the stiffness of the real aileron

| | K (Nm) | f [Hz] |
|---|---|---|
| Flexion | 1373 | 13.2 |
| Torsion | 346 | 55.1 |

with $M$ is the matrix of mass, $D$ is the matrix of damping, $K$ is the matrix of stiffness and $F_A$ are the aerodynamic forces. In order to simplify the problem, an equivalent homogeneous material is considered, so matrices are reduced to a scalar.

This equation is time marched by means of a classical four steps Runge-Kutta scheme. At each time step, the aerodynamic forces are composed of two components: one related to the phenomenon of buffet and one due to the reaction of the aerodynamic force, induced by the profile displacement. The buffet force is extracted from the numerical simulations (URANS and LES database) and the aerodynamic response is modelled. Due to the low thickness of the profile, and the fact that displacement velocity is small compared to the fluid velocity, the lift force is modelled using the thin profile theory, with a compressibility correction [1] (3):

$$F_{lift} = \frac{2\pi(\alpha - \alpha_0)}{\sqrt{1 - M^2}} \times \frac{1}{2} \rho_\infty U_\infty^2 \cdot S \tag{3}$$

The angle of the flow seen by the profile at each instant of time is estimated as (4):

$$\tan \alpha = -\frac{\dot{x}}{U_\infty} \tag{4}$$

Since the flow is responding in phase with the solid, the aerodynamic response is a positive damping term in the equation of the dynamic, Eq. 2. The main limitation of this approach is that the aerodynamic response to the profile displacement is instantaneous, while a lag is observed in practice. For this reason, this method is valid only when the ratio between the flow velocity and the displacement velocity of the solid is large (so the time lag becomes negligible). The results are expressed in terms of non-dimensional parameters $U^*$, representing the ratio between the fluid velocity and the displacement velocity of the solid and $m^*$, representing the mass ratio between the solid and the fluid:

$$U^* = \frac{U_\infty}{\frac{1}{2\pi}\sqrt{\frac{k}{m}} \cdot C} \qquad m^* = \frac{m}{\rho S L} \tag{5}$$

with k the stiffness, C the chord of the aileron and m the mass of the solid. In the case of the aileron at real dimensions, the value of the normalized velocity $U^*$ is estimated to be close to 100. Two cases are considered: without aerodynamic coupling (only the force coming from buffet is applied) and with coupling (aerodynamic response of the profile is added). The evolution of the normalized displacement, $y^* = y/C$, with respect to the normalized velocity $U^*$ is represented in the Fig. 17a (using URANS data) and in Fig. 17b (using LES data), for a large mass ratio parameter $m^* = 1600$.

In Fig. 17a, the peak close to $U^* = 10$ corresponds to the resonance between the natural frequency of the solid and the aerodynamic excitation (buffet). In the case of LES, the buffet is associated to a more complex signal in term of spectral content, so two frequencies of resonance are shown in Fig. 17b. In the uncoupled case, the maximum displacement increased with $U^*$ (corresponding to a reduction

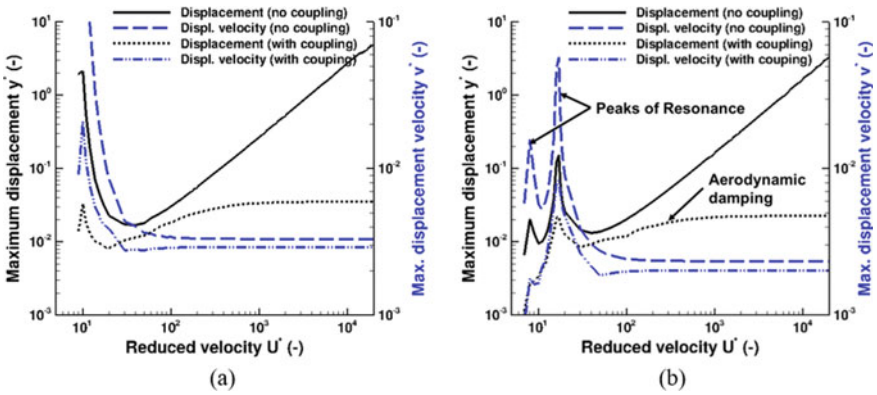


**Fig. 17** Evolution of the maximal displacement and maximal velocity displacement, with respect to the parameter $U^*$: **a** URANS and **b** LES ($m^* = 1600$)

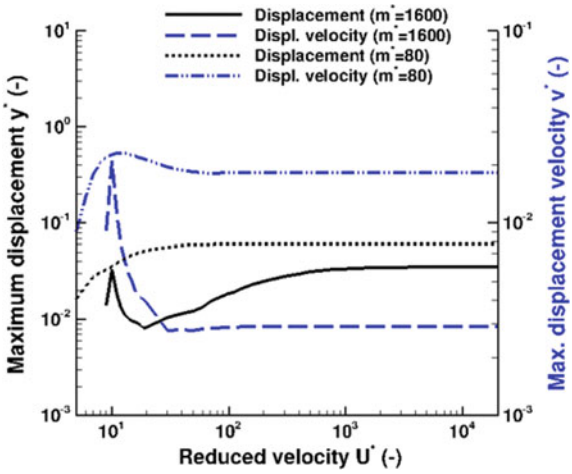


**Fig. 18** Influence of the mass ratio parameter on the displacement and displacement velocity at $U^* = 100$ (URANS data)

of the stiffness). In the coupled case, as expected, the aerodynamic forces act as a damping term, which reduced the amplitude of the displacement, especially at the resonance frequency. A plateau is also reached for value of $U^*$ higher than 500. At such velocity ratios, the periodic excitation due to buffet is no longer seen by the solid (since the time-average force of buffet is null, the solid does not react to this phenomenon). The effect of buffet predicted by LES has a weaker effect on the solid displacement compared to URANS.

Two normalized masses are compared: $m^* = 80$ (light hollow aileron) and $m^* = 1600$ (heavy plain aileron). The previous conclusions are globally unchanged with the lower mass ratio parameter ($m^* = 80$), as shown in Fig. 18. However, as expected, the maximum displacement is increased (especially at low to moderate values of $U^*$) and a smoothening of the resonance peak, due to an increase of the

aerodynamic damping (velocity displacement of the solid is increased compared to $m^* = 1600$, and so the value of the flow angle is also increased). In all cases, the value of the angle stays below 7°–8°, which is still acceptable for the thin profile theory.

## 5 Conclusion

Both experimental and numerical investigations have been performed to understand buffeting phenomenon and its impact on the composite aileron. This study can be summarized as follows. First, buffeting appears at transonic speed on a diamond aileron at zero angle of attack, as verified with both numerical simulation and measurements. Second, experimental approach reveals a 3D oscillation of the shock wave in the manner of a wind-flapping flag, but at this step there is no clear evidence of the physical phenomena promoting this 3D mode. Third, LES identifies an oscillation of the width of the shock foot ($\lambda$-width) which has a significant impact on the aerodynamics load, but this phenomenon is not seen with the URANS simulation. At last, interestingly enough, the experiments have also highlighted the chaotic behavior of the shock wave as it shifts from an oscillatory periodic state (delta state) to an erratic 3D flapping state (flag state), transiently separated by transition states, where the shock moves from a close-to-trailing edge position (delta state) to a close-to-dihedron position (flag state).

The results reported in this paper still highlight a lack of deciphering of the buffeting origin. A 3D numerical simulation (both URANS and LES) should be conducted in order to better understand the spanwise oscillation of the shock observed experimentally. More information from the wind tunnel is also needed. The use of unsteady pressure sensors on the aileron will provide a more accurate validation of the numerical simulations in the future. Fluid/Structure interaction has been investigated, considering only the bending mode. The effect of torsion should now be investigated since it should have more impact on the flow due to the increase of incidence that amplifies buffeting effects. A provision for future work will also consist in using a time-dependent stiffness, in order to represent the influence of progressive damages of unsteady loads on the aileron (fatigue).

**Acknowledgements** This work is partially funded by the French Space Agency (CNES), this support is greatly acknowledged. The authors particularly thank Jean Oswald and Florent Puel from DLA (Direction des LAnceurs) at CNES for their help on this study. The experimental campaign was conducted with the technical team of ISAE-Supaero (special thanks to Emmanuel Rivet, Patrick Cheze and Marc Grellet). The simulations performed were achieved using CALMIP computing means, under project p1425 and GENCI A0042 A07178.

## References


1. Anderson, J.-D.: Fundamental of Aerodynamics. McGraw-Hill (2007)
2. Bermejo-Moreno, L., Bodart, J., Larsson, J., Barney, B., Nichols, J.W., Jones, S.: Solving the compressible Navier-Stokes equations on up to 1.97 million cores and 4.1 trillion grid points. In: 2013 International Conference for High Performance Computing, Networking, Storage and Analysis (SC), pp. 1–10. IEEE (2013)
3. Berthelot. J.-M.: Comportement mecanique et analyse des structures. Materiaux Composites, Editions TEC DOC, 5eme édition (2012)
4. Brunet V., Deck, S.: Zonal-detached eddy simulation of transonic buffet on a civil aircraft type configuration. In: Advances in Hybrid RANS-LES Modelling., vol. 97 of Notes on Numerical Fluid Mechanics and Multidisciplinary Design. Springer (2008)
5. Caruana, D., Mignosi, A., Correge, M., Le Pourhiet, A., Rodde, A.M.: Buffet and buffeting control in transonic flow. Aerosp. Sci. Technol. **9**(7), 605–616 (2005)
6. Corre, C., Renaud, T., Lerat, A.: Transonic flow control using a Navier-Stokes solver and a multi-objective genetic algorithm. In: IUTAM Symposium Transsonicum IV, pp. 297–302 (2003)
7. Gao, C., Zhang, W., Kou, J., Liu, Y., Ye, Z.: Active control of transonic buffet flow. J. Fluid Mech. **824**, 312–351 (2017)
8. Jacquin, L., Molton, P., Deck, S., Maury, B., Soulevant, D.: Experimental study of shock oscillation over a transonic supercritical profile. AIAA J. **47**(9), 1985–1994 (2009)
9. Kawai, S., Larsson, J.: Wall-modeling in large eddy simulation: length scales, grid resolution, and accuracy. Phys. Fluids **24**(1), 015105 (2012)
10. Lee, B.H.K.: Self-sustained shock oscillations on airfoils at transonic speeds. Prog. Aerosp. Sci. **37**(2), 147–196 (2001)
11. McDevitt, J.B., Okuno. A.E.: Static and dynamic pressure measurements on a NACA 0012 airfoil in the ames high Reynolds number facility. Technical Report Technical Paper 2485, NASA (1985)
12. Menter, F.R.: Two-equation eddy-viscosity turbulence models for engineering applications. AIAA J. **32**(8), 1598–1605 (1994)
13. Pearcey, A.H., Rao, K.: The interaction between local effect at the shock and rear separation—A source of a significant scale effects in wind-tunnel tests on airfoils and wings. Technical Report, AGARD (1968)
14. Renaud, T., Corre, C., Lerat, A.: Efficient numerical simulation of buffet for airfoils transonic regime. In: International Forum on Aeroelasticity and Structural Dynamics, pp. 29–37 (2001)
15. Thiery, M., Coustols, E.: Numerical prediction of shock induced oscillations over a 2d airfoil: Influence of turbulence modelling and test section walls. Int. J. Heat Fluid Flow **27**(4), 661–670 (2006)
16. Tijdeman, J.: Investigations of the transonic flow around oscillating airfoils. Technical Report TR 77090 U, NLR (1968)
17. Vreman, A.-W.: An eddy-viscosity subgrid-scale model for turbulent shear flow: algebraic theory and applications. Phys. Fluids **16**(10), 3670–3681 (2004)

# Numerical Simulation and Modelling of a Morphing Supercritical Airfoil in a Transonic Flow at High Reynolds Numbers


**J.-B. Tô, D. M. Zilli, N. Simiriotis, I. Asproulias, D. Szubert, A. Marouf, Y. Hoarau, and M. Braza**

**Abstract** The flow dynamics and their morphing modification concerning the transonic flow around an Airbus A320 airfoil have been investigated via 2D simulations at a high Reynolds number. A distinctive flow topology, organised and chaotic occurs in this regime driven by appearance of coherent structures such as the Von-Kármán instability as well as the Kelvin-Helmholtz instability. When the Mach number and angle of attack both belong to a certain range of values, the shock wave develops a low-frequency motion along a specific distance on the suction side, issued from the development of transonic buffet instability. This phenomenon is crucial for the design because it leads to a high rise of drag and can trigger in extreme conditions dangerous dip-flutter modes. Electroactive morphing of the trailing edge region achieved by optimal vibration of piezo-actuators has proved capable to create vortex breakdown of the coherent structures and to act through an eddy-blocking mechanism to a considerable thinning of the shear layers and of the wake as has been proven in subsonic regime as shown by Scheller et al. (J Fluids Struct 55: 42–51 [10]). The eddy-blocking effect in the transonic regime has been studied in the present article in cruise-speed the conditions, following the studies by Szubert et al. (J Fluids Struct 55: 272–306 [12]) and Hunt et al. (IUTAM symposium on computational physics and new perspectives in 246 turbulence, pp 331–338. Springer, Dordrecht [6]). Accordingly, computations have been made to determine which type of actuation offers the best performance in terms of buffet dampening and aerodynamic efficiency as a whole. Lastly, it is shown that a flapping motion of the trailing edge can lock-in the frequency of the buffet phenomenon at the flapping frequency, which has potentially useful applications in terms of controlling and reducing shock oscillations.

J.-B. Tô (✉) · D. M. Zilli · N. Simiriotis · I. Asproulias · D. Szubert · M. Braza
Institut de Mécanique des Fluides de Toulouse, Unité Mixte C.N.R.S.-I.N.P.T. 5502, Av. du Prof. Camille Soula, Toulouse 31400, France
e-mail: jeromine.dumon@isae.fr

A. Marouf · Y. Hoarau
ICUBE, Unité Mixte C.N.R.S.-Université de Strasbourg 7357, Bd. Sébastien Brant, Illkirch-Graffenstaden 67400, France



M. Braza et al. (eds.), *Advances in Critical Flow Dynamics Involving Moving/Deformable Structures with Design Applications*, Notes on Numerical Fluid Mechanics and Multidisciplinary Design 147,
https://doi.org/10.1007/978-3-030-55594-8_31

**Keywords** Instability · Transition · DNS · Bluff-bodies · Wings · Incompressible flow

## 1 Introduction

A considerable number of experimental and numerical studies have been devoted to the appearance and growth of buffet on a wing, i.e. the unsteady periodic motion of the shock over a transonic wing under specific flight conditions. Pioneering research driven by Marvin et al. [8], Jacquin et al. [7], Smits and Dussauge [11] and Sajben and Kroutil [9] have given a clear insight of the transonic flows with buffet phenomenon over wings.

Another study by Grossi et al. [5] showed that the introduction of a splitter-plate at the trailing edge suppresses the Von Kármán mode, hence attenuating buffet. A strong interaction was thus identified between wake instabilities and the low frequency shock motion. While the trailing edge dynamics at the origin of buffet was relatively obscure up until then, an acoustic feedback mechanism has been found to be the source of buffet, which will be described hereinafter.

There is a strong correlation between the movement of the shock and the movement of the boundary layer, and this paper focuses on bringing to light additional insight on the mechanisms of buffet reduction thanks to hybrid morphing, while it is also shown that an appropriate trailing edge actuation can also present beneficial effects on the mean lift to drag ratio.

## 2 Description of the Numerical Experiment

### *2.1 Geometry in Use and Flow Parameters*

While transonic buffet realistically appears at high Reynolds numbers, at an order of magnitude of $10^7$ in cruising flight conditions, it was preferred to investigate buffet inside a numerical wind tunnel so that the computational mesh would be sufficiently small due to the strenuous refinement requirements that appear at very large Reynolds numbers.

The configuration used in this study is directly inspired from the wind tunnel experiments of the European project SMS—Smart Morphing and Sensing for aeronautical configurations, www.smartwing.org/SMS/EU carried out by IMP-PAN Academy of Science in Gdansk, Poland. The chord of the prototype is of 0.15 m. Buffet is thus investigated by means of a two-dimensional CFD computation as a fist step on the AIRBUS—A320 supercritical airfoil in reduced (laboratory) scale according to the ongoing experiments in free-stream Mach number of 0.78 and a chord-based Reynolds number of 2.06 M. The critical angle of attack $\alpha$ concerning the onset of

buffet will be the objective of a detailed study concerning this configuration in 3D and by respecting the geometry of the upper and lower walls of the wind tunnel. In the present case, the objective is to study the morphing effect on the flow dynamics concerning a non confined 2D configuration as a first step enabling the design of the morphing prototype. In this case, onset of buffet has been observed in our studies at $\alpha = 1.8°$. At this angle of attack and flow parameters, the buffet frequency was found to be around 111 Hz.

Another configuration at a higher angle of attack $\alpha = 5°$ is also used to enhance the buffet as well as the Shock-Wave/Boundary-Layer Interactions (SWBLI) that take place around the airfoil and within the turbulent wake. For this value of $\alpha$, a tangible separation is formed at the shock foot and the extent of the shock motion is broader than is the case for $\alpha = 1.8°$.

## *2.2 Turbulence Modelling and Numerical Parameters*

URANS modelling approaches as well as adaptive and more elaborate methods sensitizing the coherent structures development, as the OES—organised Eddy Simulation approach have been employed [1, 2, 12]. Furthermore, a $k - \omega$ Scale-Adaptive Simulation (SAS) approach was used as a first step until it was observed that the behaviour of the computed flow was non-physical, leading to an excessive suction and flow detachment.

A two-dimensional multi-block structured grid was used for the purpose of the computations.

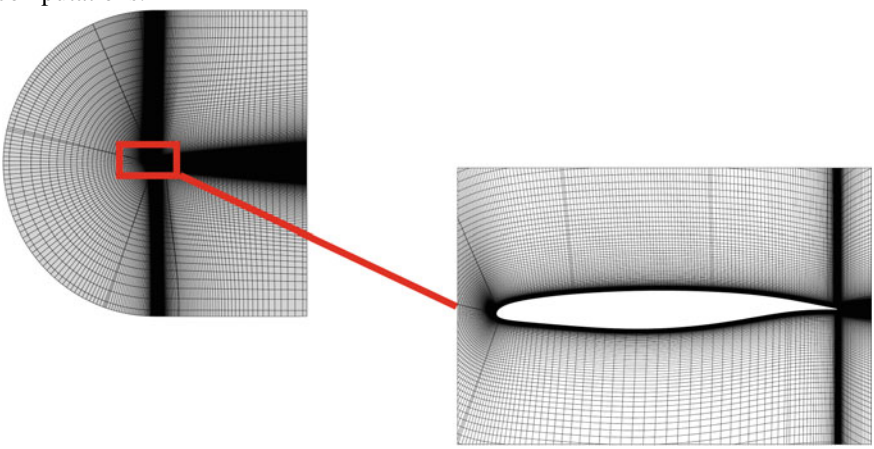

Two different grids have been examined and an exhaustive study of the grid influence, and time step has been carried out. The grid that was finally retained contains 160,000 computational cells, and presents a **C-H** topology. A 190,000-element mesh was generated afterwards with more cells in the wake region and

on the suction side in order to better capture the shock and avoid dissipating wake vortices. The $y^+$ coordinate is of the order of $10^{-1}$ in the immediate vicinity of the airfoil walls.

### *2.3 Numerical Method*

The computations have been made by using the Navier-Stokes Multi Block (NSMB) code, thanks to the partnership of our research group within the NSMB European Consortium. Structured meshes are used and the Navier-Stokes equations for compressible flows is carried out following a finite-volume formulation. For this study, the temporal integration and spatial discretization schemes are chosen similar to the study from [4]: the convective fluxes are discretized following a third-order Roe upwind scheme and time integration is performed through a dual-time stepping, second-order backward-difference scheme. The number of inner iterations was appropriately chosen to ensure a sufficient convergence rate with respect to the flow requirements.

For this particular grid and geometry, it was determined that a time step $\Delta t_s = 5 \times 10^{-6}$ s was best suited as a compromise between speed and accuracy, as the time series for the force coefficients sensibly displayed the same results for $\Delta t_s$ and smaller time steps. An example is showcased in Fig. 1 where the lift coefficient $C_l$ for the $\alpha = 1.8°$, static wing at $\Delta t_s$ is shown to be identical to a $C_l$ computed for $\Delta t = 10^{-6}$ s except for a phase shift.

## 3 Results

The buffet phenomenon associated with periodic shock motion and subsequent growth and thinning of the separated area are illustrated in the following figures.

An important issue is the appearance of the Von Kármán instability arising in the wake due to the presence of two inflection points in the velocity field, that is when $\partial_z^2 u = 0$. This instability then merges with the separated boundary layer and these two systems interact with one another in a viscous ≪zone≫: The thickening of the boundary layer correlates with the shedding of Von Kármán vortices. In Fig. 2a, it can be observed that when a coherent Von Kármán vortex is being released in the wake, where major viscous dissipation mechanisms occur, bumps appear alternatively in this viscous zone which act locally as a wedge to a compressible, transonic flow. The inviscid flow over this region is thus compressed again and gives birth to acoustic waves. These weak shocks appear intermittently whenever a vortex is shed in the wake, both over the suction side of the wing and along the pressure side. Therefore, the Von Kármán mode together with the shear-layer instability developed in the separated shear layers significantly affects by feedback mechanisms the SWBLI region and as

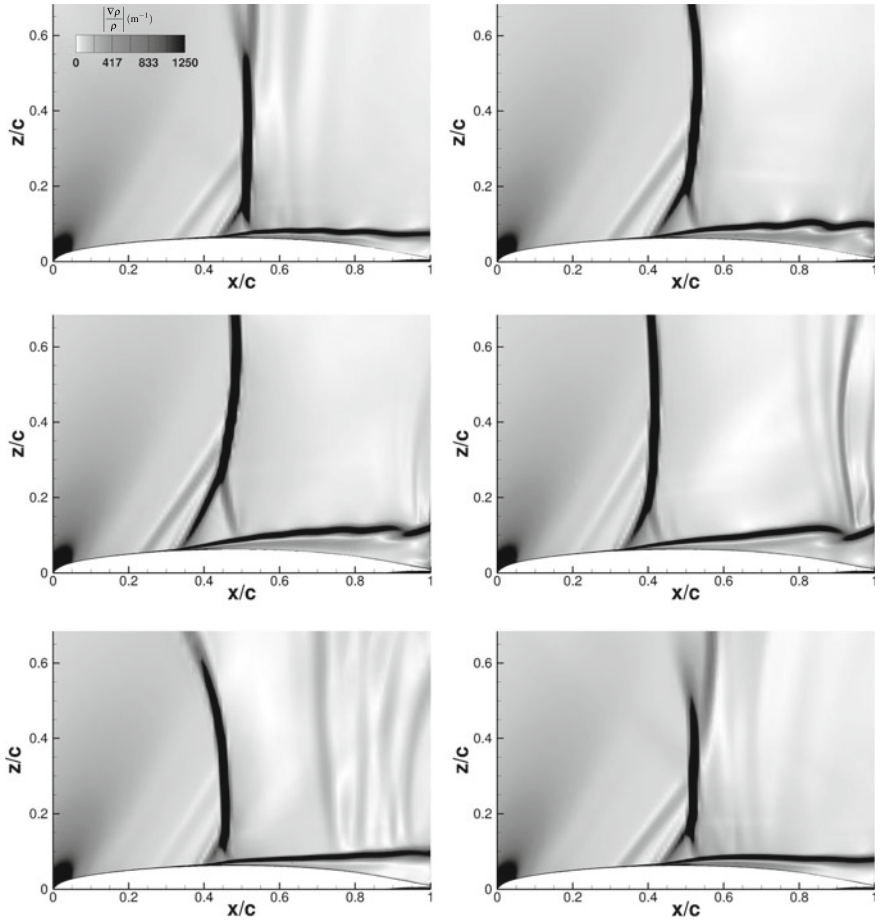


**Fig. 1** One buffet period represented by 6 snapshots. From left to right, top to bottom, the pictures correspond to times $t^* = \left\{0; \frac{1}{5}; \frac{2}{5}; \frac{3}{5}; \frac{4}{5}; 1\right\}$ where $t^*$ is a non-dimensional time defined by $t^* = \frac{t-t_0}{T_b}$, $T_b$ being the buffet period and $t_0$ the arbitrary moment chosen as the beginning of one buffet period. Here, it is chosen to be one of the moments when the shock is weakest, i.e. when it reaches its most downstream position (see [13])

seen in the next section, is able to highly affect the buffet phenomenon. Indeed, the shear layers and the Von Kármán vortices near the trailing edge constitute a specific form of an effective obstacle containing the viscous effects and being thicker than the nominal airofil's configuration. The inertia effects associated with the compressibility around this virtual obstacle are the reason of formation of acoustic waves travelling upstream and modifying the SWBLI region, as well as the boundary layer upstream of the SWBLI. By means of the morphing, this study shows how optimally this feedback can operate.

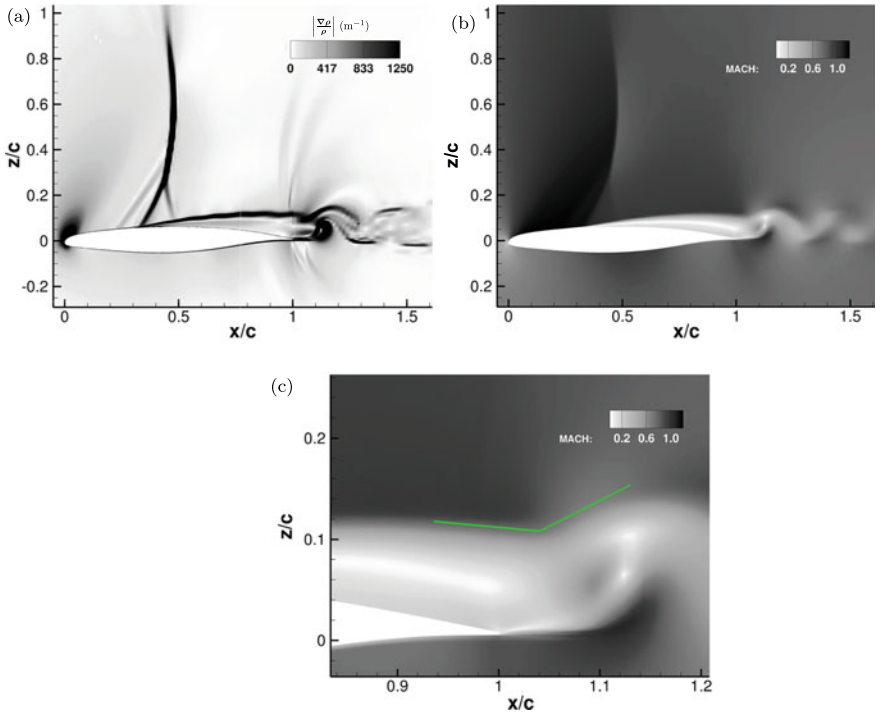


**Fig. 2** **a** A density gradient snapshot at $t* = 2/5$

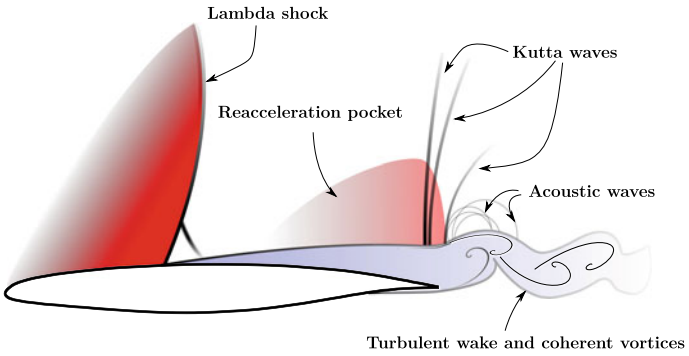


**Fig. 3** A schematic view of the main phenomena underlying buffet

These weak shocks—also known as Kutta waves—have a characteristically curved and almost circular shape (see schematic diagram Fig. 3), which comes from the diffraction they undergo when interacting with a vortex as mentioned in [3]. These shocklets then grow and their wavefront propagates both upstream and downstream. Due to the transonic flow regime in the inviscid region over the separated boundary layer, the wave fronts decelerate while propagating upstream until they hit the lambda shock and impart their energy to it while fusing together. As it becomes stronger, the shock separates the boundary layer sooner and sooner, moving upstream along the wing until the acceleration pocket upstream the shock becomes too lean to allow the flow to gain speed. The shock thus loses strength and goes back downstream. As a direct consequence of this loss of strength, the boundary layer somewhat reattaches. Meanwhile, previously created Kutta waves are reaching the shock, which allows another cycle to begin.

### *3.1 Force Coefficients Under the Buffet Effect*

The aforementioned physical mechanisms result in unsteady forces (Fig. 1) characterized by a low-frequency periodic pattern repeating itself throughout the numerical experiment. Smaller oscillations also appear periodically in the grooves of the lift and drag signals, representing all the wake and boundary layer instabilities. By moving back and forth along the suction side, the shock thickens the boundary layer and induces a strong flow separation at its foot when it advances upstream, while the boundary layer becomes thinner when the shock moves downstream. If a strongly separated flow helps the Von Kármán and shear layer instabilities happen due to separation near the trailing edge, the reattachment that ensues causes them to disappear intermittently as can be seen on the .

In Fig. 4, the lift coefficient is plotted with respect to time in the $\alpha = 1.8°$ case without morphing. Although the unstable character of buffet is barely visible at this angle of attack if one were watching flow field snapshots, and even though separation is intermittent and weak, periodic patterns in the lift and drag coefficients as well as a distinct peak of energy in the Power Spectral Density (PSD) as seen in Fig. 7 are proofs that buffet still happens at that low angle of attack. When the trailing edge is slightly deflected upwards by an angle of 2°, the oscillations disappear, albeit at the expense of a reduction in performance, as the lift coefficient decreases on average. However, Fig. 5 shows that the drag coefficient also decreases by a substantial amount which means that on average, the lift to drag coefficient augments by 10%. This can be explained by the fact that the slight upward deflection tends to re-accelerate the flow on the suction side, and the boundary layer will thus be sucked towards the surface of the wing, disfavouring both separation and the creation of wake instabilities. In turn, weakened instabilities mean weaker Kutta waves, and a very faint interaction between said waves and the shock until buffet dies out altogether.

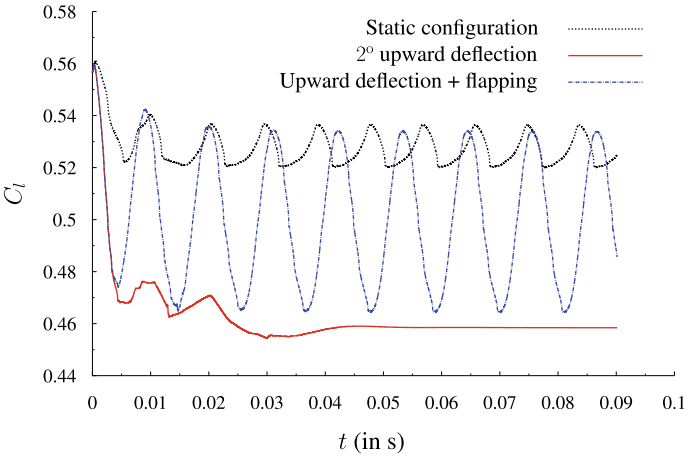


**Fig. 4** Lift coefficients for $\alpha = 1.8°$

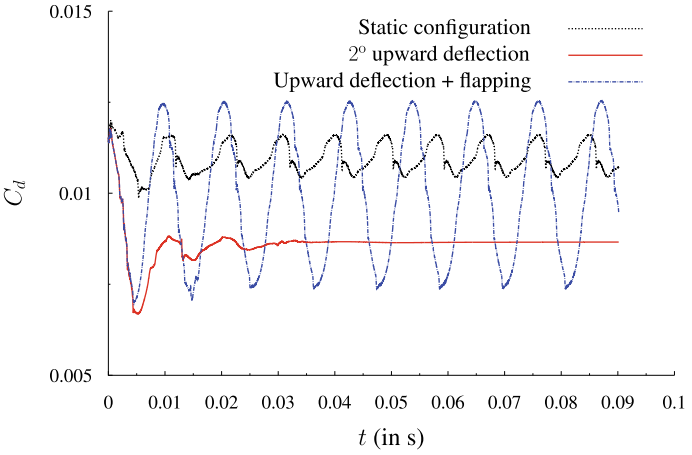


**Fig. 5** Drag coefficients for $\alpha = 1.8°$

This is less obvious for $\alpha = 5°$ because at this sharper incidence, separation is already too well-established to be suppressed by such a minimal deformation of the trailing edge. Figure 6 shows less of a difference between the static configuration and the morphing ones, although it is clear that morphing manages to reduce both lift and drag on average and to increase the mean lift to drag ratio, even at this angle of attack.

These results, computed when each signal is stationary, are summed up in Table 1:

As was already pointed out, the improvements in terms of $\langle C_l/C_d \rangle$ are more prominent in the $\alpha = 1.8°$ case, because the angle of attack is reduced and separation does not occur as strongly as in the $\alpha = 5°$ case. A slight improvement can be noticed

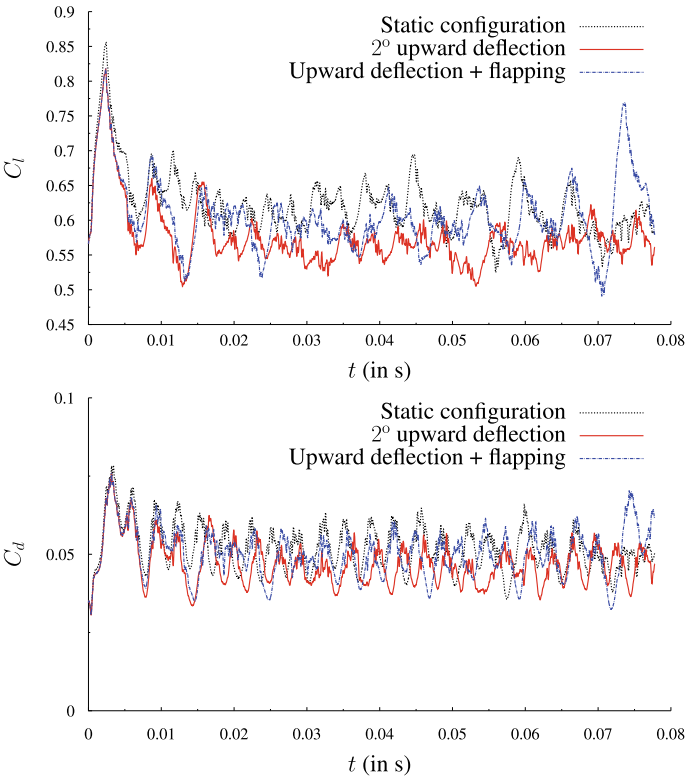


**Fig. 6** Force coefficients for $\alpha = 5°$

**Table 1** Relative mean lift over drag ratio gain compared to the static case

| Incidence | Angle of attack 1.8 | | Angle of attack 5 | |
|---|---|---|---|---|
| Type of actuation | D | D + F | D | D + F |
| $\frac{\langle C_l/C_d\rangle - \langle C_l/C_d\rangle_{\text{static}}}{\langle C_l/C_d\rangle_{\text{static}}} \times 100$ | +10.4% | +4.3% | +2.5% | +0.4% |

Note that D means "2° deflection" and "D + F" is the superposition of an immobile upward deflection and a 90 Hz flapping motion

in all these configurations, with a notable increase in $\langle C_l/C_d\rangle$ for the small trailing edge deflection when the incidence is 1.8°.

While the force coefficients RMS $C_{f,\text{rms}} = \left(\frac{1}{N}\sum_{i\in N\text{ samples}}\left(C_f(t_i) - C_{f,\text{mean}}\right)^2\right)^{1/2}$ shrink dramatically for $\alpha = 1.8°$ when a small trailing edge deflection is applied, this is less obvious for $\alpha = 5°$. An important issue of the present study is that an upward 2° deflection is sufficient to reduce both lift and drag RMS quite considerably. Most crucially, it can be seen on the energy spectra that morphing essentially modifies buffet through a dampening of flow instabilities in the wake region: By modify-

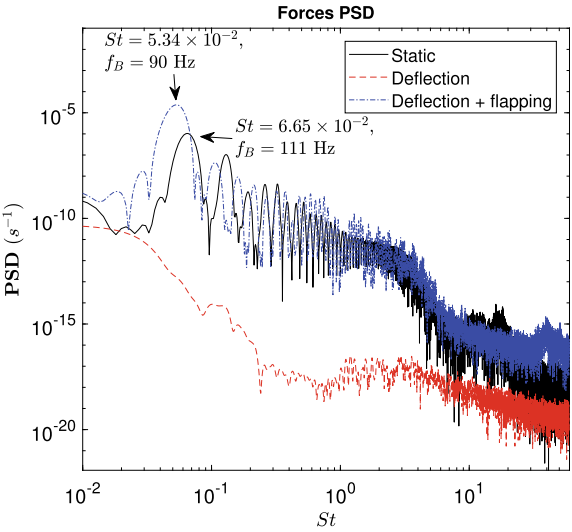


**Fig. 7** Energy spectra for $\alpha = 1.8°$

ing the high frequency region of the energy spectrum ($St > 5$) and diminishing the strength of all flow instabilities in this region, the non-linear interactions between these high-frequency modes and the buffet mode, expressed through the frequency peaks in between the buffet bump and Von Kármán mode as well as between the Von Kármán mode and the higher-frequency Kelvin-Helmholtz modes in the energy spectrum, are suppressed. This is the main mechanism of buffet annihilation.

In the energy spectrum of Fig. 7, it is noticeable that most of the modes have been dampened by the trailing edge deflection, while flapping modifies the behaviour of high frequency phenomena all the way to the left where intermediate bumps (which are harmonics of the buffet mode) are shifted to the left. This effectively displaces the natural frequency of the buffet instability which now takes the exact same value as the frequency of actuation.

## *3.2 A Frequency Lock-In*

A frequency lock-in is highlighted when the flapping frequency is modified. Flapping was performed at $f_{\text{act}} = 70$; 80; 90; 100 and 120 Hz, which corresponds to $St = 4.16 \times 10^{-2}$; $4.75 \times 10^{-2}$; $5.34 \times 10^{-2}$; $5.94 \times 10^{-2}$ and $4.16 \times 10^{-2}$ respectively.

As is shown in Fig. 8, the large bump that corresponds to buffet perfectly coincides with the actuation frequency, which shows the strong influence of morphing on the shock motion. This may also explain why it is relatively difficult to act upon buffet at a larger angle of attack. A PSD for $\alpha = 5°$ shows (cf. Fig. 9) that buffet does not occur at a single frequency, which means that it does not appear as one single peak or bump in the PSD, but as a clustering of multiple peaks.

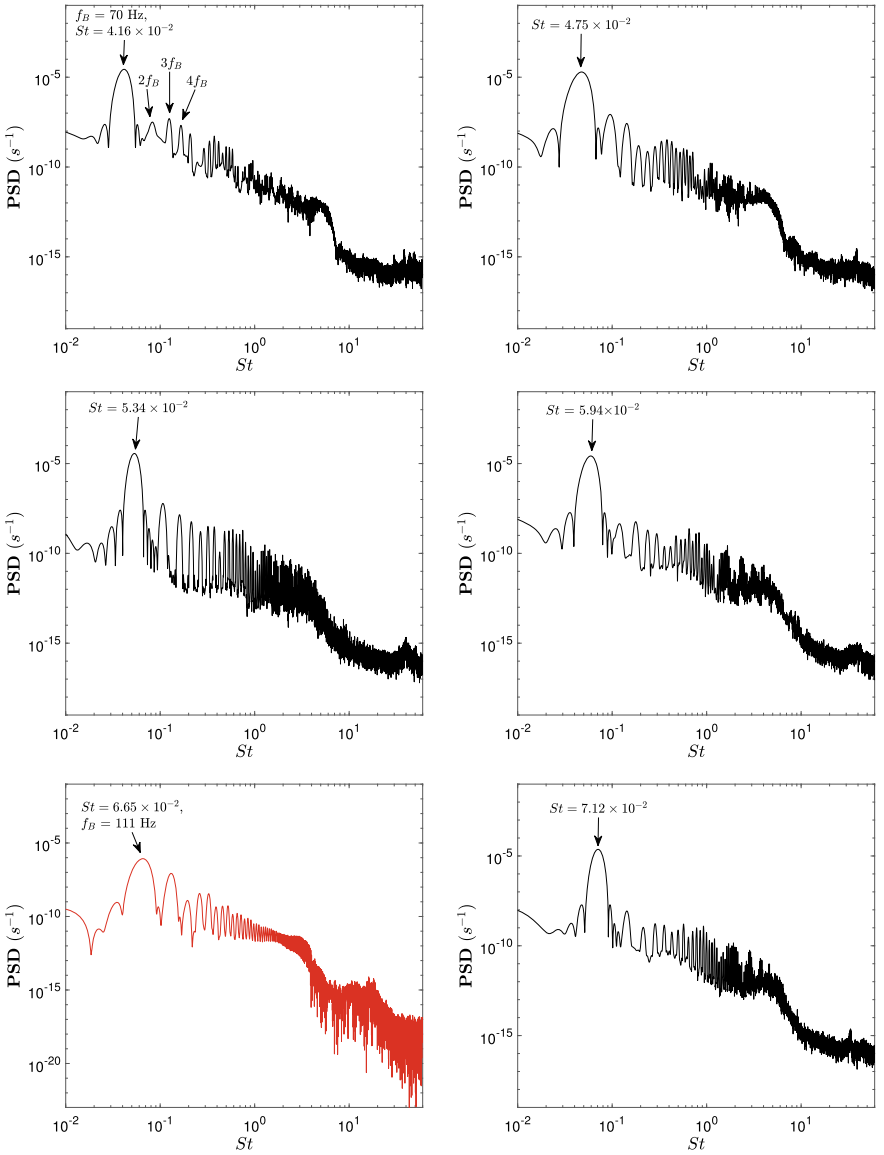


**Fig. 8** Power Spectral Density plots of the lift coefficient for different actuation frequencies. Black curves: PSD estimation via a Welch method for the following actuation frequencies: $f_{\text{act}} = \{70; 80; 90; 100; 120\}$ Hz. Red curve: Static configuration, i.e. unmorphed airfoil at an angle of attack $\alpha = 1.8°$

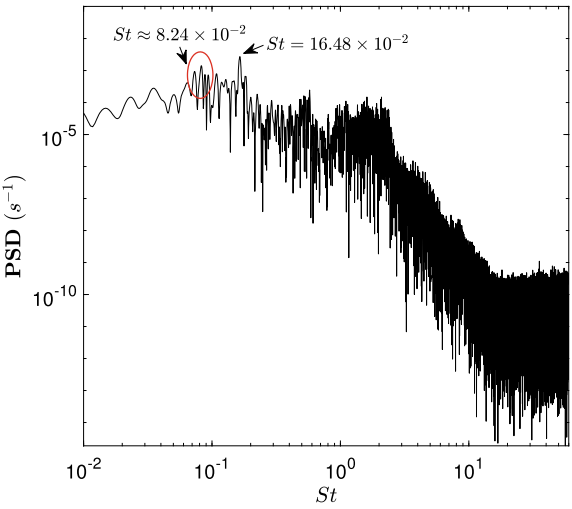


**Fig. 9** PSD for $\alpha = 5°$. A slightly predominant frequency stands out at $St = 16.48 \times 10^{-2}$, but it appears that a cluster of frequencies better characterizes buffet than just a single peak

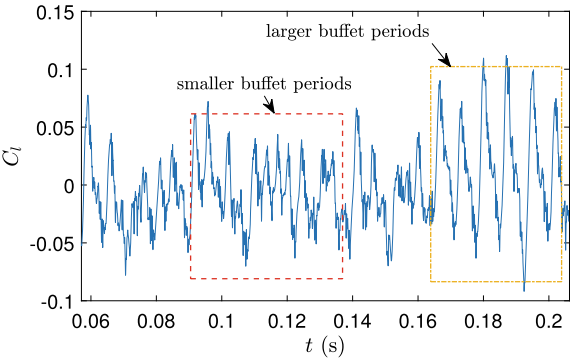


**Fig. 10** A frequency modulation can be observed, with zones corresponding to a low-frequency buffet, others to a higher-frequency phenomenon

This translates into a frequency modulation due to the intense non-linear interaction between wake instabilities and the shock, as can be seen in Fig. 10. The small upward deflection cannot influence this interaction strongly enough and the PSD remains pretty much the same, with a slight drop in energy for low frequency modes. However, even though flapping does not influence buffet as much as it did for $\alpha = 1.8°$, this actuation excites a small bump that exactly corresponds to the morphing frequency, which indicates that a frequency lock-in still arises at that angle of attack (cf. Fig. 11).

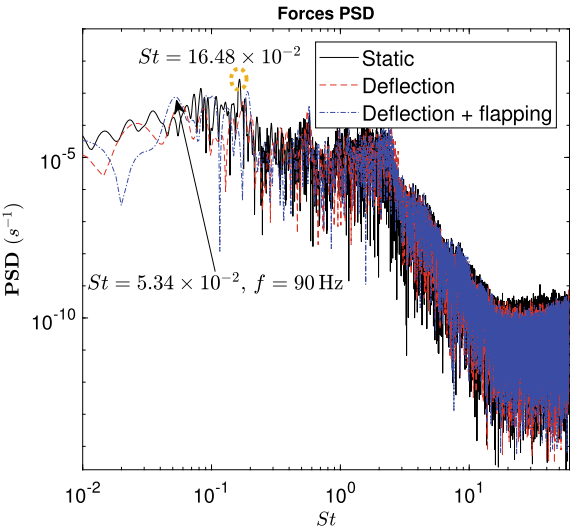


**Fig. 11** An energetic bump appears at $f = 90$ Hz for the deflection + flapping case. This is a testament of frequency lock-in at $\alpha = 5°$

## 4 Conclusions

The present study analyses the transonic buffet mechanisms related to coherent vortex formation in the separated shear layers and in the near wake, as well as their feedback effect towards the SWBLI area.

2D computations by using the OES approach around a static and morphing A320 airfoil have shown that slightly deflecting and optimally actuating the trailing edge region in the transonic regime corresponding to the cruise phases of flight, is able to considerably manipulate the surrounding vortex structures and the shear layers and affect the buffet dynamics. A frequency lock-in of the buffet mode and the actuation frequency has been shown by specific slight deformations and vibrations of the near-trailing edge area.

**Acknowledgements** The authors are grateful to the LAPLACE Laboratory team of electroactive actuators and to the national supercomputing centres CALMIP, CINES and IDRIS for their attribution of computational resource.

## References

1. Bourguet, R., et al.: Anisotropic organised Eddy simulation for the prediction of nonequilibrium turbulent flows around bodies. J. Fluids and Struct. **24**(8), 1240–1251 (2008). ISSN 08899746. https://doi.org/10.1016/j.jfluidstructs.2008.07.004
2. Braza, M., et al.: Turbulence modelling improvement for highly detached unsteady aerodynamic flows by statistical and hybrid approaches. In: ECCOMAS CFD 2006 : European Conference on Computational Fluid Dynamics, 5–8 Sept 2006 (2006)

3. Gnani, F., et al.: Experimental investigation on shock wave diffraction over sharp and curved splitters. Acta Astronautica **99**(1), 143–152 (2014). ISSN 00945765. https://doi.org/10.1016/j.actaastro.2014.02.018
4. Grossi, F., Braza, M., Hoarau, Y.: Prediction of transonic buffet by delayed detached—Eddy simulation. In: AIAA J. **52**(10), 2300–2312 (2014). ISSN 0001-1452. https://doi.org/10.2514/1.J052873, http://arc.aiaa.org/doi/10.2514/1.J052873
5. Grossi, F., Szubert, D., et al.: Numerical simulation and turbulence modelling of the transonic buffet over a supercritical airfoil at high Reynolds number. In: Proceedings of the ETMM9 9th International ERCOFTAC Symposium on Engineering Turbulence Modelling and Measurements. Thessaloniki, Greece (2012)
6. Hunt, J.C.R., Eames, I., Westerweel, J.: Vortical interactions with interfacial shear layers. In: Kaneda, Y. (ed.) IUTAM Symposium on Computational Physics and New Perspectives in Turbulence, pp 331–338. Springer, Dordrecht (2008). ISBN 978-1-4020- 6472-2
7. Jacquin, L., et al.: Experimental study of shock oscillation over a transonic supercritical profile. In: AIAA J. **47**(9), 1985–1994 (2009). ISSN 0001-1452. https://doi.org/10.2514/1.30190, http://arc.aiaa.org/doi/10.2514/1.30190
8. Marvin, J.G., Levy, Jr., L.L., Seegmiller, H.L.: Turbulence modeling for unsteady transonic flows. In: AIAA J. **18**(5), 489–496 (1980). ISSN 0001-1452. https://doi.org/10.2514/3.50782
9. Sajben, M., Kroutil, J.C.: Effects of initial boundary-layer thickness on transonic diffuser flows. In: AIAA J. **19**(11), 1386–1393 (1981). ISSN 0001-1452. https://doi.org/10.2514/3.60075
10. Scheller, J., et al.: Trailing-edge dynamics of a morphing NACA0012 aileron at high Reynolds number by high-speed PIV. J. Fluids Struct. **55**, 42–51 (2015). ISSN 10958622. https://doi.org/10.1016/j.jfluidstructs.2014.12.012
11. Smits, A.J., Dussauge, J.P.: Turbulent Shear Layers in Supersonic Flow, p. 410 (2005). ISBN 978-0-387-26305-2. http://www.springer.com/physics/classical+continuum+physics/book/978-0-387-26140-9
12. Szubert, D., et al.: Shock-vortex shear-layer interaction in the transonic flow around a supercritical airfoil at high Reynolds number in buffet conditions. J. Fluids Struct. **55**, 276–302 (2015). ISSN 10958622. https://doi.org/10.1016/j.jfluidstructs.2015.03.005
13. Tijdeman, H.: Investigation of the transonic flow around oscillating airfoils. In: National Aerospace Lab., Amsterdam, Netherlands TR-77-090U (1977). b07421b9-136d-494c-a161-b188e5ba1d0d

# Fluid-Structure Simulation of a Piston Shock-Tube Using an Adaptive ALE Scheme in the Non-ideal Compressible-Fluid Regime


**Barbara Re and Alberto Guardone**

**Abstract** Numerical simulations of the three-dimensional piston-induced shock-tube problem in Non-Ideal Compressible-Fluid Dynamics are performed by using a novel interpolation-free adaptive scheme, able to solve the Euler equations within the Arbitrary Lagrangian Eulerian (ALE) framework, including connectivity changes due to mesh adaptation. To cope with displacement- and force-imposed boundary motions, the grid is adapted by means of node insertion, deletion and edge swapping. The Geometric Conservation Law constraint is automatically fulfilled by an appropriate computation of the geometric grid quantities and no interpolation of the solution from the original to the adapted grid is required thanks to the interpretation of the connectivity changes as a sequence of fictitious continuous deformations. These capabilities represent great advantages with respect to standard interpolation-based adaptation techniques as they avoid the occurrence of spurious oscillations in the flow field, which may undermine the robustness of the numerical scheme in the non-ideal compressible-fluid dynamics regime in the close proximity of the liquid-vapor saturation curve and critical point. Numerical simulations confirm the feasibility of an oscillating-piston experiment to observe non-ideal wave propagation including non-monotone sound speed effects.

**Keywords** Non-ideal compressible fluid dynamics · Fluid-structure simulations · Mesh adaptation · Piston problem

B. Re (✉)
Institut für Mathematik, Universität Zürich, Zürich CH-8057, Switzerland
e-mail: barbara.re@math.uzh.ch

A. Guardone
Department of Aerospace Science and Technology, Politecnico di Milano, 20156 Milano, Italy
e-mail: alberto.guardone@polimi.it



M. Braza et al. (eds.), *Advances in Critical Flow Dynamics Involving Moving/Deformable Structures with Design Applications*, Notes on Numerical Fluid Mechanics and Multidisciplinary Design 147,
https://doi.org/10.1007/978-3-030-55594-8_32

## 1 Introduction

Non-Ideal Compressible-Fluid Dynamics (NICFD) concerns flows occurring within the thermodynamic region wherein the fluid thermodynamic behavior significantly departs from the one predicted by the ideal gas model, such as dense-vapor, supercritical-fluid and two-phase-fluid flows. In these conditions, attractive and repulsive molecular forces are not negligible and non-ideal gas effects, such as non-monotone Mach variation along isentropes, or non-classical phenomena, such as rarefaction shocks, may possibly occur, see [6].

In recent years, this specific branch of gas-dynamics is receiving more and more interest, as different modern applications, especially in the field of propulsion and power, have been conceived to benefit from the non-ideal flow behavior to reach better performance. An example is represented by the Organic Rankine Cycle (ORC) engines, where organic fluids of high molecular complexity are used as working fluids in the Rankine cycle to exploit low-temperature renewable-energy sources. Nevertheless, the theoretical and practical treatment of the NICFD flow behavior still presents several challenges, and further experimental and numerical investigations are required to improve the understanding and the modeling capabilities of non-ideal compressible flows.

Different efforts have been made to extend standard CFD techniques usually adopted under the perfect, i.e. polytropic ideal, gas assumption to the NICFD regime, see [16], and commercial software as well. In addition, new methods are continuously developed to tackle specific numerical tasks or applications. For example, several contributions have been dedicated to numerical schemes, to efficient evaluation of thermodynamic quantities, and to shock waves and to turbulent flows in the NICFD regime. Recently, we have discussed an assessment of an interpolation-free mesh adaptation technique for inviscid simulations in the NICFD regime [12, 13]. Thanks to a peculiar interpretation of the local grid adaptation within the Arbitrary Lagrangian-Eulerian (ALE) framework [11], this technique avoids the occurrence of spurious oscillations due to the interpolation of the solution between the original and the adapted grid, which could be detrimental in proximity of the vapor-liquid saturation curve. Furthermore, an ad-hoc description of the finite volume modification due to mesh adaptation allows to compute the grid velocities so that the Geometric Conservation Law (GCL) is fulfilled even when the mesh connectivity changes because of node insertion, deletion, or edge swap. As known, this constraint plays a crucial role in fluid-structure simulations [8]. Concurrently with the numerical techniques, the experimental activities are fundamental both to improve the comprehension of NICFD flows, as well as to assess new CFD tools.

Driven by these motivations, we present here the first results of an adaptive Fluid-Structure simulation of the piston-problem in the NICFD regime. The piston problem is a quite standard gas-dynamic test, which presents diverse numerical challenges, such as the presence of traveling waves with different spatial scales and the large displacements of the numerical boundaries that model the piston surfaces. In addition, this setup is often the core of experimental test rigs, thus the capability of perform-

ing this kind of simulation is of paramount importance for the design of new test equipment devoted to the investigation of fundamental behavior of NICFD flows. This paper stems form the previous work described in [15], where we presented the simulation of the 2D shock-tube piston-problem filled with air, under the polytropic ideal gas assumption. The main novelties here introduced concern the fluid-structure interaction in three-dimensional problems characterized by large displacements, and mesh-adaptation in non-ideal compressible flow simulations.

## 2 Methods

The ALE framework allows to solve the flow governing equations on a dynamic, i.e. deforming, computational grid. In this work, the unsteady Euler equations are spatially discretized by means of a node-centered edge-based finite-volume scheme, and the backward Euler formula is exploited for time integration. Thus, the ALE compressible governing equations over the finite volume $\mathcal{C}_i$ can be written as

$$\frac{V_i \mathsf{u}_i^{n+1} - V_i \mathsf{u}_i^n}{\Delta t} = \sum_{k \in \mathcal{K}_{i,\neq}} \boldsymbol{\phi}(\mathsf{u}_i, \mathsf{u}_k, \nu_{ik}, \boldsymbol{\eta}_{ik}) + \boldsymbol{\phi}^{\partial}(\mathsf{u}_i, \nu_i, \boldsymbol{\xi}_i) \tag{1}$$

where $\mathsf{u}_i$ is the average value of the vector of conservative variables $\mathsf{u} = [\rho, \boldsymbol{m}, E^T]^{\mathrm{T}}$ over $\mathcal{C}_i$, $\boldsymbol{\phi}$ and $\boldsymbol{\phi}^{\partial}$ are suitable integrated numerical fluxes for, respectively, the flux across the domain cell interface $\partial\mathcal{C}_{ik} = \partial\mathcal{C}_i \cap \partial\mathcal{C}_k$ and, if the node $i$ lies on the boundary, across the boundary cell interface $\partial\mathcal{C}_{i,\partial}$. Moreover, $\mathcal{K}_{i,\neq}$ is the set of the neighboring nodes of the finite volume $i$, and the integrated normals $\boldsymbol{\eta}_{ik}$, $\boldsymbol{\xi}_i$ and the interface velocities $\nu_{ik}$ and $\nu_i$ are defined as

$$\boldsymbol{\eta}_{ik} = \int_{\partial\mathcal{C}_{ik}} \boldsymbol{n}_i \,, \qquad \boldsymbol{\xi}_i = \int_{\partial\mathcal{C}_{i,\partial}} \boldsymbol{n}_i \,, \qquad \nu_{ik} = \int_{\partial\mathcal{C}_{ik}} \boldsymbol{v} \cdot \boldsymbol{n}_i \,, \qquad \nu_i = \int_{\partial\mathcal{C}_{i,\partial}} \boldsymbol{v} \cdot \boldsymbol{n}_i \,. \tag{2}$$

When solving flow equations on a moving computational domain, the evaluation of the geometric quantities connected to the grid movement, that is the ones defined in Eq. (2), is crucial. In this regard, it is usually recognized that the fulfillment of the so-called Geometric Conservation Law (GCL) positively affects the stability and the accuracy of the numerical scheme for dynamic grids and allows larger time steps with respect to non-compliant schemes [4, 9]. For the governing equations (1), this constraint can be enforced by means of the following Discrete Geometric Conservation Law (DGCL)

$$\frac{d}{dt} \int_{\mathcal{C}(t)} d\boldsymbol{x} = \oint_{\partial\mathcal{C}(t)} \boldsymbol{v} \cdot \boldsymbol{n} \, ds \,, \tag{3}$$

which can be split into contributions pertaining to the domain and to the boundary:

$$\Delta V_{ik}^{n+1} = \Delta t \; v_{ik}^{n+1} \qquad \text{and} \qquad \Delta V_{i,\partial}^{n+1} = \Delta t \; v_{i}^{n+1} \,, \tag{4}$$

where $\Delta V_{ik}^{n+1}$ and $\Delta V_{i,\partial}^{n+1}$ are the volumes swept during the interval from $t^n$ to $t^{n+1}$ by the interface portions $\partial \mathcal{C}_{ik}$ and $\partial \mathcal{C}_{i,\partial}$, respectively. When the finite volumes experience a continuous deformation, relations (4) allow to easily compute GCL-compliant interface velocities in terms of the positions of the grid nodes at the beginning and at the end of the time step, as thoroughly described in [11].

## *2.1 Adaptive GCL-Compliant Scheme*

In unsteady simulations, mesh adaptation techniques may be profitably used to tackle large boundary movements, and to accurately capture the relevant flow features that originate and move through the domain [2, 5]. For what concerns the first goal, if the fixed-connectivity redistribution of the internal nodes that is performed after the boundary movement leads to badly-shaped mesh elements, edge swapping and barycentric node relocation are exploited to restore the grid quality. This operation is not performed every a fixed number of time steps, but only when the displacement to be imposed during the time step will lead to a poor-quality or invalid grid [14]. The achievement of the second goal requires the definition of an effective adaptation criteria that can be used to determine where grid should be modified. This indicator can be built in terms of the derivatives of some relevant flow quantities, such as the Mach number or the density. The grid spacing is indeed related to the solution-behavior: it is reduced where the gradients are large, while it is increased where the solution is smooth. An in-depth investigation of these kind of adaptation criteria in NICFD regimes is presented in [12].

Local grid connectivity changes lead to modifications of the finite volumes that compose the computational domain. Intuitively, node insertion leads to new finite volumes, while after node deletion some finite volumes have to be deleted. The interpolation can be used to map the solution onto the new, adapted grid, but this operation, from a numerical point of view, is hazardous, as it can undermine positive-preserving and conservative of the solution, and it can introduce oscillations. An alternative approach is proposed in [7, 11], where a three-steps series of fictitious collapse and expansion operations are exploited to describe the grid connectivity changes as a sequence of continuous deformations, as shown for the 2D edge split in Fig. 1. In this way, the volume modifications can be taken into account in a conservative fashion within the ALE framework and the GCL is fulfilled by relations (4) even when nodes are inserted or deleted and edges are swapped, without undermining the properties of the underlying fixed-connectivity scheme. Moreover, the absence of an explicit interpolation prevents the generation of spurious oscillations that may make more difficult and less robust the solution of the flow field in the NICFD regime.

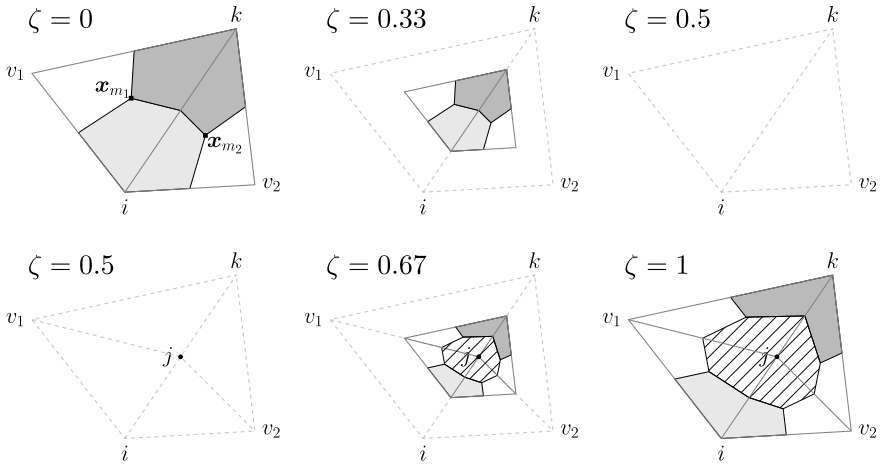


**Fig. 1** Three-steps procedure applied to the split of edge $e_{ik}$. The non-dimensional time $0 \leq \zeta \leq 1$ is used to describe the different fictitious steps. The dashed grey lines show the grid connectivity in the original/final configuration ($\zeta = 0/\zeta = 1$), while the portions of the finite volumes associated to $i$, $k$ and $j$ are shown with light grey □, dark grey ■ and the pattern ▨, respectively. The label $\boldsymbol{x}_{m_i}$ indicates the barycenter of the element $m_i$. In the first row the collapse phase $0 < \zeta < 0.5$ is depicted: the quadrilateral $i$-$k$-$v_1$-$v_2$, composed by the elements that share the edge $e_{ik}$ at $\zeta = 0$, is collapsed over its mid-point. When it reaches a null area, the connectivity is changed ($\zeta = 0.5$): the new point $j$ is inserted, the edge $e_{ik}$ is split into two edges ($i$-$j$ and $k$-$j$) and two new edges are created to connect $j$ to $v_1$ and $v_2$. The second row displays the expansion procedure $0.5 < \zeta < 1$: the nodes $i$, $k$, $v_1$, $v_2$ return to their original positions to reach the final configuration (at $\zeta = 1$)

## 2.2 Thermodynamic Modeling

A complete thermodynamic model of the fluid at equilibrium is obtained from two independent EoS, such as for example the pressure and energy EoS using the temperature $T$ and the specific volume $v = 1/\rho$ as independent variables, namely, $P = P(T, v)$ and $e = e(T, v)$, see [1]. For an ideal gas, $P(T, v) = RT/v$, and the compatible energy EoS is a function of the temperature only, which, under the further assumption of constant specific heats reads $e(T) = RT/(\gamma - 1)$, where $\gamma > 1$ is the ratio of the specific heats at constant pressure and volume, respectively. The Peng-Robinson [10] model is implemented in the CFD solver to include NICFD effects. Assuming a constant specific heat in the dilute-gas limit, the EoS for the pressure and the internal energy read

$$\begin{aligned} P(T, v) &= \frac{RT}{v - b} - \frac{a\alpha_\omega^2(T)}{v^2 + 2vb - b^2}, \\ e(T, v) &= e_0 + \phi(T) - \frac{a\alpha_\omega(T)}{b\sqrt{2}} \left[\alpha_\omega(T) + f_\omega \sqrt{T/T_c}\right] \tanh^{-1}\left(\frac{b\sqrt{2}}{v + b}\right), \end{aligned} \tag{5}$$

where $\tanh^{-1}$ is the inverse of the hyperbolic tangent, $e_0$ is a reference energy and where the constant $a$ and $b$ are given by $a = 0.45724\frac{(RT_c)^2}{P_c}$ and $b = 0.07780\frac{RT_c}{P_c}$, with $R$ gas constant, $T_c$ and $P_c$ critical temperature and pressure, respectively. The function $\alpha_\omega(T)$ is defined as $\alpha_\omega(T) = 1 + f_\omega[1 - \sqrt{T/T_c}]$, where $f_\omega = 0.37464 + 1.54226\omega - 0.26992\omega^2$ and $\omega$ is the centric factor of the fluid.

## 2.3 Computational Procedure

In the present work, the external re-mesher mmg3d library is exploited to efficiently modify the computational grid [3]. Figure 2 outlines the whole computational procedure used in unsteady simulations. At the beginning of the time step $t^n \leq t \leq t^{n+1}$, the grid and the solution are respectively label as $\mathcal{K}^n$ and $\mathsf{u}(t^n, \mathcal{K}^n)$. Then, the following operations are performed:

1. Mesh deformation: the displacement of the piston is computed, and the internal grid nodes are displaced to cope with it. A first attempt is performed by means of the elastic analogy; if it fails, the grid quality is enhanced by exploiting the mmg3d library [14]. The new grid is labeled $\mathcal{K}^{n+}$.
2. Prediction: the solution at next time step, over the grid $\mathcal{K}^{n+}$, is computed. This step prevents a delay between the solution-based mesh adaptation and the actual geometry, and allows to enforce larger time steps.

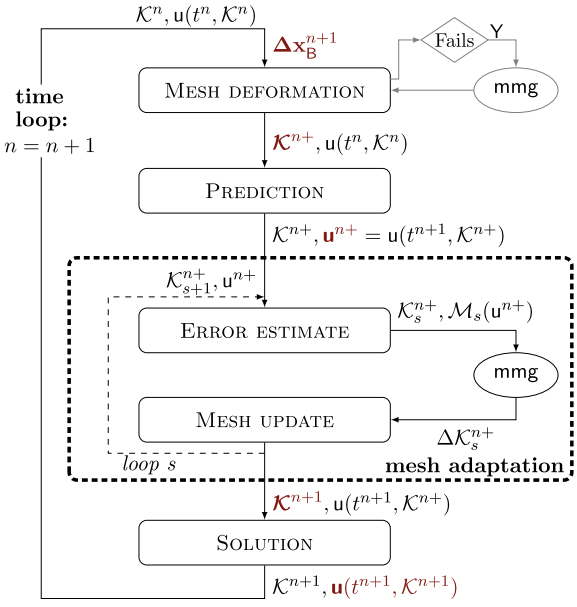


**Fig. 2** Adaptive computational procedure for unsteady problems. The grid $\mathcal{K}^{n+}$ complies with the boundary displacement at $t^{n+1}$ and, over it, the solution $\mathsf{u}^{n+}$ is computed in the *Prediction* step. The metric field $\mathcal{M}(\mathsf{u}^{n+})$ is passed as input to mmg3d which communicates to the flow solver all performed modifications $\Delta\mathcal{K}^{n+}$, so that it can compute the swept volumes $\Delta V$ due to mesh adaptation. Finally, the solution at $t^{n+1}$ over the adapted grid $\mathcal{K}^{n+1}$ is computed

3. Error estimate: the target grid spacing $\mathcal{M}$ is computed according to the derivatives of the solution just computed $\mathsf{u}^{n+} = \mathsf{u}(t^{n+1}, \mathcal{K}^{n+})$.
4. Mesh adaptation: the grid $\mathcal{K}^{n+}$ and the target grid spacing $\mathcal{M}(\mathsf{u}^{n+})$ are passed as inputs to the library mmg3d, which locally adapts the grid by means of node insertion, deletion and edge swapping.
5. Mesh update: the flow solver receives from mmg3d each performed grid modification $\Delta\mathcal{K}^{n+}$; the finite volume discretization is modified accordingly and the resulting swept volumes $\Delta V$ are computed by means of the three-steps procedure [11].
6. Computation of the solution $\mathsf{u}^{n+1}$ on the grid $\mathcal{K}^{n+1}$, using as initial guess $\mathsf{u}^{n+}$.

## 3 Results

The interpolation-free adaptive approach described in the previous section is exploited to simulate the flow field generated by a piston oscillating in a infinite-length tube. No gap between the piston and the tube walls is assumed. Two kinds of simulations are performed: first, the position of the piston is imposed directly; second, a force is imposed to the piston and the consequent displacement results from the pressure acting on the piston surfaces. The second force is calculated so that the resulting movement is the same. The second test aims at providing a first assessment of the adaptive procedure in Fluid-Structure simulation in NICFD regimes. Obviously, an inaccurate thermodynamic model as the PIG gas would lead to a completely erroneous motion of the piston. In both simulations, a combination of the Hessian of the pressure and the gradient of the Mach number is used to build the adaptation criteria.

In the first simulation, an harmonic motion is imposed to the piston, i.e. $x_P^n = x_0 + A\cos(2\pi\, f\, t^n)$, with an amplitude $A = -0.5$ m and a frequency $f = 30$ Hz. The piston has a square section of $0.05 \times 0.05$ m and a length of 0.1 m, and it is centered at $x_0 = 0$. Thus, the initial position is $x_P(0) = -0.25$ m. The tube is filled with the linear siloxane $MD_4M$,[1] initially at rest with $P_0 = 0.9\, P_c$ and $T_0 = 1.015\, T_c$, where the subscripts c indicates the variables at the critical point. Table 1 reports the thermo-physical and critical properties of $MD_4M$ used in this work.

The piston starts to move toward the right with an increasing velocity. This motion generates compressive ways on the right part of the domain, which, due to the increasing velocity in the first quarter of the period $T$, may coalesce. At the same time, rarefaction waves are generated and propagate in the left part of the piston. In the second part of the period, the opposite occurs, namely rarefaction waves are generated on the right side of the piston and compression on the left one. The first three periods of the motion are simulated. Figure 3 shows the results at the end of each period. We can noticed how the different waves propagate into the domain. A more quantitative display of the pressure evolution along the tube is given in Fig. 4.

[1] $MD_4M$ is the acronym for the tetradecamethylhexasiloxane.

**Table 1** Thermodynamic properties for $MD_4M$: $M_m$ is the molecular mass, $T_b$ is the boiling temperature, $T_c$, $P_c$, $v_c$ are the critical temperature, pressure and volume; $Z_c$ is the compressibility factor at critical point, $c_{p\infty}/R$ is isobaric specific heat capacity in the ideal gas limit, and $\omega$ is the acentric factor

| | | | | | | | |
|---|---|---|---|---|---|---|---|
| $M_m$ (kg/mol) | 0.45899 | $T_b$ (K) | 533.9 | $T_c$ (K) | 653.20 | $P_c$ (bar) | 8.7747 |
| $v_c$ ($m^3$/kmol) | 1.7309 | $Z_c$ | 0.2797 | $c_{p\infty}/R$ | 115.99 | $\omega$ | 0.7981 |

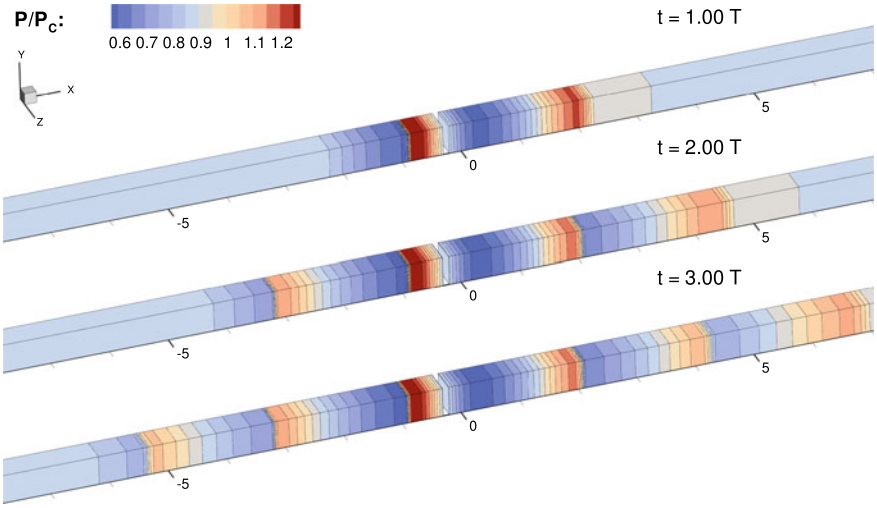


**Fig. 3** Pressure field in the displacement-imposed test. The results at end of the first three periods are shown. To improve the clearness of the picture, different aspect ratios are used between $x$ and $y$, $z$ axis, namely the lengths over $y$ and $z$ are multiplied by a factor 10

During the first simulation, the pressure force acting on the piston surfaces is evaluated at each time step. Now, this "recorded" force and the inertial force are imposed on the piston in the second (e.g. forced) simulation, in order to obtain the same motion. Assuming a mass $m = 1.0$ kg, at each time step the velocity (in the $x$ direction) of the piston is computed as

$$V_P^{n+1} = V_P^n + \frac{1}{m}\left(-\mathcal{F}_{P,1}^n - \mathcal{F}_{I,1}^n + \int_{\partial\Omega_P} P(\mathsf{u}^n)\,\boldsymbol{n}_x\,dS\right)/\Delta t\,, \tag{6}$$

where $\mathcal{F}_{P,1}$ is the pressure force computed in the first simulation, $\mathcal{F}_{I,1}$ is the inertial force of the desired motion (i.e., in this case $-m\ddot{x}_P$), $P(\mathsf{u})$ is the pressure and $\boldsymbol{n}_x$ is the $x$-component of the normal to the piston surface, labeled $\partial\Omega_P$. If, the pressure fields are the same, the integral term cancels out $-\mathcal{F}_{P,1}$, so the motion is driven by the imposed acceleration $\ddot{x}_P$. The final time of this test is the same as the one of the previous simulation. The results of this test, displayed in Fig. 5, are very similar to the

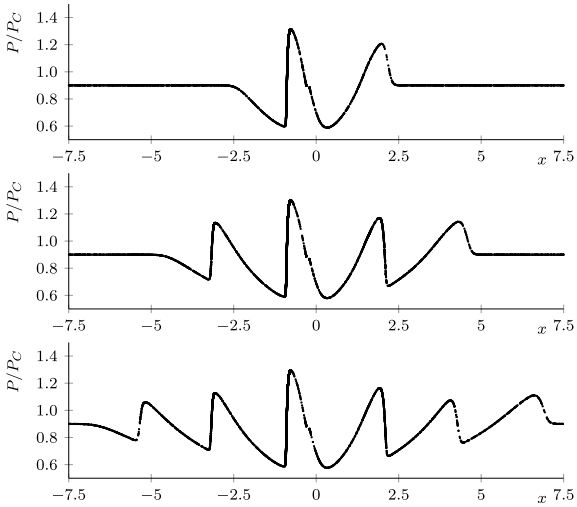


**Fig. 4** Pressure evolution in the displacement-imposed test. The results at end of the first three periods are shown

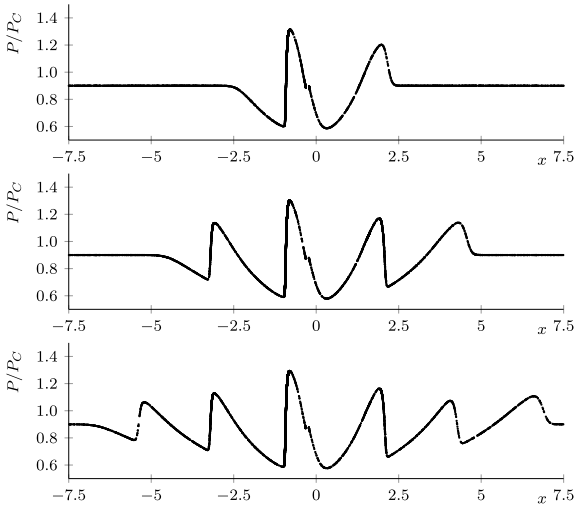


**Fig. 5** Pressure evolution in the displacement-imposed test. The results at times $t = 1\,T, t = 2\,T, t = 3\,T$ are shown

ones of the previous test, shown in Fig. 4. This fact is confirmed more clearly by the comparison of the piston position on both test, shown in Fig. 6. The good agreement between the two profiles demonstrates the capability of the proposed approach to deal with Fluid-Structure interaction for rigid bodies. More specifically, even though the fluid behavior is non-ideal, the force exerted by it on the solid walls of the piston is correctly taken into account during the motion. The discrepancies in Fig. 6 are due to the small integration error introduced by the use of quantities at $t^n$ to evaluate $V_P^{n+1}$, i.e., in the right hand side of Eq. (6). The force imposed to the piston and the one exerted by the fluid on the piston walls are shown in Fig. 7.

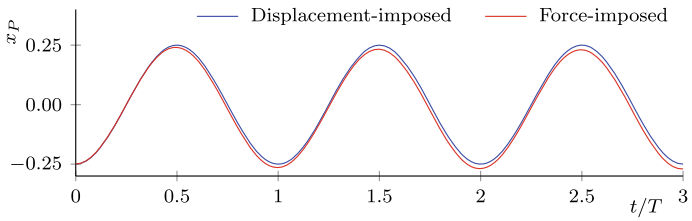


**Fig. 6** Piston position as a function of time for the displacement-imposed simulation (where an harmonic motion is imposed) and the forced-imposed simulation (where the displacement results from the difference in the force imposed on the piston and the one exerted by the fluid on the piston surfaces)

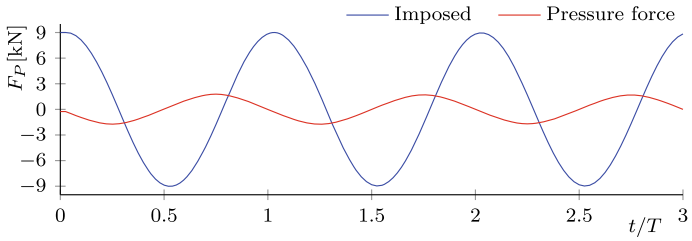


**Fig. 7** Forces imposed and resulting in the forced-imposed test. The *Imposed* force is the one imposed on the piston, that is $\mathcal{F}_{P,1} + \mathcal{F}_{I,1}$ in Eq. (6); while the *Pressure force* is the force exerted by the fluid on piston

The importance of mesh adaptation in this kind of simulations, where the computational domains experience large displacements and the flow features exhibit strong unsteadiness, is depicted in Fig. 8, which displays a detail of the flow field together with the grid in proximity to the piston.

## 4 Conclusions

In the present work, a novel adaptive ALE scheme for dynamic meshes was successfully applied to simulate the fluid-structure interaction of a piston moving inside a tube filled with the siloxane $MD_4M$. The fluid operates in highly non-ideal conditions and two different types of motion are simulated. First, a periodic displacement is applied to the piston to produce suitable pressure disturbances within the fluid; then, a time-dependent force is imposed to the piston, whose motion thus results from the difference in the external, imposed force and the pressure force exerted by the fluid on the piston surfaces. A good agreement is reached when the same acceleration is imposed, confirming the validity of the proposed approach in the non-ideal regime. Due to the large displacement experienced by the piston within the tube, mesh adaptation was used to preserve the mesh quality and to modify the

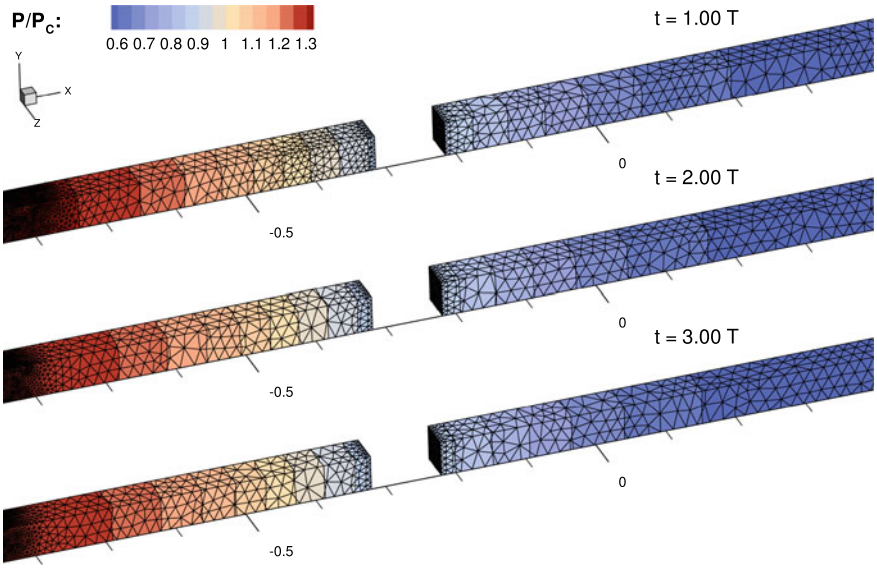


**Fig. 8** Detail of the grid in forced-imposed test, in the region near the piston, at times $t = 1\,T$, $t = 2\,T$, $t = 3\,T$. The pressure contour is also shown below the grid to highlight the connection between the solution and the grid spacing

grid spacing to detect and follow the most significant flow features. A conservative implementation of the ALE scheme for adaptive meshes was used to avoid explicit interpolation of the solution across different grids, which may introduce undesirable oscillations into the flow field. Finally, due to the primary role that the piston problem plays in several laboratories facilities, the present results could be considered a confirmation of the feasibility of a shock-tube experiment to study the non-ideal behavior of compressible-fluid in the close proximity of the liquid-vapor saturation curve and critical point.

**Acknowledgements** This work is dedicated to our late friend, mentor and colleague Cécile Dobrzynski. This research is supported by ERC Consolidator Grant N. 617603, Project NSHOCK, funded under the FP7-IDEAS-ERC scheme.

## References

1. Callen, H.B.: Thermodynamics and an Introduction to Thermostatistics, 2nd edn. Wiley (1985)
2. Compère, G., Remacle, J., Jansson, J., Hoffman, J.: A mesh adaptation framework for dealing with large deforming meshes. Int. J. Numer. Meth. Eng. **82**, 843–867 (2010)
3. Dobrzynski, C., Dapogny, C., Frey, P., Froehly, A.: Mmg3d (Computer Software)
4. Farhat, C., Geuzaine, P., Grandmont, C.: The discrete geometric conservation law and the nonlinear stability of ALEschemes for the solution of flow problems onmoving grids. J. Comput. Phys. **174**, 669–694 (2001)

5. Habashi, W.G., Dompierre, J., Bourgault, Y., Ait-Ali-Yahia, D., Fortin, M., Vallet. M.G.: Anisotropic mesh adaptation: towards user-independent, mesh-independent and solver-independent CFD. Part I: general principles. Int. J. Numer. Meth. Fluids **32**, 725–744 (2000)
6. Harinck, J., Guardone, A., Colonna, P.: The influence of molecular complexity on expanding flows of ideal and dense gases. Phys. Fluids **21**, 086101–1–14 (2009)
7. Isola, D., Guardone, A., Quaranta, G.: Finite-volume solution of two-dimensional compressible flows over dynamic adaptive grids. J. Comput. Phys. **285**, 1–23 (2015)
8. Lesoinne, M., Farhat, C.: Geometric conservation laws for flow problems with moving boundaries and deformable meshes, and their impact on aeroelastic computations. Comput. Methods Appl. Mech. Eng. **134**, 71–90 (1996)
9. Mavriplis, D.J., Yang, Z.: Construction of the discrete geometric conservation law for high-order time-accurate simulations on dynamic meshes. J. Comput. Phys. **213**(2), 557–573 (2006)
10. Peng, D.Y., Robinson, D.B.: A new two-constant equation of state. Ind. Eng. Chem. Fundam. **15**(1), 59–64 (1976)
11. Re, B., Dobrzynski, C., Guardone, A.: An interpolation-free ALE scheme for unsteady inviscid flows computations with large boundary displacements over three-dimensional adaptive grids. J. Comput. Phys. **340**, 26–54 (2017)
12. Re, B., Dobrzynski, C., Guardone, A.: Assessment of grid adaptation criteria for steady, two-dimensional, inviscid flows in non-ideal compressible fluids. Appl. Math. Comput. (2017)
13. Re, B., Guardone, A.: An adaptive ALE scheme for non-ideal compressible-fluid dynamics over dynamic unstructured meshes. Shock Waves **29**, 73–99 (2019). https://doi.org/10.1007/s00193-018-0840-2
14. Re, B., Guardone, A., Dobrzynski, C.: An adaptive conservative ALE approach to deal with large boundary displacements in three-dimensional inviscid simulations. In: Proceedings of 2017 AIAA SciTech Forum, Grapevine, Texas (2017)
15. Re, B., Guardone, Dobrzynski, C.: Numerical simulation of shock-tube piston problems with adaptive, anisotropic meshes. In: Oñate, E., Papadrakakis, M., Schrefler, B. (eds.) Proceedings of Coupled Problems in Science and Engineering, Rhodes Island, Greece, vol. VII, pp. 1227–1238 (2017)
16. Vitale, S., Gori, G., Pini, M., Guardone, A., Economon, T.D., Palacios, E., Alonso, J.J., Colonna, P.: Extension of the SU2 open source CFD code to the simulation of turbulent flows of fluids modelled with complex thermophysical laws. In: Proceedings of 22nd AIAA Computational Fluid Dynamics Conference, Dallas, USA, pp. 1–22 (2015)

# Fluid-Structure Interaction, Morphing and Control

# Fabrication and Characterization of Folded Foils Supporting Streamwise Traveling Waves


**Sam Calisch, Neil Gershenfeld, Dixia Fan, G. Jodin, and Michael Triantafyllou**

**Abstract** A body of work has grown around the use of small amplitude traveling waves on aerodynamic and hydrodynamic surfaces for boundary layer control. In particular, when the traveling wave speed exceeds the free stream velocity, significant drag reductions have been shown in simulation. Building viable prototypes to test these hypotheses, however, has proven challenging. In this paper, we describe a candidate system for constructing structural airfoils and hydrofoils with embedded electromagnetic actuators for driving high velocity traveling waves. Our approach relies on the fabrication of planar substrates which are populated with electromagnetic components and then folded into a prescribed three dimensional structure with actuators embedded. We first specify performance characteristics based on hydrodynamic requirements. We then describe the fabrication of fiber-reinforced polymer composite substrates with prescribed folding patterns to dictate three dimensional shape. We detail the development of a miniaturized single-phase linear motor which is compatible with this approach. Finally, we compare the predicted and measured force produced by these linear motors and plot trajectories for a 200 Hz driving frequency.

**Keywords** Traveling waves · Separation control · Distributed actuation · Origami

## 1 Introduction

Both computational and experimental work has grown around the use of small amplitude traveling waves on aerodynamic or hydrodynamic surfaces for boundary layer control and drag reduction. This work has demonstrated significant drag reductions

S. Calisch (✉) · N. Gershenfeld
Center for Bits and Atoms, Massachusetts Institute of Technology, Cambridge, MA, USA
e-mail: sam.calisch@cba.mit.edu

D. Fan · G. Jodin · M. Triantafyllou
Department of Ocean Engineering, Massachusetts Institute of Technology, Cambridge, MA, USA

G. Jodin
LAPLACE and IMFT , Université de Toulouse, CNRS, Toulouse, France



M. Braza et al. (eds.), *Advances in Critical Flow Dynamics Involving Moving/Deformable Structures with Design Applications*, Notes on Numerical Fluid Mechanics and Multidisciplinary Design 147,
https://doi.org/10.1007/978-3-030-55594-8_33

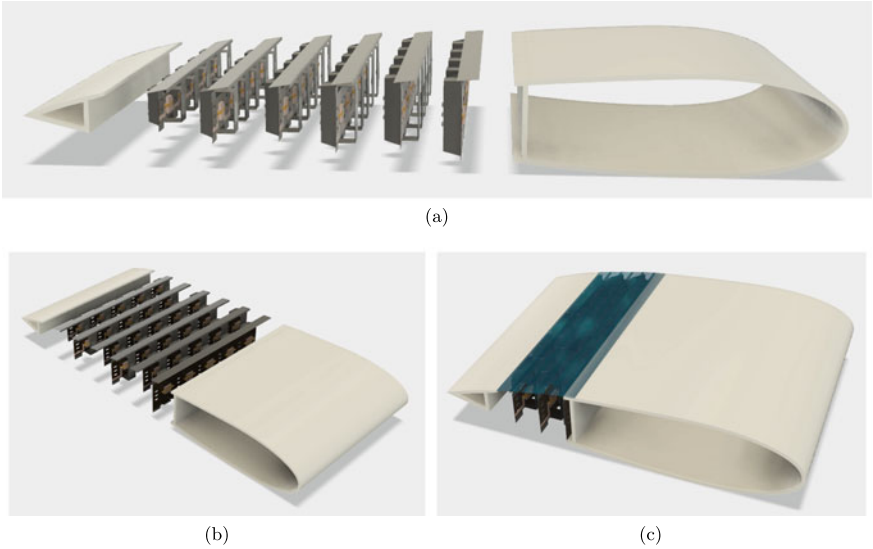


**Fig. 1** Traveling wave elements included near the 3/4 chord position of a foil. **a** Exploded side view, **b** exploded perspective view, **c** assembled perspective view

over a wide range of Reynolds numbers so long as the wave speed moderately exceeds the free stream speed [1–6]. In these cases, the energy required to drive the traveling waves can be made to be significantly less than the energy savings from drag reduction. Despite these results, fabricating viable high-speed traveling waves on aerodynamic surfaces remains a great challenge. This work investigates performance of structural systems with distributed aerodynamic actuation made using origami-inspired methods of cutting and folding fiber-reinforced composites. Such systems could be designed as airfoil sections, ship hulls, vehicle fairings, or automobile panels, potentially providing drag reduction and energy savings for these applications.

Origami-inspired fabrication methods have enjoyed considerable success in micro-robotics, where the scale of actuators and assemblies prevents manual assembly [7]. These techniques leverage CNC fabrication and lamination techniques similar to those used in printed circuit board manufacturing. Typically a sequence of cutting, consolidation, and curing steps is used to produce a laminate with fiber-reinforced members joined by flexible hinge elements with integrated actuation and electrical interconnect. Micro-robots produced this way have been shown operable at hundreds of hertz [8], and capable of using a variety of actuation (e.g. piezoelectric [9], dielectric elastomer [10], electromagnetic [11], shape memory alloy [12], and fluidic [13]) and sensing [14–18] technologies. Further, the folding mechanisms specified by hinge patterns not only create effective transmissions for motion [19] and be made self-folding [20], but also can be used to simplify delicate three dimensional assembly tasks [21–23] to repeatably produce robots with minimal manual assembly.

Origami-inspired methods have also been used at a larger scale to create high-performance structural materials. Honeycombs like those used in lightweight sandwich panels can be directly produced with a specified three-dimensional shape by simply specifying a pattern of two-dimensional cuts and folds [24, 25], thus avoiding costly and imprecise machining of honeycombs. This construction has shown potential for scalable production [26, 27], and related constructions have already been demonstrated at commercial scales [28–31]. Further, folding mechanics can be used to tailor material properties [32–35] over a range of mechanical performance.

This work seeks to leverage these two bodies of work to address the challenge of constructing high-performance structural systems with distributed actuation of traveling surface waves. In what follows, we first characterize the desired performance of a distributed actuation system based on hydrodynamic arguments. We then detail our construction approach, starting with the fabrication of a fiber-reinforced substrate with prescribed hinge lines. We then describe the development of an electromagnetic linear motor which functions when its components are populated onto the substrate, and outline assembly steps for a complete system prototype. Finally, we compare measured forces with simulation and verify high frequency operation.

## 2 Fluid Mechanical Actuation Specifications

We begin by developing a set of specifications for a distributed actuation system for driving traveling waves on a hydrodynamic surface. For the characteristics of a desired wave shape, we reference the study of Shen et al. [2] for Reynolds number $Re = U\lambda/\nu \approx 10^4$. We use three parameters to specify the wave shape: the amplitude $a$, the wavelength $\lambda$ and the wall motion phase speed $c$. The actuation frequency $f$ of the actuators is derived as $f = c/\lambda$.

The literature uses the wave number ($k = 2\pi/\lambda$) times the amplitude to specify the wave steepness. Studies suggest values of $ka$ of the order of 0.2 are appropriate. The wave speed is similarly prescribed by the dimensionless ratio $c/U$, where $U$ is the free stream flow velocity. When this ratio is made greater than 1, separation is eliminated and the wall waves generate a thrust. At $c/U \approx 1.2$, energy optimality has been observed, as the power required to actuate the wall plus the power saved due to drag reduction is minimal. The choice of the wavelength is a tradeoff between actuator manufacturing constraints and fluid mechanic considerations.

To satisfy values from the literature and be within the constraints of a feasible actuator to design, we select an amplitude $a = 1$ mm, a wavelength $\lambda = 20$ mm, and frequency $f = 60$ Hz. This gives a wave steepness of 0.314 and allocates four actuators per wavelength if each requires 5 mm of chordwise extent. With a freestream velocity $U \approx 1$ m/s and a chord of 0.15 m, this gives $c/U \approx 1.2$ and chordwise $Re \approx 7.5 \times 10^4$.

To estimate the force requirements, we consider only force normal to the wall and assume a worst case estimate of actuating the suction side with maximal acceleration under the maximum pressure and inertial forces. Assuming a hexagonal packing of

actuators with half-cell-span of 5 mm as above, each actuator is responsible for a surface patch of area $A = 100\,\text{mm}^2$. Numerical simulation provides a pressure coefficient of 0.06, leading to 30 Pa pressure. A typical hydrodynamic pressure is around 500 Pa. The total force produced by these pressures is around 53 mN.

To calculate the inertial forces, we must consider the actuator inertia and the fluid added mass. In general, the added mass in such a case of connected moving walls is not constant. In the case where the region under consideration has a small chordwise extent relative to $\lambda$, the force due to added mass can be written as $F = \rho a k A (c - U)^2$. For the parameters identified above, this added mass force is on the order of 1 mN (but increases greatly at larger values of $c/U$). Assuming a moving mass of 100 mg, the total required inertial force to operate at 60 Hz is roughly 15 mN. This gives a total force requirement of roughly 70 mN.

## 3 Construction

In this section we detail the design and fabrication of our candidate structural system with distributed actuation for traveling surface waves. We first show a method of producing stiff, fiber-reinforced composites with prescribed compliant hinge lines. We then describe a miniaturized, single-phase linear motor, suitable for embedding in a structure to produce traveling waves. Finally, we detail assembly steps of this construction, showing how folding allows much of the work to be done in a flat state, making the process more repeatable and amenable to automation.

### *3.1 Composite Construction*

To fabricate fiber-reinforced composites with prescribed hinge lines, we use a method similar to one commonly used in microrobotics (c.f. [7]) where sheets of resin-impregnated carbon fiber are cut and then bonded to a polymer layer (often Kapton or PET). In regions where the fiber reinforcements have been removed, only the polymer layer remains, forming a compliant, robust hinge. Hinge cycle lifetimes approaching $10^7$ have been shown in microrobotics applications with significant angular deflection, and an exponential relationship between hinge bending length and cycle life has been identified [36]. At larger scales where hinge lengths can be greater and angular deflections can be smaller, significantly increased lifetimes are expected and indefinite operation may be attained by staying below the material fatigue limit.

Our fabrication process is shown in Fig. 2. In Fig. 2a, a stack of resin-impregnated carbon fiber layers is cut with an oscillating knife on a flatbed cutting machine. The stack consists of three layers of unidirectional carbon with a 0-90-0 layup schedule. This cutting step removes hinge lines with a width of approximately 400 $\mu$m. Next in Fig. 2b, the carbon layer is placed between two sheets of 12 $\mu$m PET film and

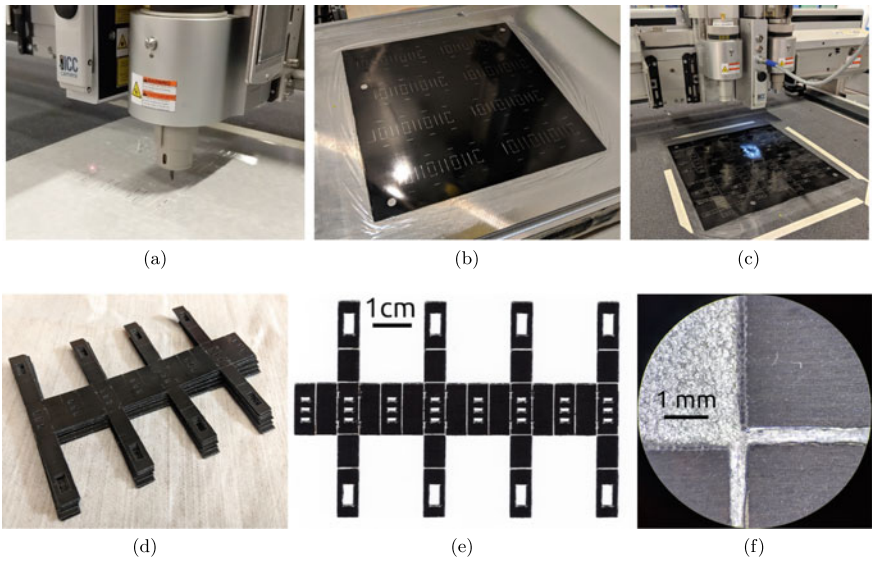


**Fig. 2** Fabrication of fiber-reinforced polymer composite laminates. **a** Cutting resin-impregnated carbon fiber using oscillating knife to form hinges, **b** curing resin-impregnated carbon fiber between two sheets of 12 micron PET film, **c** optically registering and cutting cured laminate using oscillating knife, **d** Batch of fiber-reinforced parts produced, **e** optical scan of part, showing clear hinges void of fiber reinforcement, **f** microscope image of two incident hinge lines

cured under a vacuum bag at 200 °C for two hours. In Fig. 2c, this cured laminate is optically registered on the flatbed cutting machine and cut again using an oscillating knife to form registration features and an outline. The composite strips produced in one cycle are shown in Fig. 2d. A scan of a single strip is shown in Fig. 2e and a microscope image of two hinge lines is shown in Fig. 2f. For this prototype, the finished thickness of carbon fiber layers was roughly 150 μm, while the combined PET hinge layer thickness was 25 μm.

In microrobotics applications, the polymer layer is usually sandwiched between two layers of fiber reinforcement to minimize its required bending radius. In larger scale applications with wider hinges, a single layer of fiber reinforcement can be sandwiched by two polymer layers. The wider hinge maintains safe polymer bending radii, and placing the continuous polymer layers outside of the fiber reinforcement layer makes the resulting structure more robust to delamination. As resin-impregnated carbon fiber sheets are usually available in substantially thicker dimensions than polymers like PET, this layer inversion allows for thinner resulting laminates. Finally, when a polymer is sandwiched by two fiber layers that have been precisely machined, alignment of these layers is tantamount. With a single machined fiber layer, no alignment is necessary, simplifying the fabrication process.

When assembled, the strip produced in Fig. 2 will form one layer of a hexagonal-celled honeycomb with integrated actuators and flexure bearings (one of the units

pictured in Fig. 1a). The physical example produced here has a uniform size, and so the resulting honeycomb will have a constant thickness. To produce honeycombs filling a desired shape, however, we can apply the geometric derivations of [26] or [25] to contour a given shape such as the foil shape shown in Fig. 1.

### 3.2 *Linear Motors*

To actuate the traveling waves, we now describe the design of a small, single phase linear motor ideal for embedding in folded structures. Linear motors often use three phases to extend actuation forces to large strokes, but because the required amplitudes for this application are only on the order of one millimeter, we use a single phase to simplify driving and wiring requirements and miniaturize the size of the actuator. As a large number of these actuators are required, we selected an "E" core shape which can be wound simply and fits inside a hexagonal honeycomb cell efficiently. Further, this core design can be parameterized easily to include any number $N > 2$ of electrical poles, where the force produced scales linearly with the number of poles (assuming the number of magnetic poles is always $N - 1$).

In Fig. 3, we show the fabrication of these linear motors. First, in Fig. 3a, core shapes are cut from round stock of Vimvar, a relatively inexpensive electrical iron

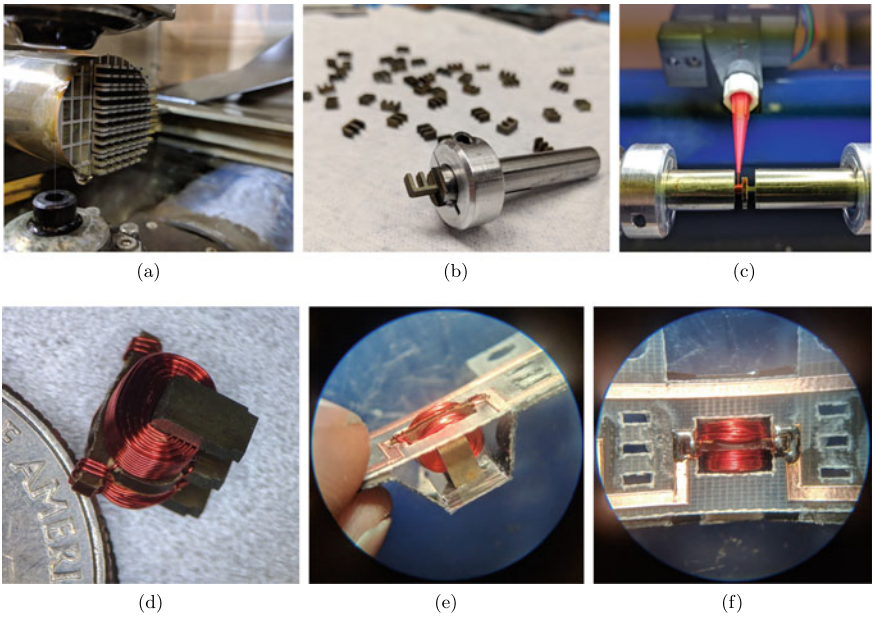


**Fig. 3** **a** Electric discharge machining cores from round Vimvar stock, **b** released cores with winding clamp, **c** core during winding, **d** wound core with terminations (U.S. Quarter coin for scale), **e** wound core placed in honeycomb scaffolding, **f** wound core soldered for electrical connection

with high permeability ($\mu_r \approx 10{,}000$), high saturation induction ($B_s \approx 2.1T$). Two wire cuts are make at 90 degrees from each other, enabling three dimensional features and producing many cores in a single machining operation. In Fig. 3b, the produced magnetic cores are parted off and prepared for winding with 34 AWG magnet wire. A custom-built precision coil winder head is used to lay two opposing coils of 90 wraps each. The coil winder uses a Luer-Lok dispensing tip for accurate magnet wire placement and high packing density, shown in Fig. 3c. The coil winding head allows the coils to be placed automatically, requiring operator intervention only when starting or finishing a coil. This significantly decreases the time required to wind a core and reduces error and inconsistencies in the actuator construction. The coils are heat-set using a hot air gun and the wire ends are terminated and wrapped around a central winding guide made of paper phenolic, shown in Fig. 3d. These terminations can be tinned with a standard soldering iron and connected with the copper traces used in our construction, shown in Figs. 3e, f.

These wound cores constitute the stator of our linear motor. The rotor consists of two Neodymium permanent magnets (N50, 3 mm × 3 mm × 0.5 mm) magnetized through thickness and oriented with opposite polarity. A wedge of Vimvar acts as a backiron flux return for this magnet pair. When the phase is energized with current, magnetic flux is directed alternately in and out of the legs of the magnetic core. This produces a force on the rotor that seeks to align the field of produced by the permanent magnets with that of the magnetic core. By alternating the direction of current periodically, the rotor can be made to oscillate at the driving frequency.

### *3.3 Assembly*

To create a functional unit, fiber-reinforced composite substrates and the magnetic components of the linear motor are combined in a set of assembly steps, shown in Fig. 4. In Fig. 4a, the wound magnetic cores, magnets, and back-iron components are populated on the composite substrate while in the flat state. This step is currently performed manually, but can be automated in much the same manner as industrial PCB manufacturing for high production rates.

In Fig. 4b, a wiring strip is attached using the magnetic cores for alignment, constraining the corrugation hinges and supplying soldered electrical connection to the motors. The wiring strips are produced using a simplified flex-PCB manufacturing process, where adhesive-backed copper foil is kiss-cut and transferred to 125 μm Garolite G10. The copper traces are optically registered, and additional features and an outline are cut. Again, while soldering was performed manually, this is amenable to reflow or wave soldering such as is used in industrial PCB manufacturing. At this stage, a skin strip is attached with cyanoacrylate glue, using magnet edges for registration. This skin strips are made with the same fiber-reinforced composite process described above, but with a overall thickness of roughly 100 μm.

In Fig. 4c, the magnets and back-iron components are brought together with the aid of attractive forces, assembling the flexure bearings for the linear motors. This

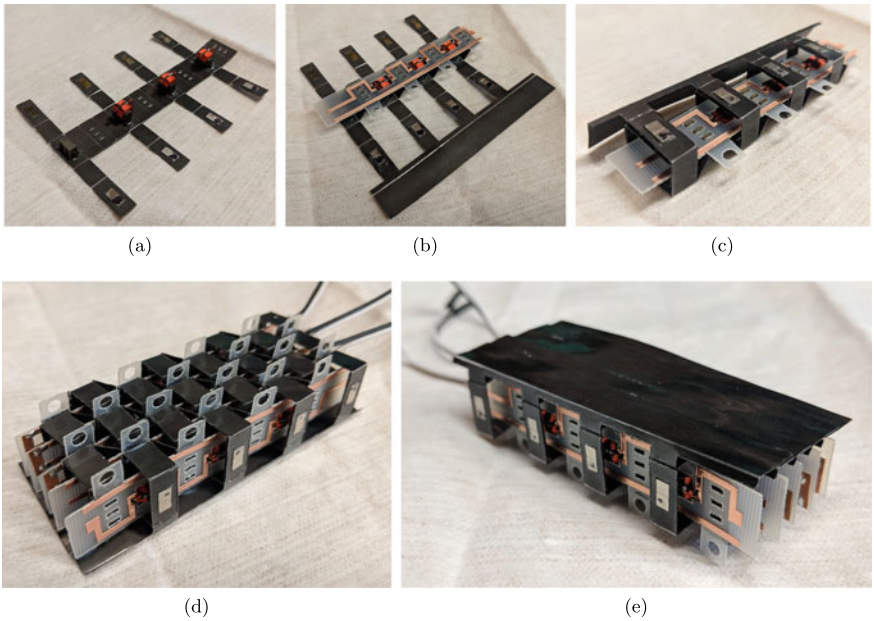


**Fig. 4** Assembly steps. **a** Populate wound cores, magnets, and back-iron components, **b** apply electrical routing and skin strips to constrain corrugation hinge angles, **c** bring magnets and back-iron components together to complete flexure bearing, **d** multiple row units are stacked, **e** skin strips lap and are joined into a continuous aerodynamic skin

connection is strengthened with cyanoacrylate glue, completing the assembly of a full strip unit. Multiple units can be assembled to create a honeycomb with embedded linear actuators. The stator of one unit align with the rotor of an adjacent unit, loading the flexure bearings in tension and setting a consistent air gap (roughly 800 $\mu$m in the prototype shown in Fig. 4). The skin strips of each row overlaps slightly with that of the adjacent row. These skins are bonded and covered with adhesive-backed PET (50 $\mu$m thickness) to create a smooth hydrodynamic surface.

## 4 Characterization

This section describes characterization work to ensure the produced force and frequencies meet the requirements of a hydrodynamic traveling wave application.

### *4.1 Force*

To evaluate force produced by the linear motors, we compare finite element simulation and experimental testing. The simulations were performed using COMSOL Multiphysics [37]. Figure 5 shows one simulation, with flux intensity and direction drawn for a linear motor in minimum (5a) and maximum (5b) configurations of the stroke when the phase current is one ampere. In Fig. 5a, the field of the permanent magnets opposes the field produced by the coils, and flux seeks alternate paths than the iron core. In Fig. 5b, the two flux distributions are aligned, providing a low reluctance magnetic circuit through the core. To simulate these effects, we assumed a planar flux distribution and ran a two-dimensional simulation, significantly lowering the computational burden. While the flux distributions are largely planar, this neglects fringing fields. Thus we expect simulations to slightly overestimate force produced but roughly preserve dependence on geometric parameters.

We simulated flux distributions and resulting force on the rotor for a range of coil currents, stroke positions, and core geometries. These studies indicated the size of the back-iron was significant in increasing actuator force but also in the moving mass. For these reasons, we designed the triangular back-iron shown in Fig. 5, which limits magnetic saturation while avoiding unnecessary moving mass.

To compare simulated values with our physical prototypes, we measured force using a materials characterization machine (Instron 4411) with 5 N load cell, shown in Fig. 6. We used linear slides to precisely position the rotor and stator and transmitted force to the load cell using a Garolite flexure to avoid off-axis loads.

Figure 7 plots force vs. stroke and current for simulated and measured actuators with an 800 μm air gap. Deviations from a planar flux distribution are responsible for roughly 20% reduction in peak force at 1 ampere phase current. We note that 800 μm is a conservative air gap, selected because smaller air gaps deformed rotor flexure under attractive forces. With a stiffer rotor, smaller air gaps could increase force

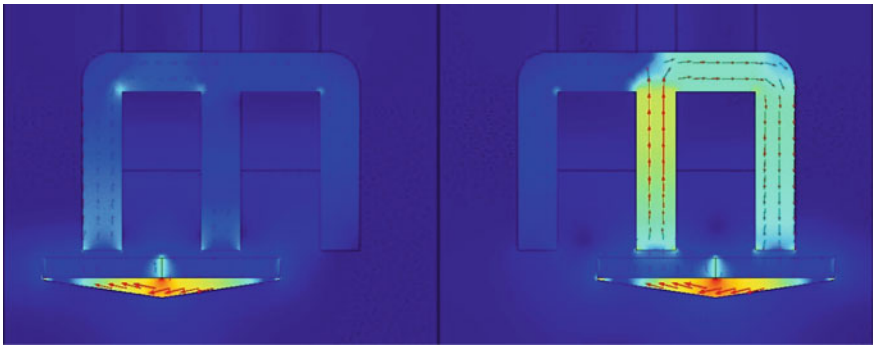


**Fig. 5** Simulated flux intensity (colormap) and direction (arrows) under positive current of 1 amp. **a** A negative most stroke limit, **b** at positive most stroke limit

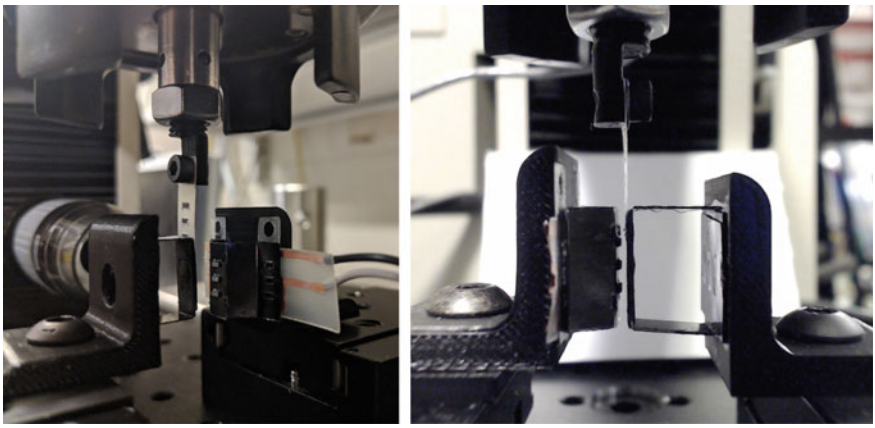

(a) (b)

**Fig. 6** Test setup for force measurement on material characterization machine. **a** Perspective view, showing 5N load cell, flexure for transmitting force, linear stages, and power wiring. **b** Side view, showing prescribed gap between magnetic core and magnets

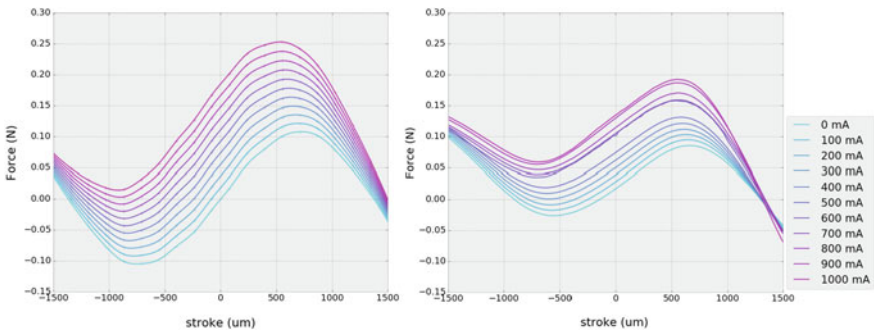


(a) (b)

**Fig. 7** **a** Two-dimensional simulation and **b** measured force with 800 μm air gap

without significantly increasing moving mass. Despite this, the force magnitudes comfortably exceed the fluid mechanical requirements derived in Sect. 2.

## *4.2 Frequency*

To characterize the high frequency operation of our actuators, we performed simple trials with square wave drive inputs of varying frequency using a single actuator with no skin attached. In a fully assembled honeycomb, the rotor travel is limited by the

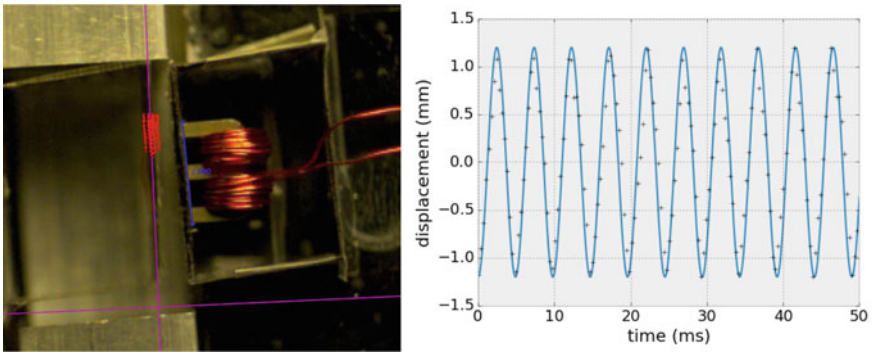


**Fig. 8** 200 Hz operation: **a** video with motion tracking, **b** Extracted trajectory

adjacent strip units, but to test variable travel limits, we implemented physical end stops using aluminum bars in these high frequency trials.

Figure 8 shows the results of sending a 200 Hz driving frequency to the actuator with a current limit of approximately 1 ampere. The resulting trajectory was recorded using a high speed video camera (Krontech Chronos 1.4) at 3000 frames per second. We used video tracking software (Physlets Tracker) to extract the trajectory and plot it in Fig. 8b. This simple test shows that our actuator is capable of driving its rotor at 200 Hz with an amplitude of approximately 1.2 mm.

## 5 Conclusions

We detailed a candidate system for fabricating foils with driven traveling surface waves. Studies suggest that traveling waves can eliminate separation and significantly reduce drag if wave speed moderately exceeds free stream speed, but building physical prototypes meeting these requirements has proven difficult. The origami-inspired manufacturing techniques described above produce structures with embedded actuation, motion guides, wiring, and structural support that may realize this engineering challenge.

In this work, we first estimated wave parameters based on hydrodynamics and developed a specification for force, frequency, and size required of an actuator system. We described a generalizable method for producing fiber-reinforced panels with prescribed hinge lines, which when populated with electromagnetic components produce shaped volumes with embedded actuators for driving surface waves. We then simulated and measured performance of our actuation system in force and frequency. In both metrics, performance showed a safe margin over stated requirements.

With these encouraging preliminary results, there is considerable future work that can improve this distributed actuation system. First, the performance testing

described above was carried out on the level of a single actuator without the contribution of bending stiffness of a skin and the interactions between adjacent actuator rows. Using fiber alignment and hinge placement, the skin strips in this work were designed to have much lower bending stiffness in the chordwise direction than in the spanwise direction. This minimizes the actuator work required to overcome bending stiffness, but this must be tested. Future work must also address the necessary compliance in mounting skin panels to accommodate the chordwise geometric effects of the wave amplitude without causing binding of the rotor flexure bearings.

It is expected that future work could considerably improve actuator performance. As mentioned, the air gap used in measurements was conservative due to deformation of the rotor under smaller air gaps. By stiffening the rotor, smaller gaps can be used, increasing generated force without significantly increasing moving mass. Further, the drive signals used were simple current-controlled voltage square waves. Better control would use the actuator transfer function to increase average force generated while maintaining safe thermal dissipation (the effective limit on driving current).

Finally, an obvious next step is to experimentally verify that the hydrodynamic performance characteristics can be realized and test hypotheses about traveling waves. If successful, the macroscopic drag reduction effects of traveling waves could be measured with a load cell, while the elimination of separation and wave-scale pheonoma could be visualized using PIV or other flow visualization techniques. This exciting work is currently an active research effort.

**Acknowledgements** Sam Calisch and Neil Gershenfeld are supported by the MIT Center for Bits and Atoms research consortia. Gurvan Jodin's contributions are carried out within the Smart Morphing and Sensing project and the EU's H2020 program for research, technological development and demonstration under grant agreement No. 723402. Michael Triantafyllou and Dixia Fan are supported by the MIT Sea Grant program.

## References

1. Chen, W., Liu, Y., Xu, F., Li, H., Hu, H.: Suppression of Vortex Shedding from a Circular Cylinder by using a Traveling Wave Wall. American Institute of Aeronautics and Astronautics, 15 Jan 2018 (2014)
2. Shen, L., Zhang, X., Yue, D.K.P., Triantafyllou., M.S.: Turbulent flow over a flexible wall undergoing a streamwise travelling wave motion. J. Fluid Mech., **484**, 197–221 (2003)
3. Triantafyllou, M.S., Hover, F.S., Techet, A.H., Yue, D.K.: Review of hydrodynamic scaling laws in aquatic locomotion and fishlike swimming. Appl. Mech. Rev. **58**(4), 226–237 (2005)
4. Wu, C.-J., Liang, W., Wu, J.-Z.: Suppression of the von kármán vortex street behind a circular cylinder by a travelling wave generated by a flexible surface. J. Fluid Mech. **574**, 365–391 (2007)
5. Xu, Feng, Chen, W.-L., Bai, W.-F., Xiao, Y.-Q., Ou, J.-P.: Flow control of the wake vortex street of a circular cylinder by using a traveling wave wall at low Reynolds number. Comput. Fluids **145**, 52–67 (2017)
6. Yao, Y., Lu, C.J., Si, T., Zhu, K.: Experimental investigation on the drag reduction characteristics of traveling wavy wall at high Reynolds number in wind tunnel. J. Hydrodyn. Ser. B, **22**(5), 719–724 (2010)

7. Wood, R.J., Avadhanula, S., Sahai, R., Steltz, E., Fearing, R.S.: Microrobot design using fiber reinforced composites. J. Mech. Des. **130**(5), 052304 (2008)
8. Ma, K.Y., Chirarattananon, P., Fuller, S.B., Wood, R.J.: Controlled flight of a biologically inspired, insect-scale robot. Science **340**(6132), 603–607 (2013)
9. Jafferis, N.T., Lok, M., Winey, N., Wei, G.-Y., Wood, R.J.: Multilayer laminated piezoelectric bending actuators: design and manufacturing for optimum power density and efficiency. Smart Mater. Struct., **25**(5), 055033 (2016)
10. Duduta, M., Clarke, D.R., Wood, R.J.: A high speed soft robot based on dielectric elastomer actuators. In: 2017 IEEE International Conference on Robotics and Automation (ICRA), pp. 4346–4351. IEEE (2017)
11. Goldberg, B., Karpelson, M., Ozcan, O., Wood, R.J.: Planar fabrication of a mesoscale voice coil actuator. In: 2014 IEEE International Conference on Robotics and Automation (ICRA), pp. 6319–6325. IEEE (2014)
12. Felton, S.M., Becker, K.P., Aukes, D.M., Wood, R.J.: Self-folding with shape memory composites at the millimeter scale. J. Micromech. Microeng. **25**(8), 085004 (2015)
13. Li, S., Vogt, D.M., Rus, D., Wood, R.J.: Fluid-driven origami-inspired artificial muscles. In: Proc. Natl. Acad. Sci. 13450 (2017)
14. Araromi, O.A., Walsh, C.J., Wood, R.J.: Hybrid carbon fiber-textile compliant force sensors for high-load sensing in soft exosuits. In: 2017 IEEE/RSJ International Conference on Intelligent Robots and Systems (IROS), pp. 1798–1803. IEEE (2017)
15. Brühwiler, R., Goldberg, B., Doshi, N., Ozcan, O., Jafferis, N., Karpelson, M., Wood, R.J.: Feedback control of a legged microrobot with on-board sensing. In: 2015 IEEE/RSJ International Conference on Intelligent Robots and Systems (IROS), pp. 5727–5733. IEEE (2015)
16. Jayaram, K., Jafferis, N.T., Doshi, N., Goldberg, B., Wood, R.J.: Concomitant sensing and actuation for piezoelectric microrobots. Smart Mater. Struct. (2018)
17. Shin, B., Felton, S.M., Tolley, M.I., Wood, R.J.: Self-assembling sensors for printable machines. In:2014 IEEE International Conference on Robotics and Automation (ICRA), pp. 4417–4422. IEEE (2014)
18. Sun, X., Felton, S.M., Wood, R.J., Kim, S.: Printing angle sensors for foldable robots. In: 2015 IEEE/RSJ International Conference on Intelligent Robots and Systems (IROS), pp. 1725–1731. IEEE (2015)
19. McClintock, H., Temel, F.-Z., Doshi, N., Koh, J., Wood, R.J.: The millidelta: A high-bandwidth, high-precision, millimeter-scale delta robot. Sci. Robot. **3**(14), eaar3018 (2018)
20. Felton, S., Tolley, M., Demaine, E., Rus, D., Wood, R.: A method for building self-folding machines. Science **345**(6197), 644–646 (2014)
21. Ma, K.Y., Chirarattananon, P., Wood, R.J.: Design and fabrication of an insect-scale flying robot for control autonomy. In: 2015 IEEE/RSJ International Conference on Intelligent Robots and Systems (IROS), pp. 1558–1564. IEEE (2015)
22. Onal, C.D., Tolley, M.I., Wood, R.J., Rus, D:. Origami-inspired printed robots. IEEE/ASME Trans. mechatron. **20**(5), 2214–2221 (2015)
23. Onal, C.D., Wood, R.J., Rus, D.: Towards printable robotics: Origami-inspired planar fabrication of three-dimensional mechanisms. In: 2011 IEEE International Conference on Robotics and Automation (ICRA), pp. 4608–4613. IEEE (2011)
24. Nojima, T., Saito, K.: Development of newly designed ultra-light core structures. JSME Int. J. Ser. A Solid Mech. Mater. Eng. **49**(1), 38–42 (2006)
25. Saito, K., Pellegrino, S., Nojima, T.: Manufacture of arbitrary cross-section composite honeycomb cores based on origami techniques. J. Mech. Des. **136**(5), 051011 (2014)
26. Calisch, S., Gershenfeld, N.: Towards continuous production of shaped honeycombs. In: ASME 2018 Manufacturing Science and Engineering Conference. American Society of Mechanical Engineers (2018)
27. Wang, L., Saito, K., Gotou, Y., Okabe, Y.: Design and fabrication of aluminum honeycomb structures based on origami technology. J. Sandwich Struct. Mater. 1099636217714646 (2017)
28. Heimbs, S.: Foldcore sandwich structures and their impact behaviour: an overview. In: Dynamic Failure of Composite and Sandwich Structures, pp. 491–544. Springer (2013)

29. Pflug, J.: Coretinium®: a new tata steel material based on econcore's innovative thermhex technology. Reinforced Plast. **60**(2), 107–109 (2016)
30. Pflug, J., Vangrimde, B., Verpoest, I., Vandepitte, D., Britzke, M., Wagenführ, A.: Continuously produced paper honeycomb sandwich panels for furniture applications. In: 5th Global Wood and Natural Fibre Composites Symposium. Kassel, Germany, April, pp. 27–28 (2004)
31. Pflug, J., Vangrimde, B., Verpoest, I., Bratfisch, P., Vandepitte, D.: Honeycomb core materials: new concepts for continuous production of honeycomb core materials. Sampe J. **39**(6), 22–30 (2003)
32. Calisch, S., Gershenfeld, N.: Kirigami fabrication of shaped, flat-foldable cellular materials based on the tachi-miura polyhedron. In: 7OSME (2018) (In Review)
33. Eidini, M., Paulino, G.H.: Unraveling metamaterial properties in zigzag-base folded sheets. Sci. Adv. **1**(8) (2015)
34. Filipov, E.T., Tachi, T., Paulino, G.: Origami tubes assembled into stiff, yet reconfigurable structures and metamaterials. Proc. Natl. Acad. Sci. **112**(40), 12321–12326 (2015)
35. Neville, R.M., Scarpa, F., Pirrera, A.: Shape morphing Kirigami mechanical metamaterials. Sci. Rep. 6:31067 EP–08 (2016)
36. Malka, R., Desbiens, A.-L., Chen, Y., Wood, R.J.: Principles of microscale flexure hinge design for enhanced endurance. In: 2014 IEEE/RSJ International Conference on Intelligent Robots and Systems (IROS 2014), pp. 2879–2885. IEEE (2014)
37. COMSOL Inc.: Comsol Multiphysics Reference Manual, Version 5.3. www.comsol.com

# The Aerodynamic and Aeroacoustic Effect of Passive High Frequency Oscillating Trailing Edge Flaplets


**Edward Talboys, Thomas F. Geyer, and Christoph Brücker**

**Abstract** Aerofoil noise reduction is a topic of great interest at the present time and as such many strategies have been presented, in previous literatures whether they are trailing edge serrations, leading edge undulations or porous aerofoils, to name a few. The present study investigates a bio-inspired solution where an array of passive flexible elements, known as flaplets, are extended over the trailing edge of the aerofoil and are allowed to oscillate freely in the flow field. The aerofoil in used in the present study is a NACA 0012 and has been analysed by using both time resolved particle image velocimetry (TR-PIV), in a close circuit wind tunnel, and aeroacoustic measurements in an open jet wind tunnel at moderate chord based Reynolds numbers; ranging from 50,000 to 350,000. The results show a clear reduction in tonal noise with a clear region of maximum noise reduction scaled with $u_{\infty}^{1.5}$.

**Keywords** Noise reduction · Trailing edge flaplets · Shear layer instability

## 1 Introduction

The main source of aerodynamic tonal noise generated on aerofoils is due to the trailing edge turbulent boundary layer interaction. And as such this noise signature plays a crucial role in practically all aerodynamic applications; from small aircraft to wind turbines and ventilation systems. To mitigate this aeroacoustic interaction many possible approaches exist, among them are serrated edges, slitted trailing edges, brush-like edge extensions or porous materials. In the present study, a flexible trailing edge consisting of an array of small elastic flaplets, mimicking the tips of bird feathers, is used.

E. Talboys · C. Brücker (✉)
Mechanical Engineering and Aeronautics, City, University of London, London EC1V 0HB, UK
e-mail: christoph.bruecker@city.ac.uk

T. F. Geyer
Fachgebiet Technische Akustik, Brandenburgische Technische Universität, 03046 Cottbus, Germany



M. Braza et al. (eds.), *Advances in Critical Flow Dynamics Involving Moving/Deformable Structures with Design Applications*, Notes on Numerical Fluid Mechanics and Multidisciplinary Design 147,
https://doi.org/10.1007/978-3-030-55594-8_34

The specific arrangement and structure of feathers on the trailing edge of an owl's wing is well known to be one of the key mechanisms that the bird used to enhance noise suppression [10]. In addition, secondary feathers on the upper side of the wings of the steppe eagle (*Aquila nipalensis*) [4] and the peregrine falcon (*Falco peregrinus*) [17], to give a few examples, have been observed to pop-up as the birds attack prey or come into land at a high angle of attack. This phenomena has been the subject of many research studies. Schlüter [24] could show that by attaching rigid flaps, via a hinge, on the upper surface of the wing, the $C_L$ max is increased for a series of tested aerofoils (NACA 0012, NACA 4412, SD 8020). Schlüter also showed that the flaps bring the additional benefit of gradual stall rather than a more severe lift crisis. Osterberg and Albertani [15] carried out a similar study on a flat plate subjected to high angles of attack, coming to the same conclusion. Brücker and Weidner [3] used flexible flaplets attached on the suction side of a NACA 0020 aerofoil that was subjected to a ramp-up motion. The results show a considerable delay in dynamic stall. Flap length and flap chordwise spacing were varied and it was found that the most successful configuration was two rows of flaps of length 0.1c spaced 0.15c–0.2c in the chordwise direction. The wavelength of the rollers in the shear layer was found to be of the same order, 0.15c–0.2c. This led to the conclusion that the flaplets resulted in a lock-in effect with these rollers, as the two spacing length scales were comparable. Concluding that this lock-in effect stabilises the shear layer. Rosti et al. [20] then built on these findings of by carrying out a DNS (direct numerical simulation) parametric study. The flap element was rigid but coupled to the aerofoil surface by a torsional spring type coupling. It was found that when the flap oscillations were at the same frequency as the shear-layer roll up, the mean lift coefficient was at it's highest.

Similar effects, as observed for aerofoils, could also be seen on tests with bluff bodies. A series of studies on cylinder flows with flaplets attached on the aft half of the cylinder have been carried out [6, 12, 13]. Kunze and Brücker [13] saw that the presence of the flexible elements allowed the shedding frequency to be locked in with the most dominant eigen-frequency of the flaplets. This hints to a similar lock-in effect of the shear layer roll-up observed for the aerofoils [20]. Consequently the flow-structure in the wake is changed and a reduced wake deficit is observed. Kamps et al. [12] then tested the same cylinder/flaplet configuration in an aeroacoustic wind tunnel and could show that the flaplets overall reduce noise, both in the tonal and the broadband components.

The present study builds off these previous studies in order to study the benefit/impact of flexible flaplets being attached to the trailing edge rather than on the aerofoil body. Tests of such modifications of the trailing edge by Kamps et al. [11] already showed promising results in noise reduction. However, no details of the flow structure and the fluid-structure interaction is known which might explain the observed aeroacoustical modification.

## 2 Experimental Set-Up

The experiments are carried out in two stages, the velocity field was measured in the Handley Page laboratory at City, University of London in a closed loop wind tunnel. And the acoustics were measured in the aeroacoustic open jet wind tunnel [23] at the Brandenburg University of Technology in Cottbus. A NACA 0012 aerofoil, with chord of 0.2 m, was tested at both locations with and without the flaplets. The span of the aerofoil was different for each experiment due to wind tunnel configurations, however this is thought to have no bearing on the presented results. A 0.3 mm thick boundary layer trip was implemented at 0.2c on both sides of the aerofoil to ensure that the boundary layer was turbulent.

The flexible flaplets are made from a polyester foil (E = 3.12 GPa, $\rho = 1440\,\mathrm{kg/m^3}$), of thickness 180 μm, which was laser-cut at one long side to form an array of individual uniform flaplets. Each flaplets has a length of L = 20 mm, a width of s = 5 mm and an interspacing of d = 1 mm in spanwise direction (see Fig. 1b). The foil was adhered to the pressure side of the aerofoil using thin double sided tape such that the flaplets face downstream, with their free end located at a distance of x/c = 1.1c downstream of the trailing edge. The flaplets form a mechanical system whereby each flaplet is a rectangular cantilever beam which is free to oscillate perpendicular to the mean-flow direction. The oscillating frequency of the flaplets was experimentally found to be 107 Hz and have a maximum displacement of approximately 1 mm when subjected to the present flow conditions [26].

### *2.1 Velocity Field Measurements*

The test section of the wind tunnel used for the Time Resolved Particle Image Velocimetry (TR-PIV) is 0.81 m by 1.22 m in cross-section, and has a turbulence intensity of 0.8%. In this instance the aerofoil span is 0.52 m whereby one side of the aerofoil spanned to the floor of the tunnel and an endplate was affixed to the exposed end to negate any end effects. The aerofoil was 3D printed in two sections with a small perspex section in the measurement window, as per Fig. 1b. The use of perspex in this region improves the quality of the PIV recordings close to the surface. Two chord based Reynolds numbers ($Re_c$) were analysed in this study, 100,000 and 150,000, at two different angles of attack, 0° and 10°.

Time Resolved Particle Image Velocimetry (TR-PIV) measurements were carried out using a 2 mm thick double pulsed Nd:YLF laser sheet in a standard planar set-up. A high speed camera (Phantom Miro M310, window size 1280 × 800 pixels) equipped with a macro lens, Tokina 100 mm, with f/8 was used in frame straddling mode. Olive oil seeding particles, of approximate size 1 μm, were added to the flow downstream of the model. 500 pairs of images were obtained at a frequency of 1500 Hz with the pulse separation time being 80 μs for the $Re_c$ = 100,000 case and 30 μs for the $Re_c$ = 150,000 case.

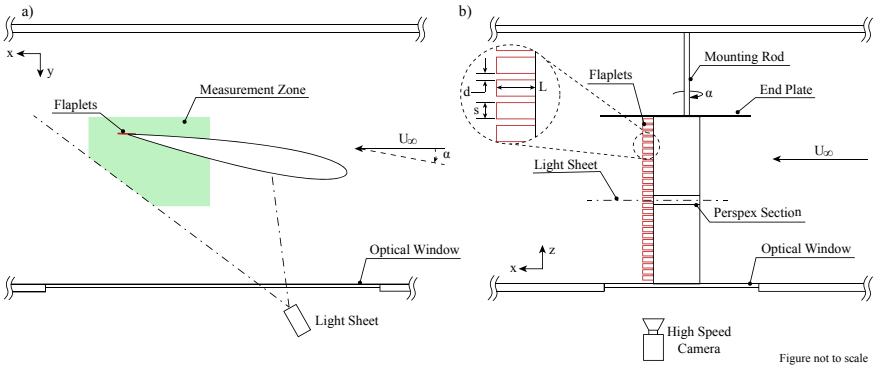


**Fig. 1** Schematic of the TR-PIV set-up. **a** Plan view, **b** side view

The raw images were then processed using the TSI Insight 4G software which uses the method of 2D cross correlation. The first pass interrogation window size was 32 × 32 pixels, with a 50% overlap. The size was then reduced to 16 × 16 pixels for the subsequent pass. A 3 × 3 median filter was then applied to validate the local vectors, any missing or spurious vectors were interpolated by using the local mean.

## *2.2 Acoustic Measurements and Data Processing*

The aeroacoustic measurements took place in the small aeroacoustic open jet wind tunnel [23] at the Brandenburg University of Technology in Cottbus, with a setup similar to that used in [7]. The wind tunnel was equipped with a circular nozzle with a contraction ratio of 16 and an exit diameter of 0.2 m. With this nozzle, the maximum flow speed is in the order of 90 m/s. At 50 m/s, the turbulence intensity in front of the nozzle is below 0.1%. During measurements, the wind tunnel test section is surrounded by a chamber with absorbing walls on three sides, which lead to a quasi anechoic environment for frequencies above 125 Hz.

For the measurements, the aerofoil is positioned at a distance of 0.05 m downstream from the nozzle. The tips of the aerofoil are attached to a wind tunnel balance to simultaneously measure the aerodynamic performance. Since the span of the aerofoil ($b$ = 0.28 m) exceeds the nozzle diameter, no aerodynamic noise is generated at the tips or the lateral mountings. A schematic of the setup is shown in Fig. 2.

The acoustic measurements were performed using a planar microphone array, consisting of 56 1/4th inch microphone capsules flush mounted into an aluminum plate with dimensions of 1.5 m × 1.5 m (see [21]). The microphone layout is included in Fig. 2. The aperture of the array is 1.3 m. The array was positioned out of the flow, in a distance of 0.71 m above the aerofoil.

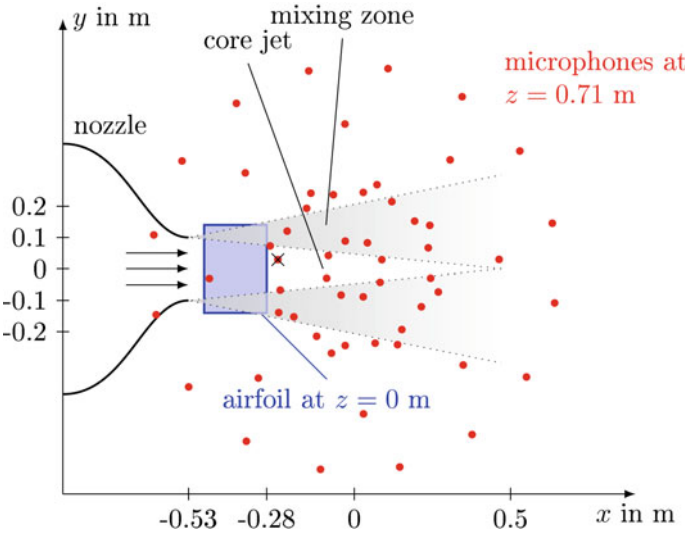


**Fig. 2** Schematic display of the measurement setup (top view, ×marks the location of the single microphone)

Data from the 56 microphones were recorded with a sampling frequency of 51.2 kHz and a duration of 60 s using a National Instruments 24 Bit multichannel measurement system. To account for the refraction of sound at the wind tunnel shear layer, a correction method was applied that is based on ray tracing [22]. In post processing, the time signals were transferred to the frequency domain using a Fast Fourier Transformation, which was done blockwise on Hanning-windowed blocks with a size of 16384 samples and 50% overlap. This lead to a small frequency spacing of only 3.125 Hz. The resulting microphone auto spectra and cross spectra were averaged to yield the cross spectral matrix. This matrix was further processed using the CLEAN-SC deconvolution beamforming algorithm [25], which was applied to a two-dimensional focus grid parallel to the array and aligned with the aerofoil. The grid has a streamwise extent of 0.5 m, a spanwise extent of 0.4 m and an increment of 0.005 m. The outcome of the beamforming algorithm is a two-dimensional map of noise source contributions from each grid point, a so-called sound map. In order to obtain spectra of the noise generated by the interaction of the turbulent boundary layer with the trailing edge of the aerofoil, a sector was defined that only contains the noise source of interest. The chosen sector has a chordwise extent of 0.2 m and a spanwise extent of 0.1 m. Thus, spectra of the noise generated by this mechanism are derived by integrating all noise contributions from within this sector, while all potential background noise sources (such as the wind tunnel nozzle or the aerofoil leading edge) are excluded from the integration. The resulting sound pressures were then converted to sound pressure levels $L_p$ $re$ 20 µPa and 6 dB were subtracted to account for the reflection at the rigid microphone array plate.

In addition to the beamforming results, auto spectra of a single array microphone close to the aerofoil trailing edge were analysed. The microphone position is highlighted in Fig. 2.

## 3 Results and Discussion

### *3.1 Velocity Field Measurements*

A virtual velocity probe was placed in the measured velocity field at a suitable location (x/c = 0.85 and y/c = 0.05) in the boundary layer to detect instabilities. This is done by means of evaluating the fluctuating vertical component ($v'$) time-series at the probe location. A peak in the $v'$ velocity corresponds to the presence of a shear layer roll-up vortex passing through the probe area as revealed by the TR-PIV results. Therefore the time history of this probe is investigated using spectral analysis in order to see the nature of the shear-layer rollers and better evaluate the effect of the flaplets.

A proper orthogonal decomposition (POD) of the fluctuating velocity field was carried out and this aids to the understanding of the spectral results as each POD mode is associated with a dominant flow feature. In the present case the dominant features are the shear layer vortices.

It is well understood that the eigenvectors of each POD mode gives the temporal signature of the mode. Therefore performing a spectral analysis on the eigenvectors yields the frequency of structure observed in the mode. From the spectral analysis of the 4th$v'$ mode, Fig. 3b, it is seen that this mode corresponds to the fundamental shear layer instability mode. In comparison, the 2nd mode, Fig. 3a, shows half of the fundamental frequency ($f_{0-1/2}$). This mode indicates the presence of a non-

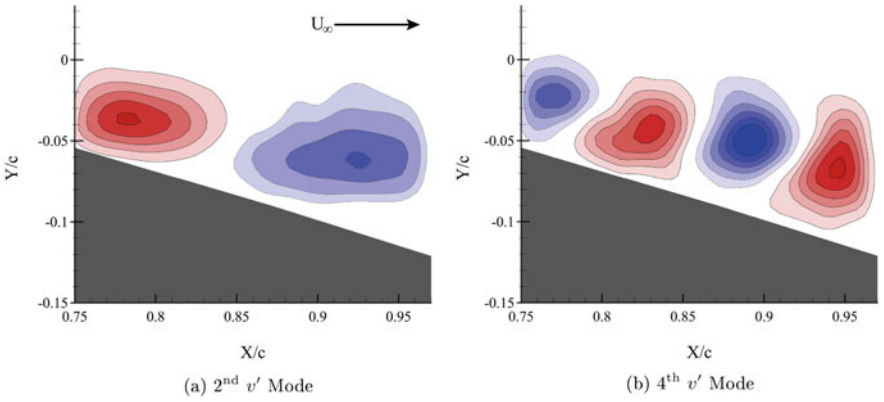


**Fig. 3** Spatial reconstruction of the $v'$ velocity POD modes at $Re_c$ = 150,000 and $\alpha = 10°$

linear state in the shear-layer which is the observed pairing of successive rollers, explaining the factor two change that can be clearly seen in Fig. 3. POD also gives a graphical representation of the dominant structures and as such the wavelength of the fundamental shear-layer mode can be estimated.

When analysing the velocity probe data for the zero degree cases, it was seen that no obvious spectral peaks were present. The shear layer at these conditions is expected to be in the sub-critical state as the adverse pressure gradient is weaker compared to the 10° angle of attack situation [9].

Table 1, shows the compiled results of Fig. 4 and the results of the $Re_c$ = 100,000 cases. The theoretical case is from the empirical equation proposed by [27] for a NACA 0012 at 10° angle of attack. Further agreement is found with experimental trends from Huang and Lin [9] who graphically present a frequency of ∼100 Hz - 200 Hz, for the tabulated cases.

When observing the $Re_c$ = 150,000; $\alpha$ = 10°; baseline spectra result from the velocity probe, Figure 4a, it is seen that the strongest peak is at $\sim f_{0-1/2}$ position. This is indicating that the non-linear state is already dominating with rows of large, merged vortices present in the flow. These vortices will carry an increased lower tonal noise signature. This merging effect has been seen in many previous planar shear flow literatures [8, 19]. It must be noted here that this dominant frequency is not truly half, and is thought to be because the position of the transition point of the instability is randomly fluctuating in the shear layer; hence giving a more 'broadband' region where this frequency is seen [5, 18, 19, 28]. Once the flaplets are attached to the aerofoil, Fig. 4b, the $f_{0-1/2}$ frequency is suppressed and the $f_0$ is now the dominant frequency. This indicates that the shear-layer is stabilised and the growth of non-linear modes is reduced, thus reducing the tendency of vortex pairing. This stabilisation is thought to be caused by a lock-on effect between the oscillating flaplets and the fundamental shear-layer instability, a similar effect to that presented by Kunze and Brücker [13].

**Table 1** Shear layer fundamental and non-linear instability frequencies detected by the PIV probe and POD modes from Fig. 4, with a theoretical result from Tam [27] for comparison

| Test cases | PIV Probe | | POD | |
|---|---|---|---|---|
| | $f_0$ (Hz) | $f_{0-1/2}$ (Hz) | $f_0$ (Hz) | $f_{0-1/2}$ (Hz) |
| $Re_c$ = 100,000; $\alpha$ = 10°; Baseline | 150 | — | 150 Hz | — |
| $Re_c$ = 100,000; $\alpha$ = 10°; Flaplets | 132 | — | 132 | — |
| Theory | 160 Hz | — | — | — |
| $Re_c$ = 150,000; $\alpha$ = 10°; Baseline | 234 | 156 | 234 | 144 |
| $Re_c$ = 150,000; $\alpha$ = 10°; Flaplets | 246 | 114 | 246 | 114 |
| Theory | 221 Hz | — | — | — |

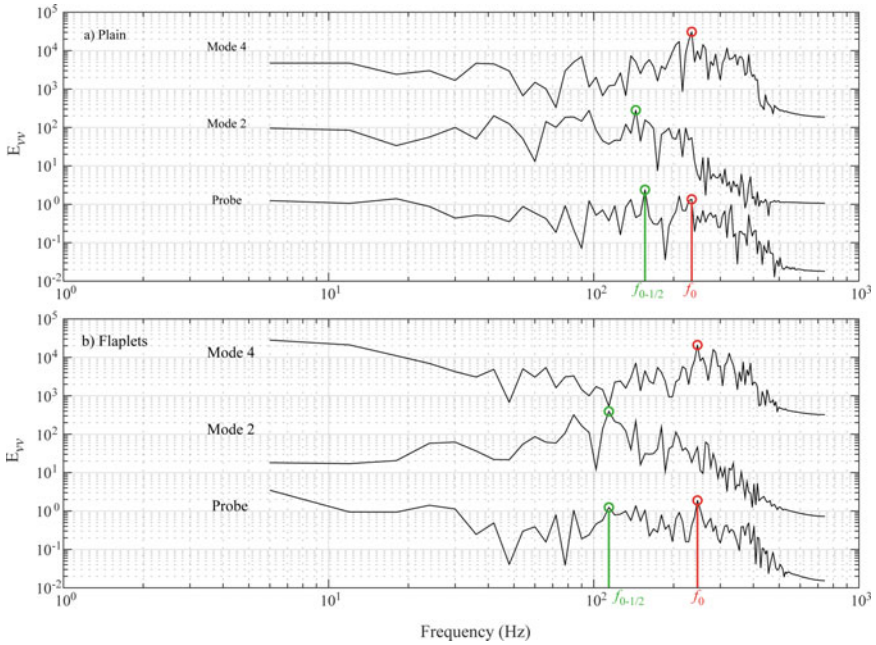


**Fig. 4** Spectral analysis of the $v'$ (probe), 4th $v'$ POD mode and 2nd $v'$ POD mode for the case at $Re_c$ = 150,000 and $\alpha$ = 10°. Each spectra is spaced by two decades for clarity

For the lowest Reynolds Number case, there was no dominating shear layer instabilities/pairing observed in the spectral analysis. And as such the flaplets had no observable effect on the flow field.

## *3.2 Aeroacoustics*

Due to the less intensive data processing of aeroacoustic measurements, when compared to TR-PIV, various chord based Reynolds numbers at different angles of attack are tested in the anechoic wind tunnel both with and without the laminar boundary layer trip. As the wind tunnel is of open jet configuration the geometric angle of attack is not the true angle of attack and a correction factor, such as the one presented by Brooks et al. [2], can be applied. In the present study the angles stated are the geometric angles of attack and not the corrected angles lending to the fact that the correction factor does not account for 3-D effects.

Figure 5 uses the third octave sound pressure levels (re 20 μPa) at the corresponding centre frequencies, $f_m$. It shows the SPL of the aerofoil with and without the flaplets at a Reynolds number of 100,000 and at two different geometric angles of attack, 0° and 10°. Figure 5b, d show the cases where the boundary layer trip

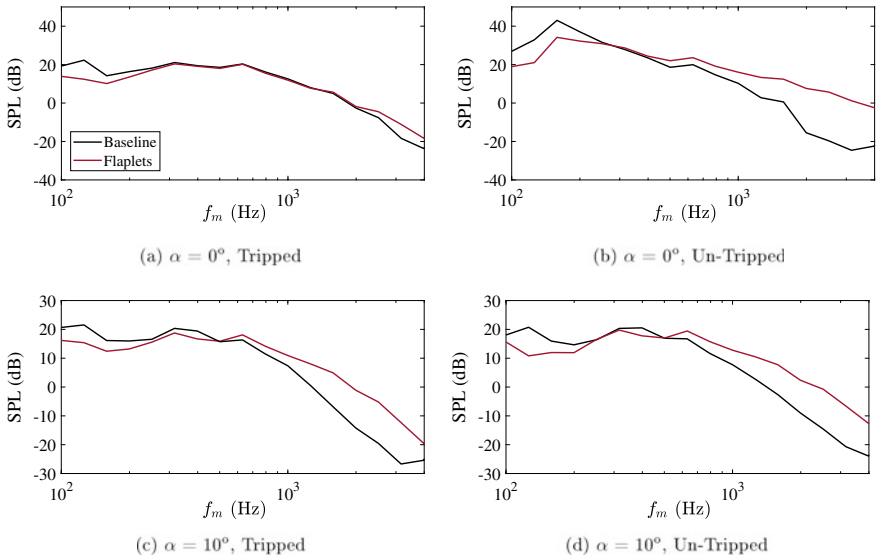


**Fig. 5** Third octave band sound pressure level (SPL), $Re_c$ = 100,000

has been removed from the aerofoil, to see the effect of the flaplets under a laminar boundary layer.

In these cases, it can be seen that, the flaplets have a benefit at very low tonal frequencies but then at higher, more broadband, frequencies there is in an increase in the noise level. Even though there is a clear change in the noise spectra in Fig. 5b compared to Fig. 5a, the flaplets still behave more or less in a similar fashion, a tonal reduction and then an increase in the broadband noise. The tonal noise reduction is thought to be due to the stabilisation of the shear layer that was observed in Sect. 3.1, and hence has changed the vortex shedding frequency of the aerofoil. This results was also been seen on a previous study using a NACA 0010 aerofoil with trailing edge flaplets by Kamps et al. [11].

To evaluate the effect of the flaplets over a wider range of $Re_c$, contours of sound pressure level difference ($\Delta$SPL) are shown in Figs. 6 and 7. These contours are the $\Delta$SPL of a single microphone which was in the region directly above the trailing edge, see Fig. 2, and $\Delta$SPL is defined as:

$$\Delta\text{SPL} = 10 \cdot \log_{10}\left(\frac{\bar{p}^2_{\text{flaplets}}}{\bar{p}^2_{\text{baseline}}}\right)\text{dB} \tag{1}$$

A negative level indicates a noise level reduction with the flaplets and vice versa for a positive $\Delta$SPL. From Fig. 6 it can be seen that over a wide range of Reynolds number there is still the low frequency benefit that was previously discussed, and then the increase in broadband noise.

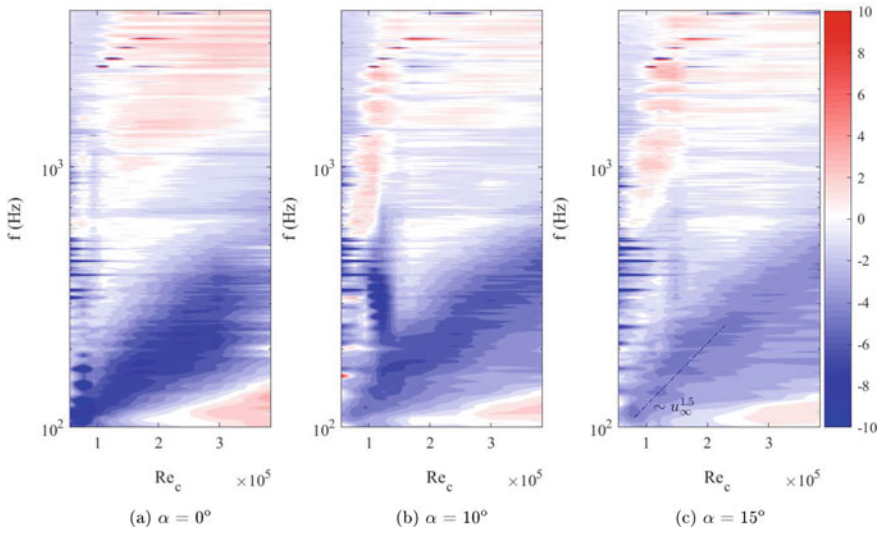


**Fig. 6** Sound pressure level difference contours in dB, ΔSPL, (see Eq. 1) of the tripped aerofoil as a function of frequency and Reynolds number at three different geometric angles of attack

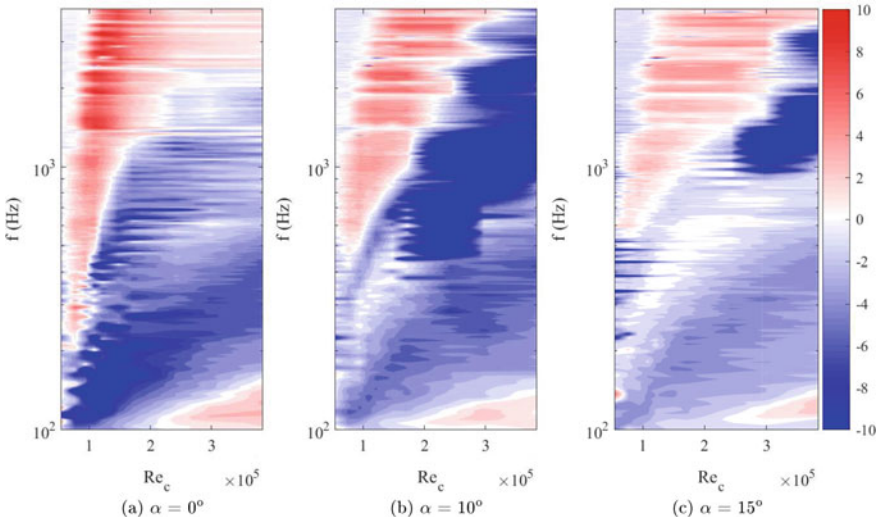


**Fig. 7** Sound pressure level difference contours in dB, ΔSPL, (see Eq. 1) of the un-tripped aerofoil as a function of frequency and Reynolds number at three different geometric angles of attack

Increasing Reynolds number shows an interesting trend, at low frequencies there is a clear region of 'maximum' noise benefit which trends with a $f \propto u_\infty^{1.5}$ relationship, (see. Fig. 6c). This region is also present in the un-tripped case (Fig. 7). This scaling has been seen in many previous literatures [1, 16, 27], where the overall trend of the most intense tonal frequency scales with $u_\infty^{1.5}$, over a wide range of moderate Reynolds number. This scaling is the subject of much controversy and it is proposed by Tam [27], that the mechanism behind the scaling is a feedback loop that consists of boundary layer instabilities and instabilities in the wake. Therefore it is clear that the flaplets stabilise these instabilities in the boundary layer, as seen in Sect. 3.1, and have modified the wake. Leading to a reduction in tonal noise.

As the angle of attack increases the magnitude of the noise reduction is reduced, however there is still a reduction of approximately 5 dB. The reason for this is due to the instabilities in the boundary layer and the onset of separation is moving further up-stream which suppresses the tonal noise and promotes a more broadband noise [14], showing that the flaplets are very good at suppressing the tonal noise component but are not as effective with broadband frequencies.

Once the flaplets are exposed to a laminar boundary layer the noise reduction benefits are increased at low frequencies and the broadband noise increase is more pronounced.

Figure 8, shows the overall sound pressure level from the third octave bands. Naturally the OSPL increases with increasing flow speed and at low angles of attack (Fig. 8a) there is a clear overall sound reduction over the range of Reynolds number investigated. However as the angle increases the difference is less but notably there is always a slight reduction in noise with the flaplets.

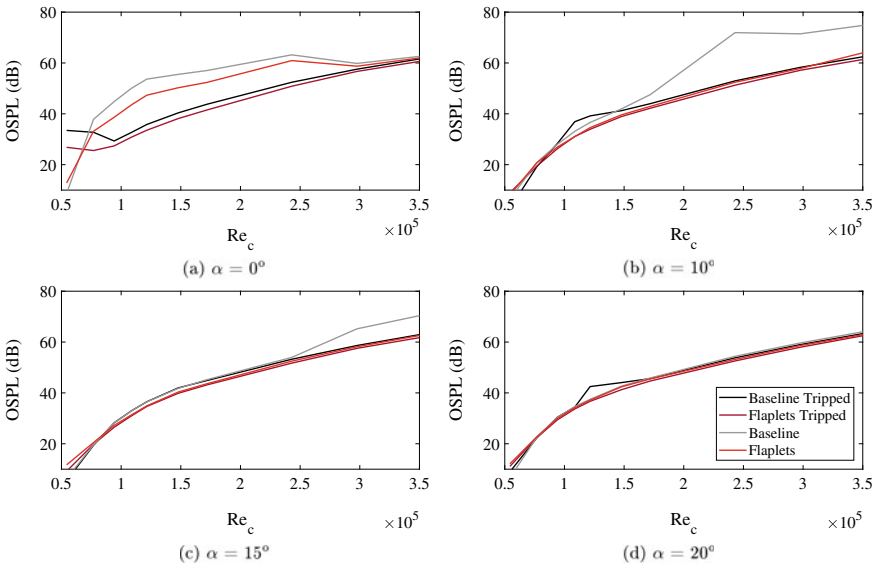


**Fig. 8** Overall third octave band sound pressure levels (OSPL) for all the investigated cases

## 4 Conclusion

Aerodynamic and aeroacoustic measurements have been taken on a NACA 0012 aerofoil in moderate Reynolds number flows, at varying angles of attack with passive high frequency oscillating trailing edge flaplets. Both time resolved PIV and aeroacoustic measurement techniques have been used in the present study and are in agreement, showing the benefit of having such a device in the tested Reynolds numbers range. A tonal noise reduction, has been concluded and is attributed to the stabilisation of the shear layer via a pacemaker effect instigated by the flaplets. An increase in broadband noise is also seen, however the overall sound pressure level data (OSPL, Fig. 8) shows that even with the high frequency noise increase, there is still a benefit. Further detailed integral force measurements is currently being investigated for the present arrangement of flaplets and a detailed DOE type experiment is also ongoing to determine how the thickness, width, length and spacing of the flaplets effects the overall performance in order to attain a greater understanding and an empirical relationship between flaplet geometry and noise reduction.

**Acknowledgements** The position of Professor Christoph Brücker is co-funded by BAE SYSTEMS and the Royal Academy of Engineering (Research Chair no. RCSRF1617\4\11), which is gratefully acknowledged.

## References

1. Arbey, H., Bataille, J.: Noise generated by airfoil profiles placed in a uniform laminar flow. J. Fluid Mech. **134**(1), 3 (1983)
2. Brooks, T.F., Pope, S., Marcolini, M.A.: Airfoil self-noise and prediction. NASA Ref. Publ. **1218**, 1–142 (1989)
3. Brücker, C., Weidner, C.: Influence of self-adaptive hairy flaps on the stall delay of an airfoil in ramp-up motion. J. Fluids Struct. **47**, 31–40 (2014)
4. Carruthers, A.C., Thomas, A.L.R., Taylor, G.K.: Automatic aeroelastic devices in the wings of a steppe eagle Aquila nipalensis. J. Exp. Biol. **210**(23), 4136–4149 (2007)
5. Dong, S., Karniadakis, G.E., Ekmekci, A., Rockwell, D.: A combined direct numerical simulation-particle image velocimetry study of the turbulent near wake. J. Fluid Mech. **569**, 185–207 (2006)
6. Geyer, T.F., Kamps, E., Sarradj, L., Brücker, C.: Passive control of the vortex shedding noise of a cylinder at low Reynolds numbers using flexible flaps. In: 23rd AIAA/CEAS Aeroacoustics Conference, pp. 1–11 (2017)
7. Geyer, T.F., Sarradj, E., Fritzsche, C.: Measurement of the noise generation at the trailing edge of porous airfoils. Exp. Fluids **48**(2), 291–308 (2010)
8. Ho, C., Huang, L.: Subharmonics and vortex merging in mixing layers. J. Fluid Mech. **119**, 443–473 (1982)
9. Huang, R.F., Lin, C.L.: Vortex shedding and shear-layer instability of a cantilever wing at low Reynolds numbers. In: 33rd Aerospace Science Meeting and Exhibit, vol. 33, no. 8, pp. 1398–1403 (1995)
10. Jaworski, J., Peake, N.: Aerodynamic noise from a poroelastic edge with implications for the silent flight of owls. J. Fluid Mech. **723**, 456–479 (2013)

11. Kamps, L., Brücker, C., Geyer, T.F., Sarradj, E.: Airfoil self noise reduction at low Reynolds numbers Using a passive flexible trailing edge. In: 23rd AIAA/CEAS Aeroacoustics Conference, Reston, Virginia, June 2017, pp. 1–10. American Institute of Aeronautics and Astronautics
12. Kamps, L., Geyer, T.F., Sarradj, E., Brücker, C.: Vortex shedding noise of a cylinder with hairy flaps. J. Sound Vib. **388**, 69–84 (2016)
13. Kunze, S., Brücker, C.: Control of vortex shedding on a circular cylinder using self-adaptive hairy-flaps. Comptes Rendus Mec. **340**(1–2), 41–56 (2012)
14. McAlpine, A., Nash, E.C., Lowson, M.V.: On the generation of discrete frequency tones by the flow around an aerofoil. J. Sound Vib. **222**(5), 753–779 (1999)
15. Osterberg, N., Albertani, R.: Investigation of self-deploying high-lift effectors applied to membrane wings. Aeronaut. J. **121**(1239), 660–679 (2017)
16. Paterson, R., Vogt, P., Fink, M., Munch, L.: Vortex noise of isolated airfoils. NACA Adv. Restr. Rept. 3G29 J. Aeronaut. Sci. J. Aircr. Low Adv. Ration J. Am. Helicop. Soc. J. Aircr. **17**(5), 3–12 (1972)
17. Ponitz, B., Schmitz, A., Fischer, D., Bleckmann, H., Brücker, C.: Diving-flight aerodynamics of a peregrine falcon (Falco peregrinus). PLoS One **9**(2) (2014)
18. Prasad, A., Williamson, C.: The instability of the shear layer separating from a bluff body. J. Fluid Mech. **333**, S0022112096004326 (1997)
19. Rajagopalan, S., Antonia, R.A.: Flow around a circular cylinder-structure of the near wake shear layer. Exp. Fluids **38**(4), 393–402 (2005)
20. Rosti, M., Kamps, L., Brücker, C., Omidyeganeh, M., Pinelli, A.: The PELskin project-part V: towards the control of the flow around aerofoils at high angle of attack using a self-activated deployable flap. Meccanica **52**(8), 1811–1824 (2017)
21. Sarradj, E.: A fast signal subspace approach for the determination of absolute levels from phased microphone array measurements. J. Sound Vib. **329**(9), 1553–1569 (2010)
22. Sarradj, E.: A fast ray casting method for sound refraction at shear layers. Int. J. Aeroacoust. **16**(1–2), 65–77 (2017)
23. Sarradj, E., Fritzsche, C., Geyer, T.F., Giesler, J.: Acoustic and aerodynamic design and characterization of a small-scale aeroacoustic wind tunnel. Appl. Acoust. **70**(8), 1073–1080 (2009)
24. Schluter, J.: Lift enhancement at low Reynolds numbers using self-activated movable flaps. J. Aircr. **47**(1), 348–351 (2010)
25. Sijtsma, P.: CLEAN based on spatial source coherence. Int. J. Aeroacoust. **6**(4), 357–374 (2007)
26. Talboys, E., Brücker, C.: Upstream shear layer stabilisation via self-oscillating trailing edge flaplets. Exp. Fluids (2018)
27. Tam, C.: Discrete tones of isolated airfoils. J. Acoust. Soc. Am. **55**(6), 1173–1177 (1974)
28. Yarusevych, S., Sullivan, P., Kawall, J.: On vortex shedding from an airfoil in low-Reynolds-number flows. J. Fluid Mech. **632**, 245 (2009)

# Electroactive Morphing Vibrating Trailing Edge of a Cambered Wing: PIV, Turbulence Manipulation and Velocity Effects


**G. Jodin, J. F. Rouchon, J. Schller, N. Simiriotis, M. Triantafyllou, S. Cazin, P. Elyakime, M. Marchal, and M. Braza**

**Abstract** Inspired from nature, deformations and vibrations are applied on aircraft wings. Thanks to smart-materials that deform a structure, an electroactive morphing wing prototype at reduced scale has been realized within the Smart Morphing and Sensing project. Force measures are carried out for different actuations at two different velocities to highlight up to 2% lift improvement with a wake's thickness reduction of around 10%. Then high speed time resolved particle image velocimetries reveal important effects on flow dynamics as well as on time average. In addition, based on turbulence manipulation, a theoretical explanation of the mechanisms from the actuator towards the near trailing edge and wake structure is highlighted. Finally, actuation ranges leading to increased aerodynamic performances are shown.

**Keywords** Bio-inspiration · Morphing wing · Piezoelectric · Smart materials · Turbulence · Flow dynamics

## 1 Introduction

The future aircrafts will be more efficient, less noisy, cheaper and more green. These guidelines are motivated by a highly competitive market within a societal context of environmental concerns linked to growing fuel prices. Therefore, the aircraft designs need to be more efficient. With respect to aerodynamic performance, current planes have fixed wing geometries, optimized for one cruise flight step. During flight, the altitude, the weight and the speed are changing so one fixed wing shape is sub-

G. Jodin (✉) · J. F. Rouchon · J. Schller
LAPLACE, Université de Toulouse, CNRS, Toulouse, France
e-mail: gurvan.jodin@ens-rennes.fr

G. Jodin · M. Triantafyllou
MIT, 77 Massachusetts Ave., Cambridge, MA 02139, USA

G. Jodin · J. Schller · N. Simiriotis · S. Cazin · P. Elyakime · M. Marchal · M. Braza
IMFT, Université de Toulouse, CNRS, Toulouse, France



M. Braza et al. (eds.), *Advances in Critical Flow Dynamics Involving Moving/Deformable Structures with Design Applications*, Notes on Numerical Fluid Mechanics and Multidisciplinary Design 147,
https://doi.org/10.1007/978-3-030-55594-8_35

optimal. Adapting the shape of the wing during the flight can save several percent of fuel burn for a regional passenger aircraft [11].

Such shape change is called morphing, and it has been of extensive research for more than 40 years [1], with little application to civil aviation. The actual aim of aircraft morphing is not to deform a structure but to adapt the flow in real time. Going further in this concept, let us have a look to nature. The graceful movements of fishes and birds moving within a fluid is fascinating. Their high level of performance in terms of maneuverability, noise emission [12] or energy consumption [10] during their moves comes from their ability to manipulate the surrounding turbulence. Imitating the natural movements of animal is not easy with conventional actuator technologies. Furthermore, airplanes fly much faster than birds, therefore bio-inspired concepts and not biomimetic concepts must be developed. Recent advances in the field of smart materials show the potential to overcome these difficulties, as well as providing a structure stiff enough to withstand the aerodynamic loads, while being flexible enough to be deformed.

Considering electroactive materials, Shape Memory Alloys (SMAs) and piezoelectric materials are commonly used. SMAs are characterized by thermomechanical behaviors, and most of applications use Joule heating to activate the SMAs. Typical applications are shape adaptation at low deformation speed [1]. Piezoelectric materials' electromechanical behavior is activated via the electric field [1]. The developments of piezoelectric composites allow for a simple implementation; piezoelectric composite patches glued on the structure are often used as bending actuators that control the shape of a wing.

The IMFT and LAPLACE laboratories have been focused on studying electroactive morphing for more than 15 years in various collaborative research projects. They aim more electric, lighter, less consuming and less noisy aircraft design, [8, 13, 14] within STAE-RTRA DYNAMORPH[1] project and Airbus project. Now, an electroactive morphing wing prototype at reduced scale has been realized within the Smart Morphing and Sensing project.[2] This prototype embeds both SMA and piezoelectric actuators. This allows both large deformations ($\approx$10% of the chord) at limited frequency ($\leq$1 Hz) and small deformations ($<$1 mm) at higher frequencies ($\leq$400 Hz). Following previous work [8, 13], the first section of the article is dedicated to this design. The second section introduces the wind tunnel experimental setup, that allowed for force measures and High Speed Time Resolved Particle Image Velocimetry (HS TR-PIV). The following sections present experimental data when the morphing vibrating trailing edge is actuated. Before the conclusion, a last section discusses how the actuation manipulate the turbulence to change the aerodynamic performance of the wing.

[1] www.fondation-stae.net.

[2] "Smart Morphing and Sensing for aeronautical configurations" is the H2020 European research project no 723402, http://smartwing.org/SMS/EU.

## 2 Prototype Design

The considered prototype is an electroactive hybrid morphing wing. It embeds both camber control and Higher Frequency Vibrating Trailing Edge (HFVTE) actuators. The baseline airfoil is a wing section of Airbus-A320. The chord is 700 mm and the span 590 mm. This aspect ratio affects the flow, but it does not affect the actual results, as the experiments are dedicated to the changes in the flow due to morphing compared to a non-morphing wing. Figure 1a presents the three sections of the prototype. The actuators are sized, simulated and implemented on the last 30% of the chord, corresponding to usual flap positions. The hollow fixed leading edge contains electronics and tubing for all temperature, pressure and position transducers as well as actuator interfaces.

The camber control actuator's working principle relies on distributed structure embedded actuators: SMA wires are spread under the upper and lower aluminum skins of the wing. The actuation of the upper wires (suction side) causes bending of the trailing edge towards higher cambered shapes. Antagonistically, the actuation of SMA wires under the pressure side skin causes a decrease in camber. Figure 1b shows the SMA actuated wing section. When warmed by means of electric current, the wires tend to retract. This bends the skin and change the wing shape.

The HFVTE actuators are composed of metallic substrates sandwiched between "Macro Fiber Composite" (MFC) piezoelectric patches on both sides. MFC patches are LZT piezoelectric fibers and electrode networks encapsulated within epoxy. When supplied by a voltage, the patches stretch out and generate bending. The whole is covered by a flexible molded silicon that provides the trailing edge shape. Figure 2a illustrate the actuator topology. The active length of the HFVTE is 35 mm chordwise. This design allows for quasi-static tip deformation peak to peak amplitude of almost 1 mm, while able to vibrate at amplitudes large enough up to 400 Hz. Figure 2b introduce the performance of the actuator: it is the maximal vibration amplitude versus frequency. These results have been obtained by means of a high speed camera focused on the trailing edge of the wing mounted inside the wind tunnel.

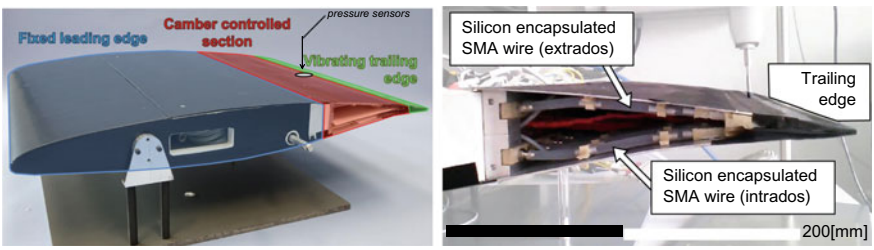


(a) (b)

**Fig. 1** (a) Reduced Scale (RS) prototype. (b) Bending through Shape Memory Alloys

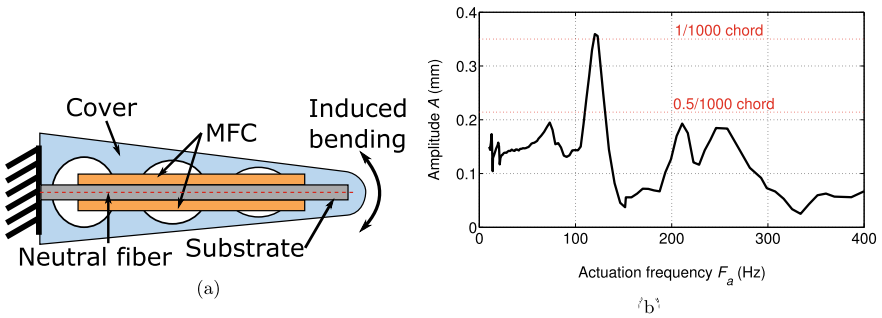


**Fig. 2** **a** Sketch of the piezoelectric trailing edge actuator. **b** Actuator performance characterization: amplitude VS frequency under 1kV supply. 1/1000 and 0.5/1000 chord fraction indications are related to peak to peak amplitudes

The authors invite the reader to refer to the previous publications [7, 9] for more details related to the design and the electromechanical characterization of this electroactive morphing wing.

## 3 Experimental Setup

The wing model is tested in a subsonic wind tunnel. The test section is 592 mm width per 712 mm high. The wing is mounted with an incidence of 10°. which are subject to the same blockage ratio. The turbulence intensity of the inlet section is about 0.1% of the free stream velocity. Measurements are carried out at ambient temperature (22 °C).

A first campaign of experiments consists of drag and lift measures, thanks to a custom made aerodynamic balance.

A second campaign of experiments followed the analysis of the data from the first one. A selection of morphing configuration has been selected for HS TR-PIV measures. Figure 3 presents a 3D view of the wind tunnel test section experimental set up. Smoke particles of 3.4 μm diameter are introduced in the airflow for this purpose. The depth of the field was focused on the 2.5 mm thick stream-wise laser light sheet—in Fig. 3 the green area corresponds to the laser sheet within the camera range. The laser pulsations are generated by a two cavity Nd:YLF (527 nm) laser (Photonics Industries International Inc. DS-527-60). Using mirrors, the laser lights up the wing's wake from the bottom and the laser sheet is reflected from up to bottom to light up the upper side of the wings trailing edge. This arrangement allows for novel PIV measures of the flow over a wing with a vibrating morphing trailing edge. Particle images are recorded during the experiment using the digital high-speed camera Phantom V1210. Each image is divided into interrogation windows. The interrogation window size is $16 \times 16$ px$^2$ (px being Pixel), which corresponds to $3.4 \times 3.4$ mm$^2$, with an overlap of 75%. The computation of the velocity fields

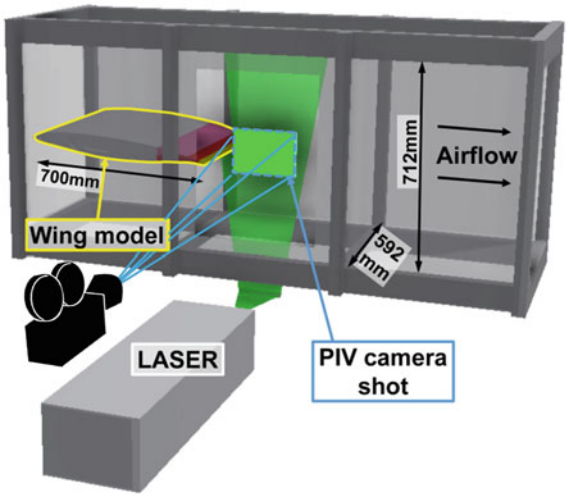


**Fig. 3** Wind tunnel test section drawing with hybrid morphing wing model. PIV setup is represented. The PIV plane is located mid-span

from the images was done using an open source MPI software CPIV-IMFT that runs on regional clusters to compute a set of more than 50,000 images in a short time (e.g. 2 h 41 min on 15 nodes of 20 CPU each). Prior using this software, a comparison with the well known reference commercial software DAVIS8 from Lavision has been performed. As a result, the pic-locking effect are similar, the average fields are in good accordance. Nevertheless, CPIV-IMFT seems to generate dynamic velocities with a bit more variance than DAVIS8. The open source MPI software has been found to be reliable enough for the investigation of morphing effects by comparing the different experiments. Acquisitions of 50,000–200,000 images (≈5–21 s) are sufficient to obtain statistical convergence of the results presented in the following.

## 4 Global Morphing effect—Force Measures

The first experimental campaign consists in the exploration of the frequency and the amplitude of the vibrations of the trailing edge. At initial camber (SMA actuators are off), lift and drag forces have been recorded when the HFVTE is supply by different sinusoidal voltages. Non-significant changes in drag have been measured (change under the measurement accuracy). The balance characterization showed that for the considered force measures have a 95% confidence interval of $\pm 0.3\%$ for the lift, and $\pm 0.2\%$ for the drag. The percentages are related to the baseline wing forces at 10° angle of attack, no morphing, and at a Reynolds number related to the chord ($Re = U \cdot c/\nu$, $U$ being the free stream velocity, $c$ the wing chord and $\nu$ the kinematic viscosity) of 500,000. The relative precision is even higher for the results at Reynolds number of 760,000. Figure 4a, b presents the processed data from 1000 experiments, each during 20 s. HFVTE frequency range is 12–450 Hz (i.e. a reduced frequency

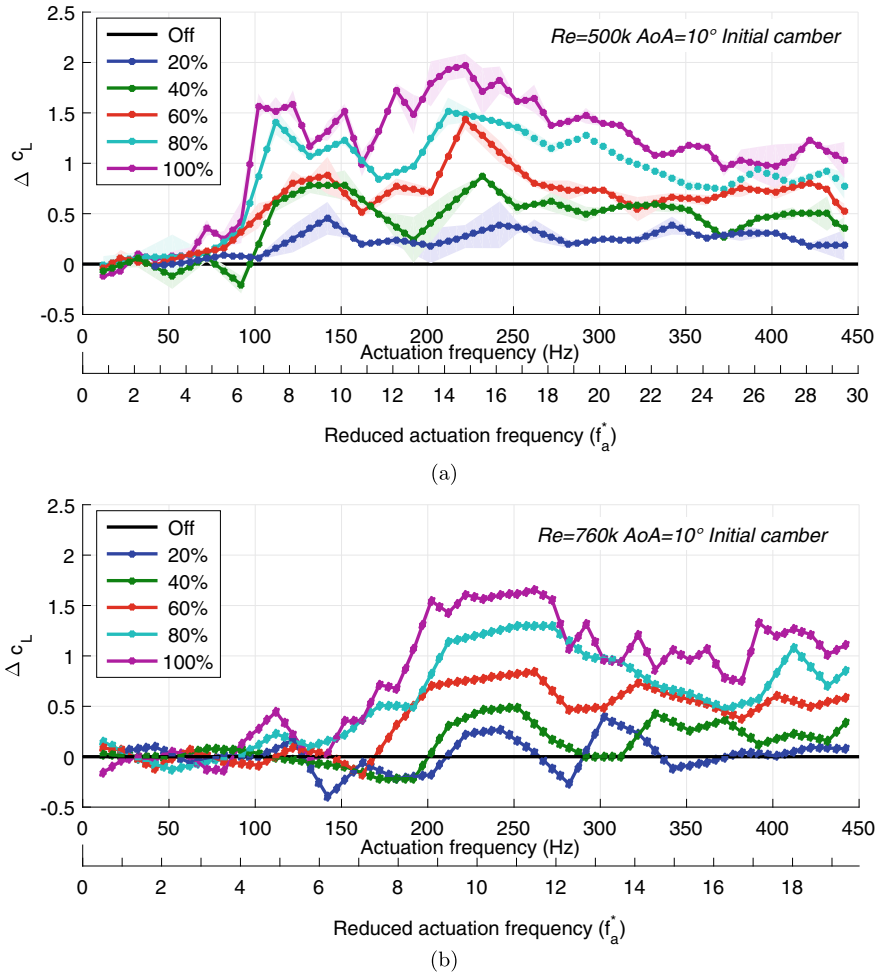


**Fig. 4** Average lift coefficient modifications due to trailing edge actuations, for different frequencies and amplitudes. **a** Reynolds number $5 \times 10^5$. **b** Reynolds number $7.6 \times 10^5$

$f_a^* = f \cdot c/U \in [0.8 \ldots 30]$, with $f$ the actuation frequency). 5 amplitude levels are tested from 20 to 100% of the maximum amplitude of the actuators, Reynolds number is $Re = 500,000$ (noted $Re$ 500 k) for Fig. 4a and $Re = 760,000$ (noted $Re$ 760 k) for Fig. 4b. Attention has been paid to repeatability and accuracy of the measures. The order of the measures has been generated randomly, to prevent any memory or hysteresis effect from the sensors. Finally, one measure at a given HFVTE setting is compared to a previous and a following reference measured data with no actuation.

Figure 4a, b show the variation of the lift coefficient in relation with the actuation frequency. The different actuation amplitudes are drawn in different colors. Pale areas described the variations of the measures between the two experiment repetitions

whereas the darker lines are the average values. The experiments are repeatable with ±0.14% lift difference.

The first observation is the effect of the amplitude. Generally, the larger the HFVTE amplitude the larger the gain. This clearly indicates that if the actuator could vibrate at larger amplitudes, more gains can be achieved. But increasing amplitude over a certain limit would decreases the gains, as reported in [3] for the forced active control of airflows.

A second observation is the low effect of the HFVTE at low frequencies, followed by a quick rise of the lift after a threshold frequency (around 90 Hz for *Re* 500 k on Fig. 4a, and respectively around 150 Hz for *Re* 760 k on Fig. 4b). For the two considered frequencies, the corresponding reduced frequencies are about $f_a^* = 6$. Also, some positive lift improvements are visible for both velocities for $f_a^* = 5$. So, the velocity is important to determine a efficient actuation frequency. The flow conditions only do not explain the whole measures. Some difference in gains between the two figures are related to the performance of the actuator: the characterization of the vibrating actuator presented in Fig. 2b reveals that a resonance with a large amplitude occurs around 120 Hz. This large amplitude leads to significant effects. On both velocities, some lift improvements are visible around 120 Hz. Specifically for *Re* 500 k (on Fig. 4a) the superposition of the threshold frequency plus the actuator resonance leads to a very sharp edge in the lift gains. After this resonance, between 150 and 200 Hz the amplitude is smaller. This can explain the smooth rising of gains for *Re* 760 k (Fig. 4b) as well as the small decrease in lift for *Re* 500 k (Fig. 4a). Over 280 Hz, the amplitude of the vibrations decreases to lower values, thus explaining the lower gains in lift at these high actuation frequencies.

To sum up the results, within the considered Reynolds numbers, actuations over a reduced frequency of 6% good lift improvements, under the condition of having a sufficient vibration amplitude. Very small vibrations are enough to enhance significantly the aerodynamic performances, e.g. a 0.7 mm peak to peak vibration—0.1% of the chord—at 220 Hz improves the lift by 2% for the *Re* 500 k case.

## 5 Flow dynamics—PIV

Following the previous force measures, HS TR-PIV measures have been performed on 5 experiments, all at a Reynolds number of $5 \times 10^5$. The first case is the static non-actuated baseline, for reference. Then, according to the Fig. 4a, the best actuation case (i.e. 220 Hz 1 kV), a frequency just after the threshold (i.e. 110 Hz 1 kV) and an intermediate frequency with low amplitude due to actuation limit but still with good lift improvement (i.e. 150 Hz 1 kV) are considered. Also, another point with low gain (i.e. 55 Hz 1 kV) has been recorded. This point is similar to previous study of the authors [8]. A good consistency with authors' previous results is fortunately obtained.

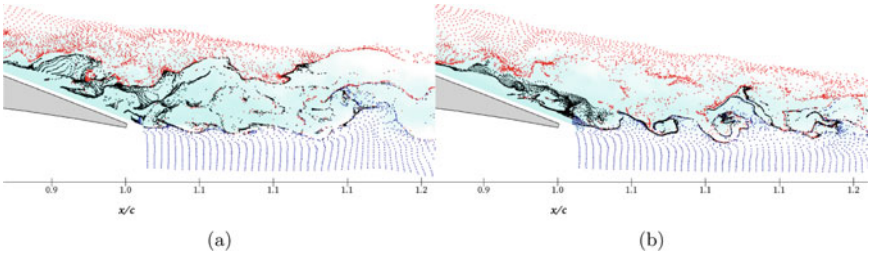


**Fig. 5** Snapshots of streaklines. Red, black and blue seeds are inserted. Flow comes from left to right. Background color indicates velocity amplitude. **a** Static baseline without actuation. **b** actuation at 220 Hz

## *5.1 Streaklines*

Presenting the streaklines is helpful to understand the flow dynamics, before getting into details. Figure 5 present two snapshots with streaklines. Blue seeds are located on the pressure side, red ones on the suction side, and black seeds are placed at from the trailing edge to roughly the separation point. Figure 5a is the static baseline. Composition of black and red vortices go downstream, interact with smaller vortices from the trailing edge and generate a large oscillating wake with both smal and large eddies. Figure 5b corresponds to the 220 Hz actuated case. The vibration of the trailing edge causes constantly spaced waves in the wake. They are clearly visible, made of lines of black particles surrounded by blue ones. Here the actuation helps to drain the black particles from the recirculation area, thus reducing the wake width before the trailing edge. The resulting wake is therefore dominated by the forced trailing edge vortices. On both actuated and reference cases, the different colored particle streams seem not to mix. This supports the Eddy Blocking Effect, described by Hunt [5]. More details are provided in the discussion section.

## *5.2 Proper Orthogonal Decomposition*

A proper orthogonal decomposition (POD) is performed on the PIV velocity fields. The POD is a mathematical tool that allows for decomposing a system dynamic into modes, ranked by energy. This approach can be viewed in the context of Reduced Order Modeling and is useful to the physical understanding. See [2] for more details about the algorithm used, as well as authors' previous studies [8].

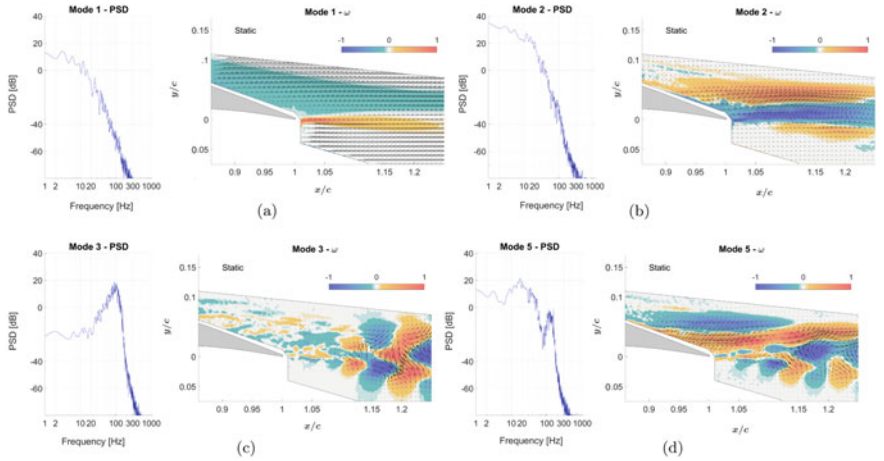


**Fig. 6** 4 POD modes of the static baseline. $Re = 500$ k. Each mode comes with PSD of its temporal coefficient, and vorticity contour with superimposed velocity vectors from spatial coefficient

### 5.2.1 Non Actuated Flow Dynamics

The first four modes – the most energetic ones – describe the main mechanisms of the flow. Figure 6 presents the modes #1, #2, #3 and #5. Mode #4 is equivalent of #3 with a 90° phase shift. Modes #5 to #12 describe the same mechanisms. Each mode is summarized by a Power Spectral Density (PSD) of its temporal coefficient, together with the vorticity field of its spatial coefficient superimposed by velocity vectors. Mode #1 is related to the average field, mode #2 represent the effect of the flow separation over the wing that is involved in the von Kármán vortices, mode #3-4 is linked to the shear layer instabilities that have frequencies in the range 50 to 170Hz, including Kelvin Helmholtz instabilities. Mode #5 describes the link among the separation, recirculation and the shear layer, as it contains space and time similitudes with the modes associated with he considered phenomena.

### 5.2.2 Morphing Effects on Main Dynamic

The HFVTE has considerable effect on flow dynamics. For instance, all the actuation tested – even the less efficient 55 Hz—cause a shift of the shear layer instabilities. Figure 7a presents mode #3 of the 55 Hz case. Peaks at fundamental and harmonic of the actuation frequency dominate the PSD. According to the spatial mode, more energy is present close to the actuated trailing edge.

The actuation with the higher amplitude—i.e. 110 Hz 1 kV—completely changes the dynamics and the order of the modes, compared to the static case. As in all cases, the first mode is linked to the time average velocity, but in the 150 Hz and 110 Hz cases, the modes #2–3 demonstrate the actuation modifying the main shear

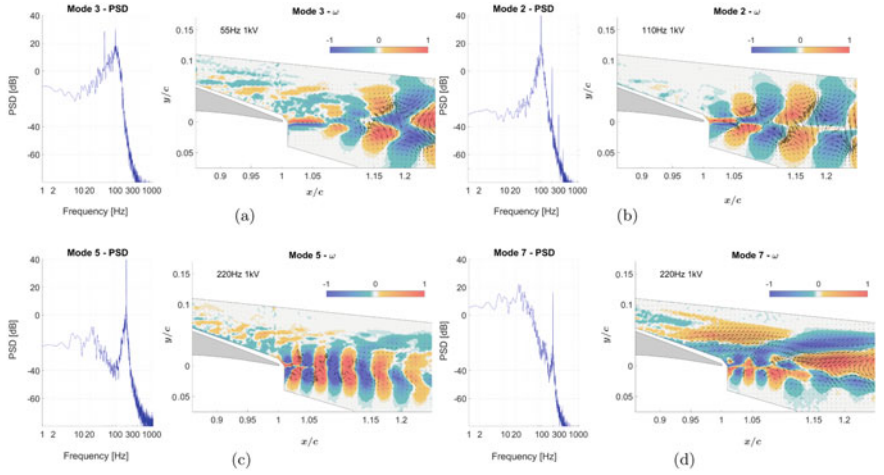


**Fig. 7** 4 POD modes of different actuation cases. $Re = 500$ k. For all the modes, PSD of its temporal coefficient and vorticity contour are drawn. Superimposed arrows correspond to velocity vectors

layer instabilities, as visible in Fig. 7b. Then, several intermediates modes appear, dedicated with the actuation. The highest energy occurrences of such modes are #5 for the 220 Hz case, #4 for 110 Hz and #18 for 150 Hz. Figure 7c illustrates the first occurrence of modes dedicated to actuation, for the 220 Hz case. The energy is mainly contained in small coherent vortices coming from the trailing edge vibrations.

Figure 7s illustrates the interaction between vortices generated through actuation versus vortices generated through separation. This mode contains space and time features linked to the two type of considered vortices.

### 5.2.3 Morphing Effects on High Order Modes

Less energetic phenomena linked to higher POD modes are interesting to explain the physics, as a small change may lead to large effects in such chaotic flows. Indeed, this study shows that a small amplitude trailing edge vibration considerably manipulated the near wake vortices. Szubert et al. had showed that introducing energy in high order POD modes leads to significant changes in the flow dynamic [15].

Mode #14 of the static baseline (presented in Fig. 8a) describes the interaction of teh the wake with alternating vortices from the suction side of the wing. Such mode is downsized to #17 of the 220 Hz actuated case. This mode is similar to the corresponding mode of the non-actuated case, but presents a peak at the actuation frequency.

Mode #18 of the 220 Hz case is a typical mode caused by the actuation. In Fig. 8b, the actuation is linked to the energy of the wake coming from both sides of the wing. This can be interpreted as a synchronization of the dynamics.

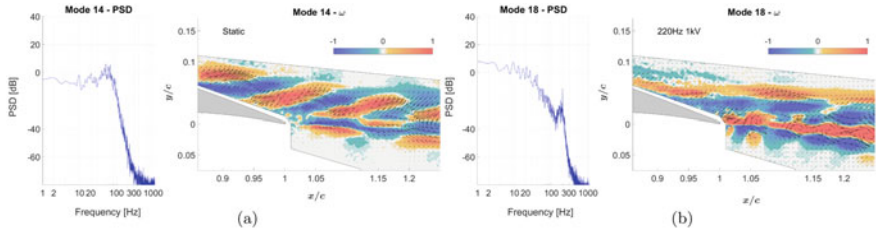


**Fig. 8** Equivalent POD modes of the static baseline and the 220 Hz actuated case

## 6 Discussion

Investigating the effect of an electroactive deformable vibrating trailing edge, the understanding of the mechanisms is decomposed threefold: a exploration of the frequencies and amplitudes macroscopic effects, the observation of the flow velocity for some selected experiments, and a modal decomposition to explain the mechanisms.

First, compared to existing studies relating active flow control, the actuation at the trailing edge provides an action on both the wake and the upstream flow. Indeed, as related by Greenblatt et al. [4], most of the harmonic flow forcing are done upstream to the separation to attempt controlling it.

Second, the amplitude seems to have second order effect on the gains. Actuation at 110, 220 and 150 Hz have 0.7 mm (0.1%$c$), 0.4 mm (0.06%) and 0.12 (0.017%) peak to peak amplitude, respectively. Nevertheless, they all provide more than 1% lift improvements. This is also visible with the POD analysis, where same significant impacts on flow dynamics occur: shift in natural vortex shedding frequency, more coherent shear layer, and energy introduction near the trailing edge. However, both force and PIV measures tend to show that the more the amplitude, the more the effect. It can be guessed that very large amplitudes would not increase the gains; nevertheless such amplitudes have not bee reached experimentally.

Third, the 220 Hz actuation case deviates the wake downwards. This effect is not visible for the 150, 110 and 55 Hz cases. A wake deviated downwards can be compared to downward jet, thus leading to an upwards resulting force, so an improved lift. This could explain why this moderate actuation amplitude is the best actuation frequency.

Fourth, if no visible deviation of the wake is visible for other actuations, how can we explain the gain in performance? Looking at Fig. 5, the black eddies, coming from the recirculation zone stay within the upper red and lower blue shear layer that form interfaces from turbulent flow to non-turbulent flow (T-NT). The black area is a turbulent to turbulent interface (T-T). It is interesting to note that none of these black eddies do not go through the other interfaces. This clearly illustrates the Eddy Blocking Effect, as in the case of free interface shear layers [6]. Therefore, the wake thickness depends on the size of the black eddy area. Actuation introduces smaller scale vortices which produce vortex breakdown of existing larger coherent vortices.

Therefore it helps controlling the size of the wake vortices and also helps to drain this detached area. The vortex breakdown occurring in the actuation manipulated area lead to a thinner wake, thanks to the eddy blocking effect.

Finally, comparison of force measures at different velocities seems to indicate that the involved mechanism are similar in the considered Reynolds range. In addition, the threshold frequency observed is linked to the flow conditions. An increase of the Reynolds number by 50% increased the threshold frequency by roughly 50%. This is the first step to determine a priori and efficient actuation range for design purpose.

## 7 Conclusions

This paper presents a hybrid electroactive morphing wing prototype equipped for wind tunnel experiment. The present study focuses on the aerodynamic performance enhancement thanks to trailing edge active vibrations.

A first part of the study explored the actuation parameters at two different velocities. It has been shown up to 2% of lift improvement. Afterwards, five actuations have been selected for Time-Resolved PIV. Important morphing effects on the flow dynamics and on the time-averaged quantities have been shown. Based on turbulence manipulation, an explanation of the mechanisms generated by the actuation and affecting the local flow structure has been put in evidence. Finally, efficient actuation range have been indicated by the present study.

**Acknowledgements**


The authors would like to thank the Fédération de Recherche FERMAT for laser and camera intensively used in this work. This work has been carried out within the Smart Morphing and Sensing for aeronautical configurations. This project has received funding from the European Union's H2020 program for research, technological development and demonstration under grant agreement no 723402.

## References

1. Barbarino, S., Bilgen, O., Ajaj, R.M., Friswell, M.I., Inman, D.J.: A review of morphing aircraft. J. Intell. Mater. Syst. Struct. **22**(9), 823–877 (2011)
2. Berkooz, G., Holmes, P., Lumley, J.L.: The proper orthogonal decomposition in the analysis of turbulent flows. Annu. Rev. Fluid Mech. **25**(1), 539–575 (2011)

3. Collis, S.S., Joslin, R.D., Seifert, A., Theofilis, V.: Issues in active flow control: theory, control, simulation, and experiment. Prog. Aerosp. Sci. **40**(4), 237–289 (2004)
4. Greenblatt, D., Wygnanski, I.J.: The control of flow separation by periodic excitation. Progr. Aerosp. Sci. **36**(7), 487–545 (2000)
5. Hunt, J., Ishihara, T., Szubert, D., Asproulias, I., Hoarau, Y., Braza, M.: Turbulence Near Interfaces-Modelling and Simulations, vol. 133 of Notes on Numerical Fluid Mechanics and Multidisciplinary Design, pp. 283–292. Springer, Switzerland: Updated contributions reflecting new findings. Presented at the ERCOFTAC Symposium on Unsteady Separation in Fluid-Structure Interaction, 17–21 June 2013. St John Resort, Mykonos, Greece (2016)
6. Hunt, J.C.R., Eames, I., Westerweel, J.: Vortical Interactions with Interfacial Shear Layers, pp. 331–338. Springer, Netherlands, Dordrecht (2008)
7. Jodin, G., Scheller, J., Duhayon, E., Rouchon, J.F., Triantafylllou, M., Braza, M.: Implementation of a hybrid electro-active actuated morphing wing in wind tunnel. To appear in Solid State Phenomena (2017)
8. Jodin, G., Motta, V., Scheller, J., Duhayon, E., Döll, C., Rouchon, J.-F., Braza, M.: Dynamics of a hybrid morphing wing with active open loop vibrating trailing edge by time-resolved piv and force measures. J. Fluids Struct. **74**, 263–290 (2017)
9. Jodin, G., Scheller, J., Rizzo, K.J., Duhayon, E., Rouchon, J.F., Braza, M.: Dimensionnement d'une maquette pour l'investigation du morphing électroactif hybride en soufflerie subsonique. In: Congrès Français de Mécanique. Association Française de Mécanique, Online AFM (2015)
10. Liao, J.C., Beal, D.N., Lauder, G.V., Triantafyllou, M.S.: Fish exploiting vortices decrease muscle activity. Science, **302**(5650), pp. 1566–1569 (2003)
11. Lyu, Z., Martins, J.R.R.A.: Aerodynamic shape optimization of an adaptive morphing trailing edge wing. J. Aircr. **52**, 1951–1970 (2015). November
12. Sarradj, E., Fritzsche, C., Geyer, T.: Silent owl flight: bird flyover noise measurements. AIAA J. **49**(4), 769–779 (2011)
13. Scheller, J., Chinaud, M., Rouchon, J.F., Duhayon, E., Cazin, S., Marchal, M., Braza, M.: Trailing-edge dynamics of a morphing NACA0012 aileron at high reynolds number by high-speed PIV. J. Fluids Struct. **55**, 42–51 (2015)
14. Scheller, J.: Electroactive morphing for the aerodynamic performance improvement of next generation airvehicles. Ph.D thesis, Institut Narional Polytechnique de Toulouse (2015)
15. Szubert, D., Grossi, E., Jimenez Garcia, A., Hoarau, Y., Hunt, J.C.R., Braza, M.: Shock-vortex shear-layer interaction in the transonic flow around a supercritical airfoil at high reynolds number in buffet conditions. J. Fluids Struct. **55**, 276–302 (2015)

# Camber Actuation of an Articulated Wing with Electromechanical Actuators


**Alexandre Giraud, Martin Cronel, Ioav Ramos, and Bertrand Nogarede**

**Abstract** This paper relates the design of electromechanical actuators for camber actuation in a morphing flap. In order to reduce fuel consumption, the camber of an articulated wing or flap is controled to reach specific aerodynamic profiles. The wing is divided in 6 parts, connected with 5 hinges. The angles of the hinges are controled by the electromechanical actuators, through a proper leverage and a linear force. The leverages are specified for each articulation from the torques applied on it, which are calculated to reach the profiles under flight conditions. The electromechanical actuators consist in a motor, a gearbox and a screw and nut transmission. Their integration and their torque close control are presented

**Keywords** Wings · Morphing · Electromechanical actuation · Camber control

## 1 Introduction

Recent studies highlighted the benefits the morphing could provide when applied to aircrafts [1], especially from an aerodynamic point of view by allowing aerodynamic shape optimization [11]. Hence, adaptive morphing wings have the potential to reduce fuel consumption of aircraft by adapting shape to flight conditions. Fuel consumption is a high issue from an environmental point of view and an economic

A. Giraud (✉) · M. Cronel · I. Ramos · B. Nogarede
NOVATEM, 27 rue d'Aubuisson, 31000 Toulouse, France
e-mail: alexandre.giraud@novatem-sas.com

M. Cronel
e-mail: martin.cronel@novatem-sas.com

I. Ramos
e-mail: ioav.ramos@novatem-sas.com

B. Nogarede
e-mail: bertrand.nogarede@novatem-sas.com



M. Braza et al. (eds.), *Advances in Critical Flow Dynamics Involving Moving/Deformable Structures with Design Applications*, Notes on Numerical Fluid Mechanics and Multidisciplinary Design 147,
https://doi.org/10.1007/978-3-030-55594-8_36

one. For instance, in 2008, civil aviation was responsible of 2% of $CO_2$ emission [17]. Moreover, one kilogram of fuel saved can allow a 1000 $ savings [4].

The work presented in this article is a part of a European project called Smart Morphing and Sensing (SMS), which deals with several kinds of morphing applied on wing shape. Here, a slow motion of morphing flap is studied: controlling its camber is the main objective. In this way, the profile of the flap can be adapted more precisely to flight conditions which depend on the flight phase, altitude, temperature or even weather conditions.

Such a flap will be integrated to a wing but the general principle of the study might be extended to a whole aircraft wing in the future. The feasibility of such a study has been proved in [10] where camber control of a small flap was using Shape Memory Alloy (SMA) actuators and proposed hybrid actuation with a high frequency actuation using piezoelectric actuators. SMA actuators are adapted to slow motion in high force conditions, [9]. We propose here to extend camber control to a larger flap. Due to reliability and acceptance in aeronautical industry, we also propose an electromechanical actuation solution, which have a higher maturity level in aero actuation, but remains a true challenge to integrate in aircraft conditions. It will provide a good comparison to SMA actuation in the future.

First, the morphing flap is presented, with all its functional parameters, such as hinges positions, torques or angles. Then, an electromechanical actuation is proposed and detailed. Finally, the integration and control of the actuators are discussed.

## 2 Presentation of the Flap and Its Actuation

### *2.1 Flap Details*

The flap profile has to be controled to reach the shapes between two positions, Shape Up and Shape Down, from a reference profile. The shape positions, presented in Fig. 1, are determined by other partners of SMS project, depending on aerodynamic forces in flight conditions.

In order to control the profile of the flap, a specific articulated wing has been designed. The wing is divided in six parts linked by five hinges or articulations, such as a dorsal vertebra. The location of articulation $a_i$, $i \in \{1, \ldots, 5\}$ (Fig. 2) is

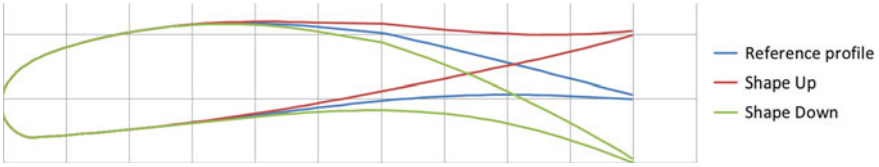


**Fig. 1** Wing profiles

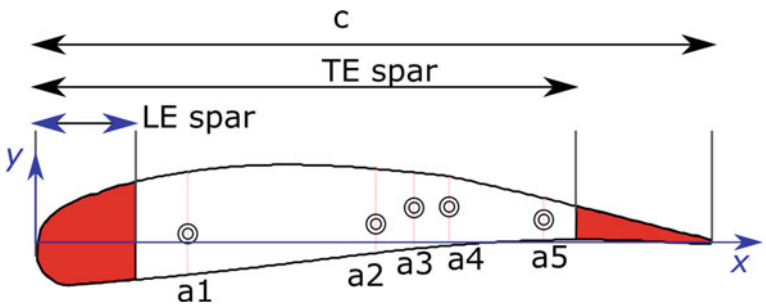


**Fig. 2** Morphing wing with hinges

**Table 1** Flap dimensions

| Distance | (m) |
|---|---|
| C | 1 |
| TE spar | 0.85 |
| LE spar1 | 0.15 |
| Hu 1 | 0.092 |
| Hu 2 | 0.082 |
| HU 3 | 0.053 |
| Hu 4 | 0.044 |
| Hu 5 | 0.033 |
| Hd 1 | 0.061 |
| Hd 2 | 0.043 |
| Hd 3 | 0.060 |
| Hd 4 | 0.058 |
| Hd 5 | 0.030 |

determined by an optimization for an actuation with Shape Memory Alloy (SMA). The corresponding dimensions of Fig. 2 are gathered in Table 1. Table 2 presents the different torques applied on each articulation and its limit angles of opening. These values are specified by other partners of SMS project in order to reach the desired aerodynamic profiles in flight conditions.

The solution presented here uses Electromechanical Actuators (EMA), providing an alternative to SMA actuation. In this way, a detailed comparison will be possible later with the researches of another work within the SMS project, which focuses on SMA actuation for the same flap. EMA are also more accepted for actuators in aeronautical industry, providing more interest to a comparison with SMA. Moreover, EMA design is faster and will provide more rapidly a morphing flap for the very first aerodynamic tests.

EMA may be used directly on the rotation axes of each hinge, like in [14]. However, due to the very high torque needed to control the camber in the specified

**Table 2** Torques and angles

| Hinge | Torque (N m) | Angle > 0 | Angle < 0 |
|---|---|---|---|
| $a_1$ | 446 | 4.8 | −2.5 |
| $a_2$ | 140 | 1.5 | −5.3 |
| $a_3$ | 88 | 1.5 | −0.1 |
| $a_4$ | 62 | 2.2 | −0.4 |
| $a_5$ | 28 | 3.4 | −4.1 |

**Fig. 3** First hinge scheme

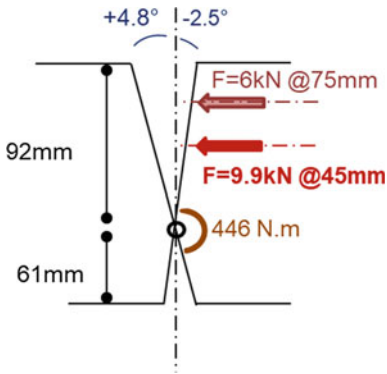


conditions of the project, we decided to use the leverage available above and below articulation (y axis of Fig. 2). In this way, the rotation is obtained with a linear force applied on x axis (Fig. 2) with a linear NOVATEM's EMA. The force depends on the torque on each hinge and the distance from the center of rotation. For instance, the torque on the first articulation ($a_1$) is 446 N m. A more detailed scheme of the first articulation is presented on Fig. 3. The evolution of lever force with the distance from the center is shown on Fig. 4. Thus, the position of the NOVATEM's EMA can be determined to apply the needed force to articulate $a_1$. The same process is used for all hinges. Table 3 sums up the different torques, leverages and force for each hinge. Depending on the leverage and the angles, the corresponding linear stroke permits the determination of the screw of the linear NOVATEM's EMA, also presented in Table 3.

## *2.2 Actuation Choices*

Several types of EMA are possibles to get a linear force. Direct linear electromagnetic actuators are a solution [22], but their design is more complex and their dynamic is not adapted to the needed actuation for the flaps. A rotational actuator connected to a gear and a screw and nut transmission is more adapted here [18]. It would also be

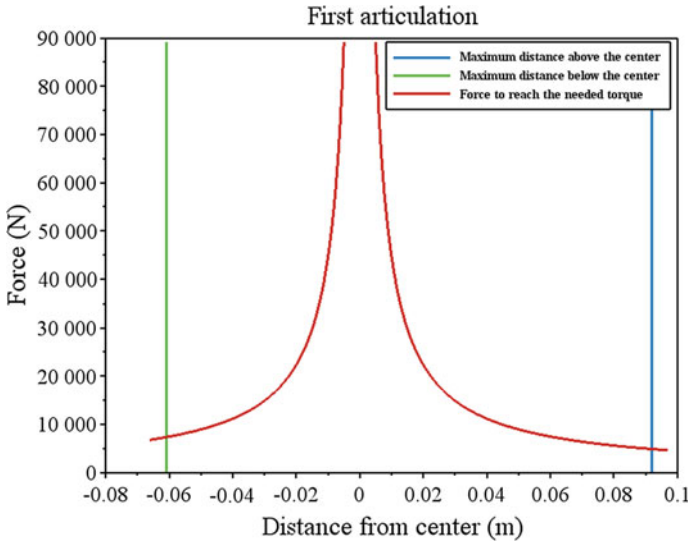


**Fig. 4** Force evolution around the first hinge

**Table 3** Torques and leverages

| Hinge | Torque (N m) | Leverage (m) | Force (kN) | Screw stroke (mm) |
|---|---|---|---|---|
| a1 | 446 | +0.05 | 9 | 7 |
| a2 | 140 | +0.04 | 3.5 | 6 |
| a3 | 88 | −0.03 | 3 | 1.5 |
| a4 | 62 | −0.03 | 2 | 1.5 |
| a5 | 28 | +0.012 | 2.35 | 2 |

conceivable to avoid gears and have a direct driven motor like in [6], connected with the screw and nut transmission. This kind if solution is attractive because avoiding gears increasing the efficiency of the chain. However, without gear, the need motor torque would be very high, leading to a bad compacity and a high current intensity and so heating issues. Generally, to increase compacity of an electromchanical actuator, the electromechanical conversion frequency has to be increased, reducing the quantity of the active parts (iron, copper, magnet) [8]. That is why the most adapted solution here is a very compact and small motor functionning at high speed, linked to a high reduction ratio gear and an adapted screw and nut transmission.

Nevertheless, such a solution involves an iron losses augmentation [13, 20], which can be estimated thanks to simple and efficient models [3] or more accurate but complex ones [7]. It is also possible to estimate iron losses experimentally with a specific bench proposed in [2]. This type of bench could also provides aerolical and mechanical losses, detailed in [16] with Joule losses. At this range of speed, losses

must be taken precisely into account in the actuation design, which has to use global optimization like in [5]. The following section details the different components of the EMA.

## 3 Electromechanical Actuator Description

### *3.1 Motor*

The synchronous permanent magnet motor is designed to get the maximum possible specific torque and efficiency, but for the highest compacity. It is thus designed around a high saturation iron cobalt stator yoke with a high density winding allowing for high linear current density. Because of the relatively high reduction ratio of the EMA assembly, the motor has a relatively high rotational speed, thus inducing iron losses. These losses are attenuated by the low magnets polarization and large airgap. A maximum efficiency of 94% was reached thanks to the implemented topology and a specific torque of almost 0.9 Nm/kg. This two combined figures make of this motor ideal for the current EMA application.

The motor general parameters are gathered in Table 4. The field distribution of magnetic flux density obtained by finite element computation is presented on Fig. 5 and a picture of the produced motor is given in Fig. 6.

### *3.2 Gearbox*

The gear of our EMA must have a high reduction ratio, to get the highest torque possible on the nut. The most adapted solution is a 4 stages planetary gearbox. This solution is classical but remains efficient. The parameters of the chosen gear are gathered in Table 5.

The efficiency $\eta_g$ of the gearbox depends of the power flow direction [15]. As the input power flow and ouput one are on the same axes, the efficiency of the gearbox is directly obtained from the efficency of the basic epicyclic gear, which depends on speed, torques and the number of teeth of the differents trains [12]. It y is usually estimated from experimental tests [15]. Here we have:

**Table 4** Motor parameters

| Outer yoke diameter (mm) | Motor shaft diameter (mm) | Stator length (mm) | Maximum torque (mN m) | Corresponding speed (rpm) |
|---|---|---|---|---|
| 18.5 | 5 | 42.5 | 35 | 10,000 |

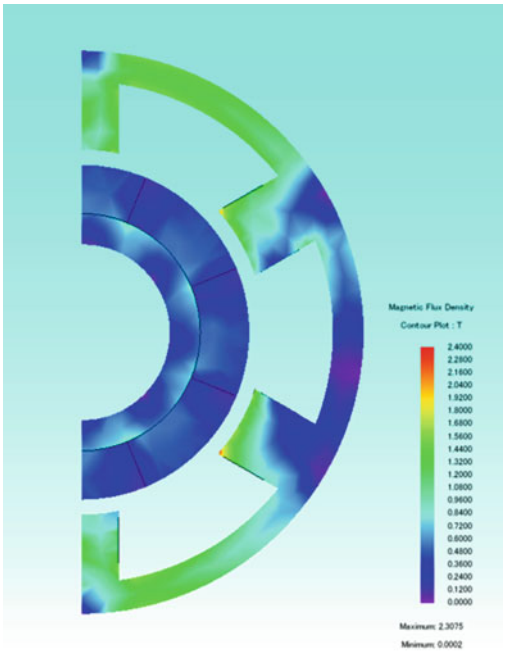


**Fig. 5** Magnetic field distribution in the motor

**Fig. 6** Picture of the motor

$$\eta_g = 64\% \tag{1}$$

The gearbox transmits the motor torque to a screw and nut, up to 12.2 N m.

## *3.3 Screw and Nut*

The screw and nut transmission (a planetary roller screw here) allows the conversion of the rotational motion provided by the motor through the gearbox into a linear

**Table 5** Gear parameters

| Outer diamater (mm) | Length (mm) | Reduction ratio |
|---|---|---|
| 42 | 84 | 546 |

**Table 6** Screw and nut parameters

| Screw diameter (mm) | Nut diameter (mm) | Nut length (mm) | Screw length (mm) | Screw thread (mm) |
|---|---|---|---|---|
| 15 | 36.5 | 50 | 20 | 5 |

motion, apply a force on a leverage (specified in Sect. 2). The output torque of the gearbox $C_{gear}$ is linked to the linear force $F_{screw}$ provided by the screw with the following equation:

$$C_{gear} = \frac{p.F_{screw}}{2\pi\eta_s} \tag{2}$$

Where $p$ is the screw thread and $\eta_s$ is the efficiency of the screw and nut, given by Eqs. (3) et (4) respectively for direct and inverse transmission.

$$\eta_s = \frac{1}{1 + \frac{d\pi\mu}{p}} = 0.88 \tag{3}$$

$$\eta_{s_{inv}} = 2 - \frac{1}{\eta} = 0.87 \tag{4}$$

The constant $\mu = 0.010$ depends on the helix angle $\alpha = 4.3°$ of the screw whose diameter is $d$. Therefor, with 12.2 N m on the nut, the screw can apply a force up to 13.37 kN.

Table 6 presents the parameters of the screw and the nut.

### *3.4 Plays*

The estimation of the different plays is essential due to their influence on the real position of the screw when it is actuated through the motor and the gearbox. The plays of direct connexion are neglected, like between the motor and the gearbox or between the gearbox and the nut. The output gearbox radial play is estimated at 1° : the accuracy of nut radial position is limited to 1°. One turn of the nut theoretically provides a 5 mm screw linear motion, due to its thread. So the gearbox play limits the accurary of the screw position to 13.9 µm.

The play of the screw and nut connexion can be avoided by applying a specific charge on the nut. However, in order to estimate the global plays in the worst case,

**Table 7** Torques and leverages

| Hinge | Screw stroke (mm) | Percentage of plays (%) |
|---|---|---|
| a1 | 7 | 0.39 |
| a2 | 6 | 0.45 |
| a3 | 1.5 | 1.79 |
| a4 | 1.5 | 1.79 |
| a5 | 2 | 1.35 |

the screw and nut connexion play is considered as equal to 23 μm, whch corresponds to the plays for low quality screw [19]. The global play is then included between these two values. Table 7 details the percentage of plays on the screw thread for each hinge, in the worst case (26.9 μm).

## 4 Mechanical Integration and Control

### *4.1 Integration and Bearing Utility*

The different parts of the EMA (Fig. 7) must be connected to each other. They are detailed on Fig. 8. The solution proposed here consists in a direct motor gear connexion. The nut is linked to the gear with a specific nut carrier and rotates at the output speed of the gearbox. That rotation provides a linear motion to the screw, with a linear force involved by the torque on the nut. The same EMA is used for the 5 hinges.

A specific frame is design in order to maintain all the parts together and to connect the EMA to the wing structure at the proper leverage above each articulation, linking the two parts on both sides of it and allowing the motion.

However, the linear force passing through the screw may damage the gearbox. Therefore, tapered roller bearings are used to transmit the force to the frame or to the nut carrier, through dedicated flanges. The force transmission depends on the motion direction whether the articulation is opening or closing. The bearings must be correctly mounted on the nut carrier and in the frame, as shown on Fig. 9.

This solution of integration is the most compact and efficient for such an application. The weigth of the motor, the gearbox, the bearings and the screw and nut transmission is equal to 1.07 kg. Depending of the material, the packaging parts (frame, carter, nut carrier, strut) can weigh between 500 g and 1 kg, increasing the total weight around 2 kg at maximum per EMA, so 10 kg at maximum for all the EMAs.

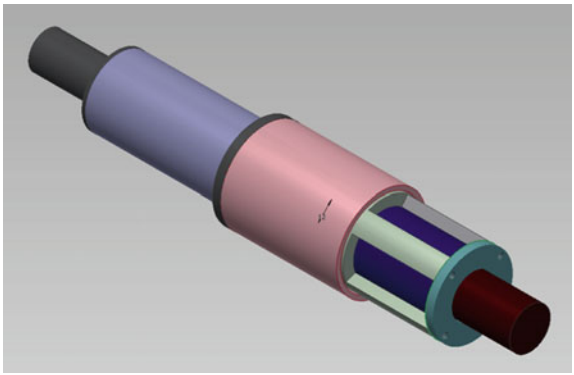

**Fig. 7** Complete electromechanical actuator

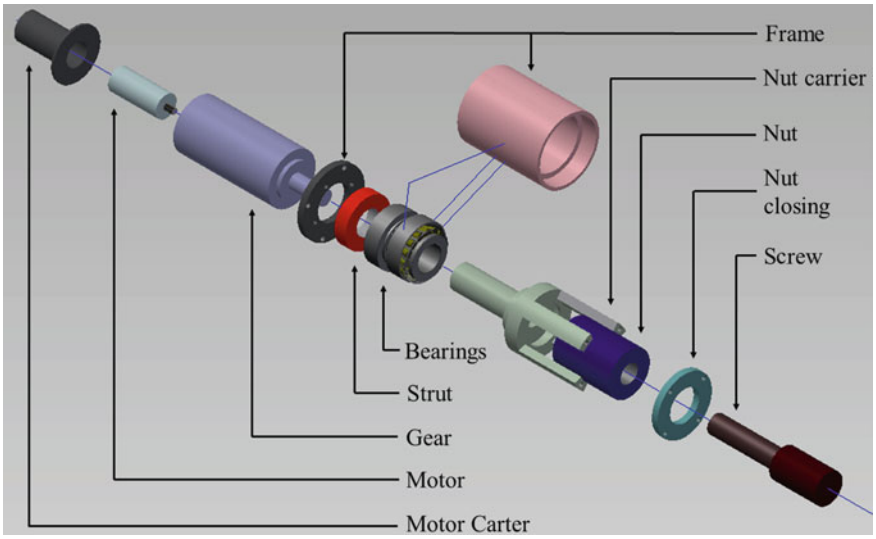


**Fig. 8** Detail of electromechanical actuator

## *4.2 Close Control Strategy*

The general camber control is not described here as it is a part of a more complexe research work, linked with aerodynamic seached profiles. However, the camber control of the wing depends on the angle control of each hinge, which is directly determined by the motion and the position of the screw, and so the linear force it provides. In this way, a close control of the torque of the motor is proposed, like in [21].

As there is a real space and weight constraint, we planned to keep a full analog close control in order to reduced to a minimum the complixity of the electronics. The reference torque ($I_{set}$) of each motor will be calculated in a central control command

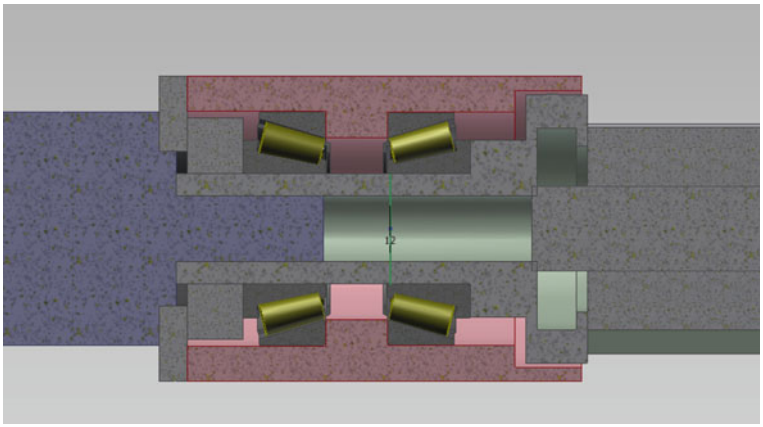

**Fig. 9** Force distribution with bearings

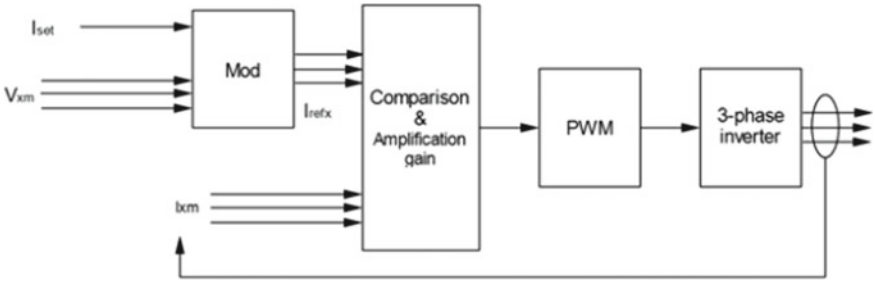


**Fig. 10** Close control diagram

strategy while each motor has a driver torque close control. The driver Torque Control strategy is described in Fig. 10 diagram.

The current set-point $I_{set}$ is provided by the central electronics and serves as a modulation for the position sensor signals ($V_{h_{1m}}$, $V_{h_{2m}}$ and $V_{h_{3m}}$) generically called $V_{h_{xm}}$. The result of the modulation is the variation in the magnitude of the $V_{h_{xm}}$ signals, thus resulting in the current reference by phase $I_{ref_x}$. A comparison to the actual value of each phase current, $I_{xm}$, is performed and corrected with an amplification gain. The resulting signals ($\alpha_x$) are directly used as current reference to be compared to a carrier in a full Pulse-Width Modulation (PWM) strategy. Finally, the resulting gate signals are sent to a 3-phase inverter with integrated drivers.

The torque close control is included in a larger speed control loop. Then, thanks to a incremental encoder in the motor, it is possible to get the position of the screw from the radial position of the motor rotor, taking into acount the differents plays in the EMA (gear and screw and nut connexion).

## 5 Conclusions

The designed electromechanical actuators produce enough force to actuate the camber of the flap. They consist in the complex integration of a permanent magnet synchronous motor, a planetary gearbox and a screw and nut tranmission. In this way, the output motor torque is producing a linear force on the screw. Each EMA use a specific leverage to articulate the parts on both sides of its hinge. Therefore, the angle of each hinge is controled by the screw thread, and so the motor rotation. A close torque control of the motor is presented. The torque control can easily give the position control of the screw.

Nevertheless, the global control of the camber is a part of another research subject in the SMS european project. It links all the actuators together in order to have a global motion, fitting the camber with specific profiles. By controling the profile camber of the flap, and even of a larger wing, the fuel consumption will decrease as the flap (or wing) morphing is adapted to flight conditions.

## References

1. Barbarino, S., Bilgen, O., Ajaj, R.M., Friswell, M.I., Inman, D.J.: A review of morphing aircraft. J. intell. Mater. Syst. Struct. **22**(9), 823–877 (2011)
2. Bernot, A., Giraud, A., Lefèvre, Y., Llibre, J.-F.: Experimental study of iron losses generated by a uniform rotating field. IEEE Trans. Magn. **53**(11), 1–5 (2017)
3. Bertotti, G.: General properties of power losses in soft ferromagnetic materials. IEEE Trans. Magn. **24**(1), 621–630 (1988)
4. Boglietti, A., Cavagnino, A., Tenconi, A., Vaschetto, S., di Torino, P.: The safety critical electric machines and drives in the more electric aircraft: a survey. In: 35th Annual Conference of IEEE Industrial Electronics, IECON'09, pp. 2587–2594. IEEE (2009)
5. Fitan, E., Messine, F., Nogarede, B.: The electromagnetic actuator design problem: A general and rational approach. IEEE Trans. Magn. **40**(3), 1579–1590 (2004)
6. Gerada, C., Bradley, K.J.: Integrated PM machine design for an aircraft EMA. IEEE Trans. Ind. Electron. **55**(9), 3300–3306 (2008)
7. Giraud, A., Bernot, A., Lefevre, Y., Llibre, J-F.: Modeling quasi-static magnetic hysteresis: a new implementation of the play model based on experimental asymmetrical b (h) loops. In: 2016 XXII International Conference on Electrical Machines (ICEM), pp. 1895–1901. IEEE (2016)
8. Jac, J., Matt, D., Ziegler, N., Enrici, P., Martire, T.: Electromagnetic actuator with high torque mass ratio. permanent magnet machine with synchronous and Vernier double effect. Application to aeronautical systems. In: International Aegean Conference on Electrical Machines and Power Electronics, ACEMP'07, pp. 81–86. IEEE (2007)
9. Jani, J.M., Leary, M., Subic, A., Gibson, M.A.: A review of shape memory alloy research, applications and opportunities. Mater. Des. (1980–2015) **56**, 1078–1113 (2014)
10. Jodin, G., Scheller, J., Duhayon, E., Rouchon, J.F., Braza, M.: Implementation of a hybrid electro-active actuated morphing wing in wind tunnel. In: Solid State Phenomena, vol. 260, pp. 85–91. Trans Tech Publications (2017)
11. Lyu, Z., Martins, J.R.R.A.: Aerodynamic shape optimization of an adaptive morphing trailing-edge wing. Journal of Aircraft **52**(6), 1951–1970 (2015)
12. Macmillan, R.H.: Epicyclic gear efficiencies. Engineer **23**, 727–728 (1949)

13. Moses, A.J., Leicht, J.: Power loss of non oriented electrical steel under square wave excitation. IEEE Trans. Magn. **37**(4), 2737–2739 (2001)
14. Pecora, R., Amoroso, F., Magnifico, M.: Toward the bi-modal camber morphing of large aircraft wing flaps: the cleansky experience. In: Industrial and Commercial Applications of Smart Structures Technologies 2016, vol. 9801, p. 980106. International Society for Optics and Photonics (2016)
15. Pennestri, E., Freudenstein, F.: The mechanical efficiency of epicyclic gear trains. J. Mech. Design **115**(3), 645–651 (1993)
16. Pfister, P.-D., Perriard, Y.: Very-high-speed slotless permanent-magnet motors: analytical modeling, optimization, design, and torque measurement methods. IEEE Trans. Ind. Electron. **57**(1), 296–303 (2010)
17. Roboam, X., Sareni, B., De Andrade, A.: More electricity in the air: toward optimized electrical networks embedded in more-electrical aircraft. IEEE Ind. Electron. Mag. **6**(4), 6–17 (2012)
18. Rosero, J.A., Ortega, J.A., Aldabas, E., Romeral, L.A.R.L.: Moving towards a more electric aircraft. IEEE Aerosp. Electron. Syst. Mag. **22**(3), 3–9 (2007)
19. SKF: Roller Screws Catalog. PUB MT/P1 14489 EN (2014)
20. Tumanski, S.: Handbook of Magnetic Measurements. CRC Press (2016)
21. Zhong, L., Mr. Rahman, F., Hu, W.Y., Lim, K.W.: Analysis of direct torque control in permanent magnet synchronous motor drives. IEEE Trans. Power Electron. **12**(3), 528–536 (1997)
22. Ziegler, N., Matt, D., Jac, J., Martire, I., Enrici, P.: High force linear actuator for an aeronautical application. association with a fault tolerant converter. In: ACEMP'07. International Aegean Conference on Electrical Machines and Power Electronics, pp. 76–80. IEEE (2007)

# Numerical Study of Trailing-Edge Dynamics of a Two Element Airfoil-Flap with Morphing Flap at High Reynolds Number


**A. Marouf, N. SImiriotis, J. B. Tô, Y. Bmegaptche, Y. Hoarau, J. F. Rouchon, and M. Braza**

**Abstract** This article examines the morphing effect of trailing-edge flap of high lift configuration at the take-off position. It includes vibrations with different frequencies and amplitudes around the supercritical Airbus A320 wing-flap. The Reynolds number is 2.25 million and the angle of attack 8.2° which corresponds to take-off and landing phases. The flap deflection angle from its initial position is 10° and translated with 30 cm horizontally from the main wing. The results have been validated with numerical data [1] that worked on a similar two-element wing named GA (W) 2. In the present study, we show through spectral analysis and Proper Orthogonal Decomposition (POD the influence on the wake's width and on the aerodynamic performances, on the predominant frequencies and instabilities.

**Keywords** Electroactive morphing · Vibration · Trailing-edge · Simulation · Wings · Aerodynamic

## 1 Introduction

Trailing-edge high-lift devices have been widely used on many kinds of aircraft previously. The structure-deformation technology has also been regarded as promising in the field of aircraft design. Traditional high-lift devices have a precedent of using the concept of deformation, which is mainly applied to the rear of wing, in order to improve the performance of takeoff and landing and this concept enables the manipulation of the near-region turbulence enhancing specific beneficial structures

A. Marouf (✉) · Y. Hoarau
ICUBE, Strasbourg, France
e-mail: amarouf@unistra.fr

A. Marouf · N. SImiriotis · J. B. Tô · Y. Bmegaptche · M. Braza
IMFT, Toulouse, France

J. F. Rouchon
LAPLACE, Toulouse, France



M. Braza et al. (eds.), *Advances in Critical Flow Dynamics Involving Moving/Deformable Structures with Design Applications*, Notes on Numerical Fluid Mechanics and Multidisciplinary Design 147,
https://doi.org/10.1007/978-3-030-55594-8_37

in the wake. In this way and thanks to the introduction of smaller-scale chaotic turbulent vortices, breaking down or suppression of preexisting predominant instability modes can be achieved. This study is a part of electroactive morphing activities in the context of the SMS (Smart Morphing and Sensing) European project (www.smartwing.org/SMS/EU). It includes numerical simulations and physical analysis issued from the hybrid morphing, operating different time scales and associating different smart actuation approaches. This article focuses on the high-lift flap in take-off configuration of Airbus A320 at high Reynolds number, using adopted turbulence modelling. This design using smart material properties in interaction with fluid flow aims at simultaneously increasing the lift, reducing the drag and the aerodynamic noise of the aircraft wings of the future. The morphing applied is partly bio-inspired. Optimal vibration and slight deformation of the trailing edge region by using smart piezo-actuators have been studied. The camber control is achieved by shape memory alloys operating at low frequencies (order of 1 Hz), whereas the trailing-edge vibration are of higher order (100–500 Hz). The association of both actuations concerns the hybrid morphing [2]. The actuation of MFC (Micro-Fiber Composite) piezo-patches in the trailing edge region [2] is simulated by using an amplitude of the vibration at 0.35 mm and a frequency range of [20–500 Hz]. The access to ongoing experimental studies in our research team contributes to the understanding of the physics and the performance of morphing. The study uses advanced numerical simulation approaches implemented in our research team and used elsewhere in the European research institutes and aeronautical industry. A first part of the study concerns simulations of the two-element A320 wing-flap in the take-off configuration with vibrating trailing edge is performed which optimal actuations will be accessed in relation to the fixed objectives in association with the experimental large-scale morphing prototype of the SMS project in full scale.

## 2 Numerical Method and Turbulence Modelling

### *2.1 Flow Configuration*

The subsonic flow over the A320 wing in the Take-off position is investigated numerically at a free-stream Mach number in the range of 0.032 and a chord-based Reynolds number of 2.25 Mio. The A320 has a main wing and a flap, the total chord for the large scale is 2.72 m. An angle of attack is chosen $\alpha = 8.2°$ that corresponds exactly to high angles of taking-off configurations. The wind tunnel properties have the same properties as the numerical. The wing was mounted wall-to-wall in the wind tunnel S4 of IMFT by Y. Bmegapche Tekap. We simulated the flow in 2D domain and compared the numerical results to numerical results of GA(w)-2 airfoil [1] which is a similar wing as the A320.

## 2.2 Numerical Methods

The simulations of the A320 airfoil in the Take-off position have been carried out with the Navier-Stokes Multi-Block (NSMB) [3] solver. The NSMB solver is the fruit of a European consortium that included Airbus from the beginning of '90s, as well as main European aeronautics research Institutes, as KTH, EPFL, IMFT, ICUBE, CERFACS, Univ. of Karlsruhe, ETH-Ecole Polytechnique de Zurich, among other. This consortium is coordinated by CFS Engineering in Lausanne, Switzerland. NSMB is a structured code that includes a variety of efficient high-order numerical schemes and of turbulence modelling closures in the context of LES, URANS and of hybrid turbulence modelling. A first reference of the code description can be found in [4] concerning the versions of this code in the decade of '90s. Since then, NSMB highly evolved up to now and includes an ensemble of the most efficient CFD methods, as well as adapted fluid–structure coupling for moving and deformable structures. These developments can be found in [5] regarding URANS modelling for strongly detached flows [6], in the area of moving body configurations [7] and [8] allowing for Detached Eddy Simulation with the NSMB code. NSMB solves the compressible Navier–Stokes equations using a finite-volume formulation on multi-block structured grids.

## 2.3 Multiblock Grid

Two 2D normal and finer multiblock grids built in our research team have a C-H topology and a size of 0.5 and 0.6 M cells approximately (Fig. 1). The grids have been tested in NSMB. A comparison of these two grids for the pressure coefficients with the experimental results is provided. The results are very similar for the two grids. The refined grid has been used for this study.

In addition, a Chimera grid that contains two independent grids, the first grid is the fluid domain including the wing and the second one is around the flap Fig. 2. The Chimera is used for optional configurations of Take-off and Landing where the flap changes its deflection angle from 10° to 40°.

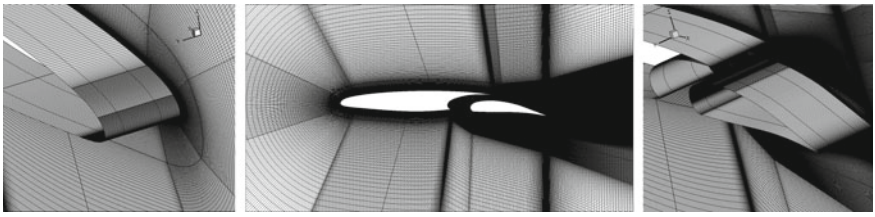

**Fig. 1** Presentation of the refined grid

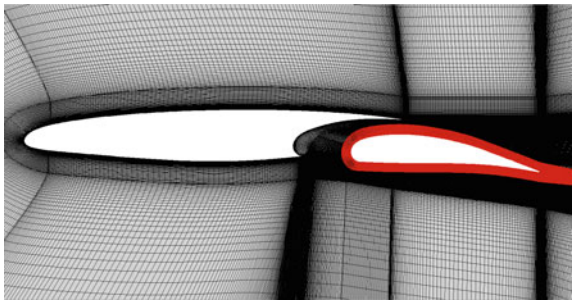

**Fig. 2** Presentation of Chimera grid

The $y^+$ length regarding the turbulence modelling near the wall is smaller than 0.5 in the whole domain.

In order to take into account, the movement of the geometry or the deformation over time, the ALE (Arbitrary Lagrangian Eulerian) formulation was introduced into the Navier-Stokes equations. The ALE formulation is particularly well suited for taking dynamic meshing into account [9]. The formulation adopted in the NSMB code adapts to discretized conversational equations using the finite volume method. The motion and slight deformation of the near-trailing edge region with a frequency of the vibration $f$ and the amplitude.

## *2.4 Results Validation*

Different cases have been studied and investigated to find the right approximation to experimental results, different grids, time stepping for a low Mach number (compressible schemes).

A study of the time step has been carried out for the 2D grid. After testing values of $\Delta t = 10^{-3}, 10^{-4}$ and $10^{-5}$ s, we continued the simulations with $10^{-5}$ that was

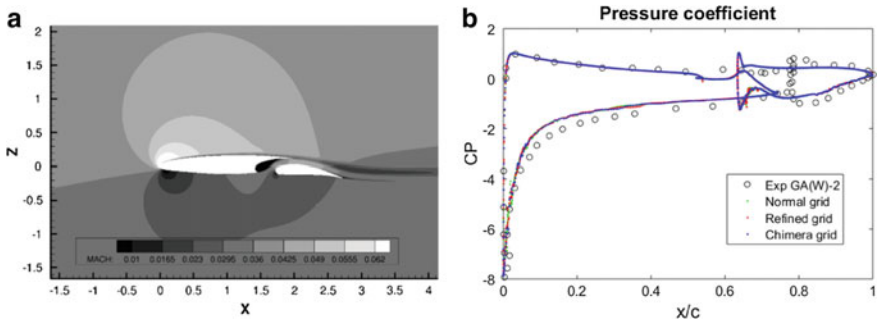


**Fig. 3** **a** Schematic diagram of the non-dimensional velocity Mach number. **b** Presentation of the pressure coefficient for different grid and experimental data

an optimal time for the independence of the solution in an adopted implicit method. A typical number between 60 and 100 inner steps Runge-Kutta was sufficient for the convergence in each time step. The grid independency is demonstrated in Fig. 3 by comparing both of normal and refind meshes, and the numerical solution is very approximate to the experiment data of GA (w) 2 airfoil Fig. 3, the only difference between both of A320 airfoil and GA (W) 2 is the thickness of the wing and the GA (W) 2 has a smaller flap.

## *2.5 Turbulence Modelling*

Based on previous studies in our research group which examined the predictive ability of various turbulence models [10, 11], it was shown that the two-equation $k - \varepsilon$ model (Chien model 1982) was not able to produce the instability and the unsteadiness at the present incidence value. The OES (Organised-Eddy Simulation), Bourguet et al. [10] provides a quite good flow detachment dynamics including the separated shear layers and wake the vortex dynamics. In the present study this turbulence modelling approach has been used and shown a clear appearance of the shear layer instability, the Kelvin-Helmholtz and von Karman vortices past the trailing edge at a first time to our knowledge concerning the two-element configuration involving a large gap between the main wing and the flap. These aspects are crucial for the modification of these dynamics thanks to morphing and are well captured by the present approach. The refined mesh has around 250 cells in 2 chords in the wake, to capture small eddies with a size around 1.5–2 cm, it explains the presence of wake instabilities shown in Fig. 4 for the static case.

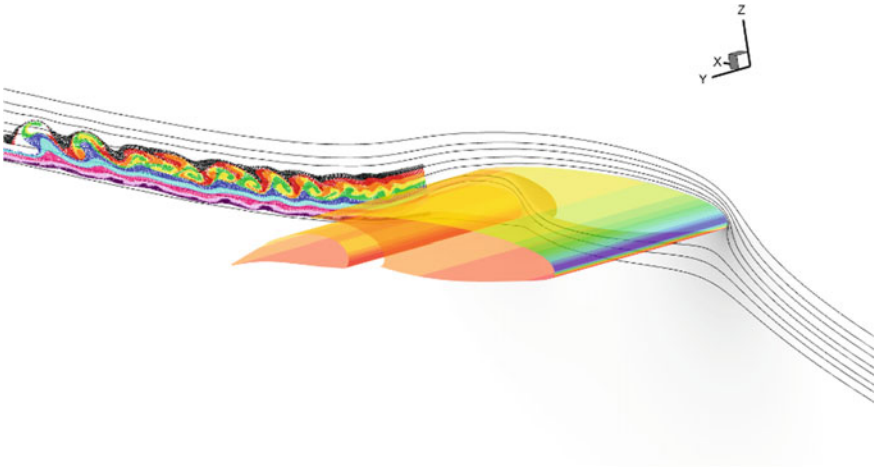


**Fig. 4** Presentation of streaklines on the wake + pressure on the surface of the A320 wing

## 3 Static Configuration Versus Morphing

The electroactive morphing applied in the experimental set-up creates vibrations of small piezo-actuators disposed long the span near the trailing edge region and able to provide small deformations (order of cm) with frequencies in the range of 100–300 Hz. It is shown in the present study that this kind of vibration has a has prominent effect on the development of vortical structures in the wake, on the wake's width and on the aerodynamic forces, as shown in the following section. The effects of the actuating case (with vibrations) compared to the static case are shown for different frequencies from a low range of 30 Hz up to a higher range of 400 Hz. The optimal results have been analysed concerning the higher-order range of the vibration frequency.

### *3.1 Wake Instabilities*

To a better understanding of the flow around the two wing-flap elements at the take-off position, we distinguish 3 elementary attached flow regions due to the presence of two objects in the flow (wing and flap), a separating area is noticed due to the presence of the gape Fig. 5. The presence of two different natural frequencies in the wake, a higher frequency of 80–90 Hz which corresponds to the turbulent structures created near to the flap and a lower frequency which is the half of the first 30 Hz that represents the bigger instabilities and structures created by the presence of the main wing Fig. 5. Drawing the streaklines Fig. 5 it is clearly seen that this frequency corresponds to Kelvin Helmholtz instability.

The understanding of the operation of vortex shedding allows their control by means of morphing. The trailing edge vibration triggers eddy blocking effects that change the wake. We compared the wake instabilities in the static and morphing cases, vibration in low frequencies and near to the natural frequencies gave a slight modification of the flow. Actuation at high frequencies has shown an interesting results Fig. 5 the vibrating the trailing edge influences the shear layer instabilities, there is an interaction between flow coming from the flap, the gap and the main wing, the actuations at 300 Hz Fig. 5 and 400 Hz can delay and suppress almost completely the formation of the Kelvin Helmholtz instabilities wake.

The signal of the crossflow velocity component is extracted for 5 points from the static and morphing cases. Figure 6 shows the wake crossflow velocity field, that exhibit the vortical structures. The monitor points are located in the wake close and far from the flap trailing edge.

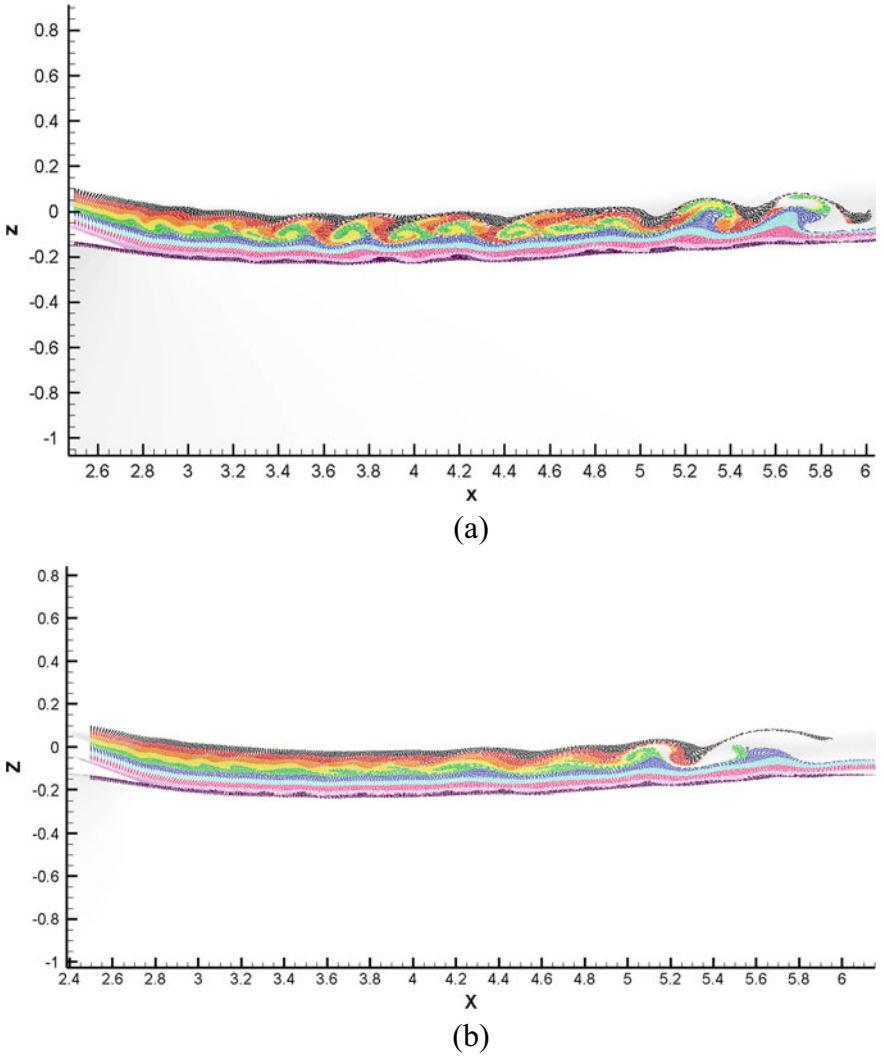


**Fig. 5** Streaklines in the wake region, **a** Static case. **b** morphing case 300 Hz

## *3.2 Modal Analysis*

The POD is applied to study the coherent structures developed in the flow and the wake specially. It was introduced at the first by Karhunen and Loweve and applied in Fluid Mechanics by Berkooz et al. [12]. The flow solution is decomposed into spatial $\phi_i$ modes and $\alpha_i$ temporal coefficients sorted by their relative energy in the flow.

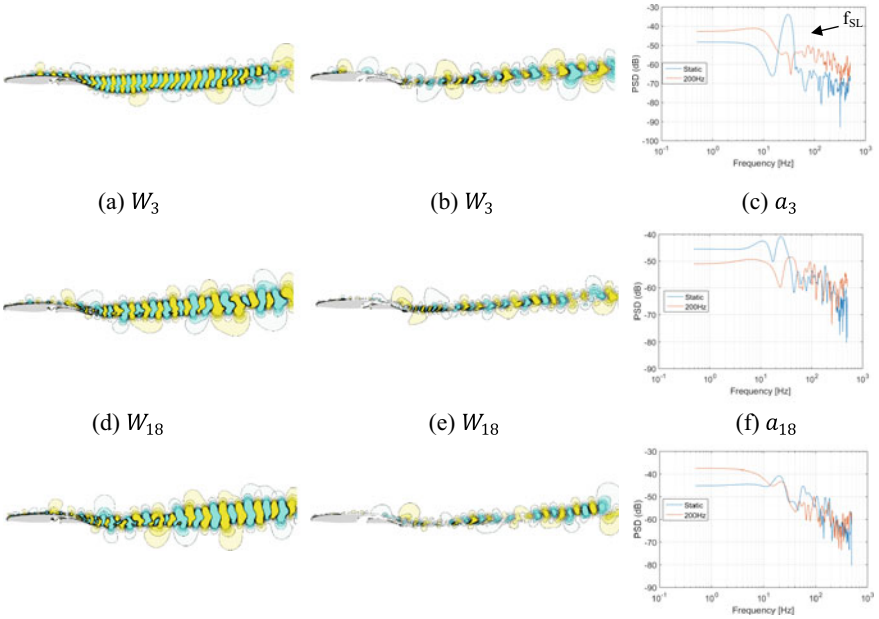


(a) $W_3$ (b) $W_3$ (c) $a_3$

(d) $W_{18}$ (e) $W_{18}$ (f) $a_{18}$

(f) $W_{27}$ (g) $W_{27}$ (h) $a_{27}$

**Fig. 6** Spatial modes and PSD ([13]) for the temporal modes computed for the crossflow velocity, the static (**a**), (**d**) and (**f**) and the morphing case (**b**), (**e**) and (**g**) at 200 Hz

The POD is applied for the crossflow velocity, the modification of the flow is highlighted when comparing the first and higher modes of the unactuated case in Fig. 6 to the cases at actuation frequencies of 200 Hz, it has shown the most prominent effects in the wake. The time step of the sampling is $10^{-3}$s which is less than inverse of the highest natural frequency on the wake. A constant number of snapshots (300) were used to construct the POD correlation matrix.

The spatial modes (shown in Fig. 6) for the unactuated and actuating case is significantly different from first to higher modes. The effect of the actuation is seen where the energy of the coherent structures in the wake is decreased, the actuation introduces additional modes which supersede the frequency of the shear layer, that was also shown by Johannes et al. [14]. In addition, the temporal coefficients (shown in Fig. 6) and their PSD such as $a_3$ underline this behaviour.

### *3.3 Mean Fields in the Wake*

The profiles of the mean axial velocity are compared for different $x/c$ positions placed respectively on the wake $x/c = 1.05$, $x/c = 1.15$, $x/c = 1.20$, $x/c = 1.40$, for the comparison of the unactuated and actuated cases (shown in Fig. 7).

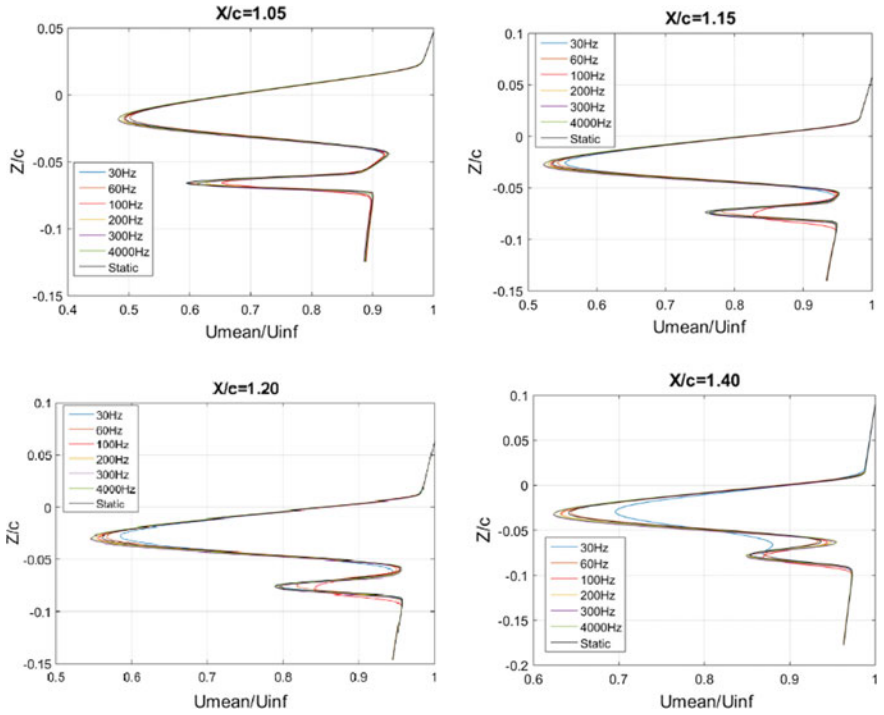


**Fig. 7** The mean longitudinal velocity profiles along the wake for various actuating frequencies

The adjacent layers coming from the flap, the gap and the main wing of fluid move parallel to each other with different speeds, it creates a shear layer due to the difference of the velocity. With an actuation frequency we can modify the behaviour of the shear layer, as shown in Fig. 7 a slight modification of the velocity profiles is visible at early *x/c* stations for low frequencies actuations as 30 Hz (near to natural frequency), but in the station $x/c = 1.40$, the region of the gap is suppressed and a mixing between the two shear layers coming from the flap and the wing. With an actuation frequency 100 Hz the changes are important and the deficit of the velocity decreases $U - U_{inf}$. Reducing this quantity causes the diminution of the shear stress $\tau = \mu.\partial u/\partial y$.

## 4 Conclusions

In this study the morphing studied by High-Fidelity numerical simulations introduces optimal vibration frequencies with a slight deformation of the flap trailing edge region. The wake dynamics are significantly affected by the application of morphing when acting in frequencies higher than the natural frequencies of the separating shear

layers. The POD has showed new modes replacing the existing of the unactuated case and the PSD that shows clearly the attenuation of the global instabilities in the wake. The aerodynamic performance are increased for some actuating cases such as for 60 Hz, the mean value of the ratio lift/drag is increased up to 1.54%, and an increase of lift of +0.57% in the case of higher frequency actuation of 300 Hz.

**Acknowledgements** The authors are grateful to the IMFT and ICUBE Laboratories, to the three national supercomputing centers: HPC-Strasbourg, CALMIP, CINES, IDRIS and CEA-HPC-TGCC for having provided a significant CPU allocation for the present study.

## References

1. Lu, W., Tian, Y., Liu, P.: Aerodynamic optimization and mechanism design of flexible variable camber trailing-edge flap. Chin. J. Aeronaut.**30**(3), 988–1003 (2017)
2. Jodin, G., Motta, V., Scheller, J., Duhayon, E., Doll, C., Rouchon, J.F., Braza, M.: Dynamics of hybrid morphing wing with active open loop vibrating trailing edge by time-resolved PIV and force measures. J. Fluids Struct. **74**, 263–290 (2017)
3. Hoarau, Y., Pena, D., Vos, J.B., Charbonier, D., Gehri, A., Braza, M., Deloze, T., Laurendeau, E.: Recent developments of the Navier Stokes multi block (NSMB) CFD solver. In: 54th AIAA Aerospace Sciences Meeting. American Institute of Aeronautics and Astronautics. https://doi.org/10.2514/6.2016-2056
4. Vos, J., Rizzi, A., Corjon, A., Chaput, E., Soinne, E.: Recent advances in aerodynamics inside the NSMB (Navier Stokes Multi Block) consortium. 36th AIAA Aerospace Sciences Meeting and Exhibit (1998)
5. Hoarau, Y.: Analyse physique par simulation numérique et modélisation des écoulements décollés instationnaires autour de surfaces portantes. Thèse de doctorat dirigée par Braza, Marianna Dynamique des fluides (2002)
6. Martinat, G., Braza, M., Hoarau, Y., Harran, G.: Turbulence modelling of the flow past a pitching NACA 0012 airfoil at and Reynolds numbers. J. Fluids Struct. **24**(8), 1294–1303 (2008)
7. Barbut, G., Braza, M., Hoarau, Y., Barakos, G., Sévrain, A., Vos, J. B.: Prediction of transonic buffet around a wing with flap. In: Progress in Hybrid RANS-LES Modelling, 191–204. Springer, Berlin, Heidelberg (2010)
8. Grossi, F., Braza, M., Hoarau, Y.: Prediction of transonic buffet by delayed detached-eddy simulation. AIAA J. **52**(10), 2300–2312 (2014)
9. Donea, J., Giuliani, S., Halleux, J.P.: An arbi- trary lagrangian-eulerian finite element method for transient dynamic fluid-structure interactions. Comput. Methods Appl. Mech. Eng. **33**(1), 689–723 (1982)
10. Bourguet, R., Braza, M., Harran, G., El Akoury, R.: Anisotropic organised Eddy simulation for the prediction of non-equilibrium turbulent flows around bodies. J. Fluids Struct. **24**(8), 1240–1251 (2008)
11. Szubert, D., Grossi, F., Jimenez Garcia, A., Hoarau, Y., Hunt, J.C.R., Braza, M.: Shock-vortex shear-layer interaction in the transonic flow around a supercritical airfoil at high Reynolds number in buffet conditions. J. Fluids Struct. 55, 276–302 (2015)
12. Berkooz, G., Holmes, P., Lumley, J.L.: The proper orthogonal decomposition in the analysis of turbulent flows. Ann. Rev. Fluid Mech. **25**(1), 539–575
13. Welch, P.D.: The use of fast Fourier transform for the estimation of power spectra: a method based on time averaging over short, modified periodograms. IEEE Trans. Audio Electroacoust. **15**(2), 70–73 (1967)

14. Scheller, J., Chinaud, M., Rouchon, J.F., Duhayon, E., Cazin, S., Marchal, M., Braza, M.: Trailing-edge dynamics of a morphing NACA0012 aileron at high Reynolds number by high-speed PIV. J. Fluids Struct. **55**, 42–51 (2015)

# The Passive Separation Control of an Airfoil Using Self-adaptive Hairy Flaps


**Chunlin Gong, Zhe Fang, Gang Chen, Alistair Revell, Adrian Harwood, and Joseph O'Connor**

**Abstract** In recent years, researchers have found that separation control could increase the mean lift, decrease the drag, delay stall, reduce noise and influence the transition to turbulence, which has a significant economic and ecological impact on society, and it has been used extensively in the design of unmanned aerial vehicles (UAVs) and micro aerial vehicles (MAVs), which operate at low Reynolds numbers. In this paper, the passive separation control of a NACA0012 airfoil at Reynolds number $\mathrm{Re} = 1000$ using self-adaptive hairy flap is investigated. The fluid motion is obtained by solving the discrete lattice Boltzmann equation, the dynamics of the flaps are calculated by the finite element method (FEM), and the coupling of flap dynamics and flow dynamics is handled by the immersed boundary method (IBM). Aerodynamic performance is quantified by the mean drag and mean lift of the NACA0012 airfoil. The influence of the flap parameters (quantity, length, rigidity and position)

C. Gong (✉) · Z. Fang
Shaanxi Aerospace Flight Vehicle Design Key Laboratory, School of Astronautics, Northwestern Polytechnical University, Xi'an, Shaanxi, China
e-mail: leonwood@nwpu.edu.cn

Z. Fang
e-mail: fangzhe@mail.nwpu.edu.cn

G. Chen
State Key Laboratory for Strength and Vibration of Mechanical Structures, School of Aerospace, Xian Jiaotong University, Xi'an, Shaanxi, China
e-mail: aachengang@xjtu.edu.cn

A. Revell · A. Harwood · J. O'Connor
School of Mechanical, Aerospace and Civil Engineering, University of Manchester, Manchester, UK
e-mail: alistair.revell@manchester.ac.uk

A. Harwood
e-mail: adrian.harwood@manchester.ac.uk

J. O'Connor
e-mail: joseph.oconnor@manchester.ac.uk



M. Braza et al. (eds.), *Advances in Critical Flow Dynamics Involving Moving/Deformable Structures with Design Applications*, Notes on Numerical Fluid Mechanics and Multidisciplinary Design 147,
https://doi.org/10.1007/978-3-030-55594-8_38

on the aerodynamic performance is investigated and a mean drag reduction and lift increment under a certain circumstance are observed.

**Keywords** Passive separation control · Lattice Boltzmann · Immersed boundary · Finite element method

## 1 Introduction

Due to their high flight efficiency, high maneuverability and low flight noise, unmanned aerial vehicles (UAVs) and micro aerial vehicles (MAVs) are becoming more and more popular and have been applied in many areas. However, these aircraft usually operate at low Reynolds numbers and high angles of attack, causing many related challenges in their design, an important one being the control of flow boundary-layer separation [1]. To solve this issue, people have proposed many biomimetic methodologies by observing that some birds pop-up their feathers when flow separation starts to develop on the upper side of their wings. Liebe [2] and Carruthers et al. [3] interpreted this self-adjusting behaviour as a biological high-lift device and assumed that a delay in flow separation resulted in higher lift at lower flight speeds. Using a wind tunnel, Meyer et al. [4] demonstrated that the lift of an airfoil (HQ17) would increase about 10% in nominally stalled conditions by setting self-deploying flexible flaps on its suction side. Similar results were also observed by Schluter [5]. Bechert et al. [6] who conducted a series of wind tunnel experiments and extensively investigated the effects of adaptive flaps mounted on the wing. Their results indicated that for a large aspect ratio wing, adaptive flaps could suppress flow separation which developed gradually from upstream of the trailing edge, enhancing the maximum lift by up to 20%. Bramesfeld and Maughmer [7] mounted small, movable tabs on the upper surface of a S824 aerofoil and tested its aerodynamic performance in a low-speed wind tunnel at a chord Reynolds number $\mathrm{Re} = 1.0 \times 10^6$. They discovered that the tabs act as pressure dams which could reduce the adverse effects of the flow separation, allowing lower pressures upstream of their location than would occur otherwise. Compared to the clean airfoil, the maximum lift coefficient could be increased by approximately 20% with these simple devices.

For the further investigation of this passive separation control mechanism, Johnston et al. [8, 9] compared the effects of free-moving and fixed flaps mounted at different deployment angles over an angle of attack range from 12° to 20°. They observed a progressive increase in the stall angle of attack with increasing flap angle, with diminishing returns beyond the effector angle of 60°. The oil flow visualization on the airfoil with and without the fixed-angle flaps proved that the effector caused the separation point to move aft on the airfoil, as compared to the clean airfoil. Bruecker and Weidner [10] investigated various configurations of self-adaptable hairy flaps located on the lower half of NACA0020 airfoil at low Reynolds number flow and

measured the flow evolution along the airfoil with and without hairy flaps in ramp-up angle of attack motion. They interpreted the stall delay as the reduction of the backflow and re-organisation of the shear layer roll-up process.

Besides the wind tunnel experiments, people have also used numerical methods to investigate passive separation control and have obtained many useful conclusions. Favier et al. [11] numerically simulated flow past a two-dimensional circular cylinder with a cilia-like hairy coating at Reynolds number $\mathrm{Re} = 200$. They found the overall drag can be reduced by 15% compared to the clean cylinder. Similar work was done by Venkataraman and Bottaro [12] who simulated a NACA0012 airfoil with hairy coatings attached to its upper surface and found that the coatings could decrease drag oscillations by approximately 11% and increase lift by approximately 9% under separated flow conditions. Rosti et al. [13] used the Navier-Stokes equations to calculate the three-dimensional turbulent flow around an NACA0020 aerofoil with hairy flaps installed on the suction side and close to the trailing edge during a ramp-up motion. In their work each flap was still modeled as a lumped 1D flexible filament.

Using a many-core fluid-structure interaction solver LUMA [14], this paper numerically investigates the influence of various hairy flaps located on the upper surface of a NACA0012 airfoil, the Reynolds number defined by chord-length of airfoil is $\mathrm{Re} = 1000$. In LUMA, the fluid motion is obtained by solving the lattice Boltzmann equation. The dynamics of the hairy flaps are calculated using the finite element method (FEM), and the interaction between fluid and structure is handled using the immersed boundary method (IBM). Aerodynamic performance is quantified by the mean drag and the mean lift of NACA0012 airfoil. And the influence of the flap parameters (length, rigidity and position) on the aerodynamic performance is investigated.

## 2 Numerical Method

This section describes the global formulations employed in LUMA to simulate the non-linear dynamics of flexible flaps which interact with a flow fluid.

### *2.1 Lattice Boltzmann Method*

Based on microscopic models and mesoscopic kinetic equations, the lattice Boltzmann method (LBM) has been proven to be a viable and efficient substitute for NS solver and put into use in many fluid-flow simulations. The evolutionary process of the LBM is simple and clear, and its computational stencil is local, making it very suitable for parallel calculations [15].

The Boltzmann equation for incompressible viscous flow is:

$$\frac{\partial f}{\partial t} + \mathbf{e} \cdot \nabla_{\mathbf{x}} f + \mathbf{F} \cdot \nabla_{\mathbf{e}} f = \Omega_f \tag{1}$$

where $f$ is the distribution function of the particles located at spatial coordinate $\mathbf{x}$ and time $t$ with velocity $\mathbf{e}$. The force term $\mathbf{F}$ accounts for any external force applied to the fluid, $\Omega_f$ represents the collision operator which includes a non-linear distribution function term $f$. The collision operator can be simplified using the Bhatnagar, Gross, and Krook (BGK) approach [16], which is given by:

$$\Omega_f = \frac{1}{\tau}\left(f^{(eq)} - f\right) \tag{2}$$

where $\tau$ is the single relaxation time parameter related to the kinematic viscosity of the fluid $\upsilon$, and $f^{(eq)}$ is the equilibrium distribution function obtained by a Taylor series expansion of the Maxwell-Boltzmann equilibrium distribution [17].

Equation (1) can be discretised in time and space, and solved on a uniform Cartesian mesh. At each point on the mesh, each particle is assigned one of a finite number of discrete velocity values. In our case we use the D2Q9 model, which refers to two-dimensional and nine discrete velocities, referred to by subscript $\alpha$.

For the discretization of the external forcing term $\mathbf{F}$, we use the representation proposed by Guo et al. [18] which accounts for the contribution of the additional force to the momentum and momentum flux. The expression can be written as:

$$F_\alpha = \left(1 - \frac{1}{2\tau}\right) w_\alpha \left[\frac{\mathbf{e}_\alpha - \mathbf{u}}{c_s^2} + \frac{\mathbf{e}_\alpha \cdot \mathbf{u}}{c_s^4}\mathbf{e}_\alpha\right] \cdot \mathbf{f} \tag{3}$$

where $c_s = 1/\sqrt{3}$ is the speed of sound, $w_\alpha$ are the weight coefficients, which take standard values [15], $\mathbf{f}$ is the force density acting on the fluid.

## 2.2 The Immersed Boundary Method

The immersed boundary method uses independent grids to discretize the fluid and structure separately. The fluid is discretized by a set of Eulerian points, which are the fixed, regular Cartesian lattice points, while the boundary of the structure immersed in the fluid is discretized by a set of markers, which are called Lagrangian points [19]. The predicted velocity **u*** simulated by the fluid in the absence of the structure is interpolated onto the embedded geometry of the obstacle, $\Gamma$, discretized using Lagrangian marker points with coordinates $\mathbf{X}_k$:

$$\mathbf{U}^*\left(\mathbf{X}_k, t^n\right) = \Im\left(\mathbf{u}^*\right) \tag{4}$$

Knowing the velocity $\mathbf{U}^*(\mathbf{X}_k, t^n)$ at the location of the Lagrangian markers, a distribution of singular forces that restore the desired velocity $\mathbf{U}^d(\mathbf{X}_k, t^n)$ on $\Gamma$ is

determined as:

$$\mathbf{F}^*\left(\mathbf{X}_k, t^n\right) = \frac{\mathbf{U}^d(\mathbf{X}_k, t^n) - \mathbf{U}^*(\mathbf{X}_k, t^n)}{\Delta t} \tag{5}$$

The singular surface force field given over $\Gamma$ is then transformed by a spreading operator $\Pi$ into a volume force-field defined on the Cartesian mesh points $\mathbf{x}_{i,j}$ surrounding $\Gamma$:

$$\mathbf{f}^*\left(\mathbf{x}_{i,j}, t^n\right) = \Pi\left[\mathbf{F}^*\left(\mathbf{X}_k, t^n\right)\right] \tag{6}$$

In the case of the lattice Boltzmann method, the force $\mathbf{f}^*\left(\mathbf{x}_{i,j}, t^n\right)$ is used directly as $\mathbf{f}$ in Eq. (3) to correct the flow field.

## 2.3 Model of Flexible Flap

The dynamic FEM is introduced as the structural solver to obtain the dynamic response of flexible flaps. In addition, the geometrical non-linearity is also taken into consideration. In the non-linear dynamic FEM, the kinetic equation of flexible flap can be written as:

$$\mathbf{M}\ddot{\mathbf{X}}(t) + \mathbf{C}\dot{\mathbf{X}}(t) + \mathbf{F}_{int}(\mathbf{X}) - \mathbf{F}_{ext}(t) = 0 \tag{7}$$

where $\mathbf{X}$, $\dot{\mathbf{X}}$ and $\ddot{\mathbf{X}}$ represent the displacement, velocity and acceleration of boundary points (Lagrangian points), respectively. $\mathbf{M}$ and $\mathbf{C}$ are the mass and damping matrices of flap. $\mathbf{F}_{int}$ represents the internal force of flap, and it is a non-linear function of the displacement $\mathbf{X}$. $\mathbf{F}_{ext}(t)$ represents the external forces such as the fluid force and gravity acting on the flap.

Equation (7) can be solved by the Newmark-β method [20] which is also an implicit method. In this method, the acceleration and velocity of flap can be written as:

$$\begin{aligned} \ddot{\mathbf{X}}_{t+\Delta t} &= c_0(\mathbf{X}_{t+\Delta t} - \mathbf{X}_t) - c_2\dot{\mathbf{X}}_t - c_3\ddot{\mathbf{X}}_t \\ \dot{\mathbf{X}}_{t+\Delta t} &= c_1(\mathbf{X}_{t+\Delta t} - \mathbf{X}_t) - c_4\dot{\mathbf{X}}_t - c_5\ddot{\mathbf{X}}_t \end{aligned} \tag{8}$$

where $c_{\mathrm{n}}$ are six variables which are related to the accuracy and stability requirements of this method.

In order to obtain the displacement of flap at time $t + \Delta t$, we use the Newton-Raphson method to process the non-linear item $\mathbf{F}_{\mathrm{int}}(\mathbf{X})$ in Eq. (7). In this method, we assume that the non-linear internal force of flap $\mathbf{F}_{\mathrm{int}}$ at time $t + \Delta t$ can be expressed as:

$$\mathbf{F}_{int,t+\Delta t} = \mathbf{F}_{int,t} + \frac{\partial \mathbf{F}_{int}}{\partial \mathbf{X}} \Delta \mathbf{X} = \mathbf{F}_{int,t} + K_{T,t} \Delta \mathbf{X} \tag{9}$$

where $K_T$ is the global tangent stiffness matrix of the flap.

The final iteration expression of Eq. (7) can be written as:

$$\begin{aligned} \left[K^i_{T,t+\Delta t} + c_0\mathbf{M} + c_1\mathbf{C}\right]\Delta \mathbf{X}^{i+1} &= F_{ext,t+\Delta t} - F^i_{\text{int},t+\Delta t} \\ &- \mathbf{M}\left[c_0\left(\mathbf{X}^i_{t+\Delta t} - \mathbf{X}_t\right) - c_2\dot{\mathbf{X}}_t - c_3\ddot{\mathbf{X}}_t\right] \\ &- \mathbf{C}\left[c_1\left(\mathbf{X}^i_{t+\Delta t} - \mathbf{X}_t\right) - c_4\dot{\mathbf{X}}_t - c_5\ddot{\mathbf{X}}_t\right] \end{aligned} \tag{10}$$

Because $K_T$, $\mathbf{M}$ and $\mathbf{C}$ are symmetric matrices, the above iteration can be solved by the triangular decomposition method. When the above iteration converges, the displacement of flap $\mathbf{X}_{t+\Delta t}$ can be obtained. Substituting $\mathbf{X}_{t+\Delta t}$ into Eq. (8), the acceleration $\ddot{\mathbf{X}}_{t+\Delta t}$ and velocity $\dot{\mathbf{X}}_{t+\Delta t}$ of flap can also be obtained.

## 3 Results and Discussion

In this section, the flow around a NACA0012 airfoil with and without hairy flaps is investigated, and the effects of flaps with different lengths and positions on aerodynamic performance, quantified by the overall mean lift and drag coefficients, is analyzed.

### *3.1 Flow Over a NACA0012 Airfiol*

The first case studies the unsteady flow around a NACA0012 airfoil at Re = 1000 and AoA = 10°, which has been investigated extensively in the literature. The Strouhal number $St$ is defined as $St = f_{\mathrm{D}}\mathrm{c}/U_\infty$, where $f_{\mathrm{D}}$ is the shedding frequency, c is the chord length of airfoil, $U_\infty$ is the free stream velocity. In the present case, the computed Strouhal number is 0.8417, which is about 2.2% smaller than the value of 0.861 reported by Falagkaris et al. [21] and the value of 0.86 reported by Johnson and Tezduyar [22].

The time evolution of the lift and drag coefficients in the present case is shown in Fig. 1a, and the time-averaged lift coefficient over the last six periods is compared with the reported values in [21, 22] in Fig. 1b. It can be seen that the present results agree well with these two references.

Figure 2 shows the boundary layer thickness around the NACA0012 airfoil and the time-averaged vorticity over six oscillation periods. From this figure, we can see that the distribution of vorticity along normal directions in present results are similar to the results reported in [21].

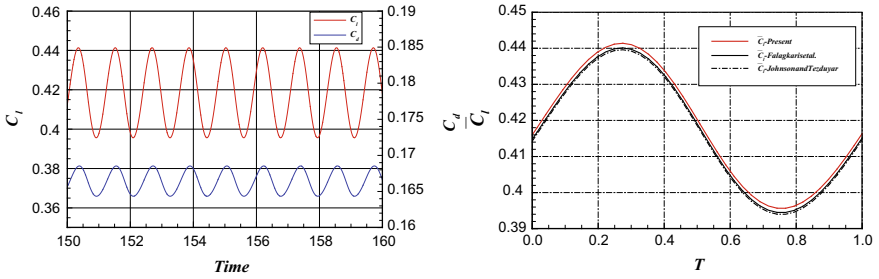


**Fig. 1** **a** Time evolution of lift and drag coefficients for the flow around a NACA0012 airfoil at Re = 1000 and AoA = 10°. **b** Averaged lift coefficient over six oscillations with period $T$

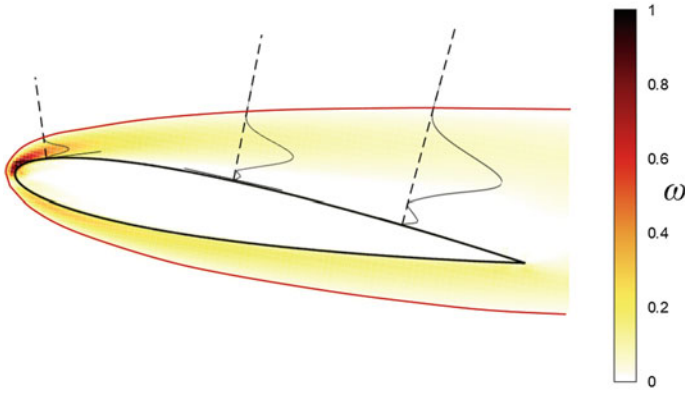


**Fig. 2** Normalized absolute vorticity field around the NACA0012 at Re = 1000 and boundary layer thickness δ (red line). The black lines show the vorticity $\omega_{\mathbf{n}l}$, scaled with the maximum value $(\omega)_{\mathbf{n}l}$, on the normal directions $\mathbf{n}_l$.

## 3.2 *Flow Over a NACA0012 Airfiol with a Rigid Fiap*

Figure 3 shows a NACA0012 airfoil with one rigid flap clamped on the suction side. Its length is $L$, the deployment angle between flap and airfoil upper surface is $\theta$, and the distance from the leading edge to the fixed end of flap measured along the chord

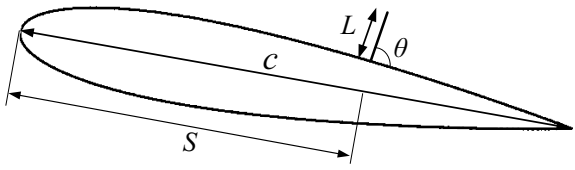


**Fig. 3** Configuration of a NACA0012 at AoA = 10° with a flap mounted on its suction side

**Table 1** The values used for length ratio $L^*$ and position ratio $S^*$

| L* | 0.04 | 0.06 | 0.08 | 0.10 | 0.12 |
|---|---|---|---|---|---|
| S* | 0.5 | 0.6 | 0.7 | 0.8 | 0.9 |

c is $S$. In this section, we investigate the effects of rigid flap length and position on aerodynamic performance.

Here we define two dimensionless parameters: the length ratio $L^* = L/c$ and the position ratio $S^* = S/c$, their values are listed in Table 1. As a preliminary calculation, the deployment angle $\theta$ is fixed at 90°.

Figure 4a, b shows the mean lift coefficients and mean drag coefficients of NACA0012 airfoil together with rigid flap in different test cases, respectively. For comparison, the results of the clean airfoil case are also included. From these two figures, it can be seen that for a rigid flap of a certain length, the closer it is to the trailing edge of airfoil, the higher the overall mean lift coefficient and the smaller the overall mean drag coefficient. When the length of flap increases, if the flap is not too close to the trailing edge ($S^* = 0.5, 0.6$), the overall mean lift coefficient decreases and the overall mean drag coefficient increases. If the flap is close to the trailing edge ($S^* = 0.7, 0.8, 0.9$), the overall mean lift coefficient increases first and then decreases. Analogously, the overall mean drag coefficient decreases first and then increases.

We can conclude that when $L^* = 0.1$ and $S^* = 0.9$, the airfoil with a rigid flap achieves its best aerodynamic performance (highest lift coefficient and smallest drag coefficient), and its performance is better than the clean airfoil. Focusing on this case, in the next step we continue to investigate the effects of deployment angles and material properties of flap on aerodynamic performance.

Figure 5 shows the mean lift and mean drag coefficients of a NACA0012 airfoil together with a rigid flap having different deployment angles $\theta$. This figure shows

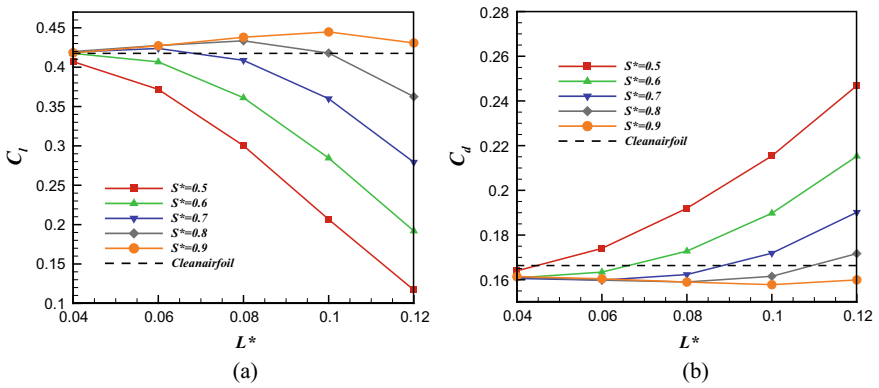


**Fig. 4** **a** The mean lift coefficients of airfoil together with rigid flap in different cases. **b** The mean drag coefficients of airfoil together with rigid flap in different cases

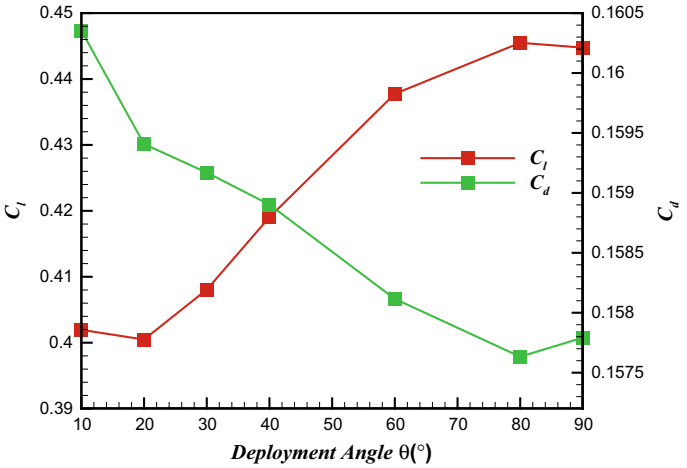


**Fig. 5** The mean lift coefficient and mean drag coefficient of NACA0012 airfoil together with rigid flap in different deployment angle cases

that when the deployment angle $\theta$ increases, the mean lift coefficient increases and mean drag coefficient decreases. At $\theta = 80°$, the airfoil and flap achieve maximum mean lift coefficient and minimum mean drag coefficient.

## *3.3 Flow Over a NACA0012 Airfiol with a Flexible Fiap*

Finally, focusing on the case $L^* = 0.1$, $S^* = 0.9$, $\theta = 80°$, we replace the rigid flap with a flexible flap and change the material properties of the flap. The values of flap density $\rho_s$ and Young's modulus $E$ used for the experiments are listed in Table 2.

Figure 6 shows the mean lift and mean drag coefficients of the NACA0012 airfoil together with flexible flap for different density $\rho_s$ and Young's modulus $E$ values. The results of the NACA0012 airfoil with the rigid flap are also included. From this figure, it can be seen that when the flap density $\rho_s$ and Young's modulus $E$ change, the overall mean lift coefficients in all case are higher than the rigid flap case. When $\rho_s = 9000$ kg/m$^3$, $E = 0.05$ MPa, the airfoil and flap achieve maximum mean lift coefficient. For the mean drag coefficients, in most cases they are higher than the rigid flap case. When $\rho_s = 4000$ kg/m$^3$, $E = 0.05$ MPa, the airfoil and flap achieve minimum mean drag coefficient.

**Table 2** The values of flap density $\rho_s$ and Young's modulus E

| $\rho_s$ (kg/m$^3$) | 1000 | 2000 | 3000 | 4000 | 5000 | 6000 | 7000 | 8000 | 9000 | 10000 |
|---|---|---|---|---|---|---|---|---|---|---|
| E (MPa) | 0.05 | 0.1 | | | | | | | | |

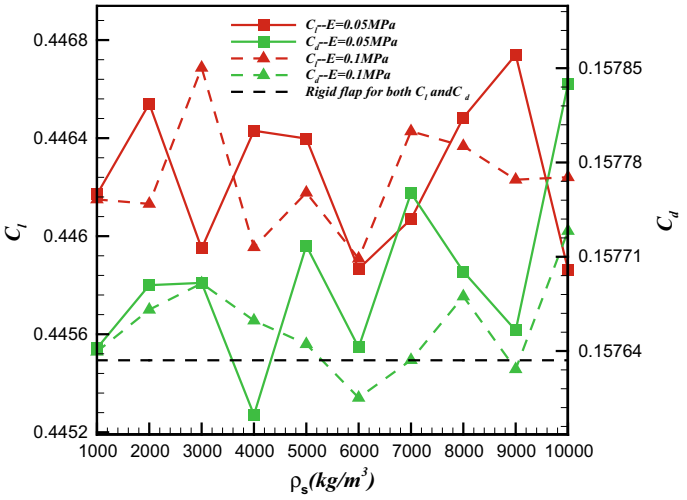


**Fig. 6** The mean lift coefficient and mean drag coefficient of NACA0012 airfoil together with flexible flap in different cases

From what is discussed above, we choose the case $\rho_s = 4000$ kg/m$^3$ and $E = 0.05$ MPa as the best case because it has the smallest mean drag coefficient and a relatively high mean lift coefficient, It also achieves a better aerodynamic performance than the rigid flap case (higher lift coefficient and smaller drag coefficient). Compared with the clean NACA0012 airfoil case, it has a 6.9% higher mean lift coefficient and a 5.27% smaller mean drag coefficient.

## 4 Conclusions

We have used the fluid-structure solver LUMA, which combines the lattice Boltzmann method, immersed boundary and finite element method, to investigate the effects of a flap mounted on a NACA0012 airfoil. The flap length, position and rigidity have been varied. For a rigid flap, the results show that when the flap is closer to the trailing edge of airfoil, the airfoil has higher mean lift and lower mean drag. When the flap is close to the trailing edge of the airfoil and its length increases, the overall mean lift coefficient increases first and then decreases, and the overall drag decreases first and then increases. When $L^* = 0.1$ and $S^* = 0.9$, the airfoil with the rigid flap achieves the best aerodynamic performance, and its performance is better than the clean airfoil. When the deployment angle $\theta$ increases, the mean lift coefficient increases and the mean drag coefficient decreases. At $\theta = 80°$, the airfoil and flap achieve a maximum mean lift coefficient and a minimum mean drag coefficient. For the flexible flap, when its density $\rho_s = 4000$ kg/m$^3$ and Young's modulus $E = 0.05$ MPa, it has better aerodynamic performance than the rigid flap

case. Compared with the clean NACA0012 airfoil case, it has a 6.9% higher mean lift coefficient and a 5.27% smaller mean drag coefficient.

**Acknowledgements** The present work was partially supported by the Fundamental Research Funds for the Central Universities of Northwestern Polytechnical University, NSFC Foundation (Grant No.1167225,No.11511130053) and the Natural Science Foundation of Shaanxi Provence (No.2016JM1007).

## References

1. Pines, Darryll, J., Bohorquez, F.: Challenges facing future micro-air-vehicle development. J. Aircraft **43**(2), 290–305 (2006)
2. Liebe, W.: Der auftrieb am tragflügel: Entstehung und zusammenbruch. Aerokurier **12**(1520), 54 (1979)
3. Carruthers, A.C., Thomas, A.L.R., Taylor, G.K.: Automatic aeroelastic devices in the wings of a steppe eagle Aquila nipalensis. J. Exp. Biol. **210**(23), 4136–4149 (2007)
4. Meyer, R., et al.: Separation control by self-activated movable flaps. AIAA J. **45**(1), 191–199 (2007)
5. Schluter, J.U.: Lift enhancement at low reynolds numbers using self-activated movable flaps. J. Aircraft **47**(1), 348–351 (2012)
6. Bechert, D.W., Hage, W., Meyer, R.: Self-actuating flaps on bird- and aircraft-wings. In: Flow Phenomena in Nature Volume 2: Inspiration, Learning and Application. DLR (2006)
7. Bramesfeld, G., Maughmer, M.D.: Experimental investigation of self-actuating, upper-surface, high-lift-enhancing effectors. J. Aircraft **39**(1), 120–124 (2002)
8. Johnston, J., Gopalarathnam, A., Edwards, J.: Experimental investigation of bio-inspired high lift effectors on a 2-D airfoil. In: 29th AIAA Applied Aerodynamics Conference, pp. 255–265 (2011)
9. Johnston, J., Gopalarathnam, A.: Investigation of a bio-inspired lift-enhancing effector on a 2D airfoil. Bioinsp. Biomimet. **7**(3), 036003 (2012)
10. Brücker, C., Weidner, C.: Influence of self-adaptive hairy flaps on the stall delay of an airfoil in ramp-up motion. J. Fluids Struct. **47**, 31–40 (2014)
11. Favier, J., et al.: Passive separation control using a self-adaptive hairy coating. J. Fluid Mech. 627 (2009), 451–483
12. Venkataraman, D., Bottaro, A.: Numerical modeling of flow control on a symmetric aerofoil via a porous, compliant coating. Phys. Fluids **24**(9), 093601 (2012)
13. Rosti, M.E., Omidyeganeh, M., Pinelli, A.: Study of flow around NACA0020 aerofoil with hairy flaps during ramp-up motion. In: European Drag Reduction and Flow Control Meeting—Edrfcm (2015)
14. Harwood, A.R.G., et al.: LUMA: a many-core, fluid–structure interaction solver based on the Lattice-Boltzmann method. Softwarex 7, 88–94 (2018)
15. Succi, S.: The Lattice Boltzmann equation—for fluid dynamics and beyond. Physics Today **55**(12), 58–60 (2002)
16. Bhatnagar, P.L., Gross, E.P., Krook, M.: A Model for Collision Processes in Gases. I. Small Amplitude Processes in Charged and Neutral One-Component Systems. Phys. Rev. **94**(3), 511–525 (1954)
17. Qian, Y.H., D'Humières, D., Lallemand, P.: Lattice BGK models for Navier-Stokes equation. Epl 17.6BIS, p. 479 (2007)
18. Guo, Z., Zheng, C., Shi, B.: Discrete lattice effects on the forcing term in the lattice Boltzmann method. Phys. Rev. E Stat. Nonlin. Soft Matter Phys. **65**(4) Pt 2B, 046308 (2002)

19. Peskin, C.S.: Flow patterns around heart valves: A numerical method. J. Comput. Phys. **10**(2), 252–271 (1972)
20. Newmark, N.M.: A method of computation for structural dynamics. Proc. ASCE **85**(1), 67–94 (1959)
21. Falagkaris, E.J., et al.: PROTEUS: a coupled iterative force-correction immersed-boundary multi-domain cascaded lattice Boltzmann solver. Comput. Math. Appl. **74**(10), 2348–2368 (2017)
22. Johnson, A.A., Tezduyar, T.E.: Mesh update strategies in parallel finite element computations of flow problems with moving boundaries and interfaces. Comput. Methods Appl. Mech. Engrg. **119**(1), 73–94 (1994)

# Dynamic Response of Wall-Mounted Flaps in an Oscillating Crossflow


**Joseph O'Connor and Alistair Revell**

**Abstract** The coupled interactions between fluids and slender structures play a number of critical roles in a broad range of physical processes. In flow control applications, poroelastic coatings consisting of arrays of passive slender structures have been shown to provide beneficial aerodynamic characteristics when applied to bluff bodies. This effect has been linked to the appearance of a travelling wave through the array which locks in to the shedding frequency of the wake. Through a simplified test case, which reduces the problem complexity while retaining the essential physics of the behaviour, the present work aims to further elucidate this phenomenon via numerical simulations. A range of array lengths are tested and the appearance and propagation of the travelling waves are monitored. The results show that for small arrays there exists one clearly defined wave, which is attributed to the advection of the primary bulk vortex over the array. However, for larger arrays, secondary vortices are generated at the tips which also induce a wave-like behaviour. These secondary vortices are smaller in size and intensity than the primary vortex and induce a smaller deflection in the flaps which dissipates quicker as it propagates though the array.

**Keywords** Fluid-structure interaction · Slender structures · Lattice Boltzmann method · Immersed boundary method · Finite element method

## 1 Introduction

The coupled interactions between fluids and slender structures play a number of critical roles in a broad range of physical processes. Cilia, for example, are ubiquitous in nature and serve several physiological functions, from cell propulsion [4] to particle regulation [15]. Moreover, the interactions between vegetation and fluid flows have

J. O'Connor (✉) · A. Revell
School of Mechanical, Aerospace and Civil Engineering, The University of Manchester, Manchester M13 9PL, UK
e-mail: joseph.oconnor@manchester.ac.uk



M. Braza et al. (eds.), *Advances in Critical Flow Dynamics Involving Moving/Deformable Structures with Design Applications*, Notes on Numerical Fluid Mechanics and Multidisciplinary Design 147,
https://doi.org/10.1007/978-3-030-55594-8_39

important consequences in terms of agriculture [3] and coastal protection [7]. A further example is in the field of biomimetics, where bioinspired designs based on slender structures are finding industrial applications in areas such as flow sensing [12] and flow control [5, 13].

The flow control capability of self-adaptive hairy coatings has been a topic of interest in several recent studies. Under the right conditions, the compliance of these coatings allows them to interact with and modify the wake pattern and shedding cycle behind bluff bodies, leading to improved aerodynamic characteristics. Favier et al. [5] developed a homogenised model to simulate such systems and noted drag reductions of 15% and reductions in the lift fluctuations of 40% under optimal conditions. These observations were later confirmed experimentally by Niu and Hu [17]. Furthermore, in the optimal regime, [5] observed a travelling wave through the array, with a frequency that matched the vortex shedding frequency. This travelling wave and its associated lock-in effect has been observed in multiple related studies [13, 16, 21], with the lock-in effect being linked to optimal aerodynamic performance.

These observations provided the motivation for the EU-funded PELskin project [6]: a consortium of partners focussed on investigating the potential flow control capability of a poroelastic (PEL) coating for aerodynamic surfaces. The aim of this project was to investigate and characterise the potential for passive slender structures to interact with bluff body wakes and improve their aerodynamic performance (e.g. reduce drag). As part of this work, a simplified test case was sought so as to reduce the complexity of the problem while still retaining the fundamental physics of the behaviour. Such a case was studied both experimentally and numerically [6, 19]. The travelling wave observed in previous studies also presented in the simplified case and a preliminary analysis suggested a link between the travelling wave and the advection of secondary vortices generated at the tips of the array. However, since the focus of the study was on examining the parameter space, this effect was not analysed in detail.

The aim of the present research is to build on the work conducted within the PELskin project. Specifically, the aim is to analyse the generation of secondary vortices at the tip of the array and how they propagate to initiate the travelling wave. Since the length of the array proved to be a limiting factor in earlier work [19], a range of array lengths (number of flaps) are tested. The case is studied numerically via a lattice Boltzmann-immersed boundary-finite element model and the resulting dynamics and behaviour are analysed in detail. The model is first validated against the experimental data from the reference case, before extending the case to explore the effect of increasing array length. Through an analysis of the flap dynamics and flow topology, the key behaviour modes are characterised and quantified and their significance is highlighted.

## 2 Methods

### 2.1 Lattice Boltzmann Method

The lattice Boltzmann method (LBM) has evolved over recent years to become an attractive alternative to the Navier-Stokes equations for certain complex flows. The LBM is derived from kinetic theory and relies on a mesoscopic description of the fluid. The driving equation behind the LBM is the Boltzmann equation, which in its discrete form is given by:

$$f_i(\boldsymbol{x} + \boldsymbol{c}_i \Delta t, t + \Delta t) - f_i(\boldsymbol{x}, t) = \frac{\Delta t}{\tau}\left[f_i^{eq}(\boldsymbol{x}, t) - f_i(\boldsymbol{x}, t)\right] + \Delta t F_i(\boldsymbol{x}, t) \tag{1}$$

where $\boldsymbol{x}$ are the spatial coordinates, $t$ is time, $\boldsymbol{c}_i$ is the $i$th component of the lattice velocity vector, and $F_i(\boldsymbol{x}, t)$ is an external force discretised on the lattice. The probability distribution function, $f_i(\boldsymbol{x}, t)$, describes the proportion of fluid molecules within an elemental volume located at $\boldsymbol{x}$ and time $t$ moving with velocity $\boldsymbol{c}_i$. The relaxation time-scale, $\tau$, is related to the (lattice) viscosity via:

$$\nu = \left(\tau - \frac{1}{2}\right) c_s^2 \Delta t \tag{2}$$

where $c_s$ is the lattice speed of sound. The equilibrium function, $f_i^{eq}(\boldsymbol{x}, t)$, is a function of local macroscopic quantities only, and can be obtained via a Taylor series expansion of the Maxwell-Boltzmann distribution [9, 10], giving:

$$f_i^{eq}(\boldsymbol{x}, t) = w_i \rho \left(1 + \frac{\boldsymbol{c}_i \cdot \boldsymbol{u}}{c_s^2} + \frac{(\boldsymbol{c}_i \cdot \boldsymbol{u})^2}{2c_s^4} - \frac{\boldsymbol{u} \cdot \boldsymbol{u}}{2c_s^2}\right) \tag{3}$$

where $w_i$ is a velocity-specific weighting factor related to the discrete lattice. The macroscopic quantities, $\rho(\boldsymbol{x}, t)$ and $\boldsymbol{u}(\boldsymbol{x}, t)$ can be calculated by taking moments of the distribution function:

$$\rho(\boldsymbol{x}, t) = \sum_i f_i(\boldsymbol{x}, t) \tag{4}$$

$$\rho \boldsymbol{u}(\boldsymbol{x}, t) = \sum_i \boldsymbol{c}_i f_i(\boldsymbol{x}, t) + \frac{\Delta t}{2} \boldsymbol{f}(\boldsymbol{x}, t) \tag{5}$$

In the present work, the force density, $\boldsymbol{f}(\boldsymbol{x}, t)$, provides the coupling between the fluid and structural dynamics. Its Cartesian form is discretised on the lattice to give [8]:

$$F_i(\boldsymbol{x}, t) = w_i \left(1 - \frac{1}{2\tau}\right)\left(\frac{\boldsymbol{c}_i - \boldsymbol{u}}{c_s^2} + \frac{\boldsymbol{c}_i \cdot \boldsymbol{u}}{c_s^4} \boldsymbol{c}_i\right) \cdot \boldsymbol{f}(\boldsymbol{x}, t) \tag{6}$$

## 2.2 Finite Element Method

The present model adopts the corotational formulation of the finite element method (FEM) to solve the structural dynamics. The main idea of the corotational formulation is to decompose the motion of each element within the assemblage into a rigid body motion and a purely deformational one [2]. Two-noded Euler-Bernoulli beam elements are used to discretise the structure. The use of such elements implies the cross sections of the structure remain rigid, so that the present model is only applicable to slender structures. Since large deformations are expected in the present work, geometric nonlinearity is handled via an incremental Newton-Raphson procedure.

Following [1], the equilibrium conditions governing the nonlinear Newton-Raphson solution are:

$$\boldsymbol{M}\ddot{\boldsymbol{U}}^{n+1,k+1} + \boldsymbol{K}^{n+1,k}\Delta\boldsymbol{U}^{k} = \boldsymbol{R}^{n+1} - \boldsymbol{F}^{n+1,k} \tag{7}$$

$$\boldsymbol{U}^{n+1,k+1} = \boldsymbol{U}^{n+1,k} + \Delta\boldsymbol{U}^{k} \tag{8}$$

where $n$ and $k$ are the time step and iteration counters, $\boldsymbol{M}$ is the mass matrix, $\boldsymbol{K}$ is the tangent stiffness matrix, $\boldsymbol{R}$ is the external load vector, $\boldsymbol{F}$ are the internal forces within the structure, $\ddot{\boldsymbol{U}}$ are the nodal accelerations, and $\Delta\boldsymbol{U}$ are the incremental nodal displacements. Second-order time stepping is achieved via the constant-average-acceleration version of the Newmark integration scheme.

## 2.3 Immersed Boundary Method

The immersed boundary method (IBM) provides the link between the fluid and structural dynamics. It relies on two separate non-conforming grids to represent the fluid and the boundary. The fluid is defined on an Eulerian grid (the lattice), which is Cartesian and fixed in space. The boundary, on the other hand, is represented on a Lagrangian grid, which is curvilinear and free to move across the computational domain. The main idea of the IBM is to mimic the effect of the boundary by introducing a source term (force) in the governing fluid equations. These forces are calculated in such a way so that the fluid feels the presence of the boundary through this force, and the no-slip condition is satisfied along the surface.

Since the two grids are separate from each other, communication between them is crucial. Moreover, since they are non-conforming, this data transfer requires specialised interpolation/spreading operators. Specifically, the momentum field must be interpolated from the fluid grid (Eulerian) to the boundary grid (Lagrangian), and the resulting forces must be spread back from the boundary grid to the fluid grid. The operators defining these communication steps are given by:

$$\Phi(\boldsymbol{X}) = \mathcal{I}[\phi(\boldsymbol{x})] = \sum_{\Omega_s} \phi(\boldsymbol{x})\ \tilde{\delta}(\boldsymbol{x} - \boldsymbol{X})\Delta x \Delta y \Delta z \tag{9}$$

$$\phi(\boldsymbol{x}) = \mathcal{S}[\Phi(\boldsymbol{X})] = \sum_{\Gamma_s} \Phi(\boldsymbol{X})\ \tilde{\delta}(\boldsymbol{x} - \boldsymbol{X})\epsilon \Delta q \Delta r \Delta s \tag{10}$$

where $\boldsymbol{x} = (x, y, z)$, $\boldsymbol{X} = (q, r, s)$, $\phi$ is a quantity defined in the Eulerian frame, $\Phi$ is the same quantity defined in the Lagrangian frame, and $\epsilon$ is a scaling factor which ensures reciprocity between the interpolation and spreading steps [18]. Here, lower-case notation denotes values in the Eulerian frame, and upper-case notation denotes values in the Lagrangian frame. The present work adopts the three-point version of the discrete Dirac Delta function, $\tilde{\delta}$, proposed by [20].

The full LBM-IBM algorithm is given by Li et al. [14] and makes use of the fact that the LBM forcing scheme [8] decomposes the velocity into a predicted and a force-corrected term [22]. After solving the LBM equation, the macroscopic fluid velocity can be written:

$$\rho \boldsymbol{u}(\boldsymbol{x}, t) = \rho \boldsymbol{u}^*(\boldsymbol{x}, t) + \frac{\Delta t}{2} \boldsymbol{f}(\boldsymbol{x}, t) \tag{11}$$

where $\boldsymbol{u}^*$ is the predicted velocity field. Since the fluid velocity at the boundary must equal the velocity of the boundary, $\boldsymbol{U}^b = \mathcal{I}[\boldsymbol{u}]$, (Eq. 11) can be converted into the Lagrangian frame to give:

$$\mathcal{I}[\rho(\boldsymbol{x}, t)]\boldsymbol{U}^b(\boldsymbol{X}, t) = \mathcal{I}[\rho \boldsymbol{u}^*(\boldsymbol{x}, t)] + \frac{\Delta t}{2} \boldsymbol{F}(\boldsymbol{X}, t) \tag{12}$$

Since the velocity of the boundary, $\boldsymbol{U}^b$, is known, (Eq. 12) can be rearranged and solved for the corrective force density, $\boldsymbol{F}$. The force is then transferred back to the Eulerian frame via the spreading operator, $\mathcal{S}$. Finally, the velocity field is updated by adding the corrective force to the predicted velocity field (Eq. 11).

## 2.4 Fluid-Structure Coupling

To enhance the stability of the coupled model, a block Gauss-Seidel implicit coupling scheme is adopted. This technique iterates over the separate field solvers within the time step until the interface conditions are met. To accelerate the convergence of these iterations, the solution is relaxed by combining the structural displacements at the current and previous iterations, such that:

$$\boldsymbol{U} = \omega \tilde{\boldsymbol{U}} + (1 - \omega)\boldsymbol{U}^{k-1} \tag{13}$$

where $\boldsymbol{U}$ is the relaxed solution which is passed to the fluid solver, $\tilde{\boldsymbol{U}}$ is the displacement computed from the structural solver, and $\boldsymbol{U}^{k-1}$ is the solution from the previous iteration. The relaxation factor is adjusted dynamically according to Aitken's delta-squared method [11]:

$$\omega_k = -\omega^{k-1} \frac{(\boldsymbol{r}_{k-1})^T (\boldsymbol{r}_k - \boldsymbol{r}_{k-1})}{|\boldsymbol{r}_k - \boldsymbol{r}_{k-1}|^2} \tag{14}$$

where $\boldsymbol{r}_k$ is the residual vector, which is also used as a stopping criterion.

$$\boldsymbol{r}_k = \tilde{\boldsymbol{U}}_k - \boldsymbol{U}_{k-1} \tag{15}$$

## 3 Simulation Setup

Figure 1 shows a schematic of the reference case from [6], which consists of an oscillating channel flow over a row of 10 flexible flaps. This setup is used to simulate the conditions of a von Kármán street behind a bluff body. The parameters describing the dimensions and physical properties of the problem are summarised in Table 1. The Womersley and Reynolds numbers are calculated based on the flap length, and the reference velocity is given as the maximum centreline velocity obtained for a clean channel (no flaps). In the original experiment, the flaps spanned most of the channel width, leading to a quasi-2D flow field. As such, only 2D simulations are conducted in the present work.

While the original experiment was conducted only for 10 flaps, the purpose of the present work is to investigate the travelling wave that arises due to secondary vortices which are generated at the tips. Therefore, to examine how this effect arises and propagates through the array, the number of flaps is varied over a range from 6 to 20. The following section presents results examining the effect of flap number while keeping all other problem parameters constant.

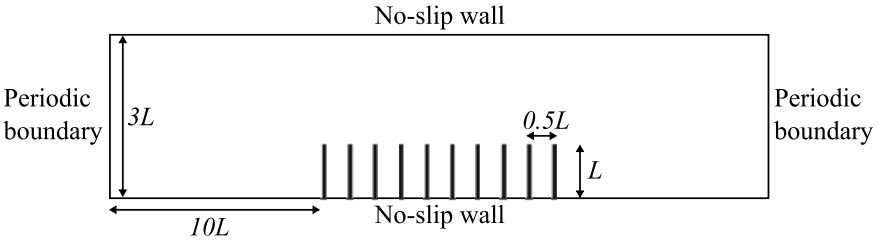


**Fig. 1** Schematic of computational domain for reference case

**Table 1** Problem parameters for test case

| Parameter | Symbol | Value |
|---|---|---|
| Channel height | $H$ | 6 cm |
| Flap height | $L$ | 2 cm |
| Flap thickness | $h$ | 1 mm |
| Fluid density | $\rho_f$ | 1200 kg/m$^3$ |
| Kinematic viscosity | $\nu$ | $1 \times 10^{-4}$ m$^2$/s |
| Flap density | $\rho_s$ | 1200 kg/m$^3$ |
| Young's Modulus | $E$ | 1.2 MPa |
| Frequency | $f$ | 1 Hz |
| Womersley number | $\alpha$ | 5 |
| Reynolds number | $Re$ | 120 |

# 4 Results

## *4.1 Validation*

To validate the current approach, the model is tested against the experimental data obtained for the reference case [6]. Figure 2 shows the experimental and numerical results for the streamwise tip deflection of each flap. Overall the agreement is good; however, some slight discrepancies are observed. These may be attributed to differences in the approximation of the experimental parameters. In particular, the bending rigidity of the flaps is extremely sensitive to the flap thickness. Another possible explanation for the noted differences is 3D effects, due to the finite span of the flaps in the experiment, which are not captured in the 2D simulation. Nevertheless, the agreement is good and shows that the present model can reproduce the dynamic motion of the system.

## *4.2 Effect of Array Length*

A range of array lengths were tested in the present work, spanning from 6 to 20 flaps. Figures 3 and 4 show the tip histories over three periods for the two extreme cases (6 flaps and 20 flaps). Both cases show a main dynamic which is governed by the driving flow (1 Hz). However, also evident is the appearance of secondary dynamics which manifest as small 'kicks' in the tip motion. This behaviour can be attributed to the travelling wave phenomenon and the overlaid dashed lines in Figs. 3 and 4 show how the wave propagates through the array.

For the shorter array (6 flaps), there exists one clearly defined wave-like motion that travels the length of the array and follows the motion of the flaps. After the flow

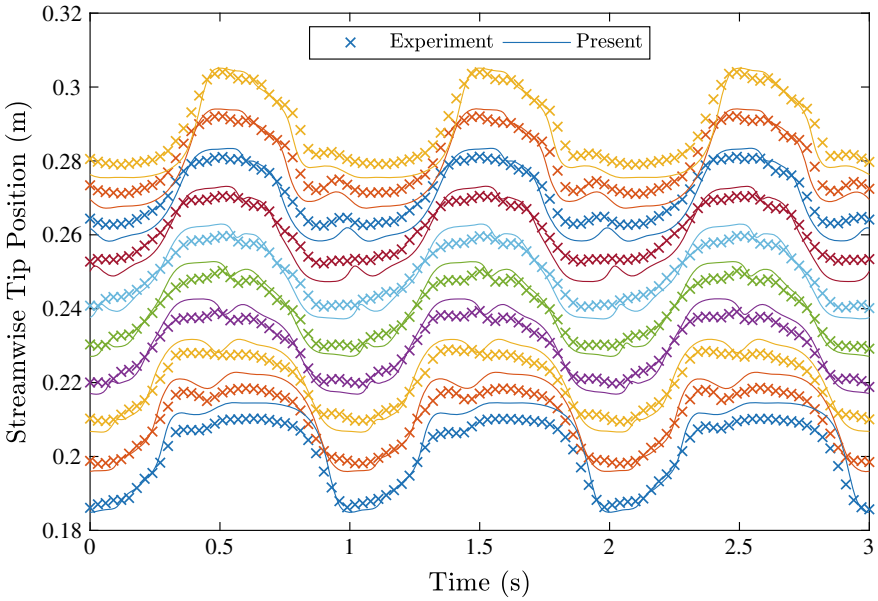


**Fig. 2** Validation of present model. Streamwise tip positions for each flap are compared against the experiment of [6]

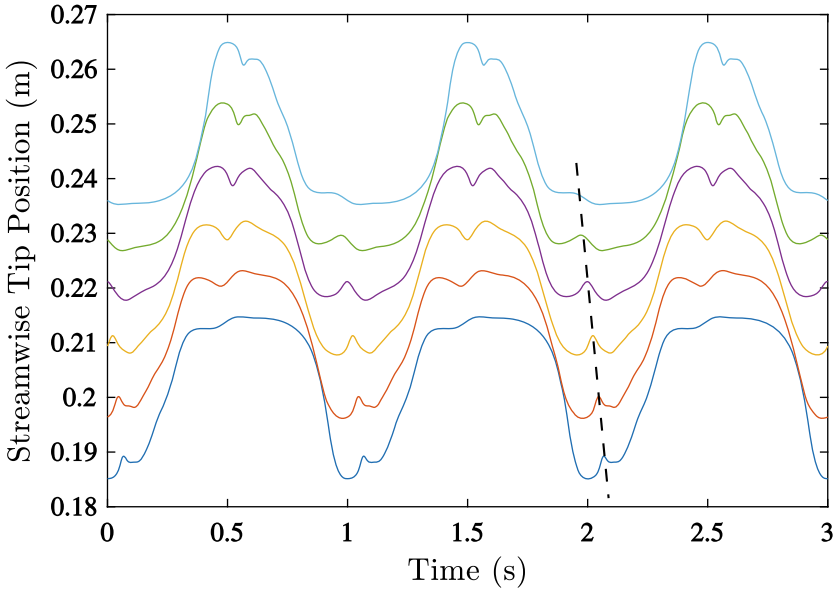


**Fig. 3** Streamwise tip positions for each flap for an array of 6 flaps. Dashed line shows propagating wave motion due to advection of vortices over the array

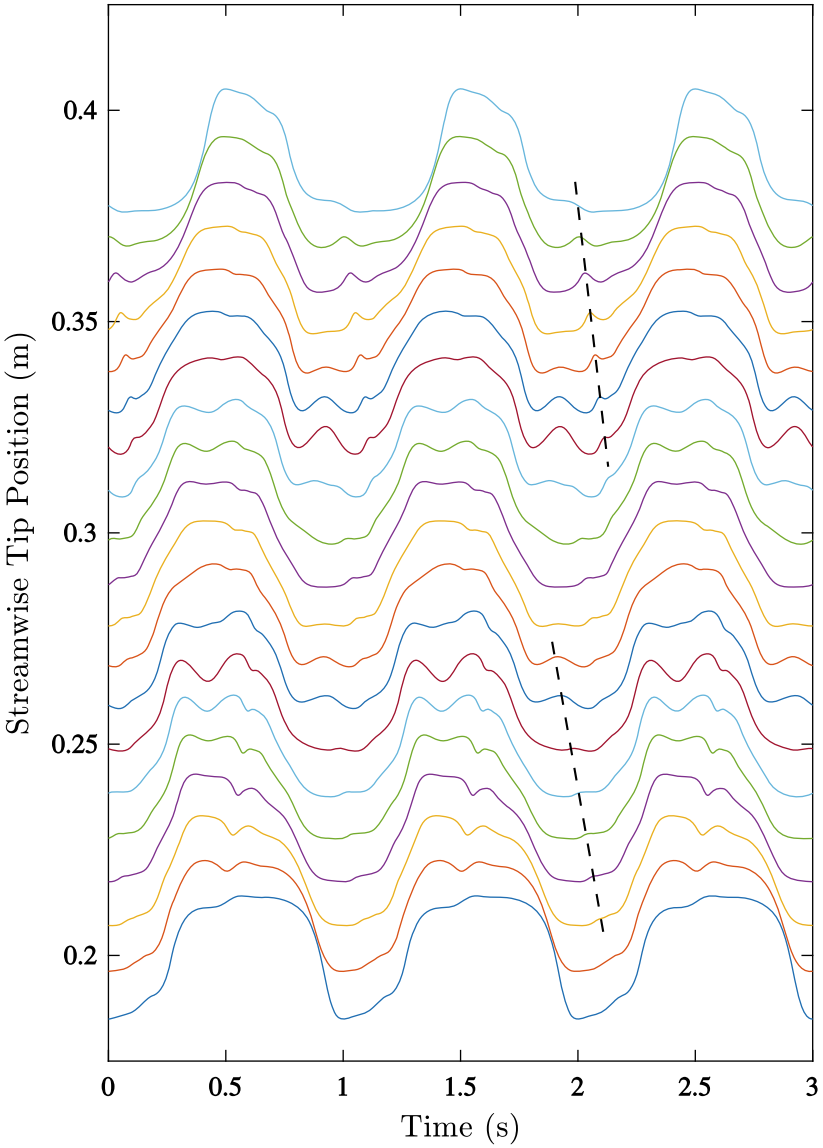


**Fig. 4** Streamwise tip positions for each flap for an array of 20 flaps. Dashed line shows propagating wave motion due to advection of vortices over the array

reverses direction the flaps deflect to the opposite side in a whip-like motion and the travelling wave follows shortly after. As will be shown later, the appearance of this clearly defined wave can be attributed to the passage of the primary bulk vortex which passes over the array periodically. In addition to the travelling wave motion, there is also a lag in the whip-like motion between the flaps. The outermost flap in the direction of the deflection initiates the whip-back motion, which is then shortly followed by the adjacent flap. This proceeds through the array until all of the flaps are deflected in the reverse direction.

In the case of the longer array (20 flaps), the 'kick' motion which results from the travelling waves is still evident. However, as opposed to the shorter array, where

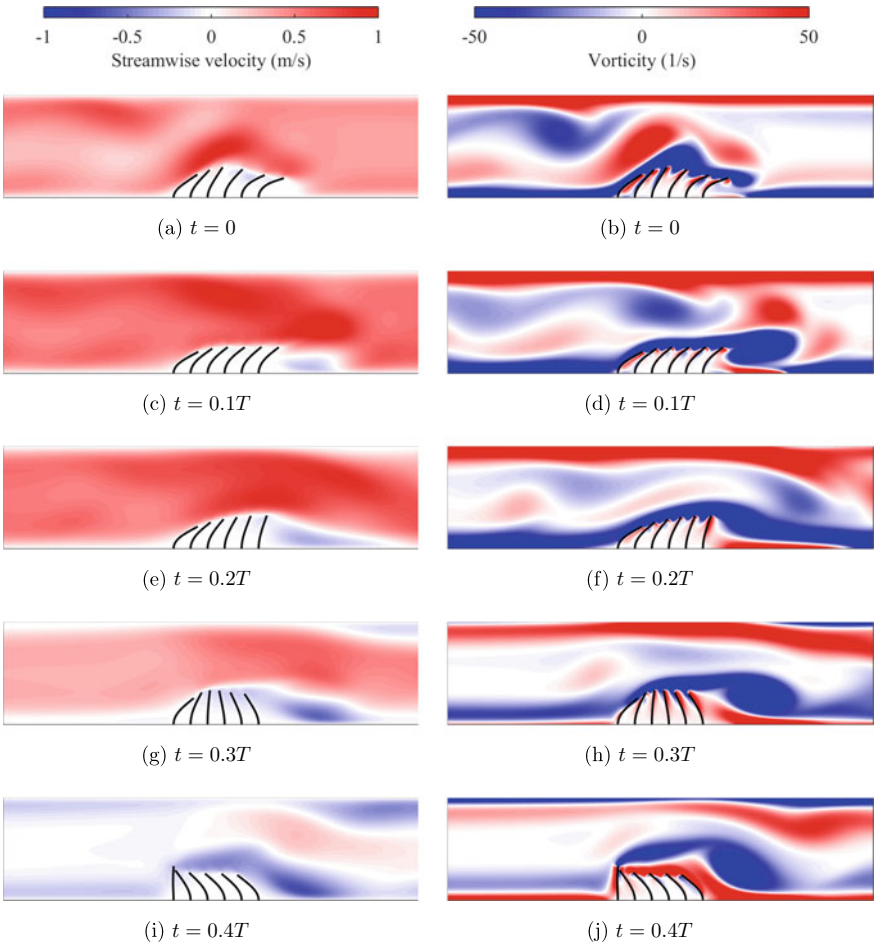


**Fig. 5** Snapshots of velocity (**a**, **c**, **e**, **g**, **i**) and vorticity (**b**, **d**, **f**, **h**, **j**) contours over one half-period for an array of 6 flaps. The second half of the period is antisymmetric

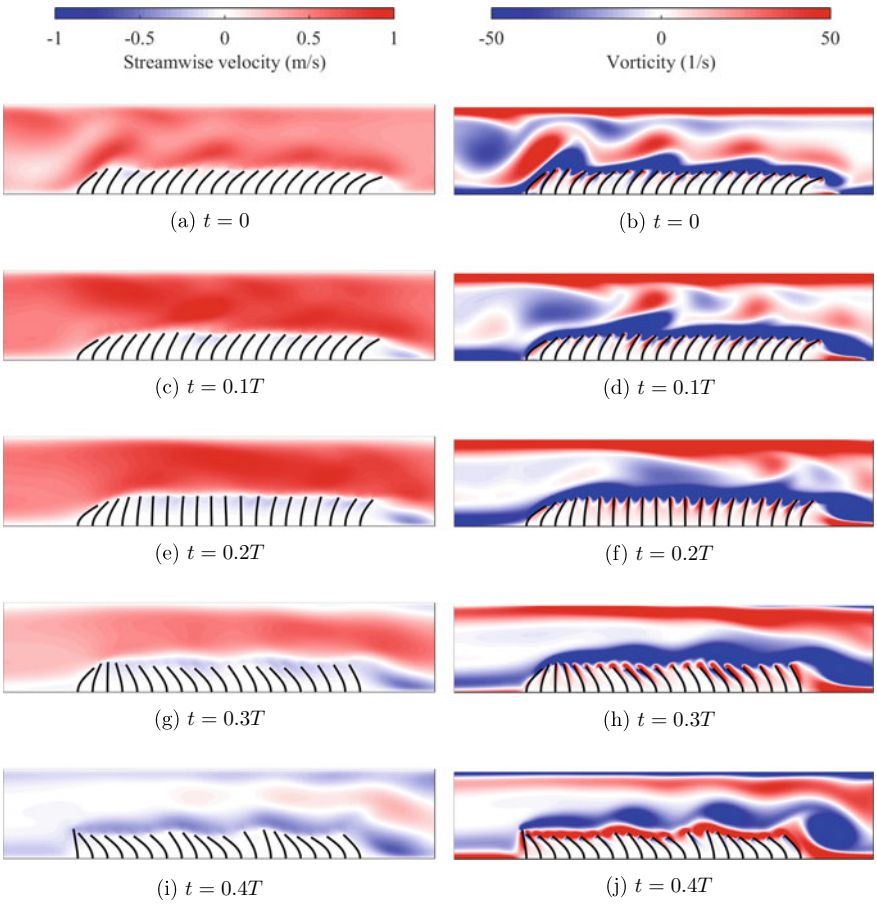


**Fig. 6** Snapshots of velocity (**a**, **c**, **e**, **g**, **i**) and vorticity (**b**, **d**, **f**, **h**, **j**) contours over one half-period for an array of 20 flaps. The second half of the period is antisymmetric

only one wave exists, multiple waves can now be observed. This effect is more pronounced towards the edges of the array, although it diminishes in strength as it propagates through the array. Also in contrast to the shorter array, the first flaps to initiate the whip-back are located at the centre of the array. After the centre flaps start to deflect backwards, the adjacent flaps also follow and this behaviour spreads out in both directions to the edges of the array.

Figure 5 shows snapshots of the streamwise velocity and vorticity contours through one-half cycle. Clearly observable is the primary bulk vortex which is shed from the array and is a feature of the finite size of the array. Due to the relatively short length of the array, only the primary bulk vortex exists and no secondary vortices form. At $t = 0$, the primary vortex is located at the centre of the array and is propagating through the array in the direction of the flow. The presence of this vortex

induces a local deflection (kick) in the surrounding flaps, which also travels through the array with the vortex. After the end of the half-cycle the flow changes direction and this is followed by the vortex and corresponding deflection wave.

Figure 6 shows the velocity and vorticity contours for the array with 20 flaps, over the same time period as Fig. 5. In addition to the primary bulk vortex which appears at the edges of the array, secondary vortices are also generated in the centre of the array at the tips of the flaps. Like the primary vortex, these vortices propagate along the array and induce a local deflection in the flaps, which appears as a travelling of deflection. Due to their small size and intensity, their effect on the flaps is less pronounced than that of the primary vortex and they quickly dissipate, as evidenced in the tip deflections shown in Fig. 4. Such behaviour could prove important in terms of flow control applications since the generation and lock-in of these travelling waves have been previously linked to optimal aerodynamic performance.

## 5 Conclusions

This work has aimed to further elucidate the flow control capability of arrays of passive slender structures. Specifically, the appearance of travelling waves propagating through the array have been investigated in relation to the length of the array. A simplified test case, which reduced the problem complexity while still retaining the essential dynamic behaviour, was studied numerically via a lattice Boltzmann-immersed boundary-finite element model. A range of array lengths were tested and the appearance and propagation of the travelling waves were monitored.

The results show that for small arrays there exists one clearly defined wave, which is attributed to the advection of the primary bulk vortex over the array. However, for larger arrays, secondary vortices are generated at the tips which also induce a wave-like behaviour. These secondary vortices are smaller in size and intensity than the primary bulk vortex and dissipate quicker as they propagate through the array, leading to decreased deflection in the flaps. This has important implications for flow control applications, since the appearance of these waves has been previously linked to optimal operating conditions in terms of drag reduction, and future work should focus on how these waves can be sustained and tuned to operate under a variety of flow conditions.

**Acknowledgements** The authors would like to acknowledge the use of the Computational Shared Facility at The University of Manchester and the ARCHER UK National Supercomputing Service. Support from the UK Engineering and Physical Sciences Research Council under the project 'UK Consortium on Mesoscale Engineering Sciences (UKCOMES)' (Grant No. EP/L00030X/1) is gratefully acknowledged

## References


1. Bathe, K.J.: Finite Element Procedures, 2nd edn. Prentice Hall (2014)
2. de Borst, R., Crisfield, M.A., Remmers, J.J.C., Verhoosel, C.V.: Non-Linear Finite Element Analysis of Solids and Structures, 2nd edn. Wiley (2012)
3. de Langre, E.: Effects of Wind on Plants. Annu. Rev. Fluid Mech. **40**(1), 141–168 (2008)
4. den Toonder, J.M.J., Onck, P.R.: Microfluidic manipulation with artificial/bioinspired cilia. Trends Biotechnol. **31**(2), 85–91 (2013)
5. Favier, J., Dauptain, A., Basso, D., Bottaro, A.: Passive separation control using a self-adaptive hairy coating. J. Fluid Mech. **627**, 451–483 (2009)
6. Favier, J., Li, C., Kamps, L., Revell, A., O'Connor, J., Brücker, C.: The PELskin project - part I: fluid-structure interaction for a row of flexible flaps: a reference study in oscillating channel flow. Meccanica **52**(8) (2017)
7. Gedan, K.B., Kirwan, M.L., Wolanski, E., Barbier, E.B., Silliman, B.R.: The present and future role of coastal wetland vegetation in protecting shorelines: answering recent challenges to the paradigm. Clim. Change **106**(1), 7–29 (2011)
8. Guo, Z., Zheng, C., Shi, B.: Discrete lattice effects on the forcing term in the lattice Boltzmann method. Phys. Rev. E **65**(4), 046308 (2002)
9. X. He and L. Luo. Theory of the lattice Boltzmann method: From the Boltzmann equation to the lattice Boltzmann equation. *Physical Review E*, 56(6):6811–6817, 1997a
10. He, X., Luo, L.: A priori derivation of the lattice Boltzmann equation. Phys. Rev. E **55**(6), R6333 (1997b)
11. Irons, B.M., Tuck, R.C.: A version of the Aitken accelerator for computer iteration. Int. J. Numer. Meth. Eng. **1**(3), 275–277 (1969)
12. Kottapalli, A.G.P., Bora, M., Asadnia, M., Miao, J., Venkatraman, S.S., Triantafyllou, M.: Nanofibril scaffold assisted MEMS artificial hydrogel neuromasts for enhanced sensitivity flow sensing. Sci. Rep. **6**, 19336 (2016)
13. Kunze, S., Brücker, C.: Control of vortex shedding on a circular cylinder using self-adaptive hairy-flaps. Comptes Rendus Mécan. **340**(1–2), 41–56 (2012)
14. Li, Z., Favier, J., D'Ortona, U., Poncet, S.: An immersed boundary-lattice Boltzmann method for single- and multi-component fluid flows. J. Comput. Phys. **304**, 424–440 (2016)
15. Masoud, H., Alexeev, A.: Harnessing synthetic cilia to regulate motion of microparticles. Soft Matter **7**(19), 8702–8708 (2011)
16. Mazellier, N., Feuvrier, A., Kourta, A.: Biomimetic bluff body drag reduction by self-adaptive porous flaps. Comptes Rendus Mécan. **340**(1–2), 81–94 (2012)
17. Niu, J., Hu, D.L.: Drag reduction of a hairy disk. Phys. Fluids **23**(10), 101701 (2011)
18. Pinelli, A., Naqavi, I.Z., Piomelli, U., Favier, J.: Immersed-boundary methods for general finite-difference and finite-volume Navier-Stokes solvers. J. Comput. Phys. **229**(24), 9073–9091 (2010)
19. Revell, A., O'Connor, J., Sarkar, A., Li, C., Favier, J., Kamps, L., Brücker, C.: The PELskin project: part II—investigating the physical coupling between flexible filaments in an oscillating flow. Meccanica **52**(8) (2017)
20. Roma, A.M., Peskin, C.S., Berger, M.J.: An adaptive version of the immersed boundary method. J. Comput. Phys. **153**(2), 509–534 (1999)
21. Venkataraman, D., Bottaro, A.: Numerical modeling of flow control on a symmetric aerofoil via a porous, compliant coating. Phys. Fluids **24**, 093601 (2012)
22. Wu, J., Shu, C.: Implicit velocity correction-based immersed boundary-lattice Boltzmann method and its applications. J. Comput. Phys. **228**(6), 1963–1979 (2009)

# Effects of an Oscillating Flap on the Main Airfoil Unsteady Lift in Grid Turbulence


**Herricos Stapountzis, Athanasios Barlas, Georgios Papageorgiou, and Athanasios Patsiouras**

**Abstract** A wing of NACA 0015 profile and Aspect Ratio 2.4 fitted with a Trailing Edge Flap was tested in a wind tunnel for both smooth and turbulent flow conditions at a Re number 108000. The unsteady lift on the wing was measured with and without the flap. Two types of flap excitation were tried: One was of the "open loop" type in which the flap was subjected to sinusoidal pitching oscillations while the wing was set to a constant angle of attack. In the second, "closed loop" mode, the excitation signal fed into the flap originated from the unsteady lift of the wing itself. The phase lag between those signals was changed and it was found that it played a significant role in the suppression of the main wing unsteady lift.

**Keywords** Trailing edge flap · Wind turbine load alleviation · Smart blades · Unsteady aerodynamics · Active flow control

## 1 Introduction

Atmospheric turbulence and gusts are responsible for inducing unsteady loads to airplane wings, helicopter blades and wind turbine rotors. The last ones however, on account of their relatively larger size, are subjected to additional cyclic load increments due yaw misalignment, tower shadow and wind shear in the atmospheric boundary layer. Flapwise bending moments near the blade root would be a serious cause for fatigue. It is desirable to maintain, as much as possible, a rather steady or prescribed blade loading in order to lower the fatigue risk and also suppress vibrations especially for helicopter blades. Various methods have been tried towards this objective, which in some cases could also result in increased annual energy production of the wind turbine, Barlas and van Kuik [1], Krzysiak and Narkiewicz [2],

H. Stapountzis (✉) · G. Papageorgiou · A. Patsiouras
Department of Mechanical Engineering, University of Thessaly, 383 34 Volos, Greece
e-mail: erikos@uth.gr; erikostap@gmail.com

A. Barlas
DTU, 4000 Roskilde, Denmark



M. Braza et al. (eds.), *Advances in Critical Flow Dynamics Involving Moving/Deformable Structures with Design Applications*, Notes on Numerical Fluid Mechanics and Multidisciplinary Design 147,
https://doi.org/10.1007/978-3-030-55594-8_41

Siala and Liburdy [3], Maldonaldo et al. [4]. Collective or individual pitching of the wind turbine blades (cyclic pitch with a phase shift) was found to effectively reduce fatigue loads, Larsen et al. [5], but rather sluggish to attenuate atmospheric turbulence effects. Better control of the blade lift would be accomplished by moving a large hinged flap through a small angle, Hassan [6]. Further load reductions could be effected by the deployment of small size trailing edge flaps, or deformable, "morphing" trailing edges, which because of their smaller moment of inertia, would be accordingly activated to account for various unsteady conditions, including shorter atmospheric gusts, Hulskamp et al. [7], Wolff et al. [8], Madsen et al. [9], Pankonien and Inman [10], Valasek [11]. Considerable research is devoted to such "smart rotor" innovations from both the experimental and computational point of view. One issue is the correct and realistic aerodynamic modelling and another one is the method of active control (open or closed loop), Bergami and Hansen [12], Frederick et al. [13]. With regard to aerodynamic problems, among the points of interest are the size and position of the flap relatively to the main wing, the amplitude of deflection $\beta_0$ and the pitch rate, in case the wing is at a steady angle of attack $\alpha$. If the wing itself oscillates along with the flap then their phase difference needs to be investigated. It was found that there exist regimes of appropriate phase difference where the undesirable unsteady lift is suppressed, Bak et al. [14], Bergami et al. [15], Krzysiak et al. [2], Wolff et al. [8].

Figure 1, adapted from the experimental results of [14], shows how the fluctuating part of the unsteady lift on the main steady fixed wing at $\alpha = 4.6°$ is influenced by the reduced frequency k of sinusoidal flap oscillation during a full cycle. The reduced frequency is defined as $k = \omega c/(2U_\infty)$, where $\omega$ is the circular frequency of oscillation $\omega = 2\pi f$, f being the frequency in Hz, c is the wing chord, including the flap chord and $U_\infty$ is the free stream speed. The instantaneous flap angle is $\beta$ (in degrees) and half amplitude of the flap oscillation is denoted by the angle $\beta_0$.

For sinusoidal motion the root mean square of $\beta$, $\beta_{RMS} = \beta_0/\sqrt{2}$. Due to experimental limitations the amplitude $\beta_0$ could be maintained at a constant level as the

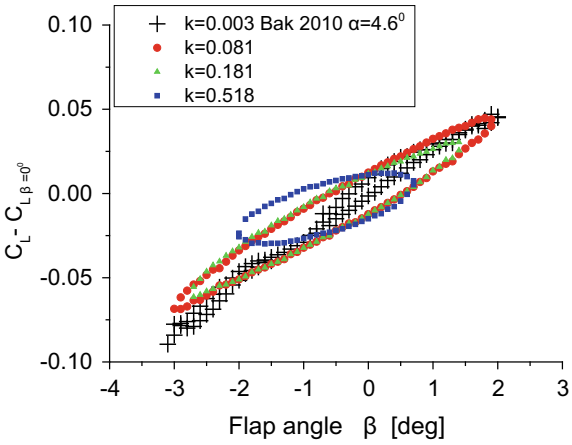


**Fig. 1** Fluctuating part of the lift with flap angle $\beta$ in sinusoidal oscillation and main wing RISOE B1-18 steady at angle of attack $\alpha = 4.6°$. Adapted from wind tunnel test results of Bak et al. [14]

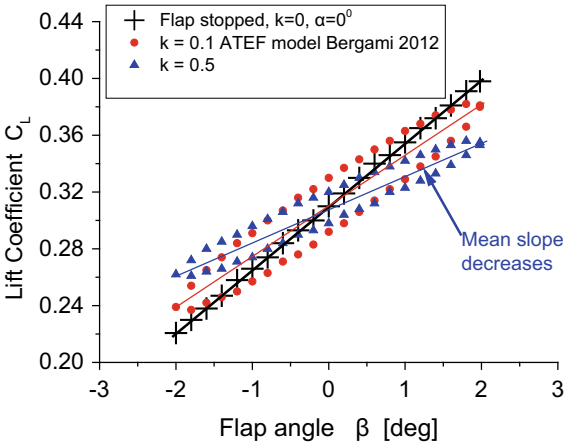


**Fig. 2** Unsteady lift coefficient for various oscillating flap reduced frequencies with wing NACA 64-418 steady at $\alpha = 0°$ Adapted from ATEF model calculation results of Bergami et al. [15]

frequency of oscillation was varied, a problem that was encountered in the experiments of the present work, as will be seen later. It is observed that the unsteady lift amplitude and consequently its RMS value decrease with reduced frequency as well as the average lift curve slope. The loop in the $C_L - \beta$ curve, as reported in [14], is counterclockwise indicating a favorable behavior towards the lowering of the unsteady lift.

Figure 2, shows similar results from the computational work of Bergami et al. [15], using their ATEF (Adaptive Trailing Edge Flap) engineering model. The main wing is set at a zero angle of attack $\alpha = 0°$.

The computations show that when the amplitude of flap oscillation $\beta_0$ was set to $\beta_0 = 2°$ there is a systematic trend to reduce the unsteady lift as k increases.

Figure 3, adapted from [14], shows the experimental results for combined sinusoidal motion of the wing and its attached flap. A phase difference of 40° yields the lowest unsteady lift fluctuation. On the other hand, inappropriate phase differences may increase the unsteady lift significantly, e.g. $\Delta\varphi = -150°$.

In the present work experiments of similar nature to those reported from [14] above are carried out in order to examine the influence of reduced frequency, turbulence intensity and manner of flap excitation on the wing unsteady lift. Comparisons with the experimental findings of [14, 15], where possible, due to the big difference in the wing chord to flap chord ratios, will be attempted.

## 2 Experimental Setup

The open, suction type wind tunnel at the University of Thessaly Mechanical Engineering Department was employed for the unsteady lift measurements using piezoelectric force transducers. The wind speed was $U_\infty = 13$ m/s and the 2-D wing/flap assembly of AR = 2.4 with end plates was positioned 20M downstream of a standard

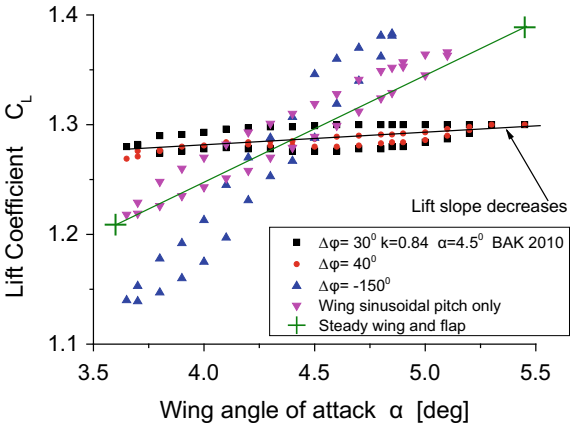


**Fig. 3** Unsteady Lift Coefficient for simultaneous wing and flap sinusoidal oscillation at k = 0.84 and main wing RISOE B1-18 angle of attack α = 4.5°. The phase difference between wing and flap is Δφ degrees. Adapted from wind tunnel test results of Bak et al. [14]

biplanar grid (M = 90 mm mesh to square bar size ratio = 4.5). At this downstream location the turbulence intensity without the grid was 0.7% and with the grid 5%.

The wing was of the NACA 0015 profile with chord c = 125 mm and the flap profile was close to that of an EPPLER 561 17% thick profile of chord length $c_F$ = 65 mm, Fig. 4. Tests were performed at Reynolds numbers Re = $U_\infty$ c/ν between 108,000 and 135,000. The wing chord to flap chord ratio $c/c_F$ in this work is equal to 1.92, which is in fact too small compared to the ratio found in the literature, [14]. Limitations in the Lab instrumentation has contributed to this decision.

Two types of flap rotary oscillation were considered (mechanically accomplished by means of a hinge and a connecting rod mounted on a powerful loudspeaker): (a) sinusoidal, of frequency $f_F$, by means of an independent signal generator of which the amplified signal was fed into the loudspeaker and (b) by feeding the unsteady (turbulent) lift signal of the wing into the amplifier and subsequently into the loudspeaker in order to vibrate the hinged flap. The wing and the flap were mounted independently, so that mechanical cross-talk of forces would be avoided. For case (a) the flap frequencies were equal to 0, 10, 12.5, 15 and 20 Hz with corresponding half amplitudes $\beta_0$ = 0 (no flap oscillation), 25.4°, 6.6°, 3.1° and 2°. For case (b) the unsteady lift signal was fed into the loudspeaker via two different ways: first, directly from the output of the amplifier and second, with its polarity reversed. In the former case, the unsteady lift and the excitation were in phase (denoted as "Phase Lift") while in the latter they were 180° out of phase ("180 Lift"). The shape of the two time records was checked visually using an oscilloscope and also numerically via the coherence function of the corresponding analogue signals, simultaneously sampled in time.

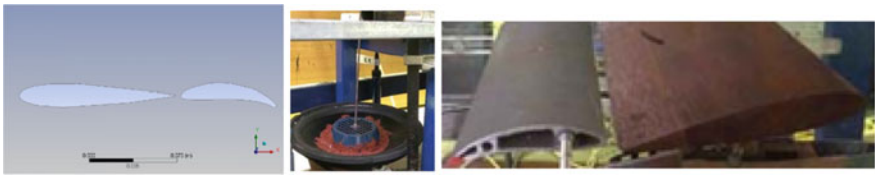

**Fig. 4** Wind tunnel models. Main wing NACA 0015, chord c = 125 mm, span b = 300 mm. Flap EPPLER 561 17% thick, chord $c_F$ = 65 mm, span = 300. Reduced frequency k is based on c

## 3 Unsteady Lift Results for the Model Wing Without a Flap

Figure 5 presents experimental data for the unsteady lift on an isolated non-oscillating wing (no flap) set at a steady angle of attack α. Variability in the unsteady lift may arise from the inherent flow unsteadiness of a wind tunnel in nominally "smooth" flow (for example acoustic excitation) or background turbulence, intentionally generated turbulence, as in this work by means of a grid, turbulent boundary layer on the wing surface, flow separation (stall) and to some extend extraneous noise from the force balance.

The root mean square of the fluctuating part of the unsteady lift coefficient, $C_{L\,RMS}$, which is plotted against α, is seen to increase with angle of attack in all cases, concerning our results and those found in the literature, e.g. Gaunaa [16], Smith et al. [17], Humphreys [18], Lysak et al. [19].

Our results show that grid turbulence with an intensity i of 5% causes significant increase in the $C_{L\,RMS}$ of the NACA 0015 wing, compared to that in the wind tunnel flow without the grid (i = 0.7%). The data of Gaunaa [16] suggest lowering of $C_{L\,RMS}$ as Re increases, partly because of the lower turbulence intensities at higher wind speeds.

As stall is approached the unsteady lift increases (α > 15°) in all data. Closer to our results are those of Smith et al. [17], who tested a NACA 0012 wing in the turbulent boundary layer of a water tunnel and those of Lysak et al. [19] (not shown in Fig. 5) who measured the unsteady lift on a NACA $65_{1A}$-012 wing in a water tunnel with grid turbulence. Their data point to a ratio $C_{L\,RMS\text{-}TURB}/C_{L\,RMS\text{-}SMOOTH} = 3.2$ for α = 0°, of the same order of magnitude found by Stapountzis [20] in earlier experiments in a wind tunnel. Increase in airfoil thickness is also known to cause higher unsteady lift.

## 4 Unsteady Lift with Flap in Steady Conditions

This section deals with the unsteady lift of the wing equipped with the flap, but not yet in oscillation, β = 0°. Values of $C_{L\,RMS}$ are again plotted against α for smooth flow and grid turbulence in Fig. 6.

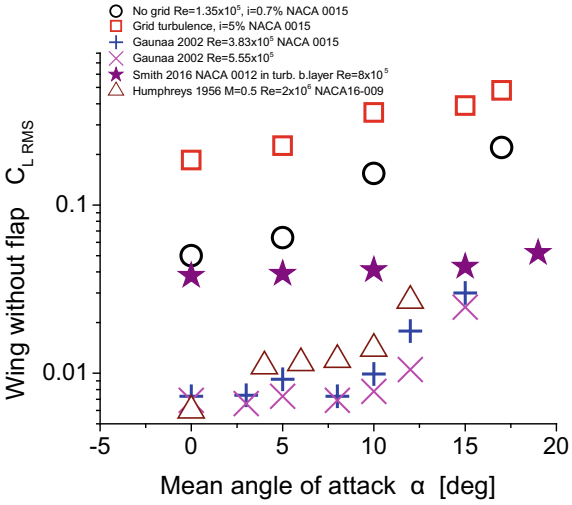


**Fig. 5** Fluctuating lift for wings without flap in smooth and turbulent flows from present experimental work and from Gaunaa et al. [16], Smith et al. [17], Humphreys [18].

The presence of the flap and for angle of attack $\alpha = 0°$, increases the unsteady lift in smooth flow by about 50%, while it has the opposite effect in turbulent flow, the unsteady lift decreases by about 15%. At $\alpha = 7.5°$ and turbulent flow, no appreciable change in the unsteady lift is noticed due to the flap presence (compare Figs. 5 and 6).

Bak et al. [14] measured the unsteady lift on a Risoe-B1-18 airfoil with $c/c_F = 10$, at quasi steady conditions ($k \approx 0.003$) at $Re = 1.66 \times 10^6$ and background wind tunnel turbulence $\approx 1\%$. The $C_{L\,RMS}$ at $\alpha = 4.6°$ was 0.04, close to our result for smooth flow at $\alpha = 0°$. It seems therefore that grid turbulence attenuates the interference caused by the flap in a steady condition ($\beta = 0°$) with regard to the unsteady lift development.

## 5 Unsteady Lift with Flap in Sinusoidal Forcing

Figures 7 and 8 demonstrate how the oscillating flap in sinusoidal excitation, $\beta(t) = \beta_0 \cos(\omega t)$, influences the unsteady lift of the main wing. The nearest (taking into account the too small value of $c/c_F$ in the present experiments) available data for comparison are those reported in [14] (experiments, $\alpha = 4.6°$) and in [15] (computations with the ATEF model, $\alpha = 0°$). Representative plots of the $\beta - C_L$ lobes with increasing k were given in Figs. 1 and 2 in the Introduction. Using their data the root mean square lift coefficients were computed. In order to bring their results to a comparable form with ours the $C_{L\,RMS}$ data were normalized with the RMS flap amplitude, $\beta_{0\,RMS}$, assuming variations of the type $\beta(t) = \beta_0 \cos(\omega t)$ (with $\omega = 2\pi f_F$).

Figure 7 shows the variation of the normalized RMS lift coefficient with reduced frequency at $\alpha = 0°$ for smooth and turbulent flow. Our data point to a non favorable

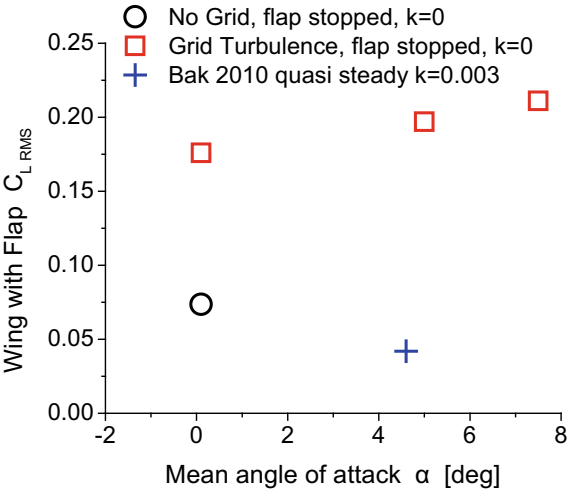


**Fig. 6** Fluctuating lift for wings with flap in smooth and turbulent flows from present experimental work with flap steady ($k = 0$, $\beta = 0°$, $Re = 1.08 \times 10^5$) and from Bak et al. [14], (quasi-steady, $k \approx 0.003$, $Re = 1.66 \times 10^6$)

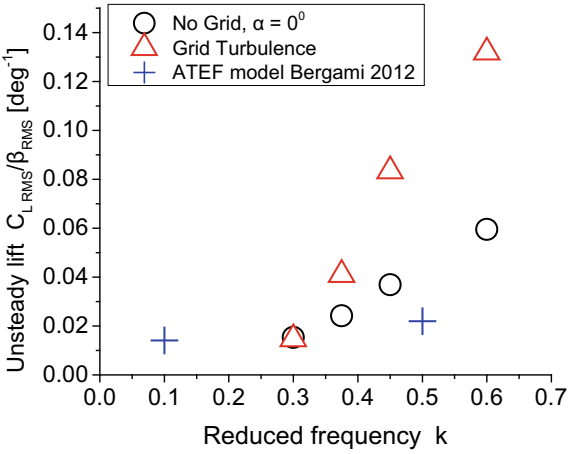


**Fig. 7** Normalized fluctuating lift for wings at $\alpha = 0°$ with flap in smooth and turbulent flows from present experimental work for flap with sinusoidal excitation and from ATEF model of Bergami et al. [15]

contribution of the flap excitation for unsteady lift alleviation especially for grid turbulence. A roughly linear increase of the normalized lift with k is observed, one of the reasons could be the large size of the flap compared to the wing and the large unsteadiness caused in its wake. The increase in the normalized lift with reduced frequency k found from the data in [15, 21] is very mild compared to ours. In their work the RMS values of the fluctuating parts of the unsteady lift for $k = 0.1$ and 0.5 are 0.019 and 0.027 respectively and the normalized values for $\beta_0 = 2°$ are shown in Fig. 7. A fair agreement might be assumed in the low reduced frequency regime, $k < 0.3$.

In Fig. 8 there are data for more angles of attack besides the zero angle, i.e. for $\alpha = 5°$, 7.5° (our experimental data) and $\alpha = 4.6°$ (experimental data in [14]).

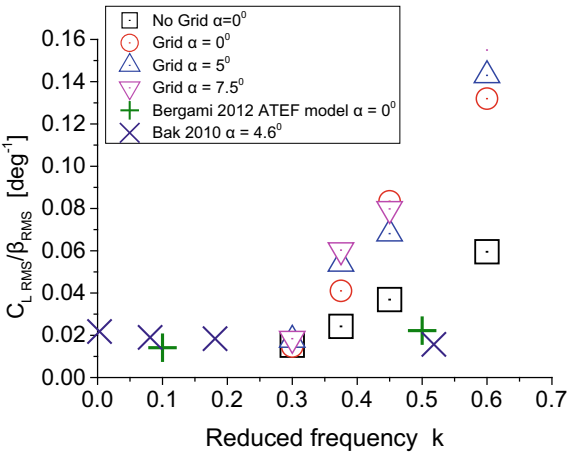


**Fig. 8** Effect of reduced frequency k and mean angle of attack α on the normalized fluctuating lift for wings with flap in smooth and turbulent flows from present experimental work for flap with sinusoidal excitation and from Bak et al. [14]

In our case the normalized lift does not seem to be significantly influenced by increases in the angle of attack at least in the range examined (0° to 7.5°) and again it increases with reduced frequency k. On the contrary, the experimental results of Bak et al. [14] indicate a mild, though favorable effect of the flap oscillation on the alleviation of the unsteady lift. The data taken from Fig. 1, [14], and normalized as described above show in Fig. 8 that the unsteady lift can indeed be lowered when k increases. There are no available data beyond $k = 0.5$ in order to ascertain whether this favorable effect reaches an optimum value for load alleviation. Research with sinusoidal excitation dealing also with phase changes is quite extensive in this respect e.g. [22, 23].

## 6 Unsteady Lift with Flap in a Closed Loop Excitation

The signal fed to the actuator moving the flap was the unsteady lift felt by the wing in turbulent flow. It was beforehand amplified in order to be able to drive the powerful loudspeaker. The two signals were followed in time and recorded for further analysis. As mentioned in Sect. 3, the phase between the two signals could be altered by changing the polarity in the actuator (loudspeaker). Then the flap would move in the opposite direction. The advantageous effect of a flap as a high lift device is well documented, i.e. when the flap moves downwards, $\beta < 0$, (assuming that upwards causes the wing nose up, $\alpha > 0$) the lift increases. Figure 9 shows that this phase lag can dramatically affect the normalized unsteady lift. In Fig. 10 time traces of the two signals are presented.

The decrease with phase change in the normalized lift is more pronounced at low angles of attack. For example at $\alpha = 0°$ the lift without phase change is about 0.075, while with 180° phase change the corresponding value is 0.05. Reverting to Fig. 8 and assuming sinusoidal excitation this would imply operation at a reduced

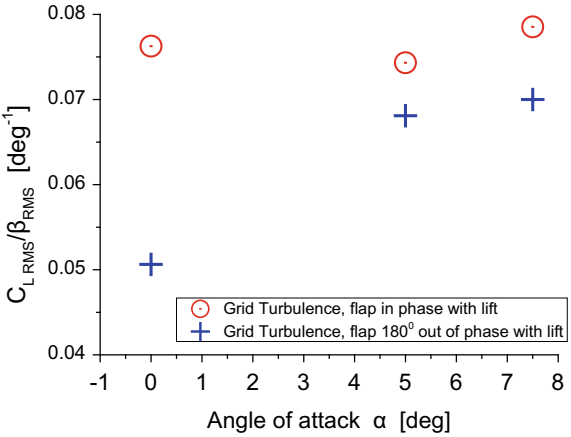


**Fig. 9** Effect of feedback method (lift-flap phase shift 0° and 180°) and mean angle of attack α on the normalized fluctuating lift for wing with flap in smooth and turbulent flow

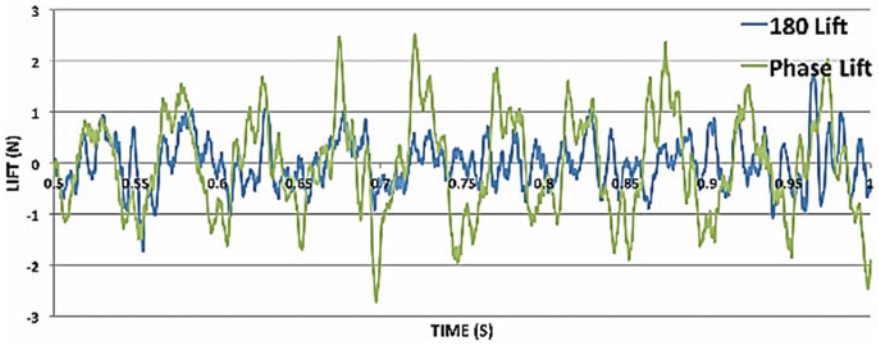


**Fig. 10** Unsteady lift record in turbulent flow with feedback flap excitation using the lift signal and phase shift for no phase shift 0° (green) and 180° (blue)

frequencies k ≈ 0.45 and 0.35 respectively. It is as if the phase change reduces the strength of the unsteadiness of lift in terms of sinusoidal excitation. Further work would be needed in order to cover a wide range of phase differences and perhaps locate an optimum for unsteady lift alleviation.

## 7 Conclusions

The experimental results of the present study show that unsteady lift is affected by trailing edge flaps but the degree of load alleviation depends on many factors like the relative size of the flap and the excitation mode. For sinusoidal excitation, the

presence of strong turbulence renders the effects of changes in mild angles of attack (e.g. $\alpha < 8°$) less important than changes in the reduced frequency of oscillation. Flap excitation with a signal originating from the unsteady lift sensed by the main wing itself seems to have potential benefits for unsteady lift alleviation provided that appropriate phase differences in the closed loop procedures are used. Smart rotors and their control strategies is currently drawing a lot of attention in the wind energy scientific and industrial sector, [24–27].

## References


1. Barlas TK, van Kuik GAM (2007) State of the art and prospectives of smart rotor control for wind turbines. Sci Making Torque Wind J Phys Conf Ser 75, 01 2080 (2007)
2. Krzysiak, A., Narkiewicz, J.: Aerodynamic loads on airfoil with trailing-edge flap pitching with different frequencies. J. Aircraft **43**(2), 407 (2006)
3. Siala, F., Liburdy, J.A.: Energy harvesting of a heaving and forward pitching wing with a passively actuated trailing edge. J. Fluids Struct. **57**, 1–14 (2015)
4. Maldonado, V., Farnworth, J., Gressick, W., Amitay, M.: Active control of flow separation and structural vibrations of wind turbine blades. Wind Energy. **13**, 221–237 (2010)
5. Larsen, T.J., Madsen, H.A., Thomsen, K.: Active load reduction using individual pitch, based on local blade flow measurements. Wind Energy **8**, 67–80 (2005)
6. Hassan, A.A.: Experimental/numerical evaluation of integral trailing edge flaps for helicopter rotor applications. J. Am. Helicopter Soc. **50**, 3–17 (2005)
7. Hulskamp, T., Champliaud, H., van Wingerden, J.-W., Barlas, A., Bersee, H,.van Kuik, G., Verhaegen, G.: Smart dynamic rotor control: Part 1, Design of a smart rotor. In: The Science of Making Torque from Wind (2010)
8. Wolff, T., Ernst, B., Seume, J.R.: Aerodynamic behavior of an airfoil with morphing trailing edge for wind turbine applications. Sci Making Torque Wind J Phys Conf Ser **524**, 012018 (2014)
9. Madsen, A.H., Andersen, P.B., Andersen, L.T., Bak, C., Buhl, T., Li, N.: The potentials of the controllable rubber trailing edge flap (CRTEF). In: EWEC Proceedings (2010)
10. Pankonien, A., Inman, D.J.: Experimental testing of spanwise morphing trailing edge concept. Proc. SPIE **8688**(15), 1–13 (2013)
11. Valasek, J. (ed.). (2012). Morphing Aerospace Vehicles and Structures. Wiley, New York (2012)
12. Bergami, L., Hansen, M.H.: High-fidelity linear time-invariant model of a smart rotor with adaptive trailing edge flaps. Wind Energy **20**(3), 431–447 (2017)
13. Frederick, M., Kerrigan, E.C., Graham, J.M.R.: Gust alleviation using rapidly deployed trailing-edge flaps. J. Wind Eng. Ind. Aerodyn. **98**, 712–723 (2010)
14. Bak, C., Gaunaa, M., Andersen, P.B., Buhl, T., Hansen, P., Clemmensen, K.: Wind tunnel test on airfoil Riso-B1-18 with an active trailing edge flap. Wind Energ. **13**, 207–219 (2010)
15. Bergami, L., Riziotis, V.A., Gauna, M.: Aerodynamic response of an airfoil section undergoing pitch motion and trailing edge flap deflection: a comparison of simulation methods. Wind Energy **18**(7), 1273–1290 (2015)
16. Gaunaa, M.: Unsteady aerodynamic forces on NACA 0015 airfoil in harmonic translator motion. Ph.D. Thesis, Technical University of Denmark
17. Smith, S.M., Pearce, B.W., Brandner, P.A., Clarke, D.B., Moreau, D.B., Xue, Y.: Steady and unsteady loads acting on a hydrofoil immersed in a turbulent boundary layer. In: 20th Australasian Fluid Mechanics Conference, Perth, Australia (2016)
18. Humphreys, M.D.: Measurements of normal-force-coefficient fluctuation on four 9-percent-thick airfoils having different locations of maximum thickness. In: NACA RM 154B22 (1954)

19. Lysak, P.D., Capone, D.E., Jonson, M.L.: Unsteady lift of thick airfoils in turbulent flows. In: Proceedings of ASME IMECE2009-11414 (2009)
20. Stapountzis, H., Graham, J.M.R.: The unsteady lift on bluff cylindrical bodies in unsteady flow. Aero. Q. **33**, 219–236 (1982)
21. Bergami, L., Gaunaa, M.: ATEFlap aerodynamic model, a dynamic stall model including the effects of trailing edge flap deflection. DTU Risoe-R No 1792 (2012)
22. Oltmann, N.-C., Sobota, D., Hoffmann, A.: Load reduction of wind turbines using trailing edge flaps. In: 4th International Conference on Energy and Environment Research, ICEER 2017, Porto, Portugal (2017)
23. Li, C.F., Xu, Y., Zhao, X.L., Xu, J.Z.: Influence of trailing edge flap on wind turbine using three-dimensional computational fluid dynamics method. In: 6th International Conference on Pumps and fans with Compressors and Wind Turbines, IOP Conference Series: Materials Science and Engineering, vol 52, 052005 (2013)
24. Bernhammer, L.O., van Kuik, G.A.M., de Breuker, R.: How far is smart rotor research and what steps need to be taken to build a full-scale prototype? Sci Making Torque Wind J Phys Conf Ser **555**, 012008 (2014)
25. Plumley, C., Leithead, W., Jamieson, P., Bossanyi, E., Graham, J.M.R., Comparison of individual pitch and smart rotor control strategies for load reduction. Sci Making Torque Wind J Phys Conf Ser **524**, 012054 (2014)
26. Shan, M.: Load reducing control for wind turbines: load estimation and higher level controller tuning based on disturbance spectra and linear models. Dr.-Ing. Dissertation, Universitat Kassel (2017)
27. Njiri, J.G., Soffker, D.: State-of-the-art in wind turbine control: Trends and challenges. Renew. Sustain. Energy Rev. **60**, 377–393 (2016)

# Fast Sensitivity Analysis for the Design of Morphing Airfoils at Different Frequency Regimes


**Felix Kramer, Marian Fuchs, Thilo Knacke, Charles Mockett, Emre Özkaya, Nicolas Gauger, and Frank Thiele**

**Abstract** An approach to produce sensitivity maps to facilitate the design of morphing aerostructures is proposed and analysed. The process assesses the effect of large-scale deformations at low actuation speeds as well as low-scale deformations at high frequencies. Emphasis is put on a fast process to obtain results within a rapid turnaround time. The resulting sensitivity maps for an industrially relevant airfoil are qualitatively matched to published experiments of the same configuration and aerodynamic interpretations. The sensitivities are calculated using an in-house flow solver and its discrete adjoint derivative. Subject to the approximations inherent to the adopted unsteady RANS methodology, some suggestions for effective deformation locations are proposed.

**Keywords** Sensitivity · Adjoint · Airfoil · Morphing

## 1 Introduction

Current wing design on commercial aircraft is commonly optimized for selected flight states such as cruise, take-off and landing. The mechanical parts required to realize these configurations limit the achievable shapes and enforce compromises on the design. During the last decade, extensive research has been conducted to implement deforming morphing wing structures to overcome this limitation [1]. Numerous trailing edge devices were conceived and investigated [2, 4, 7] all of which use servo actuators to realize the deformations. The work in the present paper was

F. Kramer (✉) · M. Fuchs · T. Knacke · C. Mockett · F. Thiele
CFD Software Entwicklungs-und Forschungsgesellschaft mbH, Berlin, Germany
e-mail: felix.kramer@cfd-berlin.com

E. Özkaya · N. Gauger
TU Kaiserslautern, Paul-Ehrlich-Str. 34, 67663 Kaiserslautern, Germany



M. Braza et al. (eds.), *Advances in Critical Flow Dynamics Involving Moving/Deformable Structures with Design Applications*, Notes on Numerical Fluid Mechanics and Multidisciplinary Design 147,
https://doi.org/10.1007/978-3-030-55594-8_42

done within the framework of the H2020 EU project "Smart Morphing and Sensing" (SMS) which combines shape memory alloys for low frequency deformations with distributed piezoelectric fiber actuators for high frequency actuations [3, 8]. Finally, this actuator concept will be complemented by fiber optic sensors to achieve a closed-loop control.

The main contribution of the present work is to numerically identify the most efficient placement for such actuators. When dealing with a distributed actuator system, a sensitivity-based approach using an adjoint solver has the inherent advantage that the costs for the sensitivity evaluation are independent of the number of control faces, rendering it very efficient for distributed controls [5, 6]. In this paper, such an adjoint solver is applied to a realistic commercial airfoil with several reference deformations closely matching the experimental campaign [3]. The resulting sensitivity maps identify efficient locations for the low (LF) and the high frequency (HF) actuation in order to increase the lift. Being a design tool, it is important to quickly assess the different designs of complex configurations. Therefore, the presented approach focuses on methods with rapid turnaround times.

## 2 Numerical Setup and Primal Flow

The LF deformation is modeled by quasi-steady simulations within a domain matched to the wind tunnel of the corresponding experiments. The computational domain in Fig. 1 demonstrates the blocking and the total dimensions of the channel $L_x = 7.7$ m and $L_y = 0.712$ m whereas the chord length of the airfoil is $c = 0.7$ m. Throughout this paper, values are kept dimensional for direct comparison with the experiments. The mesh was generated (and subsequently morphed) using ANSA from BETA CAE Systems and is based on an airfoil geometry provided by the *Institut de Mécanique des Fluides de Toulouse* (IMFT). Although all cases under investigation use an angle of attack of AoA $= 10°$, the mesh is constructed with AoA $= 0°$. It is morphed afterwards to the intended AoA as shown in Fig. 2a. The trailing edge (TE) region of the baseline case (black) in Fig. 2b is then morphed to 6 different reference deformations, of which only the maximum upwards and downwards deflections are shown.

The mesh at the important leading edge (LE) and TE regions is shown in Fig. 3a, b before morphing at AoA $= 0°$ and after morphing to AoA $= 10°$ in Fig. 3c, d. Only mild degradation of mesh quality is visible after morphing and the mesh quality

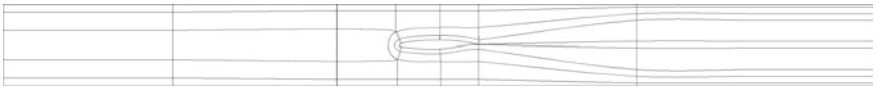

**Fig. 1** Computational domain with the blocking of the block-structured mesh. Airfoil in the channel center

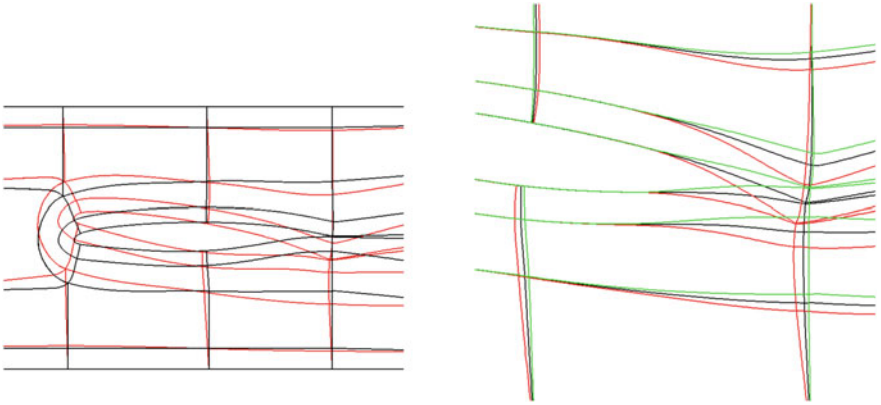

(a) Comparison of AoA = 0° (black) and the baseline at AoA = 10° (red).

(b) Range of reference deformations from $d_{TE} = -25$ mm (red) to $d_{TE} = 20$ mm (green). Baseline with $d_{TE} = 0$ mm (black).

**Fig. 2** Blocking before and after morphing

is considered sufficient for the present investigation. Currently, the meshes are 2D and consist of 196,000 cells. The wall normal size of the first cells at the airfoil is roughly $2 \times 10^{-5}$m growing with 10% in the wall normal direction. The in-house flow solver CFDFlux is a block-structured Finite Volume code solving the Navier-Stokes equations on a colocated grid and with second order accuracy in time and space. It uses a fully-implicit scheme and a pressure-based algorithm with a numerically advanced Rhie and Chow interpolation suitable for sensitive applications such as aeroacoustics. Although features like Large Eddy Simulation and newest methods for Detached Eddy Simulation are available, the present investigation uses for efficiency the unsteady RANS branch only. The sensitivities are calculated by deriving an adjoint solver from the primal solver using discrete adjoints. The correctness of the adjoint solver was verified by comparing with Finite Differences at selected locations. The excessive memory demands of the adjoint solver being caused by storing flow solutions forward in time is avoided by using a two-level checkpointing approach which carefully balances disk and memory usage in a hybrid storage scheme.

In accordance with the experiments, the Reynolds number is $\mathrm{Re} = c \cdot u_{\mathrm{in}}/\nu = 10^6$ and the Mach number $\mathrm{Ma} = u_{in}/a = 0.065$ where $c = 0.7$ m is the chord length, $u_{\mathrm{in}} = 21.5$ m/s the inflow velocity and $a$ the speed of sound. For the $k$-$\omega$ turbulence model, a turbulent intensity of $\mathrm{TU} = 0.01$ and viscosity ratio of $\nu/\nu_t = 1$ are applied as inflow conditions.

Figure 4 demonstrates the course of the unsteady lift coefficient after the initial transient phase. The time step for these simulations was set to a rather coarse value of $\Delta t = 2 \times 10^{-5}$ s to reduce unsteadiness for the LF investigation. As expected, the displacement of the trailing edge $d_{\mathrm{TE}}$ has a strong influence on the lift. The corresponding average values over the shown time interval are given in Table 1.

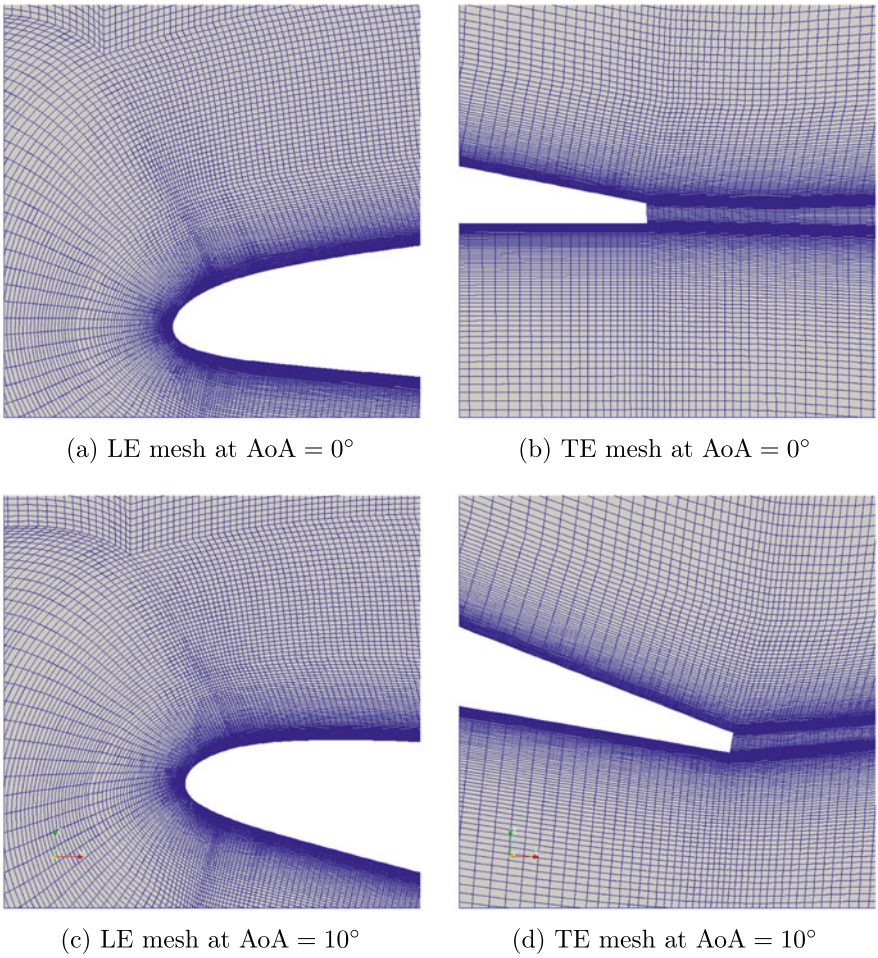

(a) LE mesh at AoA $= 0°$ (b) TE mesh at AoA $= 0°$

(c) LE mesh at AoA $= 10°$ (d) TE mesh at AoA $= 10°$

**Fig. 3** Different views of the mesh

The solver CFDFlux uses a hybrid wall boundary condition which blends smoothly between a low and a high Reynolds boundary condition, relaxing common constraints on the near wall mesh. However, the mesh in the present investigation is designed to resolve the boundary layer with a low Reynolds boundary condition. Figure 5 shows that the commonly used condition of $y^+ < 1$ is valid on most of the airfoil surface.

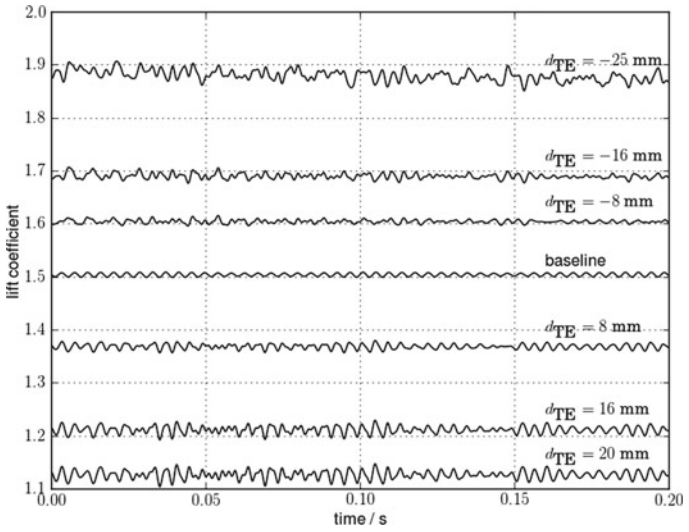


**Fig. 4** Lift coefficient for the reference cases

**Table 1** Mean lift coefficients based on an interval of $T = 0.2$ s

| $d_{TE}$ (mm) | Mean lift coefficient |
|---|---|
| 0 | 1.51 |
| 8 | 1.37 |
| 16 | 1.21 |
| 20 | 1.13 |
| −8 | 1.61 |
| −16 | 1.69 |
| −25 | 1.88 |

## 3 Sensitivities for Quasi-Steady Morphing

The low frequency actuation shall be modeled by quasi-steady simulations. The evaluation of the sensitivities on the reference deformation states intends to show where improvements of the deformation are most effective. The resulting sensitivity maps with respect to the mean lift evaluated over a time interval of $T = 0.2$ s are shown in Fig 6. Comparing with Fig. 4, the interval is large enough to achieve a meaningful statistical sample for the unsteady flow. Positive contours indicate that local outward deformation of the wall would be beneficial for the lift whereas negative contours favour inward deformation to increase the lift. The sensitivities must be interpreted strictly locally in the design space and can not predict the result of a full optimization (the sensitivities of a fully optimized airfoil would be zero). Therefore, the sensitivities show the influence of very small deformations on the lift.


**Fig. 5** Contours of the cell height $y^+$

The baseline case with no additional bending of the TE in Fig. 6a reveals a negative sensitivity in the LE region and positive values in the rest of the upper nose region. This corresponds to a flattening of the leading edge and an upward deformation of the upper nose region whereas the lower part is comparatively neutral. The trend is therefore to reduce the curvature of the LE and increase the thickness. A similar effect is commonly achieved by slats on multi-element airfoils. The outward deformation on the mid section of the upper wing surface increases the camber of the airfoil. The sensitivity in the TE region is clearly dominated by the inward deformation of the lower surface which increases the circulation (Kutta condition). This is reinforced by the local maximum of the upper surface slightly upstream of the TE.

The upwards deformed reference cases with $d_{\mathrm{TE}} > 0$ in Fig. 6b–d share the characteristics of the baseline case.

The downwards deformed reference cases in Fig. 6e, f show similar characteristics, but much more pronounced. The mid section shows a stronger trend towards camber increase, and the local maximum in the TE region is stronger and concentrated on a smaller region.

The maximum downward deformed reference case in Fig. 6g produces the maximum lift of the reference cases, and illustrates that better optimized shapes tend to show weaker sensitivities. The mid section as well as the TE region feature significantly reduced sensitivities, with only the nose and lower TE regions retaining strong sensitivity. The negative local minimum on the rear part of the airfoil might indicate that a reduction of the excessive local curvature is favourable.

Focusing on the TE region, the following conclusions can be drawn within the limitations of the numerical methods. Common to all reference cases and most important is the inward deformation at the lower surface close to the TE. On the upper surface upstream of the TE, mostly a slight outward deformation is favoured. The values located directly at the corners of the blunt TE can not be directly interpreted because sensitivities tend to show excessive values at feature edges.


(a) baseline $d_{\mathrm{TE}} = 0$ mm


(b) $d_{\mathrm{TE}} = 8$ mm


(c) $d_{\mathrm{TE}} = 16$ mm


(d) $d_{\mathrm{TE}} = 20$ mm


(e) $d_{\mathrm{TE}} = -8$ mm


(f) $d_{\mathrm{TE}} = -16$ mm


(g) $d_{\mathrm{TE}} = -25$ mm

**Fig. 6** Sensitivity of the lift with respect to wall normal outward deformation of the baseline case AoA= 10° and various reference deformations characterized by the displacement of the trailing edge $d_{\mathrm{TE}}$

## 4 Approximating Sensitivity for High Frequency Deformations

In the previous section, the quasi-steady simulations were set up to show only minor unsteadiness. To investigate the effects of the high frequency actuation it is desirable to resolve more unsteadiness. This is achieved by reducing the time step size from $\Delta t = 2 \times 10^{-5}$ to $\Delta t = 1 \times 10^{-5}$ as well as by staying in the later part of the transient phase of the simulation when the flow has not yet completely settled. Consequently, the lift oscillations in Fig. 7 are much stronger than in Fig. 4 from the low frequency investigation.

The time integration interval $T$ plays an important role for interpreting sensitivity results. A long interval like in the previous section filters out most of the unsteady effects such that the sensitivity will not change much with even longer periods. With shorter intervals, a favourable deformation along the sensitivity map might have an adverse effect outside of the used interval. However, this commonly unintended trade-off between intervals can be used to derive conclusions for high-frequency deformations. The difference to a long interval is stronger the shorter the chosen interval, as can be seen comparing Fig. 8a, g where the former is the same as in the quasi-steady investigation, and the latter is a factor 100 shorter.

The sensitivity on such short intervals can be split into two contributions: A strong contribution of larger scales, which is illustrated by the features that change only mildly with increasing $T$ in Fig. 8, and a weaker contribution linked to unsteady structures.

The large scale contribution is independent of the phase angle (i.e. starting point of the interval). This allows the contributions to be separated by shifting the phase angle in a stepwise manner and decomposing the result into an ensemble average and a fluctuating part. As an example, such a shifting interval was used in Fig. 9 for a single point on the upper surface about $0.04c$ upstream of the TE. The x-axis

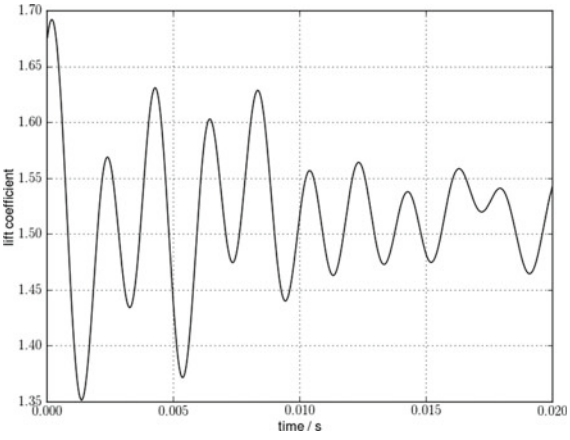


**Fig. 7** Example for the lift oscillation of the high-frequency investigation


(a) $T = 0.2$ s


(b) $T = 0.1$ s


(c) $T = 0.04$ s


(d) $T = 0.02$ s


(e) $T = 0.01$ s

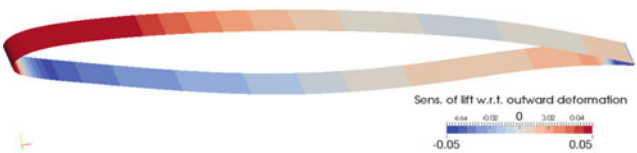


(f) $T = 0.004$ s


(g) $T = 0.002$ s

**Fig. 8** Influence of integration interval on to sensitivity of the lift with respect to wall normal outward deformation of the baseline case at AoA= 10°. Data is based on single simulations from a common starting point. The contour scalings of (**a**) and (**b**) deviate from the remaining plots

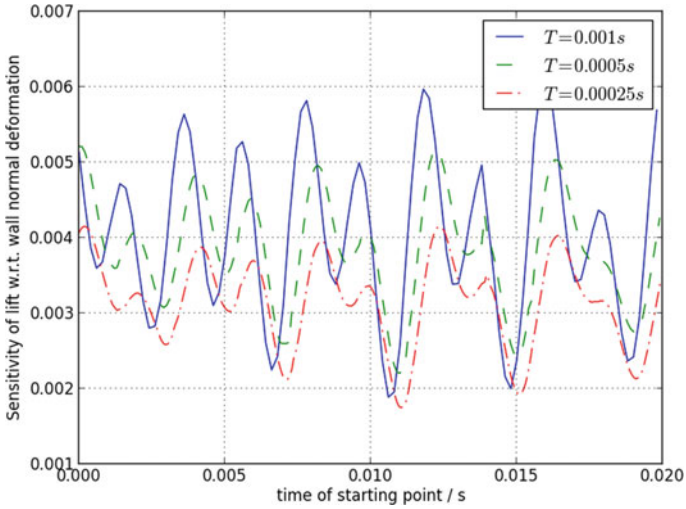


**Fig. 9** Sensitivity at an individual point 4% of the chord upstream of the TE for various phase positions and fixed intervals

denotes the shifted starting point of each interval. The sensitivities oscillate around a positive mean value with a frequency similar to the lift oscillation frequency.

The decomposition in mean and fluctuating components is performed for the whole airfoil and the strength of the fluctuation is summarized by the root-mean-square of the fluctuation in Fig. 10a, b. Except for the upper TE region, the map of the mean sensitivity is consistent with pitching the airfoil up. The RMS sensitivity demonstrates that the lower airfoil surface is of only minor relevance for the high frequency actuation whereas the upper surface is much more effective. When approaching the upper TE, the values decrease. In contrast to the quasi-steady investigation where the excessive sensitivities at the TE were restricted to the last cell face at the TE, the present high frequency evaluation shows strong RMS values distributed over multiple cell faces in the lower TE region. This is interpreted as strong indication that such an actuation is very favourable, as already shown by the experiments of the IMFT [3, 8].

With focus on the TE region, two starting points were selected in Fig. 10c, d when the sensitivity fluctuations are extreme in this region, i.e. representing a peak and trough respectively in Fig. 9.

## 5 Conclusions

The presented approach demonstrates a fast process based on efficient methods to obtain sensitivity maps for low and high frequency deformations at short turnaround times. Emphasis was initially put on a fast evaluation of the approach rather than


(a) Ensemble average


(b) RMS of fluctuation w.r.t. ensemble average


(c) Example for approximate peak of fluctuation in the rear region


(d) Example for approximate trough of fluctuation in the rear region

**Fig. 10** Decomposition of sensitivity contributions based on 100 short intervals of $T = 0.001$ s each shifted by 0.0002 s covering a total duration of 0.02 s

resolving more complex flows with higher accuracy. However, within an unsteady RANS context, this approach can easily be extended to more complex situations.

For the low frequency regime, sensitivity maps were produced for a baseline case and 6 reference deformations of an industrially-relevant airfoil. Features of the resulting sensitivity maps, such as a thicker nose with reduced curvature, more camber, and a trailing edge modification increasing the circulation could be successfully matched to aerodynamic interpretations. Within the limitations of the numerical methods applied, the lower trailing edge region is best modified by an inward deformation whereas the upper trailing edge region should be deformed slightly outwards.

Sensitivities for high-frequency deformation were successfully extracted using the same code base as for the low frequency regime avoiding additional solver complexity. From these maps, it was inferred that the high-frequency actuation at the

lower airfoil surface is ineffective except for an actuation close to the trailing edge. Here the lift is seen to be very sensitive, which agrees with experimental findings. For the upper surface, the sensitivity map suggests high frequency deformations over the whole mid wing.

In future work, similar evaluations of the sensitivity to low and high-frequency surface deformation will be made for an objective function that better reflects aerodynamic efficiency, such as lift-to-drag ratio. Furthermore, shape optimisation simulations will be carried out to find an optimal deformed steady shape starting from different trailing edge deflections.

**Acknowledgements** This project has received funding from the European Union's Horizon 2020 research and innovation programme under grant agreement No 723402 "Smart Morphing and Sensing".

## References

1. Barbarino, S., Bilgen, O., Ajaj, R.M., Friswell, M.I., Inman, D.J.: A review of morphing aircraft. J. Intell. Mater. Syst. Struct. **22**(9), 823–877 (2011)
2. Dimino, I., Ciminello, M., Concilio, A., Pecora, R., Amoroso, F., Magnifico, M., Schueller, M., Gratias, A., Volovick, A., Zivan, L.: Distributed actuation and control of a morphing wing trailing edge. In: Wölcken, P.C, Papadopoulos, M. (eds.) Smart Intelligent Aircraft Structures (SARISTU), pp. 171–186, Cham. Springer International Publishing (2016)
3. Jodin, G., Motta, V., Scheller, J., Duhayon, E., Carsten, Rouchon, J.-F., Braza, M.: Dynamics of a hybrid morphing wing with active open loop vibrating trailing edge by time-resolved PIV and force measures. J. Fluids Struct. **74**, 263–290 (2017)
4. Kota, S., Flick, P., Collier, F.: Flight testing of the flexfloil™ adaptive compliant trailing edge. In: 54th AIAA Aerospace Sciences Meeting. American Institute of Aeronautics and Astronautics Inc., AIAA (2016)
5. Lyu, Z., Joaquim R.R.A.M.: Aerodynamic shape optimization of an adaptive morphing trailing edge wing. In: Proceedings of the 15th AIAA/ISSMO Multidisciplinary Analysis and Optimization Conference, Atlanta, GA, June 2014, AIAA, pp. 2014–3275 (2014)
6. Nemili, A., Özkaya, E., Gauger, N.R., Kramer, F., Thiele, F.: Discrete adjoint based optimal active control of separation on a realistic high-lift configuration. In: Dillmann, A., Heller, G., Krämer, E., Wagner, C., Breitsamter, C., (eds.) New Results in Numerical and Experimental Fluid Mechanics X, pp. 237–246, Cham. Springer International Publishing (2016)
7. Magnifico, M., Pecora, R., Amoroso, F.: Toward the bi-modal camber morphing of large aircraft wing flaps: the cleansky experience. In: Proceedings of SPIE, vol. 9801, p. 9801 (2016)
8. Scheller, J., Jodin, G., Joseph Rizzo, K., Duhayon, E., Rouchon, J.-F., Triantafyllou, M.S., Braza, M.: A Combined Smart-Materials Approach for Next-Generation Airfoils. Solid State Phenom. **251**, 106–112 (2016)

# Thin Shear Layers in High-resolution Direct Numerical Simulations of Turbulence


**Takashi Ishihara, Koji Morishita, and J. C. R. Hunt**

**Abstract** Recent studies based on high-resolution direct numerical simulations (DNSs) of turbulence have shown that there are three different types of shear layers in homogeneous and inhomogeneous turbulent flows; at the outer edge (T/NT), in the interior (T/T) and within the buffer layer near the wall (T/W). All the layers play important roles in various turbulence phenomena in the fields of natural sciences and engineering applications. Data analyses showed that all the shear layers act as a barrier of the velocity fluctuations by blocking velocity fluctuations from the one side to the other side. It was suggested that the blocking mechanism of thin turbulent wall (T/W) layers can be used to control the turbulent wake of aerofoils. For high Reynolds number, flows over typical aerofoils at low angle of incidence in the thin turbulent boundary layers (TBLs) have a conditional structure with thin T/W layers which act as a barrier to eddies in the outer part of the TBL. Recent studies indicate that using disturbance—devices at the airfoil surface enhances the blocking effect of the TW barrier and leads—unexpectedly-to reduced shear fluctuations at the wall. This suggests that deeper understanding of the structures and properties of the T/W layers may provide ideas to consider the better strategies for aerofoils designs. In this paper, we review the recent studies on the three different types of shear layers, which are based on the high-resolution DNSs of homogeneous isotropic turbulence (HIT), turbulent boundary layer (TBL), and turbulent channel flow (TCF).

**Keywords** Turbulence · High Reynolds number · DNS · Thin shear layers · Blocking mechanism

T. Ishihara (✉)
Okayama University, Okayama 700-8530, Japan
e-mail: takashi_ishihara@okayama-u.ac.jp

K. Morishita
Kobe University, Kobe 657-8501, Japan

J. C. R. Hunt
University College London and Trinity College, Cambridge, UK



M. Braza et al. (eds.), *Advances in Critical Flow Dynamics Involving Moving/Deformable Structures with Design Applications*, Notes on Numerical Fluid Mechanics and Multidisciplinary Design 147,
https://doi.org/10.1007/978-3-030-55594-8_43

## 1 Introduction

Recent developments of supercomputer enable us to perform large-scale direct numerical simulations (DNSs) of turbulence. A history of the number of grid points used in the DNS of homogeneous isotropic turbulence shows an increase by a factor of $10^9$ times over the past 40 year. Thanks to this development, we can now analyze turbulent flow fields in detail at much higher Reynolds number than previously. Our recent studies using the DNS data of homogeneous isotropic turbulence (HIT), turbulent channel flow (TCF), and turbulent boundary layer (TBL) have shown that there are three different types of shear layers in homogeneous and inhomogeneous turbulent flows; at the outer edge (T/NT), in the interior (T/T) and within the buffer layer near the wall (T/W) [1]. Since all the layers are related to energy containing eddies (forcing at large-scales) or boundary conditions in the turbulent flow fields, they necessarily play important roles in various turbulence phenomena in the fields of natural sciences and engineering applications.

Analysis of the DNS data of turbulent boundary layers (TBLs) showed that the conditional cross correlations of streamwise velocity fluctuations near turbulent/non-turbulent (T/NT) interface are de-correlated across the T/NT interface [2]. Such de-correlation is consistent with the blocking mechanism proposed by a theoretical study [3]. Recent studies Szubert et al. [4], Hunt et al. [5] suggested that the blocking mechanism of T/W layers can be used to control the turbulent wake of aerofoils. Flows over typical aerofoils at low angle of incidence in the thin turbulent boundary layers (TBLs) have a conditional structure with thin T/W layers which act as a barrier to eddies that are generated in the outer part of the TBL. Recent studies indicate that using some device within the airfoil surface enhances the blocking effect of the T/W barrier and leads to reduced shear fluctuations at the wall. Therefore, understanding of the structures and properties of the T/W layers is necessary to consider the better strategies for aerofoils designs. Note that in typical engineering flows the Reynolds numbers are very high as shown in this study. Note also that thin shear layers (T/T) also form in the interior of these boundary layers and wake flows [6].

In this paper, we review our recent studies on the three different types of shear layers based on the DNSs of homogeneous isotropic turbulence (HIT) ($R_\lambda = 1100$), turbulent boundary layer (TBL) ($R_\theta = 900 - 2000$), and turbulent channel flow (TCF) ($R\tau = 5120$).

## 2 DNS Data of Turbulent Flows

In this study, we use the DNS data of three different types of incompressible turbulence including homogeneous isotropic turbulence (HIT), turbulent boundary layer (TBL), and turbulent channel flow (TCF). The DNS data of HIT in this study are those used in Kaneda et al. [7] and Ishihara et al. [8]. A fully alias-free Fourier spectral method was used in those DNSs. The TBL data are from Ishihara et al. [2]

in which the DNSs were performed using a Fourier spectral method in the streamwise and spanwise directions combined with a Jacobi polynomial expansions in the wall-normal direction (after changing the variable) [9]. The TBL can be assumed to be periodic in the streamwise direction by introducing a fringe region downstream, although the flow is changing in the streamwise direction as the boundary layer grows, c.f. Spalart and Watmuff [10]. The DNS data of TCF are those used in Morishita et al. [11] and Kaneda et al. [12], where a Fourier-spectral method was used in the streamwise and spanwise directions and a Chebyshev-tau method was used in the wall-normal direction. The parameters used in the DNSs of three different types of turbulence are listed in Table 1.

**Table 1.** Parameters of the DNSs; **a** HIT (from Ishihara et al. [8]), **b** TBL (from Ishihara et al. [2]), **c** TCF (from Kaneda et al. [12])

(a) HIT; $N$: number of grid points in one direction, $R_\lambda$:Taylor microscale Reynolds number, L: integral length scale, $\lambda$: Taylor microscale, $\eta$: the Kolmogorov length scale

| Run | $N$ | $R_\lambda$ | L | $\lambda$ | $\eta$ |
|---|---|---|---|---|---|
| 256-1 | 256 | 167 | 1.13 | 0.203 | 0.00797 |
| 512-1 | 512 | 257 | 1.02 | 0.125 | 0.00395 |
| 1024-1 | 1024 | 471 | 1.28 | 0.0897 | 0.00210 |
| 2048-1 | 2048 | 732 | 1.23 | 0.0558 | 0.00105 |
| 4096-1 | 4096 | 1131 | 1.09 | 0.0339 | 0.00051 |

(b) TBL; $N_x * N_y * N_z$: number of grid points in the streamwise ($x$), wall-normal ($y$), spanwise ($z$) directions, $R_\theta$: Reynolds number based on momentum thickness, $\theta_0$: momentum thickness at the inlet, $\Lambda_x$, $\Lambda_z$: domain size in $x$ and $z$ directions, $\Delta x^+$, $\Delta z^+$: grid size in $x$ and $z$ directions

| Run | $N_x * N_y * N_z$ | $R_\theta$ | $\Lambda_x/\theta_0$ | $\Lambda_z/\theta_0$ | $\Delta x^+$ | $\Delta z^+$ |
|---|---|---|---|---|---|---|
| R900 | 1920 * 256 * 384 | 344–1130 | 1221 | 91.6 | 10.4 | 3.91 |
| R2500 | 4608 * 512 * 768 | 835–2443 | 1293 | 97.0 | 10.2 | 4.72 |

(c) TCF; $R_\tau$: friction Reynolds number, $h$: channel half-width, $N_x * N_y * N_z$: number of grid points in the streamwise ($x$), wall-normal ($y$), spanwise ($z$) directions, $L_x$, $L_z$: domain size in $x$ and $z$ directions, $\Delta x^+$, $\Delta z^+$: grid size in $x$ and $z$ directions, $\Delta y_c{}^+$: grid size in $y$ direction at the center

| $R_\tau$ | $L_x/h$ | $L_z/h$ | $N_x * N_y * N_z$ | $\Delta x^+$ | $\Delta y_c{}^+$ | $\Delta z^+$ |
|---|---|---|---|---|---|---|
| 640 | $\pi$ | $\pi/2$ | 256 * 384 * 256 | 7.9 | 7.9 | 3.9 |
| 1280 | $\pi$ | $\pi/2$ | 512 * 768 * 512 | 7.9 | 7.9 | 3.9 |
| 2560 | $\pi$ | $\pi/2$ | 1024 * 1536 * 1024 | 7.9 | 7.9 | 3.9 |
| 5120 | $\pi$ | $\pi/2$ | 2048 * 1536 * 2048 | 7.9 | 15.9 | 3.9 |

## 3 Three Different Types of Thin Shear Layers

### *3.1 T/T*

In HIT studies of vorticity fields obtained by using DNS showed that there is a transition in the forms of intense vortical structures from isolated vortex tubes at $R_\lambda = O(100)$ to dense vortex clusters (thin shear layers) at $R_\lambda = O(1000)$ [13, 14]. A series of analyses of conditional statistics of the thin shear layers in HIT showed the following [14]; (i) The size and thickness of the layers are O(L) and $O(\lambda)$, respectively. (ii) Across the layer there is a velocity jump of $O(u_{rms})$. (iii) Strong micro-scale vortices are generated inside the layer with strength of order $R_\lambda^{1/2}$ greater than that predicted by K41. (iv) These vortices are associated with strong energy dissipation (of order $R_\lambda$ greater than the mean) and high net energy transfer with large fluctuations within the layer. (v) The interfaces of the layers act partly as a barrier to the fluctuations outside the layer.

Recently, Elsinga et al. [15] showed quantitatively using the eigenframes of rate-of-strain tensor that there are transitions of vortical structures in turbulent flows as Re increases. Figure 1 shows that strong microscale vortices in a layer-like region with a skewed distribution of a vortex component induce a shear flow across the layer. Similar T/T structures have been found in experiments [16]. Also, similar layers were observed in much higher Reynolds number turbulence ($R_\lambda = 2300$) obtained by recent highest resolution DNS with $12{,}288^3$ grid points [17]. Recently, it was suggested that the thin shear layer which was analyzed in detail in IKH is generated by a forcing at large-scale as a part of double spirals around a large-scale low-pressure vortex. Micro-scale double spirals around a tubular vortex were firstly observed by Kida and Miura [18] in a DNS of decaying turbulence at $R_\lambda = 106$. The double spiral structure at $R_\lambda = O\ (1000)$ is similar to that observed in Kida and Miura [18] but is different in that it is constructed as a cluster of intense microscale vortices.

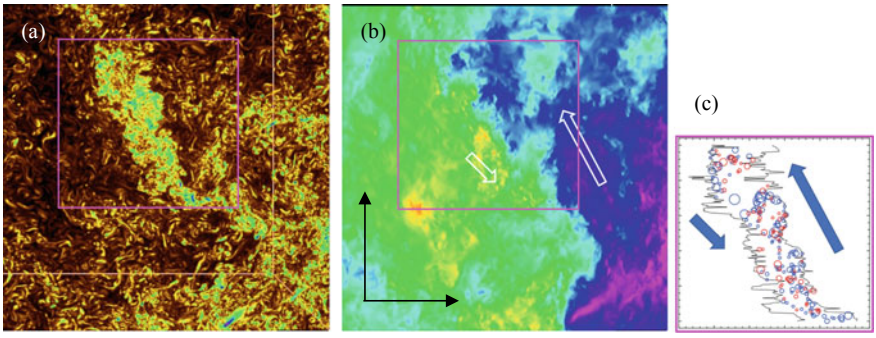


**Fig. 1.** Contour plots of **a** enstrophy and **b** $z$-component of velocity in a $x$-$z$ plane. The size of the plotted domain is $1.16L \times 1.16L$ ($L$ is the integral scale). **c** High $|\omega_y|$ peakes in the layer; blue circles are for $\omega_y > 0$ and red circles are for $\omega_y < 0$. The pink square region in (**a**, **b**) is plotted (From IKH).

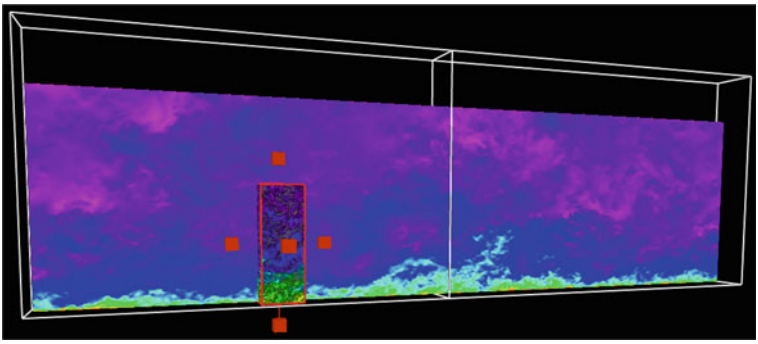

**Fig. 2.** A contour plot of streamwise velocity component in a plane perpendicular to the spanwise direction. The bottom of the bounding box is one of the wall of the TCF, the top is the channel center. The depth of the bounding box indicates a 1/8 part of the computational domain in the spanwise direction

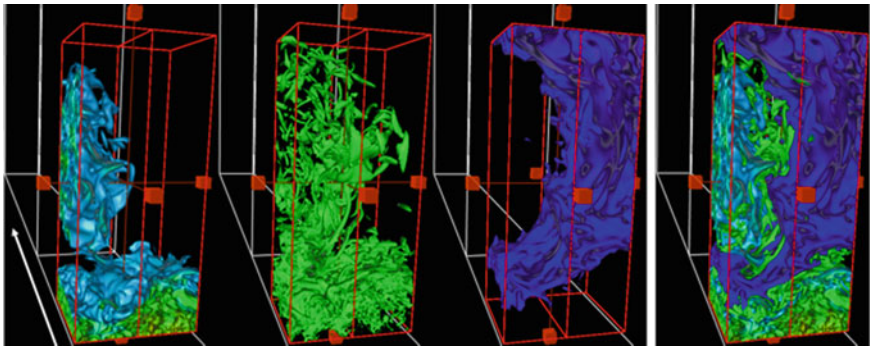

**Fig. 3.** Iso-surfaces indicating low speed zone, high enstrophy regions, high speed zone, and their superpositions, in a red subdomain shown in Fig. 2

T/T layers similar to those observed in the above studies have been also observed by experiments within turbulent boundary layers [6]. Recently, de Silva et al. [19] observed uniform momentum zones (UMZ) in TBLs. They observed that shear layers of intense vortices separate each zone. However, the relation between the UMZ and the thin shear layers in high Re wall turbulence has not been studied in detail yet. Figure 2 shows a contour plot of streamwise velocity component on a wall-normal cross section in the streamwise direction of TCF at $R_\tau = 5120$. We can observe sharp changes (jumps) in the streamwise velocity component at some parts of the contours. The observation indicates also that the edges of the UMZ are not always strong (T/T) shear layers.

Figure 3 shows low speed zone, high speed zone, and high enstrophy regions in a sample subdomain. It shows that the clusters of strong vortices are generated at the thin regions between the low speed zone and high speed zone. As observed in the

figure, high speed and low speed zones are fully three-dimensional and the internal thin shear layers are not always parallel to the wall. Therefore, the geometrical shapes of the thin shear layers are more complex and cannot be studied by two-dimensional as proposed de Silva et al. [19]. Our observations based on three-dimensional visualizations of the high Re TCF agree well with the conceptual scenario (nested packets of hairpins or cane-type vortices growing up from the wall) given by Adrian et al. [20]; see Fig. 25 in their paper. However, Fig. 3 suggests that it may be appropriate to replace the packets of large-scale hairpins or cane-type vortices in their Fig. 25 by the thin shear layers constructed by dense vortices when the Reynolds number is high enough. The similar is expected for the T/T layers within high Re TBLs.

### *3.2 T/NT (of TBL)*

Analyses of the conditional statistics near the external turbulent/non-turbulent (T/NT) interface of the TBLs (the momentum-thickness-based Reynolds numbers, $R_\theta = 500 - 2200$) [2] showed that the T/NT interface can be well determined as the outer-most iso-surfaces of the vorticity-amplitude. We used $\omega = \alpha U/\delta$ ($\alpha = 0.7$) as the threshold, where U is the streamwise velocity at $y = \infty$ and $\delta$ is the boundary layer thickness (see Fig. 4a). The average height of the T/NT interface is about $0.8\delta$. We observe that there is a velocity jump of order $u_{\rm rms}$, where $u_{\rm rms}$ is the rms value of the streamwise velocity component near the T/NT interace.

Analyses of the conditional statistics near the T/NT interface showed that the T/NT layer has an inertia-viscous double structure which consists of a turbulent sublayer with a thickness of the order of the Taylor micro-scale and its outer boundary with a thickness of the order of the Kolmogorov length scale. The analysis also showed that the conditional cross correlations of the streamwise or the wall-normal velocity fluctuations change sharply across the interface, suggesting that the T/NT layer acts as a barrier to the external velocity fluctuations.

### *3.3 T/W*

In general wall-bounded turbulent flows, we observe a change of functional form of mean velocity profile at the region (about $10\nu/u_\tau$ from the wall) between the viscus layer and log-law region, where $\nu$ is kinematic viscosity and $u_\tau$ is the friction velocity. In the actual snapshots of velocity profiles it is expected that we may observe much sharper velocity jumps near the wall. To characterize such a sharp velocity jump, we tried to determine the T/W interface by using $\omega = \alpha U/\delta$ ($\alpha = 7.0$, 8.0, and 9.0) as the threshold values for the TBL ($R_\theta = 900$). The resulting PDFs of the heights of the interface are plotted in Fig. 5. The average heights, which are 40, 31, and 25 in wall units for $\alpha = 7.0$, 8.0, and 9.0, respectively, depend on the threshold values, while the peak heights of the PDFs (12.7, 11.9, and 10.4, respectively) have

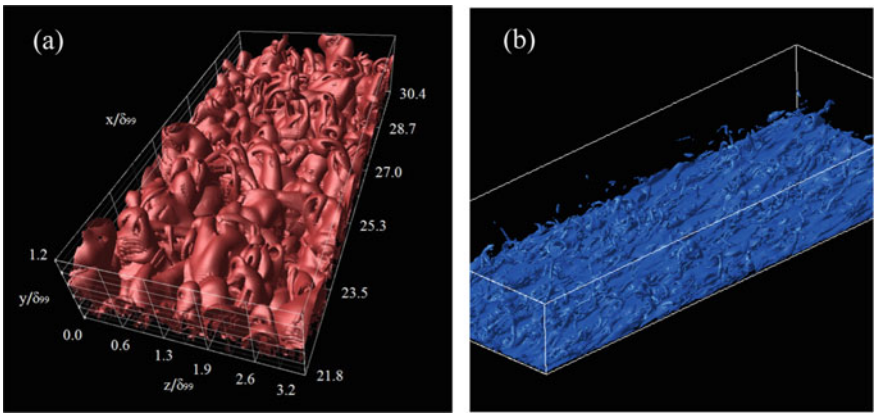


**Fig. 4.** Iso-surfaces of vorticity amplitude showing **a** T/NT interface determined by $\omega = 0.7U/\delta$ and **b** T/W interface determined by $\omega = 7U/\delta$

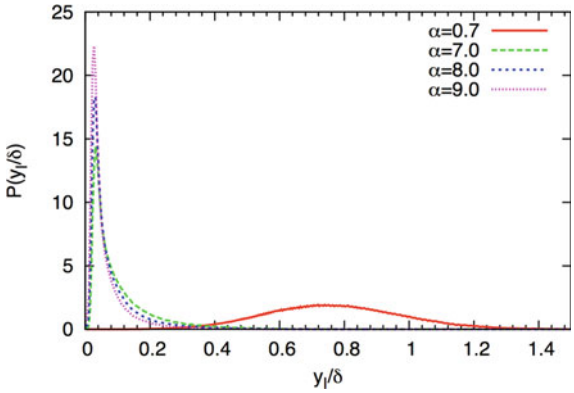


**Fig. 5.** PDFs of the height of the T/W interface in the TBL ($R_\theta = 900$) determined by $\omega = \alpha U/\delta$ ($\alpha = 7.0, 8.0, 9.0$). The corresponding data for the T/NT interface ($\alpha = 0.7$) are also plotted for comparison

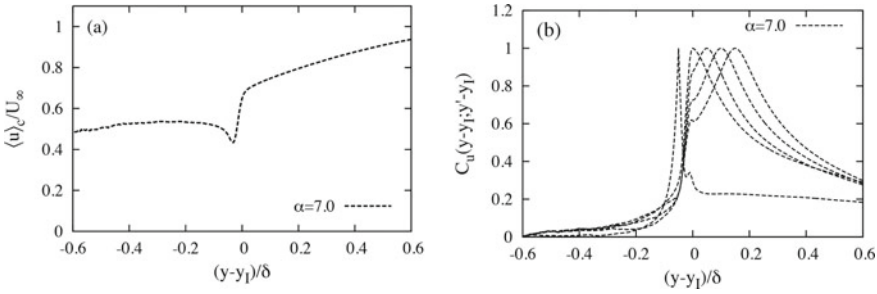


**Fig. 6.** **a** Conditional average of the streamwise velocity component near the T/W interface defined by $\omega = 7.0U/\delta$ in the TBL ($R_\theta = 900$). **b** Conditional cross correlations of the streamwise velocity fluctuations for the T/W interface

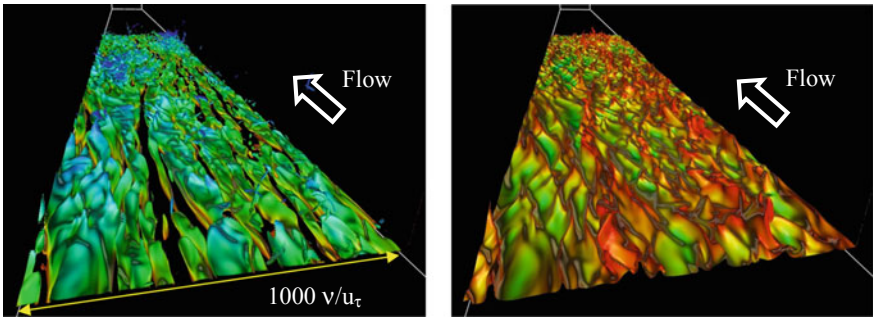


**Fig. 7.** Visualizations of the T/W layer in a DNS of the TCF at $R_\tau = 5120$; **a** iso-surface of vorticity amplitude ($\omega^+ = 0.6$) colored by the value of $u$ (Blue is fast and yellow is slow) and **b** iso-surface of streamwise velocity component ($u^+ = 10$) colored by the value of vorticity amplitude (Green is large and red is small).

weak dependence on the threshold values. Figure 4b shows the iso-surface of vorticity amplitude determined by $\omega = 7.0U/\delta$. As observed in Fig. 4b, the iso-surface consists of the base part and hairpin vortices. The results in Fig. 5 with the visualization in Fig. 4b suggest that the majority of the T/W interfaces lies in the region about $10\nu/u_\tau$ from the wall. Note that $\omega = 7.0$–$9.0U/\delta$ for $R_\theta = 900$ corresponds to $\omega^+$ ~0.4–0.5. Therefore, for the extraction of the T/W interface, the threshold values of $\omega^+$ ~0.4–0.5 are appropriate for different Reynolds numbers.

Figure 6 shows the conditional average of the streamwise velocity component and conditional cross correlations of the streamwise velocity fluctuations. We observe sharp velocity jumps of order (0.2–0.3U) across the T/W interface. Also, we can observe the strong de-correlation of velocity fluctuations at the T/W interface. This indicates that the blocking mechanism at T/W interfaces is stronger than that at T/NT interfaces.

To understand the structure of the T/W layer in high Reynolds number TBLs, we investigate the T/W layer in a DNS of the TCF at $R_\tau = 5120$ in Fig. 7. As in the case of low Reynolds number TBL, the T/W layer in Fig. 7a is constructed by the base part and hairpin vortices. The base part of the T/W layer has scale-like thin structures and has cracks in the streamwise direction. The top of the base part is blue and the bottom is yellow. We confirm from these colors that the T/W layer is a shear layer. The iso-surface of the streamwise velocity in Fig. 7b has flame-like structures and has mountain ranges extending in the streamwise direction. The mountain ranges correspond to low-speed streaks (see, e.g., [21]). Their positions agree well with those of cracks observed in Fig. 7b.

## 4 Conclusions

In this paper, we have compared the characteristics and role of the thin shear layers that are found in the high-resolution DNSs of HIT, TCF, and TBL. Three types of thin shear layers are found in high Re turbulence; internal T/T layer in HIT and in TCF, external T/NT layer in TBL, and T/W layers in TBL and in TCF. We observed that the T/T layer in high Re HIT and TCF has a velocity jump across the layer, which is composed by dense microscale vortices. Also, we observe the decorrelation of velocity fluctuations at all the layers and that the decorrelation of velocity fluctuations at the T/W interface of TBLs are stronger than that at T/NT interfaces of TBLs. The T/W layers are at $y^+$ ~10 and they have scale-like vortical structures when the Reynolds number is high. Stabilizing the T/W layers may be the key to controlling the wall-bounded turbulent flows.

As shown by Xu et al. [22], the velocity fluctuations in T/W is highly non-Gaussian. Numerical experiments to confirm these results would be interesting.

**Acknowledgements** The computational resources of the K computer provided by the RIKEN Advanced Institute for Computational Science through the HPCI System Research project (Projects ID:hp170087 and ID:hp180109) were partly used in this study. This research was supported in part by JSPS KAKENHI Grant Number JP15H03603 and by MEXT as "Exploratory Challenge on Post-K computer" (Elucidation of the Birth of Exoplanets [Second Earth] and the Environmental Variations of Planets in the Solar System).

## References

1. Ishihara, T., Morishita, K., Hunt J.C.R.: Three types of thin shear layers observed in high *Re* turbulence. In: Proceeding of IMA Conference on Turbulence, Waves and Mixing, King's College Cambridge, UK, pp. 5–8 (2016)
2. Ishihara, T., Ogasawara, H., Hunt, J.C.R.: Analysis of conditional statistics obtained near the turbulent/non-turbulent interface of turbulent boundary layers. J. Fluids Struct. **53**, 50–57 (2015)
3. Hunt, J.C.R., Durbin, P.A.: Perturbed vortical layers and shear sheltering. Fluid Dyn. Res. **24**, 375–404 (1999)
4. Szubert, D., Grossi, F., Garcia, A.J., Hoarau, Y., Hunt, J.C.R., Braza, M.: Shock-vortex shear-layer interaction in the transonic flow around a supercritical airfoil at high Reynolds number in buffet conditions. J. Fluids Struct. **55**, 276–302 (2015)
5. Hunt, J.C.R., Ishihara, T., Szubert, D., Asproulias, I., Hoarau Y., Braza M. (2016) Turbulence near interfaces—modelling and simulations. In: Braza, M., Bottaro, A., Thompson, M. (eds.) Advances in Fluid-Structure Interaction. Notes on Numerical Fluid Mechanics and Multidisciplinary Design, vol. 133. Springer, Cham (2016)
6. Eisma, J., Westerweel, J., Ooms, G., Elsinga, G.E.: Interfaces and internal layers in a turbulent boundary layer. Phys. Fluids (1994–Present) **27**, 055103 (2015)
7. Kaneda, Y., Ishihara, T., Yokokawa, M., Itakura, K., Uno, A.: Energy dissipation rate and energy spectrum in high resolution direct numerical simulations of turbulence in a periodic box. Phys. Fluids **15**, L21–L24 (2003)

8. Ishihara, T., Kaneda, Y., Yokokawa, M., Itakura, K., Uno, A.: Small-scale statistics in high-resolution direct numerical simulation of turbulence: Reynolds number dependence of one-point velocity gradient statistics. J. Fluids Mech. **592**, 335–366 (2007)
9. Spalart, P.R., Moser, R.D., Rogers, M.M.: Spectral methods for the Navier-Stokes equations with one infinite and two periodic directions. J. Comp. Phys. **96**, 297–324 (1991)
10. Spalart, P.R., Watmuff, J.H.: Experimental and numerical study of a turbulent boundary layer with pressure gradients. J. Fluid Mech. **249**, 337–371 (1993)
11. Morishita, K., Ishihara, T., Kaneda, Y.: Small-scale statistics in direct numerical simulation of turbulent channel flow at high-Reynolds number. J. Phys: Conf. Ser. **318**, 022016 (2011)
12. Kaneda, Y., Morishita, K., Ishihara, T.: Small scale universality and spectral characteristics in turbulent flows. In Proceedings the 8th International Symposium on Turbulence and Shear Flow Phenomena, Poitiers, France, INV2 (2013)
13. Ishihara, T., Gotoh, T., Kaneda, Y.: Study of high–Reynolds number isotropic turbulence by direct numerical simulation. Annu. Rev. Fluid Mech. **41**, 165–180 (2009)
14. Ishihara, T., Kaneda, Y., Hunt, J.C.R.: Thin shear layers in high Reynolds number turbulence—DNS results. Flow Turbul. Combust. **91**(4), 895–929 (2013)
15. Elsinga, G.E., Ishihara, T., Goudar, M.V., da Silva, C.B., Hunt, J.C.R.: The scaling of straining motions in homogeneous isotropic turbulence. J. Fluid Mech. **829**, 31–64 (2017)
16. Hunt, J.C.R., Ishihara, T., Worth, N.A., Kaneda, Y.: Thin shear layer structures in high Reynolds number turbulence. Flow Turbul. Combust. **92**(3), 607–649 (2014)
17. Ishihara, T., Morishita, K., Yokokawa, M., Uno, A., Kaneda, Y.: Energy spectrum in high-resolution direct numerical simulations of turbulence. Phys. Rev. Fluids **1**, 082403(R) (2016)
18. Kida, S., Miura, H.: Double spirals around a tubular vortex in turbulence. J. Phys. Soc. Jpn. **69**(10), 3466–3467 (2000)
19. de Silva, C.M., Hutchins, N., Marusic, I.: Uniform momentum zones in turbulent boundary layers. J. Fluid Mech. **786**, 309–331 (2016)
20. Adrian, R.J., Meinhart, C.D., Tomkins, C.D.: Vortex organization in the outer region of the turbulent boundary layer. J. Fluid Mech. **422**, 1–54 (2000)
21. Kline, S., Reynolds, W., Schraub, F., Runstadler, P.: The structure of turbulent boundary layers. J. Fluid Mech. **30**(4), 741–773 (1967)
22. Xu, C., Zhang, Z., den Toonder, J. M. J., Nieuwstadt, F. T. M.: Origin of high kurtosis levels in the viscous sublayer. Direct numerical simulation and experiment. Phys. Fluids **8**, 1938–1944 (1996)

# Scaling Laws for an Airfoil with MFC-Actuated Trailing Edge Plate


**F. Auteri, P. Bettini, and N. Bonfanti**

**Abstract** This study describes the steady effects on the lift coefficient of an airfoil with a plate mounted on the trailing edge and actuated with MFC piezoelectric devices. The problem is analysed numerically with a low fidelity model which has been validated experimentally. A linear structural model is developed taking into account large beam rotations. Finite differences have been used to solve the structure equations, while XFoil is employed to solve the aerodynamic problem by virtue of its speed, accuracy, and widespread use. The performance of the system is evaluated by the derivative of the lift coefficient with respect to the actuation force. The behaviour of this scalar value as a function of both structural and aerodynamic parameters is modelled with approximate, closed form scaling laws when possible. A rather simple but accurate scaling law can be envisaged for the inviscid, uncoupled results. The viscous ones can be described as functions of the boundary layer properties over the actuation system. The coupled formulation suggests that aeroelastic effects decrease the actuation efficacy and can be modelled as a power law of both flight velocity and actuator length. The new insight provided in the present paper can be useful in preliminary design to rapidly evaluate the performance advantage that can be obtained from this morphing technology.

**Keywords** Morphing wing · MFC

## 1 Introduction

In the aerospace sector, the term "morphing" indicates aerospace structures that are able to change their shape to increase the performance of an aircraft, see [13]. The concept of morphing structure has been inspired by nature. Birds, for instance, rely on their capability to change the geometry of the wings to improve the controllability

F. Auteri (✉) · P. Bettini · N. Bonfanti
Dipartimento di Scienze e Tecnologie Aerospaziali, Politecnico di Milano,
via La Masa 34, 20156 Milano, Italy
e-mail: franco.auteri@polimi.it



M. Braza et al. (eds.), *Advances in Critical Flow Dynamics Involving Moving/Deformable Structures with Design Applications*, Notes on Numerical Fluid Mechanics and Multidisciplinary Design 147,
https://doi.org/10.1007/978-3-030-55594-8_44

and efficiency of flight and to extend their flight envelope. While morphing has always been present to a certain extent on aircraft, e.g. ailerons or flaps, a more extensive application of this concept is recently obtaining increased attention from the aerospace industry by the development of new enabling technologies, such as ShapeMemory Alloys (SMA), piezoelectric actuators and compliant mechanisms [9].

A particular kind of morphing that has received a limited attention to date is related to thin plates that are actuated by piezoelectric devices and are installed on the trailing edge of the wing, see [1] and [5]. The actuation for these devices is provided by Micro Composite Fiber (MFC) piezoelectric actuators, first developed at the NASA Langley Research Center. These actuators exploit uniaxial fibres surrounded by a polymeric matrix and the voltage is applied through an interdigitated electrode pattern deposed on a polyimide film [14]. Owing to their simplicity, low weight and high bandwidth, they could have several applications, ranging from the optimisation of the load distribution to gust-load attenuation.

In this work, a low-fidelity investigation of the performance of an airfoil, equipped with a morphing trailing-edge plate, is carried out. MFC actuators are flush mounted on a thin plate that is installed as a cantilever on the trailing edge of the airfoil, as shown in Fig. 1. This configuration is particularly interesting for its simplicity, since the plate can be quite easily retrofitted on an existing wing. The paper is organised as follows. In Sect. 2, the mathematical models employed to describe the actuated plate and the aerodynamic forces acting on the airfoil-plate system are described. Section 3 is devoted to the experimental validation of the models adopted. In Sect. 4 the obtained results are reported and discussed. Finally, some concluding remarks are drawn in Sect. 5.

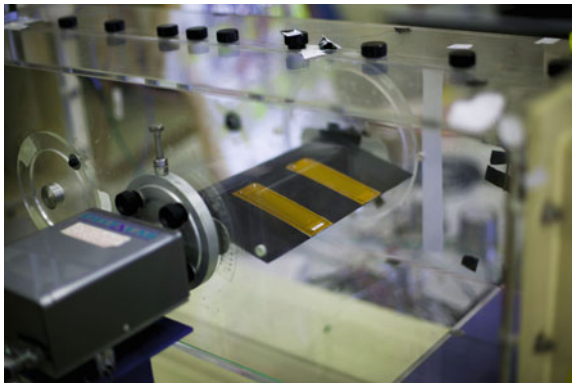

**Fig. 1** Airfoil with MFC-actuated trailing-edge installed in the wind tunnel

## 2 The Mathematical Model

Owing to the discrete character of the MFC actuators, the structure is actually 3D, as shown in Fig. 2 (left), as is also the wing. We can assume, however, that the actuators will be densely distributed along the span, that loads do not vary sensibly along it and that the bending stiffness of the plate is higher along the span than along the chord, then a homogenisation along the span allows us to obtain a more manageable 2D problem. Assuming also that the wing has a high aspect ratio, we can deal with the single wing section, while the full wing properties can be obtained by Prandtl's finite wing theory [7] for a sufficiently slender wing.

The aforementioned hypotheses permit a substantial simplification of the problem, the deformation becoming a plane function $\varepsilon(x, y, z) \approx \varepsilon(x, y)$. The virtual deformation work per unit span can be written $\int_x \int_y \overline{\varepsilon}_x(x, y) E_M(x, y)\, \varepsilon_x(x, y)\, \mathrm{d}y\, \mathrm{d}x$, where the overbar denotes the virtual deformation, $E$ is the material Young modulus and $E_M(x, y) = \frac{1}{L_{\mathrm{ref}}} \int_z E(x, y, z)\, \mathrm{d}z$ is the average of the plate/MFC Young moduli over $L_{\mathrm{ref}}$. Considering a spanwise uniform Young modulus for both the plate and the actuator, the equivalent Young modulus ($E_M$) is $E(x, y) = E_{B3\mathrm{D}}$ for $(x, y) \in \mathcal{V}_B$ and $E(x, y) = E_P = N_{\mathrm{act}} L_{\mathrm{act}} E_{P3\mathrm{D}} / L_{\mathrm{ref}}$ for $(x, y) \in \mathcal{V}_P$, where $\mathcal{V}_B$ and $\mathcal{V}_P$ are the section areas of the plate and of the actuator, respectively, see Fig. 2 (right), $E_{B3\mathrm{D}}$ and $E_{P3\mathrm{D}}$ are the Young moduli of the plate and piezo-actuators, respectively, while $L_{\mathrm{ref}}$ and $L_{\mathrm{act}}$ are the plate and MFC spans while $N_{\mathrm{act}}$ is the number of MFCs per $L_{\mathrm{ref}}$. The structure is composed of the just derived 2D beam, with the two active MFCs on the top and bottom side, as shown in Fig. 2 (right). Using the virtual displacement principle (VDP) leads to the governing equations and natural boundary conditions. Since the plate is very thin, it is safe to use the Euler–Bernoulli beam model. This implies a null beam shear energy, and the VDP simply reads $\int_{\mathcal{V}} \overline{\varepsilon}_x \sigma_x\, \mathrm{d}\mathcal{V} = 0$. The integral can be divided in two different domains: the beam one ($\mathcal{V}_B$) and the piezo-actuator one ($\mathcal{V}_P$):

$$\int_{\mathcal{V}} \overline{\varepsilon}_x \sigma_x\, \mathrm{d}\mathcal{V} = \int_{\mathcal{V}_B} \overline{\varepsilon}_x \sigma_x\, \mathrm{d}\mathcal{V}_B + \int_{\mathcal{V}_P} \overline{\varepsilon}_x \sigma_x\, \mathrm{d}\mathcal{V}_P. \tag{1}$$

A linear approximation is used for both the piezo-actuator and the beam, and a strain definition that takes large rotations into account has been used for the beam.

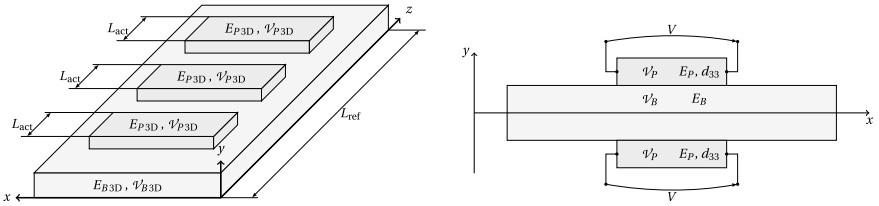


**Fig. 2** 3D plate-MFC configuration (left). Visual representation of a beam ($\mathcal{V}_B$) with the installed piezo-actuators ($\mathcal{V}_P$) (right). Figures are not to scale

We start by modelling the effect of the MFC actuator on the plate, which is considered as a 1D beam. A more detailed modelling, considering the three-dimensional nature of the actuator, according to the techniques employed in [2] or, more recently, [3], would be possible, but it is actually out of the scope of the present work. Here we will look for a simple 1D beam model using the virtual work principle. By virtue of linearity, we consider the effect of the upper and lower MFC separately. A substitution of the piezoelectric characteristic equation in the single piezo-actuator work gives

$$\left.\begin{array}{l}\sigma_x = E_P\varepsilon_x - d_{33}\frac{V}{d_e}E_P \\ W_P = \int_{\mathcal{V}_P}\overline{\varepsilon}_x\sigma_x\,\mathrm{d}\mathcal{V}_P\end{array}\right\} \Rightarrow W_P = \int_{\mathcal{V}_P}\overline{\varepsilon}_x\left(E_P\varepsilon_x - d_{33}\frac{V}{d_e}E_P\right)\mathrm{d}\mathcal{V}_P, \tag{2}$$

where $d_{33}$ is the piezoelectric-effect coefficient [12], $d_e$ the distance between electrodes, and $V$ the applied voltage. We can assume a linear strain $\varepsilon_x = \mathrm{d}u_0/\mathrm{d}x - y\mathrm{d}v_0/\mathrm{d}x$. Substituting this definition in Eq. (2) and integrating over the beam section gives

$$\begin{aligned}W_P = &\int_{x_P}\frac{\mathrm{d}\overline{u}_0}{\mathrm{d}x}EA_P\frac{\mathrm{d}u_0}{\mathrm{d}x}\,\mathrm{d}x_P + \int_{x_P}\frac{\mathrm{d}^2\overline{v}_0}{\mathrm{d}x^2}EJ_P\frac{\mathrm{d}^2v_0}{\mathrm{d}x^2}\,\mathrm{d}x_P - \int_{x_P}\frac{\mathrm{d}^2\overline{v}_0}{\mathrm{d}x^2}ES_P\frac{\mathrm{d}u_0}{\mathrm{d}x}\,\mathrm{d}x_P \\ &- \int_{x_P}\frac{\mathrm{d}\overline{u}_0}{\mathrm{d}x}ES_P\frac{\mathrm{d}^2v_0}{\mathrm{d}x^2}\,\mathrm{d}x_P - d_{33}\frac{V}{d_e}EA_P\int_{x_P}\frac{\mathrm{d}\overline{u}_0}{\mathrm{d}x}\,\mathrm{d}x_P + d_{33}\frac{V}{d_e}ES_P\int_{x_P}\frac{\mathrm{d}^2\overline{v}_0}{\mathrm{d}x^2}\,\mathrm{d}x_P,\end{aligned} \tag{3}$$

where $S_P$ and $J_P$ are the section first and second order moment, respectively, and $EJ(x) = \int_y E(x,y)J(x,y)\,\mathrm{d}y$. Integrating the last two terms of Eq. (3), we obtain the virtual work of the actuator

$$W_{P,\mathrm{act}} = -d_{33}\frac{V}{d_e}EA_P\left(\overline{u}_0\Big|_{x_{Pf}} - \overline{u}_0\Big|_{x_{Pi}}\right) + d_{33}\frac{V}{d_e}ES_P\left(\frac{\mathrm{d}\overline{v}_0}{\mathrm{d}x}\Big|_{x_{Pf}} - \frac{\mathrm{d}\overline{v}_0}{\mathrm{d}x}\Big|_{x_{Pi}}\right). \tag{4}$$

The two terms can be separated, and written as the effect of two axial forces $-F(\overline{u}_0(x_f) - \overline{u}_0(x_i))$ and two moments $M(\overline{\theta}_z(x_f) - \overline{\theta}_z(x_i))$. It is possible to easily find the blocking force from the piezo-actuator datasheets, and the force distance is obtainable by geometric considerations of the beam-actuator system. This means that F and M are calculated as $F = F_{\mathrm{up}} + F_{\mathrm{low}}$ and $M = (H_B + H_P)(F_{\mathrm{up}} - F_{\mathrm{low}})/2$. The linear dependence between the applied force and the induced displacement typical of MFCs is taken into account by increasing the plate stiffness where the actuator is present.

A simple linear Euler–Bernoulli model has been employed for the structure. By virtue of simplifications, it takes the contribution of large rotations into account [10] but neglects the effect of the axial load applied by the MFC since its effect on the displacement is irrelevant. The equation and boundary conditions read

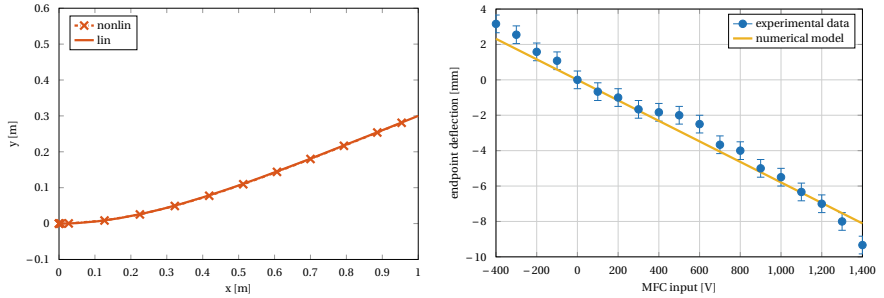


**Fig. 3** Left: comparison of beam deformations for a uniform distributed load of 12N m$^{-1}$ computed with the linear and nonlinear solver. Right: endpoint deflection of the actuated plate in still air: comparison between the numerical model and the experimental values

$$\widehat{EJ}\frac{\mathrm{d}^4 v_0}{\mathrm{d}x^4} = q, \quad v_0(0) = 0, \quad \left.\frac{\mathrm{d}v_0}{\mathrm{d}x}\right|_0 = 0, \quad \widehat{EJ}\left.\frac{\mathrm{d}^2 v_0}{\mathrm{d}x^2}\right|_l = M, \quad \widehat{EJ}\left.\frac{\mathrm{d}^3 v_0}{\mathrm{d}x^3}\right|_l = 0, \tag{5}$$

where $q$ is the distributed normal load acting on the plate and $M$ is the moment applied by the MFC. In Fig. 3 (left), beam deformations computed with the present linear model and with a nonlinear model are compared. It is evident how at a given $x$ value the two methods output very similar $y$, so that the use of a linear model is perfectly justified.

The aerodynamic forces were computed using the open source code Xfoil [4] that uses a panel method with linear vorticity and constant source distribution along straight panels to compute the 2D potential flow. The laminar/turbulent boundary layer is taken into account by an integral, compressible formulation, and the inviscid/viscous coupling is obtained by Lighthill's transpiration velocity [8]. Compressibility is taken into account, where indicated, using the Kármán–Tsien correction [11].

## 3 Experimental Validation

To test the structural model, a simple experimental setup was used. A plate, 0.085 m long, 0.028 m wide and $0.2718 \times 10^{-3}$ m thick, made of unidirectional carbon fibre with Young modulus 3.4 GPa, was equipped with a Smart Material M-8528-P1 MFC. The endpoint normal deflection was measured as a function of the input voltage. The average over three sets of measures is compared with the numerical results in Fig. 3 (right). A satisfactory agreement is found between the model and the experiment.

The aerodynamic tests were performed in an open-circuit wind tunnel with $0.30 \times 0.30 \times 1.00$ m test section and maximum wind speed of 45 m s$^{-1}$. A NACA 63(.2)-218 airfoil with 0.29 m span and end plates was employed equipped with the actuated plate, see Fig. 1. The wind speed was measured by a Pitot-static tube

mounted in the upstream side of the test section. The endpoint displacement of the plate was measured by processing the images acquired with a Canon 1DS Mark-I camera equipped with a 50 mm lens and a macro ring. The focus plane was aligned with the lateral end of the plate. The mean value obtained from 80 measures was taken. The plate, 12 cm long, 6.5 cm wide and 0.2 mm thick, has been made of two sheets of pre-impregnated unidirectional carbon fibre (Hexcel Hexply 913/CHTA/12K/5/34) with fibres aligned along the span, and an intermediate teflon sheet extending approximately to one third of the plate chord. Two Smart Material M-8528-P1 MFCs were mounted on the suction side with non- technical adhesive tape to allow disassembly. The plate was laminated in a press, with 2-bar pressure and at a temperature of 120° C. One of the carbon sheets was attached to the suction side of the airfoil trailing edge and one to the pressure side by non-technical adhesive tape also to allow disassembly, so that the plate formed a 13° angle with the airfoil chord.

The experimental model had two important differences from the ideal one: first, a very high compliance of the plate where it is attached to the airfoil trailing edge; second, a suboptimal gluing of the MFC. These effects have been modelled by a concentrated spring $K_t$ and a performance-degradation coefficient $\epsilon$. The values of the parameters have been identified by comparing experiments and calculations at fixed angle of attack, varying the actuation voltage and wind speed. The torsional spring stiffness is computed fitting the measured 0V deformations with the computed ones, Fig. 4 (left), obtaining $8\,\mathrm{N\,rad^{-1}}$. The actuation effectiveness is estimated by comparison between the computed and measured $C_{L,F}$, Fig. 4 (right), obtaining $\epsilon = 0.5$. The numerical simulations used viscous and compressibility corrections.

Validation results are shown in Fig. 5. The matching is very good at high speeds, while it is definitely poor for speeds under $10\,\mathrm{m\,s^{-1}}$ due to numerical and experimental errors.

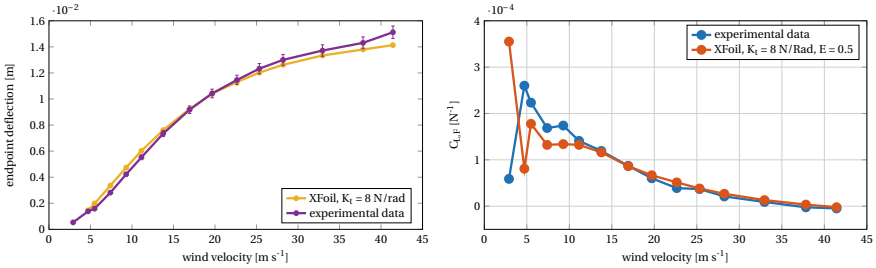


**Fig. 4** Left: Endpoint deflection as a function of the velocity compared with the experimental data; the error bars represent the uncertainty due to the pixel-to-length conversion. Actuation voltage: 0 V. Right: measured and computed $C_{L,F}$ for a 3° angle of attack, obtained with −500, 0, +500, +1500 V actuation voltages

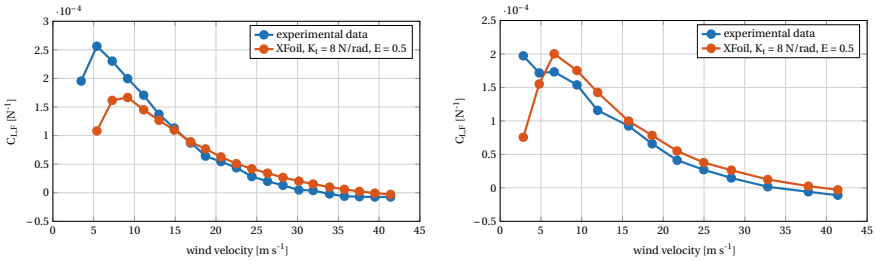


**Fig. 5** Measured and computed $C_{L,F}$ as a function of speed for 0° (left) and −3° (right) angle of attack, obtained with −500, 0, +500, +1500 V actuation voltages

## 4 Results and Discussion

First, the aerodynamic performance of the actuated airfoil, a NACA 0012, is investigated neglecting the aeroelastic coupling. The aim is to isolate the effects of MFC actuation from the aeroelastic effects to have a clearer picture of the actuation behaviour and provide a bound for static aeroelastic calculations. Table 1 shows the default configuration of the tested airfoil. All the computations have been performed varying one or two parameters at a time, leaving the other ones unchanged.

Smart Material Corp.'s datasheet gave the MFC properties for the M-8557-P1 model. The upper and lower side where symmetrically operated in the $-500 \div 500$ V range.

First, we investigate the relationship between the actuation force $F$ and the lift coefficient $C_L$. The results, not reported for conciseness, clearly show the linearity of $C_L(F)$. The linear behaviour of the $C_L$ with respect to the actuation force allows us to describe the actuation effectiveness by the derivative of the lift coefficient w.r.t. the actuation force

**Table 1** System properties used in the simulation

| Parameter | Value | Parameter | Value |
|---|---|---|---|
| Airfoil | NACA 0012 | MFC width | $0.64 \times 10^{-1}$ m |
| Airfoil points | 100 | MFC plate coverage | 100% |
| Plate thickness | $0.3 \times 10^{-3}$ m | MFC Young modulus | 30 GPa |
| Plate length | $0.1 \times 10^{0}$ m | MFCs per spanwise meter | 5 |
| Plate angle | 0 | MFC forces range | −308 to 308 N |
| Plate Young modulus | 20 GPa | Angle of attack | 0 |
| Plate points | 30 | Reynolds number | Inviscid |
| MFC thickness | $0.3 \times 10^{-3}$ m | Mach number | 0 |

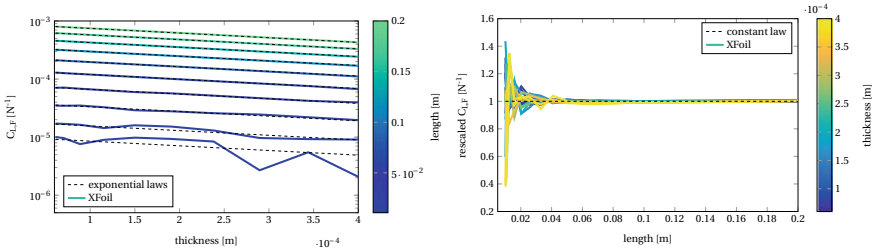


**Fig. 6** Left: $C_{L,F}$ plotted as a function of the plate thickness for several plate lengths, with semilogarithmic axes; the dashed lines are exponential fits. Right: ratio between numerical results and $\tilde{C}_{L,F}$ as function of $l$ for several values of $t$; the closer the curve to the constant law, the more accurate the proposed scaling law

$$C_{L,F} \stackrel{\text{def}}{=} \frac{\partial C_L(\ldots, F)}{\partial F}, \tag{6}$$

where $F$ is the mean actuation force applied by the upper and lower actuators. Having opposite positive direction, the positive upper force is a traction while the lower is a compression. The force has been preferred to the voltage to avoid any dependence on the MFC model, and to the torque to avoid dependence on the plate thickness, which is part of the parameter space.

Next, we investigate how $C_{L,F}$ depends on the structural and aerodynamic properties of the system. For convenience, all lengths are normalized with respect to the airfoil chord, not considering the length of the actuated plate. The dependence of $C_{L,F}$ on the geometry of the plate length and thickness is reported in Fig. 6 (left). It clearly shows an exponential dependence of $C_{L,F}$ on the plate thickness. A similar plot, not shown for conciseness, shows that a power law relates $C_{L,F}$ to the plate length. The scaling law can be therefore expressed as $\tilde{C}_{L,F}(l,t) = e^{K_1+K_2\,t}\,l^{K_3}$, where $K_1$, $K_2$ and $K_3$ are constants that can depend on the other parameters. Figure 6 (right) shows the ratio between the computed $C_{L,F}$ and the value predicted by the approximate scaling law $\tilde{C}_{L,F}$. The values tend to collapse on unity for sufficiently long plates, indicating the accuracy of the scaling law. The oscillations observed for low plate lengths are related to the fact that errors become more and more important as the plate length is reduced.

A very similar scaling law can be derived for $C_{L,F}$ as a function of the Young modulus $E$. The results, not shown for conciseness, allow us to obtain a unique scaling law taking into account the plate thickness, length and Young modulus:

$$\tilde{C}_{L,F}(l,t,E) = \mathrm{e}^{K+K_t t+K_{Et}E\,t}\,l^{K_l}, \tag{7}$$

where $K$, $K_t$, $K_{Et}$ and $K_l$ are all constants depending on the other parameters. The computed constant values for the present case are $K = 4.554$, $K_t = 1.486 \times 10^3$, $K_{Et} = 1.631 \times 10^{-8}$, $K_l = 1.524$. A Montecarlo approach has been used to test the accuracy of this scaling law, to avoid spanning a three-dimensional parameter space,

obtaining a mean error of 0.4%, therefore the scaling law is quite accurate if related to the low fidelity models adopted and provides the designer with a quick tool to explore the parameter space and select the main design parameters in a preliminary design phase. Pearson correlation coefficients indicate a weak correlation with the length that can be explained with a slight misestimation of the $K_l$ coefficient. A similar error analysis has been conducted for other airfoil shapes with comparable results, proving that this formulation is robust since it remains valid irrespective of the shape of the considered airfoil.

After the impact of the main structural properties on performance has been analysed, we discuss the dependence of $C_{L,F}$ on the aerodynamic parameters such as the angle of attack, the Reynolds and Mach numbers.

First, the effect of the angle of attack was evaluated by plotting $C_{L,F}/l^{K_l}$ as a function of the angle of attack and another parameter, either the plate length or the thickness or the Young modulus, with similar results, not reported for conciseness. They show that the effect of the angle of attack is to simply rescale $C_{L,F}$ by $\cos\alpha$. The scaling law for $C_{L,F}(\alpha, l, t, E)$ can therefore be expressed as

$$C_{L,F}(\alpha, l, t, E) = \mathrm{e}^{K+(K_t+K_{El}E)t} l^{K_l} \cos\alpha. \tag{8}$$

A further Monte Carlo analysis with this last formulation and the angle of attack as additional free parameter reveals that the model retains almost the same accuracy as the previous one, the mean error being 0.5%.

Then, we analysed the effect of Mach number on the airfoil performance exploiting XFoil compressibility correction, which is valid well below the airfoil critical Mach number. The results, not reported for conciseness, show that the actuation performance increases significantly with the Mach number, especially at high angles of attack where the airfoil load is higher, velocities are higher and therefore the correction is higher, with an increase going from 30 to 60% at a Mach number of 0.6. These results are neither power laws, exponential, or logarithmic, and the scaling law for the dependence of $C_{L,F}$ on the Mach number is still elusive.

The effect of viscosity is subtler. A clearer insight can be obtained by plotting $C_{L,F}$, corrected by $\cos\alpha$ to isolate the viscous effects, as a function of the mean displacement thickness on the actuated plate and of the flow Reynolds number for a turbulent boundary layer with almost constant shape factor, $H < 1.5$, Fig. 7 (left). It is evident from the figure that reducing the boundary layer thickness, either by increasing the Reynolds number or by changing the angle of attack, increases the effectiveness of the actuation. In fact, the boundary layer slows down the flow near the wall, thus decreasing the sensitivity to the plate displacement [6]. Notably, in these conditions $C_{L,F}$ is a decreasing linear function of the displacement thickness. The combined effect of the angle of attack, Reynolds number and of the average shape factor, rescaled to lie in the interval [0, 1], can be appreciated in Fig. 7 (right). The effectiveness of the actuator grows with the Reynolds number, it is quite independent on the angle of attack but depends dramatically on the shape factor. In particular, it drops dramatically when the shape factor approaches its maximum value, typical of incipient separation. As a matter of fact, high shape factors are associated with

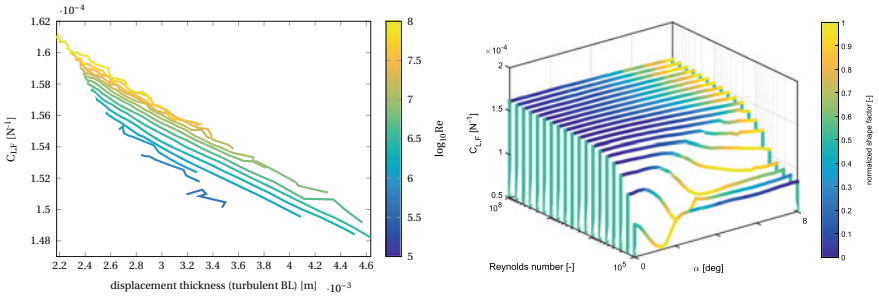


**Fig. 7** Left: $C_{L,F}$ plotted against the displacement thickness over the actuator, plotted only for turbulent boundary layers; the curves vary along the $\alpha$, not shown in this graph. Right: $C_{L,F}$ as a function of the angle of attack, Reynolds number and shape factor (colour)

boundary layer velocity profiles with a low derivative of the velocity with respect to the wall distance at the wall, and therefore small velocities near the wall that limit the effectiveness of the actuated plate [6]. The complex behaviour of viscous flows prevents a simple representation of $C_{L,F}$ as a function of the Reynolds number in closed form, but these observations on the connection between the shape of the boundary layer velocity profile and the effectiveness of the control plate allow one to predict when such actuation systems could be ineffective. In particular, we can infer that the plate effectiveness will be maximum in cruise conditions and will be limited in take-off and landing conditions, where we can expect the shape factor of the boundary layer to be higher near the airfoil trailing edge. Another interesting result can be obtained by plotting $C_{L,F}$ as a function of the Reynolds number and of the actuator length, Fig. 8. The $C_{L,F}$ dependence on the Reynolds number and length can be modelled as a decrease of the apparent length, as Fig. 8 (left) shows. The data can be collapsed on the same curve when appropriately translated by a function of the Reynolds number, that we will call apparent shortening in the sequel. The apparent shortening and the average displacement thickness show the same dependence on the Reynolds number up to a multiplicative constant, so that the apparent shortening can be directly related to the average displacement thickness, as shown in Fig. 8 (right) for $l = 0.0158$ m, and represented by the function

$$\begin{cases} l_s(l, \mathrm{Re}) = S_{1t}\overline{\delta}^*(\xi; l, \mathrm{Re}) + S_{2t}(l) \ : & \textbf{turbulent boundary layer}, \\ l_s(l, \mathrm{Re}) = S_{1l}(l)\overline{\delta}^*(\xi; l, \mathrm{Re}) + S_{2l}(l) \ : & \textbf{laminar boundary layer}. \end{cases} \tag{9}$$

where $\overline{\delta}^*$ denotes the average boundary-layer displacement thickness over the actuated plate. Figure 8 (right) shows that two different regions in the graph display a linear behaviour, with different slopes, one corresponds to a laminar boundary layer, the other one to a turbulent boundary layer. A transition region that cannot be described by a simple curve connects the two linear trends. The same qualitative behaviour, not reported here for conciseness, can be observed for different plate

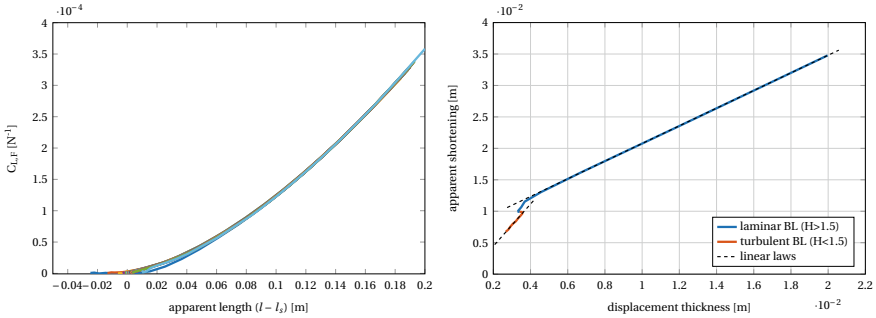


**Fig. 8** Left: $C_{L,F}$ as function of the plate length, for different Reynolds numbers. The curves are nicely collapsed by plotting them as a function of the length corrected by the apparent shortening described in Eq. (9). Right: Apparent shortening as a function of the displacement thickness. The dashed lines represent the linear regression for the two regions of the curve. The slope changes with transition

lengths, the main difference being a shift for the portion associated with a turbulent boundary layer, and both a shift and a slope change for the laminar part. The only fit parameter not varying with $l$ is the curve slope when the boundary layer over the actuator is turbulent, with a value of $0.289 \pm 0.0249$. The others vary substantially, and a simple algebraic description of this variation has to be found yet.

Up to now, the aerodynamic calculation was not coupled with the structural deformation for simplicity. The results thus overestimated the actual effect of compliant surfaces. Compliance can hardly be neglected in the present problem, where very thin control surfaces are considered. We now investigate how the deformation of the control surface due to aerodynamic loads may influence its performance. Owing to the nonlinearity of the problem, an iterative procedure is adopted. The coupled simulations take generally 15–40 iterations to converge, therefore the $C_{L,F}$ calculation is significantly slower than in the uncoupled case. We checked that, despite the problem is intrinsically nonlinear, the $C_L(F)$ is still substantially linear with respect to actuation force, for reasonable values of the force, and $C_{L,F}$ can still be considered a meaningful parameter to evaluate the plate performance.

The $C_{L,F}$ analysis varying the plate length and thickness was carried out with a plate and calculation parameters almost identical to that described in Table 1 but for the plate young modulus that was higher, 70 GPa. The air speed was $50\,\mathrm{m\,s^{-1}}$ and its density $0.9\,\mathrm{kg/m^3}$. The results reveal a quite different behaviour with respect to the uncoupled case. While, in the uncoupled case, we observed a monotonic behaviour for $C_{L,F}(l)$ and $C_{L,F}(t)$, in the present case the behaviour is no longer monotonic, Fig. 9 (left). The reason is that the deformation of the actuation plate due to aerodynamic loads increases with the plate length, decreasing its effectiveness. Since the computation of the complete $(l, t, V)$ space is computationally onerous, the optimal thickness envelope, shown in red in Fig. 9 (left), is investigated. The envelope presents a maximum, that is the maximum inviscid $C_{L,F}$ achievable at a given velocity ($50\,\mathrm{m\,s^{-1}}$). The optimal thickness is shown in Fig. 9 (right) as a

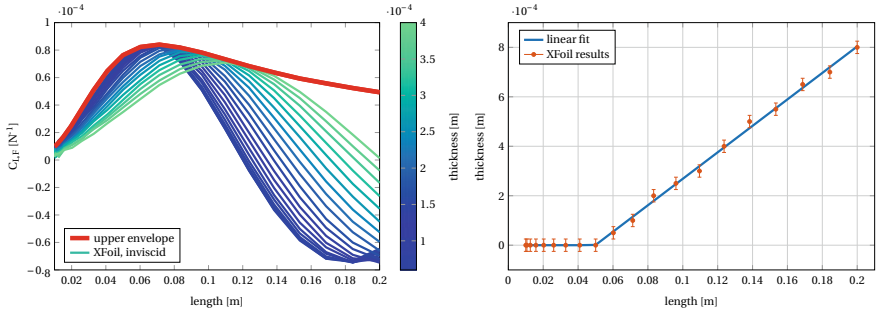


**Fig. 9** *Left* : $C_{L,F}$ plotted as a function of the plate length for several values of thickness (blue-green line as), at 50 m s$^{-1}$. The envelope of the curves is also reported (red line). Right: optimal thickness as a function of the plate length; the error bar represents the resolution of the method used to identify the envelope

function on the length. It is reasonably represented by a piecewise linear behaviour. For small lengths the optimum thickness is zero, meaning that the stiffness of the actuator (30 GPa) is sufficient or even excessive for the purpose.

It is useful to define now the aeroelastic efficiency of the system as the ratio between the uncoupled $C_{L,F}$ and the coupled one, $\mathcal{E}_c = C_{L,F}^{\text{coupled}} / C_{L,F}^{\text{uncoupled}} \in [0, 1]$. We can observe in Fig. 10 that this ratio has two regions: for low values of the independent variable, be it the length or the velocity, it is one, meaning that aeroelastic effects do not play a role when the plate is stiff enough or the aerodynamic forces are sufficiently small. For large lengths or velocities, it asymptotically decreases as a power law.

The scaling law for $\mathcal{E}_c$ can therefore be expressed as

$$\tilde{\mathcal{E}}_c(l, V) = \begin{cases} Q\, V^{Q_V} l^{Q_l} & l > l_c(V), \\ 1 & l < l_c(V), \end{cases} \tag{10}$$

where $l_c$ is the length at which the power laws intersect with the value $\mathcal{E}_c = 1$, and the computed constants are $Q = 0.505$, $Q_V = -1.398$ and $Q_l = -2.136$. Notice that these values can depend on other parameters, as, for instance, the Young modulus. A more complete parameter space exploration is left for a future investigation.

As can be observed in the figure, the scaling law (10) does not work well when $l \approx l_c$. If higher precision is needed in the transition region between unit efficiency and the decreasing power law, it is possible to model the aeroelastic efficiency as a fractional power law,

$$\tilde{\mathcal{E}}_c(l, V) = \frac{1}{1 + G\, V^{G_V} l^{G_l}}, \qquad l < (1 + P)\, l_c(V), \tag{11}$$

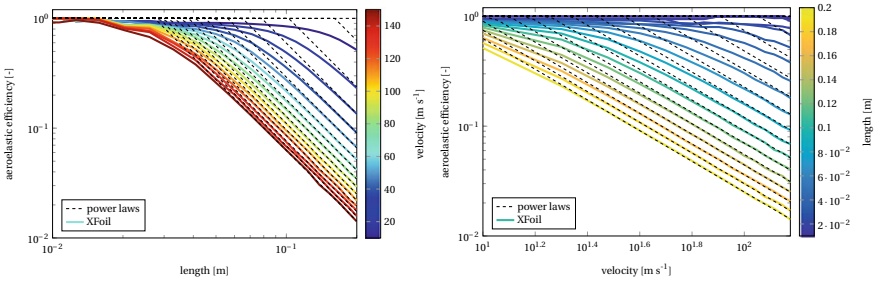


**Fig. 10** Aeroelastic efficiency $\mathcal{E}_c$ as a function of the length of the plate, for several values of the air speed (left) and plate length (right)

where $G = 1.33$, $G_V = 1.7168$, $G_l = 2.6387$ and $P$ is a positive value that extends the applicability range of the scaling law also to actuators slightly longer than $l_c$. This model works better in the transition between the two behaviours, but it becomes inaccurate when lengths and velocities are high enough.

## 5 Conclusions

This work describes the steady behaviour of compliant MFC-actuated plates mounted on the airfoil trailing edge. The numerical results show that the actuation behaviour can be modelled with simple laws, providing a good starting point to explore the parameter space when searching for optimal configurations in the preliminary design. When considering the optimum thickness for a given length, the scaling law describing the sensitivity of the lift coefficient to the actuation force in the inviscid case can be summarised by Eqs. (10) and (11). This simple scaling law can be particularly useful for a fast evaluation the actuation effects. Indeed, just a few simulations will be sufficient to estimate the values of the coefficients.

Viscous effects are more involved, but some observations are in order. First, for a turbulent boundary layer, the $C_{L,F}$ decreases linearly as a function of the mean displacement thickness measured on the actuated plate, when varying the angle of attack. Second, an apparent actuator shortening, function of the Reynolds number, appears to be a simple but effective method to take the boundary layer effects into account. Third, high shape factors of the boundary layer velocity profile over the actuated plate cause the $C_{L,F}$ to drop, especially at low Reynolds numbers. The wind tunnel tests showed good agreement with the numerical model.

The MFC installation is rather simple, this means that they could be retrofitted on existing aircraft. Real case analyses, not reported here, provided very promising results.

**Acknowledgements** This project has received funding from the European Union's H2020 program for research, technological development and demonstration under grant agreement no 723402.

## References


1. Bilgen, O., Butt, L., Day, S., Sossi, C., Weaver, J., Wolek, A., Mason, W., Inman, D.: A novel unmanned aircraft with solid-state control surfaces: analysis and flight demonstration. In: 52nd AIAA/ASME/ASCE/AHS/ASC Structures, Structural Dynamics and Materials Conference. Denver, Colorado (2011)
2. Deraemaeker, A., Tondreau, G., Bourgeois, F.: Equivalent loads for two-dimensional distributed anisotropic piezoelectric transducers with arbitrary shapes attached to thin plate structures. J. Acoust. Soc. Am. **129**(2), 681–690 (2011)
3. Dong, Z., Faria, C., Hromčík, M., Pluymers, B., Šebek, M., Desmet, W.: Equivalent force modeling of macro fiber composite actuators integrated into non-homogeneous composite plates for dynamic applications. Smart Mater. Struct. **26**(9), 095040–13 (2017)
4. Drela, M.: Xfoil: An analysis and design system for low reynolds number airfoils. In: Low Reynolds Number Aerodynamics, pp. 1–12. Springer (1989)
5. Dwarakanathan, D., Ramkumar, R., Raja, S., Siva Subba Rao, P.: Design, development and ground testing of hingeless elevons for mav using piezoelectric composite actuators. Adv. Aircraft Spacecraft Sci. **2**, 303–328 (2015)
6. Foster, D.N., Ashill, P.R., Williams, B.R.: The nature, development and effect of the viscous flow around an aerofoil with high-lift devices. R. A. E., Farnborough, Aerodynamics Department (1974)
7. Katz, J., Plotkin, A.: Low-Speed Aerodynamics. Cambridge University Press, Cambridge Aerospace Series (2001)
8. Lighthill, M.J.: On displacement thickness. J. Fluid Mech. **4**(4), 383–392 (1958)
9. Lu, K.-J., Kota, S.: Design of compliant mechanisms for morphing structural shapes. J. Intell. Mater. Syst. Struct. **14**, 379–391 (2003)
10. Reddy, J.N.: An Introduction to Nonlinear Finite Element Analysis. Oxford Scholarship Online (2004)
11. Tsien, H.S.: Two-dimensional subsonic flow of compressible fluids. J. Aeronaut. Sci. **6**, 399–407 (1939)
12. Uchino, K.: Materials issues in design and performance of piezoelectric actuators: an overview. Acta Mater. **46**(11), 3745–3753 (1998)
13. Valasek, J. (ed.): Morphing Aerospace Vehicles and Structures. Wiley, New York (2012)
14. Wilkie, W.K., Bryant, R.G., High, J.W., Fox, R.L., Hellbaum, R.F., Jalink Jr., A., Little, B.D., Mirick, P.H.: Low-cost piezocomposite actuator for structural control applications. Proc. SPIE—Int. Soc. Opt. Eng. **3991**, 323–334 (2000)

# CFD Simulations with Dynamic Morphing on the Airbus A320 Airfoil


**Konstantinos Diakakis and Georgios Tzabiras**

**Abstract** Dynamic flapping simulations were performed on the Airbus A320 airfoil in a closed tunnel configuration. Various frequencies paired with different amplitude values were examined. The analysis showed that improvement of the aerodynamic performance is definitely possible. There exists some interaction with the natural frequency of the airfoil that tends to amplify oscillations when the vibrating frequency is close to the observed natural frequency or it is a first harmonic. For vibrating frequencies that are high enough but are not competing with the natural, increase in aerodynamic performance was observed.

**Keywords** Morphing wings · Aerodynamics · Simulation · Trailing-edge vibration

## 1 Introduction

Limiting energy consumption is always an important goal in contemporary aviation applications. For most aircraft, energy consumption is directly tied to fuel consumption during the flight. Most airfoil shapes are mainly optimized for nominal cruise conditions. However, during the actual flight these conditions are constantly changing and thus the initial design for the nominal conditions is rendered sub-optimal.

Changing the wing shape during flight can have a significant effect on airfoil consumption [1]. Traditional methods for wing shape control and adaptation, which commonly utilize flaps and slats, are solutions that do not have a wide performance range

K. Diakakis (✉)
Department of Mechanical Engineering,
National Technical University of Athens, Athens, Greece
e-mail: diak@fluid.mech.ntua.gr

G. Tzabiras
Department of Naval and Marine Hydrodynamics,
National Technical University of Athens, Athens, Greece
e-mail: tzab@fluid.mech.ntua.gr



M. Braza et al. (eds.), *Advances in Critical Flow Dynamics Involving Moving/Deformable Structures with Design Applications*, Notes on Numerical Fluid Mechanics and Multidisciplinary Design 147,
https://doi.org/10.1007/978-3-030-55594-8_45

[2]. For this reason, recent advances in materials science as well as actuation technologies have led to an increasing interest in wing morphing, which is a real time adaptation of the wing shape that enables optimization based on current flow conditions.

In aviation, morphing has been known for decades. In the work of Lyu and Martins [1], it was demonstrated that camber control of the trailing edge is an efficient way to improve overall aerodynamic performance on commercial airliners. Subsequently, the concept of trailing edge morphing was tackled by many European research programs [3, 4]. Initially, adaptive structures were actuated through conventional servomotors. A more novel approach in morphing actuation is via the use of smart materials, mainly Smart memory Alloys (SMAs) and piezoelectrics, which show potential in making a wing both flexible enough to be easily deformed and stiff enough to withstand aerodynamic loads. The purpose of morphing is to have a favorable effect in the macroscopic behavior of the airflow; improved lift and drag, increased aeroelasticity, and load alleviation.

The purpose of this paper is to examine the aerodynamic performance of the Airbus A320 airfoil equipped with a high frequency vibrating trailing edge (HFVTE). The experimental setup is described in [5], where a reduced-scale prototype with a piezoelectric patch that enabled high frequency morphing of the trailing edge was tested. In the work presented, simulations are carried out for various frequencies and amplitudes, in an effort to observe performance trends and locate optimal morphing parameters. Effects of trailing edge morphing on aerodynamic performance as well as near wake behavior are assessed and discussed.

## 2 Flow Modeling

### *2.1 Solver*

The in-house CFD solver MaPFlow [6] is used. MaPFlow solves the compressible RANS equations using a cell centered finite volume discretization method based on the Roe approximate Riemann solver [7] for the convective fluxes. Low Mach preconditioning and Venkatakrishnan's limiter [8] are also implemented. In space and time the scheme is second order accurate defined for unstructured grids and implicit with dual time stepping for facilitating convergence.

The original version of the SST $k-\omega$ two-equation model proposed by Menter [9] is used for turbulence closure. In order to have the turbulence level measured in the experiment, the SST model is augmented with ambient values in both $k$ and $\omega$ equations, as suggested by Spalart [10]. These terms counteract turbulent decay and help maintain freestream $Tu_\infty$ and viscosity ratio $\mu_t/\mu$ values in the computational domain.

## 2.2 Deformation

The high frequency vibrating trailing edge (HFVTE) is defined by a polynomial offset on the $y$ axis. For all stations on the airfoil with $x$ coordinate greater than the designated value $x_s$, the offset is calculated based on the following sinusoidal equation:

$$dy(x, t) = a((x - x_s)/(C - x_s))^2 \sin(2\pi ft) \tag{1}$$

where $a$ is the morphing amplitude, $C$ is the airfoil chord, $x_s$ is the $x$ coordinate that the actuation starts, $f$ is the morphing frequency, and $t$ is the time. Note that, as described by the equation, the flapping is considered non-articulated, so the deformation only refers to the $y$ axis, whereas $x$ coordinates of deformable stations are not affected. An example of trailing edge deformation, depicting the original, maximum up, and maximum down positions is given in Fig. 1.

Arbitrary Langrangian-Eulerian(ALE) polynomial deformation is employed in the simulations for the deformation of the internal nodes.

## 2.3 Grid Generation

The domain extent is based on the experimental configuration described in (REFERENCE). The airfoil was rotated 10° around the axis origin. The inlet and outlet walls were set approximately 5 chords away from the airfoil, whereas the top and bottom

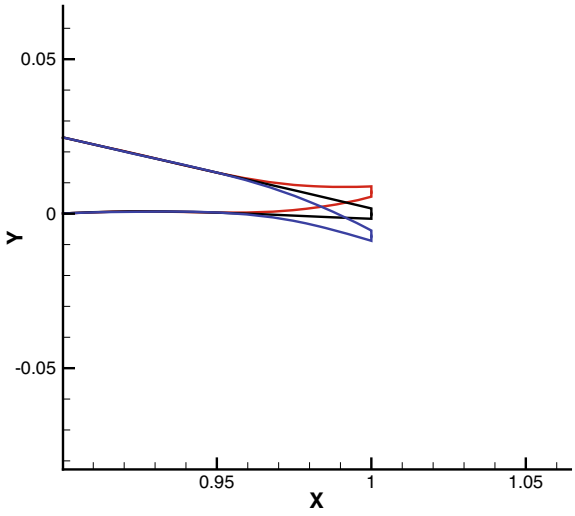


**Fig. 1** Example of trailing edge morphing

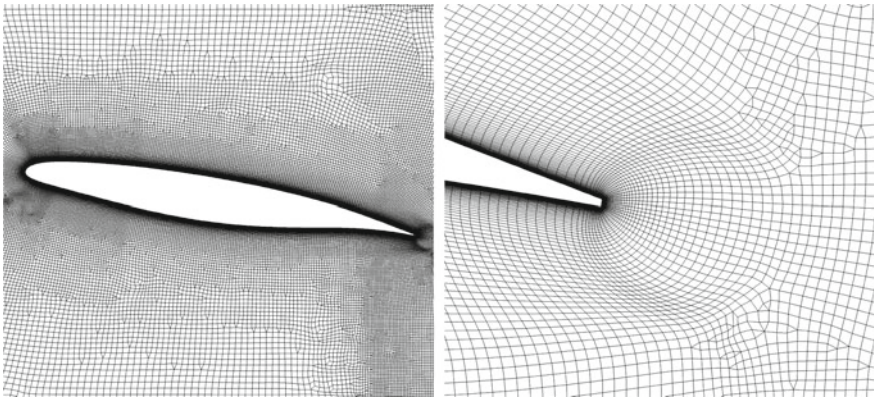

**Fig. 2** Hybrid grid for the Airbus A320 tunnel configuration. **Left**: airfoil close-up, **Right**: trailing edge detail

walls were located approximately 0.5 chords away from the leading and trailing edge, respectively.

For the simulations, hybrid grids were generated. Using a hybrid grid helps alleviate some of the difficulties in grid generation that are commonly present when using structured grids for tunnel configurations (i.e. too many cells towards the trailing edge, skewed elements when airfoil blocks meet with tunnel wall blocks). The airfoil has a structured region up to approximately 10% of the chord in the normal direction, with the rest of the domain being unstructured using quads and triangles. Since this work focuses on airfoil morphing and grid deformation, extra care was taken in order to make sure that the region around the trailing edge was sufficiently refined and able to withstand the desired grid deformation. The resulting grid had approximately 500 points around the airfoil, whereas the structured region around the airfoil had 80 elements in the normal direction. The height of the first cell was set to $5 \times 10^{-6}$ chords, following common CFD practice. This resulted in $y^+ < 1$ at all times. The resulting grid had 70 thousand elements. Neumann boundary conditions were used for the upper and lower walls of the tunnel. The grid around the airfoil and the trailing edge is shown in Fig. 2.

## 3 Computational Results

Two dimensional simulations were carried out, with flow conditions $Re = 1 \times 10^6$, and $M_\infty = 0.1$. Inlet $Tu$ was set to 1%, which yields $\frac{k}{U_\infty} = 1.5 \times 10^{-4} U_\infty^2$. This value for $k$ was also used for the ambient term in the $k$ equation of the SST model. In order to keep the viscosity ratio relatively low, inlet and ambient $\omega$ were set to $\omega \frac{L}{U_\infty} = 50$, which yields a freestream $\mu_t/\mu$ of approximately 3. It has been shown (REF Spalart) that the range for the inlet and ambient $\omega$ is not too narrow and that values up to 100

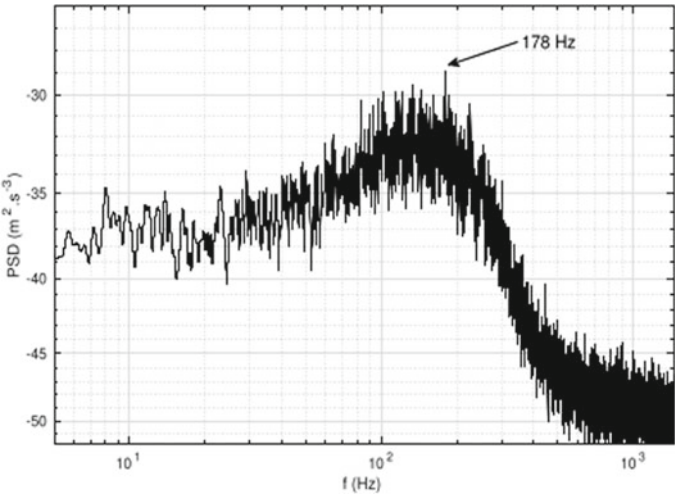


**Fig. 3** A320 airfoil, $Re = 10^6, \alpha = 10°$, PSD of averaged streamwise velocity from the experiment, courtesy of G. Jodin

are safe when fully turbulent calculations are considered. Simulations with morphing always employed 360 time steps per morphing period. The airfoil was deformed from 95% of the chord, towards the trailing edge.

Figure 3 shows the Power Spectral Density (PSD) of the averaged streamwise velocity in the near wake measured in the experiment. This PSD diagram is produced by taking the velocity history in a fixed position in the near wake and, via fast fourier transformation (FFT), analyzing the amount of energy that each frequency carries. It is shown 178 Hz is the frequency that carries the highest amount of energy. In the simulations, the natural frequency of the airfoil in simulations without morphing was approximately 150 Hz, which is adequately close to value observed in the experiment. Figure 4 shows the averaged streamlines and the contour of averaged streamwise velocity near the trailing edge, showing the region of separation as well as flow recirculation.

Various frequencies and amplitudes were simulated. At first, the amplitude was fixed to a value of 0.2 mm. Figure 7 shows the effect of vibrating frequency on the mean velocity in the near wake. With a vibrating frequency 60 and 100 Hz, wake behavior has only minor differences when compared to the static case. When the vibrating frequency is set to 150 Hz, which is the same as the natural frequency, the contour differs considerably, with a significantly smaller recirculation region past the airfoil. A similar, but less pronounced, behavior is observed in 300 Hz case, which is the first harmonic of the natural frequency. For 600 Hz, the wake is again similar to the static one, as is expected due to the fact that the frequency is much higher than the natural.

In addition, Fig. 5 shows the profiles of averaged streamwise velocity at three different positions in the near wake ($x/c = 1.1$, 1.2, and 1.4). The observed trend is

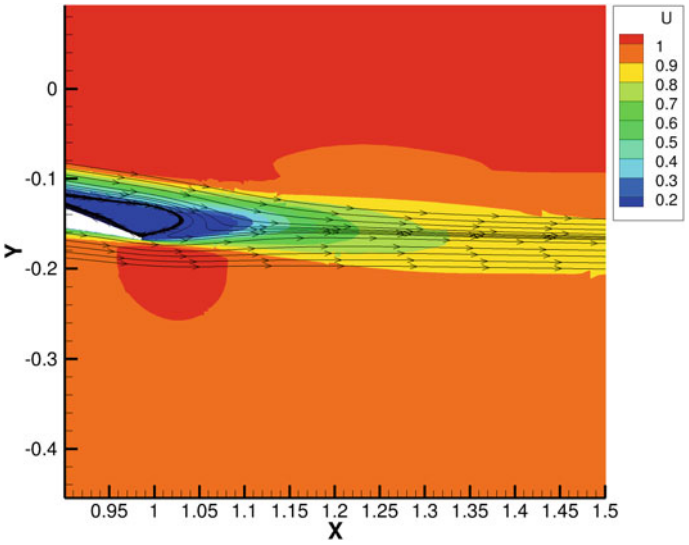


**Fig. 4** A320 airfoil, $Re = 10^6$, $\alpha = 10°$, $Tu_\infty = 1\%$, computational separation and flow recirculation with averaged streamlines

that an increase in vibrating frequency slightly decreases the minimum $U$ value in the profile, as observed for frequencies 60, 100, 300 Hz compared to the static case. The frequencies of 150, 300 Hz differ, though, as they exhibit a significantly lower $U$ deficit in both $x/c = 1.1$ and 1.2 positions. For the most downstream position of $x/c = 1.4$, it is observed that all vibrating frequencies apart 150, 300 Hz have almost converged to the same profile, with 150 Hz case now exhibiting a lower minimum in $U$ velocity. T300 Hz case has a similar difference in $U$ profile, although less pronounced.

Figure 8 shows instantaneous snapshots of wake vorticity at nondimensional $t = 35$. It is evident that both 150, 300 Hz exhibit significantly less irregular vortices, having more coherent structures that start forming at the trailing edge. This behavior is responsible for the higher minima in $U$ velocity observed for these two frequencies, as well as the slower recovery observed in the most downstream position, due to the fact that one of the two vortices in strongly more coherent than the other, whereas in all other cases velocity is diffused much faster since both vortices behave the same.

A parametric investigation was also carried out for various amplitudes per examined frequency. In this part of the analysis, amplitudes of 0.2, 0.5, 1, 2, 5 mm were considered. The resulting $C_L$ and $C_D$ polars, as well as aerodynamic performance $L/D$, are shown in Fig. 6. An interesting finding was that 100 and 150 Hz, an amplification occurred, which resulted in high lift and drag coefficient oscillations. This did not occur for the case of 200 Hz, which yielded lower amplitudes than 100 and 150 Hz, as depicted in Fig. 6, top left and right. This behavior is probably attributed to 100, 150 Hz being too close to the natural frequency of the airfoil, 200 Hz was

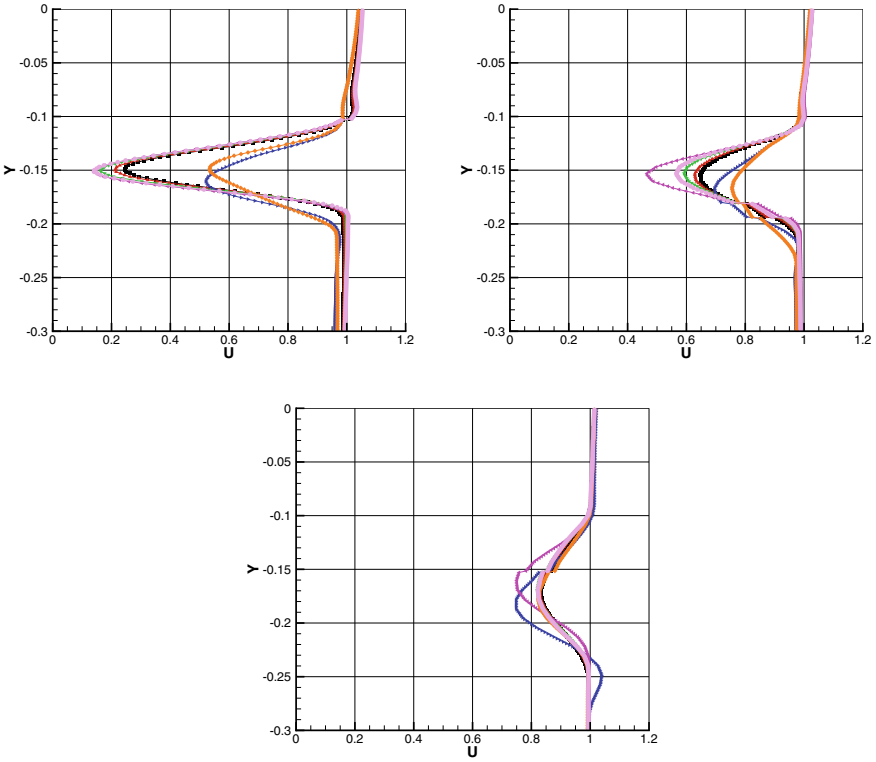


**Fig. 5** A320 airfoil, $Re = 1 \cdot 10^6$, $M = 0, 1$, $Tu_\infty = 1\%$, averaged streamwise velocity profiles at various positions in the near wake with different morphing frequencies, amplitude fixed at 0.2mm. **Top left**: $x/c = 1.1$, **Top right**: $x/c = 1.2$, **Bottom**: $x/c/1.4$

high enough to supress the amplification. Moreover, the case 300 Hz also exhibited an amplification in lift and drag oscillations, due to the fact that it is the first harmonic of the natural frequency. For most cases beyond 100 Hz, amplitudes of 25 mm are omitted, as they gave very high amplitudes.

When overall aerodynamic performance is considered, 150 and 300 Hz gave high aerodynamic performance but, unfortunately, exhibited higher amplitude oscillations. On the other hand, the cases of 100 and 200 Hz, while both being close to the natural frequency of 150 Hz, produced slightly higher performance than the static case, without significant oscillations. For frequencies below 60 Hz, no increase in performance was observed for the examined amplitudes. This suggests that these frequencies will probably be more suitable for even lower amplitudes than those examined and presented in the scope of this work.

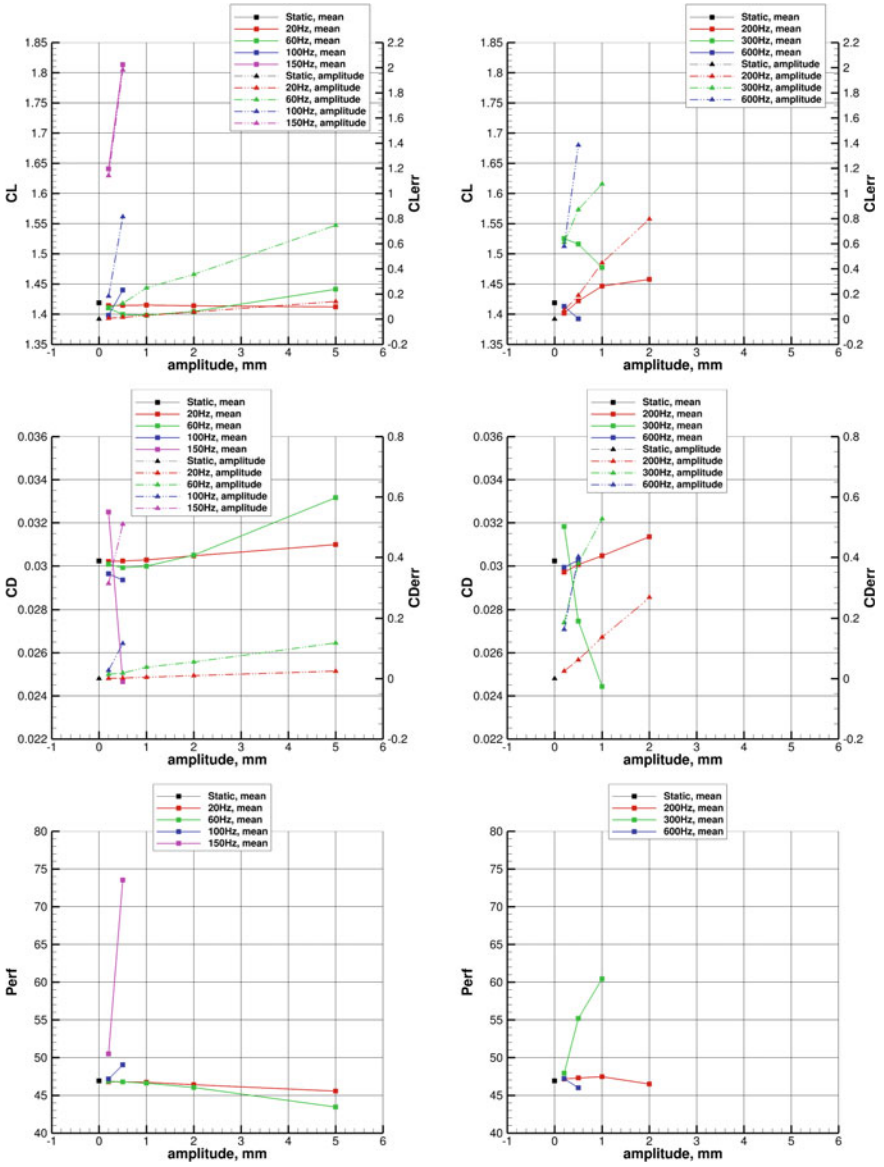


**Fig. 6** A320 airfoil, $Re = 1 \times 10^6$, $M = 0, 1$, $Tu_\infty = 1\%$, aerodynamic performance with varying frequency and amplitude. **Top left**: mean $C_L$ and error, frequencies 60–150 Hz, **Top right**: mean $C_L$ and error, frequencies 200–600 Hz, **Middle left**: mean $C_D$ and error, frequencies 60–150 Hz, **Middle right**: mean $C_D$ and error, frequencies 200-600 Hz, **Bottom left**: mean $L/D$, frequencies 60–150 Hz, **Bottom right**: mean $L/D$, frequencies 200–600 Hz

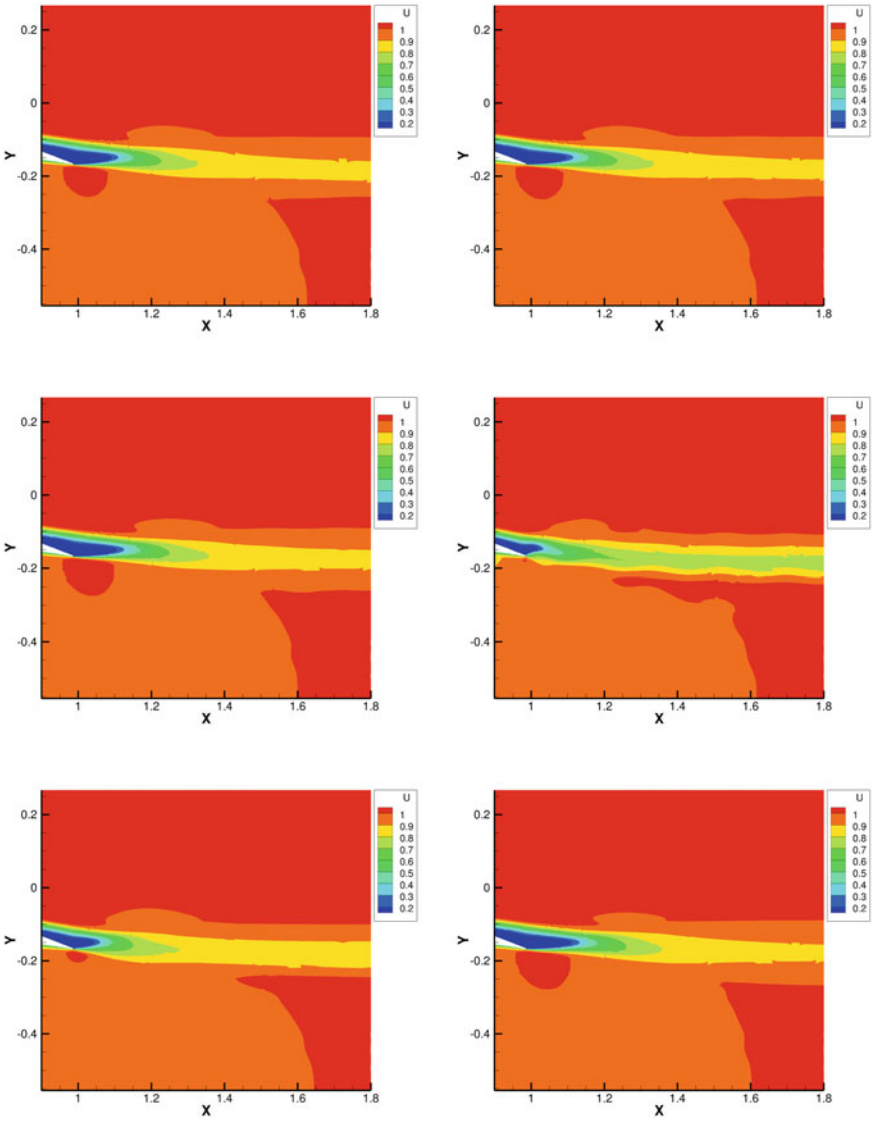


**Fig. 7** A320 airfoil, $Re = 1 \cdot 10^6$, $M = 0, 1$, $Tu_\infty = 1\%$, averaged streamwise velocity contour in the near wake with different morphing frequencies, amplitude fixed at $0.2mm$. **Top left**: static, **Top right**: 60 Hz, **Middle left**: 100 Hz, **Middle right**: 150 Hz, **Bottom left**: 300 Hz, **Bottom right**: 600 Hz

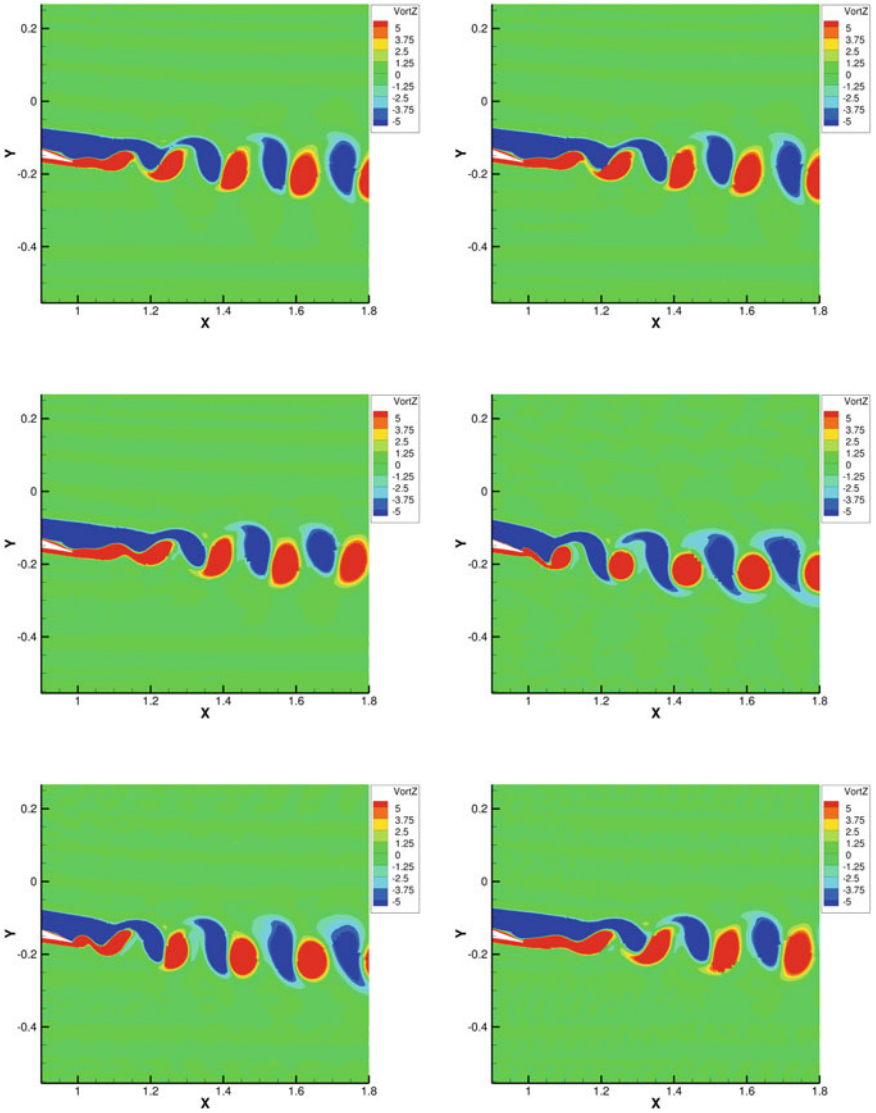


**Fig. 8** A320 airfoil, $Re = 1 \times 10^6$, $M = 0, 1$, $Tu_\infty = 1\%$, instantaneous snapshots of vorticity contour (nondimensional $t = 35$) in the near wake with different morphing frequencies, amplitude fixed at 0.2 mm. **Top left**: static, **Top right**: 60 Hz, **Middle left**: 100 Hz, **Middle right**: 150 Hz, **Bottom left**: 300 Hz, **Bottom right**: 600 Hz

## 4 Discussion and Conclusion

Simulations carried out showed that there exists the possibility to improve aerodynamic performance using a HFVTE. The morphing parameters have to be carefully evaluated, since the aerodynamic behavior does not always exhibit a predictable trend. The fact that this particular flow case is characterized by an initial natural frequency may lead to amplifications that can have a significant effect on the aerodynamic performance. For frequencies that competed with the natural frequency or its natural harmonics, amplifications and instabilities were observed, wheres for high enough frequencies that did not compete with the natural, the aerodynamic behavior was overall better. In particular, the cases of 100 and 200 Hz seemed to be able to improve aerodynamic performance for the amplitudes tested in this work (Figs. 7 and 8).

A more detailed analysis should be carried out, testing even lower amplitude values with lower and higher frequencies. It should be again noted that this work utilized 360 timesteps per morphing period which for high frequencies may not be able to provide an accurate flow solution. Perhaps 720 or even more timesteps should be used in order to resolve high frequencies. Similarly, high amplitudes even in low frequencies may need a more detailed analysis for the simulations to give a more clear view on their effect on aerodynamic performance. Lastly, another parameter that may need to be examined is the morphing patch length. For this work, it was set to $95\%x/c$ but for low frequencies perhaps a larger deformed area will give more favorable aerodynamic results.

**Acknowledgements** This work has been carried out within the scope of the Research Project "SMS—Smart Morphing and Sensing". SMS has received funding from the European Union's Horizon H2020 program for research, technological development and demonstration under grant agreement no 723402.

## References

1. Lyu, Z., Martins, J.R.R.A.: Aerodynamic shape optimization of an adaptive morphing trailing-edge wing. J. Aircraft **52**, 1951–1970 (2011)
2. Barbarino, S., Bilgen, O., Ajaj, R.M., Friswell, M.I., Inman, D.J.: A review of morphing aircraft. J. Intell. Mater. Syst. Struct. **22**, 823–877 (2011)
3. Dimino, I., Ciminello, M., Concilio, A., Pecora, R., Amoroso, F., Magnifico, M., Schueller, M., Gratias, A., Volovick, A., Zivan, L.: Distributed Actuation and Control of a Morphing Wing Trailing Edge Springer International Publishing, Cham, pp. 171–186 (2016)
4. Pecora, R., Amoroso, F., Magnifico, M.: Toward the Bi-Modal Camber Morphing of Large Aircraft Wing Flaps: the Cleansky Experience (2016)
5. Jodin, G., Motta, V., Scheller, J., Duhayon, E., Doll, C., Rouchon, J.F., Braza, M.: Dynamics of a hybrid morphing wing with active open loop vibrating trailing edge by time-resolved piv and force measures. J Fluids Struct (2017)
6. Papadakis, G., Voutsinas, S.G.: In view of accelerating CFD simulations through coupling with vortex particle approximations the science of making torque from wing. J. Phys. Conf. Ser. (2014)

7. Roe, P.L.: Approximate Riemann solvers, parameter vectors and difference schemes. J. Comput. Phys. **43**, 357–372 (1981)
8. Venkatakrishnan, V.: On the Accuracy of Limiters and Convergence to Steady State Solutions AIAA Paper **93–0880**, (1993)
9. Menter, F.R.: Two-equation Eddy viscosity turbulence models for engineering applications. AIAA J. **32** (1994)
10. Spalart, P., Rumsey, C.L.: Effective inflow conditions for turbulence models in aerodynamic calculations. AIAA J. **45** (2007)

# URANS Flow Calculations Around a Morphing and Heaving Airfoil


**Stylianos Polyzos and George Tzabiras**

**Abstract** The present work is concerned with the numerical prediction of the incompressible flow past a 2D airfoil with a morphing trailing edge. Also considered is the problem of a simultaneously heaving and morphing airfoil. The above problems are solved using the incompressible URANS solver, developed in-house at the Laboratory for Ship and Marine Hydrodynamics (LSMH) of the National Technical University of Athens (NTUA). Turbulence is modelled using the Spalart-Almaras and Menter k-ω-SST two-equation turbulence model. A fully implicit scheme is used to study the evolution in time. Using the conformal mapping technique, the software generates an orthogonal curvilinear C-type grid around the morphed profile of the 2D airfoil at each time step. By employing this method, the problem is solved around a 2D morphing airfoil at free-stream and at a Reynolds Number of 1e6, for 30 and 300 Hz of morphing frequencies and amplitudes of 1 and 5 mm. The effect of the morphing trailing edge on the lift and drag characteristics is examined. Also two cases of a heaving and morphing airfoil are examined.

**Keywords** CFD · Incompressible flow · URANS · SST · Conformal mapping · Morphing airfoil · Heaving airfoil

## 1 Introduction

In recent years there is increasing demand of the aerospace industries for safer, more economic and environmentally greener transport. Although the modern aircraft wing is highly optimized, there is still room for improvement. One aspect of the flow that can be exploited, is related the trailing-edge vortex dynamics (the well-known Kelvin-Helmholtz vortices) and finer-scale vortices. These flow structures can be manipulated in order to breakdown harmful vortex structures and to enhance

S. Polyzos (✉) · G. Tzabiras
Laboratory for Ship and Marine Hydrodynamics, National Technical University of Athens, Zografou Campus, 9, Iroon Polytechniou str, 15780 Zografou, Athens, Greece
e-mail: spolyzos@mail.ntua.gr



M. Braza et al. (eds.), *Advances in Critical Flow Dynamics Involving Moving/Deformable Structures with Design Applications*, Notes on Numerical Fluid Mechanics and Multidisciplinary Design 147,
https://doi.org/10.1007/978-3-030-55594-8_46

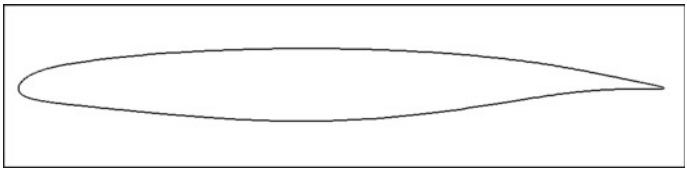

**Fig. 1** The profile of the Airbus A320 airfoil

beneficial ones, achieving reduced pressure fluctuations, responsible for the trailing-edge noise, at the same time attenuating flow separation and modifying the boundary-layer, both related to drag. The above can be achieved through active devices that morph the airfoil profile in real-time. Such a technology thus, enhances the flight performance, reduces noise and increases efficiency.

In recent years extensive research is performed regarding the performance of morphing airfoils [1]. In this present work an effort was made to numerically solve the unsteady free-stream flow around a 2D Airbus A320 airfoil (Fig. 1) the trailing edge of whom is oscillating with a set frequency and specific amplitude. To achieve that, the CFD software developed in-house at the Laboratory for Ship and Marine Hydrodynamics (LSMH) of the National Technical University of Athens (NTUA) was modified to generate and handle a changing grid. Also the problem of a simultaneously morphing and heaving airfoil was examined.

## 2 Method

### *2.1 Numerical Flow Solver*

It is assumed that the Reynolds and the continuity equations describe the incompressible flow around a 2-D airfoil. A local curvilinear coordinate system in conjunction with a curvilinear orthogonal grid is employed due to the advantages of such a setup in terms of accuracy and convergence [2]. In such a curvilinear coordinate system, the Reynolds averaged Navier-Stokes equations can be written as [3]:

$$\begin{aligned} \mathrm{C}(\mathrm{u}_1) &= -\frac{1}{\mathrm{h}_1}\frac{\partial \mathrm{p}}{\partial \mathrm{x}_1} + \rho u_2^2 \mathrm{k}_{21} - \rho u_1 \mathrm{u}_2 \mathrm{k}_{12} + (\sigma_{11} - \sigma_{22})\mathrm{k}_{21} \\ &\quad + 2\sigma_{12}\mathrm{k}_{12} + \frac{1}{\mathrm{h}_1}\frac{\partial \sigma_{11}}{\partial \mathrm{x}_1} + \frac{1}{\mathrm{h}_2}\frac{\partial \sigma_{12}}{\partial \mathrm{x}_2} \\ \mathrm{C}(\mathrm{u}_2) &= -\frac{1}{\mathrm{h}_2}\frac{\partial \mathrm{p}}{\partial \mathrm{x}_2} + \rho u_1^2 \mathrm{k}_{12} - \rho u_1 \mathrm{u}_2 \mathrm{k}_{21} + (\sigma_{22} - \sigma_{21})\mathrm{k}_{12} \\ &\quad + 2\sigma_{21}\mathrm{k}_{21} + \frac{1}{\mathrm{h}_2}\frac{\partial \sigma_{22}}{\partial \mathrm{x}_2} + \frac{1}{\mathrm{h}_1}\frac{\partial \sigma_{12}}{\partial \mathrm{x}_1} \end{aligned} \tag{1}$$

where $C(u_i)$ is the time derivative and the convection term:

$$C(u_i) = \rho \frac{\partial u_i}{\partial t} + \frac{\rho}{h_1 h_2}\left[\frac{\partial h_2 u_1 u_i}{\partial x_1} + \frac{\partial h_1 u_2 u_i}{\partial x_2}\right] \tag{2}$$

In the above equations, $h_1$, $h_2$ are the grid metrics and $k_{12}$, $k_{21}$ the curvatures. The stress tensor $\sigma_{ij}$ includes the viscous stresses and the double velocity correlations and can is expressed as:

$$\sigma_{11} = 2\mu_e\left[\frac{1}{h_1}\frac{\partial u_1}{\partial x_1} + u_2 k_{12}\right] = 2\mu_e e_{11},\ \ \sigma_{22} = 2\mu_e\left[\frac{1}{h_2}\frac{\partial u_2}{\partial x_2} + u_1 k_{21}\right] = 2\mu_e e_{22}$$
$$\sigma_{12} = \mu_e\left[\frac{1}{h_1}\frac{\partial u_2}{\partial x_1} + \frac{1}{h_2}\frac{\partial u_1}{\partial x_2} - u_2 k_{21} - u_1 k_{12}\right] = \mu_e e_{12} \tag{3}$$

The calculation domain is covered by an orthogonal curvilinear C-type structured grid and the finite volume method is applied to numerically solve the system of transport Eq. (1). A staggered grid arrangement is adopted to solve the strongly coupled momentum and continuity equations, i.e. the velocity components are defined at different points from the pressure. Each transport equation is integrated in the corresponding control volume and results in a discretized equation of the general form:

$$A_P \Phi_P = A_E \Phi_E + A_W \Phi_W + A_N \Phi_N + A_S \Phi_S + S_\Phi \tag{4}$$

where N, S, D and U correspond to the neighbouring nodes of the central node P, in the physical space. The coefficients $A_i$, $i = N, S, D, U$, represent the combined effect of the convection and diffusion terms appearing in the original differential Eq. (1). Diffusion terms are approximated by central differences while the convective part of $A_i$ is approximated by the first-order upstream scheme.

The integrated time derivative (first term on the RHS of (2)) is decomposed in two terms that are included respectively in $A_P$ and $S_\Phi$ as follows:

$$A_P : \frac{V(t)}{\delta t},\ \ S_\Phi : \frac{V(t)}{\delta t}\Phi_{old} \tag{5}$$

where $V(t)$ is the volume of the corresponding cell in the running time t and $\Phi_{old}$ is the value of the corresponding velocity component at $t - \delta t$ which is calculated by linear interpolation among the grid points in t and $t - \delta t$. This treatment corresponds to a first-order implicit time-marching scheme, since all other variables are evaluated at t.

In order to model turbulence, the k-ω-SST (Shear stress transport, [4, 5]) model is employed. SST is a widely used two-equation model based upon the Boussinesq approximation. This model divides the domain into two regions, the outer where the k-ε model is applied and the inner where the k-ω model is applied. In the expression

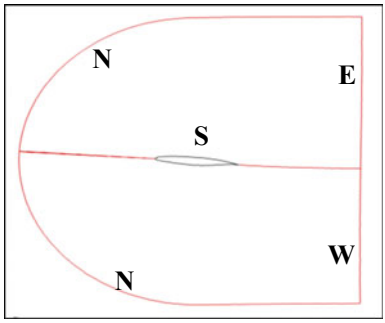


**Fig. 2** Definition of the computational domain

for the effective viscosity, eddy viscosity $\mu_e$ is a function of k and ω, the latter being the specific rate of dissipation of the turbulence kinetic energy k.

The numerical solution of the elliptic-in-space, discretized Eq. (1) requires the specification of boundary conditions on all boundaries of the calculation domain (Fig. 2). On the external boundary N the pressure and velocity components are specified by Dirichlet conditions according the considered laminar free stream flow. On the South boundary, no-slip conditions are applied on the airfoil, i.e. both $u_1$ and $u_2$-velocity components are set equal to zero, while Neumann-open type conditions [6] are applied for the pressure. On the East and West boundaries, the outflow boundaries, Newmann conditions are applied to all variables, except for the pressure where the value on the boundary is calculated by linear extrapolation of the corresponding values on the two finite volumes nearest to the boundary, as calculated in the previous iteration.

An iterative algorithm is followed to solve the time-dependant flow. In each time step the momentum and continuity equations are solved until a specified number of internal iterations is completed, making sure that convergence has been achieved. A SIMPLE-type pressure correction method is applied to solve the pressure field, Tzabiras [7]. To achieve convergence in any case, the application of under-relaxation factors is necessary. After convergence of a particular time step, the new airfoil profile is calculated from the original profile, by deforming it near the trailing edge by dy:

$$dy(x, t) = a\left[(x - x_s/c - x_s)^2 \sin(2\pi ft)\right], \quad x > x_S \tag{6}$$

where x is the chord-wise length, measuring from the leading edge, a is the deformation amplitude, $x_s$ is the chrod-wise length at which deformation begins, c is the chord and f is the morphing frequency. Then, a new grid is generated through the conformal mapping method and the momentum and continuity equations are solved.

## 2.2 Conformal Mapping and Grid Generation

In order to generate the numerical grids required by the finite volume method, the well-known conformal mapping method is employed in this work [8]. First the morphed airfoil profile is analytically represented through the coefficients $c_n = a_n + i * b_n$, of the conformal mapping of the profile onto the complex plane of the unit circle [9, 10]:

$$\zeta = c_0 + c_{-1}\frac{z}{R_C} + \sum_{n=1}^{N} c_n \frac{R_c^n}{z^n} \tag{7}$$

where $\zeta$ is the complex plane of the airfoil, z the complex plane of the circle with a radius $R_C$. Then each angle $\varphi$ on the circle corresponds to a point of the profile with coordinates $x(\varphi)$ and $y(\varphi)$. The calculation of the coefficients $a_i$, $b_i$, is straightforward, provided the relation between the angle $\varphi$ and the coordinates x, y. Since, in general, this relation is not known, an iterative procedure is required [2].

The conformal mapping coefficients are then employed to generate the 2-D orthogonal-curvilinear c-type grid (Fig. 3). Fist, the profile is analytically represented

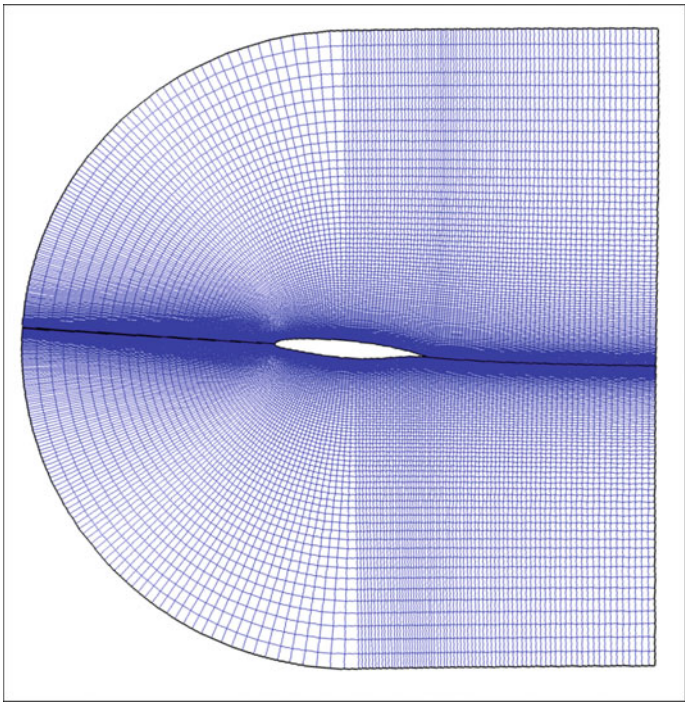

**Fig. 3** C-type orthogonal curvilinear grid around the A320 airfoil

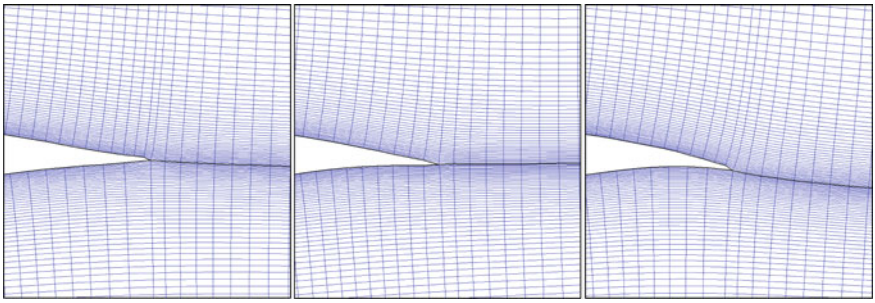

**Fig. 4** Detail of a C-type orthogonal curvilinear grid near the trailing edge of a morphed A320 airfoil, with an upwards trailing edge deflection of 5 mm (**a**, on the left) no trailing edge deflection of 5 mm (**b**, centre) and a downwards trailing edge deflection of 5 mm (**c**, on the right)

in terms of the coefficients of the conformal mapping to a unit circle. Then a c-type orthogonal curvilinear grid is generated around the unit circle, on ζ-plane, made up of four sub grids. The two sub-grids around the upstream half comprise homocentric circles and radii. The grid lines of the two sub-grids around the downstream half are calculated as flow and equipotential lines of the potential flow around the circle. Since the employed mapping is conformal, the inverse mapping is also conformal. Consequently, the grid nodes that result from the inverse mapping of the z-plane nodes, form an orthogonal curvilinear grid on the original ζ-plane. The distribution of nodes on both radial and peripheral directions is variable. When the distribution is prescribed on the z-plane, the corresponding radii and angles are calculated through the direct mapping.

It is worth noting here that this type of grid generation is quite fast and requires negligible CPU time compared to the time required to solve the Navier-Stokes. The time-consuming work is to perform an initial transformation of the specified sections, required to calculate and tabulate the corresponding conformal mapping coefficients.

At each time step, a new grid is generated around the morphed airfoil (Fig. 4a–c). Then an interpolation procedure is employed in order to calculate the values of the flow variables at the centres of their respective control volumes, from the calculated values at the centres of the control volumes of the previous time step.

## 3 Results and Discussion

In order to examine the effect of a morphing trailing edge on the lift and drag of a 2D airfoil, a series of numerical experiments were conducted for an A320 airfoil in free-stream. The chord length was 0.70 m, the free-steam air speed was $U = 21.5$ m/s corresponding to a Reynold's Number of $Re = 10^6$. Three values for the angle-of-attack were examined, 0.75° (zero degrees with respect to the chord line), 6.00 and 10.00°. In the tests with a morphing profile, the part of the airfoil near the trailing

**Table 1** Results for the steady-state numerical experiments

| Angle-of-attack (°) | 0.75 | 6.00 | 10.00 |
|---|---|---|---|
| Morphing frequency (Hz) | – | – | – |
| Morphing amplitude (m) | 0.000 | 0.000 | 0.000 |
| Lift coefficient $C_L$ (E + 01) | 1.944 | 7.064 | 1.032 |
| Drag coefficient $C_D$ (E + 02) | 1.145 | 1.646 | 2.307 |
| Lift-to-drag $C_L/C_D$ | 16.98 | 42.92 | 44.73 |

edge was periodically deforming. Two deformation amplitudes were tested, 0.001 and 0.005 m. In the first case, the last 0.035 m (5%) of the airfoil was deforming while in the later, 0.080 m (11.5%). Regarding the frequency of the deformation, two values were examined, 30 and 300 Hz as well as the static case without deformation. Finally two cases with a morphing and heaving airfoil were examined, with 0.001 and 0.005 m deformation amplitudes respectively. In both cases the angle-of-attack was 6.00°, the morphing frequency was 50 Hz, while the heaving frequency was 5 Hz and the heaving amplitude 0.070 m, or 10% of the chord.

In all numerical experiments, the same grid setup was utilised. Specifically each grid measured NI × NJ = 1000 × 300 grid nodes, in the peripheral and radial directions respectively. Of the NI = 1000 nodes, 600 were on the airfoil and a further 400 behind the trailing edge. The numerical grid extended 8 chord lengths in the radial direction, as well as ahead of the leading edge. Behind the trailing edge, the grid extended for 6 chord lengths. For each numerical experiment, the lift and drag coefficients are presented, along with the lift-to-drag ratio. For the tests with the morphing profile, the mean values are presented, calculated over eight periods.

## *3.1 Steady State Calculations*

As a base-line, three steady-state numerical experiment were conducted, one for each angle-of-attack, 0.75, 6.00 and 10.00°. In Table 1, the results are presented for the steady-state case, with regards to the lift coefficient, the drag coefficient and the lift-to-drag ratio.

## *3.2 Morphing Airfoil at 30 Hz*

A first group of tests was concerned with a morphing frequency of 30 Hz. Four numerical experiment were conducted, two for 0.75° angle-of-attack and a further two, one for 6.00 and one for 10.00° of angle-of-attack. In Table 2, the results are presented for the 30 Hz morphing cases, with regards to the lift coefficient, the drag coefficient and the lift-to-drag ratio. In parentheses are provided the per cent differences with regards to the respective steady-state test. In Fig. 5a, b the time

**Table 2** Results for the numerical experiments with a morphing frequency of 30 Hz

| Angle-of-attack (°) | 0.75 | 0.75 | 6.00 | 10.00 |
|---|---|---|---|---|
| Morphing frequency (Hz) | 30 | 30 | 30 | 30 |
| Morphing amplitude (m) | 0.001 | 0.005 | 0.005 | 0.005 |
| Lift coefficient $C_L$ (E + 01) | 1.718 (−11.61%) | 1.757 (−9.61%) | 7.176 (+1.58%) | 1.093 (+5.90%) |
| Drag coefficient $C_D$ (E + 02) | 1.156 (+1.00%) | 1.206 (+5.33%) | 1.430 (−13.15%) | 2.126 (−7.86%) |
| Lift-to-drag $C_L/C_D$ | 14.86 (−12.49%) | 14.57 (−14.18%) | 50.19 (+16.96%) | 51.41 (+14.93%) |

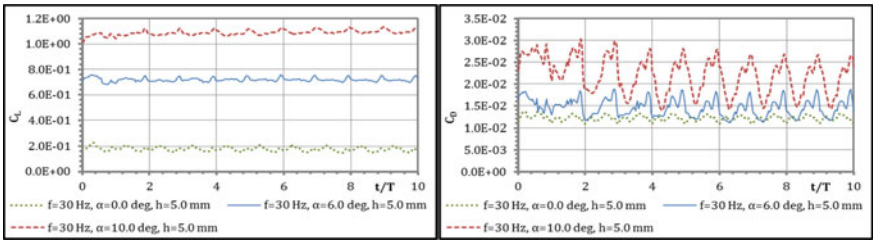


**Fig. 5** Time history of the lift ($C_L$, **a**) on the left and drag ($C_D$, **b**) on the right, coefficients, morphing frequency 30 Hz, amplitude 0.005 m, angle-of-attack 0.75, 6.00 and 10.00°

history of the lift and drag coefficients are presented respectively for the above cases.

## *3.3 Morphing Airfoil at 300 Hz*

Then a morphing frequency of 300 Hz was examined. Four numerical experiment were conducted, two for 6.00° angle-of-attack and another two for 10.00° of angle-of-attack. For each frequency one test had a morphing amplitude of 0.001 m and one had 0.005 m amplitude. In Table 3, the results are presented for the 300 Hz morphing cases, with regards to the lift coefficient, the drag coefficient and the lift-to-drag ratio. In parentheses are provided the per cent differences with regards to the respective steady-state test. In Fig. 6a, b the time history of the lift and drag coefficients are presented respectively for the 6.00° angle-of-attack cases, while in Fig. 7a, b, the time history of the lift and drag coefficients are presented for the 10.00° of angle-of-attack cases.

**Table 3** Results for the numerical experiments with a morphing frequency of 300 Hz

| Angle-of-attack (°) | 6.00 | 6.00 | 10.00 | 10.00 |
|---|---|---|---|---|
| Morphing frequency (Hz) | 300 | 300 | 300 | 300 |
| Morphing amplitude (m) | 0.001 | 0.005 | 0.001 | 0.005 |
| Lift coefficient $C_L$ (E + 01) | 7.673 (+8.62%) | 7.656 (+8.38%) | 1.166 (+12.98%) | 1.175 (+13.87%) |
| Drag coefficient $C_D$ (E + 02) | 1.888 (+14.71%) | 1.972 (+19.80%) | 2.691 (+16.65%) | 2.840 (+23.09%) |
| Lift-to-drag $C_L/C_D$ | 40.64 (−5.31%) | 38.83 (−9.53%) | 43.33 (−3.14%) | 41.38 (−7.49%) |

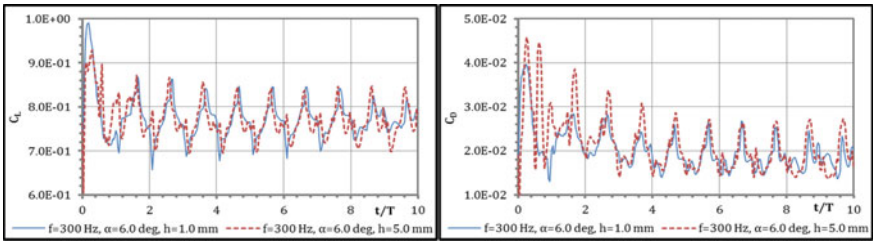


**Fig. 6** Time history of the lift ($C_L$, **a**) on the left and drag ($C_D$, **b**) on the right, coefficients, morphing frequency 300 Hz, angle-of-attack 6.00°, amplitude 0.001 and 0.005 m

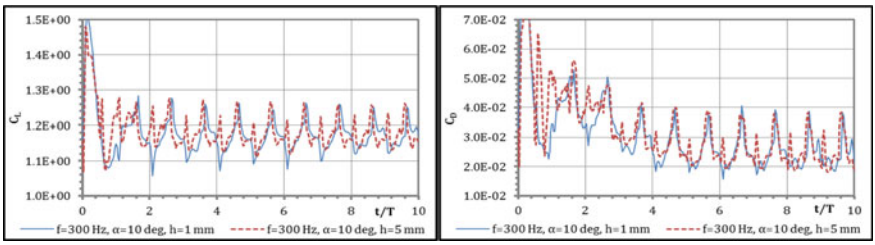


**Fig. 7** Time history of the lift ($C_L$, **a**) on the left and drag ($C_D$, **b**) on the right, coefficients, morphing frequency 300 Hz, angle-of-attack 10.00°, amplitude 0.001 and 0.005 m

## *3.4 Morphing and Heaving Airfoil at 50 Hz*

Two cases of a morphing and heaving airfoil were examined. In both cases the angle-of-attack was 6.00°, the morphing frequency was 50 Hz, while the heaving frequency was 5 Hz and the heaving amplitude 0.070 m, or 10% of the chord. The deformation amplitude was 0.001 and 0.005 m respectively. In Table 4, the results are presented for the morphing and heaving cases, with regards to the lift coefficient, the drag coefficient and the lift-to-drag ratio. The values are the RMS values through

**Table 4** Results for the numerical experiments with a morphing and heaving airfoil

| Morphing amplitude (m) | 0.001 | 0.005 |
|---|---|---|
| Lift coefficient $C_L$ (E + 01) | 7.776 | 7.898 |
| Drag coefficient $C_D$ (E + 02) | 3.624 | 3.652 |
| Lift-to-drag $C_L/C_D$ | 21.46 | 21.63 |

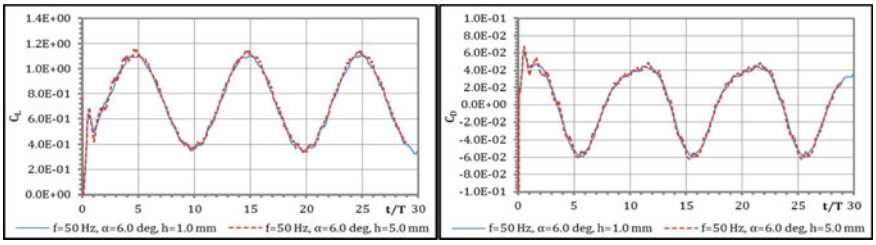


**Fig. 8** Time history of the lift on the left ($C_L$, **a**) and drag ($C_D$, **b**) on the right, coefficients, morphing frequency 50 Hz, angle-of-attack 6.00°, amplitude 0.001 and 0.005 m, heaving frequency 5 Hz, heaving amplitude 0.070 m

20 morphing periods or 2 heaving periods. In Fig. 8a, b the time history of the lift and drag coefficients are presented for the heaving cases.

## *3.5 Discussion*

In order to aid the extraction of useful conclusions, the results presented in previous paragraphs are now presented in Figs. 9, 10 and 11 as graphs. Specifically in Fig. 9a–c the lift and drag coefficients and the lift-to-frag ratio are presented as functions of the morphing frequency. In Fig. 10a–c the lift and drag coefficients and the lift-to-frag ratio are presented as functions of the morphing amplitude. In Fig. 11a–c the lift and drag coefficients and the lift-to-frag ratio are presented as functions of the angle-of-attack.

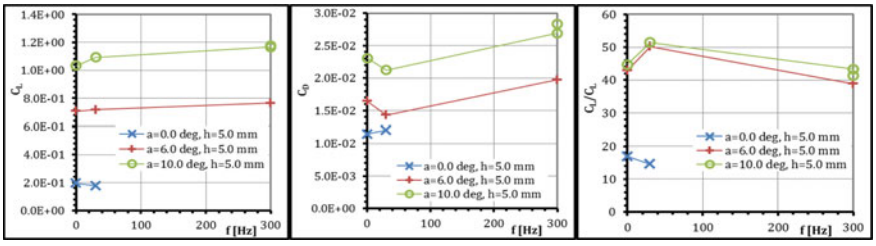


**Fig. 9** Lift (CL, **a**) and drag (CD, **b**) coefficients as well as the lift-to-drag (CD, **c**) ratio, as a function of the morphing frequency

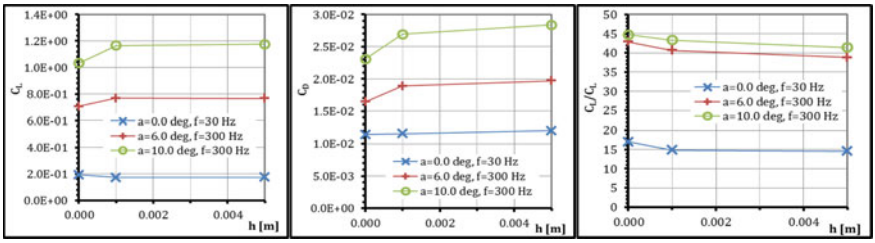


**Fig. 10** Lift (CL, **a**) and drag (CD, **b**) coefficients as well as the lift-to-drag (CD, **c**) ratio, as a function of the morphing amplitude

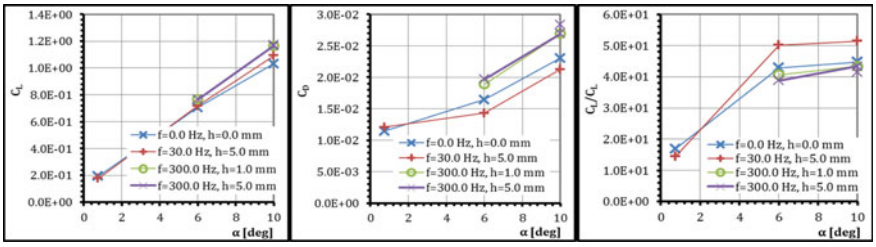


**Fig. 11** Lift ($C_L$, **a**) and drag ($C_D$, **b**) coefficients as well as the lift-to-drag ($C_D$, **c**) ratio, as a function of the angle-of-attack

The main conclusion to be drawn is that the low frequency (30 Hz) morphing is more efficient than the high frequency (300 Hz). Specifically all 30 Hz tests present an increase in lift and a reduction in drag, regardless from the angle-of-attack. On the other hand the 300 Hz tests present increased lift but also a significantly increased drag, leading to a decreased lift-to-drag ratio. Another interesting result is that the morphing amplitude has negligible effect on lift and a negative, though small, effect on drag. At this point it should be pointed out that the results at the higher frequency may be affected by the use of a relatively coarse grid.

Regarding the angle-of-attack, all tests indicate a near linear increase of lift, with respect to the angle-of-attack, up to the maximum tested angle of 10°. This indicates a small effect of the flow detachment, although morphing actually forces the flow to detach earlier. In Fig. 12a, b, the time histories of the detachment point on the suction side are presented, as a percentage of the chord, at 10° angle-of-attack, 300 Hz morphing frequency and 0.001 m and 0.005 m deformation respectively. In both figures, the dashed line corresponds to the steady-state detachment point.

Also interesting is the prediction of the drag coefficient for each of the morphing cases, in order to achieve the lift of the two steady-state cases. Using linear interpolations, the predictions for the 6.00 and 10.00° angle-of-attack are presented in Tables 5 and 6 respectively. In both cases, the lower frequency (30 Hz) is more efficient.

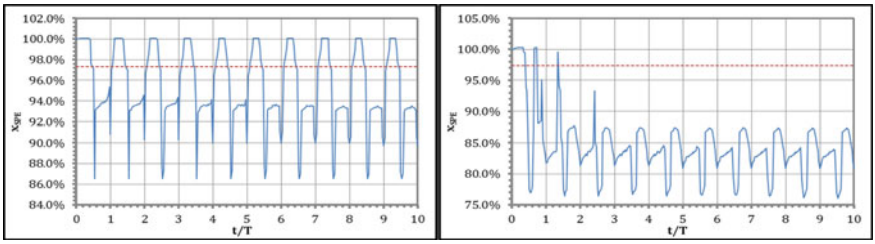


**Fig. 12** Time history of the point of suction side detachment (as a percentage of the chord), morphing frequency 300 Hz, angle-of-attack 10.00°, amplitude 0.001 (**a** on the left) and 0.005 m (**b** on the right)

**Table 5** Prediction of the drag coefficient at 6.00° angle-of-attack

| Morphing frequency (Hz) | – | 30 | 300 | 300 |
|---|---|---|---|---|
| Morphing amplitude (m) | – | 0.005 | 0.001 | 0.005 |
| Angle-of-attack (°) | 6.00 | 5.89 | 5.52 | 5.54 |
| Lift coefficient $C_L$ (E + 01) | 7.064 | 7.064 | 7.064 | 7.064 |
| Drag coefficient $C_D$ (E + 02) | 1.646 | 1.425 (−15.51%) | 1.738 (+5.31%) | 1.819 (+9.53%) |
| Lift-to-drag $C_L/C_D$ | 4.292 | 4.957 (+13.43%) | 4.064 (−5.61%) | 3.883 (−10.53%) |

**Table 6** Prediction of the drag coefficient at 10.00° angle-of-attack

| Morphing frequency (Hz) | – | 30 | 300 | 300 |
|---|---|---|---|---|
| Morphing amplitude (m) | – | 0.005 | 0.001 | 0.005 |
| Angle-of-attack (°) | 10.00 | 9.35 | 8.66 | 8.60 |
| Lift coefficient $C_L$ (E + 01) | 1.032 | 1.032 | 1.032 | 1.032 |
| Drag coefficient $C_D$ (E + 02) | 2.307 | 2.013 (−14.61%) | 2.421 (+4.72%) | 2.536 (+9.04%) |
| Lift-to-drag $C_L/C_D$ | 4.473 | 5.127 (+12.57%) | 4.262 (−4.95%) | 4.069 (−9.94%) |

A final conclusion, relative to heaving is that its effect is at least one order of magnitude greater, than that of morphing as indicated by the amplitude in the oscillations of Fig. 8a, b.

## 4 Conclusions

The present study is a first attempt to analyse the effect of morphing and heaving on the characteristics of subsonic airfoils. The necessary changes were made to the in-house developed software including the time-dependant grid deformation. The presented results indicate that the software is working well and is able to capture the effect of the morphing profile. According to the presented results, low frequency

morphing is more efficient than higher frequency morphing, though this position should be reinforced by more data points. A further result is that the effect of heaving is at least one order of magnitude greater than that of morphing. The effort towards understanding the behaviour of a morphing airfoil should continue with more extensive studies.

**Acknowledgements** This work has been carried out within the scope of the Research Project "SMS—Smart Morphing and Sensing". SMS has received funding from the European Union's Horizon H2020 program for research, technological development and demonstration under grant agreement no 723402.

## References

1. Chinaud, M., Rouchon, J.F., Duhayon, E., Scheller, J., Cazin, S., Marchal, M., Braza, M.: Trailing-edge dynamics and morphing of a deformable flat plate at high Reynolds number by time-resolved PIV. J. Fluids Struct. **47**, 41–54 (2014)
2. Tzabiras, G.D., Dimas, A., Loukakis, T.A.: A numerical method for the calculation of incompressible, steady, separated flows around aerofoils. Int. J. Numer. Meth. Fluids **6**, 789–809 (1986)
3. Tzabiras, G.D.: Numerical study of the viscous flow past a ship's model with asymmetric stern. In: Proceedings of MARIND-96 Conference, pp. III.41–III.57 (1996)
4. Menter, F.R.: Two-equation eddy-viscosity turbulence models for engineering applications. AIAA J. **32**(8), 1598–1605 (1994)
5. Tzabiras, G., Papakonstantinou, V., Voutsinas, S.: A numerical study of the flow past a wind generator. In: Braza, M., Bottaro, A., Thomson, M. (eds.) Advances in Fluid-Structure Interaction. NNFM, vol. 133, pp. 269–282. Springer (2016)
6. Tzabiras, G.D.: Resistance and self-propulsion simulations for a series-60, CB $=$ 0.6 hull at model and full scale. Ship Technol. Res. **51**, 21–34 (2004)
7. Tzabiras, G.D.: A numerical investigation of 2D, steady free surface flows. Int. J. Numer. Meth. Fluids **25**, 567–598 (1997)
8. Tzabiras, G.D., Kontogiannis, K.: An integrated method for predicting the hydrodynamic resistance of low-Cb ships. Comput. Aided Des. **1568**, 1–16 (2009)
9. Tzabiras, G.D., Vafiadou, M., Nassos, G.: A numerical method for the generation of 2D orthogonal curvilinear grids. In: 1st International Conference on Numerical Grid Generation, Landshut, W. Germany (1986)
10. von Kerczek, C., Tuck, E.O.: The representation of ship hulls by conformal mapping functions. J. Ship Res. **19**, 284–298 (1969)

# Bifurcations and Analytic Modelling in FSI

# General Boundary Identification Through Surface Pressure Measurements on a 2-D Foil


**Jack H. Clark and Jason M. Dahl**

**Abstract** Digital twins can be used as model representations of physical systems given adequate information about the physics through environmental measurements. For moving bodies in the presence of boundaries, knowledge of the local boundary conditions is necessary to develop a model that can be used in a control system or decision making process. This paper presents a method using a viscous numerical simulation as a model combined with pressure measurements on the surface of a foil in order to estimate general wall boundary conditions in the vicinity of the foil. The method uses an Unscented Kalman Filter and presents a weighted estimate approach that outperforms the standard Unscented Filter for estimation of wall shape. B-splines are used to generalize the shape of the wall. The algorithm is demonstrated to be capable of identifying an individual wall protrusion and multiple wall protrusions in order to update the wall boundary conditions for a real time numerical simulation.

**Keywords** Lateral line · Digital twin · Flow sensing

## 1 Introduction

A digital twin is an artificial representation of a physical system which properly captures the environmental loading on the system in order to provide information about the health of the system, lifetime performance of the system, or it may be used in decision making or control of the system. While cyber-physical systems have been in large use for structural health monitoring purposes [15], the combination of physical measurements with simulations of dynamically moving bodies pose additional challenges. The development of digital twins has been underway in aeronautics, particularly for structural health monitoring and fatigue estimation in aircraft materials

J. H. Clark · J. M. Dahl (✉)
Department of Ocean Engineering, University of Rhode Island, 215 South Ferry Rd, Narragansett, RI 02882, USA
e-mail: jmdahl@uri.edu



M. Braza et al. (eds.), *Advances in Critical Flow Dynamics Involving Moving/Deformable Structures with Design Applications*, Notes on Numerical Fluid Mechanics and Multidisciplinary Design 147,
https://doi.org/10.1007/978-3-030-55594-8_47

[16]. In aircraft, however, the majority of an aircraft's flight path occurs in what can be considered an unbounded fluid, such that numerical simulation of the surrounding flow field does not define solid boundary conditions other than those defining the geometry of the aircraft. In marine flows, such as ships and submarines, these vessels often operate in shallow water with near bottom conditions, they operate in a mutliphase flow environment at the interface of water and air, and these local boundary conditions change in time, particularly when the vessel is moving. In situations with unknown boundary conditions, a digital twin could deviate significantly from the physical system, particularly where fluid-structure interactions are strong. The following work develops a method for determining unknown general boundary conditions using a simple two-dimensional viscous flow model of a wing passing by an object on a wall. The method assumes the use of simple hydrodynamic measurements available at the surface of the foil (pressure in particular), to estimate the local boundary shape, which can provide a more representative simulation of the nearby flow field. The presented method is an initial step towards realizing a real time computational model integrated with real time measurements for the operation of a moving body in a fluid that could be used for decision making and control. The general method based on a B-spline representation of the boundary provides for natural extensions to 3-D surfaces and flow fields and provides an extension from previous biologically inspired work on artificial lateral line systems.

The integration of physical measurements for object detection has a natural biological analog with the mechanosensory lateral line system of fish. The lateral line is a sensory system in fish and aquatic amphibians that allows for the sensing of pressure and velocity changes in the surrounding fluid [6]. The structure of the biological sensory system is complex with significant variability amongst fishes that have evolved in different environments [18], which has lead to different types of fish using the system in different ways, such as detecting flow perturbations in different flow conditions [7], encoding a Karman vortex street [2], or recognizing and avoiding objects [4]. The expansive functionality of this system in nature has lead to research in the implementation of artificial lateral lines systems for use in underwater vehicles as navigation and environmental sensing are inherently difficult in turbid underwater environments.

Much research has focused on the development of novel pressure and velocity sensor systems that can mimic the functionality of a lateral line system [1, 12] and algorithms have been developed for interpreting these measurements in a variety of applications. Fernandez et al. [8] demonstrated object detection and tracking using embedded pressure sensors in a foil. Using a simple potential flow panel method to describe the geometry of the foil and a generalized transform for the shape of a simple body [3], it was shown that the location, size, and general geometry can be found through inversion of the pressure measurements using an unscented Kalman filter. Maertens et al. [14] elaborated on this technique, applying the method to a variety of different shapes and multiple bodies, however it was found that the technique can break down when flow separation results in measured pressures that significantly differ from the potential flow model. Additionally, the use of the generalized transform

limited the ability for detecting objects to predefined shapes assuming truncation of the transform.

Viscous effects in physical lateral line systems are known to be critically important in affecting flow behaviors in the boundary layer and at the scale of the physical receptors [21]. Maertens and Triantafyllou [13] showed that even with separation, if viscous information is known about the flow field, potential flow modeled pressures may be corrected using the displacement thickness, such that shape information derived from pressure sensing may be preserved. The fluctuating boundary layer information in this case is shown to act as an amplifier, improving object characteristic estimates. The viscous information used in object detection, however, are determined a priori through a learning algorithm, such that the technique is not applied in real time. The present study looks to improve upon this previous work in two major aspects: (1) Applying a fully viscous model of the fluid to directly incorporate viscous effects for object detection and (2) Developing a technique for the general characterization of an object's shape based on standard spline geometry. These modifications look to enhance the integration of physical measurements with a viscous flow model for boundary identification, which will help to enable general boundary updating in a real time digital twin.

## 2 Experimental Methods

In order to develop an algorithm for feature detection based on hydrodynamic measurements, we define a basic problem of interest around which the algorithm is developed. For our problem, we define a streamlined body (NACA 0012 wing section) at zero angle of attack, that passes by a feature protruding from a flat wall. Figure 1 shows the basic setup of the problem, with the NACA foil section in the vicinity of a protrusion from a flat wall. In the present study, all measurements are generated through simulations, so no physical measurements are used. It is assumed that measurements of pressure are taken at the surface of the foil section (indicated by circles in Fig. 1). The measurements of pressure are then used to infer the shape of the wall as the foil passes by the wall in time. A viscous model of the flow field is used as a forward model in order to estimate the unknown boundary conditions.

### *2.1 Simulation Model Definition*

The numerical model of the system is generated using an open source, 2-D, Cartesian-grid, Navier-Stokes solver called LilyPad [19]. LilyPad is a numerical tool designed to help researchers perform complex dynamic fluid-structure simulations at low computational cost and with immediate visual feedback. For simulating dynamically moving bodies, the numerical model implements the boundary data immersion method (BDIM) [20], an immersed boundary technique that uses kernal functions to

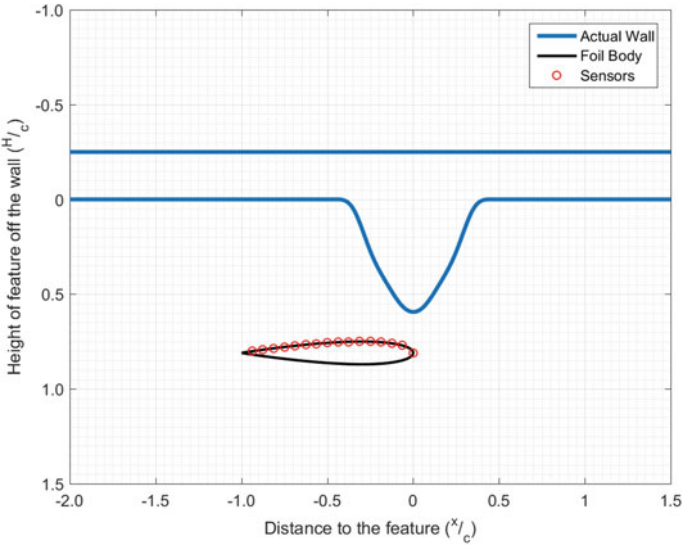


**Fig. 1** A diagram of the simulation showing the distribution of pressure sensors

blend field equations and boundary conditions for the fluid and solid in the vicinity of solid boundaries. The technique has been demonstrated to be capable of achieving second order accuracy in force estimates and has been validated against a variety of complex dynamic fluid-structure interaction problems [13]. The simple structure of the LilyPad code allows it to run quickly on a single computer processor, such that multiple simulations may be run in parallel on a single computer with multiple processors.

In typical numerical simulations, it is necessary to perform convergence and validation studies in order to ensure that the chosen grid scales and parameterization of the model will produce meaningful numerical results that properly model the physics of the system. In the present study, we are interested in developing an algorithm that utilizes the numerical model as an estimate of a physical system, but in this sense, it does not need to necessarily perfectly model all aspects of the physical system. For this purpose, we choose to run a simulation of the system that is underresolved in space, but sufficiently resolved in time to give a stable solution, as this speeds up computational time in the development of the algorithm. Since we use the numerical model to generate simulated measurements, it is okay if the model is not fully resolved to perfectly capture the true physics. In contrast, extension of the algorithm to a physical system using physical measurements will require that the numerical model sufficiently resolves the flow field in space to produce a meaningful estimate of pressure and velocity for the physical system.

The simulation is set up by defining a long wall in the presence of a NACA 0012 foil. The NACA 0012 foil is defined to have a body length of 10 grid points, while the length and height of the Cartesian grid domain is defined to be $2^7$ or 128 grid

points. Proper resolution of the flow field requires about 20 grid points over the length of the foil and a domain length of $2^9$–$2^{10}$. Rather than moving the foil through the simulation, the foil remains stationary in the simulation and the wall along with features defined on the wall are moved at a defined velocity that is equivalent to the velocity of the free stream flow field. This is an equivalent condition to a foil moving through a still flow field and it ensures that a boundary layer does not form on the surface of the wall due to fluid motion. Sixteen points over the wall side of the foil are defined where the field pressure is evaluated on the foil as a function of time (shown in Fig. 1).

In order to define a general wall condition that can be modified to represent a variety of general shapes, a cubic B-spline definition of the wall shape is defined. Using a cubic B-spline representation of the wall has two particular advantages: (1) The wall shape may be defined based on the location of control points, which can be considered states of a system defining the general shape of the wall; and (2) B-splines have a natural extension to three-dimensional NURBS surfaces, such that the method could be extended to three-dimensional space.

The wall surface is defined using a standard B-spline representation as in Eq. (1), where a 2-D line is defined by a set of control points multiplied by a set of weighted basis functions [5],

$$S_{m,\mathbf{t}}(x) = \sum_{i=0}^{D-1} P_i B_{i,m}(x) \tag{1}$$

where $S_{m,t}(x)$ is a particular spline segment of polynomial order $m$ at point $x$ relative to the knot vector $\mathbf{t}$, $P_i$ are the $D$ control points, and $B_{i,m}(x)$ is the basis function relative to the knot vector. The basis function is defined as in De Boor [5]. Choosing the order, number of control points, and knot vector a priori allows for the spline boundary to be modified simply by the locations of the control points. Figure 1 shows an example wall shape defined using a B-spline definition.

## 2.2 Estimation Algorithm Definition

Estimation of the wall boundary condition in the presence of the foil is performed using an Unscented Kalman Filter [17]. The Unscented Kalman Filter ($UKF$) is an extension of the Linear Kalman Filter, which has the ability to account for highly non-linear state and measurement relationships by assuming Gaussian statistics for the unknown states. The $UKF$ uses a sigma transform and an unscented transform to estimate the first and second moments of the random variable measurement and state distributions, while limiting the number of random realizations necessary to obtain a statistical representation of these variables. The sigma transform and unscented transform are able to account for high order statistical moments with low added computational cost.

In our algorithm, we define the location of control points that define the surface of the wall to be unknown system state variables that we wish to estimate. Measurements of pressure on the surface of the foil are assumed to be measured observations that are known at specific instances in time. If we wish to estimate the location of control points using our pressure observations, the system can described in a state equation (Eq. 2) and a measurement equation (Eq. 3),

$$\mathbf{P}[k+1] = \mathbf{P}[k] + \mathbf{v}[k] \tag{2}$$

$$\mathbf{p}[k] = F(\mathbf{P}[k]) + \mathbf{w}[k] \tag{3}$$

where $k$ is discrete time, $\mathbf{P}$ are the y-location of $N$ control points with covariance $C^P$, $\mathbf{p}$ is a windowed time history of pressure modeled at defined locations on the foil from the numerical simulation (denoted as non-linear process $F$) with covariance $C^F$, and $\mathbf{v}[k]$ and $\mathbf{w}[k]$ are uncorrelated additive noise associated with the state and measurement respectively [17]. The state and measurement noise have variances $q$ and $r$, and covariance of the form $Q = qI$ and $R = rI$ where $Q$ is size $N \times N$ and $R$ has size $\mathcal{O}(\mathbf{p}^F)$.

For simplicity in demonstrating the algorithm and to avoid ambiguity in our solution, the control point locations $\mathbf{P}$, are chosen to have evenly spaced, pre-defined horizontal locations, such that only the vertical position of the $N$ control points is variable and unknown. Pressure measurements must be sampled sufficiently in time over a large enough length of time to satisfy the assumptions of a Gaussian distribution. In the present study, we use $M \geq 50N$ measurements per pressure time history.

The sigma transformation [17] is a method to select a set of weighted sample points that contain information about the true mean and covariance of a Gaussian random variable. The number of sigma points ($L$), are determined by the number of states as $L = 2N + 1$. The value of each sigma point is determined by Eqs. (4), (5), and (6) based on the estimated mean state, $\bar{\mathbf{P}}$, and the estimated state covariance $C^x$,

$$X_0 = \bar{\mathbf{P}} \tag{4}$$

$$X_i = \bar{\mathbf{P}} + (\sqrt{(N+\lambda)C^x})_i, \quad i = 1, \ldots, N \tag{5}$$

$$X_i = \bar{\mathbf{P}} - (\sqrt{(N+\lambda)C^x})_{n-i}, \quad i = N+1, \ldots, 2N \tag{6}$$

where $\lambda = \alpha^2(N + \kappa) - N$ is a scaling parameter corresponding to the mean and covariance weights, $W^m$ and $W^c$ in Eqs. (7) and (8). The unscented transform constant $\alpha > 0$ controls the spread of the sigma points about the estimated mean state and is typically a small number, though it can vary depending on the type of estimated variable [17]. A value of $\kappa \geq 0$ guarantees that the estimate of the covariance will remain positive semi-definite, but can vary depending on the type of estimated parameter.

$$W_0^m = \frac{\lambda}{N+\lambda}, \quad W_i^m = \frac{1}{2(N+\lambda)}, \quad \text{for } i = 1, \ldots, 2N \tag{7}$$

$$W_0^c = W_0^m + (1 - \alpha^2 + \beta), \quad W_i^c = W_i^m \tag{8}$$

$\beta \geq 0$ is used to incorporate statistical information about higher order moments of the random variable distribution, where $\beta = 2$ produces a standard normal distribution. The unscented transform is a method to estimate the mean and covariance of a transformed random variable distribution from the sigma points using the defined weights. Using the sigma points as determined above, we pass the sigma points through the state and measurement equations, Eqs. (2) and (3). This allows us to define $\mu_P$ and $\mu_F$, the current state and measurement estimates, as a weighted average based on the sigma points as in Eqs. (9) and (10).

$$\mu_P = \sum_{i=0}^{2N} W_i^m X_i \tag{9}$$

$$\mu_F = \sum_{i=0}^{2N} W_i^m p_i^F \tag{10}$$

$p_i^F$ is the measurement of pressure from a numerical simulation run using the boundary conditions determined through the sigma transformation $X_i$. From these estimates, we can define the covariance matrices of the state and measurement using Eqs. (11) and (12).

$$C^x = \sum_{i=0}^{2N} W_i^c (X_i - \mu_P)(X_i - \mu_P)^T \tag{11}$$

$$C^y = \sum_{i=0}^{2N} W_i^c (p_i^F - \mu_F)(p_i^F - \mu_F)^T \tag{12}$$

Ultimately, the unscented transform passes the statistical properties of the estimated random variable through the non-linear relationship between state and measurement, while properly transforming the distribution and mean of the random variable. When used with a Kalman filter, the unscented transform then allows one to correct the estimate of a particular system state based on the error of the measurement estimate compared with the observed measurement, while performing fewer random realizations through the Sigma transform, than would be necessary to fully statistically sample the random variables.

Following the method of Wan and Van Der Merwe [17], the cross-variance between the state and measurement estimates is computed as in Eq. (13).

$$C^{x,y} = \sum_{i=0}^{2N} W_i^c (X_i - \mu_P)(p_i^F - \mu_F)^T \tag{13}$$

The gain of the filter, $K$ is then calculated as in Eq. (14), and the mean and covariance of the system states are updated based on the measurement $\mathbf{p}^{meas}$, gain, and estimated states, as in Eqs. (15) and (16).

$$K = C^{x,y}(C^{y})^{-1} \tag{14}$$

$$\bar{\mathbf{P}} = \mu_P + K(\mathbf{p}^{meas} - \mu_F) \tag{15}$$

$$C^{P} = C^{x} - K(C^{x,y})^{T} \tag{16}$$

## 2.3 Estimation Algorithm Implementation

Implementation of the estimation algorithm requires a set of a priori decisions about how to define the states and measurements in the system. In the B-spline definition of a wall, we can choose an arbitrary number of control points to define the surface of the wall, however, as each control point is a state variable to be estimated, we would like to limit the number of states to be estimated at any point in time. One of the useful features of a B-spline is that the shape of the spline is determined only by the nearest local control points, hence if one moves a single control point, the curve only varies its shape in that local vicinity. This implies that one does not necessarily need to estimate the location of all control points at once, but rather can estimate the locations of a subset of control points that shift with the location of the foil. We first define that at each discrete time step, $k$, the foil advances forward due to its forward speed. The shape of the wall is initially assumed to be flat, and defined by $D$ control points (i.e. all control point positions are zeroed to the wall and the covariance of the states is initialized as the identity matrix). The discrete time step, $k$, is defined such that each control point exists at a location $Uk$, where $U$ is the forward speed of the foil. A subset, $N$, number of control points is selected in a window region near the location of the foil to be updated according to the $UKF$ algorithm. It is important to note that each time step $k$ is not related to the numerical simulation time, it is instead the global time that defines the current location of the foil. At each time step, the sigma points are computed, which define $L$ number of simulations to be performed using wall shapes defined by the sigma point choices (i.e. the sigma points define different locations of the control points, which vary the shape of the wall where the $L$ simulations will allow for computation of the statistics associated with the variability of the sigma points). The states of the system are then updated according to the previously defined $UKF$ algorithm and a comparison is made between the state estimated pressures and the measured pressure, computing the root mean square error (RMSE) for all of the pressure estimates. The $UKF$ process is then repeated until a convergence criteria has been met for the RMSE of the modeled and measured pressure at time $k$. In the presented results, the convergence criteria is defined as when the RMSE changes by less than one percent of the previous value. At this point, $n$ control points on the downstream side within the window of $N$ states become fixed and are not allowed to change, the foil moves forward in time by $k$, and $n$ control

points are included in the new window of $N$ states to be estimated. This algorithm repeats as the foil moves forward in time.

One important challenge of this method is the fact that fluids contain memory, such that the pressure at any instant in time is dependent on the time history of the wake of the object. Even though the physical foil is moving forward in time, in order to compute the pressure on the surface of the foil at a particular time $k$, simulations must all begin at the same point in the past, otherwise the history of the wake will be different and the modeled pressure will be incorrect. This requires that as the foil moves forward in time, simulations using the sigma parameters become longer. Also, any errors in control points that become fixed due to the propagation of the algorithm in time, will also propagate errors in the estimate of pressure over time. While the length of simulations could be reduced by altering the initial conditions of the simulations based on the current global time of the foil, the propagation of errors in simulations due to errors in fixed estimated states will need to be considered in future work.

## 3 Results and Discussion

Initial results are shown for a window of $N = 19$ control points, with the window shifting by $n = 1$ control point at each discrete time step. The numerical simulation noise level was assumed to be $Q = \underline{0}$ and the measurement noise level was set to be proportional to the resolution of the LilyPad simulation, such that $R = 0.5 \times 10^{-3} I$, based on previous observations on the estimation of splines using recursive methods [9, 10]. For this implementation, following guidelines from [11, 17] on the implementation of the $UKF$ algorithm, we chose $\alpha = 1$, $\beta = 5$, and $\kappa = 1$.

### *3.1 Standard Estimation Method*

To construct the measurement matrix in the $UKF$ algorithm, we can consider each pressure measurement at a given point in time to be an observation of the system. In this way, we construct the measurement matrix, $\mathbf{p}^{meas}$ as a single column array of each pressure measurement time history $\mathbf{p}_i$ at measurement location $i$, with $i = 1 \ldots 16$ over the chord of the foil. This evenly weights any observation of pressure on the surface of the foil to be used to estimate the location of the control points.

Figure 2a shows the wall estimate from the algorithm as the foil moves forward to three discrete positions in time. The shapes near each line indicate the positions of the windowed estimated control points for that discrete position in time. One can see from the figure, that the algorithm is capable of distinguishing that a protrusion exists at the wall, giving a relative estimate of the size and location of the feature (i.e. the height of the protrusion is captured well and the width of the protrusion is somewhat identified), however there are small fluctuations in the spline estimate of

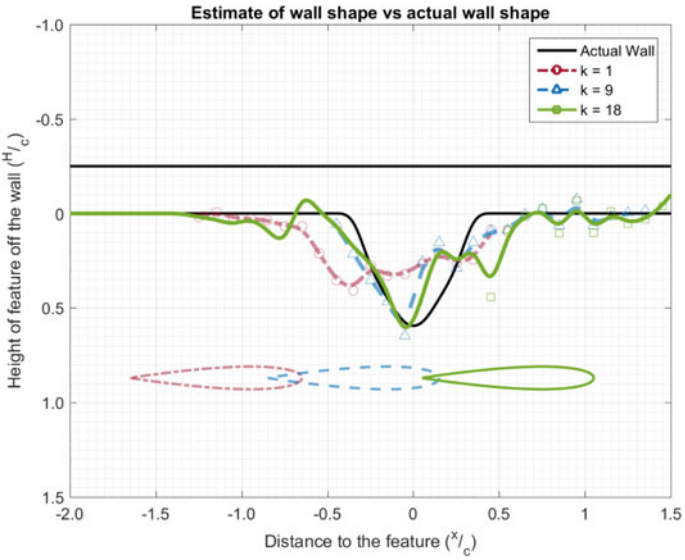


(a) Standard Estimate

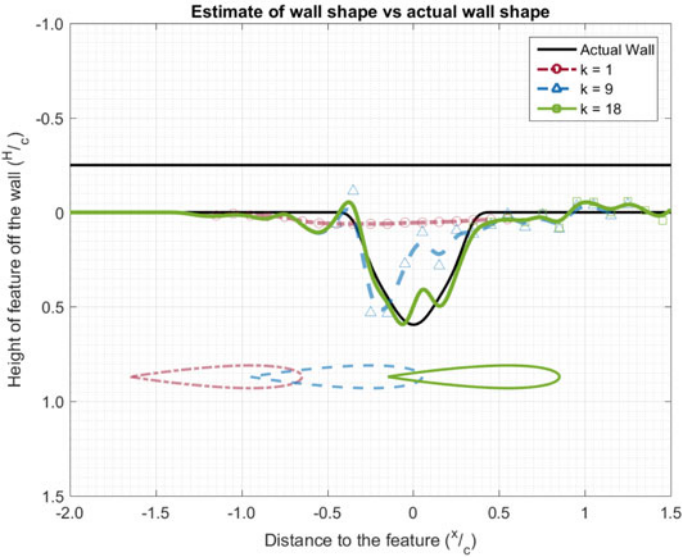


(b) Weighted Estimate

**Fig. 2** Standard (top) and weighted (bottom) estimate of wall shape and foil position shown at 3 discrete time steps of the filter, where color denotes each time step and shapes (circles, triangles, and squares) show control point locations in that time step

the flat wall regions and large deviations from the true wall shape on the back side of the feature. The fluctuations in the flat wall region are likely due to insensitivity of the algorithm to pressure changes for features that are relatively far from the foil. Bouffanais et al. [3] showed that specific shape features are only sensitive to pressure in the vicinity of one body length. Additionally, by evenly weighting the influence of each pressure observation, the estimate of the wall shape can be skewed by pressure measurements that may have little or no useful information in estimating the feature.

### *3.2 Weighted Estimation Method*

Figure 2b shows the estimate of the wall feature at the same instances in time as Fig. 2a, however in this case, we slightly alter the algorithm to weight certain pressure measurements differently. Instead of constructing a measurement matrix from all pressure measurements, we construct the measurement matrix only from each single measurement location $i$ and make an estimate of the wall shape from the time histories obtained from that single measurement point. Using each measurement location separately, we can obtain a separate estimate of the control point locations from each separate pressure location. The separate estimates of control point locations are then averaged, using a weighted average, to obtain the estimate for control point locations. The weights of the average are determined by computing the RMSE between the pressure measurement and estimation for a given point, then inverting and normalizing the value to obtain a weight between 0 and 1, where the weights sum to 1 over the number of pressure measurements used. The advantage of this method is that pressure measurements that give more information about the feature on the wall will be given more preference in determining the shape of the wall. One can see from Fig. 2b, that there is a marked improvement in capturing the true shape of the feature. The height and width of the feature are now captured well, although slight fluctuations still exist along the flat wall and a slight dip in the feature exists near the peak.

### *3.3 Multiple Shapes*

Applying the weighted estimation algorithm to multiple shapes, we can see how the algorithm performs for more general estimation problems. In this case, two protrusions extend from the flat wall, where we vary the distance between the protrusions. Figure 3 shows the comparison of the estimated shape once the foil has passed the second shape with the true shape of the wall. While the algorithm is capable of identifying multiple shapes in a single pass of the foil, some limitations exist. When the object shapes are close to one another, as in Fig. 3a, the estimation of the individual features tend to blend together as the resulting wake produces a stagnant region in between the two features.

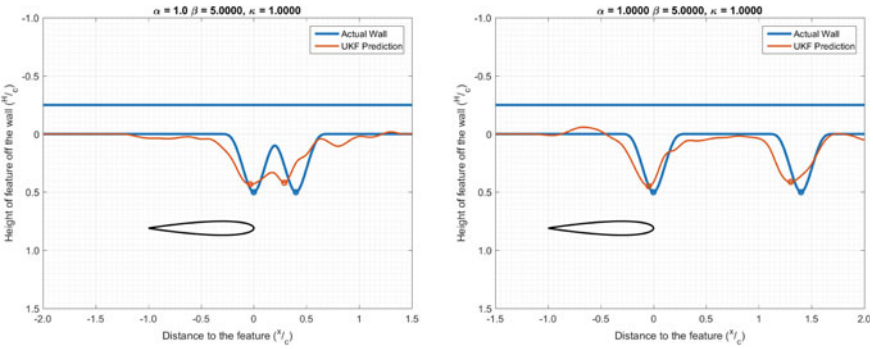


(a) Case 1 - Near shapes (b) Case 2 - Far shapes

**Fig. 3** Estimate of wall shape with two features

While the two peaks of the features are inferred by the algorithm and the width of the two features is reasonably estimated, there is error in the height of the feature and significant error in distinguishing two separate features. It is important to note that in this simulation, the forward speed of the foil is not varied, hence if we were to slow the forward speed of the foil, this might help with more refined detection of the wall shape. When the features are further apart from one another, the features are identified much more distinctly, with clear protrusions identified at each feature location. Estimation of the height and width of the features is reasonable, although the second feature is estimated to be shorter and wider than the true feature.

## *3.4 Error Discussion*

Error was previously only shown visually, however Table 1 quantifies the quality of the feature estimation in each of the shown examples based on the RMSE in the estimate of the peak value (closest point to the foil), the overall RMSE of the

**Table 1** Error metrics for the B-spline *ukf*

| | Peak RMSE | Total RMSE | Mean error | Max error |
|---|---|---|---|---|
| Standard estimation | 0.0312 | 0.0627 | 0.0047 | 0.3327 |
| Weighted estimation | 0.0443 | 0.0263 | 0.0012 | 0.1062 |
| Close shapes | 0.0780 | 0.0422 | 0.0061 | 0.2450 |
| Far shapes | 0.0745 | 0.0431 | 0.0107 | 0.2774 |

Values are in terms of a root mean square error. Mean and max error are presented as absolute values. Units are in chord lengths

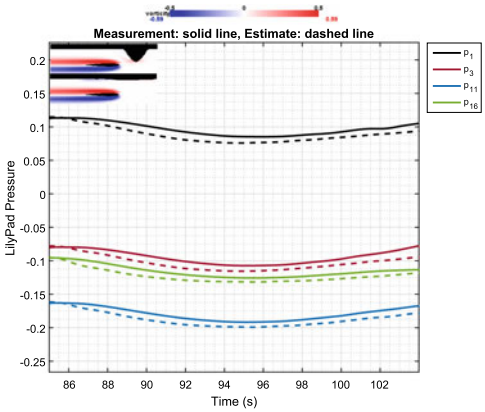


(a) $k = 1$

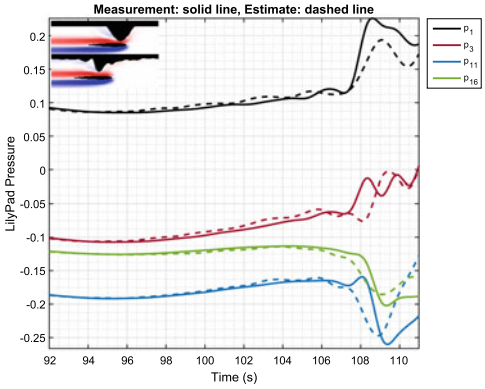


(b) $k = 9$

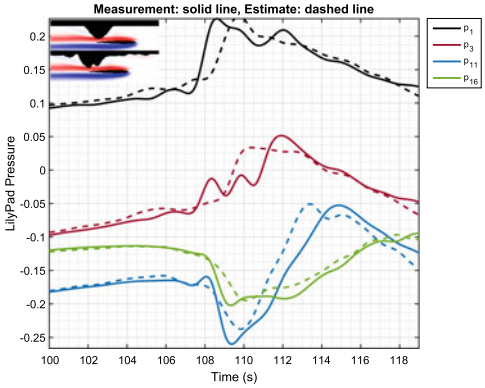


(c) $k = 18$

**Fig. 4** Pressure time histories corresponding to three timesteps of the *ukf*. Actual and estimated simulations are shown in the upper left corner with vorticity

total shape, the mean error of the total shape, and the max error in the total shape. Although the standard unweighted method is slightly better at estimating the peak value of the feature, the weighted estimation method demonstrates a better overall estimate of the total shape, reducing the mean overall error and max error. While visually, estimation of the features for the two shapes that are far from one another appears to be a better estimate than when the shapes are close together, based on the quantitative metrics, there is little difference in the quality of the estimates.

While we quantify the error in estimates based on the resulting estimated shape of the feature, the measurements by which the shape is estimated are only a proxy of the object shape, since we measure pressure. In order to estimate the true shape of the object, the estimated pressure would need to perfectly match the measured pressure over time. Figure 4 shows a comparison of the resulting pressure estimates at four points on the foil compared with the measured pressure from the true object shape, using the weighted estimation method. The upper left images in each subfigure show the true feature (top) and the current estimated feature (bottom) corresponding to the shown pressure time histories. Although the algorithm tends to follow the pressure in each time history fairly closely, minor deviations from each pressure time history lead to minor adjustments to the wall shape, such that the exact shape is difficult to recover. While this method may be useful in identifying the presence of a general wall feature, utilizing this technique for updating boundary conditions in a digital twin may require refinements due to propagation of error from minor differences in estimated boundaries.

## 4 Conclusion

In conclusion, we present an algorithm for determining general boundary features in the presence of a foil based on pressure measurements at the surface of the foil. By representing the wall feature with B-spline control points, estimated using an unscented Kalman filter, it is possible to estimate the general shape. A weighted estimation technique is shown to improve the algorithm, where fine features are better identified. The algorithm is shown to be capable of handling the identification of multiple objects as well. Utilizing the method for boundary condition updating in a CFD digital twin would require further analysis of how boundary errors would propagate in time. While the estimate of the wall is not an exact model of the true system, it could provide valuable information to a control system for avoiding collisions or for identifying fine features. This paper only presents a limited sample of the algorithm applied to a specific identification problem. It is important to note that the $UKF$ algorithm is sensitive to the statistical coefficients which may need to be tuned for different estimation problems.

**Acknowledgements** The authors would like to acknowledge support for this project from the Office of Naval Research under program manager Kelly Cooper, grant #N00014-16-1-2968.

## References


1. Asadnia, M., Kottapalli, A., Karavitaki, D., Warkiani, M., Miao, J., Corey, D., Triantafyllou, M.: From biological cilia to artificial flow sensors: biomimetic soft polymer nanosensors with high sensing performance. Sci. Rep. (2016). https://doi.org/10.1038/srep32955
2. Bleckmann, H., Zelick, R.: Lateral line system of fish. Integr. Zool. **4**(1), 13–25 (2009)
3. Bouffanais, R., Weymouth, G.D., Yue, D.K.: Hydrodynamic object recognition using pressure sensing. In: Proceedings of the Royal Society of London A: Mathematical, Physical and Engineering Sciences, p. rspa20100095. The Royal Society (2010)
4. Coombs, S., Braun, C.B., Donovan, B.: The orienting response of lake Michigan mottled sculpin is mediated by canal neuromasts. J. Exp. Biol. **204**(2), 337–348 (2001)
5. De Boor, C.: A Practical Guide to Splines, vol. 27. Springer, New York (1978)
6. Dijkgraaf, S.: The functioning and significance of the lateral-line organs. Biol. Rev. **38**(1), 51–105 (1963)
7. Engelmann, J., Hanke, W., Mogdans, J., Bleckmann, H.: Neurobiology: hydrodynamic stimuli and the fish lateral line. Nature **408**(6808) (2000)
8. Fernandez, V.I., Maertens, A., Yaul, F.M., Dahl, J., Lang, J.H., Triantafyllou, M.S.: Lateral-line-inspired sensor arrays for navigation and object identification. Mar. Technol. Soc. J. **45**(4), 130–146 (2011)
9. Harashima, M., Ferrari, L.A., Sankar, P.: Spline approximation using Kalman filter state estimation. IEEE Trans. Circ. Syst. II Anal. Dig. Sig. Process. **44**(5), 421–424 (1997)
10. Jauch, J., Bleimund, F., Rhode, S., Gauterin, F.: Recursive B-spline approximation using the Kalman filter. Eng. Sci. Technol. Int. J. **20**(1), 28–34 (2017)
11. Julier, S.J.: The scaled unscented transformation. In: American Control Conference, 2002. Proceedings of the 2002, vol. 6, pp. 4555–4559. IEEE (2002)
12. Kottapalli, A., Asadnia, M., Miao, J., Triantafyllou, M.: Artificial fish skin of self-powered micro-electromechanical systems hair cells for sensing hydrodynamic flow phenomena. J. R. Soc. Interface **12**, 1–14 (2015)
13. Maertens, A.P., Triantafyllou, M.S.: The boundary layer instability of a gliding fish helps rather than prevents object identification. J. Fluid Mech. **757**, 179–207 (2014)
14. Maertens, A.P., Dahl, J.M., Triantafyllou, M.S.: Distributed pressure sensing to locate and identify obstacles. In: 17th International Unmanned Untethered Submersible Technology (UUST 2011) Conference. Portsmouth, NH, USA, Aug 2011
15. Rice, J.A., Mechitov, K., Sim, S.-H., Nagayama, T., Jang, S., Kim, R., Spencer Jr., B.F., Agha, G., Fujino, Y.: Flexible smart sensor framework for autonomous structural health monitoring. Smart Struct. Syst. **6**(5–6), 423–438 (2010)
16. Tuegel, E.J., Ingraffea, A.R., Eason, T.G., Spottswood, S.M.: Reengineering aircraft structural life prediction using a digital twin. Int. J. Aerosp. Eng. (2011)
17. Wan, E.A., Van Der Merwe, R.: The unscented Kalman filter for nonlinear estimation. In: Adaptive Systems for Signal Processing, Communications, and Control Symposium 2000. AS-SPCC. The IEEE 2000, pp. 153–158. IEEE (2000)
18. Webb, J.: Lateral line structure. Encycl. Fish Physiol. Gen. Environ. **1**, 336–346 (2011)
19. Weymouth, G.D.: Lily pad: towards real-time interactive computational fluid dynamics. In: Numerical Towing Tank Symposium, vol. 18, Oct 2015
20. Weymouth, G.D., Yue, D.K.-P.: Boundary data immersion method for cartesian-grid simulations of fluid-body interaction problems. J. Comput. Phys. **230**(16), 6233–6247 (2011)
21. Windsor, S.P., McHenry, M.J.: The influence of viscous hydrodynamics on the fish lateral-line system. Integr. Comp. biol. **49**(6), 691–701 (2009)

# Analytic Modeling of a Size-Changing Swimmer


**Gabriel D. Weymouth and Francesco Giorgio-Serchi**

**Abstract** Cephalopods use large-scale structural deformation to propel themselves underwater, changing their internal volume by 20–50%. In this work, the hydroelastic response of a swimmer comprised of a fluid-filled elastic-membrane is studied via an analytic formulation of two coupled non-linear dynamic equations. This model of the self-propelled soft-body dynamics incorporates the interplay of the external and internal added-mass variations. We compare the model against recent experiments for a body which abruptly reduces its cross-section to eject a single jet of fluid mass. Using the model we study the impact of size-change excitation on sustained swimming speeds and efficiency.

**Keywords** Fluid-structure interaction · Biological flow · Swimming · Modeling

## 1 Introduction

The maritime sector requires complex tasks to be performed in always more forbidding environments and with a constantly increasing degree of autonomy. These requirements are fostering the incremental improvement of the manoeuvring capabilities of state-of-the-art underwater vehicles [2, 13, 14] either by refining navigation and positioning systems or by undertaking completely disruptive design processes. This is the case of biomimetics, where water dwelling organisms are taken as the source of inspiration for the development of innovative vehicles. Underwater robotics has extensively employed the swimming biomechanics of fish and other aquatic creatures in order to endow new prototypes with the capability of hovering, short radius

G. D. Weymouth (✉)
Faculty of Engineering and Physical Sciences, University of Southampton, Southampton SO17 1BJ, UK
e-mail: g.d.weymouth@soton.ac.uk

F. Giorgio-Serchi
School of Engineering, University of Edinburgh, Edinburgh EH9 3FF, UK
e-mail: F.Giorgio-Serchi@ed.ac.uk



M. Braza et al. (eds.), *Advances in Critical Flow Dynamics Involving Moving/Deformable Structures with Design Applications*, Notes on Numerical Fluid Mechanics and Multidisciplinary Design 147,
https://doi.org/10.1007/978-3-030-55594-8_48

turning, fast start/slowdown and low-speed manoeuvring [1, 9, 18]. The propulsion routines of biologically- inspired robots entails, for the most part, cyclic oscillations of one or more body parts. These commonly drive the onset of momentum-rich vortical flow structures responsible for generating unsteady hydrodynamical forces which propel the vehicles. Flapping foil propulsion, for instance, relies on actuators which mimic the continuous deformation of fins and tails by means of discrete sequences of rigid links and joints. However, new actuators which more closely resemble the compliant nature of living tissues are now being developed by exploiting soft structures [10] which offer the advantage of intrinsic safer physical interaction with the environment as well as a higher degree of agility [11, 17].

The employment of compliant body parts or entirely soft-bodied vehicles and actuators not only provides a higher degree of structural resilience and the need for less-refined control strategies, but it also lends itself to mimic those organisms which rely extensively on large body-volume variations to propel themselves, such as squids and octopi. These sea-dwelling creatures sport a repertoire of extremely aggressive manoeuvres thanks to their pulsed-jetting propulsion which is driven by the inflation and deflation of a cavity of their body [7]. While the study on pulsed-jet locomotion has mainly revolved around the contribution to thrust from the vortex generated at the nozzle exit-plane [8], it is becoming apparent that the role of the external shape variation represents a prominent factor in this mode of propulsion, [3, 15]. The analysis performed on submerged bodies subject to abrupt shape-changes confirms that the forces associated with added-mass variation participate in the generation of thrust to a large extent, [6, 16]. Thus, the exploitation of added-mass variation as a potential source of thrust can have a major impact on the design [3] and control [4, 12] of new kinds of underwater vehicles. To this end, in this paper we devise a model for capturing the coupled fluid-structure-interaction effects of such kind of vehicles. The purpose of this model is to offer a fast tool for exploring the design space of new prototypes and shed light over the potential to employ added-mass variation effect as a source of thrust in aquatic vehicles.

## 2 Methodology

We consider a canonical self-propelled size-changing swimmer consisting of a hollow ellipsoidal neutrally buoyant elastic shell completely immersed in fluid, Fig. 1. In the manner of squids and cephalapods, the swimmer propels itself by contracting its cross section, characterized by the minor semi-axis $B$, while maintaining the major semi-axis length $L$ fixed, and ejecting a portion of the internal fluid mass through an exit nozzle with area $A_e$. For sustained propulsion, the shell re-inflates with fluid via an opening at the center of mass to avoid ambiguity, and repeats the process.

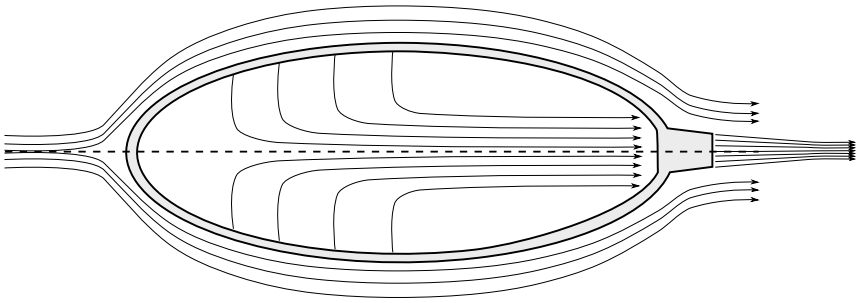

**Fig. 1** Flow kinematics inside and outside a self-propelled hollow membrane oscillating around its equilibrium configuration

## 2.1 Coupled Swimming Model

The length and time scales of the body are set by the invariant major semi-axis length $L$ and frequency of pulsation $\omega$. The mass scale is set by the water density $\rho$. We describe the dynamics of this system with two-degrees of freedom; the body's dimensionless translation velocity $u = U/(L\omega)$ and dimensionless minor semi-axis length $b = B/L$.

Using a superscript notation to denote the coefficients related to each of the two modes, the dynamical equations are expressed as

$$m^{(u)}\dot{u} + c^{(u)}u = \tau \tag{1}$$

$$m^{(b)}\ddot{b} + c^{(b)}\dot{b} + k^{(b)}(b - b_0) = \psi \tag{2}$$

where $m, c, k$ are the dimensionless lumped inertia, damping, and stiffness coefficients for the translation and deformation, $\tau$ is the jet thrust, $b_0$ is the resting semi minor-axis length and $\psi$ is the deformation excitation. The goal is to determine the form of these coefficients, making simplifications as appropriate.

## 2.2 Translation Model

Building on previous work [5, 15] the translation mode can be modeled as

$$(M_s + M_f)\frac{dU}{dT} = \sum F = -\frac{dM_f}{dT}U_j - \frac{d}{dT}(M_{xx}U) - \frac{1}{2}C_D A_f |U|U \tag{3}$$

where $M_s$ is the (constant) mass of the structure and $M_f$ is the (variable) mass of the internal fluid and $\sum F$ are the sum of the fluid contributions. The first fluid forcing term is the thrust due to mass flux out of the jet at speed $U_j$. The second term is the

*dynamic* added-mass force based on the added mass in the translation direction $M_{xx}$. The third is a quasi-steady drag force based on the frontal area $A_f$ and an empirical drag coefficient $C_D$ for slender ellipsoids.

The kinematics of the system link the changes in vehicle volume $V = \frac{4}{3}\pi B^2 L$ to the changes in internal mass and jet velocity.

$$M_s + M_f = \rho L^3(\tfrac{4}{3}\pi b^2), \quad \frac{dM_f}{dT} = \rho L^3 \omega(\tfrac{8}{3}\pi b\dot{b}) \propto A_e U_j \tag{4}$$

As stated above, we will consider the jet thrust to only be active during deflation. Similarly, the external added mass is modeled as that of the inscribed spherical body

$$M_{xx} = \rho L^3(\tfrac{2}{3}\pi b^3), \quad \frac{dM_{xx}}{dT} = \rho L^3 \omega(2\pi b^2 \dot{b}) \tag{5}$$

which is within $0.01\rho L^3$ of the analytic added mass of an ellipsoid for all values of $B < 2L$. The variational term is critical because as the ellipsoid changes size during translation, the variation in added-mass produces a force $-\frac{dM_{xx}}{dT}U$, which significantly changes the dynamics of the swimmer.

Grouping terms shows that the inertia of the translation mode is the sum of the hollow body mass, the mass of internal fluid, and the added-mass of the external flow. Translation damping includes forces from the fluid drag and the added-mass variation. Applying the dimensional scaling defined above gives the translation model coefficients as

$$m^{(u)} = \tfrac{2}{3}\pi b^2(2+b), \quad c^{(u)} = \pi b^2(2\dot{b} + \tfrac{1}{2}C_D|u|), \quad \tau = \alpha(\tfrac{8}{3}\pi b\dot{b})^2 \tag{6}$$

where $\alpha = L^2/A_e$ during deflation and $\alpha = 0$ during inflation. Note that each term is coupled to the deformation mode (via $b$ or $\dot{b}$), that the drag term is nonlinear (as expected), and that $A_e$ is the only free design parameter in the translation model.

## 2.3 Deformation Model

As a first step toward modeling jetting swimmers, only the radial expansion mode of the membrane deformation is considered. Therefore the membrane remains ellipsoidal at all times[1] and the radius $R$ along the body length is defined as

$$R = B\sqrt{1-x^2} = Lb\sqrt{1-x^2} \tag{7}$$

[1]Note that if the length and exit size are fixed, we can't maintain a perfect ellipsoidal shape while shrinking. However, for modest size changes and small exit areas, the error will be small and confined to the region near the exit plane.

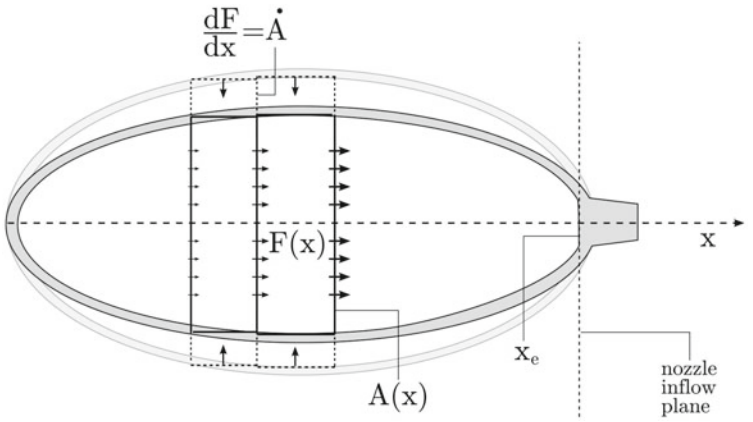


**Fig. 2** Relevant terms in the definition of the internal added-mass

where the body-fixed coordinate runs along $X = -L \ldots L$ and $x = X/L$. The governing equation for this mode is then

$$(I_s + I_f)\frac{d^2B}{dT^2} + (C_s + C_f)\frac{dB}{dT} + (K_s + K_f)B = K_s B_0 + \Psi \tag{8}$$

where $I_s$ is the modal inertia of the structure and $I_f$ is the added inertia of the fluid due to acceleration of this mode. Similarly, $C_{s,f}$ and $K_{s,f}$ are the structural/fluid damping/restoring coefficients. $K_s B_0$ is the resting force needed to achieve a non-zero resting size $B_0$ and $\Psi$ is the excitation force. The structural coefficients depend on the design and material of the structure and will not be investigated in detail here. However, we will link the fluid coefficients to the kinematics of the swimmer, as we did for the translation model.

First, we investigate the added inertia by determining the fluid kinetic energy induced by deformation. Since the ellipsoid is streamlined, the confined *internal* flow causing the jet can be conceptualized as 1D, Fig. 2. As is well known, confined flows amplify the kinetic energy for a given motion, and so the internal flow will be the dominant fluid contribution:

$$E_f \approx \frac{1}{2}\rho \int U_i^2 dV = \frac{1}{2}\rho L \int_{-1}^{x_e} \frac{F^2(x)}{A(x)} dx \tag{9}$$

where $U_i$ is the internal flow velocity, $F$ is the flux through area $A = \pi R^2 = L^2 \pi b^2 (1 - x)$ and $x_e < 1$ is the exit location.

Incompressible flow requires that the change of the section area due to shrinking is equal to the increase in the flux through that section. Therefore the differential equation for $F$ is

$$\frac{dF}{dX} = \frac{dA}{dT} = 2\pi L^2 \omega_n b \dot{b}(1 - x^2) \tag{10}$$

And integration gives

$$\frac{F(x)}{L^3\omega} = 2\pi b\dot{b}\int_{-1}^{x}(1-\tilde{x}^2)d\tilde{x} = \frac{2}{3}\pi b\dot{b}(2+3x-x^3) \tag{11}$$

Substituting $F$ and $A$ gives

$$\begin{aligned}\frac{1}{L^4\omega^2}\int_{-1}^{x_e}\frac{F^2}{A}dx &= \frac{4}{9}\pi\dot{b}^2\int_{-1}^{x_e}\frac{(2+3x-x^3)^2}{1-x^2}dx \\ &= \frac{4}{9}\pi\dot{b}^2\left(-4x+2x^2+\frac{5x^3}{3}-\frac{x^5}{5}-8\log(x-1)\right)\Bigg|_{-1}^{x_e}\end{aligned}$$

We can simply this formula by using $x_e \approx 1$ for the nonlinear polynomial parts. The fluid inertia, defined by $E_f = \frac{1}{2}I_f(\frac{dB}{dT})^2$, is therefore

$$\frac{I_f}{\rho L^3} = \frac{16}{9}\pi\left(2\log\left(\frac{2}{1-x_e}\right)+x_e-\frac{34}{15}\right) \tag{12}$$

As an example, if the body is slender with $b = 0.2$ and $x_e = 0.8$ then $I_f \approx 17\rho L^3 \approx 100(M_s + M_f)$! It is clear that this term greatly dominates over structural inertia for a density matched body.

Similarly, the fluid damping term will also be dominated by the internal flow. We model this loss using a Darcy friction factor. The pressure head loss at the jet exit and due to wall shear stresses approaching the jet can be written:

$$\Delta p = \tfrac{1}{2}\rho C_F U_j|U_j| \tag{13}$$

where $C_F$ is Darcy's friction factor

$$C_F = \frac{32}{Re}\frac{1}{\sqrt{1-x_e^2}}+\frac{1}{2} \tag{14}$$

which comprises of the term for head loss along constant radius cylindrical pipes at Re $< 2100$ and of an additional coefficient which accounts for viscous effect at square-edged inlets.

Finally, we consider if there are any fluid restoring forces. There is no fluid restoring force if $u = 0$ since the fluid is static regardless of the value of $b$. However, when the body is in motion the pressure distribution on the external surface depends on the shape, and therefore $b$. This scaling argument shows that $k_f = K_f/(\rho L^3\omega_n^2) \propto -u^2 b$, therefore its relative importance is quantified by a Weber number $We = u^2 b/k_s$. The dynamics of the fluid and body are strongly coupled at high $We$ and the structural model will require more than a single deformation mode. We assume $We \ll 1$ for the slender and stiff elastic body considered in this work.

Using these approximations, modal deformation coefficients are dominated by the internal flow and structural stiffness, i.e.

$$m^{(b)} = I_f/\rho L^3, \quad c^{(b)} = \frac{1}{2} C_F |\dot{b}|, \quad k^{(b)} = k_s \tag{15}$$

Note that in this case the deformation equation is decoupled from $u$ and when the deformation amplitude $|b| = \max(b) - b_0$ is small, we have an effectively linear oscillator with natural frequency $\omega_n = \sqrt{k_s/m^{(b)}}$ and damping ratio $\zeta = \frac{2}{3\pi} C_F \omega |b| / \sqrt{m^{(b)} k_s}$.

### 2.4 *Jetting Escape Model Validation*

Next our dynamical model is compared to the experimental results of Weymouth, Subramaniam, and Triantafyllou, *Bioinspiration and Biomimetics*, 2015. In that work, an elastic membrane was stretched over a rigid hull, inflated with water, and allowed to freely translate as it deflated. The body jetted away at high-speed, similar to the escape maneuver of an octopus. The experimental vehicle has $L = 18\,\text{cm}$, $A_e/L^2 = 0.05$ and $b_0 = 0.2$ and the initial mass was 3.5 times the resting mass $M_f = 3.5 M_0$, and the stiffness $k_s$ is set to achieve approximately the same emptying time as the experiment $T \approx 1\,\text{s}$. These model was set to match these values and $C_D = 0.05$ and $C_F = 0.25$ are chosen from the literature (and did not significantly impact the results). Finally, the excitation $\psi$ is set to zero and the model Eq. (1) is integrated numerically.

An important difference between the analytic model described above and the experiment is that the vehicle's rigid endo-skeleton causes the ejection period to abruptly stop 1.0 kg limit. Instead, the current model allows the shell to oscillate around the equilibrium width $b_0$, the point where the fluid content in the shell is about 1.0 kg.

Despite these differences the comparison in Fig. 3 is remarkably good. The model results replicate the essential acceleration curve, as well as the measured peak velocity. This model enables us to estimate the role of thrust and added-mass variation effect in determining the burst of acceleration of the body. In agreement with the postulated mechanics in Weymouth et al. [16], the contribution from added-mass variation approaches 25% of the jet force on the vehicle.

## 3 Pulsed Swimming Results

These results give some confidence in the model to predict swimming performance. The next step is to use the model to study the impact of the excitation $\psi$ to the pulsed swimming characteristics.

In this set of tests we maintain the same parameters as in the validation test, but define the excitation as

$$\psi = \|\psi\| \cos(\omega t) \tag{16}$$

where the amplitude $\|\psi\|$ is chosen to achieve a characteristic deformation of $\delta b = b - b_0 = 0.025$, i.e. $\|\psi\| = 0.025 k_s$. This amplitude is somewhat arbitrary, but the corresponding volume change of 50% is similar to the levels found in nature.

Figure 4 shows the results as the excitation frequency is varied with respect to the swimmer's natural frequency in water. As with the validation case, we've initialized

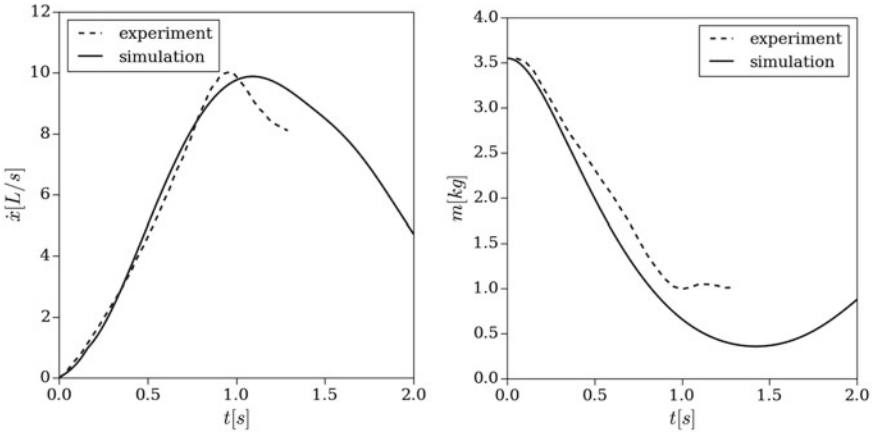


**Fig. 3** Comparison of the analytic model of Eq. (1) to to the experimental measurements for the translation speed $\dot{x} = U/L$ (left) and the internal mass $m \approx \rho \frac{4}{3} \pi L^3 b^2$ (right)

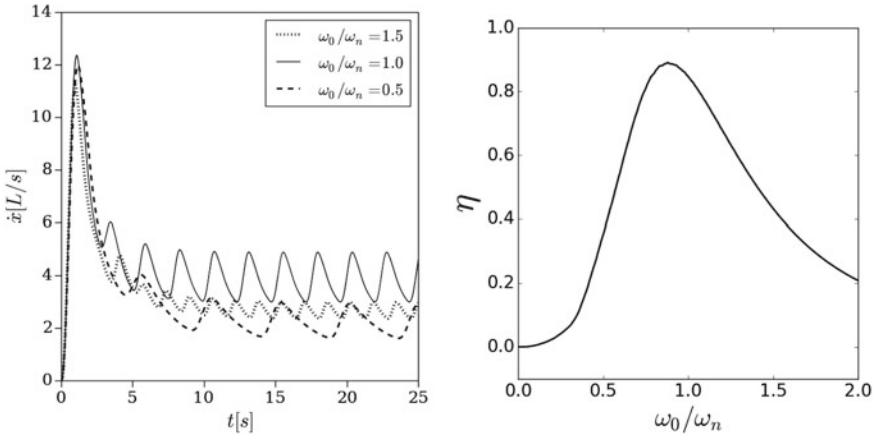


**Fig. 4** Performance of the size changing swimmer based on the coupled analytic model Eq. (1). The velocity $\dot{x}$ over time (left) and the quasi-propulsive efficiency $\eta$ (right) as the excitation frequency ratio is varied

the swimmer at 350% of its resting volume and so we see the same initial peak in the velocity response. However, the long term behavior of the swimmer is determined by the frequency ratio $\omega/\omega_n$. When the ratio is greater than one, the amplitude of deformation and therefore the magnitude of velocity variation decreases. In contrast, when $\omega/\omega_n < 1$ the deformation magnitude remains fairly large, but the jet velocity is reduced, leading to an overall decrease in average swimming velocity down to $\overline{u} = 2.5\, L/s$. Excitation at the natural frequency generates the largest deformation as expected, and maintains a swimming speed of $\overline{u} = 4\, L/s$.

A similar trend is observed in terms of the efficiency. As the body is freely swimming, the thrust and drag forces are balanced on average making the net force an inappropriate metric for the efficiency. Instead, the quasi-propulsive efficiency is used

$$\eta = \frac{\overline{P}_{\text{in}}}{\overline{P}_{\text{tow}}} \tag{17}$$

where $P_{\text{in}} = \psi \dot{b}$ is the power put into the motion by the excitation force, $P_{\text{tow}} = \sum fu$ is the power it would take to tow the body at its resting size through the same velocity history. Both of these powers are averaged over a steady cycle. The result in Fig. 4 shows that it is far more efficient to swim when exciting at the natural frequency, with the peak value reaching just above 90% for the chosen model parameters.

## 4 Conclusions

This study has developed a simplified analytic model for size changing swimmers. The model uses only two degrees of freedom, translation and radial deformation, but is found to capture the essentially features of previous experiments, namely:

1. The translation of an impulsive swimmer during an escape maneuver was found to reach peak velocities above 10 $L/s$.
2. The translation model accounts for the variation in added mass which produces a thrust approaching 25.

In addition, the model highlights previously unexplored features related to the deformation, namely:

1. The deformation model accounts for the internal inertia of the fluid, which completely dominates over the structural inertia and so sets the natural frequency of the swimmer.
2. The deformation mode was found to be effectively uncoupled from the translation mode for stiff membranes ($k_s \gg u^2 b$). Since the inertia of the flooded systems is high, large oscillation frequencies would only be possibly with stiff membranes, making this an important case to consider.

The model was then applied to the case of a swimmer which is excited in its deformation mode. The results show that the excitation at the natural frequency

results in a mean swimming speed of 4 $L/s$ and a quasi-propulsive efficiency of 90%. Excitation off of the natural frequency resulted in a rapid drop-off in efficiency and swimming speed.

Despite these promising results, there are still many issues to improve in this model. The fundamental weakness is in limiting the structure to a single radial deformation mode shape. In addition, visco-elastic damping in the structure may be important, depending on the manner of the swimmer's design. These elements and others are part of ongoing work, with the goal of developing a freely swimming experimental prototype in the near future.

## References

1. Colgate, J.E., Lynch, K.M.: Mechanics and control of swimming: a review. IEEE J. Ocean. Eng. **29**, 660–673 (2004)
2. Elvander, J., Hawkes, G.: ROVs and AUVs in support of marine renewable technologies. In: MTS/IEEE Oceans 2012, pp. 1–6. Hampton Roads, VA (2012)
3. Giorgio-Serchi, F., Arienti, A., Laschi, C.: Underwater soft-bodied pulsed-jet thrusters: actuator modeling and performance profiling. Int. J. Robot. Res. (2016)
4. Giorgio-Serchi, F., Renda, F., Calisti, M., Laschi, C.: Thrust depletion at high pulsation frequencies in underactuated, soft-bodied, pulsed-jet vehicles. In: MTS/IEEE OCEANS. Genova, Italy (2015)
5. Giorgio-Serchi, F., Weymouth, G.D.: Drag cancellation by added-mass pumping. J. Fluid Mech. **798** (2016)
6. Giorgio-Serchi, F., Weymouth, G.D.: Underwater soft robotics, the benefit of body-shape variations in aquatic propulsion. In: Soft Robotics: Trends, Applications and Challanges. Biosystems & Biorobotics, vol. 17, pp. 37–46. Springer (2016)
7. Johnson, W., Soden, P.D., Trueman, E.R.: A study in met propulsion: an analysis of the motion of the squid, Loligo Vulgaris. J. Exp. Biol. **56**, 155–165 (1972)
8. Krieg, M., Mohseni, K.: Modelling circulation, impulse and kinetic energy of starting jets with non-zero radial velocity. J. Fluid Mech. **79**, 488–526 (2013)
9. Licht, S., Polidoro, V., Flores, M., Hover, F., Triantafyllou, M.: Design and projected performance of a flapping foil AUV. IEEE J. Ocean. Eng. **29**, 786–794 (2004)
10. Marchese, A.D., Onal, C.D., Rus, D.: Autonomous soft robotic fish capable of escape maneuvers using fluidic elastomer actuators. Soft Robot. **1**, 75–87 (2014)
11. Mörtl, A., Lawitzky, M., Kucukyilmaz, A., Sezgin, M., Basdogan, C., Hirche, S.: The role of roles: physical cooperation between humans and robots. Int. J. Robot. Res. **31**, 1656–1674 (2012)
12. Renda, F., Giorgio-Serchi, F., Boyer, F., Laschi, C.: Modelling cephalopod-inspired pulsed-jet locomotion for underwater soft robots. Bioinspir. Biomim. **10** (2015)
13. Vaganay, J., Gurfinkel, L., Elkins, M., Jankins, D., Shurn, K.: Hovering autonomous underwater vehicle-system design improvements and performance evaluation results. In: International Symposium on Unmanned Untethered Submarine Technology, Durham, USA (2009)
14. Vasilescu, I., Detweiler, C., Doniec, M., Gurdan, D., Sosnowski, S., Stumpf, J., Rus, D.: AMOUR V: a hovering energy efficient underwater robot capable of dynamic payloads. Int. J. Robot. Res. **29**, 547–570 (2010)
15. Weymouth, G., Triantafyllou, M.S.: Ultra-fast escape of a deformable jet-propelled body. J. Fluid Mech. **721**, 367–385 (2013)
16. Weymouth, G.D., Subramaniam, V., Triantafyllou., M.S.: Ultra-fast escape maneuver of an octopus-inspired robot. Bioinspir. Biomim. **10**, 1–7 (2015)

17. Woodman, R., Winfield, A.F.T., Harper, C., Fraser, M.: Building safer robots: safety driven control. Int. J. Robot. Res. **31**, 1603–1626 (2012)
18. Yu, J., Ding, R., Yang, Q., Tan, M., Wang, W., Zhang, J.: On a bio-inspired amphibious robot capable of multimodal motion. IEEE Trans. Mech. 1–10 (2011)

# Author Index





M. Braza et al. (eds.), *Advances in Critical Flow Dynamics Involving Moving/Deformable Structures with Design Applications*, Notes on Numerical Fluid Mechanics and Multidisciplinary Design 147,
https://doi.org/10.1007/978-3-030-55594-8